Developing Kinase Inhibitors as Chemical Tools and Potential Drugs

by

Frank Kwarcinski

A dissertation submitted in partial fulfillment
of the requirements for the degree of
Doctor of Philosophy
(Medicinal Chemistry)
in the University of Michigan
2016

Doctoral Committee:

Assistant Professor Matthew B. Soellner, Chair
Professor Charles L. Brooks III
Professor George A. Garcia
Professor Anna K. Mapp
Assistant Professor Brent R. Martin

DEDICATION

To my family,
Steph, Mom, Pops and Mom & Dad

ACKNOWLEDGEMENTS

I would like to thank all of the people who have positively influenced both my career and character over the years. I specifically wanted to recognize my undergraduate mentor, Dr. James Dye for introducing me to research and for showing me how to genuinely enjoy coming to work every day. I also want to thank my advisor, Dr. Matthew Soellner, for not only his scientific advice over the last five years, but for his active commitment to my success as a scientist and as an individual. Matt has continually challenged me to better myself since he took me on as a rotator and I sincerely appreciate everything that he has done for me. Additionally, I want to thank my dissertation committee members, Prof. George Garcia, Prof. Anna Mapp, Prof. Charles Brooks III and Asst. Prof. Brent Martin for their valuable contributions to the studies presented herein and for additional discussions on other collaborative efforts. I also want to recognize Dr. Jennifer Meagher, Dr. Jeanne Stuckey and Dr. Markus Seeliger for mentoring me during my kinase crystallography endeavors and Dr. John Montgomery for his mentorship during my time in the CBI program.

A deserved thanks goes out to all current and former members of the Soellner lab that have taught me one thing or another, including Christel Fox, Michael Steffey, Dr. Steve Bremmer, Dr. Kristoffer Brandvold, Dr. Meghan Breen, Dr. Sameer Phadke, Dr. Shana Santos, Dr. Kristin Ko, Taylor Johnson, Michael Agius, Eric Lachacz, and Omar Beleh. I could not imagine working with a better group of scientists or people. I especially want to highlight the contributions of Mike S., Chris, Kris, Sameer, Meg, Eric, Taylor and Omar to the work presented below. I would like to thank Dr. George Georghiou and Ivan Lebedev for their advice on protein crystallography during my stay at Stony Brook and for helping me adjust to life on the island. Furthermore, I want to thank medicinal chemistry friends I have met along the way, including Dr. Ron Jenkins, Dr. Kyle Heslip, Dr. Doug Hansen and Dr. Anthony Emanuele.

Finally, I am most grateful for the support of my friends and family during my time at UofM. I especially want to thank my parents, Roman and Debbie Kwarcinski, my brother Mike and his soon-to-be wife Shivangee, my sister Dee, her husband Justin and baby Weston, as well as my wife's parents, Al and Donna Shock, my sister-in-law Ang and her soon-to-be husband Josh and the girl, Lola, for everything that they have done for me. All of the good things in my life are because of them. To my wife, thank you for pushing me to be better when I needed to, for telling me to relax when I was doing too much and for loving and supporting me always. I cannot wait for what comes next for us in life. You are my everything.

TABLE OF CONTENTS

LIST OF TABLES

LIST OF FIGURES

FIGURE

LIST OF SCHEMES

LIST OF APPENDICES

APPENDIX

ABSTRACT

Kinase inhibitors have experienced a dramatic evolution over the last two decades, as multi-targeted kinase chemical probes have gradually given way to highly specific, clinically approved drugs. Recent advances in molecular targeted therapies, especially those involved in cancer, have also created a demand for novel inhibitors that can potently and selectively target any of the more than 200 kinases implicated in disease. The work described herein details our efforts toward designing these needed methodologies.

Our first strategy utilized irreversible kinase inhibition to target a nonconserved cysteine residue located within the phosphate-binding loop (P-loop) of c-Src kinase. A promiscuous kinase inhibitor scaffold served as the design basis, providing for a stringent test of inhibitor selectivity. Lead covalent compounds, **2.6** and **2.7**, both displayed an 8-fold improvement in potency for c-Src over a reversible analog, compound **2.1**. Profiling against homologous kinases c-Abl and Hck ultimately resulted in a >60-fold improvement in selectivity relative to compound **2.1**. This modular design strategy also led to the creation of an irreversible analog of dasatinib, compound **2.8**. This inhibitor was successful in targeting a dasatinib-resistant mutant of c-Src (T338M c-Src, IC_{50} = 44 nM) as well as improving the fairly non-selective binding nature of dasatinib amongst a panel of 124 wt kinases (dasatinib, S_{35} = 12%; **2.8**, S_{35}= 7%).

The design of a second methodology centered on a proximity-based, enzyme-templated fragment screen for the discovery of selective bivalent kinase inhibitors. This approach rapidly identified fragment hits through use of an activity assay without the need for biophysical detection methods or prior structural knowledge. Acrylamide library members formed potential Michael adducts to compound **3.1**, a thiol-containing ATP pocket small molecule, as opposed to with the protein itself (conventional disulfide tethering). A hit-to-lead campaign following an initial screen with c-Src kinase resulted

in two potent furanyl derivatives, compounds **3.8** (wt c-Src, K_i = 70 nM) and **3.10** (wt c-Src, K_i = 130 nM). Both inhibitors demonstrated a dramatic improvement in selectivity (>9-fold average selectivity) over the initial ATP pocket binder amongst a panel of homologous kinases (c-Abl, Hck, c-Yes). In fact, compound **3.8** represents the most c-Src over c-Yes selective (8.7-fold) inhibitor reported to date. This methodology has the potential to be applied to numerous kinase and non-kinase targets.

Another kinase targeting approach evaluated the impact that conformation-selective inhibition has on kinome-wide selectivity. A crystallographically confirmed 'matched set' of active and inactive inhibitors sharing the same kinase hinge-binding scaffold was used to determine trends in inhibitor selectivity. We observed that DFG-out inactive (type II) kinase inhibitors experienced an identical selectivity score (average S_{35} = 22%) to dasatinib (S_{35} = 21%), an inhibitor that binds to the active conformation of the kinase. Conversely, our designed αC-helix out inactive (CHO) inhibitors produced a far superior selectivity profile (average S_{35} = 11%). Interestingly, while dasatinib and the CHO inhibitors saw no specific kinase binding preferences, we found that our type II inhibitors preferentially bound to kinases with bulky gatekeeper residues.

A final study characterized the relative conformation of the kinase P-loop as a means for selective inhibition. The P-loop is a structural feature implicated in inhibitor selectivity and drug resistance, yet it is often not resolved in kinase X-ray crystal structures. The synthesis of a unique 'molecular ruler' series of covalent compounds (based on compound **2.7**) resulted in an unprecedented tool to measure the native, in-solution positioning (extended or kinked) of this critical loop. Further mutational studies suggest that regions distal to the P-loop may actually contribute to its relative conformation, which can be exploited for selective kinase inhibition.

All of these methods have greatly improved our knowledge regarding kinase inhibitor selectivity and should aid in the development of future chemical probes and clinical drug candidates.

CHAPTER I

Developing Methodologies for the Discovery of Novel Kinase Inhibitors

Abstract

Kinases make up almost 2% of the human genome and play a critical role in cell signaling. Consequently, countless pharamacological approaches have been set forth to control abberrant kinase activity. This has resulted in the development of 30 FDA-approved small molecule kinase inhibitors over the last 15 years. While successful for several specific targets, these agents are clincially used to inhibit only a portion of the more than 200 kinases implicated in disease. This chapter briefly details some of the current methods of kinase inhibition and their limitations. It also introduces strategies for the development of future kinase inhibitors.

Methods for Kinase Inhibition

Kinases are responsible for the transfer of the gamma phosphate of ATP to the hydroxyl group of either a serine, threonine or tyrosine residue of a given protein or peptide substrate. Nearly a third of the entire proteome is phosphorylated, leading to diverse cellular events such as protein docking, substrate recruitment, and kinase localization.[1-5] Although highly regulated, kinases are susceptible to several modes of deregulation (overexpression, absence of negative regulator, activating mutations), which can result in diseases related to their roles in cellular growth, differentiation, and motility.[6-11]

Drug discovery efforts to correct these cellular abnormalities look to inhibit the specific kinase responsible. The ensuing inhibitor design strategies focus on improving target potency and selectivity to 1) compete against millimolar levels of intracellular ATP, and to 2) prevent undesired binding to one or more of the other 500 kinases in the human genome.[12-13] Most clinically approved kinase inhibitors potently inhibit several targets, yet paradoxically display low toxicity profiles.[14] This suggests that pan kinase inhibition may actually be advantageous in the treatment of some cancers.[15]

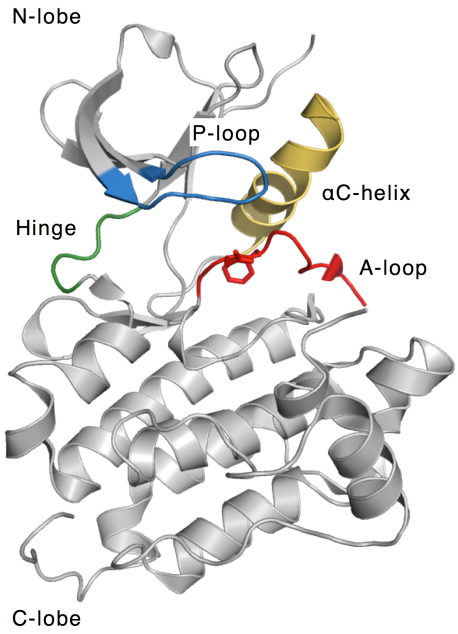

Figure 1.1. Cartoon depiction of a typical kinase catalytic domain fold. Key features are highlighted, included the hinge region (green), P-loop (blue), αC-helix (yellow) and activation loop (red).

All FDA approved kinase inhibitors bind to the ATP pocket of the kinase.[16-17] This well-defined, hydrophobic pocket is situated between the N-terminal (N-lobe) and C-terminal (C-lobe) lobes of the kinase catalytic domain (**Figure 1.1**).[18-19] The smaller N-lobe consists of five anti-parallel ß strands and a single αC helix. The larger C-lobe is primarily α-helical in nature. A short loop or hinge region connects the two lobes to one another and forms the back wall of the pocket. It also makes two critical backbone hydrogen bonds to the adenine ring of ATP. The phosphate-binding loop (P-loop) or glycine-rich loop of the kinase defines the ceiling of the pocket and properly orients the phosphate groups of ATP for catalysis. A majority of kinase inhibitors bind to the conserved hinge kinase region and utilize select van der Waals interactions for potent inhibition. Increasingly diverse inhibitor binding modes, however, have begun to take advantage of the positioning of the activation loop (A-loop), which is required for substrate binding and subsequent phosphorylation.[20] Notably, the Asp-Phe-Gly (DFG) motif is located at the start of this loop and its 'in' or 'out' orientation defines binding of either a Type I or Type II inhibitor respectively.[21]

Despite almost half of the kinome being implicated in disease, only a fraction of all kinases (< 5%) have been successfully targeted in the clinic.[16] Moreover, selective inhibitors only exist for a third of all kinases, making cellular signaling studies difficult to employ and interpret.[12] Taken together, there is a tremendous need for the development of novel kinase inhibitors. Several recent approaches for kinase inhibition are described herein with the goal of understanding their impact on kinase selectivity for use in the design of future therapeutics. While these approaches are applicable to most of the kinome, the primary focus of the next few sections will be on the development of c-Src inhibitors. c-Src is a cytosolic protein tyrosine kinase that has been validated as a target in the treatment of several cancers.[22-24] It has been well characterized over time, both biochemically and structurally, making it an ideal model system to study.[25-27] Despite the tremendous amount of information known about c-Src and other cytosolic tyrosine kinases, a significant need still exists to properly understand any molecular determinants responsible for controlling inhibitor selectivity.

Covalent Kinase Inhibition

While generally avoided in most drug discovery efforts, irreversible inhibition has begun to emerge in the kinase field as a means to dramatically improve both inhibitor potency and selectivity.[28-29] The reward of discovering a new molecularly targeted therapy in the treatment of cancer has alleviated concerns over the potential risk of drug-protein adduct off-target toxicity.[30-32] The main approach for covalent kinase inhibition involves targeting a solvent-exposed, noncatalytic, nonconserved cysteine residue located near (~10 Å) the ATP pocket of the kinase (lysine trapping agents will not be discussed in this work). Nearly 40% of the kinome fits into this category[20], making covalent inhibition highly amendable to a large number of kinase targets.

Irreversible kinase inhibitors present many advantages over conventional reversible compounds, including a non-ATP competitive mode of inhibition (once bound), lower in vivo dosing for desired efficacy, an ideal protein residence time (limited only by protein turnover), and an ability to target clinically relevant inhibitor resistant mutations.[28, 33] Consequently, pharmaceutical companies have optimized these parameters leading to the FDA-approval of two separate covalent kinase inhibitors;

1) afatinib[34], a quinazoline-based EGFR inhibitor used in the treatment of non-small cell lung cancer, and 2) ibrutinib[35], a pyrazolopyrimidine-based BTK inhibitor used in the treatment of mantle cell lymphoma and chronic lymphocytic leukemia.

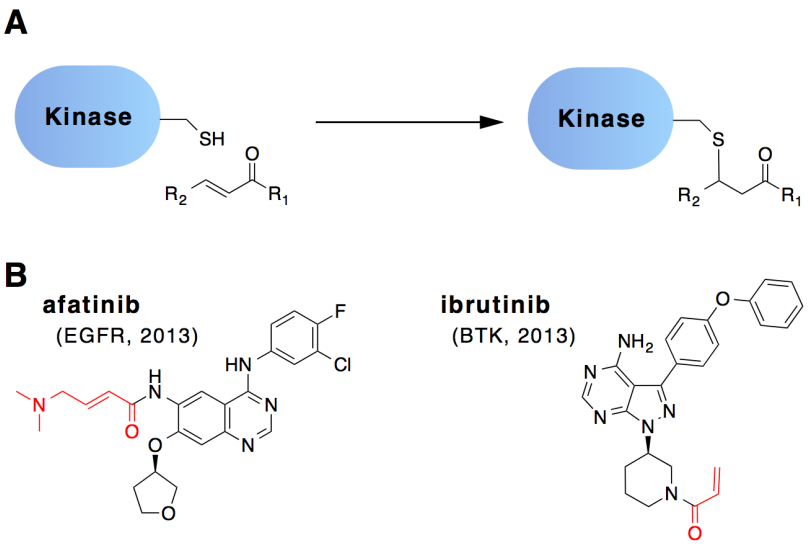

Figure 1.2. Covalent inhibition example. (**A**) Schematic for irreversible kinase inhibitors with nonconserved cysteine residue of the kinase. (**B**) Chemical structures of both FDA-approved kinase inhibitors.

Aside from EGFR and BTK, several additional kinases have been successfully targeted with covalent kinase inhibitors, including RSK, HER2, FGFR, VEGFR2, JNK and c-Src.[36] This research focused on the careful selection of the reversible inhibitor scaffold with optimal electrophile placement for the greatest improvement in inhibitor potency. The characterization of these irreversible inhibitors ranges widely, from simply comparing relative half-maximal inhibitory concentrations (IC_{50}), to the full calculation of binding affinities (K_i) and rate of inactivation constants (k_{inact}).[37] Our research in this area, as described in **Chapter II**, developed the first irreversible inhibitors of wild type (wt) c-Src.[38] We designed our inhibitors with the intent of determining the direct contribution of the electrophile to inhibitor selectivity, an approach not routinely taken in the medicinal chemistry field. Consequently, we managed to create covalent inhibitors with dramatically improved potency and selectivity relative to their reversible

counterparts, which could be applied to a number of different kinases for a variety of biochemical applications.

Fragment-Based Drug Discovery Applied to Kinases

Fragment-based drug discovery (FBDD) uses either NMR or X-ray crystallographic methods to identify hits from a small molecular weight (< 300 Da) chemical library.[39] Lead compounds can then be further optimized for potency and validated against the target with orthogonal assays. The simple, yet elegant nature of FBDD results in a vast amount of chemical space being explored by a small number of fragments in comparison to standard high throughput-screening (HTS). Additionally, fragment screens generally demonstrate higher hit rates and the opportunity for improved physiochemical properties of lead chemical candidates over more commonly employed HTS campaigns.

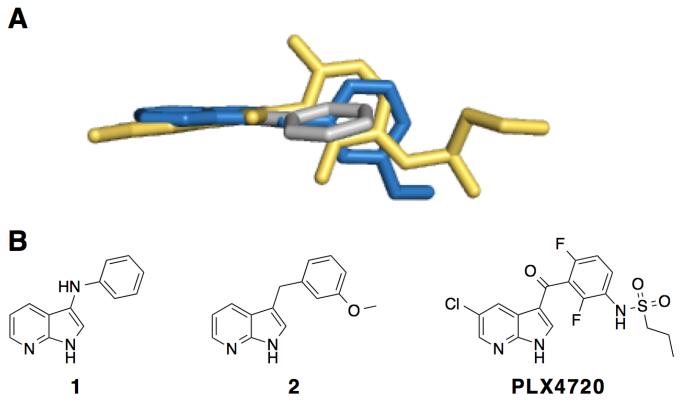

Figure 1.3. Fragment-based drug discovery basis for FDA-approved kinase inhibitor, vemurafenib. (**A**) Crystal structure overlay demonstrating the progression from fragment 1 (gray, initial screening hit) to fragment 2 (blue, substituted fragment) to PLX4720 (yellow), the chemical precursor to vemurafenib. (**B**) Chemical structures of each fragment. The structure of vemurafenib has one additional phenyl ring at the C5 position of the 7-azaindole ring.

Fragment-based screens have been used with mixed success in the discovery of novel kinase inhibitors. Labor-intensive detection methods (surface plasmon resonance, NMR, X-ray crystallography) for low affinity fragments and ATP pocket centric design strategies are partly to blame for its limited usage in kinases.[40] Even though higher throughput assays are generally more attractive, kinase-fragment screens have gained

increasingly more attention in drug discovery programs over the last decade, as evidenced by productive screens against targets such as PDK1, CDK2, PI3Kγ, and p38α.[39] The wealth of kinase structural information available and the great potential for identifying novel chemotypes has allowed hit-to-lead campaigns to become more rapid and efficient with time. In fact, vemurafenib (**Figure 1.3**), an FDA-approved V600E B-Raf selective kinase inhibitor, just recently (2011) became the first marketed drug to have its origins from a fragment-based screen.[41]

Research groups have alternatively employed fragment tethering to circumvent some of the more commonly observed pitfalls of fragment screening (time-consuming detection methods, optimization of weak hits). Tethering, as initially described in work by Sunesis and the Wells group[42], screens disulfide fragments against a protein of interest containing a native or engineered cysteine. Here, any fragment with moderate-to-weak affinity for the target rapidly undergoes thiol exchange, and the fragment hit is verified using mass spectrometry. Fragment tethering has several benefits, including knowledge of the ligand-binding site and efficient detection of weak fragment binders. A variant of this method known as extended tethering has been utilized in the design of Aurora A and PDK1 kinase inhibitors[43-44], although these studies suffered from lower throughput mass spectrometry detection methods and the necessity of prior knowledge of the protein site being targeted.

Work performed by our research group, as outlined in **Chapter III**, illustrates a unique approach to improving the throughput of traditional fragment-based screening. It differs from traditional tethering by utilizing a Michael reaction between an ATP-competitive hit compound with a pendent thiol and an acrylamide fragment. It benefits from using a proximity-based, enzyme-templated approach, where increases in local concentration of both reactive components lead to in situ formation of a bivalent inhibitor.[45-47] In our method, bivalent hits are identified using a kinase activity assay, which can be used to rapidly screen diverse libraries of acrylamide fragments.[48] This type of kinetic, proximity-based approach has been utilized before[49-51], but not in an assay-screening format with a small molecule thiol.

Conformation-Selective Kinase Inhibition

Kinases are dynamic proteins that can be turned 'on' or 'off' based on the conformational state that they are sampling.[52] Both states are susceptible to small molecule inhibition and numerous inhibitors are available that bind to the active and inactive conformation of the kinase.[53] Predicting which state to target for optimal potency and specificity, however, is extremely challenging. Conformation-selective inhibitors binding to the inactive kinase state (specifically the DFG-out inactive state) have conventionally been thought to display the greatest kinome-wide selectivity[54], yet recent studies have suggested that these inhibitors are not inherently more selective than those that bind to the active kinase state.[21] Moreover, conformation-selective inhibitors can impact several noncatalytic kinase functions (phosphorylation status, cellular localization, interacting protein partners) further obscuring our cellular understanding of these inhibitor binding modes.[55-59]

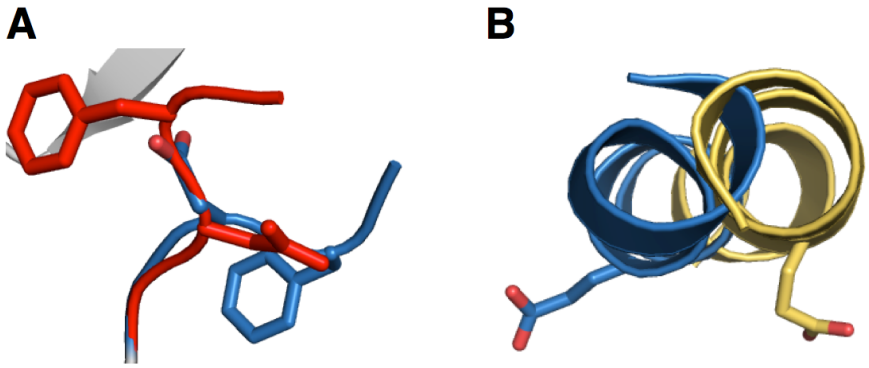

Figure 1.4. Inactive kinase conformations. (**A**) The aspartate and phenylalanine residues of the DFG-in active kinase (blue) are contrasted against the DFG-out inactive (red) structure. (**B**) The conserved glutamate on the αC-helix of the kinase is shown in its active, in conformation (blue) and inactive, outward rotated conformation (yellow).

Compounds that bind to the 'on' or active state of the kinase are known as Type I inhibitors. These agents bind in a similar manner as ATP, with the kinase ready to accept and phosphorylate substrates. Two-thirds of all FDA-approved inhibitors adopt this binding mode.[16] While active kinase conformations are structurally fairly conserved, inactive kinase conformations can be quite diverse amongst the kinome. Two main inactive kinase categories exist; DFG-out inactive and αC-helix out (CHO) inactive.

DFG-out refers to a 180° flipping of the DFG motif found at the start of the A-loop of the kinase (**Figure 1.4A**). Compounds that bind to the DFG-out inactive state of the kinase are known as Type II inhibitors.[21] Many early kinase inhibitors were developed to bind to this specific conformation, following its complete characterization in the crystal structure of imatinib bound to c-Abl.[60] Subsequent drug discovery efforts sought to duplicate the incredible selectivity profile of imatinib, seeing as it only potently inhibits three kinases (c-Abl, c-Kit, and PDGFR).[14]

The alternate inactive kinase conformation mode, CHO inactive, prevents catalysis by rotating the αC-helix of the kinase N-lobe outward. This breaks a conserved salt bridge between a conserved lysine within the ATP pocket and a glutamate of the αC-helix while simultaneously causing the kinase to adopt a more compact state (**Figure 1.4B**).[59, 61-64] Inhibitors of this binding mode are often incorrectly termed Type I inhibitors, although they bind to an inactive state of kinase.[21, 65-66] Four FDA-approved inhibitors bind in this conformational state, including lapatinib[67], one of the most selective kinase inhibitors known to date.[14] No comprehensive selectivity analysis of inhibitors that bind this conformation has been performed, making it of interest to study.

Work in **Chapter IV** specifies our efforts to properly characterize the effects of conformation-selective inhibition on kinome-wide selectivity. To this end, we synthesized a 'matched set' of conformation-selective analogs of dasatinib, an FDA-approved pan-kinase inhibitor that binds the active kinase conformation.[53] We crystallographically confirmed the binding mode for our inhibitors and then profiled them against a panel of kinases to understand their contributions to inhibitor selectivity.

The P-loop as an Underexplored Region for Inhibitor Development

Most kinases share a high degree of conservation within the ATP pocket, making it difficult for ATP-competitive inhibitors to distinguish between them.[17] Recent efforts have begun to target less structurally conserved kinase regions as inhibitor selectivity filters[20], including the kinase P-loop[68-69]. This loop is located between the ß1 and ß2 strands of the kinase N-lobe and comprises the roof of the ATP pocket. The glycine-rich composition of the P-loop (–LGXGXXGXV–) allows it to make significant hydrophobic contacts to both ATP and a majority of kinase inhibitors.[70]

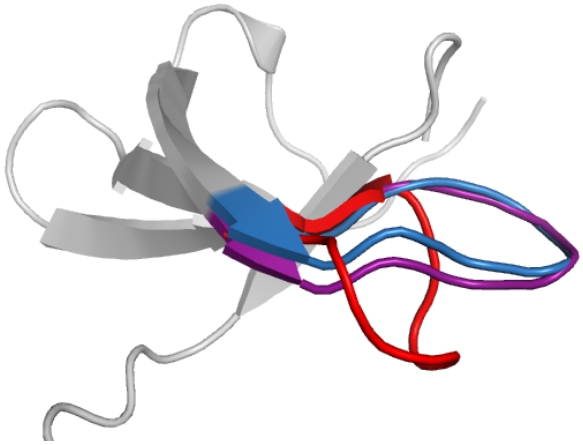

Figure 1.5. Overlay of homologous kinases illustrating variable P-loop conformations. The fully extended P-loop of c-Src kinase (blue) is compared to the extended P-loop of Fyn (purple) and the kinked P-loop of c-Abl (red).

X-ray crystallography has revealed that homologous kinases can adopt considerably different P-loop conformations. These range from a completely extended P-loop, as exemplified in the structure of c-Src[62], to the less frequently observed folded-in or kinked P-loop, illustrated in several structures of c-Abl[60] (Figure 1.5). Interestingly, these two kinases share 75% identity to one another in the ATP pocket[66], yet demonstrate two opposite ends of the P-loop conformational spectrum. Studies swapping the P-loop residues of c-Src for those found in c-Abl have failed to produce a kinked P-loop, suggesting that molecular determinants outside of the ATP pocket are responsible for determining its relative conformation.[68, 71]

Analysis of the seven different kinases (ABL, AURA, MET, FGFR1, p38α, MAP4K4, ACK1) that adopt a kinked P-loop also confirms that primary sequence does not play a role in the positioning of this loop.[72] Although these kinases share a consensus –LGXGXØGXV– P-loop amino acid sequence, where Ø is an aromatic residue and X is typically a polar residue, more than half of the kinome also shares this similar sequence. Furthermore, this folding event is not limited to a specific chemotype, as more than 40 unique scaffolds have been crystallized in a kinase with a kinked P-loop conformation.

The rare nature of the kinked P-loop makes it an obvious choice for a selectivity filter. While some research has focused on designing inhibitors complementary to this kinked structure[72], research by our group and others has looked to design ligands that preferentially bind to kinases with extended P-loops.[68-69] These purported ‘P-loop pocket’

binders have been useful for improving inhibitor selectivity, but interestingly do not always have their selectivity correlate to the static P-loop conformations found within the protein data bank. Consequently, our work in **Chapter V** looked to understand factors that control P-loop conformational variability amongst homologous kinases and to relate this positioning to trends in inhibitor selectivity.

Conclusions

The enormous amount of information in the kinase field confirms that there is no right or wrong way to target a deregulated kinase. Clinical small molecule kinase inhibitors, however, only treat a portion of the validated kinases implicated in disease demonstrating a critical need for improved design strategies. These approaches need to employ a variety of assays and be applicable to kinases with and without prior structural information to improve second-generation inhibitors. Ideally, these novel small molecules will also provide methodology to interrogate complex biological pathways in a fast, dose-dependent manner with varying levels of kinase inactivation.[12] Future studies may prove that single kinase inhibition is not feasible or necessary from a clinical standpoint, as combination therapies potentially become more widely utilized. Improved inhibitors are needed to determine the physiological relevancy of a specific kinase within a given disease, especially with the advent of personalized health care.

References

(1) Johnson, S. A.; Hunter, T. Kinomics: methods for deciphering the kinome. *Nat. Methods.* **2005,** *2*, 17–25.

(2) Hunter, T. Protein kinases and phosphatases: the Yin and Yang of protein phosphorylation and signaling. *Cell.* **1995,** *80*, 225–236.

(3) Graves, J. D.; Krebs, E. G. Protein phosphorylation and signal transduction. *Pharmacol. Ther.* **1999,** *82*, 111–121.

(4) Pawson, T.; Scott, J. D. Protein phosphorylation in signaling – 50 years and counting. *Trends in Biochemical Sciences.* **2005,** *30*, 286–290.

(5) Ryslava, H.; Doubnerova, V.; Kavan, D.; Vanek, O. Effect of posttranslational modifications on enzyme function and assembly. *Journal of Proteomics.* **2013,** *92*, 80–109.

(6) Dhanasekaran, D. N.; Reddy, E. P. JNK signaling in apoptosis. *Oncogene.* **2008,** *27*, 6245–6251.

(7) Manning, B. D.; Cantley, L. C. AKT/PKB signaling: navigating downstream. *Cell.* **2007,** *129*, 1261–1274.

(8) Olsson, A. K.; Dimberg, A.; Kreuger, J.; Claesson-Welsh, L. VEGF receptor signalling - in control of vascular function. *Nat. Rev. Mol. Cell Biol.* **2006,** *7*, 359–371.

(9) Mitra, S. K.; Hanson, D. A.; Schlaepfer, D. D. Focal adhesion kinase: in command and control of cell motility. *Nat. Rev. Mol. Cell Biol.* **2005,** *6*, 56–68.

(10) Zarubin, T.; Han, J. Activation and signaling of the p38 MAP kinase pathway. *Cell Res.* **2005,** *15*, 11–18.

(11) Birchmeier, C.; Birchmeier, W.; Gherardi, E.; Vande Woude, G. F. Met, metastasis, motility and more. *Nat. Rev. Mol. Cell Biol.* **2003,** *4*, 915–925.

(12) Knight, Z. A.; Shokat, K. M. Features of selective kinase inhibitors. *Chem. Biol.* **2005,** *12*, 621–637.

(13) Vulpetti, A.; Bosotti, R. Sequence and structural analysis of kinase ATP pocket residues. *Farmaco.* **2004,** *59*, 759–765.

(14) Davis, M. I.; Hunt, J. P.; Herrgard, S.; Ciceri, P.; Wodicka, L. M.; Pallares, G.; Hocker, M.; Treiber, D. K.; Zarrinkar, P. P. Comprehensive analysis of kinase inhibitor selectivity. *Nat. Biotechnol.* **2011,** *29*, 1046–1051.

(15) Knight, Z. A.; Lin, H.; Shokat, K. M. Targeting the cancer kinome through polypharmacology. *Nat. Rev. Cancer.* **2010,** *10*, 130–137.

(16) Blue Ridge Institute for Medical Research. USFDA approved protein kinase inhibitors compiled by Robert Roskoski Jr. http://www.brimr.org/PKI/PKIs.htm. **2015**.

(17) Breen, M. E.; Steffey, M. E.; Lachacz, E. J.; Kwarcinski, F. E.; Fox, C. C.; Soellner, M. B. Substrate activity screening with kinases: discovery of small-molecule substrate-competitive c-Src inhibitors. *Angew. Chem. Int. Ed. Engl.* **2014,** *53*, 7010–7013.

(18) Hanks, S. K.; Hunter, T. The eukaryotic protein kinase superfamily: kinase (catalytic) domain structure and classification. *The FASEB Journal.* **1995,** *9*, 576–596.

(19) Hubbard, S. R.; Till, J. H. Protein tyrosine kinase structure and function. *Annu. Rev. Biochem.* **2000,** *69*, 373–398.

(20) Zhang, J.; Yang, P. L.; Gray, N. S. Targeting cancer with small molecule kinase inhibitors. *Nat. Rev. Cancer.* **2009,** *9*, 28–39.
(21) Zhao, Z.; Wu, H.; Wang, L.; Liu, Y.; Knapp, S.; Liu, Q.; Gray, N. S. Exploration of type II binding mode: A privileged approach for kinase inhibitor focused drug discovery? *ACS Chem. Biol.* **2014,** *9*, 1230–1241.
(22) Kim, L. C.; Song, L.; Haura, E. B. Src kinases as therapeutic targets for cancer. *Nat. Rev. Clin. Oncol.* **2009,** *6*, 587–595.
(23) Roskoski, R., Jr. Src protein-tyrosine kinase structure, mechanism, and small molecule inhibitors. *Pharmacol. Res.* **2015,** *94*, 9–25.
(24) Finn, R. S. Targeting Src in breast cancer. *Ann. Oncology.* **2008,** *19*, 1379–1386.
(25) Martin, G. S. The hunting of the Src. *Nat. Rev. Mol. Cell. Biol.* **2001,** *2*, 467–475.
(26) Thomas, S. M. B., J. S. Cellular functions regulated by Src family kinases. *Ann. Rev. Cell. Dev. Biol.* **1997,** *13*, 513–609.
(27) Seeliger, M. A.; Young, M.; Henderson, M. N.; Pellicena, P.; King, D. S.; Falick, A. M.; Kuriyan, J. High yield bacterial expression of active c-Abl and c-Src tyrosine kinases. *Protein Sci.* **2005,** *14*, 3135–3139.
(28) Barf, T.; Kaptein, A. Irreversible protein kinase inhibitors: balancing the benefits and risks. *J. Med. Chem.* **2012,** *55*, 6243–6262.
(29) Liu, Q.; Sabnis, Y.; Zhao, Z.; Zhang, T.; Buhrlage, S. J.; Jones, L. H.; Gray, N. S. Developing irreversible inhibitors of the protein kinase cysteinome. *Chem. Biol.* **2013,** *20*, 146–159.
(30) Evans, D. C.; Watt, A. P.; Nicoll-Griffith, D. A.; Baillie|, T. A. Drug-protein adducts: an industry perspective on minimizing the potential for drug bioactivation in drug discovery and development. *Chem. Res. Toxicol.* **2004,** *17*, 3–16.
(31) Uetrecht, J. Idiosyncratic Drug Reactions: Past, Present, and Future. *Chem. Res. Toxicol.* **2008,** *21*, 84–92.
(32) Singh, J.; Petter, R. C.; Baillie, T. A.; Whitty, A. The resurgence of covalent drugs. *Nat. Rev. Drug Discov.* **2011,** *10*, 307–317.
(33) Singh, J.; Petter, R. C.; Kluge, A. F. Targeted covalent drugs of the kinase family. *Curr. Opin. Chem. Biol.* **2010,** *14*, 475–480.
(34) Keating, G. M. Afatinib: a review of its use in the treatment of advanced non-small cell lung cancer. *Drugs.* **2014,** *74*, 207–221.
(35) Cameron, F.; Sanford, M. Ibrutinib: first global approval. *Drugs.* **2014,** *74*, 263–271.
(36) Miller, R. M.; Taunton, J. Targeting protein kinases with selective and semipromiscuous covalent inhibitors. *Methods Enzymol.* **2014,** *548*, 93–116.
(37) Krippendorff, B. F.; Neuhaus, R.; Lienau, P.; Reichel, A.; Huisinga, W. Mechanism-based inhibition: deriving K(I) and k(inact) directly from time-dependent IC(50) values. *J. Biomol. Screen.* **2009,** *14*, 913–923.
(38) Kwarcinski, F. E.; Fox, C. C.; Steffey, M. E.; Soellner, M. B. Irreversible inhibitors of c-Src kinase that target a nonconserved cysteine. *ACS Chem. Biol.* **2012,** *7*, 1910–1917.
(39) Mortenson, P. N.; Berdini, V.; O'Reilly, M. Fragment-based approaches to the discovery of kinase inhibitors. *Methods Enzymol.* **2014,** *548*, 69–92.
(40) Scott, D. E.; Coyne, A. G.; Hudson, S. A.; Abell, C. Fragment-based approaches in drug discovery and chemical biology. *Biochemistry.* **2012,** *51*, 4990–5003.

(41) Tsai, J.; Lee, J. T.; Wang, W.; Zhang, J.; Cho, H.; Mamo, S.; Bremer, R.; Gillette, S.; Kong, J.; Haass, N. K.; Sproesser, K.; Li, L.; Smalley, K. S.; Fong, D.; Zhu, Y. L.; Marimuthu, A.; Nguyen, H.; Lam, B.; Liu, J.; Cheung, I.; Rice, J.; Suzuki, Y.; Luu, C.; Settachatgul, C.; Shellooe, R.; Cantwell, J.; Kim, S. H.; Schlessinger, J.; Zhang, K. Y.; West, B. L.; Powell, B.; Habets, G.; Zhang, C.; Ibrahim, P. N.; Hirth, P.; Artis, D. R.; Herlyn, M.; Bollag, G. Discovery of a selective inhibitor of oncogenic B-Raf kinase with potent antimelanoma activity. *Proc. Natl. Acad. Sci. U S A.* **2008,** *105*, 3041–3046.

(42) Erlanson, D. A.; Braisted, A. C.; Raphael, D. R.; Randal, M.; Stroud, R. M.; Gordon, E. M.; Wells, J. A. Site-directed ligand discovery. *Proc. Natl. Acad. Sci. U S A.* **2000,** *97*, 9367–9372.

(43) Cancilla, M. T.; He, M. M.; Viswanathan, N.; Simmons, R. L.; Taylor, M.; Fung, A. D.; Cao, K.; Erlanson, D. A. Discovery of an Aurora kinase inhibitor through site-specific dynamic combinatorial chemistry. *Bioorg. Med. Chem. Lett.* **2008,** *18*, 3978–3981.

(44) Erlanson, D. A.; Arndt, J. W.; Cancilla, M. T.; Cao, K.; Elling, R. A.; English, N.; Friedman, J.; Hansen, S. K.; Hession, C.; Joseph, I.; Kumaravel, G.; Lee, W. C.; Lind, K. E.; McDowell, R. S.; Miatkowski, K.; Nguyen, C.; Nguyen, T. B.; Park, S.; Pathan, N.; Penny, D. M.; Romanowski, M. J.; Scott, D.; Silvian, L.; Simmons, R. L.; Tangonan, B. T.; Yang, W.; Sun, L. Discovery of a potent and highly selective PDK1 inhibitor via fragment-based drug discovery. *Bioorg. Med. Chem. Lett.* **2011,** *21*, 3078–3083.

(45) Krasinski, A. R., Z.; Manetsch, R.; Raushel, J.; Taylor, P.; Sharpless, K. B.; Kold, H. C. In situ selection of lead compounds by click chemistry: target-guided optimization of acetylcholinesterase inhibitors. *J. Am. Chem. Soc.* **2005,** *127*, 6686–6692.

(46) Namelikonda, N. K.; Manetsch, R. Sulfo-click reaction via in situ generated thioacids and its application in kinetic target-guided synthesis. *Chem. Commun.* **2012,** *48*, 1526–1528.

(47) Levitsky, K.; Ciolli, C. J.; Belshaw, P. J. Selective inhibition of engineered receptors via proximity-accelerated alkylation. *Org. Let.* **2003,** *5*, 693–696.

(48) Kwarcinski, F. E.; Steffey, M. E.; Fox, C. C.; Soellner, M. B. Discovery of bivalent kinase inhibitors via enzyme-templated fragment elaboration. *ACS Med. Chem. Lett.* **2015,** *6*, 898–901.

(49) Kathman, S. G.; Xu, Z.; Statsyuk, A. V. A fragment-based method to discover irreversible covalent inhibitors of cysteine proteases. *J. Med. Chem.* **2014,** *57*, 4969–4974.

(50) Oueis, E.; Nachon, F.; Sabot, C.; Renard, P. Y. First enzymatic hydrolysis/thio-Michael addition cascade route to synthesis of AChE inhibitors. *Chem. Commun.* **2014,** *50*, 2043–2045.

(51) Oueis, E.; Sabot, C.; Renard, P.-Y. New insights into the kinetic target-guided synthesis of protein ligands. *Chem. Commun.* **2015,** *51*, 12158–12169.

(52) Huse, M.; Kuriyan, J. The conformational plasticity of protein kinases. *Cell.* **2002,** *109*, 275–282.

(53) Wang, Q.; Zorn, J. A.; Kuriyan, J. A structural atlas of kinases inhibited by clinically approved drugs. *Methods Enzymol.* **2014,** *548*, 23–67.

(54) Fabbro, D.; Cowan-Jacob, S. W.; Moebitz, H. Ten things you should know about protein kinases. *Brit. J. Pharmacol.* **2015,** *172*, 2675–2700.
(55) Sullivan, J. E.; Holdgate, G. A.; Campbell, D.; Timms, D.; Gerhardt, S.; Breed, J.; Breeze, A. L.; Bermingham, A.; Pauptit, R. A.; Norman, R. A.; Embrey, K. J.; Read, J.; VanScyoc, W. S.; Ward, W. H. J. Prevention of MKK6-dependent activation by binding to p38α MAP kinase. *Biochemistry.* **2005,** *44*, 16475–16490.
(56) Agius, M. P.; Soellner, M. B. Modulating noncatalytic function with kinase inhibitors. *Chem. Biol.* **2014,** *21*, 569–571.
(57) Hari, S. B.; Merritt, E. A.; Maly, D. J. Conformation-selective ATP-competitive inhibitors control regulatory interactions and noncatalytic functions of mitogen-activated protein kinases. *Chem. & Biol.* **2014,** *21*, 628–635.
(58) Wang, L.; Perera, B. G.; Hari, S. B.; Bhhatarai, B.; Backes, B. J.; Seeliger, M. A.; Schürer, S. C.; Oakes, S. A.; Papa, F. R.; Maly, D. J. Divergent allosteric control of the IRE1a endoribonuclease using kinase inhibitors. *Nat. Chem. Biol.* **2012,** *8*, 982–989.
(59) Krishnamurty, R.; Brigham, J. L.; Leonard, S. E.; Ranjitkar, P.; Larson, E. T.; Dale, E. J.; Merritt, E. A.; Maly, D. J. Active site profiling reveals coupling between domains in SRC-family kinases. *Nat. Chem. Biol.* **2013,** *9*, 43–51.
(60) Schindler, T.; Bornmann, W.; Pellicena, P.; Miller, W. T.; Clarkson, B.; Kuriyan, J. Structural mechanism for STI-571 inhibition of abelson tyrosine kinase *Science.* **2000,** *289*, 1938–1942.
(61) Sicheri, F.; Moarefi, I.; Kuriyan, J. Crystal structure of the Src family tyrosine kinase Hck. *Nature.* **1997,** *385*, 602–609.
(62) Xu, W.; Harrison, S. C.; Eck, M. J. Three-dimensional structure of the tyrosine kinase c-Src. *Nature.* **1997,** *385*, 595–602.
(63) Jura, N.; Zhang, X.; Endres, N. F.; Seeliger, M. A.; Schindler, T.; Kuriyan, J. Catalytic control in the EGF receptor and its connection to general kinase regulatory mechanisms. *Mol. Cell.* **2011,** *42*.
(64) Georghiou, G.; Kleiner, R. E.; Pulkoski-Gross, M.; Liu, D. R.; Seeliger, M. A. Highly specific, bisubstrate-competitive Src inhibitors from DNA-templated macrocycles. *Nat. Chem. Biol.* **2012,** *8*, 366–374.
(65) Zuccotto, F.; Ardini, E.; Casale, E.; Angiolini, M. Through the Data for ATP K_m Determination gatekeeper door": exploiting the active kinase conformation. *J. Med. Chem.* **2010,** *53*, 2681–2694.
(66) Liu, Y.; Gray, N. S. Rational design of inhibitors that bind to inactive kinase conformations. *Nat. Chem. Biol.* **2006,** *2*, 358–364.
(67) Wood, E. R.; Truesdale, A. T.; McDonald, O. B.; Yuan, D.; Hassell, A.; Dickerson, S. H.; Ellis, B.; Pennisi, C.; Horne, E.; Lackey, K.; Alligood, K. J.; Rusnak, D. W.; Gilmer, T. M.; Shewchuk, L. A unique structure for epidermal growth factor receptor bound to GW572016 (Lapatinib): Relationships among protein conformation, inhibitor off-rate, and receptor activity in tumor cells. *Cancer Research.* **2004,** *64*, 6652–6659.
(68) Brandvold, K. R.; Steffey, M. E.; Fox, C. C.; Soellner, M. B. Development of a highly selective c-Src kinase inhibitor. *ACS Chem. Biol.* **2012,** *7*, 1393–1398.

(69) Chaikuad, A.; Tacconi, E. M. C.; Zimmer, J.; Liang, Y.; Gray, N. S.; Tarsounas, M.; Knapp, S. A unique inhibitor binding site in ERK1/2 is associated with slow binding kinetics. *Nat. Chem. Biol.* **2014,** *10*, 853–862.

(70) Patel, R. Y.; Doerksen, R. J. Protein Kinase−inhibitor database: Structural variability of and inhibitor interactions with the protein kinase P-loop. *J. Proteome Res.* **2010,** *9*, 4433–4442.

(71) Seeliger, M. A.; Nagar, B.; Frank, F.; Cao, X.; Henderson, M. N.; Kuriyan, J. c-Src binds to the cancer drug imatinib with an inactive Abl/c-Kit conformation and a distributed thermodynamic penalty. *Structure.* **2007,** *15*, 299–311.

(72) Guimaraes, C. R.; Rai, B. K.; Munchhof, M. J.; Liu, S.; Wang, J.; Bhattacharya, S. K.; Buckbinder, L. Understanding the impact of the P-loop conformation on kinase selectivity. *J. Chem. Inf. Model.* **2011,** *51*, 1199–1204.

CHAPTER II

Utilizing Covalent Inhibition for Kinase Selectivity and Characterizing P-loop Conformations

Abstract

Current research efforts have focused on designing inhibitors to compete with ATP in the catalytically active site of the kinase. There are, however, more than 500 protein kinases in the human kinome that share nearly identical ATP-binding domains, making selectivity and subsequent cellular characterization difficult to achieve. To overcome this issue, we synthesized the first fully characterized irreversible inhibitors of wt c-Src. The protein is covalently modified at a cysteine residue (Cys277) found in less than 2% of all human kinases located within the glycine-rich P-loop. The designed irreversible inhibitors display an enhanced biochemical potency and selectivity in comparison to their reversible analogs, as well as in increase in cellular efficacy. Finally, these covalent modifiers were used to target clinically observed c-Src mutations and to study the P-loop conformation of several different kinase systems, an important loop that can affect inhibitor selectivity. This methodology provides a robust framework for generating irreversible kinase inhibitors from almost any reversible, chemical scaffold to target a specific kinase of interest.

Introduction

Despite more than 150 small molecule kinase inhibitors in clinical and preclinical trials, only a fraction of the approximate 200 kinases implicated in disease have been selectively inhibited. Most of the inhibitors currently in development are exceptionally potent, but generally non-selective as a result of targeting the highly conserved ATP-binding pocket. Reversible kinase inhibition strategies have generally been pursued towards this means[1-3], while irreversible methods are considerably underrepresented (**Chapter I**).[4-5] Covalent targeting of nonconserved, noncatalytic cysteine residues offers

significant advantages towards achieving both potent and selective compounds, including longer drug residence times, inhibition of resistance mutations and non-ATP-competitive modes of action.[6-7] Potential concerns over adverse immune responses from drug-protein adducts have largely been alleviated by several favorable toxicity profiles from recently approved small molecule-targeted therapies in cancer.[8-12]

Herein we report the design and characterization of the first irreversible inhibitors of wt c-Src. We targeted c-Src given its overexpression in numerous cancers and its role in tumor metastasis (see **Chapter I**).[13-14] Although reversible c-Src inhibitors have been previously developed, very few of these can boast the desired potency and selectivity required for use as an effective cellular probe.[15-17] Moreover, we deconvulated the role of covalent modification on inhibitor selectivity from canonical reversible scaffold binding interactions. We accomplished this by modifying two separate promiscuous kinase inhibitor scaffolds with an electrophile that targets Cys277 of c-Src kinase. Both of these compounds showed much improved selectivity and potency in comparison to their reversible counterparts. Our work demonstrated covalent inhibition overcoming resistance mutations and helping to characterize the relative conformation of an important kinase loop region involved in inhibitor binding.

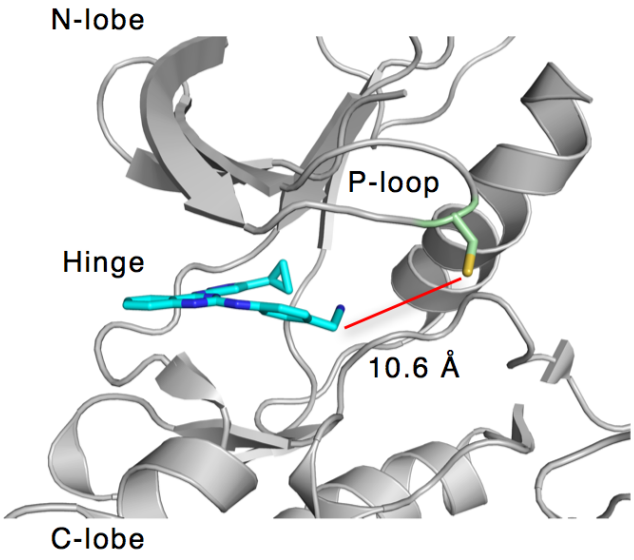

Figure 2.1. Crystal structure of c-Src bound to aminopyrazole inhibitor (PDB: 3F6X). The distance (10.5 Å) from the core scaffold to the sulfhydryl atom of Cys277 is shown in red.

The Design and Characterization of Irreversible Inhibitors of c-Src Kinase

Of the six noncatalytic cysteine residues present on the catalytic domain of c-Src, only Cys277 (chicken numbering) is positioned near the ATP binding pocket and solvent-exposed for potential electrophile reactivity. This cysteine is located within the P-loop (phosphate-binding loop or glycine-rich loop) and found in < 2% of all kinases (P-loop sequence alignment found in **Appendix Figure A.1** for SRC, FGR, FGFR-1,2,3,4, LIMK1, TNK1 & YES).[4] We reasoned that this nonconserved cysteine residue would provide an ideal selectivity filter for our designed irreversible inhibitors.

Our inhibitor design centered on a previously reported promiscuous kinase-binding scaffold.[18] Crystal structure analysis (PDB: 3F6X) revealed an approximate 10-Å distance that needed to be spanned from the core aminopyrazole to the nucleophilic sulfhydryl group (**Figure 2.1**). Slight modification of this inhibitor starting point led to the synthesis of control compound **2.1**. Profiling data revealed potent binding for **2.1** at 2 μM to nearly 60% of the kinases present in the panel (see **Appendix Figure A.2** for KINOMEscan profiling results). The uniqueness of starting with a promiscuous inhibitor enabled us to determine if selective c-Src inhibition could occur through a covalent mechanism of action alone. A series of analogs (compounds **2.2**–**2.7**) of compound **2.1** were synthesized with differing linkers (glycine and ß-alanine) and electrophiles (acrylamide, α-chloro ketone and vinyl sulfonamide) to create a putative library of covalent c-Src inhibitors of differing length and reactivity.

IC_{50} measurements at 0 and 120 min were performed using a previously reported continuous, fluorimetric activity assay[19] to initially assess relative potency for the inhibitor set (**Table 2.1**). Compounds **2.2**–**2.7** each displayed time-dependent inhibition, while compound **2.1** did not have an observable change in its IC_{50} value over the same time frame. Compounds **2.6** and **2.7** displayed the most significant c-Src inhibition and were consequently used to confirm the specific covalent bond between electrophile and Cys277.

Table 2.1. IC_{50} values for compounds **2.1**–**2.7** against wt c-Src.

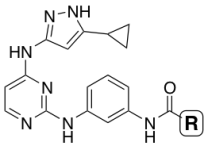

Compound	R	IC_{50} Values 0 min	IC_{50} Values 120 min
1		670	720
2	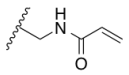	4400	350
3	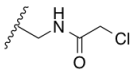	3200	340
4	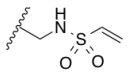	1700	570
5	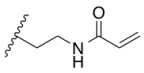	3200	610
6	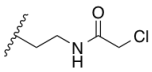	1200	91
7	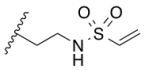	760	93

Both **2.6** and **2.7** saw a significant loss in potency (>6-fold) upon mutation of Cys277 to Ser (**Figure 2.2**). Compound **2.1**, conversely, had nearly identical potency for both wt and C277S c-Src (**Table 2.2**). Gel filtration experiments using wt c-Src treated with compound **2.1**, **2.6** or **2.7** further confirmed this precise interaction. While wt c-Src incubated with compound **2.1** regained its basal kinase activity, c-Src treated with either compound **2.6** or **2.7** did not (**Appendix Figure A.3**). Identical experiments performed with C277S c-Src and compound **2.7** did regain activity following gel filtration. Finally, the previously described wt c-Src–inhibitor complexes with compound **2.6** and **2.7** (after gel filtration) were analyzed by mass spectrometry to confirm single covalent adducts in both cases (**Appendix Figure A.4**). Taken together, these results validate that inhibitor irreversibility is solely dependent on the presence of Cys277.

After confirming Cys277 as the site of covalent modification, compounds **2.6** and **2.7** were subjected to further biochemical assays to determine their true binding affinities. IC_{50} values are often used to characterize irreversible inhibitors despite the fact that they are time dependent and can only be used to compare relative inhibitor potencies.[20] For a more definitive analysis, we opted to determine binding affinities (K_i) and rates of covalent bond formation (k_{inact}) for both compounds **2.6** and **2.7** with c-Src (**Figure 2.2**). Briefly, we determined IC_{50} values for a range of enzyme–inhibitor preincubation times at

RT, which were then used to directly calculate K_i and k_{inact} constants via nonlinear regression fits of the time-dependent IC_{50} values as previously reported.[20] While IC_{50} values (**Table 2.1**) could not discriminate between compounds **2.6** and **2.7**, our follow-up analysis determined compound **2.7** to have a better affinity (K_i = 360 nM) and larger rate of inactivation constant (k_{inact} = 1.5 X 10^{-3} s^{-1}) compared to that of **2.6**. Based on this dramatically better binding to the target, compound **2.7** was selected for selectivity and cellular studies.

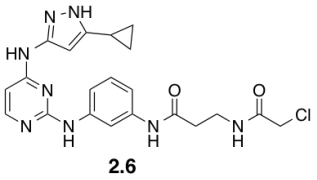

2.6

wt c-Src, IC_{50} = 91 nM
C277S c-Src, IC_{50} = 530 nM

k_{inact} = 1.0 x 10^{-3} s^{-1}
K_i = 600 nM

k_{inact}/K_i = 1700 M^{-1} s^{-1}

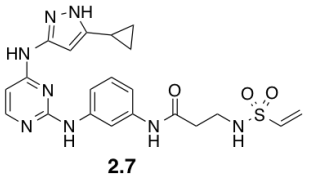

2.7

wt c-Src, IC_{50} = 93 nM
C277S c-Src, IC_{50} = 1200 nM

k_{inact} = 1.5 x 10^{-3} s^{-1}
K_i = 360 nM

k_{inact}/K_i = 4000 M^{-1} s^{-1}

Figure 2.2. Biochemical data for compounds **2.6** and **2.7**.

Selectivity and Cellular Efficacy of Irreversible Inhibitors

According to our methodology, covalent inhibitor **2.7** was predicted to display an improved selectivity profile over compound **2.1** as a result of an increase in binding to c-Src. Consequently, remarkable specificity was obtained with compound **2.7**, as it displayed a >80-fold improvement in potency for c-Src over two other closely related PTKs, c-Abl and Hck (≥70% similarity for all three kinases, **Table 2.2**). In comparison, compound **2.1** only had a 3-fold improvement against the same targets. This result is particularly interesting given the past difficulty in obtaining any selectivity amongst these kinases. A past comprehensive study of 72 preclinical and clinical kinase inhibitors demonstrated a lack of any compound that was more than 20-fold selective for c-Src over both c-Abl and Hck.[21]

Table 2.2. Selectivity panel for compounds **2.1** and **2.7**.

Compound	IC_{50} Values, 120 min		
	wt c-Src	wt c-Abl	wt Hck
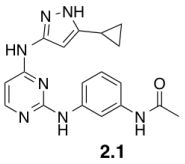 **2.1**	720 nM (---)	807 nM (---)	2800 nM (**4x**)
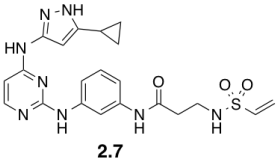 **2.7**	93 nM (---)	7700 nM (**83x**)	8000 nM (**86x**)

The above data demonstrates that exceptional selectivity can be obtained for our covalent inhibitors against a specific Cys277-containing kinase over targets lacking the identical P-loop residue. Selectivity amongst the additional kinases with the same P-loop Cysteine is dependent on the reversible binding (or lack thereof) of the core aminopyrazole. This has been reported previously with irreversible inhibitors of FGFR. These compounds target a cysteine in the equivalent position as c-Src but do not inhibit c-Src itself, seeing as the reversible scaffold does not bind to c-Src.[22] Since our starting scaffold does bind to all nine cysteine containing P-loop kinases with measureable affinity, we anticipated compound **2.7** to potently inhibit these targets as well. To confirm this, we tested compound **2.7** against the SFK c-Yes and observed potent inhibition (IC_{50} = 46 nM at 120 min). Modification of the reversible scaffold can generate selective inhibitors amongst these specific kinases.

To be effective in a cellular context, irreversible inhibitors must remain relatively inert toward physiological concentrations (mM) of endogenous nucleophiles, such as glutathione. We consequently re-evaluated the potency of compound **2.7** against wt c-Src in the presence of 1 mM reduced glutathione and found no change in biochemical IC_{50} (**Appendix Table A.1**). Similar results were obtained with a high concentration (1 mM) of DTT. These results indicate a lack of reactivity between electrophile and nucleophile, mirroring earlier studies that demonstrate that vinyl sulfonamides are kinetically slow substrates in intermolecular Michael reactions.[23]

Work was then conducted to assess the *in cellulo* activity of compound **2.7**. We found that **2.7** is cell permeable and efficient at inhibiting cellular Src phosphorylation (**Appendix Figure A.5**). An additional Src-dependent proliferation assay in 3D cell culture comparing compound **2.7** to its reversible complement, **2.1**, was also performed. Compound **2.1** had a GI_{50} of 14.3 μM while the irreversible compound **2.7** had a GI_{50} of 4.4 μM (**Appendix A** for individual curves). This observed increase in efficacy for **2.7** nicely parallels the earlier performed biochemical work that displayed greater c-Src potency for the irreversible inhibitors.

Dasatinib Irreversible Inhibitor Analogs

The modular design of our irreversible inhibitor series made it reasonable to apply this strategy to other scaffolds that bind c-Src. We focused our efforts on dasatinib, one of two (bosutinib) FDA-approved kinase inhibitors that potently target c-Src kinase.[24] Based on our success with the prior aminopyrazole scaffold, we sought to synthesize an irreversible counterpart to dasatinib to (1) improve its potency against clinically relevant mutations and (2) improve its selectivity for c-Src (binds 52 kinases with K_d < 100 nM).[21]

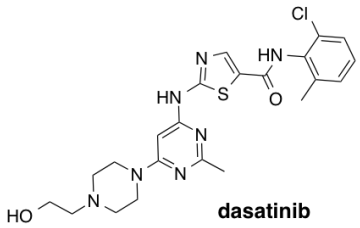

dasatinib

wt c-Src, IC_{50} < 5 nM

T338M c-Src, IC_{50} = 14,300 nM

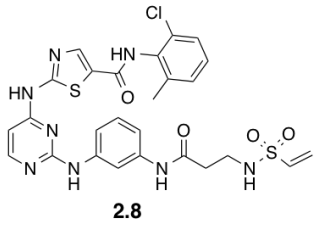

2.8

wt c-Src, IC_{50} < 5 nM

T338M c-Src, IC_{50} = 44 nM

k_{inact} = 3.9 x 10^{-3} s^{-1}

K_i = 98 nM

k_{inact}/K_i = 40,000 M^{-1} s^{-1}

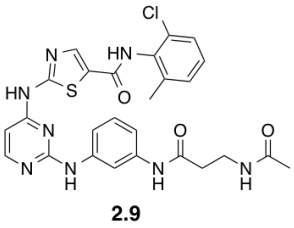

2.9

wt c-Src, IC_{50} < 5 nM

T338M c-Src, IC_{50} = 29,600 nM

Figure 2.3. Biochemical data for dasatinib and compounds **2.8** and **2.9**.

An analog of dasatinib was subsequently synthesized utilizing the same optimal ß-alanine linker and vinyl sulfonamide electrophile combination from compound **2.7**, affording compound **2.8** (**Figure 2.3**). Compound **2.9** was also prepared as an extra reversible-binding control compound. We were unfortunately unable to characterize these

three compounds against wt c-Src due to the enzyme requirements for our activity assay (IC_{50} < 5 nM for wt c-Src at 0 min), which agrees with the known tight binding capabilities of dasatinib for c-Src (reported K_i = 16 pM).[25] We next tested our inhibitor set against a gatekeeper variant (T338M) of c-Src that is highly resistant to dasatinib (IC_{50} = 14 μM) and compound **2.9** (IC_{50} = 30 μM) binding. Compound **2.8**, conversely, is a highly potent inhibitor of this gatekeeper c-Src construct (IC_{50} = 44 nM). This is significant because not all irreversible inhibitors can target gatekeeper mutations, as evidenced by a set of reported covalent inhibitors of wt FGFR1 that did not inhibit the corresponding gatekeeper mutant (V561M).[22] This compound represents one of the most potent inhibitors of T338M c-Src known to date and demonstrates the effectiveness of irreversible inhibition in targeting reversible-compound resistant kinases.

After achieving inhibition of T338M c-Src, we turned our attention to evaluating the selectivity profile of **2.8** relative to dasatinib. We reasoned that maintaining even comparable potency to dasatinib would enhance selectivity, especially if enzyme engagement of **2.8** with off-target kinases was compromised by the addition of an enthalpically nonproductive binding moiety (linker/electrophile). Both **2.8** and dasatinib had externally measured (Luecome Biotechnologies[26-27]) IC_{50} values of roughly 3 nM, so we opted to profile a panel of 124 wt kinases at 15 nM (5x IC_{50} value) against both compounds using a 120-min incubation. Selectivity differences were determined via inhibitor S-scores, which represent the fraction of kinases inhibited to a particular level (S_{35} is the percentage of total wt kinases in the panel with <35% of DMSO control activity). A lower S-score percentage indicates higher kinome selectivity. In this specific panel, compound **2.8** demonstrated an overall improvement in selectivity by having an S_{35} score of 7% compared to an S_{35} score of 12% for dasatinib (**Table 2.3**). Full profiling results for both inhibitors can be found in **Appendix A**.

Table 2.3. Selectivity scores for dasatinib and compound **2.8** against a panel of 124 diverse wt kinases.

	Selectivity Scores	
Compound	S(15)	S(35)
dasatinib	8%	12%
2.8	3%	7%

A more thorough look at the profiling data reinforces the fact that the reversible binding portion of the scaffold contributes to a significant portion of the inhibitor selectivity. Five of the nine kinases with c-Src P-loop Cysteine residues were present in the Luceome panel (SRC, FGFR1, FGFR2, LIMK1, YES), yet only c-Src and c-Yes displayed significant binding to compound **2.8**. This is directly attributed to dasatinib being a tight binder of both Src-family kinases. No binding of **2.8** was observed for either FGFR1 or LIMK1, with only weak binding to FGFR2 (78.7% of control, POC), indicating that the main reversible scaffold must have some appreciable interaction with the target for covalent inhibition to occur. Consequently, careful consideration of the starting point for irreversible inhibitors must be taken into account for optimal selectivity to occur.

While it was assumed that compound **2.8** would lose binding to kinases without a P-loop cysteine, it was less apparent if **2.8** would pick up additional kinase off-targets that contain cysteine residues outside of the kinase P-loop. In our panel, TEC and TXK saw modest increases in binding to compound **2.8** (TEC = 48.6 POC; TXK = 54.1 POC) compared to that of dasatinib. Interestingly, TEC and TXK contain a cysteine residue in their respective sugar-binding pockets.[4] This implies that it is possible to inhibit kinases with cysteines located elsewhere in the catalytic domain. Modification of the flexible linker in **2.8** to a more conformationally restricted version could eliminate covalent labeling of these undesired cysteine residues.

Table 2.4. Cellular efficacy of compound **2.8**. SK-BR-3 (breast cancer); HT-29 (colorectal cancer); HMEC (human mammary epithelial cells, healthy control cell line).

	GI_{50} Values		
Compound	SK-BR-3	HT-29	HMEC
dasatinib	1,600 nM	7.0 nM	2,300 nM
2.8	44 nM	220 nM	1,000 nM

Our biochemical studies were followed up with additional *in cellulo* work to assess the potential usage of our irreversible dasatinib analogs as selective cellular probes. Compound **2.8** efficiently reduced the proliferation of HT-29 colon cancer cells

(GI_{50} = 220 nM) growing *in vitro* (**Table 2.4**), comparable to that of dasatinib (GI_{50} = 7 nM). Evaluation of both compounds in a Src-dependent breast cancer cell line, SK-BR-3, demonstrated a significant improvement for **2.8** over dasatinib (**2.9**: GI_{50} = 91 nM; dasatinib: GI_{50} = 1600 nM). This highlights the potential for irreversible inhibitors to outperform their reversible counterparts within a specific cellular context, although further work is required to completely analyze specific signaling pathways affected by either dasatinib or the more selective, compound **2.8**, in each cell line. For good measure, the toxicity of each inhibitor was also evaluated using human mammary cells (HMEC), a healthy cell line control. Compound **2.8** and dasatinib performed similarly to one another (**Table 2.4**) with GI_{50} values in the single digit micromolar range.

Insight into P-loop Conformation

Another advantage of our covalent targeting strategy is the ability to study the conformation of the kinase P-loop. This highly flexible and dynamic loop has been associated with both inhibitor selectivity and resistance, but few tools existed prior to our involvement to accurately study its structural tendencies.[28-30] Previously determined time-dependent IC_{50} values for compound **2.7** with several kinases were used to calculate rate of inactivation (k_{inact}) constants, values capable of reporting on the distance between the inhibitor electrophile and cysteine nucleophile pair. Rate of inactivation constants are ideal parameters for approximating this interaction since these values are independent of inhibitor binding affinity (K_i).[20] In this simplified model, a larger k_{inact} constant is representative of a closer distance between bound inhibitor **2.7** and Cys277 of the P-loop.

As a proof-of-principle, we initially investigated the relative P-loop conformation of c-Src compared to that of c-Abl. Crystal structures of both kinases bound to dasatinib illustrate the extended P-loop of c-Src and the bent-in P-loop of c-Abl (**Figure 2.4**). We reasoned that covalent modification of a cysteine-containing P-loop Abl mutant would be dramatically faster than that for wt c-Src, based on the 7 Å difference between the two P-loop structures. To test this, we produced a Q252C c-Abl kinase mutant with a cysteine in the analogous position to Cys277 in c-Src. It is well established that enzymatic activity is not disrupted by mutation within the P-loop[30-31], making this chemical genetic approach applicable to most kinases. While compound **2.7** has modest, reversible binding for wt c-

Abl (IC_{50} = 7700 nM), it potently inhibits Q252C c-Abl (IC_{50} = 145 nM at 120 min). We next determined the rate of inactivation value of this c-Abl mutant and compared it to our previously calculated value for wt c-Src. The k_{inact} constant for Q252C c-Abl was 2-fold larger ($p < 0.05$) than the value for c-Src, which is consistent with the known kinked conformation of the c-Abl P-loop. This suggests that the P-loop of c-Abl positions Cys252 much closer to the vinyl sulfonamide of **2.7** for more rapid electrophile reactivity.

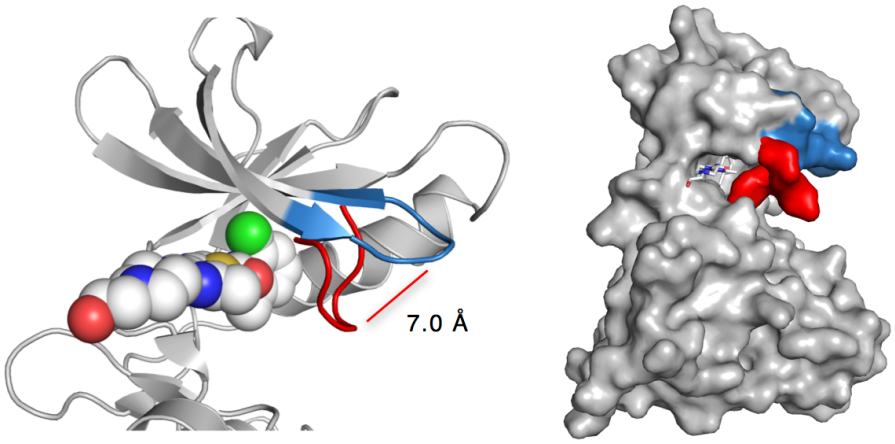

Figure 2.4. Alignment of crystal structures with dasatinib bound to c-Src (PDB: 3QLG) and c-Abl (2GQG). (Left) Cartoon overlay of the extended P-loop of c-Src (blue) and bent-in P-loop of c-Abl (red). (Right) Surface representation of the 'P-loop pocket' of c-Src being filled by the collapsed P-loop of c-Abl (red).

Although inhibitor selectivity amongst homologous kinases is notoriously difficult, our group recently reported a series of reversible inhibitors that were specific for c-Src and not c-Abl or SFK c-Yes.[15] It was hypothesized that these inhibitors directly interact with the 'P-loop pocket' of c-Src, the protein surface under the extended P-loop of the kinase.[15] Given the lack of such a pocket in c-Abl (**Figure 2.4**), it was supposed that the kinase P-loop conformation controls selectivity for this class of inhibitors.[28] A similar hypothesis could also be extended to inhibitor selectivity for c-Src over its most closely related SFK, c-Yes. Up until our involvement, however, this was not a valid model since c-Yes has no known crystal structures or computational models. We addressed this by employing our methodology to study the relative P-loop conformation of c-Yes (contains native Cys277 residue). The determined k_{inact} constant for wt c-Yes

was nearly identical to the value for c-Abl, suggesting a bent-in P-loop conformation. This result is particularly intriguing given that there are only 29 different amino acids between the catalytic domains of c-Src and c-Yes (95% similarity, 90% identity).

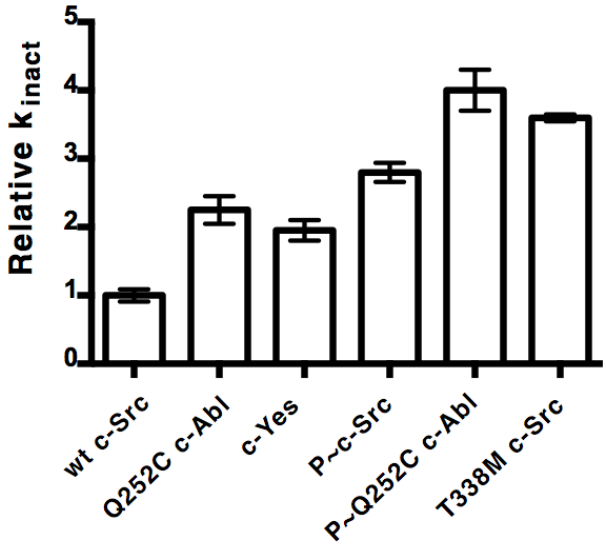

Figure 2.5. Relative kinact values for compound **2.7**. Statistical analysis was performed in GraphPad Prism 4.0 using a two-tailed *t* test (c-Src *vs* Q252C c-Abl, $p < 0.05$; c-Src *vs* c-Yes, $p < 0.05$; c-Src *vs* P~c-Src, $p < 0.01$; c-Abl *vs* P~Q252C c-Abl, $p < 0.01$; c-Src *vs* T338M c-Src, $p < 0.005$).

With our methodology in hand, we decided to explore how other kinase modifications affect the relative conformation of the P-loop. The stabilization of the active kinase conformation has been reported to cause the movement of the kinase P-loop,[32-33] making this a perfect case study to explore. We hypothesized that phosphorylation of the activation loop (P~Y416) and subsequent stabilization of the active kinase conformation would significantly alter the rate of the covalent modification of the P-loop cysteine. The k_{inact} constant of compound **2.7** with P~Y416 c-Src was 2-fold larger than that of wt c-Src, implying a more closed P-loop conformation (**Figure 2.5**). This results was duplicated with c-Abl, where P~Q252C c-Abl demonstrated a similar 2-fold improvement in rate of covalent modification relative to the dephosphorylated form. Both pieces of data support the idea of cross talk between distal regions of the kinase catalytic domain, in this case communication from a phosphorylated tyrosine residue almost 15 A away from the P-loop of the kinase.

We also revisited the earlier described gatekeeper mutation with our k_{inact} constant determination strategy, which plays a significant role in dictating kinase inhibitor binding, Despite adding hydrophobic bulk to the ATP pocket, gatekeeper mutations in a kinase generally increase the affinity for ATP relative to wt kinase.[30] We reasoned that this increase in affinity might result from a slight closing of the P-loop onto its nucleotide substrate. Thus, we determined a k_{inact} value for T338M c-Src and found it to be 3-fold larger than that of wt c-Src ($p < 0.01$). Although we did measure a kinking of the P-loop, the specific mechanism behind this specific observed closure is unknown. Past molecular dynamics simulations with c-Abl and receptor kinase EGFR have reported that gatekeeper mutations can cause movement of both the αC-helix and the P-loop, in agreement with our experimental data.[34-35]

Conclusions

This work reported the development and characterization of the first, irreversible inhibitors of wt c-Src. A known promiscuous kinase binding-scaffold was modified into a Src-specific inhibitor by attaching an electrophile positioned to covalently target a nonconserved cysteine residue located within the P-loop of the kinase. The methodology was applied to two separate chemical scaffolds and resulted in irreversible inhibitors with improved potency and selectivity over their reversible counterparts. Cellular results also paralleled this biochemical result with a noticeable increase in efficacy for the irreversible inhibitors over the reversible ones.

This approach for developing irreversible inhibitors can be reasonably applied to wide number of cysteine-containing kinases, as it has been calculated that nearly 20% of the kinome has a solvent-exposed cysteine residue near the ATP pocket.[4] This method can be extended to target kinases without naturally occurring cysteines nearby the nucleotide-binding site by using chemical genetic techniques as well (Q252C c-Abl). Finally, we demonstrated that inactivation rate constants (k_{inact}) for irreversible inhibitors could be utilized to study the conformation of the kinase P-loop. We applied this approach to three homologous kinases (c-Src, c-Abl, c-Yes) and to two different Src constructs and gained insight into why certain inhibitors may preferentially bind c-Src over other PTKs. Additional work characterizing how irreversible inhibitors can utilized

to investigate kinase structure–function relationships important in the discovery of Src-selective inhibitors will be discussed in **Chapter V**. All of these results provide a very detailed blueprint for the creation of irreversible kinase inhibitors to improve both target potency and selectivity.

Materials and Methods

General Synthetic Methods

Unless otherwise noted, all reagents were obtained via commercial sources and used without further purification. Dasatinib was purchased from LC labs. ^{1}H and ^{13}C NMR spectra were measured with a Varian MR400 or Inova 500 spectrometer. Mass spectrometry (HRMS) was carried out by the University of Michigan Mass Spectrometry Facility (J. Windak, director).

Synthetic Protocols

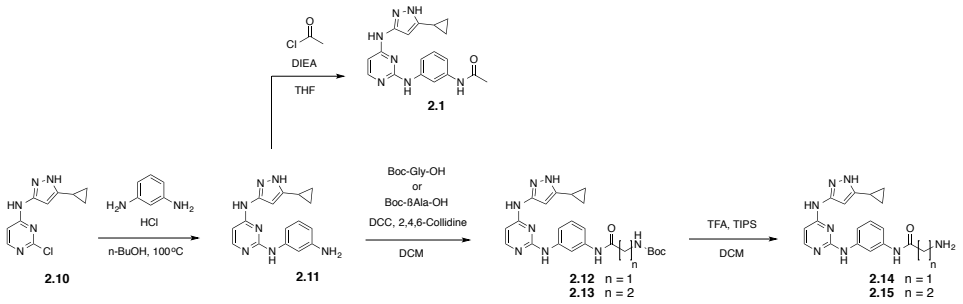

Scheme 2.1. Synthesis of compound **2.1** and compounds **2.11**–**2.15**.

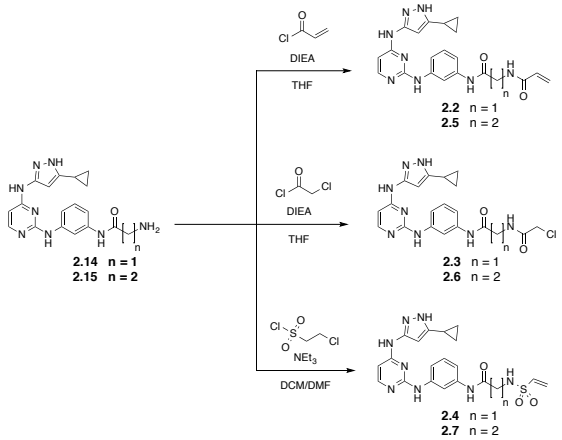

Scheme 2.2. Synthesis of compounds **2.2**–**2.7**.

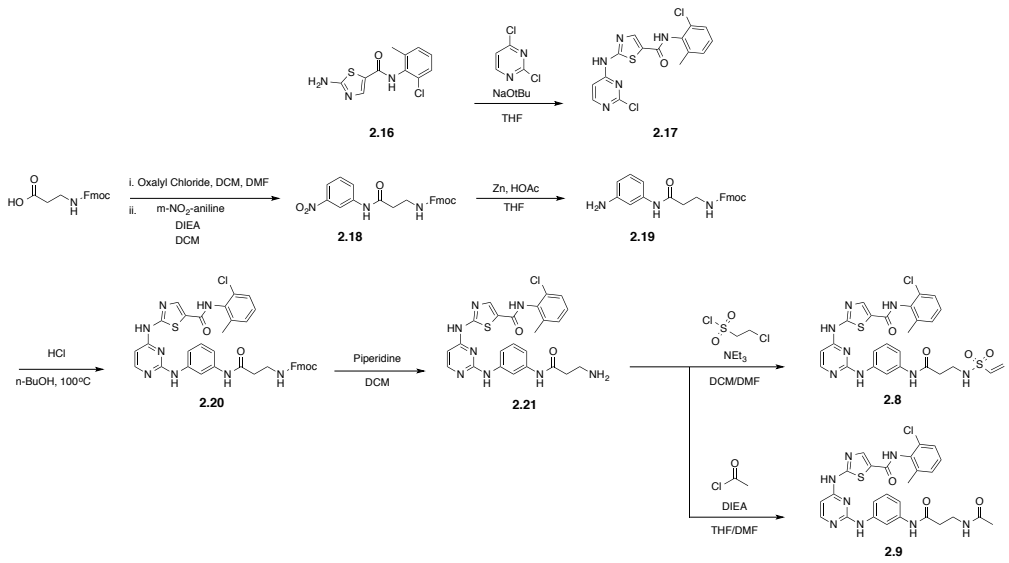

Scheme 2.3. Synthesis compounds **2.8** and **2.9**.

Synthesis of **2.10**. This compound was prepared as previously reported.[18]

Synthesis of **2.11**. This compound was prepared in an analogous way to previous reports.[18] Pyrimidine monochloride **2.10** (500 mg, 2.13 mmol) and *m*-phenylenediamine (345 mg, 3.19 mmol) were dissolved in n-BuOH (8 mL) followed by the addition of concentrated HCl (0.1 mL). Resulting mixture was kept at 100 °C overnight. Gray precipitate was collected by filtration, solubilized in THF/H_2O (20 mL), brought to pH 10 with 2N NaOH and organics were removed under reduced pressure prior to vacuum filtration to yield crude **2.11**. The product was purified by automated silica gel chromatography (linear gradient of 0 → 10% methanol in DCM) to yield compound **2.11** as a tan solid (471 mg, 72% yield). **Spectral data**. ^{1}H NMR (400 MHz, $CDCl_3$:MeOH-d_4): δ 7.92 (d, J = 6.12 Hz, 1 H), 7.08–7.01 (m, 2 H), 6.85–6.79 (m, 1 H), 6.39–6.33 (m, 1 H), 6.20–6.11 (m, 1 H), 5.81 (br s, 1 H), 1.85–1.75 (m, 1 H), 0.92–0.83 (m, 2 H), 0.70–0.62 (m, 2 H) ppm; ^{13}C NMR (100 MHz, $CDCl_3$:MeOH-d_4) δ 159.52, 156.22, 146.83, 142.58, 140.42, 129.51, 110.745, 109.88, 107.10, 97.41, 7.60 ppm. HRMS-ESI (*m*/*z*): [M + H]$^+$ calcd for $C_{16}H_{17}N_7$, 308.1618; found 308.1627.

Synthesis of **2.1**. Compound **2.11** (100 mg, 0.326 mmol) was added to a flame-dried flask that was flushed with N_2, followed by THF (3 mL) and DIEA (0.113 mL, 0.651 mmol)

addition. The contents of the flask were cooled to 0 °C prior to addition of acetylchloride (23 μL, 0.326 mmol). The reaction was allowed to stir for 1.5 h (0 °C → RT). The solvent was removed under reduced pressure to provide the crude product, which was purified via reverse-phase chromatography (linear gradient of 5 → 35% CH_3CN in H_2O) to yield compound **2.1** as a white solid (25.2 mg, 22% yield). **Spectral data**. ^{1}H NMR (400 MHz, $CDCl_3$:MeOH-*d*$_4$): δ 7.58–7.43 (m, 1 H), 7.27–7.10 (m, 1 H), 6.20–6.07 (m, 1 H), 6.03–5.87 (m, 1 H), 1.96 (s, 3 H), 1.70–1.56 (m, 1 H), 0.85–0.72 (m, 2 H), 0.54–0.36 (m, 2 H) ppm; ^{13}C NMR (100 MHz, $CDCl_3$:MeOH-*d*$_4$) δ 169.81, 159.92, 158.01, 149.37, 139.18, 138.62, 128.85, 116.31, 114.71, 112.06, 97.74, 23.28, 7.23 ppm. HRMS-ESI (*m*/*z*): $[M + H]^+$ calcd for $C_{18}H_{19}N_7O$, 350.1724; found 350.1734.

Synthesis of **2.12**. Boc-Gly-OH (627 mg, 3.58 mmol) was added to a flame-dried flask that was flushed with N_2. DCC (738 mg, 3.58 mmol) was then added, followed by DCM (30 mL) and 2,4,6-collidine (1.3 mL, 9.77 mmol) and allowed to stir at RT for 0.5 h. Aniline **2.11** was added and allowed to stir for 10 h. Contents of flask were filtered through a glass frit and washed with DCM (3 x 10 mL). The solvent was removed under reduced pressure and the crude product was dissolved in EtOAc (30 mL), washed with brine (1 x 10 mL), dried over anhydrous $MgSO_4$ (s) and filtered, and then the solvent was removed under reduced pressure to yield crude **2.12**. The product was purified by automated silica gel chromatography (linear gradient of 40 → 100% ethyl acetate in hexanes) to yield **2.12** as a pale yellow solid (596 mg, 39% yield). **Spectral data**. ^{1}H NMR (400 MHz, $CDCl_3$:MeOH-*d*$_4$): δ 7.86–7.81 (m, 1 H), 7.74–7.69 (m, 1 H), 7.23–7.18 (m, 1 H), 7.16–7.11 (m, 2 H), 6.18–6.10 (m, 1 H), 5.87 (br s, 1 H), 5.67 (br s, 1 H), 3.81–3.77 (m, 2 H), 1.77–1.69 (m, 1 H), 1.33 (s, 9 H), 0.84–0.78 (m, 2 H), 0.61–0.55 (m, 2 H) ppm; ^{13}C NMR (100 MHz, $CDCl_3$:MeOH-*d*$_4$) δ 168.11, 159.94, 159.20, 156.42, 155.60, 140.07, 137.85, 128.84, 115.91, 113.82, 111.36, 97.49, 79.92, 43.85, 27.80, 7.30 ppm. HRMS-ESI (*m*/*z*): $[M + H]^+$ calcd for $C_{23}H_{28}N_8O_3$, 465.2357; found 465.2373.

Synthesis of **2.13.** Boc-ßAla-OH (305 mg, 1.62 mmol) was added to a flame-dried flask that was flushed with N_2. DCC (333 mg, 1.62 mmol) was then added, followed by DCM (15 mL) and 2,4,6-collidine (0.59 mL, 4.41 mmol) and allowed to stir at RT for 0.5 h.

Amine **2.11** was added and allowed to stir for 10 h. The reaction mixture was filtered through a glass frit and washed with DCM (3 x 10 mL). The solvent was removed under reduced pressure and the crude product was dissolved in EtOAc (30 mL), washed with brine (1 x 10 mL), dried over anhydrous $MgSO_4$ (s) and filtered, and then the solvent was removed under reduced pressure to yield crude **2.13**. The product was purified by automated silica gel chromatography (linear gradient of 40 → 100% ethyl acetate in hexanes) to yield compound **2.13** as a yellow/white solid (309 mg, 44% yield). **Spectral data.** ^{1}H NMR (400 MHz, $CDCl_3$:MeOH-d_4): δ 7.90 (d, J = 5.85 Hz 1 H), 7.86–7.80 (m, 1 H), 7.40–7.32 (m, 1 H), 7.21–7.15 (m, 1 H), 7.14–7.07 (m, 1 H), 6.26 (br s, 1 H), 5.77 (br s, 1 H), 5.63–5.55 (m, 1 H), 3.40–3.33 (m, 2 H), 2.49 (t, J = 6.49 Hz, 2 H), 1.84–1.75 (m, 1 H), 1.35 (s, 9 H), 0.91–0.85 (m, 2 H), 0.70–0.63 (m, 2 H) ppm. ^{13}C NMR (100 MHz, $CDCl_3$:MeOH-d_4) δ 170.43, 160.12, 159.02, 156.41, 155.26, 139.97, 138.46, 128.98, 115.85, 114.02, 111.40, 97.53, 79.50, 36.91, 36.46, 28.05, 7.42 ppm. HRMS-ESI (m/z): $[M + H]^+$ calcd for $C_{24}H_{30}N_8O_3$, 479.2514; found 479.2526.

Synthesis of **2.14**. Compound **2.12** (132 mg, 0.284 mmol) was dissolved in DCM/TFA (1:1 10 mL) and TIPS (0.1 mL) was added and allowed to stir at RT for 1 h. The solvent was removed under reduced pressure and crude product was precipitated with Et_2O (10 mL). Solid was collected by filtration and washed with cold Et_2O (3 x 5 mL) and dried under vacuum. The crude salt was dissolved in THF/H_2O (10 mL), brought to pH 10 with 2N NaOH, and organics were removed under reduced pressure prior to vacuum filtration to yield **2.14** as a light brown solid (94 mg, 91% yield). **Spectral data**. ^{1}H NMR (500 MHz, $CDCl_3$:MeOH-d_4): δ 7.95 (d, J = 6.00 Hz, 1 H), 7.51–7.45 (m, 1 H), 7.23–7.18 (m, 1 H), 7.07–6.98 (m, 1 H), 6.37–6.21 (m, 1 H), 5.81 (br s, 1 H), 3.40–3.38 (m, 2 H), 1.85–1.78 (m, 1 H), 0.92–0.86 (m, 2 H), 0.72–0.66 (m, 2 H) ppm; ^{13}C NMR (100 MHz, $CDCl_3$:MeOH-d_4): δ 171.49, 159.27, 158.18, 155.80, 140.16, 137.86, 128.98, 115.83, 113.55, 111.09, 97.57, 93.23, 44.42, 7.40 ppm. HRMS-ESI (m/z): $[M + H]^+$ calcd for $C_{18}H_{20}N_8O$, 365.1833; found 365.1839.

Synthesis of **2.15.** Compound **2.13** (290 mg, 0.606 mmol) was dissolved in DCM/TFA (1:1 10 mL) and TIPS (0.1 mL) was added and allowed to stir at RT for 1 h. The solvent

mixture was removed under reduced pressure and crude product was precipitated with Et_2O (10 mL). Solid was collected by filtration and washed with Et_2O (3 x 5 mL) and dried under vacuum. The crude salt was dissolved in THF/H_2O (10 mL), brought to pH 10 with 2N NaOH, and organics were removed under reduced pressure prior to vacuum filtration to yield **2.15** as a light brown solid (218 mg, 95% yield). **Spectral data.** ^{1}H NMR (400 MHz, $CDCl_3$:MeOH-d_4): δ 7.80 (d, J = 5.94 Hz, 1 H), 7.76–7.71 (m, 1 H), 7.18–7.08 (m, 3 H), 6.17–6.06 (m, 1 H), 5.64 (br s, 1 H), 2.92 (t, J = 6.31 Hz, 2 H), 2.42 (t, J = 6.31 Hz, 2 H), 1.75–1.66 (m, 1 H), 0.83–0.74 (m, 2 H), 0.60–0.51 (m, 2 H) ppm; ^{13}C NMR (100 MHz, $CDCl_3$:MeOH-d_4) δ 166.88, 159.26, 156.41, 137.69, 135.18, 129.00, 126.77, 116.60, 114.49, 111.88, 97.80, 45.52, 29.36, 7.35 ppm. HRMS-ESI (m/z): $[M + H]^+$ calcd for $C_{19}H_{22}N_8O$, 379.1989; found 379.1998.

Synthesis of **2.2**. Compound **2.14** (75 mg, 0.206 mmol) was added to a flame-dried flask that was flushed with N_2, followed by THF (5 mL) and DIEA (72 μL, 0.412 mmol) addition. The contents of the flask were cooled to 0 °C prior to addition of acryloyl chloride (17 μL, 0.206 μmol). The reaction was allowed to stir for 1.5 h (0 °C → RT). The solvent was removed under reduced pressure to provide the crude product, which was purified via reverse-phase chromatography (linear gradient of 5 → 100% CH_3CN in H_2O) to yield compound **2.2** as a white solid (23.1 mg, 27% yield). **Spectral data**. ^{1}H NMR (400 MHz, $CDCl_3$:MeOH-d_4): δ 7.83 (d, J = 5.97 Hz, 1 H), 7.76–7.72 (m, 1 H), 7.20–7.13 (m, 3 H), 6.20 (dd, J = 17.22 Hz, J = 2.35 Hz, 1 H), 6.13 (dd, J = 17.22 Hz, J = 9.45 Hz, 1 H), 5.76 (br s, 1 H), 5.59 (dd, J = 9.97 Hz, J = 2.35 Hz, 1 H), 3.98–3.95 (m, 2 H), 1.77–1.68 (m, 1 H), 0.85–0.78 (m, 2 H), 0.61–0.54 (m, 2 H) ppm; ^{13}C NMR (100 MHz, $CDCl_3$:MeOH-d_4) δ 167.30, 166.66, 159.77, 158.95, 154.87, 139.87, 137.90, 129.71, 128.63, 126.37, 115.94, 113.89, 111.50, 97.55, 42.81, 6.97 ppm. HRMS-ESI (m/z): $[M + H]^+$ calcd for $C_{21}H_{22}N_8O_2$, 419.1938; found 419.1947.

Synthesis of **2.3**. Compound **2.14** (75 mg, 0.206 mmol) was added to a flame-dried flask that was flushed with N_2, followed by THF (3 mL) and DIEA (72 μL, 0.412 mmol) addition. The contents of the flask were cooled to 0 °C prior to addition of chloroacetylchloride (17 μL, 0.206 mmol). The reaction was allowed to stir for 1.5 h (0

°C → RT). The solvent was removed under reduced pressure to provide the crude product, which was purified via reverse-phase chromatography (linear gradient of 5 → 100% CH_3CN in H_2O) to yield compound **2.3** as a white solid (34 mg, 38% yield). **Spectral data.** ^{1}H NMR (500 MHz, $CDCl_3$:MeOH-d_4): δ 7.53 (d, J = 5.72 Hz, 1 H), 7.47–7.41 (m, 1 H), 6.96–6.91 (m, 1 H), 6.88–6.83 (m, 2 H), 5.96–5.77 (m, 1 H), 5.50 (br s, 1 H), 3.73 (s, 2 H), 3.69–3.67 (m, 2 H), 1.50–1.43 (m, 1 H), 0.56–0.50 (m, 2 H), 0.32–0.27 (m, 2 H) ppm; ^{13}C NMR (125 MHz, $CDCl_3$:MeOH-d_4): δ 167.53, 166.73, 164.89, 158.92, 154.75, 139.83, 137.75, 128.37, 115.76, 113.62, 111.34, 97.43, 42.45, 41.34, 6.67 ppm. HRMS-ESI (*m/z*): $[M + H]^+$ calcd for $C_{20}H_{21}N_8O_2$, 441.1549; found 441.1558.

Synthesis of **2.4.** Compound **2.14** (75 mg, 0.206 mmol) was added to a flame-dried flask that was flushed with N_2, followed by DCM/DMF (1:1, 2 mL) and NEt_3 (57 μL, 0.412 mmol) addition. The contents of the flask were cooled to 0 °C prior to addition of 2-chloro-1-ethane sulfonyl chloride (34 μL, 0.206 mmol). The reaction was allowed to stir for 1.5 h (0 °C → RT). Majority of the solvent was removed under reduced pressure to provide the crude product in DMF, which was purified via reverse-phase chromatography (linear gradient of 5 → 100% CH_3CN in H_2O) to yield compound **2.4** as a white solid (6.0 mg, 6% yield). **Spectral data.** ^{1}H NMR (500 MHz, $CDCl_3$:MeOH-d_4): δ 7.75 (d, J = 6.05 Hz, 1 H), 7.68–7.62 (m, 1 H), 7.19–7.08 (m, 4 H), 6.44 (dd, J = 16.22 Hz, J = 9.97 Hz, 1 H), 6.17–6.11 (m, 1 H), 6.09 (dd, J = 16.22 Hz, J = 0.49 Hz, 1 H), 5.81 (dd, J = 9.97 Hz, J = 0.49 Hz, 1 H), 5.65 (br s, 1 H), 3.64–3.63 (m, 2 H), 1.73–1.65 (m, 1 H), 0.80–0.75 (m, 2 H), 0.55–0.50 (m, 2 H) ppm; ^{13}C NMR (125 MHz, $CDCl_3$:MeOH-d_4): δ 166.88, 159.25, 156.41, 139.64, 137.69, 129.00, 126.77, 116.59, 114.50, 111.88, 97.81, 96.83, 45.52, 29.36, 7.35 ppm. HRMS-ESI (*m/z*): $[M + H]^+$ calcd for $C_{20}H_{22}N_8O_3S$, 455.1608; found 455.1606.

Synthesis of **2.5.** Compound **2.15** (20 mg, 0.053 mmol) was added to a flame-dried flask that was flushed with N_2, followed by THF (3 mL) and DIEA (11 μL, 0.064 mmol) addition. The contents of the flask were cooled to 0 °C prior to addition of acryloyl chloride (4.3 μL, 0.053 mmol). The reaction was allowed to stir for 1.5 h (0 °C → RT). The solvent was removed under reduced pressure to provide the crude product, which

was purified via reverse-phase chromatography (linear gradient of 5 → 100% CH_3CN in H_2O) to yield compound **2.5** as a white solid (4.0 mg, 18% yield). **Spectral data**. ^1H NMR (400 MHz, $CDCl_3$:MeOH-d_4): δ 7.83–7.76 (m, 1 H), 7.65–7.53 (m, 1 H), 7.33–7.16 (m, 2 H), 6.27–6.14 (m, 1 H), 6.09–5.98 (m, 1 H), 5.66 (br s, 1 H), 3.90 (s, 2 H), 3.49 (t, J = 6.35 Hz, 2 H), 2.51 (t, J = 6.35 Hz, 2 H), 1.79–1.64 (m, 1 H), 0.93–0.81 (m, 2 H), 0.59–0.44 (m, 2 H) ppm; ^{13}C NMR (100 MHz, $CDCl_3$:MeOH-d_4) δ 170.40, 166.71, 159.93, 139.92, 138.43, 130.53, 129.02, 126.45, 115.86, 113.99, 111.38, 97.61, 67.80, 36.23, 35.53, 25.33, 7.49 ppm. HRMS-ESI (m/z): $[M + H]^+$ calcd for $C_{22}H_{24}N_8O_2$, 433.7095; found 433.2102.

Synthesis of **2.6.** Compound **2.15** (218 mg, 0.578 mmol) was added to a flame-dried flask that was flushed with N_2, followed by THF (6 mL) and DIEA (0.3 mL, 1.73 mmol) addition. The contents of the flask were cooled to 0 °C prior to addition of chloroacetylchloride (46 μL, 0.578 mmol). The reaction was allowed to stir for 1.5 h (0 °C → RT). The solvent was removed under reduced pressure to provide the crude product, which was purified via reverse-phase chromatography (linear gradient of 5 → 100% CH_3CN in H_2O) to yield compound **2.6** as a white solid (31.3 mg, 12% yield). **Spectral data.** ^1H NMR (400 MHz, $CDCl_3$:MeOH-d_4): δ 7.83–7.76 (m, 1 H), 7.65–7.53 (m, 1 H), 7.33–7.16 (m, 2 H), 6.27–6.14 (m, 1 H), 6.09–5.98 (m, 1 H), 5.66 (br s, 1 H), 3.90 (s, 2 H), 3.49 (t, J = 6.35 Hz, 2 H), 2.51 (t, J = 6.35 Hz, 2 H), 1.79–1.64 (m, 1 H), 0.93–0.81 (m, 2 H), 0.59–0.44 (m, 2 H) ppm; ^{13}C NMR (100 MHz, $CDCl_3$:MeOH-d_4) δ 170.34, 167.15, 162.24, 159.94, 152.87, 148.29, 144.97, 141.68, 138.87, 136.51, 129.17, 118.79, 117.12, 113.99, 98.97, 93.80, 42.11, 40.07, 35.72, 7.76, 6.67 ppm. HRMS-ESI (m/z): $[M + H]^+$ calcd for $C_{21}H_{23}ClN_8O_2$, 455.1705; found 455.1713.

Synthesis of **2.7.** Compound **2.15** (300 mg, 0.79 mmol) was added to a flame-dried flask that was flushed with N_2, followed by DCM/DMF (1:1, 6 mL) and NEt_3 (0.133 mL, 0.95 mmol) addition. The contents of the flask were cooled to 0 °C prior to addition of 2-chloro-1-ethane sulfonyl chloride (83.5 μL, 0.79 mmol). The reaction was allowed to stir for 1.5 h (0 °C → RT). Majority of the solvent was removed under reduced pressure to provide the crude product in DMF, which was purified via reverse-phase chromatography

(linear gradient of 5 → 100% CH_3CN in H_2O) to yield compound **2.7** as a white solid (46 mg, 12% yield). **Spectral data.** ^{1}H NMR (500 MHz, DMSO-d_6): δ 12.01 (br s, 1 H), 9.92 (s, 1 H), 9.67 (br s, 1 H), 9.20 (br s, 1 H), 7.99–7.92 (m, 1 H), 7.86–7.76 (m, 1 H), 7.47–7.43 (m, 1 H), 7.38–7.34 (m, 1 H), 7.30–7.23 (m, 1 H), 7.20–7.15 (m, 1 H), 6.71 (dd, J = 16.27 Hz, J = 10.07 Hz, 1 H), 6.42 (br s, 1 H), 6.28 (br s, 1 H), 6.05 (dd, J = 16.27 Hz, J = 0.25 Hz, 1 H), 5.98 (dd, J = 10.07 Hz, J = 0.20 Hz, 1 H), 3.16–3.10 (m, 2 H), 2.55 (t, J = 7.29 Hz, 2 H), 1.87–1.80 (m, 1 H), 0.93–0.83 (m, 2 H), 0.69–0.62 (m, 2 H) ppm; ^{13}C NMR (100 MHz, DMSO-d_6) δ 168.67, 159.50, 155.80, 141.13, 139.12, 137.79, 136.69, 128.37, 125.50, 116.28, 114.42, 112.37, 98.27, 38.72, 36.78, 7.64 ppm. HRMS-ESI (m/z): $[M + H]^+$ calcd for $C_{21}H_{24}N_8O_3S$, 469.1765; found 469.1773.

Synthesis of **2.16.** This compound was prepared as previously reported.[36]

Synthesis of **2.17.** Compound **2.16** (485 mg, 1.81 mmol) and 2,4-dichloropyrimidine (324 mg, 2.17 mmol) were dissolved in THF (5 mL). Then sodium tert-butoxide (609 mg, 6.34 mmol) in THF (5 mL) was added into the stirring solution dropwise at 0 °C. The contents of the flask were stirred at RT for 1.5 h and then cooled back down to 0 °C. Reaction was slowly quenched with 2N HCl (5 mL) and the reaction was allowed to stir for 1.75 h at 0 °C. The THF was removed under reduced pressure and the resulting aqueous mixture was extracted with EtOAc (3 x 15 mL), dried over anhydrous $MgSO_4$ (s) and filtered, and then the solvent was removed under reduced pressure to yield crude **2.17**. The product was purified by automated silica gel chromatography (linear gradient of 25 → 60% ethyl acetate in hexanes) to yield **2.17** (120 mg, 17% yield). **Spectral data**. ^{1}H NMR (500 MHz, DMSO-d_6): δ 12.48 (br s, 1 H), 10.07 (s, 1 H), 8.45–8.41 (m, 1 H), 8.35–8.33 (m, 1 H), 7.43–7.39 (m, 1 H), 7.33–7.24 (m, 2 H), 7.10–7.06 (m, 1 H), 2.25 (s, 3 H) ppm; ^{13}C NMR (125 MHz, DMSO-d_6) δ 159.42, 158.49, 158.30, 140.68, 138.73, 133.22, 132.32, 129.06, 128.30, 127.70, 127.03, 117.11, 106.96, 100.05, 18.24 ppm. HRMS-ESI (m/z): $[M + H]^+$ calcd for $C_{15}H_{11}Cl_2N_5OS$, 380.0134; found 380.0137.

Synthesis of 2.18. Fmoc-ßAla-OH (5.00 g, 16.1 mmol) was added to a flame-dried flask that was flushed with N_2, followed by addition of DCM (100 mL), oxalyl chloride (1.66

mL, 19.3 mmol) and DMF (0.1 mL). After 1 h, the solvent and HCl (g) generated were removed under reduced pressure to yield the crude acetyl chloride intermediate, which was dissolved in THF (100 mL) and DIEA (3.36 mL, 19.3 mmol) and *m*-nitroaniline (2663 mg, 19.3 mmol) were added and allowed to proceed overnight at RT under N_2. Then the solvent was removed under reduced pressure to yield crude **2.18**, which was washed with aqueous saturated $NaHCO_3$ (1 x 75 mL), and then 1N HCl (2 x 75 mL), cooled to 0 ºC, vacuum filtered and finally with H_2O (3 x 25 mL). Solid was dried on lyophilizer to yield **2.18** (5.78 g, 83% yield). **Spectral data**. ^{1}H NMR (500 MHz, $CDCl_3$:MeOH-d_4): δ 8.34 (s, 1 H), 7.76–7.69 (m, 2 H), 7.56 (d, J = 7.58 Hz, 2 H), 7.39 (d, J = 7.42 Hz, 2 H), 7.28 (t, J = 8.22 Hz, 1 H), 7.22–7.16 (m, 2 H), 7.12–7.06 (m, 2 H), 4.19 (d, J = 6.99 Hz, 2 H), 4.04–3.99 (m, 1 H), 3.31 (t, J = 6.14 Hz, 2 H), 2.43 (t, J = 6.14 Hz, 2 H) ppm; ^{13}C NMR (100 MHz, $CDCl_3$:MeOH-d_4) δ 170.73, 157.10, 148.28, 143.56, 141.08, 139.37, 129.47, 127.55, 126.87, 125.19, 124.79, 119.79, 118.34, 114.27, 66.71, 46.89, 36.68, 36.64. HRMS-ESI (*m/z*): $[M + H]^+$ calcd for $C_{24}H_{21}N_3O_5$, 432.1554; found 432.1557.

Synthesis of 2.19. Compound **2.18** (5.4 g, 12.5 mmol) was added to a flame-dried flask that was flushed with N_2, followed by addition of THF (90 mL), glacial acetic acid (10 mL) and zinc metal (3.26 g, 50 mmol). Flask was stirred under N_2 at RT overnight. Crude contents were filtered through celite, which was then washed with THF (3 x 30 mL). The combined filtrate and washings were concentrated down under reduced pressure and the crude mixture was suspended in saturated $NaHCO_3$ (200 mL) and extracted with EtOAc (3 x 50 mL). The organic layers were dried over anhydrous $MgSO_4$ (s) and filtered, and then removed under reduced pressure to yield crude **2.19**. The crude product was purified via silica gel plug (100% EtOAc) to yield **2.19** (3.24 g, 64.6% yield). **Spectral data.** ^{1}H NMR (400 MHz, $CDCl_3$:MeOH-d_4): δ 7.55 (d, J = 7.56 Hz, 2 H), 7.37 (d, J = 7.56 Hz, 2 H), 7.21–7.15 (m, 2 H), 7.10–7.05 (m, 2 H), 6.91–6.84 (m, 2 H), 6.60–6.56 (m, 1 H), 6.27–6.22 (m, 1 H), 4.16 (d, J = 7.07 Hz, 2 H), 4.02–3.96 (m, 1 H), 3.27 (t, J = 6.33 Hz, 2 H), 2.34 (t, J = 6.33 Hz, 2 H) ppm; ^{13}C NMR (100 MHz, $CDCl_3$:MeOH-d_4) δ 170.25, 157.01, 146.76, 143.56, 141.00, 138.74, 129.35, 127.45, 126.81, 124.76, 119.69, 111.23, 110.10, 106.80, 65.58, 46.85, 36.83, 36.61. HRMS-ESI (*m/z*): $[M + H]^+$ calcd for

$C_{24}H_{23}N_3O_2$, 402.1812; found 402.1820.

Synthesis of 2.20. Compound **2.17** (810 mg, 2.13 mmol) was added to a flame-dried flask that was flushed with N_2, followed by addition of dioxane (10 mL), compound **2.19** (1026 mg, 2.56 mmol) and HCl (0.1 mL). The contents of the flask were refluxed for 13 h and cooled to RT. Saturated $NaHCO_3$ (10 mL) was added to the reaction flask, and the dioxane was removed under reduced pressure. Resulting solid was filtered, suspended in DCM, triturated and refiltered to yield a pale brown solid of **2.20 (**847 mg, 53% yield). **Spectral data.** ^{1}H NMR (400 MHz, DMSO-d_6): δ 9.90 (s, 1 H), 9.86 (s, 1 H), 9.34 (s, 1 H), 8.28 (s, 1 H), 8.19–8.16 (m, 1 H), 7.97 (s, 1 H), 7.90–7.85 (m, 2 H), 7.68 (d, J = 7.48 Hz, 2 H), 7.44–7.35 (m, 5 H), 7.34–7.23 (m, 5 H), 7.21–7.14 (m, 1 H), 6.50–6.46 (m, 1 H), 4.27 (d, J = 6.68 Hz, 2 H), 4.24–4.17 (m, 1 H), 3.30–3.23 (m, 2 H), 2.48–2.44 (m, 2 H), 2.24 (s, 3 H) ppm; ^{13}C NMR (125 MHz, DMSO-d_6) δ 169.18, 162.24, 159.84, 159.03, 157.22, 156.96, 156.08, 143.90, 140.83, 140.71, 140.31, 139.42, 139.19, 138.84, 137.42, 133.55, 132.46, 129.07, 128.94, 128.31, 128.21, 127.61, 127.30, 127.08, 126.67, 125.20, 121.40, 120.12, 120.05, 115.63, 113.26, 111.44, 109.81, 99.47, 65.37, 46.68, 36.87, 36.55, 18.33 ppm. HRMS-ESI (m/z): $[M + H]^+$ calcd for $C_{39}H_{33}ClN_8O_4S$, 745.2107; found 745.2104.

Synthesis of 2.21. Compound **2.20** (95 mg, 0.127 mmol) was dissolved in THF (2 mL) and piperidine (0.5 mL) was added and allowed to stir at RT for 1 h. The solvent was removed under reduced pressure to yield crude **2.21**, which was suspended in Et_2O (10 mL) and vacuum filtered. The resulting solid was washed with H_2O (2 x 4 mL) followed by Et_2O (2 x 4 mL). The solid was then triturated with DCM (10 mL) to yield **2.21** (46 mg, 69% yield). **Spectral data.** ^{1}H NMR (400 MHz, DMSO-d_6): δ 10.29 (s, 1 H), 10.09 (s, 1 H), 8.91–8.88 (m, 3 H), 8.55–8.49 (m, 1 H), 8.38 (s, 1 H), 8.20–8.17 (m, 1 H), 8.03–7.97 (m, 3 H), 7.91–7.89 (m, 1 H), 7.43–7.39 (m, 1 H), 7.37–7.33 (m, 1 H), 7.31–7.28 (m, 1 H), 6.67–6.62 (m, 1 H), 3.07–3.00 (m, 2 H), 2.74–2.69 (m, 2 H), 2.24 (s, 3 H) ppm; ^{13}C NMR (100 MHz, DMSO-d_6) δ 170.90, 168.80, 161.47, 159.87, 158.61, 145.47, 143.32, 140.98, 139.82, 139.22, 138.23, 133.81, 132.84, 129.53, 129.44, 128.60, 127.29,

118.12, 115.77, 113.60, 100.09, 35.32, 33.64, 18.75 ppm. HRMS-ESI (*m/z*): $[M + H]^+$ calcd for $C_{24}H_{23}ClN_8O_2S$, 523.1426; found 523.1428.

Synthesis of 2.8. Compound **2.21** (300 mg, 0.574 mmol) was added to a flame-dried flask that was flushed with N_2, followed by DCM/DMF (1:1, 3 mL) and NEt_3 (0.120 mL, 0.861 mmol) addition. The contents of the flask were cooled to 0 °C prior to addition of 2-chloro-1-ethane sulfonyl chloride (72.4 μL, 0.688 mmol). The reaction was allowed to stir for 1.5 h (0 °C → RT). Majority of the solvent was removed under reduced pressure to provide the crude product in DMF, which was purified via reverse-phase chromatography (linear gradient of 5 → 100% CH_3CN in H_2O) to yield compound **2.8** as a faint yellow solid (57.1 mg, 16% yield). **Spectral data.** ^{1}H NMR (400 MHz, DMSO-d_6): δ 11.77 (s, 1 H), 9.94–9.87 (m, 2 H), 9.38 (s, 1 H), 8.29 (s, 1 H), 8.21–8.18 (m, 1 H), 7.97–7.94 (m, 1 H), 7.43–7.38 (m, 2 H), 7.36–7.21 (m, 4 H), 7.20–7.14 (m, 1 H), 6.70 (dd, J = 16.72 Hz, J = 9.92 Hz, 1 H), 6.53–6.48 (m, 1 H), 6.04 (dd, J = 16.72 Hz, J = 0.20 Hz, 1 H), 5.97 (dd, J = 9.92 Hz, J = 0.20 Hz, 1 H), 3.14–3.08 (m, 2 H), 2.57-2.51 (m, 2 H), 2,25 (s, 3 H) ppm; ^{13}C NMR (125 MHz, DMSO-d_6) δ 168.67, 161.95, 159.77, 158.99, 157.07, 156.98, 140.74, 140.25, 139.07, 138.82, 136.66, 133.49, 132.43, 129.07, 128.30, 128.22, 127.04, 126.86, 125.54, 115.69, 113.25, 111.43, 99.21, 38.68, 36.74, 18.30 ppm. HRMS-ESI (*m/z*): $[M + H]^+$ calcd for $C_{26}H_{25}ClN_8O_4S_2$, 613.1201; found 613.1200.

Synthesis of 2.9: Compound **2.21** (45 mg, 0.086 mmol) was added to a flame-dried flask that was flushed with N_2, followed by THF/DMF (1:1, 3 mL) and DIEA (30 μL, 0.172 mmol) addition. This was cooled to 0 °C prior to addition of acetyl chloride (9.2 μL, 0.129 mmol). The reaction was allowed to stir for 1.5 hr (0°C → RT). Majority of the solvent was removed under reduced pressure to provide the crude product in DMF, which was purified via reverse-phase chromatography (linear gradient of 5 → 100% CH_3CN in H_2O) to yield compound **2.9** as a white solid (28.5 mg, 58.6% yield). **Spectral data.** ^{1}H NMR (400 MHz, DMSO-d_6): δ 10.89 (br s, 1 H), 10.15 (s, 1 H), 10.12 (s, 1 H), 8.95–8.91 (m, 1 H), 8.41 (s, 1 H), 8.17–8.12 (m, 1 H), 8.10–8.05 (m, 1 H), 7.98–7.92 (m, 1 H), 7.90–7.86 (m, 1 H), 7.42–7.36 (m, 2 H), 7.35–7.23 (m, 3 H), 6.72–6.66 (m, 1 H), 3.30–3.23 (m, 2 H), 2.48–2.42 (m, 2 H), 2.23 (s, 3 H), 1.77 (s, 3 H) ppm; ^{13}C NMR (100 MHz,

DMSO-d_6) δ 169.74, 169.37, 162.92, 160.55, 159.31, 158.91, 146.25, 142.05, 140.42, 140.07, 138.83, 133.33, 132.43, 129.40, 129.18, 128.42, 127.30, 127.15, 118.87, 116.65, 114.34, 99.91, 36.44, 35.11, 22.61, 18.35 ppm. HRMS-ESI (*m/z*): $[M + H]^+$ calcd for $C_{26}H_{25}ClN_8O_3S$, 565.1532; found 565.1542.

Spectral Data for Compounds

Spectral data (^1H, ^{13}C NMR) for compounds **2.1**-**2.21** is shown in **Appendix A**.

General Biochemical Methods

Black, opaque-bottom 96 well plates were used for fluorescence assays and were purchased from Nunc. wt c-Src, wt c-Abl and wt Hck plasmids containing a TEV protease cleavable N-terminal 6x-His tag were a generous gift from M. Seeliger (SUNY, Stony Brook) and J. Kuriyan (UC Berkeley) and were expressed in *E. coli* and purified by C. Fox using previously published procedures (see ***Kinase Expression and Purification*** below).[37] Q252C c-Abl and T338M c-Src were prepared by C. Fox (see ***Mutant Kinase Production*** below) and c-Yes was purchased from SignalChem. Chicken c-Src and human c-Abl 1a numbering is used unless otherwise noted. Data was obtained using a Molecular Devices SpectraMax M5 plate reader or Biotek Synergy 4 plate reader. Curve fitting was performed using GraphPad Prism 4 software, while k_{inact} and K_i determination was performed using ExcelFit software according to published procedures.[20]

Determination of Inhibitor IC_{50} Values

A continuous fluorescence assay was used to determine K_i.[19] Reaction volumes of 100 μL were used in 96-well plates. 85 μL of enzyme in buffer was added to each well. 2.5 μL of the appropriate inhibitor dilution (typically 2500, 833, 278, 93, 31, 10, 3.4, 1.1, 0.38, 0 μM in DMSO) was then added. 2.5 μL of a substrate peptide ("compound 3" as described in Wang et al)[19] solution (1.8 mM in DMSO) was added. The reaction was initiated with 10 μL of ATP (1 mM in water), and reaction progress was immediately monitored at 405 nm (ex. 340 nm) for 10 minutes. Reactions had final concentrations of 30 nM enzyme, 45 μM peptide substrate, 100 μM ATP, 100 μM TCEP, 100 μM Na_3VO_4, 100 mM Tris buffer (pH 8), 10 mM $MgCl_2$, 0.01% Triton X-100. The initial rate data collected was used for determination of IC_{50} values. For IC_{50} determination, the kinetic

values were obtained directly from nonlinear regression of substrate-velocity curves in the presence of various concentrations of the inhibitor. The equation Y = Bottom + (Top – Bottom)/(1 + 10^X – LogEC50), X = log(concentration) and Y = binding; was used in the nonlinear regression. Each inhibitor IC_{50} value was determined using at least three independent experiments; a representative inhibition curve is shown in **Appendix A** for each inhibitor.

General procedure for k_{inact} and K_i determination

The aforementioned continuous fluorescence assay[19] was used to determine time-dependent IC_{50} values. 85 μL of the appropriate enzyme in buffer was incubated with 2.5 μL of inhibitor dilution (typically 2500, 833, 278, 93, 31, 10, 3.4, 1.1, 0.38, 0 μM in DMSO) at RT with varying enzyme pre-incubation times (2, 10, 20, 30, 45, 60, 75, 90, 105, 120 min). Then 2.5 μL of a substrate peptide solution (1.8 mM in DMSO) was added followed by addition of 10 μL of ATP (1 mM in water), and reaction progress was immediately monitored at 405 nm (ex. 340 nm) for 10 minutes. Reactions had final concentrations of 30 nM enzyme, 45 μM peptide substrate, 100 μM ATP, 100 μM TCEP, 100 μM Na_3VO_4, 100 mM Tris buffer (pH 8), 10 mM $MgCl_2$ and 0.01% Triton X-100. IC_{50} values were determined as previously described. For k_{inact} and K_i determination, the values were obtained directly from nonlinear regression of time-dependent IC_{50} values as previously reported.[20] The substrate concentration was set to 100 μM for each curve fit, while the ATP K_m value varied based on the particular enzyme being tested (see **Appendix A** for individual values–note that no ATP K_m value was determined for c-Yes due to a limited quantity of enzyme, value taken from literature[3]). Each inhibitor k_{inact} and K_i value was determined using at least two independent time course experiments; a representative time-dependent IC_{50} value curve is shown in **Appendix A**.

Determination of ATP K_M

The previously described continuous fluorescence assay was used to determine K_M for ATP described in Wang *et al*.[19] Reaction volumes of 100 μL were used in 96-well plates. 85 μL of enzyme in buffer was added to each well. 2.5 μL of DMSO was then added followed by 2.5 μL of a substrate peptide ("compound 3" as described in Wang et al)[19] solution (1.8 mM in DMSO). The reaction was initiated with 10 μL of the

appropriate ATP dilution (typically 1000, 500, 250, 125, 62.5, 31.3, 15.6, 7.8, 3.9, 2.0 μM in H_2O) and reaction progress was immediately monitored at 405 nm (ex. 340 nm) for 10 minutes. Reactions had final concentrations of 30 nM enzyme, 45 μM peptide substrate, 100 μM Na_3VO_4, 100 mM Tris buffer (pH 8), 10 mM $MgCl_2$, 0.01% Triton X-100. The initial rate data collected was used for determination of K_m values. For K_m determination, the kinetic values were obtained directly from nonlinear regression of substrate-velocity curves in the presence of varying concentrations of ATP. The equation $Y = (V_{max} * X)/(K_m + X)$, X = substrate concentration (μM) and Y = enzyme velocity (RFU/s); was used in the nonlinear regression. Each ATP K_m value was determined using at least three independent experiments; a representative K_m curve is shown in **Appendix A**.

Mutant Kinase Production

The Q252C c-Abl and T338M c-Src mutants were prepared by C. Fox. The unmodified wt plasmids (human c-Abl kinase domain and chicken c-Src kinase domain), both in pET28a modified with a TEV protease cleavable N-terminal 6x-His tag, were provided to the lab by M. Seeliger (SUNY, Stony Brook) and J. Kuriyan (UC Berkeley). The desired mutation (Q252C c-Abl or T338M c-Src) was added to the specific plasmid with mutagenesis using the Agilent QuikChange II kit. The mutated plasmid was then transformed by electroporation into Bl21DE3 electrocompetent cells containing YopH in pCDFDuet-1 for cell growth, kinase expression and purification (below).

Kinase Expression and Purification

E. Coli cell growth, kinase expression and purification were performed using modified literature protocols for expression of wild-type c-Src kinase domain.[37] Briefly, the plasmid containing the kinase (pET28a or pSKBR3) was transformed into *E. Coli* BL21DE3 cells already containing YopH phosphatase (pCDFDuet-1 plasmid) and plated on LB agar with kanamycin (50 μg/mL, kan) and streptomycin (50 μg/mL, SM) and grown overnight at 37 ºC. A single colony was picked for a starter culture (LB containing kan/SM) and subsequently grown overnight at 37 ºC. The next day, scaled up cultures (TB containing kan/SM) were grown to an OD_{600nm} of 1.2 at 37 ºC and cooled to 18 ºC with shaking prior to induction for 16 h at 18 ºC with 0.2 mM IPTG. Cells were harvested

by 20 min centrifugation at 4,000 rpm at 4 ºC and resuspended in 50 mM Tris (pH 8.0), 500 mM NaCl, 5% glycerol, 25 mM imidazole (buffer A) supplemented with 0.1 mM PMSF for immobilized Ni metal affinity chromatography. Cells were lysed via sonication and insoluble protein and cell debris was sedimented through a 50-min centrifugation at 14,000 rpm at 4 ºC. The clear supernatant was loaded onto the Ni-NTA agarose affinity column (batch, QIAGEN) column. The resin was washed with 50 column volumes of buffer A and five column volumes (3X) of buffer QB (20 mM Tris, pH 8.0, 5% glycerol, 1 M NaCl). Protein was eluted with five column volumes (4X) of buffer B (buffer A plus 0.5 M imidazole). The buffer B fractions were pooled together and cleaved with 0.1 mg of TEV per 2.5 mg of crude kinase.

Cleaved protein was loaded onto an anion exchange column (Q Sepharose, Fast Flow, GE Healthcare Life sciences) equilibrated with buffer QA (buffer QB without 1 M NaCl). Proteins were eluted with a linear gradient of 0–35% buffer QB and peak fractions were combined (based on kinase activity assay) and concentrated down in order to be loaded onto a size-exclusion column (HiLoad Superdex S75, GE Healthcare Life sciences) equilibrated with buffer D (50 mM Tris, pH 8.0, 5% glycerol, 200 mM NaCl, 1 mM DTT). Pure fractions via SDS-PAGE were combined and used for biochemical assays.

Gel Filtration Procedure

The appropriate enzyme was incubated with inhibitor for 1 h at RT at final concentrations of 10 μM enzyme and 100 μM inhibitor in 25 μL of total volume (5% DMSO). Then the samples were eluted with Buffer D (100 mM Tris buffer pH 8, 10 mM $MgCl_2$, 5% Glycerol) through separate Sephadex G25 columns. Concentrations were determined via absorbance at 280 nm, and then assayed as previously described. A chart of percent kinase activity remaining can be found in **Appendix A**.

ESI-MS Characterization

Previously incubated inhibitor-enzyme samples that were passed through G25 Sephadex columns (see above) were submitted to the University of Michigan Mass Spectrometry Facility for analysis. Numerical values can be found in **Appendix A**.

Cancer Cell Growth Inhibition Assays

Growth inhibition assays were performed by M. Steffey. SK-BR-3 (ATCC® HTB-30™), HT-29 (ATCC® HTB-38™) and HMEC (human mammary epithelial, Lonza®) cells were grown and maintained using complete growth media (DMEM for SK-BR-3, McCoy's 5a Modified Medium for HT-29, supplemented with 10% fetal bovine serum, and MEGM™ for HMEC) in a 37 ºC, 5% CO_2, humidified air incubator. Cells were then plated into 96 well plates in complete growth media (100 μL/well) at a concentration of 5000 cells per well and allowed to attach overnight. The cells were dosed with compound at 1% DMSO in media every 24 h for 72 h total (three times total) prior to addition of 10 μL/well of Cell Proliferation Agent WST-1 (Roche) for SK-BR-3 and HT-29 cells. The absorbance at 450 and 630 nm was read on a Biotek Synergy 4 multimode reader after incubation for 1 h at 37 ºC. The raw $\Delta(A_{450}-A_{630})$ data were converted into percent of the average of the vehicle treated wells for each cell line and the IC_{50} value was determined using nonlinear regression. For each cell line, there were n = 3 data points for each concentration. Each dose response curve was performed at least twice, providing $n \geq 6$ for each data point. The dose-response curve for each cell line with compounds **2.1**, **2.7**, **2.8** and dasatinib is shown in **Appendix A**.

3D Cell Culture Growth Inhibition

3D cell culture growth inhibition assays were performed by M. Steffey. Prior to plating cells, 50 μL Cultrex basement membrane extract (BME, Trevigen) was added to each well of a 96-well plate incubated on ice and then allowed to gel (cushion formation) over a 30-min time period in a 37 ºC incubator. v-Src 3T3 cells stably transfected with v-Src were provided by K. Shokat (UCSF) and were grown and maintained using complete growth media (DMEM) in a 37 ºC, 5% CO_2, humidified air incubator. Cells were then dispersed from flasks and collected by centrifugation (200xg for 5 min at room temperature). An aliquot of the resuspended cells was mixed with trypan blue solution and the cell number was quantified using a hemacytometer. 100% DMSO compound stocks were prepared to 100X the final concentration that is desired in the assay. 3 μL of the DMSO stock solution was then added to 297 μL of the cell suspension supplemented with 5% BME to give a DMSO concentration of 1%. The cells were plated at about

10,000 cells per well (100 μL/well) in triplicate for each compound concentration. The plate was then placed within the Essen IncuCyte imager in the 37 °C, 5% CO_2 humidified incubator and camera images were taken every 2 h to measure confluency percentages over time. The data was plotted as a percentage of the vehicle (1% DMSO alone) and analysis and curve fitting was performed using Graphpad Prism. Kinetic growth curves were based off of the first 24 h of cell growth inhibition and used to construct GI_{50} curves. There were n = 2 data points for the two lower concentrations tested (0.3 μM, 1 μM) while all other concentrations (10 μM, 30 μM, 100 μM) used n = 3 data points. Representative images and GI_{50} curves can be found in **Appendix A**.

Kinome Profiling of Compound 2.8

Kinome profiling of dasatinib and compound **2.8** was performed by Luceome Biotechnologies (Tucson, AZ).[26-27] To select an appropriate concentration, IC_{50} values for dasatinib and compound **2.8** were obtained using the Luceome technology. Nearly identical IC_{50} values were obtained (3.1 nM for dasatinib, 3.7 nM for compound **2.8**). Both dasatinib and compound **2.8** were profiled at a concentration of 15 nM. Full profiling results are available in **Appendix A**.

Western Blot Procedure

NIH-3T3 cells stably transfected with v-Src were plated into a 6-well plate in complete growth media (1 mL/well) at a concentration of 80,000 cells per well and allowed to attach overnight. After the overnight incubation the cell growth media was removed by aspiration and replaced with 1 ml per well of the dosing solution containing the compound in growth media at a final DMSO concentration of 1%. Cells were incubated for 60 min in the 37 °C, 5% CO_2 humidified incubator after which the dosing solution was removed by aspiration. The cell monolayer was washed once with 1 ml per well of ice cold PBS and the cells were scraped and lysed in 200 μL per well of ice-cold PerkinElmer lysis buffer. The lysates were then removed to new tubes on ice and protein concentrations were determined via Bradford assay. Proteins were resolved on 20% SDS polyacrylamide gels under constant voltage. Following a 20-min semi-dry Immobilon-P PVDF membrane transfer, protein bands were developed using the SNAP i.d.™ Protein Detection System methodology (Millipore). The membrane was blocked with 30 mL

blok™-PO (Millipore), followed by a 20 min incubation with 1:1,000 diluted p-Tyr anti-mouse monoclonal antibody HRP conjugate (Cell Signaling Technology). The membrane was washed (3 x 30 mL) with TBS-T (Tris-buffered saline with 0.1% Tween-20) and then incubated in 6 mL of Luminata™ Crescendo Western HRP Substrate (Millipore) for 5 min at RT. The proteins were visualized using the chemiluminescent signal under medium sensitivity at 650V on a GE Typhoon Imager and ImageQuant software. Western blot image can be found in **Appendix Figure A.5**.

References

(1) Levitzki, A.; Gazit, A. Tyrosine kinase inhibition: an approach to drug development. *Science.* **1995,** *267*, 1782–1788.

(2) Manning, G.; Whyte, D. B.; Martinez, R.; Hunter, T.; Sudarsanam, S. The protein kinase complement of the human genome. *Science.* **2002,** *298*, 1912–1934.

(3) Knight, Z. A.; Shokat, K. M. Features of selective kinase inhibitors. *Chem. Biol.* **2005,** *12*, 621–637.

(4) Zhang, J.; Yang, P. L.; Gray, N. S. Targeting cancer with small molecule kinase inhibitors. *Nat. Rev. Cancer.* **2009,** *9*, 28–39.

(5) Leproult, E.; Barluenga, S.; Moras, D.; Wurtz, J. M.; Winssinger, N. Cysteine mapping in conformationally distinct kinase nucleotide binding sites: application to the design of selective covalent inhibitors. *J. Med. Chem.* **2011,** *54*, 1347–1355.

(6) Barf, T.; Kaptein, A. Irreversible protein kinase inhibitors: balancing the benefits and risks. *J. Med. Chem.* **2012,** *55*, 6243–6262.

(7) Singh, J.; Petter, R. C.; Kluge, A. F. Targeted covalent drugs of the kinase family. *Curr. Opin. Chem. Biol.* **2010,** *14*, 475–480.

(8) Evans, D. C.; Watt, A. P.; Nicoll-Griffith, D. A.; Baillie|, T. A. Drug-protein adducts: an industry perspective on minimizing the potential for drug bioactivation in drug discovery and development. *Chem. Res. Toxicol.* **2004,** *17*, 3–16.

(9) Uetrecht, J. Idiosyncratic Drug Reactions: Past, Present, and Future. *Chem. Res. Toxicol.* **2008,** *21*, 84–92.

(10) Singh, J.; Petter, R. C.; Baillie, T. A.; Whitty, A. The resurgence of covalent drugs. *Nat. Rev. Drug Discov.* **2011,** *10*, 307–317.

(11) Keating, G. M. Afatinib: a review of its use in the treatment of advanced non-small cell lung cancer. *Drugs.* **2014,** *74*, 207–221.

(12) Cameron, F.; Sanford, M. Ibrutinib: first global approval. *Drugs.* **2014,** *74*, 263–271.

(13) Thomas, S. M. B., J. S. Cellular functions regulated by Src family kinases. *Ann. Rev. Cell. Dev. Biol.* **1997,** *13*, 513–609.

(14) Martin, G. S. The hunting of the Src. *Nat. Rev. Mol. Cell. Biol.* **2001,** *2*, 467–475.

(15) Brandvold, K. R.; Steffey, M. E.; Fox, C. C.; Soellner, M. B. Development of a highly selective c-Src kinase inhibitor. *ACS Chem. Biol.* **2012,** *7*, 1393–1398.

(16) Breen, M. E.; Steffey, M. E.; Lachacz, E. J.; Kwarcinski, F. E.; Fox, C. C.; Soellner, M. B. Substrate activity screening with kinases: discovery of small-molecule substrate-competitive c-Src inhibitors. *Angew. Chem. Int. Ed. Engl.* **2014,** *53*, 7010–7013.

(17) Brandvold, K. R.; Santos, S. M.; Breen, M. E.; Lachacz, E. J.; Steffey, M. E.; Soellner, M. B. Exquisitely specific bisubstrate inhibitors of c-Src kinase. *ACS Chem. Biol.* **2015,** *10*, 1387–1391.

(18) Statsyuk, A. V. M., D. J.; Seeliger, M. A.; Fabian, M. A.; Biggs III., W. H.; Lockhart, D. J.; Zarrinkar, P. P.; Kuriyan, J.; Shokat, K. M. . Tuning a Three-Component Reaction for Trapping Kinase Substrate Complexes. *J. Am. Chem. Soc.* **2008,** *130*, 17568–17574.

(19) Wang, Q. C., S. M.; Blumenstein, M.; Lawrence, D. S. Self-reporting fluorescent substrates of protein tyrosine kinases. *J. Am. Chem. Soc.* **2006,** *128*, 1808–1809.
(20) Krippendorff, B. F.; Neuhaus, R.; Lienau, P.; Reichel, A.; Huisinga, W. Mechanism-based inhibition: deriving K(I) and k(inact) directly from time-dependent IC(50) values. *J. Biomol. Screen.* **2009,** *14*, 913–923.
(21) Davis, M. I.; Hunt, J. P.; Herrgard, S.; Ciceri, P.; Wodicka, L. M.; Pallares, G.; Hocker, M.; Treiber, D. K.; Zarrinkar, P. P. Comprehensive analysis of kinase inhibitor selectivity. *Nat. Biotechnol.* **2011,** *29*, 1046–1051.
(22) Zhou, W.; Hur, W.; McDermott, U.; Dutt, A.; Xian, W.; Ficarro, S. B.; Zhang, J.; Sharma, S. V.; Brugge, J.; Meyerson, M.; Settleman, J.; Gray, N. S. A structure-guided approach to creating covalent FGFR inhibitors. *Chem. Biol.* **2010,** *17*, 285–295.
(23) Reddick, J. J.; Cheng, J.; Roush, W. R. Relative rates of michael reactions of 2'-(phenylethyl)thiol with vinyl sulfones, vinyl sulfonate esters, and vinyl sulfonamides relevant to vinyl sulfonyl cysteine protease inhibitors. *Org. Lett.* **2003,** *5*, 1967–1970.
(24) Wang, Q.; Zorn, J. A.; Kuriyan, J. A structural atlas of kinases inhibited by clinically approved drugs. *Methods Enzymol.* **2014,** *548*, 23–67.
(25) Lombardo, L. J.; Lee, F. Y.; Chen, P.; Norris, D.; Barrish, J. C.; Behnia, K.; Castaneda, S.; Cornelius, L. A.; Das, J.; Doweyko, A. M.; Farichild, C.; Hunt, J. T.; Inigo, I.; Johnston, K.; Kamath, A.; Kan, D.; Klei, H.; Marathe, P.; Pang, S.; Peterson, R.; Pitt, S.; Schieven, G. L.; Schmidt, R. J.; Tokarski, J.; Wen, M. L.; Wityak, J.; Borzilleri, R. M. Discovery of N-(2-chloro-6-methyl-phenyl)-2-(6-(4-(2-hydroxyethyl)-piperazin-1-yl)-2-methylpyrimidin-4-ylamino)thiazole-5-carboxamide (BMS-354825), a dual Src/Abl kinase inhibitor with potent antitumor activity in preclinical assays. *J. Med. Chem.* **2004,** *47*, 6658–6661.
(26) Jester, B. W.; Cox, K. J.; Gaj, A.; Shomin, C. D.; Porter, J. D.; Ghosh, I. A coiled-coil enabled split-luciferase three-hybrid system: applied toward profiling inhibitors of protein kinases. *J. Am. Chem. Soc.* **2010,** *132*, 11727–11735.
(27) Jester, B. W.; Gaj, A.; Shomin, C. D.; Cox, K. J.; Ghosh, I. Testing the promiscuity of commercial kinase inhibitors against the AGC kinase group using a split-luciferase screen. *J. Med. Chem.* **2012,** *55*, 1526–1537.
(28) Patel, R. Y.; Doerksen, R. J. Protein Kinase−inhibitor database: Structural variability of and inhibitor interactions with the protein kinase P-loop. *J. Proteome Res.* **2010,** *9*, 4433–4442.
(29) Guimaraes, C. R.; Rai, B. K.; Munchhof, M. J.; Liu, S.; Wang, J.; Bhattacharya, S. K.; Buckbinder, L. Understanding the impact of the P-loop conformation on kinase selectivity. *J. Chem. Inf. Model.* **2011,** *51*, 1199–1204.
(30) Krishnamurty, R.; Maly, D. J. Biochemical mechanisms of resistance to small-molecule protein kinase inhibitors. *ACS Chem. Biol.* **2010,** *5*, 121–138.
(31) Seeliger, M. A.; Ranjitkar, P.; Kasap, C.; Shan, Y.; Shaw, D. E.; Shah, N. P.; Kuriyan, J.; Maly, D. J. Equally potent inhibition of c-Src and Abl by compounds that recognize inactive kinase conformations. *Cancer Res.* **2009,** *69*, 2384–2392.

(32) Hubbard, S. R. Crystal structure of the activated insulin receptor tyrosine kinase in complex with peptide substrate and ATP analog. . *EMBO J.* **1997,** *16*, 5572–5581.
(33) Vajpai, N.; Strauss, A.; Fendrich, G.; Cowan-Jacob, S. W.; Manley, P. W.; Grzesiek, S.; Jahnke, W. Solution conformations and dynamics of ABL kinase-inhibitor complexes determined by NMR substantiate the different binding modes of imatinib/nilotinib and dasatinib. *J. Biol. Chem.* **2008,** *283*, 18292–18302.
(34) Lee, T. S.; Potts, S. J.; Kantarjian, H.; Cortes, J.; Giles, F.; Albitar, M. Molecular basis explanation for imatinib resistance of BCR-ABL due to T315I and P-loop mutations from molecular dynamics simulations. *Cancer.* **2008,** *112*, 1744–1753.
(35) Dixit, A.; Verkhivker, G. M. Hierarchical modeling of activation mechanisms in the ABL and EGFR kinase domains: thermodynamic and mechanistic catalysts of kinase activation by cancer mutations. *PLoS Comput. Biol.* **2009,** *5*, e1000487.
(36) Chen, B.-C.; Zhao, R.; Wang, B.; Droghini, R.; Lajeunesse, J.; Sirard, P.; Endo, M.; Balasubramanian, B.; Barrisha, J. C. A new and efficient preparation of 2-aminothiazole-5-carbamides: applications to the synthesis of the anti-cancer drug dasatinib. *ARKIVOC.* **2010,** *6*, 32–38.
(37) Seeliger, M. A.; Young, M.; Henderson, M. N.; Pellicena, P.; King, D. S.; Falick, A. M.; Kuriyan, J. High yield bacterial expression of active c-Abl and c-Src tyrosine kinases. *Protein Sci.* **2005,** *14*, 3135–3139.

CHAPTER III

A Novel Enzyme-Templated Fragment-Based Screen for Discovering Bivalent Kinase Inhibitors

Abstract

Even with a significant emphasis on the development of kinase inhibitors within the drug discovery field, current FDA-approved small molecules only target a subset of the kinases implicated in disease. Several factors contribute to this problem, including an inability to generate truly selective kinase inhibitors amongst this conserved phosphotransferase superfamily. Herein we describe a novel enzyme-templated fragment-based drug discovery approach for the creation of potent and selective inhibitors. The screen utilizes a library of irreversible fragments being tethered to a thiol-containing small molecule via increases in local concentration. Our 110-member electrophile library produced two final compounds with improved biochemical potency and selectivity over the starting parent scaffold. The robust detection of fragments via an activity assay over other biophysical methods can potentially be applied to any small molecule/protein system devoid of a reactive cysteine residue.

Introduction

Since the approval of imatinib in the treatment of CML in 2001[1], many drug discovery efforts have focused on duplicating its success through subsequent targeting of other kinases associated in disease. This has resulted in a boom in inhibitor development for the control of dysregulated cell signaling pathways.[2-4] A majority of these inhibitor strategies focus on targeting the ATP pocket of the kinase, the cleft between the N- and C-terminal lobes of the kinase catalytic domain (**Figure 3.1**). This defined pocket is highly amendable to drug discovery because it contains many potential hydrophobic surfaces for inhibitor interactions and can accommodate a number of heterocyclic scaffolds commonly employed in screening libraries. Consequently, all FDA-approved

kinase inhibitors bind within this conserved pocket, due to its tractable targeting nature.[5] While this has been successful for a number of clinical kinase inhibitors, many compounds of this class suffer from poor selectivity profiles and subsequent off-target toxicity.[6-7] To improve inhibitor selectivity, less conserved features adjacent to or outside the ATP-binding site have been recently targeted.[3, 8] While seemingly a simple solution to the problem, the systematic discovery of inhibitors that bind outside the ATP site is extremely difficult and often serendipitous.[9-10]

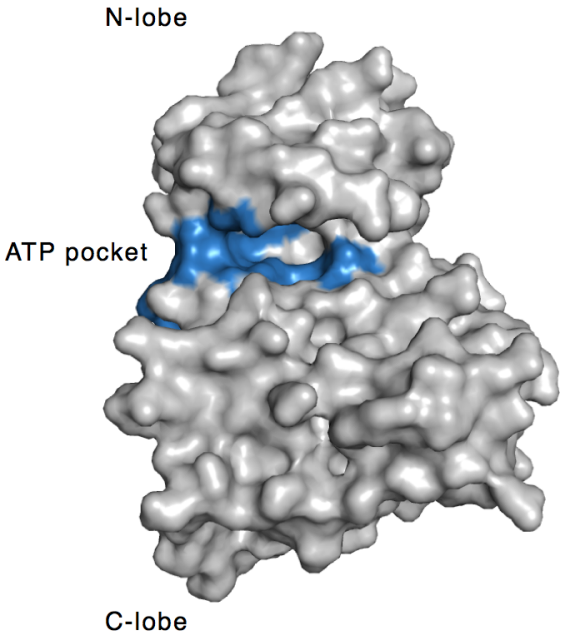

Figure 3.1. Surface map representation of kinase catalytic domain. ATP pocket is highlighted in blue.

Fragment-based drug discovery (FBDD) provides one potential methodology to address this issue (see **Chapter I**). Here, initial hits from biochemical screening are identified from a library of low-molecular weight compounds that is designed to cover an immense amount of chemical space. Further inhibitor optimization can then occur to transform a weak-binding fragment into a potent final compound. FBDD has had a tremendous impact for a number of biological targets, yet labor-intensive NMR or X-ray crystallography detection methods and ATP-pocket centric design strategies have limited its usage for kinases.[11] Instead, most kinase drug discovery platforms rely on structure-based design strategies with complementary high throughput structure-activity

relationship (SAR) inhibitor optimization. In order to apply the principles of FBDD to kinases in an unbiased manner without the need for structural information, we developed a fragment elaboration screen where hits can be identified through an activity assay.

Our strategy differs from traditional tethering, which relies on mixed disulfide formation with the protein[12], by utilizing a Michael reaction between an ATP-competitive hit compound with a pendent thiol and an acrylamide fragment (**Figure 3.2**). We benefit from using a proximity-based, enzyme-templated approach where increases in local concentration of both reactive components lead to formation of a bivalent inhibitor in situ.[13-17] This technique also allows us to screen the same fragment library multiple times for any number of targets (as opposed to synthesizing and purifying bivalent inhibitors for each target).

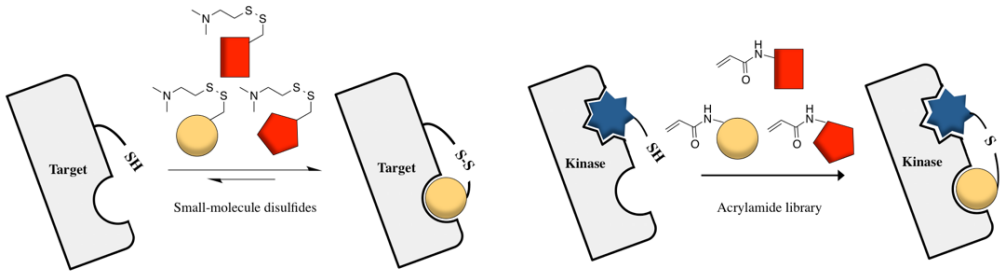

Figure 3.2. Comparison of traditional tethering (left) to our hybrid approach (right).

Enzyme-Templated Fragment Screening

Three major components needed to be carefully selected in order for a successful screen to occur: (1) the small-molecule thiol; (2) the electrophile library and (3) the kinase system. We opted to pursue our previously characterized, promiscuous kinase-binding starting scaffold from **Chapter II (Figure 3.3)**, compound **2.1**, as the basis for our reactive thiol. This invaluable tool had the potential to be applied to almost 60% of the kinome, or the percentage bound by **2.1**.[18] We consequently synthesized an analog of **2.1** that contains a thiol functionality, compound **3.1** (**Figure 3.3**), to enable enzyme-templated Michael reactions with a library of acrylamides. Compound **3.2** was additionally synthesized as a control absent a reactive thiol. As the electrophile component, we selected a commercially available acrylamide fragment library (110

members with an average molecular weight = 235 Da, see **Appendix Table B.1** for structures). This was an attractive because the low intrinsic reactivity of acrylamides would ensure that the screen would selectively identify enzyme-templated reactions.[18-19] Conversely, electrophiles with high intrinsic reactivity (e.g., vinylsulfonamides) could produce undesired conjugates in the absence of enzyme.[19] Finally we chose c-Src, a non-receptor tyrosine kinase, as the initial target to develop our methodology. As already noted in **Chapter I**, c-Src has been validated as a target of importance in a variety of diseases including the metastasis of several cancers[20-21] and few selective inhibitors are available to study its biology.[5, 8] Most important, compound **2.1** is a competent inhibitor of c-Src (K_i = 0.36 ± 0.08 μM). To ensure that our assay would identify only acrylamides that react with **3.1** and not c-Src itself, we made a mutant c-Src kinase with three non-essential, solvent-accessible cysteines mutated to serines on the surface of c-Src ('3M' c-Src: C277S, C483S, C496S). Of note, we found that compound **3.1** is a time-dependent, irreversible inhibitor of wild-type c-Src, but not of 3M c-Src.

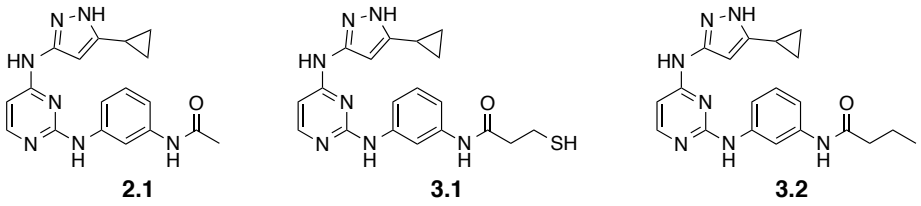

Figure 3.3. Structures of promiscuous kinase inhibitors **2.1**, **3.1** and **3.2**.

The library of 110 acrylamide fragments was incubated with 3M c-Src in the presence and absence of **3.1** (**3.1** was added at a concentration that approximates its IC_{20} value). Following a 30 min incubation, we used a continuous activity assay[22] to identify fragments that had significant inhibition difference (>2 standard deviations) between screens performed with and without thiol **3.1** (see **Appendix Table B.2** for primary screening data). From the 110 acrylamide fragments, we identified 4 hits that met our criteria (**Figure 3.4**, hit rate of 3.6%). Each of the four hits was confirmed in three subsequent enzyme-templated validation screens (see **Appendix Table B.3** for confirmation screening data).

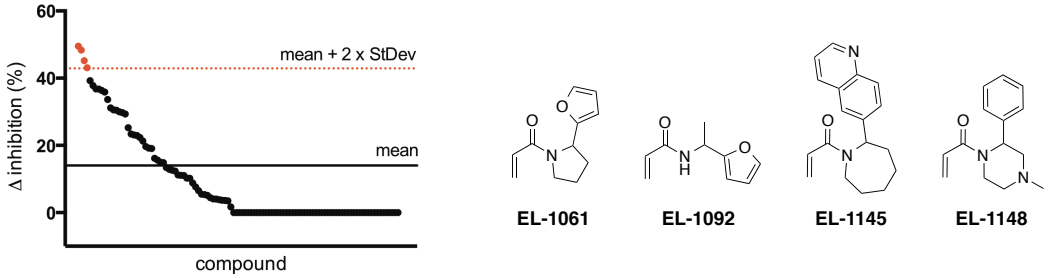

Figure 3.4. Graph of enzyme-templated screen using 3M c-Src and a library of 110 acrylamides (left). Structures of fragment hits (right).

Confirmation of Identified Hits

To demonstrate that the predicted enzyme-templated Michael additions were occurring, we performed a mass spectrometry analysis of thiol **3.1** + acrylamide **EL-1148** in the presence and absence of c-Src kinase. Only when c-Src was present could we detect a mass for the Michael adduct (compound **3.3**). We next synthesized **3.3** and found it to have improved binding potency compared to **3.2** and **EL-1148**, the individual starting fragments (**Figure 3.5**). Because **3.1** is an irreversible inhibitor of wild-type c-Src, we compared compound **3.2**, where the thiol of **3.1** is replaced with a carbon. Compound **3.2** (K_i = 0.40 ± 0.02 μM) was found to be less potent than bivalent inhibitor **3.3** (K_i = 0.09 ± 0.02 μM) for wt c-Src. To enable a comparison of thiol **3.1** with bivalent inhibitor **3.3**, we tested both for inhibition of 3M c-Src and found **3.3** to be a more potent inhibitor of this construct (**3.1**: 3M c-Src K_i = 0.20 ± 0.06 μM, **3.3**: 3M c-Src K_i = 0.12 ± 0.02 μM).

EL-1148, is a very weak inhibitor of c-Src (3M c-Src, IC_{50} = 470 ± 110 μM) but was readily identified in our method. In traditional fragment-based screening, it could be difficult to identify weak binding fragments using activity-based assays and even more difficult to discriminate between ATP-competitive and non-ATP-competitive fragments. Using biochemical activity assays, we further demonstrated that **EL-1148** is non-competitive with ATP, suggesting that it is binding in a pocket adjacent to the ATP pocket (see **Appendix Figure B.1**).

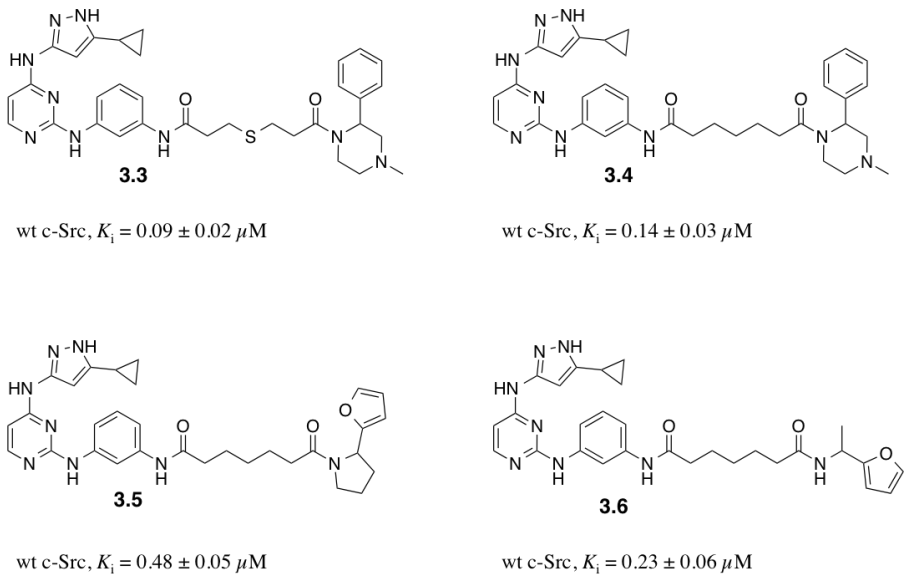

Figure 3.5. Structures of bivalent kinase inhibitors.

Inhibitor Construction and Selectivity Evaluation

Because thioethers can undergo retro-Michael reactions in assay buffer conditions (and thus lose inhibitory potency), we synthesized **3.4**, which contains an all-carbon linker between the two fragments (**Figure 3.5**). Gratifyingly, **3.4** was able to inhibit c-Src with identical potency as **3.3**. We then synthesized bivalent inhibitors, again using an all-carbon linker, derived from the two furan-containing fragments (**EL-1061** and **EL-1092**) that were identified in our enzyme-templated screen (bivalent inhibitors **3.5** and **3.6**, respectively). In addition, because both **3.5** and **3.6** are a mixture of enantiomers, we synthesized both R- and S- enantiomers (compounds **3.7**–**3.10**) of the furan-containing amine fragments and subsequently produced enantiopure bivalent inhibitors. The amines were synthesized using Ellman sulfinylimine chemistry (see Materials and Methods for details).[23-24] Upon characterization of the bivalent inhibitor series, we found that the bivalent inhibitors with R- stereochemistry had improved binding to c-Src (**Table 3.1**). A preference for a particular stereochemistry indicates specific binding to c-Src, despite the relatively weak binding observed with the acrylamide fragments.

Table 3.1. K_i values for **3.2** and enantiomerically pure bivalent kinase inhibitors. [a]Value is with 3M c-Src to avoid potential covalent labeling. [b]Not available due to potential covalent labeling of c-Yes with this inhibitor.

Compound	K_i Values, μM			
	c-Src	c-Yes	Hck	c-Abl
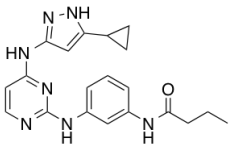 **3.2**	0.40 ± 0.02	0.47 ± 0.02	0.65 ± 0.11	0.98 ± 0.16
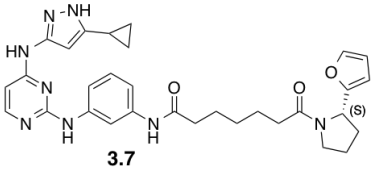 **3.7**	0.33 ± 0.05			
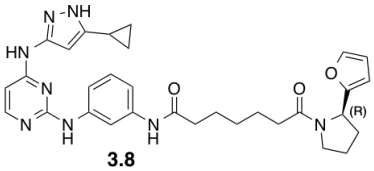 **3.8**	0.07 ± 0.02	0.61 ± 0.13	0.71 ± 0.03	0.73 ± 0.16
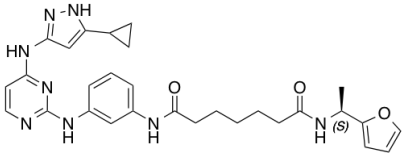 **3.9**	0.37 ± 0.02			
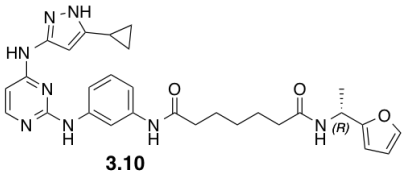 **3.10**	0.13 ± 0.06	0.80 ± 0.16	1.8 ± 0.1	1.2 ± 0.4
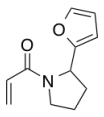 **EL-1061**	160 ± 20[a]	N/A[b]	>1250	>1250

Bivalent inhibitors **3.8** and **3.10** have 6- and 3-fold improvements in binding affinity for c-Src, respectively, compared to the control ATP-competitive fragment **3.2** (**Table 3.1**). We next sought to determine whether **3.8** and **3.10** had improved selectivity compared to fragment **3.2**. As a measure of selectivity, we assayed for inhibition against

a small panel of homologous kinases (c-Yes, 95% similar to c-Src; Hck, 80% similar to c-Src; c-Abl, 69% similar to c-Src). While **3.2** has virtually no selectivity within this panel (average selectivity = 1.8-fold), both **3.8** and **3.10** have dramatically improved selectivity (average selectivity = 9.5- and 9.4-fold, respectively). Compounds selective for c-Src over c-Yes have application in pharmacological manipulation of embryonic stem cells[25] and bivalent inhibitor **3.8** is the most selective c-Src over c-Yes inhibitor reported to date.[8, 26] In addition, while c-Src has been validated as a target in triple-negative breast cancer (TNBC)[8, 27] c-Abl has been reported to be a tumor suppressor in TNBC.[8, 28-29] Thus, compounds that have selectivity for c-Src over these homologous kinases will be useful probe compounds for the biology community.

To explore the role of the non-ATP-competitive fragment in providing selectivity to bivalent inhibitor **3.8**, we determined the selectivity of **EL-1061** (the parent fragment of **3.8**) in our homologous kinase panel. **EL-1061** is a weak inhibitor of 3M c-Src (K_i = 160 ± 20 μM), however, it was found not to inhibit Hck and c-Abl at concentrations up to 1,250 μM. Because c-Yes has a P-loop cysteine we cannot determine a reversible binding constant for this enzyme. Overall, fragment **EL-1061** has a >8-fold selectivity and that is consistent with the high selectivity obtained from bivalent inhibitor **3.8** (10-fold selectivity for c-Src over Hck and c-Abl).

It is worth noting that the potency gained going from **3.2** to **3.8** was modest (6-fold) and was at the expense of ligand efficiency (LE = 1.4(-log Ki)/(# Heavy Atoms)).[30] ATP-competitive inhibitor **3.2** has a LE = 0.32, while bivalent inhibitor **3.8** has a LE = 0.24. Despite lowering the overall ligand efficiency, there is a large increase in selectivity due to the addition of the non-ATP-competitive fragment. It is possible that with larger acrylamide fragment libraries (our library is only 110 members), a more optimal-binding fragment could be identified.

Predicted Binding Mode

On the basis of the selectivity data (**Table 3.1**), we propose that the non-ATP-competitive fragments are binding in the P-loop (also called the glycine-rich loop) pocket of c-Src (see **Appendix Figure B.2**). This pocket has previously been exploited to improve the selectivity of ATP-competitive kinase inhibitors, however, all previously

reported P-loop binding ligands were obtained using structure-based drug design.[8, 31] One of the key advantages of our methodology is that no structural information is required to identify fragments capable of assembling into bivalent inhibitors.[32] Our hypothesis is supported by structural information for analogs of **2.1** in which the amide functionality would be pointing in the direction of the P-loop pocket (**Appendix Figure B.2**). The P-loop of c-Src has a unique extended conformation resulting from a three-residue salt bridge between Lys272, Gln275, and Glu280.[33] We disrupted this salt bridge by mutating Glu280 to glycine, a mutation previously shown to modulate the P-loop conformation of Lyn, a Src-family kinase.[33] We produced E280G c-Src and tested the ability of bivalent inhibitor **3.8** to inhibit this construct of c-Src. Consistent with our hypothesis, we found that **3.8** is a four-fold weaker inhibitor (wt c-Src K_i = 0.07 ± 0.02 μM, E280G c-Src K_i = 0.26 ± 0.03 μM). Meanwhile, the potency of compound **2.1** (does not extend into P-loop pocket) is identical for this construct (wt c-Src K_i = 0.36 ± 0.08, E280G c-Src K_i = 0.41 ± 0.03 μM), illustrating that the hinge binding capabilities of the inhibitor scaffold is unaffected by this P-loop mutation. While our screen identified fragments proposed to bind in the P-loop pocket of c-Src, one could vary the linker length and/or position of the thiol to discover fragments that bind in other locations adjacent to the ATP pocket.

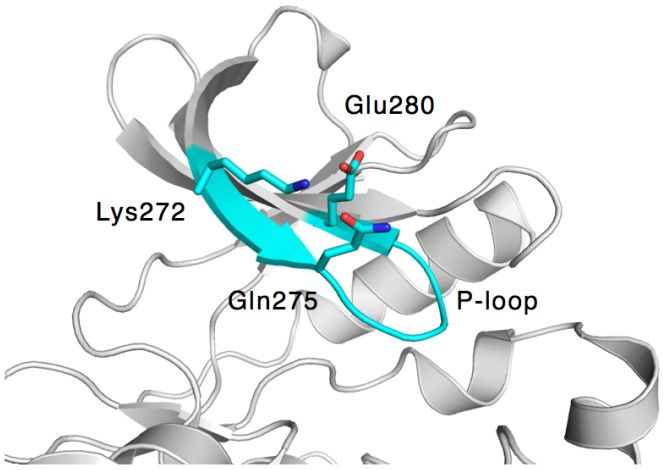

Figure 3.6. Illustration of three critical residues involved in the extended P-loop conformation of c-Src (PDB: 2SRC). When Glu280 is mutated to glycine, this extended conformation is predicted to collapse in toward the ATP pocket.

Conclusions

Herein, we have demonstrated the application of a fragment elaboration method using thiol–acrylamide chemistry to generate bivalent enzyme inhibitors. While this chemistry has been used in several applications in the past, we are the first group to use this type of system in a full-fledged fragment screening effort. We applied our method to c-Src kinase; however, our methodology could easily be applied to other kinases or enzyme systems, including proteases and phosphatases. The assembled bivalent inhibitors possess improved potency and selectivity compared to the starting fragments. This is a particularly important result, seeing as past inhibitor design efforts have struggled to improve specificity for a target amongst homologous kinases. Work applying this methodology to additional kinases targeted by **2.1** is the subject of further work by the laboratory.

Materials and Methods

General Synthetic Methods

Unless otherwise noted, all reagents were obtained via commercial sources and used without further purification. ^{1}H and ^{13}C NMR spectra were measured with a Varian MR400 or Inova 500 spectrometer. Mass spectrometry (HRMS) was carried out by the University of Michigan Mass Spectrometry Facility (J. Windak, director).

Synthetic Protocols

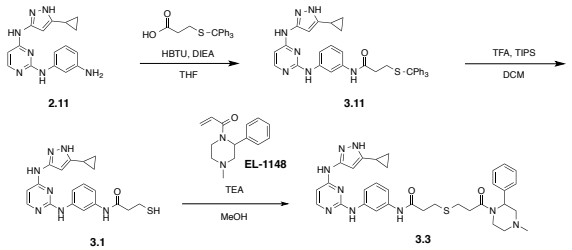

Scheme 3.1. Synthesis of compounds **3.1**, **3.3** and **3.11**.

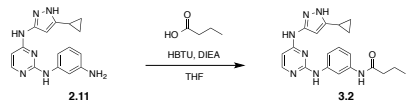

Scheme 3.2. Synthesis of compound **3.2**.

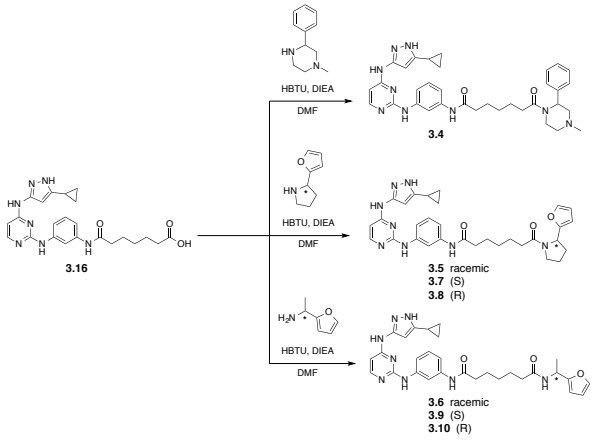

Scheme 3.3. Synthesis of compounds **3.4**–**3.10**.

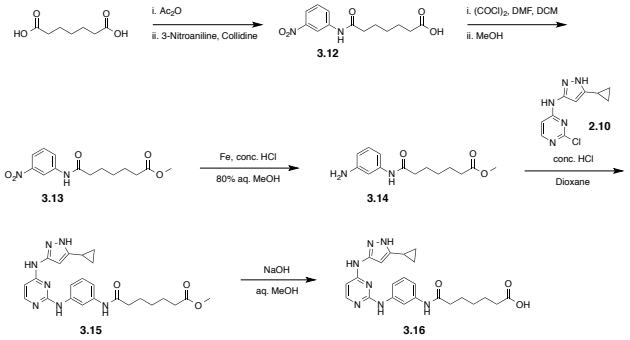

Scheme 3.4. Synthesis of compounds **3.12**–**3.16**.

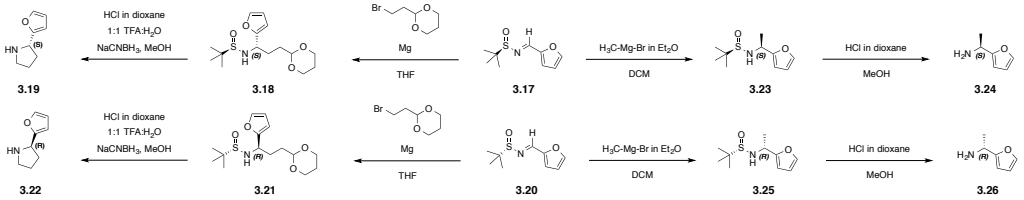

Scheme 3.5. Synthesis of compounds **3.17**–**3.26**.

Synthesis of **3.1**. Compound **3.11** (121 mg, 0.19 mmol) and TIPS (0.2 mL, 5%) were added into a 1:1 mixture of TFA:DCM (4 mL) and stirred at rt for 4 h. The solvent was removed and the crude material was suspended in Et_2O and filtered to yield the TFA salt

of the product. This was taken up in saturated $NaHCO_3$ aq. and extracted with EtOAc (3X), brine washed (1X) and dried over anhydrous Na_2SO_4 (s). Crude solid was HPLC purified (linear gradient of 5 → 95% CH_3CN in water) to yield compound **3.1** as a white solid (35 mg, 47% yield). **Spectral data**. ^{1}H NMR (400 MHz, DMSO-d_6) δ 11.98 (s, 1H), 9.90 (s, 1H), 9.59 (s, 1H), 9.13 (s, 1H), 7.97 (d, J = 5.7 Hz, 1H), 7.85 (s, 1H), 7.48 (d, J = 8.0 Hz, 1H), 7.24 (d, J = 8.2 Hz, 1H), 7.16 (t, J = 8.0 Hz, 1H), 6.55 (s, 1H), 6.34 (s, 1H), 2.74 (q, J = 7.2 Hz, 2H), 2.63 (t, J = 6.8 Hz, 2H), 2.37 (t, J = 7.9 Hz, 1H), 1.84 (tt, J = 8.8, 5.0 Hz, 1H), 0.89 (d, J = 8.2 Hz, 2H), 0.67 (d, J = 5.3 Hz, 2H). ^{13}C NMR (126 MHz, DMSO-d_6) δ 169.17, 159.49, 155.68, 141.19, 139.16, 128.45, 114.37, 112.34, 110.39, 98.32, 40.27, 39.09, 19.77, 7.70. HRMS-ESI (*m/z*): $[M + H]^+$ calcd for $C_{19}H_{21}N_7OS$, 396.1601; found 396.1606.

Synthesis of **3.2**. Compound **2.11** (11 mg, 0.036 mmol), HBTU (15 mg, 0.039 mmol), butyric acid (3.7 µL, 0.039 mmol) were dissolved in THF (1 mL) and followed by the addition of DIEA (6.9 µL, 0.039 mmol). Resulting mixture was kept at rt for 17 h. THF was removed and then the crude material was purified by automated silica gel chromatography (linear gradient of 50 → 100% EtOAc in hexanes) to yield compound **3.2** as a light tan solid (6.8 mg, 50% yield). **Spectral data**. ^{1}H NMR (500 MHz, $CDCl_3$:MeOH-d4) δ 7.77–7.73 (m, 1H), 7.62–7.58 (m, 1H), 7.15–7.06 (m, 3H), 6.14–6.02 (m, 1H), 5.72–5.53 (m, 1H), 2.16 (t, J = 7.6 Hz, 2H), 1.71–1.63 (m, 1H), 1.60–1.51 (m, 2H), 0.81 (t, J = 7.6 Hz, 3H), 0.78–0.73 (m, 2H), 0.55–0.50 (m, 2H). ^{13}C NMR (126 MHz, $CDCl_3$:MeOH-d4) δ 172.86, 159.20, 155.45, 139.90, 138.63, 128.95, 114.32, 111.80, 109.99, 97.57, 38.94, 38.25, 18.96, 13.33, 7.44. HRMS-ESI (*m/z*): $[M + H]^+$ calcd for $C_{20}H_{23}N_7O$, 378.2037; found 378.2035.

Synthesis of **3.3**. Compound **3.1** (35 mg, 90 µmol), **EL-1148** (5 mg, 20 µmol) and TEA (5 µL, 30 µmol) were added to a flame-dried flask that was flushed with N_2, followed by addition of anhydrous MeOH (0.6 mL). Resulting mixture was stirred at rt for 2 h, organics removed and then purified via reverse-phase chromatography (linear gradient of 20 → 80% CH_3CN in H_2O) to yield compound **3.3** as a white solid (10 mg, 74% yield). **Spectral data**. ^{1}H NMR (400 MHz, DMSO-d_6) δ 11.96 (s, 1H), 9.88 (s, 1H), 9.47 (s,

1H), 9.03 (s, 1H), 7.96 (s, 1H), 7.81 (s, 1H), 7.48 (d, *J* = 8.2 Hz, 1H), 7.38 – 7.24 (m, 3H), 7.24 – 7.19 (m, 2H), 7.19 – 7.11 (m, 1H), 6.40 (s, 2H), 5.61 (s, 1H), 4.28 (s, 1H), 3.72 (d, *J* = 13.3 Hz, 1H), 3.12 – 2.96 (m, 1H), 2.87 – 2.65 (m, 6H), 2.65 – 2.53 (m, 2H), 2.14 (s, 3H), 1.98 – 1.89 (m, 1H), 1.84 (tt, *J* = 8.6, 5.0 Hz, 1H), 0.95 – 0.80 (m, 2H), 0.73 – 0.61 (m, 2H). ^{13}C NMR (126 MHz, DMSO-d_6) δ 169.40, 159.47, 155.66, 141.15, 139.93, 139.21, 128.40, 128.13, 127.30, 126.51, 114.44, 112.28, 110.19, 98.32, 56.88, 54.89, 54.42, 50.26, 45.71, 41.21, 39.08, 36.82, 33.24, 32.80, 27.15, 26.87, 7.69, 6.96. HRMS-ESI (*m/z*): $[M + H]^+$ calcd for $C_{33}H_{39}N_9O_2S$, 626.3020; found 626.3021.

Synthesis of **3.4**. Compound **3.16** (15 mg, 33 μmol), 1-methyl-3-phenylpiperazine (7 mg, 40 μmol) and HBTU (15 mg, 40 μmol) were added to a flame-dried flask that was flushed with N_2, followed by addition of DIEA (7 μL, 40 μmol) and anhydrous DMF (1.5 mL). Resulting mixture was stirred at rt for 3 h, filtered and then purified via reverse-phase chromatography (linear gradient of 5 → 90% CH_3CN in H_2O) to yield compound **3.4** as a white solid (17 mg, 81% yield). **Spectral data**. ^{1}H NMR (400 MHz, DMSO-d_6) δ 11.95 (s, 1H), 9.77 (s, 1H), 9.47 (s, 1H), 9.01 (s, 1H), 7.96 (s, 1H), 7.81 (s, 1H), 7.51 – 7.43 (m, 1H), 7.37 – 7.26 (m, 3H), 7.26 – 7.18 (m, 2H), 7.18 – 7.11 (m, 1H), 6.35 (s, 2H), 5.62 (s, 1H), 3.71 (d, *J* = 13.2 Hz, 1H), 3.10 – 2.99 (m, 1H), 2.70 (d, *J* = 10.9 Hz, 1H), 2.41 (s, 2H), 2.34 – 2.24 (m, 3H), 2.15 (s, 4H), 1.92 (s, 1H), 1.84 (tt, *J* = 8.5, 5.1 Hz, 1H), 1.65 – 1.50 (m, 4H), 1.40 – 1.27 (m, 3H), 0.89 (d, *J* = 8.0 Hz, 3H), 0.67 (d, *J* = 5.2 Hz, 2H). ^{13}C NMR (126 MHz, DMSO-d_6) δ 174.92, 171.50, 171.15, 159.38, 157.84, 140.08, 139.60, 137.56, 128.71, 128.52, 127.14, 126.53, 125.28, 115.48, 113.00, 111.10, 98.42, 54.88, 53.68, 53.30, 49.07, 44.10, 36.30, 32.00, 28.40, 25.01, 24.49, 7.74, 7.15. HRMS-ESI (*m/z*): $[M + H]^+$ calcd for $C_{34}H_{41}N_9O_2$, 608.3456; found 608.3457.

Synthesis of **3.5**. Compound **3.16** (60 mg, 0.13 mmol), 2-(2-furyl)pyrrolidine HCl (26 mg, 0.15 mmol) and HBTU (56 mg, 0.15 mmol) were added to a flame-dried flask that was flushed with N_2, followed by addition of DIEA (51 μL, 0.29 mmol) and anhydrous DMF (1 mL). Resulting mixture was stirred at rt for 19 h and then purified via reverse-phase chromatography (linear gradient of 20 → 100% CH_3CN in H_2O) to yield compound **3.5** as an off-white solid (38 mg, 50% yield). **Spectral data**. ^{1}H NMR (400

MHz, DMSO-d_6) δ 12.01 (s, 1H), 9.77 (d, J = 10.9 Hz, 1H), 9.65 (s, 1H), 9.14 (s, 1H), 7.97 (d, J = 5.7 Hz, 1H), 7.83 (s, 1H), 7.47 (d, J = 9.1 Hz, 1H), 7.23 (t, J = 6.3 Hz, 1H), 7.14 (t, J = 8.0 Hz, 1H), 6.40 – 6.24 (m, 2H), 5.12 – 5.02 (m, 1H), 3.61 (dt, J = 10.5, 5.2 Hz, 1H), 3.52 – 3.35 (m, 1H), 2.35 – 2.09 (m, 4H), 2.11 – 1.78 (m, 4H), 1.59 (p, J = 7.3 Hz, 1H), 1.49 (dq, J = 15.4, 7.6 Hz, 2H), 1.45 – 1.26 (m, 1H), 1.19 (dt, J = 14.2, 7.6 Hz, 1H), 0.88 (dt, J = 8.8, 3.2 Hz, 2H), 0.71 – 0.63 (m, 2H). ^{13}C NMR (126 MHz, DMSO-d_6) δ 171.10, 159.56, 155.78, 142.32, 141.34, 141.14, 139.43, 128.38, 114.29, 112.34, 110.42, 110.22, 105.95, 105.30, 98.29, 54.44, 53.56, 46.09, 45.61, 36.33, 33.70, 33.23, 32.38, 30.31, 28.43, 25.09, 24.31, 24.09, 23.78, 21.96, 7.72. HRMS-ESI (*m/z*): $[M + H]^+$ calcd for $C_{31}H_{36}N_8O_3$, 569.2983; found 569.2975.

Synthesis of **3.6**. This compound was prepared as a 1:1 DMSO mixture of compounds **3.9** and **3.10** prior to biochemical testing.

Synthesis of **3.7**. Compound **3.16** (33 mg, 0.073 mmol), compound **3.19** (14 mg, 0.081 mmol) and HBTU (31 mg, 0.081 mmol) were added to a flame-dried flask that was flushed with N_2, followed by addition of DIEA (28 μL, 0.162 mmol) and anhydrous DMF (1 mL). Resulting mixture was stirred at rt for 4 h and then purified via reverse-phase chromatography (linear gradient of 20 → 100% CH_3CN in H_2O) to yield compound **3.7** as a white solid (7.9 mg, 19% yield). **Spectral data**. ^{1}H NMR (500 MHz, DMSO-d_6) δ 11.90 (s, 1H), 9.76 (d, J = 13.7 Hz, 1H), 9.64 (s, 1H), 9.12 (s, 1H), 8.00 – 7.94 (m, 1H), 7.83 (s, 1H), 7.51 – 7.44 (m, 2H), 7.22 (s, 1H), 7.14 (t, J = 8.0 Hz, 1H), 6.37 (q, J = 2.8, 2.4 Hz, 0H), 6.35 (s, 2H), 6.31 (t, J = 2.5 Hz, 0H), 6.06 (d, J = 3.2 Hz, 0H), 5.07 (dd, J = 14.9, 7.7 Hz, 1H), 3.61 (s, 1H), 3.51 – 3.34 (m, 2H), 2.32 – 2.24 (m, 4H), 2.26 – 2.11 (m, 1H), 2.02 (s, 1H), 1.94 (dq, J = 10.5, 6.1, 5.2 Hz, 1H), 1.89 – 1.79 (m, 3H), 1.59 (t, J = 7.7 Hz, 1H), 1.51 (q, J = 7.8 Hz, 2H), 1.35 – 1.28 (m, 1H), 1.25 – 1.17 (m, 1H), 0.88 (dq, J = 6.8, 3.6 Hz, 2H), 0.67 (dp, J = 6.3, 3.7 Hz, 2H). ^{13}C NMR (126 MHz, dmso) δ 171.08, 170.98, 170.54, 159.60, 155.82, 142.33, 141.34, 141.13, 139.42, 128.36, 112.31, 110.41, 110.22, 105.95, 105.30, 98.28, 54.43, 53.55, 46.09, 45.60, 36.33, 33.69, 33.22, 32.38, 30.30, 28.44, 28.40, 25.10, 24.30, 24.08, 23.78, 21.96, 7.71. HRMS-ESI (*m/z*): $[M + H]^+$ calcd for $C_{31}H_{36}N_8O_3$, 569.2983; found 569.2982.

Synthesis of **3.8**. Compound **3.16** (70 mg, 0.16 mmol), compound **3.22** (22 mg, 0.164 mmol) and HBTU (65 mg, 0.17 mmol) were added to a flame-dried flask that was flushed with N_2, followed by addition of DIEA (30 µL, 0.17 mmol) and anhydrous DMF (1 mL). Resulting mixture was stirred at rt for 4 h and then purified via reverse-phase chromatography (linear gradient of 5 → 100% CH_3CN in H_2O) to yield compound **3.8** as a white solid (12 mg, 14% yield). **Spectral data**. ^{1}H NMR (500 MHz, DMSO-d_6) δ 11.97 (s, 1H), 9.77 (d, *J* = 13.5 Hz, 1H), 9.52 (s, 1H), 9.07 (s, 1H), 7.97 (d, *J* = 5.7 Hz, 1H), 7.84 (s, 1H), 7.66 – 7.51 (m, 1H), 7.47 (dd, *J* = 8.7, 4.7 Hz, 1H), 7.24 (d, *J* = 8.5 Hz, 1H), 7.14 (t, *J* = 8.0 Hz, 1H), 6.40 – 6.25 (m, 3H), 6.21 (d, *J* = 3.2 Hz, 0H), 6.06 (d, *J* = 3.2 Hz, 0H), 5.11 – 5.02 (m, 1H), 3.61 (dt, *J* = 10.6, 5.2 Hz, 1H), 3.58 (s, 1H), 3.53 – 3.34 (m, 1H), 2.35 – 2.25 (m, 3H), 2.28 – 2.10 (m, 2H), 2.08 – 1.89 (m, 2H), 1.84 (td, *J* = 9.3, 8.5, 4.9 Hz, 2H), 1.63 – 1.56 (m, 1H), 1.58 – 1.31 (m, 3H), 1.33 – 1.26 (m, 1H), 1.20 (ddt, *J* = 11.4, 7.9, 3.7 Hz, 1H), 1.10 (t, *J* = 7.2 Hz, 0H), 0.88 (d, *J* = 8.1 Hz, 2H), 0.73 – 0.63 (m, 2H). ^{13}C NMR (126 MHz, DMSO-d_6) δ 171.16, 171.03, 170.59, 159.58, 155.82, 142.34, 141.36, 141.14, 139.44, 128.40, 112.36, 110.44, 110.24, 105.97, 105.32, 98.30, 54.46, 53.58, 46.12, 45.63, 36.33, 33.72, 33.64, 32.40, 30.32, 28.46, 25.12, 24.10, 23.79, 21.98, 7.74. HRMS-ESI (*m/z*): $[M + H]^+$ calcd for $C_{31}H_{36}N_8O_3$, 569.2983; found 569.2980.

Synthesis of **3.9**. Compound **3.16** (15 mg, 33 µmol), compound **3.24** (6 mg, 40 µmol) and HBTU (15 mg, 40 µmol) were added to a flame-dried flask that was flushed with N_2, followed by addition of DIEA (14 µL, 80 µmol) and anhydrous DMF (1.5 mL). Resulting mixture was stirred at rt for 3 h and then purified via reverse-phase chromatography (linear gradient of 5 → 95% CH_3CN in H_2O) to yield compound **3.9** as a white solid (13 mg, 69% yield). **Spectral data.** ^{1}H NMR (400 MHz, DMSO-d_6) δ 11.96 (s, 1H), 9.78 (s, 1H), 9.50 (s, 1H), 9.03 (s, 1H), 8.17 (d, *J* = 8.4 Hz, 1H), 7.96 (s, 1H), 7.81 (s, 1H), 7.54 (d, *J* = 1.8 Hz, 1H), 7.47 (d, *J* = 8.0 Hz, 1H), 7.24 (d, *J* = 8.0 Hz, 1H), 7.15 (t, *J* = 8.0 Hz, 1H), 6.38 – 6.33 (m, 1H), 6.18 (d, *J* = 3.2 Hz, 1H), 4.99 (p, *J* = 7.0 Hz, 1H), 2.29 (t, *J* = 7.4 Hz, 2H), 2.09 (t, *J* = 7.4 Hz, 2H), 1.84 (tt, *J* = 8.4, 4.9 Hz, 1H), 1.55 (dp, *J* = 22.3, 7.4 Hz, 4H), 1.32 (d, *J* = 7.2 Hz, 3H), 1.30 – 1.21 (m, 2H), 0.89 (d, *J* = 7.6 Hz, 2H), 0.67 (d,

J = 5.3 Hz, 2H). ^{13}C NMR (126 MHz, dmso) δ 171.24, 171.07, 156.39, 145.41, 141.71, 139.46, 128.39, 117.46, 114.83, 112.62, 110.18, 104.99, 98.34, 41.62, 36.28, 35.15, 28.30, 25.09, 24.95, 19.39, 7.69. HRMS-ESI (*m/z*): $[M + H]^+$ calcd for $C_{29}H_{34}N_8O_3$, 543.2827 found 543.2819.

Synthesis of **3.10**. Compound **3.16** (15 mg, 33 μmol), compound **3.26** (6 mg, 40 μmol) and HBTU (15 mg, 40 μmol) were added to a flame-dried flask that was flushed with N_2, followed by addition of DIEA (14 μL, 80 μmol) and anhydrous DMF (1.5 mL). Resulting mixture was stirred at rt for 3 h and then purified via reverse-phase chromatography (linear gradient of 5 → 90% CH_3CN in H_2O) to yield compound **3.10** as a white solid (8 mg, 44% yield). **Spectral data.** ^{1}H NMR (500 MHz, DMSO-d_6) δ 11.96 (s, 1H), 9.77 (s, 1H), 9.48 (s, 1H), 9.02 (s, 1H), 8.17 (d, *J* = 8.3 Hz, 1H), 7.95 (s, 1H), 7.79 (s, 1H), 7.55 (d, *J* = 1.8 Hz, 1H), 7.50 – 7.44 (m, 1H), 7.24 (s, 1H), 7.15 (d, *J* = 8.3 Hz, 1H), 6.35 (dd, *J* = 3.3, 1.8 Hz, 1H), 6.18 (d, *J* = 3.2 Hz, 1H), 4.99 (p, *J* = 7.2 Hz, 1H), 2.29 (t, *J* = 7.4 Hz, 2H), 2.09 (t, *J* = 7.4 Hz, 2H), 1.84 (tt, *J* = 8.6, 5.0 Hz, 1H), 1.55 (dp, *J* = 22.9, 7.6 Hz, 4H), 1.33 (d, *J* = 7.2 Hz, 3H), 1.31 – 1.24 (m, 2H), 0.90 (s, 2H), 0.68 (s, 2H). ^{13}C NMR (126 MHz, DMSO-d_6) δ 171.39, 171.32, 156.42, 146.28, 141.77, 139.99, 129.00, 117.42, 115.10, 112.74, 110.24, 105.05, 98.94, 41.67, 36.35, 35.17, 28.31, 25.11, 24.94, 19.42, 8.58, 7.86. HRMS-ESI (*m/z*): $[M + H]^+$ calcd for $C_{29}H_{34}N_8O_3$, 543.2827 found 543.2822.

Synthesis of **3.11**. Compound **2.11** (418 mg, 1.36 mmol), HBTU (567 mg, 1.5 mmol), *S*-tritylpropionic acid (497 mg, 1.43 mmol) were dissolved in THF (13 mL) and followed by the addition of DIEA (0.26 mL, 1.5 mmol). Resulting mixture was kept at rt for 3.5 h. THF was removed and the crude material was taken up in EtOAc, brine washed (1X) and dried over anhydrous Na_2SO_4 (s). This was filtered prior to solvent removal to yield crude **3.11** product. This was purified by automated silica gel chromatography (linear gradient of 40 → 90% EtOAc in hexanes) to yield compound **3.11** as an off-white solid (314 mg, 36% yield). **Spectral data**. ^{1}H NMR (400 MHz, DMSO-d_6) δ 11.96 (s, 1H), 9.83 (s, 1H), 9.50 – 9.45 (m, 1H), 9.02 (s, 1H), 7.95 (d, *J* = 5.9 Hz, 1H), 7.77 (s, 1H), 7.48 (d, *J* = 8.3 Hz, 1H), 7.39 – 7.29 (m, 12H), 7.29 – 7.19 (m, 4H), 7.19 – 7.10 (m, 1H), 6.41 (s, 1H), 6.32 (s, 1H), 2.42 (t, *J* = 7.2 Hz, 2H), 2.34 (t, *J* = 7.3 Hz, 2H), 1.83 (tt, *J* =

8.7, 5.0 Hz, 1H), 0.87 (t, *J* = 12.3 Hz, 2H), 0.67 (d, *J* = 5.7 Hz, 2H). ^{13}C NMR (126 MHz, DMSO-d_6) δ 168.92, 159.63, 155.73, 148.22, 145.37, 144.43, 141.18, 139.05, 129.09, 128.33, 128.04, 126.73, 114.63, 112.26, 110.40, 98.33, 92.97, 66.08, 38.25, 35.05, 27.37, 7.69, 6.87. HRMS-ESI (*m/z*): $[M + H]^+$ calcd for $C_{38}H_{35}N_7OS$, 638.2697; found 638.2706.

Synthesis of **3.12**. Pimelic acid (4 g, 25 mmol) and Ac_2O (24 mL, 250 mmol) were dissolved in THF (60 mL) and refluxed for 2 h using a heating mantle. Organics were distilled off and toluene was added (3X) and distilled away to ensure complete Ac_2O removal. Crude material was taken up in THF (60 mL) and had 3-nitroaniline (2.88 g, 20.8 mmol) added to it followed by collidine (5.5 mL, 41.6 mmol). The reaction was stirred for 12 h at rt prior to organic solvent removal. The crude had 1N NaOH added to it and the aqueous layer was washed with Et_2O (6X) before acidifying the mixture (pH < 5) to allow an off-white solid to precipitate out, which was collected via vacuum filtration (2.83 g, 49% yield). **Spectral data**. ^{1}H NMR (400 MHz, DMSO-d_6) δ 12.00 (s, 1H), 10.38 (s, 1H), 8.64 (t, *J* = 2.2 Hz, 1H), 7.89 (ddd, *J* = 7.2, 4.2, 2.3 Hz, 2H), 7.59 (t, *J* = 8.2 Hz, 1H), 2.35 (t, *J* = 7.4 Hz, 2H), 2.21 (t, *J* = 7.3 Hz, 2H), 1.61 (h, *J* = 8.2, 7.6 Hz, 2H), 1.52 (p, *J* = 7.4 Hz, 2H), 1.31 (qd, *J* = 9.9, 9.1, 6.1 Hz, 2H). ^{13}C NMR (126 MHz, DMSO-d_6) δ 174.44, 171.95, 147.94, 140.41, 130.09, 124.91, 117.47, 113.04, 36.29, 33.54, 28.16, 24.66, 24.27. HRMS-ESI (*m/z*): $[M + H]^+$ calcd for $C_{13}H_{16}N_2O_5$, 281.1132; found 281.1134.

Synthesis of **3.13**. Compound **3.12** (1.8 g, 6.43 mmol) had DCM (60 mL) added to it followed by $(COCl)_2$ (0.66 mL, 7.71 mmol) and DMF (0.1 mL) addition. After 1.5 h of stirring at rt, the flask was cooled to 0 ^{o}C and then MeOH (10 mL) was slowly added in over 15 min. The flask was warmed to rt and allowed to stir for 2.5 h. The organic layer was directly washed with saturated $NaHCO_3$ aq. (1X) and brine (1X) before being dried over anhydrous Na_2SO_4 (s). Product was concentrated on SiO_2 and purified by automated silica gel chromatography (linear gradient of 0 → 60% EtOAc in hexanes) to yield compound **3.13** as a pale yellow solid (1.51 g, 80% yield). **Spectral data**. ^{1}H NMR (500 MHz, Chloroform-*d*) δ 8.37 (t, *J* = 2.2 Hz, 1H), 8.00 (dt, *J* = 8.2, 1.4 Hz, 1H), 7.92 (ddd,

J = 8.3, 2.2, 1.0 Hz, 1H), 7.66 (s, 1H), 7.46 (t, *J* = 8.2 Hz, 1H), 3.67 (s, 3H), 2.41 (t, *J* = 7.3 Hz, 2H), 2.34 (t, *J* = 7.2 Hz, 2H), 1.74 (q, *J* = 7.4 Hz, 2H), 1.66 (p, *J* = 7.3 Hz, 2H), 1.41 (tt, *J* = 9.4, 6.4 Hz, 2H). ^{13}C NMR (126 MHz, Chloroform-*d*) δ 172.05, 139.39, 129.90, 125.62, 118.72, 114.56, 51.78, 37.21, 33.78, 28.49, 25.08, 24.33. HRMS-ESI (*m/z*): $[M + H]^+$ calcd for $C_{14}H_{18}N_2O_5$, 295.1288; found 295.1300.

Synthesis of **3.14**. Compound **3.13** (455 mg, 1.55 mmol), iron (433 mg, 7.73 mmol) and conc. HCl (0.1 mL) were combined with 80% MeOH aq. (20 mL) and heated to 80 ^{o}C for 3 h. The hot solution was filtered through celite prior to MeOH removal. Resulting aqueous layer was basicified using saturated $NaHCO_3$ aq. (30 mL) and the product was extracted using EtOAc (3X), brine washed (1X) and dried over anhydrous Na_2SO_4 (s). Organics were removed to reveal the final product as a tan solid (298 mg, 73% yield). **Spectral data**. ^{1}H NMR (500 MHz, Chloroform-*d*) δ 7.17 (t, *J* = 2.2 Hz, 1H), 7.11 (s, 1H), 7.04 (t, *J* = 8.0 Hz, 1H), 6.62 (dd, *J* = 8.3, 2.0 Hz, 1H), 6.40 (dd, *J* = 7.7, 2.2 Hz, 1H), 3.67 (s, 2H), 3.64 (s, 3H), 2.31 (t, *J* = 7.4 Hz, 4H), 1.69 (dq, *J* = 31.7, 7.6 Hz, 4H), 1.38 (qd, *J* = 9.5, 8.8, 6.4 Hz, 2H). ^{13}C NMR (126 MHz, Chloroform-*d*) δ 171.41, 147.34, 139.15, 129.70, 110.99, 109.76, 106.66, 51.64, 37.48, 33.89, 28.68, 25.27, 24.59. HRMS-ESI (*m/z*): $[M + H]^+$ calcd for $C_{14}H_{20}N_2O_3$, 265.1547; found 265.1556.

Synthesis of **3.15**. Compound **2.10** (528 mg, 2.24 mmol) was added to a flame-dried flask that was flushed with N_2, followed by addition of anhydrous dioxane (25 mL), compound **3.14** (650 mg, 2.46 mmol) and HCl (0.1 mL). The contents of the flask were heated to 80 ^{o}C for 12 h and cooled to rt. Dioxane was removed, then the crude material was precipitated using saturated $NaHCO_3$ aq. and vacuum filtered. This crude solid was purified by automated silica gel chromatography (linear gradient of 80 → 100% EtOAc in hexanes) to yield compound **3.15** as an off-white solid (822 mg, 79% yield). **Spectral data**. ^{1}H NMR (400 MHz, DMSO-d6) δ 11.95 (s, 1H), 9.77 (s, 1H), 9.47 (s, 1H), 9.01 (s, 1H), 7.97 (s, 1H), 7.81 (s, 1H), 7.51 – 7.43 (m, 1H), 7.25 – 7.19 (m, 1H), 7.14 (t, *J* = 8.0 Hz, 1H), 6.35 (s, 2H), 3.57 (s, 3H), 2.30 (q, *J* = 7.5 Hz, 4H), 1.84 (td, *J* = 8.4, 4.2 Hz, 1H), 1.64 – 1.49 (m, 4H), 1.30 (p, *J* = 7.6 Hz, 2H), 0.89 (d, *J* = 8.1 Hz, 2H), 0.67 (d, *J* = 5.3 Hz, 2H). ^{13}C NMR (126 MHz, DMSO-d_6) δ 173.32, 170.99, 159.54, 155.74, 148.25,

145.43, 141.11, 139.38, 128.35, 114.38, 112.33, 110.31, 98.29, 93.01, 51.17, 36.21, 33.18, 28.15, 24.85, 24.24, 7.69, 6.95. HRMS-ESI (*m/z*): $[M + H]^+$ calcd for $C_{24}H_{29}N_7O_3$, 464.2405; found 464.2402.

Synthesis of **3.16**. Compound **3.15** (79 mg, 0.17 mmol) and NaOH (27 mg, 0.68 mmol) were combined with 33% MeOH aq. (9 mL) and heated to 80 ^oC for 3 h. MeOH was removed in vacuo and then 2N HCl added to adjust the pH to 2–5. Precipitate that formed was vacuum filtered to reveal the product as a white solid (57 mg, 75% yield). **Spectral data**. ^1H NMR (500 MHz, DMSO-d_6) δ 12.06 (s, 1H), 9.82 (s, 1H), 9.29 (s, 1H), 7.96 (d, J = 5.9 Hz, 1H), 7.83 (s, 1H), 7.44 (d, J = 8.0 Hz, 1H), 7.25 (d, J = 8.1 Hz, 1H), 7.17 (t, J = 8.1 Hz, 1H), 6.36 (s, 1H), 6.11 (s, 1H), 2.29 (t, J = 7.4 Hz, 2H), 2.21 (t, J = 7.3 Hz, 2H), 1.83 (td, J = 8.5, 4.3 Hz, 1H), 1.55 (dp, J = 29.8, 7.5 Hz, 4H), 1.35 – 1.25 (m, 2H), 0.93 – 0.85 (m, 2H), 0.69 – 0.62 (m, 2H) ppm. ^{13}C NMR (126 MHz, DMSO-d_6) δ 174.48, 171.06, 159.32, 155.54, 147.28, 146.16, 141.04, 139.42, 128.40, 114.29, 112.43, 110.27, 98.31, 91.54, 36.28, 33.60, 28.27, 24.95, 24.34, 7.72, 7.54. HRMS-ESI (*m/z*): $[M + H]^+$ calcd for $C_{23}H_{27}N_7O_3$, 450.2248; found 450.2260.

Synthesis of **3.17**. This compound was prepared as previously reported.[23]

Synthesis of **3.18**. Crushed magnesium turnings (1185 mg, 48.8 mmol) were flame-dried with catalytic amounts of I_2 in the RBF and subsequently suspended in anhydrous THF (3M, 16 mL). 2-(2-Bromoethyl)-1,3-dioxane (2.22 mL, 16.3 mmol) in THF (3M, 5.5 mL) was added dropwise and the reaction was kept in a rt water bath for 1 h with stirring. The solution was transferred to a new flask and promptly cooled to -48 ^oC. Compound **S9** (648 mg, 3.25 mmol) dissolved in THF (1M, 3.25 mL) was added dropwise to the Grignard solution. The reaction was kept at -48 ^oC for ~2 h and allowed to warm to rt overnight. After 13 h the reaction was quenched with saturated NH_4Cl aq. and EtOAc extracted (3X), brine washed (1X) and dried over anhydrous Na_2SO_4 (s). Product was purified by automated silica gel chromatography (linear gradient of 20 → 60% EtOAc in hexanes) to yield compound **3.18** as a pale yellow oil (868 mg, 85% yield). **Spectral data**. ^1H NMR (400 MHz, Chloroform-*d*) δ 7.32 (s, 1H), 6.29 – 6.23 (m, 2H), 4.48 (q, J

= 4.4 Hz, 1H), 4.40 – 4.30 (m, 1H), 4.14 – 4.00 (m, 2H), 3.70 (t, *J* = 12.0 Hz, 2H), 3.46 (d, *J* = 6.9 Hz, 1H), 2.00 (tdd, *J* = 17.0, 11.4, 6.4 Hz, 3H), 1.62 (dq, *J* = 23.8, 8.8, 7.7 Hz, 2H), 1.25 – 1.20 (m, 1H), 1.17 (s, 9H). ^{13}C NMR (126 MHz, Chloroform-*d*) δ 154.81, 142.00, 110.19, 107.00, 101.63, 66.80, 56.03, 53.82, 31.32, 29.13, 25.68, 22.55. HRMS-ESI (*m/z*): $[M + H]^+$ calcd for $C_{15}H_{25}NO_4S$, 316.1577; found 316.1576.

Synthesis of **3.19**. Compound **3.18** (120 mg, 0.38 mmol) was taken up in MeOH (2 mL) with 0.25 mL of 4N HCl in dioxane added in and stirred for 1 h at rt. The organics were removed in vacuo and then TFA:H_2O (4 mL, 1:1) was added in along with MeOH (2 mL) and the mixture was stirred for 3 h at rt. The TFA was removed in vacuo and then the aqueous layer was neutralized with 6N NaOH prior to MeOH (2 mL) and $NaCNBH_3$ (239 mg, 3.8 mmol) addition. This mixture was stirred at rt for 16 h. Organics were removed and crude material was basicified with 1N NaOH, EtOAc extracted (4X), brine washed (1X) and dried over anhydrous Na_2SO_4 (s). Product was purified by silica gel chromatography (isocratic gradient of 10% MeOH in EtOAc with NH_3 in MeOH added) to yield compound **S11** as an oil. The free base of the product was briefly taken up in 4N HCl in dioxane (1 mL), which was then removed and the HCl salt precipitated out upon Et_2O (10 mL) addition to yield compound **3.19** as an off-white solid (64 mg, 58% yield). **Spectral data**. ^{1}H NMR (400 MHz, DMSO-d_6) δ 10.38 (s, 1H), 9.20 (s, 1H), 7.77 (d, *J* = 1.8 Hz, 1H), 6.65 (d, *J* = 3.4 Hz, 1H), 6.51 (dd, *J* = 3.3, 1.9 Hz, 1H), 4.68 (q, *J* = 7.6, 7.1 Hz, 1H), 3.26 – 3.13 (m, 2H), 2.33 – 2.22 (m, 1H), 2.17 – 2.02 (m, 2H), 1.97 (dtd, *J* = 11.9, 8.1, 7.7, 3.9 Hz, 1H). ^{13}C NMR (126 MHz, DMSO-d_6) δ 148.90, 14.09, 111.02, 110.03, 54.72, 44.57, 28.74, 23.47. HRMS-EI (*m/z*): $[M]^+$ calcd for $C_8H_{11}NO$, 137.0841; found 137.0846.

Synthesis of **3.20**. This compound was prepared as previously reported.[23]

Synthesis of **3.21**. Prepared in an analogous way to **3.18**. Crushed magnesium turnings (1622 mg, 66.8 mmol) were flame-dried with catalytic amounts of I_2 in the RBF and subsequently suspended in anhydrous THF (3M, 22 mL). 2-(2-Bromoethyl)-1,3-dioxane (3 mL, 22.2 mmol) in THF (3M, 7.5 mL) was added dropwise and the reaction was kept

in a rt water bath for 1 h with stirring. The solution was transferred to a new flask and promptly cooled to -48 ^{o}C. Compound **3.20** (886 mg, 4.5 mmol) dissolved in THF (1M, 4.5 mL) was added dropwise to the Grignard solution. The reaction was kept at -48 ^{o}C for ~2 h and allowed to warm to rt overnight. After 13 h the reaction was quenched with saturated NH_4Cl aq. and EtOAc extracted (3X) and brine washed (1X) and dried over anhydrous Na_2SO_4 (s). Product was purified by automated silica gel chromatography (linear gradient of 20 → 60% EtOAc in hexanes) to yield compound **3.21** as a slight yellow oil (920 mg, 66% yield). **Spectral data**. ^{1}H NMR (400 MHz, Chloroform-*d*) δ 7.32 (dt, *J* = 1.7, 0.8 Hz, 1H), 6.30 – 6.22 (m, 2H), 4.48 (t, *J* = 5.0 Hz, 1H), 4.35 (q, *J* = 7.0 Hz, 1H), 4.05 (ddd, *J* = 12.1, 5.3, 1.4 Hz, 2H), 3.71 (td, *J* = 12.4, 2.4 Hz, 2H), 3.47 (d, *J* = 6.8 Hz, 1H), 2.11 – 1.87 (m, 3H), 1.72 – 1.49 (m, 2H), 1.32 – 1.26 (m, 1H), 1.18 (s, 9H). ^{13}C NMR (126 MHz, Chloroform-*d*) δ 154.89, 142.16, 110.32, 107.15, 101.79, 66.97, 56.15, 53.94, 31.47, 29.28, 25.82, 22.68. HRMS-ESI (*m/z*): $[M + H]^+$ calcd for $C_{15}H_{25}NO_4S$, 316.1577; found 316.1583.

Synthesis of **3.22**. Prepared in an analogous way to **3.19**. Compound **3.21** (93 mg, 0.30 mmol) was taken up in MeOH (2 mL) with 0.25 mL of 4N HCl in dioxane added in and stirred for 1 h at rt. The organics were removed in vacuo and then TFA:H_2O (4 mL, 1:1) was added in along with MeOH (2 mL) and the mixture was stirred for 3 h at rt. The TFA was removed in vacuo and then the aqueous layer was neutralized with 6N NaOH prior to MeOH (2 mL) and $NaCNBH_3$ (188 mg, 3 mmol) addition. This mixture was stirred at rt for 12 h. Organics were removed and crude material was basicified with 1N NaOH, EtOAc extracted (4X), brine washed (1X) and dried over anhydrous Na_2SO_4 (s). Product was purified by silica gel chromatography (isocratic gradient of 10% MeOH in EtOAc with NH_3 in MeOH added) to yield compound **3.22** as an oil. The free base of the product was briefly taken up in 4N HCl in dioxane (1 mL), which was then removed and the HCl salt precipitated out upon Et_2O (10 mL) addition to yield compound **S14** as an off-white solid (23 mg, 45% yield). **Spectral data**. ^{1}H NMR (500 MHz, DMSO-d_6) δ 10.52 – 10.47 (m, 1H), 9.26 (s, 1H), 7.76 (d, *J* = 1.7 Hz, 1H), 6.65 (d, *J* = 3.3 Hz, 1H), 6.51 (dd, *J* = 3.3, 1.9 Hz, 1H), 4.66 (t, *J* = 7.1 Hz, 1H), 3.22 (dq, *J* = 10.9, 5.6 Hz, 2H), 2.30 (ddt, *J* = 11.3, 7.8, 4.3 Hz, 1H), 2.15 – 2.02 (m, 2H), 2.05 – 1.89 (m, 1H). ^{13}C NMR (126 MHz, dmso) δ

148.88, 143.88, 110.82, 109.79, 54.49, 44.33, 28.70, 23.34. HRMS-EI (*m/z*): $[M]^+$ calcd for $C_8H_{11}NO$, 137.0841; found 137.0836.

Synthesis of **3.23**. Compound **3.17** (470 mg, 2.36 mmol) was dissolved in DCM (10 mL) and cooled to -48 ^oC. Then methyl magnesium Grignard (3M, 0.94 mL) was added in slowly and stirred for 0.5 h prior to being warmed to rt overnight. Reaction was quenched with saturated NH_4Cl aq. and EtOAc extracted (3X), brine washed (1X) and dried over anhydrous Na_2SO_4 (s). Product was purified by automated silica gel chromatography (linear gradient of 0 → 50% EtOAc in hexanes) to yield compound **3.23** as an off-white, waxy solid (427 mg, 84% yield). **Spectral data.** ^1H NMR (400 MHz, Chloroform-*d*) δ 7.33 (d, *J* = 1.8 Hz, 1H), 6.29 (dd, *J* = 3.3, 1.8 Hz, 1H), 6.18 (d, *J* = 3.2 Hz, 1H), 4.56 (p, *J* = 6.7 Hz, 1H), 3.26 (d, *J* = 6.2 Hz, 1H), 1.58 (d, *J* = 6.8 Hz, 3H), 1.17 (s, 9H). ^{13}C NMR (126 MHz, Chloroform-*d*) δ 155.92, 142.06, 110.14, 106.12, 55.93, 49.79, 22.55, 21.82. HRMS-ESI (*m/z*): $[M + H]^+$ calcd for $C_{10}H_{17}NO_2S$, 216.1053 found 216.1054.

Synthesis of **3.24**. Compound **3.23** (116 mg, 0.54 mmol) was dissolved in 4N HCl in dioxane (0.27 mL, 1.1 mmol) and MeOH (2 mL) and allowed to stir at rt for 1 h. MeOH was removed in vacuo and then Et_2O (5 mL) was added to precipitate out the HCl salt of the amine, which was filtered and dried under vacuum to yield compound **3.24** as a brown solid (61 mg, 76% yield). **Spectral data.** ^1H NMR (500 MHz, DMSO-d_6) δ 8.65 (s, 3H), 7.73 (d, *J* = 1.8 Hz, 1H), 6.56 – 6.47 (m, 2H), 4.50 – 4.43 (m, 1H), 1.52 (d, *J* = 6.8 Hz, 3H). ^{13}C NMR (126 MHz, DMSO-d_6) δ 151.71, 143.15, 110.79, 108.17, 43.49, 17.49. HRMS-ESI (*m/z*): $[M + H]^+$ calcd for C_6H_9NO, 112.0757 found 112.0757.

Synthesis of **3.25**. Prepared in an analogous way to **3.23**. Compound **S12** (159 mg, 0.8 mmol) was dissolved in DCM (5 mL) and cooled to -48 ^oC. Then methyl magnesium Grignard (3M, 0.33 mL) was added in slowly and stirred for 0.5 h prior to being warmed to rt overnight. Reaction was quenched with saturated NH_4Cl aq. after 19 h and EtOAc extracted (3X), brine washed (1X) and dried over anhydrous Na_2SO_4 (s). Product was purified by automated silica gel chromatography (linear gradient of 0 → 50% EtOAc in hexanes) to yield compound **3.25** as an off-white, waxy solid (160 mg, 93% yield).

Spectral data. ^{1}H NMR (500 MHz, Chloroform-*d*) δ 7.33 (dd, *J* = 1.8, 0.8 Hz, 1H), 6.29 (dd, *J* = 3.2, 1.8 Hz, 1H), 6.18 (d, *J* = 3.2 Hz, 1H), 4.56 (p, *J* = 6.7 Hz, 1H), 3.25 (d, *J* = 6.2 Hz, 1H), 1.58 (d, *J* = 6.8 Hz, 3H), 1.17 (s, 9H). ^{13}C NMR (126 MHz, Chloroform-*d*) δ 155.97, 142.09, 110.17, 106.15, 55.96, 49.82, 22.58, 21.87. HRMS-ESI (*m/z*): $[M + H]^+$ calcd for $C_{10}H_{17}NO_2S$, 216.1053 found 216.1056.

Synthesis of **3.26**. Prepared in an analogous way to **3.24**. Compound **3.25** (113 mg, 0.53 mmol) was dissolved in 4N HCl in dioxane (0.26 mL, 1.1 mmol) and MeOH (2 mL) and allowed to stir at rt for 1 h. MeOH was removed in vacuo and then Et_2O (5 mL) was added to precipitate out the HCl salt of the amine, which was filtered and dried under vacuum to yield compound **3.26** as a brown solid (61 mg, 80% yield). **Spectral data.** ^{1}H NMR (500 MHz, DMSO-d_6) δ 8.57 (s, 3H), 7.73 (d, *J* = 2.0 Hz, 1H), 6.55 – 6.47 (m, 2H), 4.48 (s, 1H), 1.52 (d, *J* = 6.9 Hz, 3H). ^{13}C NMR (126 MHz, DMSO-d_6) δ 151.65, 143.17, 110.76, 108.13, 43.43, 17.42**.** HRMS-ESI (*m/z*): $[M + H]^+$ calcd for C_6H_9NO, 112.0757 found 112.0756.

Spectral Data for Compounds

Spectral data (^{1}H and^{13}C NMR) for compounds **3.1-3.26** is shown in **Appendix B**.

General Biochemical Methods

Black, opaque-bottom 96 well plates were used for fluorescence assays and were purchased from Nunc. wt c-Src, wt c-Abl and wt Hck plasmids containing a TEV protease cleavable N-terminal 6x-His tag were a generous gift from M. Seeliger (SUNY, Stony Brook) and J. Kuriyan (UC Berkeley) and were expressed in *E. coli* and purified by C. Fox using previously published procedures (see ***Kinase Expression and Purification*** below).[34] 3M c-Src (C277S, C483S, C496S) was prepared by C. Fox, while E280G c-Src and c-Yes were prepared by F. Kwarcinski using standard molecular biology techniques (see ***Mutant Kinase and c-Yes Production*** below). Chicken c-Src and human c-Abl 1a numbering is used unless otherwise noted. Data was obtained using a Molecular Devices SpectraMax M5 plate reader or Biotek Synergy 4 plate reader. Curve fitting was performed using GraphPad Prism 4 software.

Acrylamide Library Screening

A working stock of 100 μM was made for each acrylamide in the library in kinase buffer. A continuous fluorescence assay[22] was used to determine single point inhibition values both with and without compound **3.1** (thiol) present. Reaction volumes of 50 μL were used in 96-well plates. 10 μL of kinase buffer was added to all wells, followed by 10 μL of each library member and 10 μL of 125 μM substrate peptide. Then 10 μL of 3M c-Src enzyme was added with either no compound **3.1** (to establish baseline alkene values) present or with 7.5 μM compound **3.1** present. Contents were then incubated at rt for 30 min prior to having the reaction initiated with 10 μL of ATP (5 mM in buffer). Reaction progress was immediately monitored at 405 nm (ex. 340 nm) for 10 min. Reactions had final concentrations of 20 μM acrylamide, 50 nM enzyme, 1.5 μM compound **3.1**, 25 μM peptide substrate, 1 mM ATP, 100 μM TCEP, 100 μM Na_3VO_4, 100 mM Tris buffer (pH 8), 10 mM $MgCl_2$ and 0.01% Triton X-100. The initial rate data collected was used for single point inhibition values for two data sets, one with only the acrylamide present and the second with both the acrylamide library member and compound **3.1** in the well. The top seven library hits were followed up in triplicate to confirm positive inhibition values. The four hits from the initial library screen were determined to have percent differences greater than 2 standard deviations away from the mean. Any acrylamide–thiol combination that did not produce a positive inhibition value was not considered as a hit

Determination of Inhibitor IC_{50} and K_i Values

A continuous fluorescence assay[22] was used to determine IC_{50} and K_i values. Reaction volumes of 60 μL were used in 96-well plates. 51 μL of enzyme in buffer was added to each well. 1.5 μL of the appropriate inhibitor dilution (typically 2500, 833, 278, 93, 31, 10, 3.4, 1.1, 0.38, 0 μM in DMSO) was then added. 1.5 μL of a substrate peptide ("compound 3" as described in Wang et al)[22] solution (1.8 mM in DMSO) was added. The reaction was initiated with 6 μL of ATP (1 mM in water), and reaction progress was immediately monitored at 405 nm (ex. 340 nm) for 10 minutes. Reactions had final concentrations of 30 nM enzyme, 45 μM peptide substrate, 100 μM ATP (unless noted differently), 100 μM Na_3VO_4, 100 mM Tris buffer (pH 8), 10 mM $MgCl_2$, 0.01% Triton

X-100. The initial rate data collected was used for determination of IC_{50} values. For IC_{50} determination, the kinetic values were obtained directly from nonlinear regression of substrate-velocity curves in the presence of various concentrations of the inhibitor. The equation Y = Bottom + (Top – Bottom)/(1 + 10^X – LogEC50), X = log(concentration) and Y = binding; was used in the nonlinear regression. Some kinase ATP K_m values were calculated previously[5, 18, 35] except for 3M c-Src and E280G c-Src, which were both determined in this work (**Appendix B**). Some K_i values for compound 2.1 (c-Src, Hck & c-Abl) were determined previously.[18] Each inhibitor IC_{50} or K_i value was determined using at least three independent experiments; a representative inhibition curve is shown in **Appendix B**.

Determination of ATP K_M

The previously described fluorescence assay[22] was used to determine K_m values. Reaction volumes of 60 µL were used in 96-well plates. 51 µL of enzyme in buffer was added to each well. 1.5 µL of DMSO was then added followed by 1.5 µL of a substrate peptide ("compound 3" as described in Wang et al)[22] solution (1.8 mM in DMSO). The reaction was initiated with 6 µL of the appropriate ATP dilution (typically 1250, 625, 313, 156, 78, 39, 20, 10, 5, 2.4 µM in H_2O) and reaction progress was immediately monitored at 405 nm (ex. 340 nm) for 10 min. Reactions had final concentrations of 30 nM enzyme, 45 µM peptide substrate, 100 µM Na_3VO_4, 100 mM Tris buffer (pH 8), 10 mM $MgCl_2$, 0.01% Triton X-100. The initial rate data collected was used for determination of K_m values. For K_m determination, the kinetic values were obtained directly from nonlinear regression of substrate-velocity curves in the presence of varying concentrations of ATP. The equation $Y = (V_{max} * X)/(K_m + X)$, X = substrate concentration (µM) and Y = enzyme velocity (RFU/s); was used in the nonlinear regression. Each ATP K_m value was determined using at least three independent experiments; a representative K_m curve is shown in **Appendix B**.

Mutant Kinase and c-Yes Production

The 3M c-Src mutant (C277S, C483S, C496S) was prepared by C. Fox. E280G c-Src was prepared by F. Kwarcinski. The unmodified wt plasmid (chicken c-Src kinase domain) in pET28a modified with a TEV protease cleavable N-terminal 6x-His tag, was

provided to the lab by M. Seeliger (SUNY, Stony Brook) and J. Kuriyan (UC Berkeley). The desired mutation(s) for 3M c-Src and E280G were added to this plasmid using iterative rounds of mutagenesis using a standard PCR protocol with DpnI digest and transformation. The mutated plasmid was then transformed by electroporation into Bl21DE3 electrocompetent cells containing YopH in pCDFDuet-1 for cell growth, kinase expression and purification (below). The DNA for wt c-Yes kinase domain was ordered through IDT (pIDTSMART plasmid), cut with XhoI and NdeI restriction enzymes, separated on a DNA agarose gel and ligated into a cut pET28a expression vector prior to transformation. The c-Yes plasmid (in pET28a) was then transformed by electroporation into Bl21DE3 electrocompetent cells containing YopH (pCDFDuet-1) and GroEL (for cell growth, kinase expression and purification (below).

Kinase Expression and Purification

E. Coli cell growth, kinase expression and purification were performed using modified literature protocols for expression of wild-type c-Src kinase domain.[36] Briefly, the plasmid containing the kinase (pET28a) was transformed into *E. Coli* BL21DE3 cells already containing YopH phosphatase (pCDFDuet-1 plasmid) and plated on LB agar with kanamycin (50 μg/mL, kan) and streptomycin (50 μg/mL, SM) and grown overnight at 37 ^{o}C. The pET28a plasmid containing the c-Yes DNA was transformed into *E. Coli* BL21DE3 cells already containing YopH phosphatase (pCDFDuet-1 plasmid) and GroEL and plated on LB agar with kanamycin (50 μg/mL, kan), streptomycin (50 μg/mL, SM) and chloramphenicol (34 μg/mL, cam) and grown overnight at 37 ^{o}C. E. Coli cells for c-Yes expression without exogenously expressed GroEL did not yield discernable amounts of active kinase. A single colony was picked for a starter culture (LB containing kan/SM or LB containing kan/SM/cam) and subsequently grown overnight at 37 ^{o}C. The next day, scaled up cultures (TB containing kan/SM or TB containing kan/SM/cam) were grown to an OD_{600nm} of 1.2 at 37 ^{o}C and cooled to 18 ^{o}C with shaking prior to induction for 16 h at 18 ^{o}C with 0.2 mM IPTG. Cells were harvested by 20 min centrifugation at 4,000 rpm at 4 ^{o}C and resuspended in 50 mM Tris (pH 8.0), 500 mM NaCl, 5% glycerol, 25 mM imidazole (buffer A) supplemented with 0.1 mM PMSF for immobilized Ni metal affinity chromatography. Cells were lysed via sonication and insoluble protein and cell debris was sedimented through a 50-min centrifugation at 14,000 rpm at 4 ^{o}C. The clear

supernatant was loaded onto the Ni-NTA agarose affinity column (batch, QIAGEN) column. The resin was washed with 50 column volumes of buffer A and five column volumes (3X) of buffer QB (20 mM Tris, pH 8.0, 5% glycerol, 1 M NaCl). Protein was eluted with five column volumes (4X) of buffer B (buffer A plus 0.5 M imidazole). The buffer B fractions were pooled together and cleaved with 0.1 mg of TEV per 2.5 mg of crude kinase.

Cleaved protein was loaded onto an anion exchange column (Q Sepharose, Fast Flow, GE Healthcare Life sciences) equilibrated with buffer QA (buffer QB without 1 M NaCl). Proteins were eluted with a linear gradient of 0–35% buffer QB and peak fractions were combined (based on kinase activity assay) and concentrated down in order to be loaded onto a size-exclusion column (HiLoad Superdex S75, GE Healthcare Life sciences) equilibrated with buffer D (50 mM Tris, pH 8.0, 5% glycerol, 200 mM NaCl, 1 mM DTT). Pure fractions via SDS-PAGE were combined and used for biochemical assays.

References

(1) Cohen, M. H.; Grant Williams; Johnson, J. R.; Duan, J.; Gobburu, J.; Rahman, A.; Kimberly Benson; Leighton, J.; Kim, S. K.; Wood, R.; Rothmann, M.; Chen, G.; U, K. M.; Staten, A. M.; Pazdur, R. Approval summary for imatinib mesylate capsules in the treatment of chronic myelogenous leukemia. *Clin. Cancer Res.* **2002,** *8*, 935–942.

(2) Cohen, P. Protein kinases – the major drug targets of the twenty-first century? *Nat. Rev. Drug Discov.* **2002,** *1*, 309–315.

(3) Zhang, J.; Yang, P. L.; Gray, N. S. Targeting cancer with small molecule kinase inhibitors. *Nat. Rev. Cancer.* **2009,** *9*, 28–39.

(4) Cohen, P.; Alessi, D. R. Kinase drug discovery--what's next in the field? *ACS Chem. Biol.* **2013,** *8*, 96–104.

(5) Breen, M. E.; Steffey, M. E.; Lachacz, E. J.; Kwarcinski, F. E.; Fox, C. C.; Soellner, M. B. Substrate activity screening with kinases: discovery of small-molecule substrate-competitive c-Src inhibitors. *Angew. Chem. Int. Ed. Engl.* **2014,** *53*, 7010–7013.

(6) Knight, Z. A.; Shokat, K. M. Features of selective kinase inhibitors. *Chem. Biol.* **2005,** *12*, 621–637.

(7) Morphy, R. Selectively nonselective kinase inhibition: striking the right balance. *J. Med. Chem.* **2010,** *53*, 1413–1437.

(8) Brandvold, K. R.; Steffey, M. E.; Fox, C. C.; Soellner, M. B. Development of a highly selective c-Src kinase inhibitor. *ACS Chem. Biol.* **2012,** *7*, 1393–1398.

(9) Fang, Z.; Grutter, C.; Rauh, D. Strategies for the selective regulation of kinases with allosteric modulators: exploiting exclusive structural features. *ACS Chem. Biol.* **2013,** *8*, 58–70.

(10) Breen, M. E.; Soellner, M. B. Small molecule substrate phosphorylation site inhibitors of protein kinases: approaches and challenges. *ACS Chem. Biol.* **2015,** *10*, 175–189.

(11) Scott, D. E.; Coyne, A. G.; Hudson, S. A.; Abell, C. Fragment-based approaches in drug discovery and chemical biology. *Biochemistry.* **2012,** *51*, 4990–5003.

(12) Erlanson, D. A.; Braisted, A. C.; Raphael, D. R.; Randal, M.; Stroud, R. M.; Gordon, E. M.; Wells, J. A. Site-directed ligand discovery. *Proc. Natl. Acad. Sci. U S A.* **2000,** *97*, 9367–9372.

(13) Krasinski, A. R., Z.; Manetsch, R.; Raushel, J.; Taylor, P.; Sharpless, K. B.; Kold, H. C. In situ selection of lead compounds by click chemistry: target-guided optimization of acetylcholinesterase inhibitors. *J. Am. Chem. Soc.* **2005,** *127*, 6686–6692.

(14) Namelikonda, N. K.; Manetsch, R. Sulfo-click reaction via in situ generated thioacids and its application in kinetic target-guided synthesis. *Chem. Commun.* **2012,** *48*, 1526–1528.

(15) Levitsky, K.; Ciolli, C. J.; Belshaw, P. J. Selective inhibition of engineered receptors via proximity-accelerated alkylation. *Org. Let.* **2003,** *5*, 693–696.

(16) Oueis, E.; Nachon, F.; Sabot, C.; Renard, P. Y. First enzymatic hydrolysis/thio-Michael addition cascade route to synthesis of AChE inhibitors. *Chem. Commun.* **2014,** *50*, 2043–2045.
(17) Oueis, E.; Sabot, C.; Renard, P.-Y. New insights into the kinetic target-guided synthesis of protein ligands. *Chem. Commun.* **2015,** *51*, 12158–12169.
(18) Kwarcinski, F. E.; Fox, C. C.; Steffey, M. E.; Soellner, M. B. Irreversible inhibitors of c-Src kinase that target a nonconserved cysteine. *ACS Chem. Biol.* **2012,** *7*, 1910–1917.
(19) Kathman, S. G.; Xu, Z.; Statsyuk, A. V. A fragment-based method to discover irreversible covalent inhibitors of cysteine proteases. *J. Med. Chem.* **2014,** *57*, 4969–4974.
(20) Thomas, S. M. B., J. S. Cellular functions regulated by Src family kinases. *Ann. Rev. Cell. Dev. Biol.* **1997,** *13*, 513–609.
(21) Martin, G. S. The hunting of the Src. *Nat. Rev. Mol. Cell. Biol.* **2001,** *2*, 467–475.
(22) Wang, Q.; Cahill, S. M.; Blumenstein, M.; Lawrence, D. S. Self-reporting fluorescent substrates of protein tyrosine kinases. *J. Am. Chem. Soc.* **2006,** *128*, 1808–1809.
(23) Liu, G.; Cogan, D. A.; Owens, T. D.; Tang, T. P.; Ellman, J. A. Synthesis of enantiomerically pure *N*-*tert*-butanesulfinyl imines (*tert*-butanesulfinimines) by the direct condensation of *tert*-butanesulfinamide with aldehydes and ketones *J. Org. Chem.* **1999,** *64*, 1278–1284.
(24) Brinner, K. M.; Ellman, J. A. A rapid and general method for the asymmetric synthesis of 2-substituted pyrrolidines using tert-butanesulfinamide. *Org. Biomol. Chem.* **2005,** *3*, 2109–2113.
(25) Zhang, X.; Meyn, M. A., III; Smithgall, T. E. c-Yes tyrosine kinase is a potent suppressor of ES cell differentiation and antagonizes the actions of its closest phylogenetic relative, c-Src. *ACS Chem. Biol.* **2014,** *9*, 139–146.
(26) Davis, M. I.; Hunt, J. P.; Herrgard, S.; Ciceri, P.; Wodicka, L. M.; Pallares, G.; Hocker, M.; Treiber, D. K.; Zarrinkar, P. P. Comprehensive analysis of kinase inhibitor selectivity. *Nat. Biotechnol.* **2011,** *29*, 1046–1051.
(27) Finn, R. S. Targeting Src in breast cancer. *Ann. Oncology.* **2008,** *19*, 1379–1386.
(28) Allington, T. M.; Schiemann, W. P. The Cain and Abl of epithelial-mesenchymal transition and transforming growth factor-beta in mammary epithelial cells. *Cells Tissues Organs.* **2011,** *193*, 98–113.
(29) Allington, T. M.; Galliher-Beckley, A. J.; Schiemann, W. P. Activated Abl kinase inhibits oncogenic transforming growth factor-beta signaling and tumorigenesis in mammary tumors. *FASEB J.* **2009,** *23*, 4231–4243.
(30) Hopkins, A. L.; Keseru, G. M.; Leeson, P. D.; Rees, D. C.; Reynolds, C. H. The role of ligand efficiency metrics in drug discovery. *Nat. Rev. Drug Discov.* **2014,** *13*, 105–121.
(31) Chaikuad, A.; Tacconi, E. M. C.; Zimmer, J.; Liang, Y.; Gray, N. S.; Tarsounas, M.; Knapp, S. A unique inhibitor binding site in ERK1/2 is associated with slow binding kinetics. *Nat. Chem. Biol.* **2014,** *10*, 853–862.
(32) Gower, C. M.; Chang, M. E.; Maly, D. J. Bivalent inhibitors of protein kinases. *Crit. Rev. Biochem. Mol. Biol.* **2014,** *49*, 102–115.

(33) Barouch-Bentov, R.; Che, J.; Lee, C. C.; Yang, Y.; Herman, A.; Jia, Y.; Velentza, A.; Watson, J.; Sternberg, L.; Kim, S.; Ziaee, N.; Miller, A.; Jackson, C.; Fujimoto, M.; Young, M.; Batalov, S.; Liu, Y.; Warmuth, M.; Wiltshire, T.; Cooke, M. P.; Sauer, K. A conserved salt bridge in the G loop of multiple protein kinases is important for catalysis and for in vivo Lyn function. *Mol. Cell.* **2009,** *33*, 43–52.
(34) Seeliger, M. A.; Young, M.; Henderson, M. N.; Pellicena, P.; King, D. S.; Falick, A. M.; Kuriyan, J. High yield bacterial expression of active c-Abl and c-Src tyrosine kinases. *Protein Sci.* **2005,** *14*, 3135–3139.
(35) Ko, K. S.; Steffey, M. E.; Brandvold, K. R.; Soellner, M. B. Development of a chimeric c-Src kinase and HDAC inhibitor. *ACS Med. Chem. Lett.* **2013,** *4*, 779–783.
(36) Seeliger, M. A.; Young, M.; Henderson, M. N.; Pellicena, P.; King, D. S.; Falick, A. M.; Kuriyan, J. High yield bacterial expression of active c-Abl and c-Src tyrosine kinases. *Protein Sci.* **2005,** *14*, 3135-3139.

CHAPTER IV

The Effect of Conformation-Selective Inhibition on Kinase Selectivity

Abstract

In the kinase field, there are many widely held tenants about conformation-selective inhibitors that have yet to be validated using controlled experiments. We have designed, synthesized, and characterized a series of kinase inhibitor analogs of dasatinib, an FDA-approved kinase inhibitor that binds the active conformation. This inhibitor series includes two Type II inhibitors that bind the DFG-out inactive conformation and two inhibitors that bind the αC-helix out inactive conformation. Using this series of compounds, we analyze the impact that conformation-selective inhibitors have on target binding, kinome-wide selectivity, and cellular activity.

Introduction

Protein kinases (PKs) play a key role in cellular signal transduction pathways and regulate important cellular processes such as cell growth through post-translational phosphorylation. PKs are one of the largest protein families; the human kinome encodes for 518 protein kinases, which corresponds to 1.7% of the entire genome.[1] For these reasons, they continue to be an attractive target for drug discovery.

All FDA-approved small molecule kinase inhibitors bind in the nucleotide-binding site and prevent ATP from binding the kinase (all approved kinase inhibitors are ATP-competitive inhibitors).[2,3] Structural analysis of the FDA-approved kinase inhibitors reveals three distinct kinase conformations amenable to inhibitor binding: DFG-in active, DFG-out inactive, and αC-helix out inactive.[4] The majority of approved kinase inhibitors (19 of 30) bind the active kinase conformation and these inhibitors have previously been classified as 'Type I' inhibitors. There are 7 approved kinase inhibitors that bind the inactive, DFG-out conformation and these inhibitors have been termed 'Type II'

inhibitors. Finally, 4 approved inhibitors bind an alternate inactive conformation, the αC-helix out conformation.

Type I inhibitors are the most common kinase inhibitor class, both among approved and non-approved inhibitors. These inhibitors bind their target kinase(s) in a manner similar to ATP, where the kinase is in an active conformation (in which the activation loop is poised for phosphate transfer).[5] Meanwhile, Type II inhibitors bind an inactive kinase conformation in which the activation loop is forced to undergo a large conformational change due to the kinase inhibitor occupying an allosteric pocket adjacent to the nucleotide-binding site.[6] The specific inactive conformation bound by Type II inhibitors is termed the DFG-out inactive conformation. In this conformation, the conserved Asp-Phe-Gly (DFG) motif required for catalysis is flipped outward so that the Asp faces into the solvent and can no longer coordinate ATP/Mg^{2+}. Finally, αC-helix out inhibitors stabilize the kinase in a conformation where a key salt bridge between the catalytic lysine and a glutamate in helix ✔C is disrupted due to displacement (and/or outward rotation) of the αC-helix.[7-11]

Because the kinase ATP pocket is highly conserved, developing selective kinase inhibitors remains a key challenge for the drug discovery and chemical biology fields. Since the discovery of imatinib[12,13], a selective Type II inhibitor of c-Abl, the prevailing opinion has been that Type II inhibitors are more selective than their Type I counterparts.[14,15] It is commonly believed that not all kinases can adopt the DFG-out conformation.[16-18] These beliefs originate in the finding that imatinib does not inhibit c-Src, a protein kinase with homology to c-Abl.[19,20] The prevailing hypothesis was that imatinib did not bind c-Src, because c-Src cannot adopt the DFG-out conformation.[21] Kinome-wide analysis of kinase inhibitors initially strengthened the idea that Type II inhibitors were more selective[22], however, recent analyses suggest that the DFG-out conformation is conserved across the kinome.[6,23] Nonetheless, Type II inhibitors are still today claimed to be more selective than Type I kinase inhibitors.[24] No comprehensive selectivity analysis of inhibitors that bind the αC-helix out (CHO) conformation has been performed, however, three FDA-approved inhibitors that bind this specific inactive conformation (lapatinib, vemurafenib, and ibrutinib) are among the most selective kinase

inhibitors known.[22,25,26] Complicating matters, CHO inhibitors are often incorrectly considered Type I inhibitors in analyses of kinome profiling data.[6,17,27]

In an effort to understand the role of conformation on the selectivity of kinase inhibitors, we have created a set of conformation-selective analogs of dasatinib, an FDA-approved pan-kinase inhibitor.[4] Dasatinib is a potent inhibitor of c-Src (along with many other tyrosine kinases) and binds the active kinase conformation.[28,29] Herein, we designed analogs of dasatinib that bind the DFG-out and αC-helix out conformations of c-Src. Crystallographic characterization of our conformation-selective dasatinib analogs confirms the desired inactive conformations. Selectivity profiling across a diverse kinome panel yields insight into the divergent selectivity of conformation-selective inhibitors. Furthermore, characterization of each analog in cellular proliferation assays demonstrates that cellular potency is independent from any biochemical measurement obtained or inhibitor selectivity. Notably, these inhibitors represent the first 'matched set' of conformation-selective kinase inhibitors that share the same hinge-binding scaffold and have been verified crystallographically. Using this unique inhibitor set, our results provide a deeper understanding of kinase inhibitor structure–function and selectivity.

Design and Structural Characterization of DFG-out Dasatinib Analogs

To design an analog of dasatinib that invokes the DFG-out conformation, we applied a hybridization strategy developed by Gray and colleagues for converting Type I kinase inhibitors into Type II inhibitors.[27,30] Specifically, we created an overlay of dasatinib bound to c-Src (PDB: 3G5D) with imatinib bound to c-Src (PDB: 2OIQ) (Figure **4.1A**). The overlaid structures suggested that addition of a benzamide group to the meta-position of dasatinib's distal phenyl could result in a potent Type II analog of dasatinib. Following this design strategy, we synthesized two putative Type II inhibitors: **DAS-DFGO-I** and **DAS-DFGO-II**. These compounds vary only in the inclusion of a so-called 'flag methyl', a methyl group found both in dasatinib and in many Type II kinase inhibitors[6], including imatinib.

Dasatinib is a highly potent inhibitor of both c-Src and c-Abl (K_i < 1 nM). In activity assays, both **DAS-DFGO-I** and **DAS-DFGO-II** titrated the lowest enzyme concentration that can be used in this assay (K_i < 1 nM for both Type II analogs;

Appendix Figure C.1). To confirm that these Type II analogs invoke the DFG-out conformation, we obtained a crystal structure of **DAS-DFGO-I** bound to c-Src kinase domain (PDB: 4YBJ, **Figure 4.1B**). Several dasatinib:c-Src interactions were conserved in this crystal structure, including hydrogen bond contacts to the hinge and gatekeeper residues of c-Src (Figure **4.1C**). Gratifyingly, c-Src is in the DFG-out inactive conformation when bound to **DAS-DGFO-I**, highlighted by the outward flip of Phe-405. The benzamide group we appended to dasatinib occupies the DFG-pocket, with the amide hydrogen bonding to Glu-310 and Asp-404, all of which are prototypical features of Type II inhibitors. Notably, a previously obtained crystal structure of imatinib bound to c-Src illustrates an identical, DFG-out binding mode (**Appendix Figure C.2**).

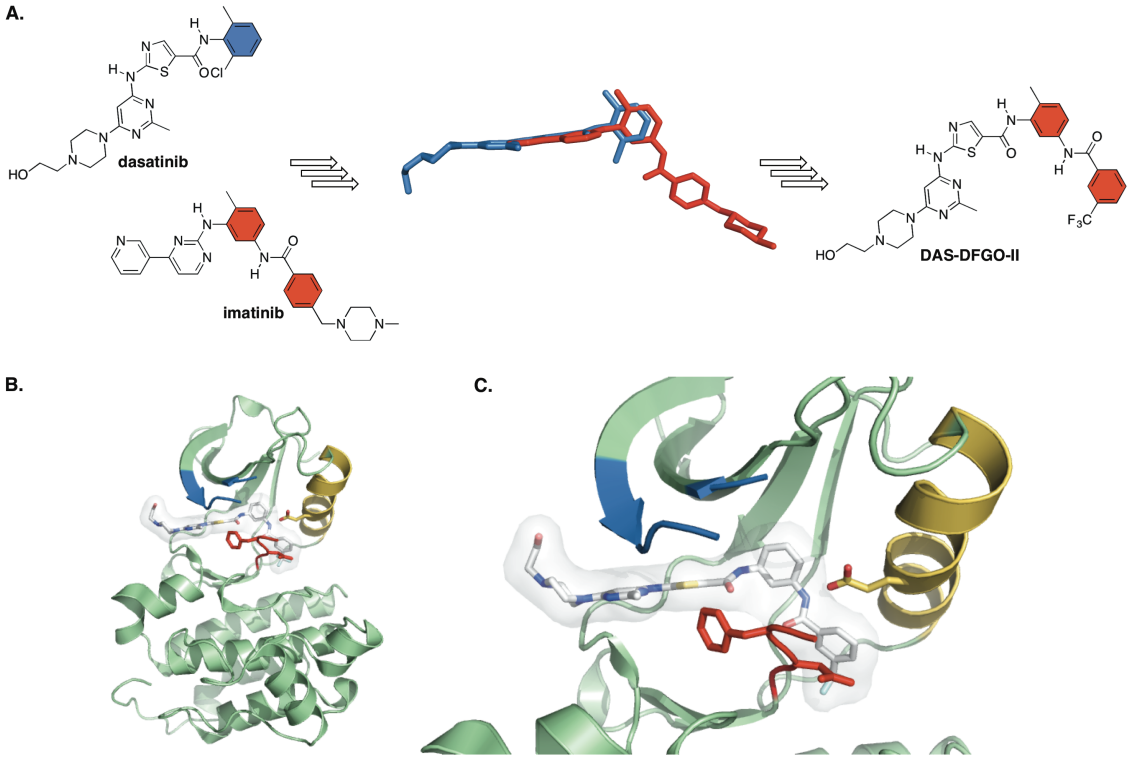

Figure 4.1. DFG-out dasatinib analog characterization. (**A**) Overlay of dasatinib (blue) and imatinib (red) kinase inhibitors used in the design of dasatinib DFG-out analogs, **DAS-DFGO-I** and **DAS-DFGO-II**. (**B**) DAS-DFGO-I (white) bound to c-Src (PDB: 4YBJ). P-loop (blue), αC-helix (yellow) and DFG motif (red) are shown. (**C**) The trifluoromethyl benzamide group is positioned within the DFG pocket, resulting in the DFG-out, inactive kinase conformation.

Design and Structural Characterization of αC-helix-out Dasatinib Analogs

While design strategies exist for the conversion of Type I kinase inhibitors into Type II inhibitors are known[27,30], no such strategy has been proposed for the conversion of Type I inhibitors into αC-helix out (CHO) binding analogs. Thus, we first analyzed the binding space occupied by existing CHO inhibitors that have co-crystal structures available (for a list of CHO inhibitors used, see **Appendix Table C.1**) (van Linden et al., 2014).[31] In contrast to Type II inhibitors, CHO inhibitors typically contain a bulky substituent that extends directly toward the αC-helix and lack hydrogen bond donors typically found in Type II inhibitors. Indeed, phenoxy or benzyloxy groups are commonly employed in the design of CHO inhibitors.[11,32,33] An overlay of dasatinib:c-Src (PDB: 3G5D) with a panel of known and verified CHO inhibitors (**Figure 4.2A**), suggested that addition of a para-phenoxy group to dasatinib could lead to an optimal CHO analog of dasatinib. Thus, we synthesized two putative CHO inhibitors: **DAS-CHO-I** and **DAS-CHO-II**, where **DAS-CHO-II** incorporates the 'flag methyl' found in dasatinib and **DAS-DFGO-II**.

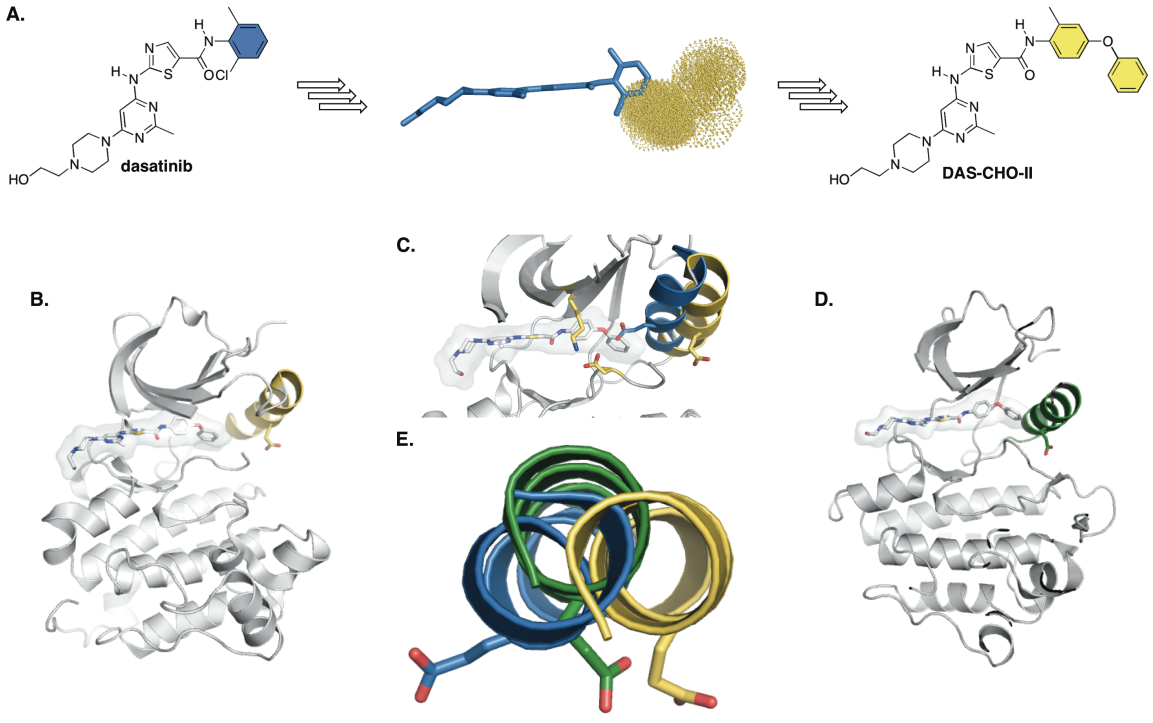

Figure 4.2. αC-helix out dasatinib analog characterization. (**A**) Overlay of dasatinib (blue) with the binding space (yellow) of structurally confirmed CHO inhibitors. A para-

phenoxy group addition to dasatinib led to the generation of **DAS-CHO-I** and **DAS-CHO-II**. (**B**) **DAS-CHO-I** bound to c-Src (PDB: 4YBK). (**C**) An overlay with dasatinib bound to c-Src (PDB: 3G5D) shows the magnitude of the αC-helix shift (~5 Å) and incompatible binding between the CHO inhibitor and the Glu310 side chain of the kinase. (**D**) **DAS-CHO-I** bound to c-Abl (PDB: 4YC8). (E) The possible range of αC-helix positioning, from αC-helix in (blue) to c-Abl αC-helix out (green) to c-Src αC-helix out (yellow).

Consistent with dasatinib and the DFG-out analogs of dasatinib, both **DAS-CHO-I** and **DAS-CHO-II** are exceptionally potent in biochemical activity assays against both c-Src and c-Abl (**Appendix Figure C.3**). To confirm the proposed CHO conformation, we obtained a crystal structure of **DAS-CHO-I** bound to both c-Src kinase domain (**Figure 4.2B**; PDB: 4YBK). c-Src bound to **DAS-CHO-I** adopts the classic CHO (also termed Src/Cdk-like) inactive conformation[7-11], as evidenced by the outward rotation of the αC-helix and outward projection of Glu-310 side chain from the ATP pocket. The phenoxy group cannot be accommodated within the DFG pocket and thus occupies the empty space that results from the outward movement of the αC-helix. As with the DFG-out analog, the hinge contacts are conserved and the Type I portion of the molecule bears striking similarity to dasatinib's binding mode. In the c-Src:**DAS-CHO-I** structure the αC-helix is rotated nearly 5 Å from the active conformation of c-Src (**Figure 4.2C**), a change consistent with the binding of other CHO inhibitors to c-Src.[10,11]

Recent evidence has suggested that many kinases can adopt the DFG-out inactive conformation, however, relatively little is known about which kinases can adopt the CHO inactive conformation. Because our results showed that c-Abl was potently inhibited by **DAS-CHO-I**, we obtained a crystal structure of this CHO inhibitor bound to c-Abl (**Figure 4.2D**). In this structure, there is less movement of the αC-helix (**Figure 4.2E**), however, the key lysine-glutamate salt bridge is disrupted, which is a unique feature of CHO inhibitors. A recently reported structure of a CHO inhibitor bound to Erk2 possesses the same features (minimal movement of αC-helix and disruption of Lys-Glu salt bridge[33]). Notably, our structure is the first of c-Abl bound to a small molecule inhibitor that binds the CHO inactive conformation.[34]

Characterization of Conformation-selective Dasatinib Analogs Binding to Target Kinases

Due to the constraints of our activity-based assays for c-Src and c-Abl (the main targets of dasatinib), we used the KINOMEscan service[35] to obtain quantitative K_d values for both c-Src and c-Abl (**Table 4.1**). Each compound is a very potent inhibitor of both c-Src and c-Abl without discrimination between targets.

We also examined the ability of our probes to bind to c-Abl that has been phosphorylated on the activation loop. Largely on the basis of imatinib's strong preference for non-phosphorylated c-Abl[20,36,37], an often reported 'feature' of Type II inhibitors is that they bind c-Abl tighter than c-Abl~pY393.[30,38,39] Given this frequently claimed feature, we were surprised to see that both **DAS-DFGO-I** and **DAS-DFGO-II** have no preference between the activation state of the kinase (**Table 4.2**). To follow up on these results, we screened a panel of bone fide Type II inhibitors of c-Abl (imatinib, nilotinib, rebastinib, and ponatinib) for which a crystal structure verifies the DFG-out inactive conformation[36,40-42] and found that only imatinib has a preference for c-Abl over c-Abl-pY393. From these studies, we can state that Type II kinase inhibitors do not have an inherent activation-state preference in biochemical assays and this type of measurement cannot be relied upon to determine inhibitor binding mode.

Table 4.1. KINOMEscan K_d profiling of conformation-selective dasatinib analogs.

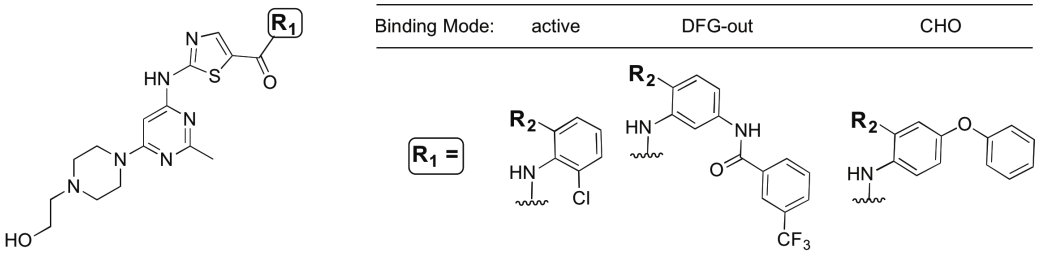

Inhibitor	R_1	R_2	c-Src K_d, nM	c-Abl K_d, nM
dasatinib	active	Me	0.07	0.03
DAS-DFGO-I	DFG-out	H	0.53	2.2
DAS-DFGO-II	DFG-out	Me	2.7	3.0
DAS-CHO-I	CHO	H	15	14
DAS-CHO-II	CHO	Me	1.7	0.32

Table 4.2. Type II inhibitor phosphorylation state dependence comparison.

Inhibitor	c-Abl K_d, nM	c-Abl~pY393 K_d, nM
DAS-DFGO-I	2.2	1.8
DAS-DFGO-II	3.0	2.0
imatinib	1.5	24
nilotinib	11	15
rebastinib	7.2	11
ponatinib	0.7	0.7

In general, Type II inhibitors have been reported to have longer residence times, compared to Type I kinase inhibitors.[20,43-45] However, these studies have not been performed using a controlled set of inhibitors, such as our dasatinib analogs. Thus, we synthesized BODIPY-labeled analogs (**Figure 4.3A**) for four of our dasatinib analogs (**DAS-**, **DAS-DFGO-I-**, **DAS-DFGO-II**, and **DAS-CHO-II-BODIPY;** for all probe data with wt c-Src and c-Abl, see **Appendix Table C.2**). We first obtained K_d values for each probe and verified that binding was not impacted by addition of BODIPY-FL on the solvent-exposed piperizine ring. We then determined off-rates for each probe with both c-Src and c-Abl. Consistent with previous reports, our Type II probes have significantly longer half-lives compared to the active-binding analog with both c-Src and c-Abl (**Figure 4.3B**). Relatively little is known about the binding kinetics of CHO kinase inhibitors, however, lapatinib (an FDA-approved CHO kinase inhibitor), has an exceptionally long half-life with its primary target EGFR ($t_{1/2}$ = 300 min).[32] We found that **DAS-BODIPY** and **DAS-CHO-II-BODIPY** have nearly identical off-rates (**Appendix Table C.2**) for both c-Src and c-Abl, suggesting that a slow off-rate is not an inherent feature of CHO kinase inhibitors.

A significant amount of effort has been spent on understanding the binding preference of imatinib for c-Abl over c-Src.[20,46,47] Initial reports suggested that c-Src was unable to adopt the DFG-out conformation (a hypothesis that has since been clearly refuted).[21] Despite evidence to the contrary[38,45,48,49], the belief that there is an energetic penalty for c-Src to invoke the DFG-out conformation persists.[50-52] Our probes represent a unique opportunity to examine whether there is any penalty (kinetic or thermodynamic)

for the DFG-out conformation in c-Src. Using **DAS-BODIPY** and **DAS-DFGO-II-BODIPY**, we compared the binding of each probes to both c-Src and c-Abl. With **DAS-BODIPY**, we observed no significant change in kinetics (k_{on} and k_{off}) or thermodynamics (K_d) of binding (**Figure 4.3C**). Likewise, we observed no significant change in the kinetics and thermodynamics for binding of **DAS-DFGO-II-BODIPY**. From these data, we conclude that imatinib's preference for c-Abl over c-Src is inherent to the ligand structure of imatinib and not conserved between Type II inhibitors.[45]

A.

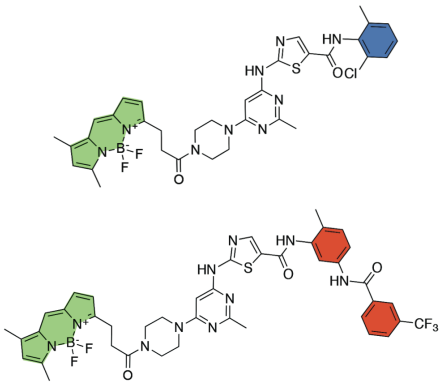

B.

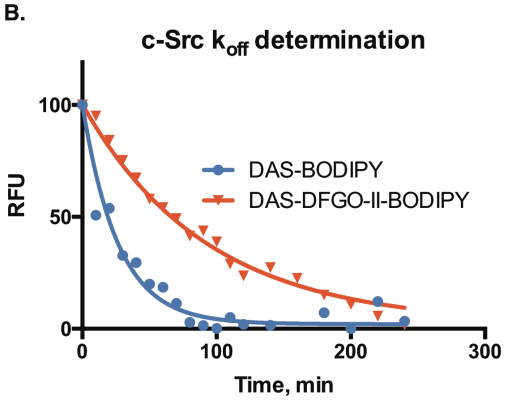

C.

	c-Src				c-Abl			
BODIPY-	**K_d, nM**	**$t_{1/2}$, min**	**k_{on}, sec^{-1}**	**k_{off}, sec^{-1}**	**K_d, nM**	**$t_{1/2}$, min**	**k_{on}, sec^{-1}**	**k_{off}, sec^{-1}**
DAS	0.50	15	1.6×10^{-3}	7.9×10^{-4}	0.15	20	3.8×10^{-3}	5.7×10^{-4}
DAS-DFGO-II	2.8	65	6.4×10^{-5}	1.8×10^{-4}	0.75	75	2.1×10^{-4}	1.5×10^{-4}

Figure 4.3. Dasatinib analog BODIPY data. (**A**) **DAS-** and **DAS-DFGO-II-BODIPY** structures. (**B**) Determination of BODIPY probes half-life values. A significantly longer half-life measurement was observed for **DAS-DFGO-II-BODIPY** (red) in comparison to **DAS-BODIPY** (blue) (**C**) Kinetic and thermodynamic data comparison for type I and type II BODIPY probes.

To complement our thermodynamic data (K_d values, **Table 4.2**) that suggests Type II inhibitors do not have a preference for a specific kinase activation-state, we examined the kinetics of **DAS-BODIPY** and **DAS-DFGO-II-BODIPY** for binding to c-Src~pY416 (activation-loop phosphorylated c-Src). We found no significant change in the binding of either inhibitor (**Appendix Figure C.4**). These data reinforce our findings that conformation-selective inhibitors do not have an inherent activation-state preference in biochemical assays.

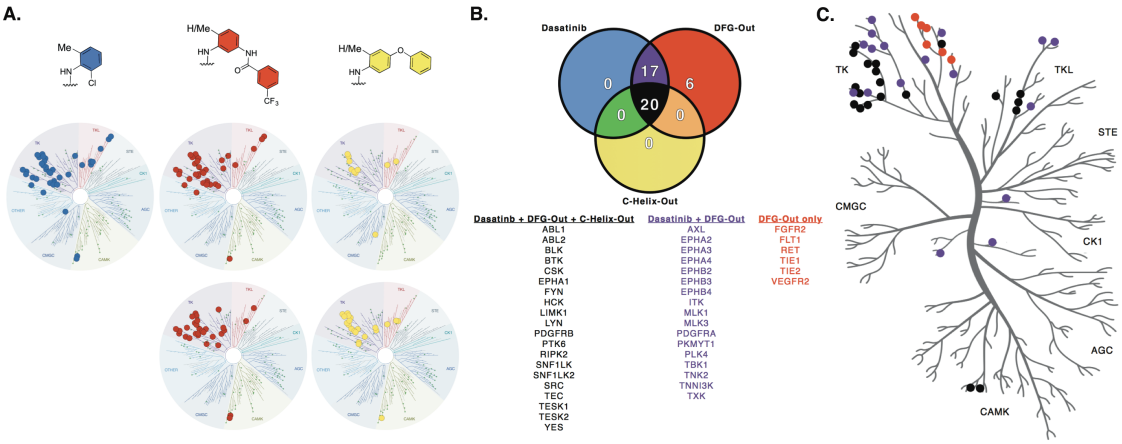

Figure 4.4. Dasatinib analog kinome-wide selectivity. (**A**) Kinase target comparison for conformation-selective dasatinib analogs utilizing a 50% cutoff value. (**B**) Analysis of kinase targets amongst the three conformation-selective modes of inhibition. Twenty kinases are targeted equally by the inhibitor set, while six kinases demonstrate a preference for DFG-out binding. Seventeen kinases show shared inhibition between dasatinib and the two DFG-out inhibitors. (**C**) Kinome tree representation of kinase targets. Colors correspond to the Venn diagram.

Selectivity Profiling of Conformation-selective Dasatinib Analogs

Type II inhibitors have been repeatedly stated to be more selective, in general, than Type I inhibitors.[24] These analyses hinge upon the profiling of a collection of unrelated kinase inhibitors. Recent analyses[6] have pointed out that several previously profiled Type II inhibitors are highly promiscuous, however, kinome-wide profiling of a matched set of conformation-selective kinase inhibitors has not been reported. Thus, we wanted to determine how the selectivity of dasatinib, a relatively promiscuous Type I inhibitor, compares to our panel of conformation-selective dasatinib analogs. We used a commercially available profiling service (Luceome Biotechnologies[53,54]) to profile each of the 5 analogs using a competition-binding assay for 124 non-mutant kinases (**Figure 4.4A**; for individual kinase data, see **Appendix C**). We selected 500 nM as the screening concentration for each analog, a concentration that represents is significantly higher than each analog's binding affinity for c-Src and c-Abl, the primary targets of dasatinib. Kinome-wide selectivity differences between the 5 compounds can be compared using their *S*-score. *S*-score represents the fraction of kinases inhibited to a particular level (e.g., S_{35} is the number of kinases with <35% of control activity divided by the total number of nonmutant kinases in the panel, here 124). In this panel, dasatinib has S_{35} = 0.21 at 500

nM. The Type II analogs (**DAS-DFGO-I** and **DAS-DFGO-II**) have similar S_{35} scores (0.24 and 0.20, respectively). Meanwhile, the CHO analogs are significantly more selective (**DAS-CHO-I** S_{35} = 0.05, **DAS-CHO-II** S_{35} = 0.16). It is worth noting that these selectivity scores do not correlate to inhibitor potency for an individual target (e.g., **DAS-CHO-I**, (S_{35} = 0.05) binds LIMK1 more potently than dasatinib (S_{35} = 0.21), see **Appendix C** for details).

This is the first kinome-wide selectivity analysis for a matched set of conformation-selective kinase inhibitors. Our findings suggest that conversion of a Type I inhibitor into a Type II inhibitor leads to similar or even reduced selectivity. This is in stark contrast to the dogma that Type II inhibitors are inherently more selective than their Type I counterparts.[24] Of interest, is that while dasatinib is a poor inhibitor of non-Thr gatekeeper kinases, the Type II inhibitors (**DAS-DFGO-I** and **DAS-DFGO-II**) can potently inhibit many non-Thr gatekeeper kinases (**Figure 4.4B**). We confirmed this with by obtaining K_d values using an orthogonal assay (KINOMEscan K_d determinations) and found that several non-Thr gatekeeper kinases can be preferentially inhibited by the DFG-out analogs (**Appendix Table C.3**). Notably, there are no kinases (in this panel) that bind dasatinib and do not also bind to the Type II analogs. Thus, the ability of the DFG-out analogs to bind kinases with non-Thr gatekeeper residues is responsible for the observed loss of selectivity compared to dasatinib. The decrease in selectivity when going from Type I to Type II is small, and the overall selectivity for Type I and Type II inhibitors appears to result from the Type I hinge-binding scaffold. This has two important implications: 1) These data imply that the DFG-out conformation is likely conserved, which is in agreement with recently published analyses of promiscuous Type II inhibitors[6], and 2) Analyzing kinome-wide selectivity data using inhibitor sets with varied hinge-binding scaffolds likely reports only on the selectivity of the hinge binder. In addition, these data suggest that kinase inhibitor selectivity should best be optimized through modification of the Type I hinge binder.

Interestingly, there have been recent publications claiming that the gatekeeper residue is a primary determinant for a kinase's ability to bind a Type II inhibitor.[55] Specifically, it has been proposed that non-Thr gatekeeper residues can prevent a kinase's ability to bind a Type II inhibitor. Our data clearly demonstrates that kinases with non-

Thr gatekeeper residues can be inhibited by Type II inhibitors. In fact, in our panels many such kinases (e.g., FLT1, RET, TIE2) are only inhibited by the Type II analogs (**Figure 4.4**).

We found that both of the dasatinib CHO analogs (**DAS-CHO-I** and **DAS-CHO-II**) are more selective than dasatinib. Several kinases are bound potently by both dasatinib and the CHO analogs (e.g., c-Src, c-Abl, LIMK1), however, there are many kinases that dasatinib potently binds to which the CHO analogs cannot bind (e.g., EPHB2, PDGFRA, and TXK) (**Figure 4.4B**; **Appendix Table C.4**). The inability of certain kinases, including the entire Ephrin family, to bind the CHO inhibitors is responsible for the increase in selectivity for the CHO analogs. We did not identify any kinases that can accommodate the CHO analog that do not also potently bind the Type I analog. These results are intriguing and suggest that invoking the CHO inactive conformation could be a useful method to improve inhibitor selectivity, provided that the target kinase can adopt this inactive conformation. Furthermore, it suggests that the CHO inactive conformation is less conserved across protein kinases than the DFG-out inactive conformation (in contrast to the DFG-out conformation which is conserved kinome-wide).

Cellular Characterization of Conformation-selective Dasatinib Analogs.

We next wanted to compare the cellular efficacy of our panel of conformation-selective dasatinib analogs. Specifically, we tested the ability of each kinase inhibitor to slow the proliferation of Bcr-Abl transformed BaF3 cells. Dasatinib is FDA-approved for the treatment of Ph^+ CML[56] and its efficacy for this indication is a direct result of dasatinib's potent enzymatic inhibition of Bcr-Abl kinase. BaF3 cells transformed with Bcr-Abl become growth-dependent on Bcr-Abl's kinase activity and have been extensively used to evaluate kinase inhibitors.[57] As a measure of toxicity, we also measured the ability of each compound to inhibit the growth of parental IL3-dependent BaF3 cells.

Relative to their ability to inhibit c-Abl in biochemical assays, the Type II dasatinib analogs are the most efficient in cell-based assays (**Table 4.3**; the Type II inhibitors lose less potency when transitioning from biochemical to cell assays).

However, dasatinib has the best cellular therapeutic index (therapeutic index = GI_{50} parental BaF3 divided by GI_{50} Bcr-Abl/ BaF3). Compared to dasatinib, the Type II analogs have dramatically increased toxicity, possibly resulting from their ability to potently inhibit non-Thr gatekeeper kinases. The CHO analogs of dasatinib suffer from both poor cellular efficiencies and low therapeutic indices. Together, these results demonstrate that, in this compound series, the Type I analog (dasatinib) has the highest therapeutic potential (as judged by disease-relevant cell-based assays).

Table 4.3. Cellular comparison of conformation-selective dasatinib analogs.

Inhibitor	c-Abl, K_d	Bcr-Abl BaF3, GI_{50}	Efficiency	BaF3 Parental, GI_{50}	Therapeutic Index
dasatinib	0.03 nM	6.0 nM	200X	>10,000 nM	1640X
DAS-DFGO-I	2.2 nM	54 nM	25X	5,900 nM	110X
DAS-DFGO-II	3.0 nM	59 nM	20X	350 nM	6X
DAS-CHO-I	14 nM	5,400 nM	380X	3,000 nM	0.6X
DAS-CHO-II	0.32 nM	550 nM	1,700X	3,800 nM	7X

Compounds with long biochemical off-rates have previously been suggested to be optimal due to their longer residence times on the target.[58-61] Interestingly, with our series of matched inhibitors, there appears to be no correlation between biochemical off-rates and cellular activity. With c-Abl, **DAS-DFGO-I** has a significantly longer half-life compared to dasatinib ($t_{1/2}$ = 79 and 20 min, respectively), however, dasatinib is nearly 10x more potent in the cell proliferation assay. In all, no biochemical parameter that we measured (K_d, k_{on}, or k_{off}) was found to be predictive of the cellular activity for this closely related set of compounds.

Inhibitor selectivity is traditionally considered to correlate to toxicity. Parental BaF3 cells (grown in the presence of IL3) are well established as a measure of toxicity.[57] Interestingly, we found that there was no overall correlation between inhibitor selectivity and cellular toxicity to BaF3 cells. For example, **DAS-CHO-I** is the most selective compound in our series (S_{35} = 0.05), however, it is significantly more toxic than the two most non-selective inhibitors in our series (dasatinib S_{35} = 0.21, **DAS-DFGO-I** S_{35} = 0.24) (**Figure 4.4A**). These data suggest that optimization of selectivity might not be necessary to achieve a high therapeutic index (which is consistent with the high number of promiscuous kinase inhibitors that are FDA-approved).

Conclusions

Since the FDA-approval of imatinib in 2001, extensive effort has focused on the development of kinase inhibitors that target the inactive conformation(s) of kinases. On the basis of imatinib's binding properties, many (incorrect) theories about kinase inhibitor were established, many of which are still widely believed.[24] In an effort to evaluate how kinase inhibitor binding mode impacts selectivity, target binding, and cellular activity, we designed and characterized the first set of kinase inhibitor analogs that bind the active and inactive conformations (DFG-out and αC-helix out).

We have demonstrated that conversion of dasatinib to a Type II analog can decrease kinome-wide selectivity. The diminished selectivity observed with the Type II binding mode is a result of these analogs potently inhibiting non-Thr gatekeeper kinases (in contrast to the Type I analog). We also demonstrate that Type II inhibitors do not inherently prefer to bind the un-activated kinase state in biochemical assays.

Our results suggest that cellular efficacy and therapeutic indicies are independent from biochemical measurements. Specifically, we demonstrate that neither selectivity score, K_d, k_{on}, nor k_{off} correlate to cellular efficacy or toxicity. Overall, the Type I analog in our compound series was the most potent and least toxic in cell assays.

Our series of inhibitors represent the first set of kinase inhibitors that bind the active, DFG-out inactive, and αC-helix out conformations and represent a useful compound series to interrogate how kinase conformation impacts inhibitor binding and selectivity.

Materials and Methods

General Synthetic Methods

Unless otherwise noted, all reagents were obtained via commercial sources and used without further purification. Dasatinib was purchased from LC Labs. BODIPY-FL-NHS (N-hydroxysuccinimide) ester was purchased from LumiProbe. ^{1}H, ^{13}C, and ^{19}F NMR spectra were measured with a Varian MR400 or Inova 500 spectrometer. Mass

spectrometry (HRMS) was carried out by the University of Michigan Mass Spectrometry Facility (J. Windak, director).

Synthetic Protocols

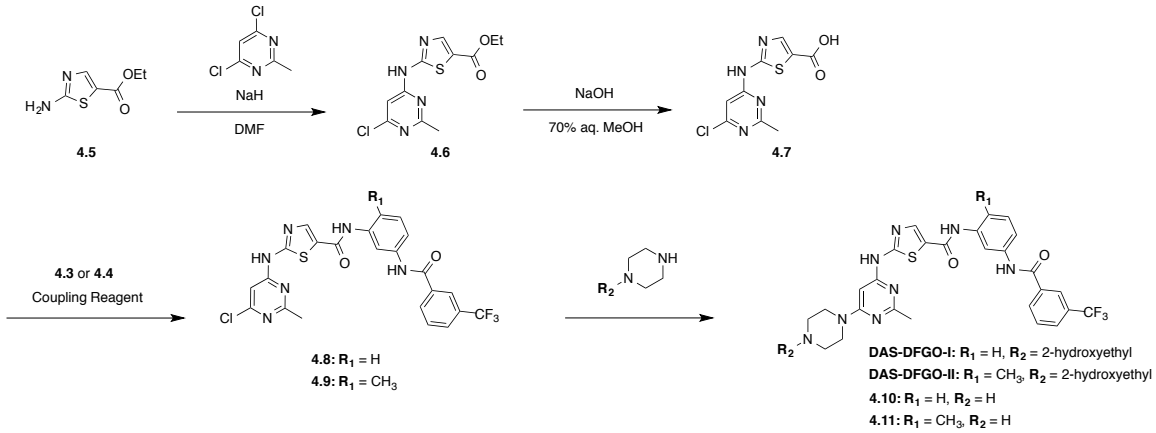

Scheme 4.1. Synthesis of **DAS-DFGO-I** and **DAS-DFGO-II**, compounds **4.5**–**4.11**.

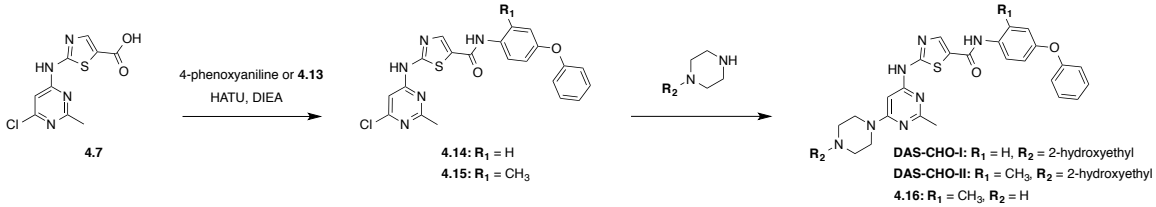

Scheme 4.2. Synthesis of **DAS-CHO-I** and **DAS-CHO-II**, compounds **4.14**–**4.16**.

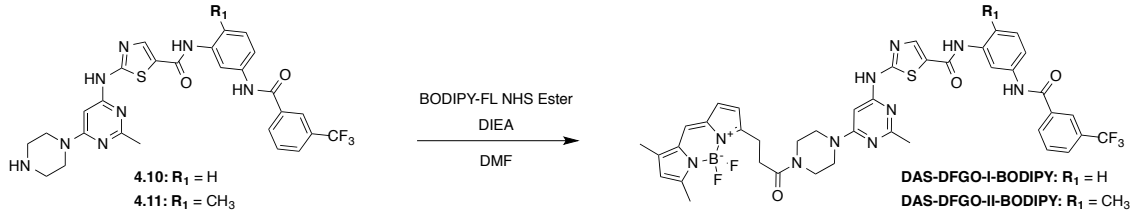

Scheme 4.3. Synthesis of compounds **DAS-DFGO-I-** and **DAS-DFGO-II-BODIPY**.

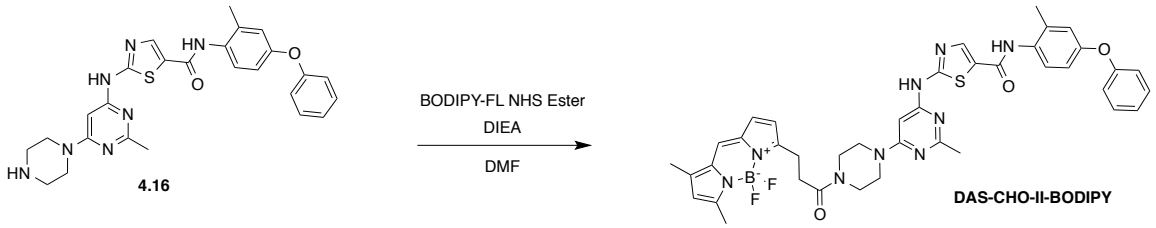

Scheme 4.4. Synthesis of **DAS-CHO-II-BODIPY**.

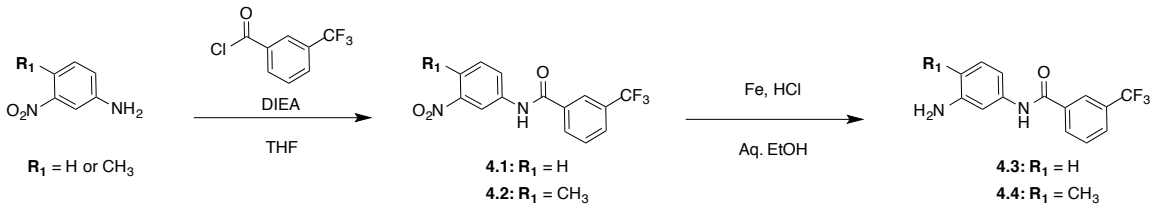

Scheme 4.5. Synthesis of compounds **4.1**–**4.4**.

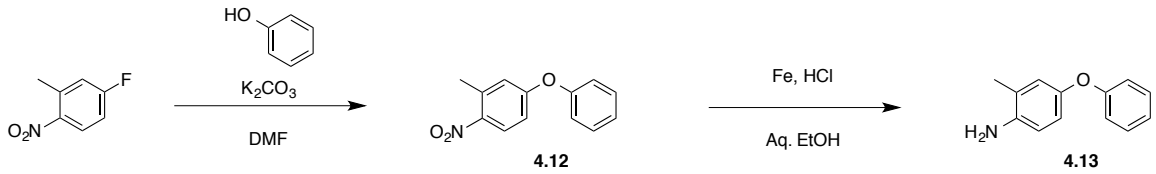

Scheme 4.6. Synthesis of compound **4.12** and **4.13**.

Synthesis of DAS-DFGO-I. Compound **4.8** (0.035 g, 0.066 mmol) was added to an oven-dried round bottom flask. Dioxane (0.5 mL) was added. 1-(2-hydroxyethyl)piperazine (0.086 g, 0.657 mmol) was then added. The reaction was heated to reflux overnight. The reaction mixture was then concentrated under reduced pressure. The crude mixture was then purified using reverse-phase HPLC to afford **DAS-DFGO-I** as a white solid (5 mg, 12% yield). **Spectral data.** ^{1}H NMR (400 MHz, DMSO-d_6) δ 11.47 (s, 1H), 10.48 (s, 1H), 10.14 (s, 1H), 8.26 (s, 2H), 8.30 – 8.15 (m, 2H), 7.94 (d, J = 7.9 Hz, 1H), 7.76 (t, J = 7.8 Hz, 1H), 7.49 – 7.39 (m, 2H), 7.29 (t, J = 8.1 Hz, 1H), 6.04 (s, 1H), 3.58 – 3.53 (m, 8H), 2.40 (s, 3H); ^{19}F NMR (471 MHz, DMSO-d_6) δ -61.07; HRMS-ESI (*m/z*): $[M + H]^+$ calcd for $C_{29}H_{29}F_3N_8O_3S$, 627.2108; found 627.2107.

Synthesis of DAS-DFGO-II. Compound **4.9** (0.250 g, 0.457 mmol) was added to an oven-dried round bottom flask. Dioxane (1.5 mL) was added. 1-(2-hydroxyethyl)piperazine (1.190 g, 9.14 mmol) was then added. The reaction was heated to reflux overnight. The reaction mixture was then concentrated under reduced pressure. The crude mixture was then purified using reverse-phase Biotage C18 column to afford **DAS-DFGO-II** as a white solid (25 mg, 9% yield). **Spectral data.** ^{1}H NMR (400 MHz, DMSO-d_6) δ 11.42 (s, 1H), 10.43 (s, 1H), 9.74 (s, 1H), 8.29 – 8.20 (m, 2H), 8.17 (s, 1H), 7.93 (d, J = 8.0 Hz, 1H), 7.82 – 7.71 (m, 2H), 7.55 (dd, J = 8.3, 2.2 Hz, 1H), 7.22 (d, J = 8.4 Hz, 1H), 6.02 (s, 1H), 4.44 (s, 1H), 3.48 (m, 4H), 3.28 (s, 8H), 2.38 (s, 3H), 2.18 (s,

3H); ^{19}F NMR (376 MHz, DMSO-d_6) δ -61.09; HRMS-ESI (*m/z*): $[M + H]^+$ calcd for $C_{30}H_{31}F_3N_8O_3S$, 641.2265; found 641.2279.

Synthesis of DAS-CHO-I. Compound **4.14** (10 mg, 0.023 mmol) was added to an oven-dried round bottom flask. Dioxane (0.228 mL) was then added, followed by 1-(2-hydroxyethyl)piperazine) (0.028 mL, 0.228 mmol). The reaction was then refluxed overnight. The reaction was then allowed to cool to rt, and the dioxane was removed under reduced pressure. The crude residue was the purified using reverse-phase HPLC using a 5→95% acetonitrile in water gradient. Product **DAS-CHO-I** was isolated as 3 mg of a white solid (25% yield). **Spectral data.** ^{1}H NMR (400 MHz, DMSO-d_6) δ 11.46 (s, 1H), 10.08 (s, 1H), 8.21 (s, 1H), 7.72 – 7.64 (m, 2H), 7.35 (dd, *J* = 8.6, 7.3 Hz, 2H), 7.08 (t, *J* = 7.4 Hz, 1H), 7.04 – 6.92 (m, 4H), 6.03 (s, 1H), 3.29 (s, 3H), 3.21 (s, 0H), 2.39 (s, 4H), 0.79 (s, 0H). ^{13}C NMR (126 MHz, DMSO-d_6) δ 165.66, 163.01, 162.75, 160.24, 157.71, 157.41, 152.43, 141.04, 135.20, 130.42, 127.11, 123.49, 122.18, 119.73, 118.44, 83.18, 52.83, 26.04; HRMS-ESI (*m/z*): $[M + H]^+$ calcd for $C_{27}H_{29}N_7O_3S$, 532.2125; found 532.2118.

Synthesis of DAS-CHO-II. Compound **4.15** (40 mg, 0.089 mmol) was added to an oven-dried round bottom flask. Dioxane (0.9 mL) was then added, followed by 1-(2-hydroxyethyl)piperazine) (0.11 mL, 0.885 mmol). The reaction was then refluxed overnight. The reaction was then allowed to cool to rt, and the dioxane was removed under reduced pressure. The crude residue was the purified using reverse-phase HPLC using a 5→95% acetonitrile in water gradient. Product **DAS-CHO-II** was isolated as 7 mg of a white solid (15% yield). **Spectral data.** ^{1}H NMR (500 MHz, DMSO-d_6) δ 11.44 (s, 1H), 9.69 (s, 1H), 8.17 (s, 1H), 7.43 – 7.36 (m, 2H), 7.30 (d, *J* = 8.6 Hz, 1H), 7.14 (tt, *J* = 7.3, 1.1 Hz, 1H), 7.05 – 6.99 (m, 2H), 6.97 – 6.92 (m, 1H), 6.85 (dd, *J* = 8.5, 2.9 Hz, 1H), 6.04 (s, 1H), 4.45 (t, *J* = 5.4 Hz, 1H), 3.57 – 3.47 (m, 6H), 2.51 – 2.39 (m, 9H), 2.21 (s, 3H). ^{13}C NMR (126 MHz, DMSO-d_6) δ 165.78, 162.82, 162.68, 160.73, 157.38, 157.17, 154.90, 140.95, 136.59, 131.75, 130.52, 128.77, 123.89, 120.66, 118.93, 116.62, 83.25, 70.16, 59.70, 52.45, 43.03, 25.95, 18.38; HRMS-ESI (*m/z*): $[M + H]^+$ calcd for $C_{28}H_{30}ClN_7O_3S$, 546.2282; found 546.2286.

Synthesis of **DAS-DFGO-I-BODIPY**. The characterization of this compound matched previous literature reports.[62]

Synthesis of **DAS-DFGO-I-BODIPY**. Compound **4.10** (5.83 mg, 10 μmol), and BODIPY-FL NHS ester (3.81 mg, 10 μmol) were dissolved in DMF (0.5 mL). DIEA (1.8μL, 10 μmol) was added after 10 min, and the resulting mixture was stirred at rt for 15 h. The crude reaction mixture was diluted into DMF and HPLC purified (linear gradient of 20 → 80% CH_3CN in water) to yield compound **DAS-DFGO-I-BODIPY** as a bright red solid (4.13 mg, 48% yield). **Spectral data**. ^{1}H NMR (400 MHz, DMSO-d_6) δ 11.83 (s, 1H), 10.84 (s, 1H), 10.49 (s, 1H), 8.65 – 8.55 (m, 4H), 8.29 (d, J = 7.7 Hz, 1H), 8.11 (t, J = 7.7 Hz, 1H), 8.02 (d, J = 4.8 Hz, 1H), 7.79 (t, J = 9.3 Hz, 2H), 7.65 (t, J = 8.0 Hz, 1H), 7.42 (d, J = 4.2 Hz, 1H), 6.76 (d, J = 4.1 Hz, 1H), 6.63 (d, J = 4.6 Hz, 1H), 6.39 (d, J = 4.4 Hz, 1H), 3.91 (d, J = 4.7 Hz, 8H), 3.43 (t, J = 7.5 Hz, 2H), 3.10 (t, J = 7.7 Hz, 2H), 2.79 (s, 3H), 2.76 (s, 3H), 2.59 (d, J = 4.6 Hz, 3H). ^{19}F NMR (376 MHz, DMSO-d_6) δ -60.55, -142.47. HRMS-ESI (*m/z*): $[M + H]^+$ calcd for $C_{41}H_{38}BF_5N_{10}O_3S$, 857.2935; found 857.2943.

Synthesis of **DAS-DFGO-II-BODIPY**. Compound **4.11** (6 mg, 10 μmol) and BODIPY-FL NHS ester (4 mg, 10.7 μmol) were dissolved in DMF (0.4 mL). DIEA (1.8 μL, 10 μmol) was added after 10 min, and the resulting mixture was stirred at rt for 16 h. The crude reaction was diluted into DMF and HPLC purified (linear gradient of 20 → 80% CH_3CN in water) to yield compound **DAS-DFGO-II-BODIPY** as a bright red solid (2.96 mg, 34% yield). **Spectral data**. ^{1}H NMR (400 MHz, DMSO-d_6) δ 11.65 (s, 1H), 10.63 (s, 1H), 9.96 (s, 1H), 8.49 – 8.41 (m, 2H), 8.38 (d, J = 1.8 Hz, 1H), 8.13 (d, J = 7.9 Hz, 1H), 7.97 (dd, J = 16.2, 8.2 Hz, 2H), 7.87 (d, J = 1.7 Hz, 1H), 7.76 (d, J = 8.2 Hz, 1H), 7.43 (d, J = 8.5 Hz, 1H), 7.27 (d, J = 3.9 Hz, 1H), 6.61 (d, J = 3.9 Hz, 1H), 6.47 (s, 1H), 6.24 (s, 1H), 3.74 (d, J = 11.9 Hz, 8H), 3.28 (t, J = 7.8 Hz, 2H), 2.95 (t, J = 7.8 Hz, 2H), 2.64 (s, 3H), 2.60 (d, J = 1.8 Hz, 3H), 2.43 (s, 3H), 2.39 (s, 3H) ^{19}F NMR (376 MHz, DMSO-d_6) δ -60.69, -142.60. HRMS-ESI (*m/z*): $[M + H]^+$ calcd for, $C_{42}H_{40}BF_5N_{10}O_3S$, 871.3092; found 871.3094.

Synthesis of **DAS-CHO-II-BODIPY**. Compound **4.16** (10.2 mg, 20 μmol), and BODIPY-FL NHS ester (8 mg, 21 μmol) were dissolved in DMF (1 mL). DIEA (4 μL, 21 μmol) was added after 10 min, and the resulting mixture was stirred at rt for 17 h. The crude reaction mixture was diluted into DMF and HPLC purified (linear gradient of 25 → 80% CH_3CN in water) to yield slightly impure compound. A second HPLC purification using 0.1% TFA (linear gradient of 20 → 80% CH_3CN in water) was performed and the final compound, **DAS-CHO-II-BODIPY**, was obtained as a TFA salt, appearing as a bright red solid (3.2 mg, 20.3% yield). **Spectral data**. ^{1}H NMR (400 MHz, DMSO-d_6) δ 11.46 (s, 1H), 9.69 (s, 1H), 8.18 (s, 1H), 7.70 (s, 1H), 7.40 (t, J = 7.8 Hz, 2H), 7.30 (d, J = 8.4 Hz, 1H), 7.17–7.09 (m, 2H), 7.03 (d, J = 7.9 Hz, 2H), 6.96–6.93 (m, 1H), 6.87–6.82 (m, 1H), 6.44 (d, J = 4.0 Hz, 1H), 6.30 (s, 1H), 6.07 (s, 1H), 3.64–3.52 (m, 8H), 3.11 (t, J = 7.4 Hz, 3H), 2.78 (t, J = 7.4 Hz, 3H), 2.47 (s, 3H), 2.43 (s, 3H), 2.26 (s, 3H), 2.21 (s, 3H). ^{19}F NMR (376 MHz, DMSO-d_6) δ -73.45 (TFA counter ion), -143.13. HRMS-ESI (*m/z*): $[M + H]^+$ calcd for $C_{40}H_{40}BF_2N_9O_3S$, 776.3109; found 776.3113.

Synthesis of 4.1. 3-nitroaniline (7.5 g, 54.3 mmol) was added to an oven-dried flask. Dichloromethane (271 mL) was added. The reaction mixture was then cooled to 0^{o}C using an ice bath. 3-trifluoromethylbenzoyl chloride (12.4 g, 59.7 mmol) was then added, followed by diisopropylethylamine (8.42 g, 65.2 mmol). The reaction mixture was then allowed to warm to rt and stir overnight. Dichloromethane (270 mL) was then added. The reaction mixture was then washed with 1 N HCl (270 mL), the aqueous layer was then back-extracted three times with dichloromethane (100 mL). The organic layers were then collected and dried over sodium sulfate. The solvent was then removed under reduced pressure. The crude reaction mixture was then purified via silica gel chromatography using a Biotage Isolera One to yield 16 g of compound **4.1** as a light yellow solid (95 % yield). **Spectral data.** ^{1}H NMR (400 MHz, DMSO-d_6): δ 10.92 (s, 1 H), 8.77-8.74 (m, 1 H), 8.32-8.26 (m, 2 H), 8.21-8.17 (m, 1 H), 7.98-7.92 (m, 2 H), 7.80-7.74 (m, 1 H), 7.66-7.61 (m, 1 H); ^{19}F NMR (376 MHz, DMSO-d_6) δ -61.15; HRMS-ESI (*m/z*): $[M + H]^+$ calcd for $C_{14}H_9F_3N_2O_3$, 311.0638; found 311.0638.

Synthesis of 4.2. 4-methyl-3-nitroaniline (2.0 g, 13.1 mmol) was added to an oven-dried flask. Tetrahydrofuran (66 mL) was added. The reaction mixture was then cooled to 0 ^{o}C using an ice bath. 3-trifluoromethylbenzoyl chloride (2.742 g, 13.1 mmol) was then added, followed by diisopropylethylamine (2.039 g, 15.77 mmol). The reaction mixture was then allowed to warm to room temperature and stir overnight. Tetrahydrofuran was then removed via rotary vaporization. The crude mixture was then suspended in water, filtered, and then rinsed with water twice. After drying 4.1 g of **4.2** as a light yellow solid was obtained (96 % yield). **Spectral data.** ^{1}H NMR (400 MHz, DMSO-d_6) δ 10.77 (s, 1H), 8.50 (d, J = 2.3 Hz, 1H), 8.31 – 8.22 (m, 2H), 7.97 (t, J = 9.4 Hz, 2H), 7.77 (t, J = 7.8 Hz, 1H), 7.47 (d, J = 8.4 Hz, 1H), 1.23 (s, 3 H); ^{19}F NMR (376 MHz, DMSO-d_6) δ -61.60; HRMS-ESI (*m/z*): $[M + H]^+$ calcd for $C_{15}H_{11}F_3N_2O_3$, 325.0795; found 325.0794.

Synthesis of 4.3. Compound **4.1** (2.3 g, 7.4 mmol) and iron (2.1 g, 37.1 mmol) were added to a round-bottom flask. Ethanol (32 mL) and water (8 mL) were then added, followed by the addition of several drops of concentrated Hydrochloric Acid. The reaction mixture was then heated to reflux for 16 h. The reaction mixture was then filtered through celite and the celite was washed with additional hot ethanol. The ethanol was removed via rotary vaporization and the crude reaction was then suspended in water and filtered. After drying 2.0 g of **4.3** as an off-white solid was obtained (96 % yield). **Spectral data.** ^{1}H NMR (400 MHz, DMSO-d_6): δ 10.15 (s, 1 H), 8.23-8.17 (m, 2 H), 7.93-7.89 (m, 1 H), 7.76-7.70 (m, 1 H), 7.06-7.03 (m, 1 H), 6.97-6.91 (m, 1 H), 6.85-6.80 (m, 1 H), 6.32-6.27 (m, 1 H), 5.09 (s, 2 H); ^{19}F NMR (376 MHz, DMSO-d_6) δ -61.15; HRMS-ESI (*m/z*): $[M + H]^+$ calcd for $C_{14}H_{11}F_3N_2O$, 281.0896; found 281.0905.

Synthesis of 4.4. Compound **4.2** (2.0 g, 6.2 mmol) and iron (1.72 g, 30.8 mmol) were added to a round-bottom flask. Ethanol (25 mL) and water (6.2 mL) were then added, followed by the addition of several drops of concentrated Hydrochloric Acid. The reaction mixture was then heated to reflux for 90 minutes. The reaction mixture was then filtered through celite and the celite was washed with additional hot ethanol. The ethanol was removed via rotary vaporization and the crude reaction was then suspended in water and filtered. After drying 1.4 g of **4.4** as an off-white solid was obtained (78 % yield). **Spectral data.** ^{1}H NMR (400 MHz, DMSO-d_6) δ 10.11 (s, 1H), 8.24 – 8.15 (m, 2H), 7.90

(d, J = 7.7 Hz, 1H), 7.72 (t, J = 7.9 Hz, 1H), 7.06 (s, 1H), 6.87 – 6.75 (m, 2H), 4.85 (s, 2H), 1.99 (s, 3H); ^{19}F NMR (376 MHz, DMSO-d_6) δ -61.08; HRMS-ESI (m/z): $[M + H]^+$ calcd for $C_{15}H_{13}F_3N_2O$, 295.1053; found 295.1061.

Synthesis of 4.5. The characterization of this compound matched previous literature reports.[28]

Synthesis of 4.6. ethyl 2-aminothiazole-5-carboxylate (**4.5**, 1.0 g, 5.8 mmol) and 4,6-dichloro-2-methylpyrimidine (0.95 g, 5.8 mmol) were added to an oven dried flask. Dimethylformamide (20 mL) was then added. The reaction mixture was then cooled to 0^o C, and sodium hydride (0.510 g, 12.8 mmol) was added. The reaction was allowed to warm to rt and stir for an additional 3 h. Excess base was quenched using ammonium chloride. The reaction was then suspended in water and filtered. After drying the **4.6** was obtained as a white solid (1.4g, 81% yield). **Spectral data.** ^{1}H NMR (400 MHz, DMSO-d_6) δ 12.30 (s, 1H), 8.07 (s, 1H), 6.88 (s, 1H), 4.24 (q, J = 7.1 Hz, 2H), 2.54 (s, 3H), 1.26 (t, J = 7.1 Hz, 3H); ^{13}C NMR (126 MHz, DMSO-d_6) δ 167.85, 162.83, 161.96, 159.07, 157.88, 145.84, 122.02, 104.11, 61.22, 25.61,14.70; HRMS-ESI (m/z): $[M + H]^+$ calcd for $C_{11}H_{11}ClN_4O_2S$, 299.0364; found 299.0371.

Synthesis of 4.7. Compound **4.6** (1.4 g, 4.7 mmol) and sodium hydroxide (1.5 g, 37.5 mmol) were added to an oven-dried round bottom flask. Methanol (11 mL) and water (4 mL) were then added. The reaction was stirred at room temperature for 48 hours. Methanol was then removed under reduced pressure. The crude reaction mixture was then suspended in 1 N HCl and filtered. After drying **4.7** (0.95 g, 75 % yield) was obtained as a white solid. **Spectral data.** ^{1}H NMR (500 MHz, DMSO-d_6) δ 8.03 (s, 1H), 6.97 (s, 1H), 2.56 (s, 3H); ^{13}C NMR (126 MHz, DMSO-d_6) δ 167.79, 163.39, 162.56, 158.94, 157.97, 145.28, 123.38, 104.03, 40.46, 40.29, 40.21, 40.13, 40.05, 39.96, 39.79, 39.62, 39.46, 25.57; HRMS-ESI (m/z): $[M + H]^+$ calcd for $C_9H_7ClN_4O_2S$, 271.0051; found 271.0055.

Synthesis of 4.8. Acid **4.7** (0.075 g, 0.277 mmol), aniline **4.3** (0.078 g, 0.277 mmol), and HATU (0.116 g, 0.305 mmol) were added to an oven-dried round bottom flask. Dimethylformamide (1.4 mL) was then added, followed by DIEA (0.143 g, 1.1 mmol). The reaction was allowed to stir at rt overnight. The reaction was then diluted in ethyl acetate (100 mL), and washed with water followed by brine. The organic layer was then dried over sodium sulfate. The crude reaction mixture was then purified via silica gel chromatography using a Biotage Isolera One (linear gradient 40 → 100% EtOAc in hexanes) to yield 0.035 g of compound **4.8** as a white solid (24 % yield). **Spectral data.** ^{1}H NMR (500 MHz, DMSO-d_6) δ 12.20 (s, 1H), 10.51 (s, 1H), 10.27 (s, 1H), 8.37 (s, 1H), 8.31 – 8.24 (m, 3H), 7.95 (d, J = 7.8 Hz, 1H), 7.77 (t, J = 7.8 Hz, 1H), 7.47 (dd, J = 16.4, 8.0 Hz, 2H), 7.32 (t, J = 8.1 Hz, 1H), 6.93 (s, 1H), 2.58 (s, 3H); ^{19}F NMR (471 MHz, DMSO-d_6) δ -61.09; HRMS-ESI (*m/z*): $[M + H]^+$ calcd for $C_{23}H_{16}ClF_3N_6O_2S$, 533.0769; found 533.0778.

Synthesis of 4.9. Acid **4.7** (0.9 g, 3.3 mmol) was added to an oven-dried round bottom flask. Tetrahydrofuran (11 mL) was then added. The reaction was cooled to 0^{o} C. Oxalyl chloride (0.5 g, 4.0 mmol) was added, followed by a drop of dimethylformamide. The reaction was allowed to warm to room temperature and stir for an additional twenty minutes. The crude mixture was then concentrated under reduced pressure. The crude reaction mixture was then again dissolved in tetrahydrofuran (11mL). Aniline **4.4** (1.0 g, 3.3 mmol) was then added followed by DIEA (0.43 g, 3.3 mmol). The reaction was then allowed to stir overnight at rt. The crude reaction mixture was then purified via silica gel chromatography using a Biotage Isolera One (linear gradient 40 → 100% EtOAc in hexanes) to yield 0.250 g of compound **4.9** as a white solid (14 % yield). **Spectral data.** ^{1}H NMR (400 MHz, DMSO-d_6) δ 12.19 (s, 1H), 10.45 (s, 1H), 9.90 (s, 1H), 8.30 – 8.11 (m, 3H), 7.93 (d, J = 7.8 Hz, 1H), 7.86 – 7.71 (m, 2H), 7.56 (dd, J = 8.2, 2.3 Hz, 1H), 7.24 (d, J = 8.3 Hz, 1H), 6.91 (s, 1H), 2.56 (s, 3H), 2.19 (s, 3H); ^{19}F NMR (376 MHz, DMSO-d_6) δ -61.10; HRMS-ESI (*m/z*): $[M + H]^+$ calcd for $C_{24}H_{18}ClF_3N_6O_2S$, 547.0925; found 547.0924.

Synthesis of **4.10**. Compound **4.8** (230 mg, 0.43 mmol), and piperazine (740 mg, 0.86 mmol) were dissolved in dioxane (1.3 mL) and the resulting mixture was refluxed overnight at 120 °C. The solvent was removed and the crude solid was purified using reverse phase C18 column chromatography (linear gradient of 30 → 100% CH_3CN in water) to yield compound **4.10** as a light brown solid (110 mg, 44% yield). **Spectral data**. ^{1}H NMR (400 MHz, DMSO-d_6) δ 10.64 (s, 1H), 10.28 (s, 1H), 8.41 (d, J = 13.6 Hz, 4H), 8.11 (s, 1H), 7.92 (s, 1H), 7.60 (s, 2H), 7.45 (s, 1H), 6.14 (s, 1H), 4.00 (s, 1H), 3.57 (s, 4H), 2.86 (s, 4H), 2.54 (s, 3H), 1.35 (s, 1H). ^{19}F NMR (376 MHz, DMSO-d_6) δ -60.76. HRMS-ESI (*m/z*): $[M + H]^+$ calcd for $C_{27}H_{25}F_3N_8O_2S$, 583.1846; found 583.1847.

Synthesis of **4.11**. Compound **4.9** (170 mg, 0.31 mmol) and piperazine (267 mg, 3.1 mmol) were dissolved in n-butanol (1.5 mL) and followed by the addition of DIEA (0.11 mL, 0.62 mmol). Resulting mixture was refluxed at 120 °C for 18 h. The reaction mixture was cooled slowly to rt and poured into water. The precipitated solid was filtered and washed several times with water. The crude solid was purified using reverse phase C18 column chromatography (linear gradient of 40 → 60% CH_3CN in water) to yield compound **4.11** as an off-white solid (74 mg, 40% yield). **Spectral data**. ^{1}H NMR (500 MHz, DMSO-d_6) δ 11.32 (s, 1H), 10.47 (s, 1H), 9.77 (s, 1H), 8.32 – 8.24 (m, 2H), 8.20 (s, 1H), 7.96 (d, J = 7.8 Hz, 1H), 7.84 – 7.75 (m, 2H), 7.59 (dd, J = 8.3, 2.2 Hz, 1H), 7.26 (d, J = 8.3 Hz, 1H), 6.01 (s, 1H), 3.43 (t, J = 5.0 Hz, 4H), 2.73 (dd, J = 6.1, 3.9 Hz, 4H), 2.53 (s, 1H), 2.40 (s, 3H), 2.21 (s, 3H). ^{19}F NMR (376 MHz, DMSO-d_6) δ -60.75. HRMS-ESI (*m/z*): $[M + H]^+$ calcd for $C_{28}H_{27}F_3N_8O_2S$, 597.2003; found 597.2001.

Synthesis of 4.12: 4-fluoro-2-methyl-1-nitrobenzene (1 g, 6.45 mmol), phenol (0.61 g, 6.45 mmol), and potassium carbonate (2.67 g, 19.34 mmol) were added to an oven-dried flask. N,N-dimethylformamide (21.5 mL) was then added and the reaction mixture was heated to 85 ^{o}C overnight. The reaction mixture was cooled to rt and subsequently diluted with ethyl acetate. The organic solution was then washed with neutral water twice, followed by one wash with brine. The organic layer was then dried over sodium sulfate. The solvent was then removed under reduced pressure. The product, **4.12**, was isolated as 2.1 g (86% yield) of an oil. **Spectral data.** ^{1}H NMR (400 MHz, $CDCl_3$) δ 8.07 – 7.99 (m, 1H), 7.46 – 7.30 (m, 2H), 7.22 (dt, J = 7.2, 1.3 Hz, 1H), 7.10 – 7.00 (m, 2H), 6.87 – 6.74

(m, 2H), 2.58 (s, 3H). ^{13}C NMR (126 MHz, $CDCl_3$) δ 161.62, 154.86, 143.45, 137.10, 130.24, 127.46, 125.17, 120.53, 120.43, 115.05, 21.42; HRMS-EI (*m/z*): calcd for $C_{13}H_{11}NO_3$, 229.0739; found 229.0736.

Synthesis of 4.13. Compound **4.12** (0.96 g, 4.19 mmol) was added to an oven-dried round bottom flask. Ethanol (16.75 mL) and water (4.2 mL) were then added followed by iron (1.17 g, 21 mmol). Several drops of concentrated hydrochloric acid were then added, and the reaction was refluxed for 90 min. After cooling to rt the crude reaction was filtered through celite. Ethanol was removed under reduced pressure. The crude residue was dissolved in ethyl acetate, and the organic solution was washed with water. The organic layer was then dried over sodium sulfate. The crude residue was subjected to silica gel chromatography (0→40% Ethyl acetate in hexanes). Removal of the organic solvent provided (0.37 g, 1.86 mmol) of product **4.13** as a dark brown oil (44% yield). **Spectral data.** ^{1}H NMR (400 MHz, $CDCl_3$) δ 7.32 – 7.21 (m, 2H), 6.99 (td, *J* = 7.4, 1.1 Hz, 1H), 6.95 – 6.88 (m, 2H), 6.81 – 6.70 (m, 2H), 6.64 (d, *J* = 8.4 Hz, 1H), 3.50 (s, 2H), 2.14 (s, 3H). ^{13}C NMR (126 MHz, $CDCl_3$) δ 159.03, 148.37, 140.89, 129.50, 123.97, 122.30, 121.95, 118.67, 117.18, 115.85, 17.60; HRMS-ESI (*m/z*): $[M + H]^+$ calcd for $C_{13}H_{13}NO$, 200.1070; found 200.1075.

Synthesis of 4.14. 2-((6-chloro-2-methylpyrimidin-4-yl)amino)thiazole-5-carboxylic acid (44 mg, 0.162 mmol) and HATU (68 mg, 0.178 mmol) were added to an oven-dried round bottom flask. N,N-dimethylformamide (0.8 mL) was then added, followed by diisopropylethylamine (0.085 mL, 0.486 mmol). The reaction was allowed to stir at rt for 45 min. 4-phenoxyaniline (30 mg, 0.162 mmol) was then added, and the reaction was allowed to stir overnight at rt. The reaction mixture was then precipitated by addition of water. The crude mixture was filtered, and the solid that was collected was then subjected to silica gel chromatography using a 30 → 100% ethyl acetate in hexanes gradient. Product **4.14** was isolated as tan solid. **Spectral data.** ^{1}H NMR (400 MHz, DMSO-d_6) δ 12.20 (s, 1H), 10.19 (s, 1H), 8.29 (s, 1H), 7.68 (d, *J* = 8.4 Hz, 2H), 7.35 (t, *J* = 7.8 Hz, 2H), 7.09 (t, *J* = 7.4 Hz, 1H), 7.04 – 6.89 (m, 5H), 2.57 (s, 3H). ^{13}C NMR (100 MHz, DMSO-d_6): ^{13}C NMR (126 MHz, DMSO-d_6) δ 167.88, 161.69, 159.87, 158.96, 157.94,

157.63, 152.65, 141.04, 134.94, 130.44, 123.55, 122.32, 119.71, 118.50, 118.32, 103.85, 25.65; HRMS-ESI (*m/z*): $[M + H]^+$ calcd for $C_{21}H_{16}ClN_5O_2S$, 438.0786; found 438.0792.

Synthesis of 4.15. 2-((6-chloro-2-methylpyrimidin-4-yl)amino)thiazole-5-carboxylic acid (**4.7**, 75 mg, 0.28 mmol) and HATU (116 mg, 0.305 mmol) were added to an oven-dried round bottom flask. N,N-dimethylformamide (1.4 mL) was then added, followed by diisopropylethylamine (0.194 mL, 1.108 mmol). The reaction was allowed to stir at rt for 45 min. Compound **4.13** (59 mg, 0.28 mmol) was then added, and the reaction was allowed to stir overnight at rt. The reaction mixture was then dissolved in ethyl acetate and the organic solution was washed with water twice, followed by a brine wash. The crude mixture was then subjected to silica gel chromatography using a 0 → 100% ethyl acetate in hexanes gradient. Product **4.15** was isolated as a tan solid. **Spectral data.** ^{1}H NMR (400 MHz, DMSO-d_6) δ 12.18 (s, 1H), 9.80 (s, 1H), 8.25 (s, 1H), 7.42 – 7.32 (m, 2H), 7.28 (d, *J* = 8.6 Hz, 1H), 7.11 (td, *J* = 7.4, 1.2 Hz, 1H), 7.04 – 6.87 (m, 4H), 6.82 (dd, *J* = 8.6, 2.8 Hz, 1H), 2.56 (s, 3H), 2.18 (s, 3H). ^{13}C NMR (126 MHz, DMSO-d_6) δ 165.58, 162.85, 160.57, 157.42, 157.29, 154.76, 141.00, 136.46, 131.95, 130.48, 128.68, 126.71, 123.79, 120.73, 118.90, 116.64, 83.04, 45.07, 44.22, 31.14, 29.45, 28.99, 26.06, 18.47. HRMS-ESI (*m/z*): [M + H]+ calcd for $C_{26}H_{27}N_7O_2S$, 502.2020; found 502.2014.

Synthesis of **4.16**. Compound **4.15** (100 mg, 0.22 mmol) and piperazine (190 mg, 2.2 mmol) were dissolved in n-butanol (1 mL) and followed by the addition of DIEA (77 µL, 0.44 mmol). Resulting mixture was refluxed at 120 °C for 18 h. The reaction mixture was cooled slowly to rt and poured into water. The precipitated solid was filtered and washed several times with water. The crude solid was purified using reverse phase C18 column chromatography (linear gradient of 40 → 60% CH_3CN in water). An impurity remained so the crude material was purified a second time by HPLC (20 → 80% CH_3CN in water) to yield compound **4.16** as an off-white solid (6 mg, 5.5% yield). **Spectral data**. ^{1}H NMR (500 MHz, DMSO-d_6) δ 11.48 (s, 1H), 9.70 (s, 1H), 8.18 (s, 1H), 7.43 – 7.35 (m, 2H), 7.29 (d, *J* = 8.6 Hz, 1H), 7.14 (tt, *J* = 7.2, 1.1 Hz, 1H), 7.05 – 6.98 (m, 2H), 6.95 (d, *J* = 2.8 Hz, 1H), 6.85 (dd, *J* = 8.5, 2.8 Hz, 1H), 6.05 (s, 1H), 3.55 (s, 4H), 2.91 (s, 4H), 2.41 (s, 3H), 2.20 (s, 3H), 1.23 (s, 1H). ^{13}C NMR (126 MHz, DMSO-d_6) δ 165.58, 162.85,

160.57, 157.42, 157.29, 154.76, 141.00, 136.46, 131.95, 130.48, 128.68, 126.71, 123.79, 120.73, 118.90, 116.64, 83.04, 45.07, 44.22, 31.14, 29.45, 28.99, 26.06, 18.47. HRMS-ESI (*m/z*): $[M + H]^+$ calcd for $C_{26}H_{27}N_7O_2S$, 502.2020; found 502.2014.

Spectral Data for Compounds

Spectral data (^1H, ^{13}C and ^{19}F NMR) for **DAS-DFGO-I**, **DAS-DFGO-II**, **DAS-CHO-I**, **DAS-CHO-II**, **DAS-DFGO-I-**, **DAS-DFGO-II-**, and **DAS-CHO-II-BODIPY** and compounds **4.1**-**4.16** is shown in **Appendix C**.

Protein Purification and Crystallization Conditions

Wild type chicken c-Src kinase domain (residues 251–533) and human c-Abl kinase domain (residues 229–512) in pET28a, modified with a TEV protease cleavable N-terminal 6x-His tag were provided by M. Seeliger (SUNY, Stony Brook) and J. Kuriyan (UC Berkeley). Cell growth and expression and protein purification were performed using modified literature protocols for expression of wild-type c-Src and c-Abl kinase domain.[63] Briefly, the plasmid containing the kinase (pET28a) was transformed into *E. Coli* BL21DE3 cells already containing YopH phosphatase (pCDFDuet-1 plasmid) and plated on LB agar with kanamycin (50 μg/mL, kan) and streptomycin (50 μg/mL, SM) and grown overnight at 37 ^oC. A single colony was picked for a starter culture (LB containing kan/SM) and subsequently grown overnight at 37 ^oC. The next day, scaled up cultures (TB containing kan/SM) were grown to an OD_{600nm} of 1.2 at 37 ^oC and cooled to 18 ^oC with shaking prior to induction for 16 h at 18 ^oC with 0.2 mM IPTG. Cells were harvested by 20 min centrifugation at 4,000 rpm at 4 ^oC and resuspended in 50 mM Tris (pH 8.0), 500 mM NaCl, 5% glycerol, 25 mM imidazole (buffer A) supplemented with 0.1 mM PMSF for immobilized Ni metal affinity chromatography. Cells were lysed via sonication and insoluble protein and cell debris was sedimented through a 50-min centrifugation at 14,000 rpm at 4 ^oC. The clear supernatant was loaded onto the Ni-NTA agarose affinity column (batch, QIAGEN) column. The resin was washed with 50 column volumes of buffer A and five column volumes (3X) of buffer QB (20 mM Tris, pH 8.0, 5% glycerol, 1 M NaCl). Protein was eluted with five column volumes (4X) of buffer B (buffer A plus 0.5 M imidazole). The buffer B fractions were pooled together and cleaved with 0.1 mg of TEV per 2.5 mg of

crude kinase. Cleaved protein was loaded onto an anion exchange column (Q Sepharose, Fast Flow, GE Healthcare Life sciences) equilibrated with buffer QA (buffer QB without 1 M NaCl). Proteins were eluted with a linear gradient of 0–35% buffer QB and peak fractions were combined (based on kinase activity assay) and concentrated down in order to be loaded onto a size-exclusion column (HiLoad Superdex S75, GE Healthcare Life sciences) equilibrated with buffer D (50 mM Tris, pH 8.0, 5% glycerol, 200 mM NaCl, 1 mM DTT). Pure fractions via SDS-PAGE were combined and concentrated down to a concentration of ~8 mg/mL (~260 μM).

Kinase-inhibitor complexes were formed in solutions of 163 μM kinase domain, 250 μM inhibitor, 50 mM Tris (pH 8.0), 200 mM NaCl, 5% (v/v) DMSO and 5-6% (v/v) glycerol. Crystals grew overnight at 20 ^{o}C using hanging-drop vapor diffusion. Drops contained 1 μL of complex + 1 μL well solution (0.1 M MES (pH 6.5), 16-22% (w/v) PEG 3350 and 100-420 mM sodium acetate). Prior to data collection, crystals were cryoprotected in well solution plus 20% (v/v) glycerol. X-ray diffraction data for both c-Src complexes were collected at 100 K and at a wavelength of 0.9787 Å at the Advanced Photon Source at Argonne National Laboratories on the 21-ID-F beamline. Data for the c-Abl complex was collected at 100 K and at a wavelength of 0.9793 Å on the 21-ID-D beamline.

Structure Determination of Kinase-Inhibitor Complexes

For the three protein-inhibitor complexes, diffraction data were processed and scaled with HKL2000.[64] The structures were solved by molecular replacement using PHASER (McCoy et al., 2007).[65] The inactive conformation of the kinase domain of chicken c-Src (PDB code 2OIQ[20]; residues 260–520 and PDB code 4DGG[11]; residues 266–519) without the αC-helix (residues 298–310) and the activation loop (residues 400–425) were the search models for the Src–**DAS-DFGO-I** and Src–**DAS-CHO-I** structures, respectively. The inactive conformation of the kinase domain of human c-Abl (PDB code 2G1T[34]; residues 232–502) without the αC-helix (residues 275–287) and the activation loop (residues 377–402) was the search model for the Abl–**DAS-CHO-I** complex. The structures were built with iterative rounds of electron density fitting in Coot[66] and refinement in autoBUSTER.[67] After the initial refinement, clear Fo-Fc density was

visible for each compound in the ATP pocket of the protein. Three-dimensional coordinates and restraint files for each ligand were generated using smiles string in GRADE[68] (Smart et al., 2011) employing the mogul+qm option. The structures were analyzed with Molprobity[69] (Chen et al., 2010) and EDS server.[70] Statitstics and electron density map images are found in **Appendix C**.

BODIPY Proble K_d Determination

An endpoint fluorescence assay[71] was used to determine K_d values. Reaction volumes of 50 µL were used in 96-well plates. 34 µL of buffer A 1X (100 mM Tris pH 8, 10 mM $MgCl_2$) was added to a single row, followed by 15 µL of enzyme (3.3X concentration) in buffer A with 3-fold dilutions (typically 125 nM, 42, 14, 4.6, 1.5, 0.5, 0.17, 0.06, 0.02, 0.01 and 0 µM final well concentration in buffer A). Then 1 µL of a 500 nM stock of the appropriate dasatinib analog BODIPY probe in DMSO was added (2% DMSO final). Wells were incubated at rt for 30 minutes prior to end point read (ex/em 485/535 nm). Reactions had final concentrations of 10 nM BODIPY-probe, 100 mM Tris buffer (pH 8) and 10 mM $MgCl_2$. For K_d determination, the values were obtained directly from the nonlinear regression one-site binding curves (using normalized data) in the presence of various concentrations of the enzyme. The equation $Y = (B_{max} * X)/(K_d + X)$; was used in the nonlinear regression. All 4 runs were averaged together for each reported value. Raw data for K_d determination can be found in **Appendix C**.

Inhibitor Off-rate Determination

A multiple time point read fluorescence assay[71] was used to determine dasatinib analog BODIPY off-rates. Briefly, 60 µL of total volume with 700 nM enzyme and 500 nM probe in buffer A 1X (Master Mix) was incubated at rt for 4 h along with 60 µL of 500 nM probe alone in buffer A 1X (Blank Mix). Following this incubation period, 4 µL of the master mix was added into 5 wells and 4 µL of the blank mix was added into 2 wells via multichannel pipette into 116 µL of buffer A 1X containing 5 µM (final concentration) unlabeled dasatinib (120 µL total, 30-fold dilution). Additionally, 4 µL of master mix was added into a single well of 116 µL of buffer A 1X containing 100 nM (final concentration) probe to maintain consistent plate reader gain values over the course of the fluorescent reads. Master mix dilutions with competitor had final concentrations of

23 nM enzyme, 17 nM BODIPY-probe, 5 μM unlabeled dasatinib, 100 mM Tris buffer pH 8 and 10 mM $MgCl_2$. Reads (ex/em 485/535 nm) were taken every 10 minutes for the first 2 h, then every 20 min for next two hours and finally every 30 min for the remainder of the assay (12 h total). The values for k_{off} determination were obtained directly from the nonlinear regression fits for one-phase decay curves (using blanked data). The equation Y = (Y0 - Plateau)*exp(-K*X) + Plateau; was used in the nonlinear regression. An average of 5 wells at each time point was utilized for the final fit values produced. Raw data for kinetic data determination can be found in **Appendix C**

Kinome-wide Inhibitor Profiling

Inhibitor selectivity profiles were obtained through Luceome Biotechnologies (Tuscon, AZ).[53,54] Each inhibitor was screened at 0.5 μM against a panel of 124 wt kinases. Tabulated kinase data can be found in **Appendix C**

Cellular Characterization

All Ba/F3 cell lines were cultured in RPMI 1640 media with 10% FBS. Parental Ba/F3 cell culture additionally contained 15% WEHI-3 conditioned media. An aliquot of the cells was mixed with Trypan Blue solution and the cell number was quantified using a hemacytometer. The cells were plated 100 μL in each well at 50,000 cells/mL so that each well contained 5,000 cells. The cells were plated into sterile, clear bottom 96 well plates and then immediately dosed with compound. Additionally, 3 wells were created containing 100 μL of media with no cells. The compounds were made in 100% DMSO at 1,000X the final concentrations that were desired for the assay generally covering a concentration range of 6 log units. These DMSO stocks were diluted 10X in RPMI 1640 media. 1 μL of the compound diluted in media was added to each well for a final concentration of 0.1% DMSO. The wells containing only media were not dosed. In general, each compound concentration was dosed in triplicate wells. The plates were returned to normal culture conditions (per ATCC) for 72 hours. After 72 hours, the plates were removed from the incubator, and 10 μL of WST-1 reagent was added to each well. The plates were returned to the incubator and the color change was visually monitored for 0.5 – 2 hours. When sufficient color change had occurred, the plates were shaken on a

plate shaker for 30 seconds, and absorbance at 450 and 630 nm was read in a Biotek Synergy 4 plate reader. The absorbance at 630 nm was subtracted from the absorbance at 450 nm. The average absorbance value from wells containing media without cells was subtracted from the absorbance value for all the wells containing cells. The absorbance values were then taken as a percentage of the absorbance for the vehicle wells (0.1% DMSO - no compound). The percent compared to vehicle was then plotted vs. log(Concentration). Data analyses and curve fitting were performed using Graphpad Prism 6. For each compound, there were n = 3 data points for each concentration. Individual GI50 curves can be found in **Appendix C**.

Accesssion Numbers

Crystallographic coordinates for the **DAS-DFGO-I**:c-Src, **DAS-CHO-I**:c-Src and **DAS-CHO-I**:c-Abl complexes have been deposited at the RCSB Protein Data Bank under accession numbers 4YBJ, 4YBK, 4YC8 (respectively).

References

(1) Manning, G.; Whyte, D.B.; Martinez, R.; Hunter, T.; Sudarsanam, S. The protein kinase complement of the human genome. *Science* **2002,** *298*, 1912.

(2) Blue Ridge Institute for Medical Research. (2015). USFDA approved protein kinase inhibitors compiled by Robert Roskoski Jr. http://www.brimr.org/PKI/PKIs.htm

(3) Breen, M.E.; Steffey, M.E.; Lachacz, E.J.; Kwarcinski, F.E.; Fox, C.C.; Soellner, M.B. Substrate activity screening with kinases: discovery of small-molecule substrate-competitive c-Src inhibitors. *Angew. Chem. Int. Ed. Engl.* **2014,** *53*, 7010–7013.

(4) Wang, Q.; Zorn, J. A.; Kuriyan, J. Chapter Two. A structural atlas of kinases inhibited by clinically approved drugs. *Methods In Enzymology* **2014,** *548*, 23–67.

(5) Zhang, J.; Yang, P. L.; Gray, N. S. Targeting cancer with small molecule kinase inhibitors. *Nat. Rev. Cancer* **2009,** *9*, 28–39.

(6) Zhao, Z.; Wang, L.; Liu, Y.; Knapp, S.; Liu, Q.; Gray, N.S. Exploration of type II binding mode: a privileged approach for kinase inhibition focused drug discovery? *ACS Chem. Biol.* **2014,** *9*, 1230–1240.

(7) Sicheri, F.; Moarefi, I.; Kuriyan, J. Crystal structure of the Src family tyrosine kinase Hck. *Nature* **1997,** *385*, 602–609.

(8) Xu, W.; Harrison, S.C.; Eck, M.J. Three-dimensional structure of the tyrosine kinase c-Src. *Nature* **1997,** *385*, 595–602.

(9) Jura, N.; Zhang, X.; Endres, N.F.; Seeliger, M.A.; Schindler, T.; Kuriyan, J. Catalytic control in the EGF receptor and its connection to general kinase regulatory mechanisms. *Mol. Cell* **2011,** *42*, 9–22.

(10) Georghiou, G.; Kleiner, R.E.; Pulkoski-Gross, M.; Liu, D.R.; Seeliger, M.A. Highly specific, bisubstrate-competitive Src inhibitors from DNA-templated macrocycles. *Nat. Chem. Biol*. **2012,** *8*, 366–374.

(11) Krishnamurty, R.; Brigham, J.L.; Leonard, S.E.; Ranjitkar, P.; Larson, E.T.; Dale, E.J.; Merritt, E.A.; Maly, D.J. Active site profiling reveals coupling between domains in SRC-family kinases. *Nat. Chem. Biol*. **2013,** *9*, 43–51.

(12) Capdeville, R.; Buchdunger, E.; Zimmermann, J.; Matter, A. Glivec (STI571, imatinib), a rationally developed, targeted anticancer drug. *Nat. Rev. Drug Discov*. **2002,** *1*, 493–502.

(13) Sawyers, C.L. Disabling Abl-perspectives on Abl kinase regulation and cancer therapeutics. *Cancer Cell* **2002,** *1*, 13–15.

(14) Mol, C.D.; Fabbro, D.; Hosfield, D.J. Structural insights into the conformational selectivity of STI-571 and related kinase inhibitors. *Curr. Opin. Drug Discov. Devel.* **2004,** *7*, 639–648.

(15) Backes, A.C.; Zech, B.; Felber, B.; Klebl, B.; Müller, G. Small-molecule inhibitors binding to protein kinase. Part II: the novel pharmacophore approach of type II and type III inhibition. *Expert Opin. Drug Discov*. **2008,** *3*, 1427–1449.

(16) Morphy, R. Selectively nonselective kinase inhibition: striking the right balance *J. Med. Chem*. **2010,** *53*, 1413–1437.

(17) Zuccotto, F.; Ardini, E.; Casale, E.; Angiolini, M. Through the "gatekeeper door": exploiting the active kinase conformation. *J. Med. Chem*. **2010,** *53*, 2681–2694.

(18) Hari, S.B.; Merritt, E.A.; Maly, D.J. Sequence determinants of a specific inactive protein kinase conformation. *Chem. Biol*. **2013,** *20*, 806–815.

(19) Deininger, M.; Buchdunger, E.; Druker, B.J. The development of imatinib as a therapeutic agent for chronic myeloid leukemia. *Blood* **2005,** *105*, 2640–2653.
(20) Seeliger, M.A, Nagar, B.; Frank, F.; Cao, X.; Henderson, M. N.; Kuriyan, J. c-Src binds to the cancer drug imatinib with an inactive Abl/c-Kit conformation and a distributed thermodynamic penalty. *Structure* **2007,** *15*, 299–311.
(21) Cowan-Jacob, S.W.; Fendrich, G.; Manley, P.W.; Jahnke, W.; Fabbro, D.; Liebetanz, J.; Meyer, T. The crystal structure of a c-Src complex in an active conformation suggests possible steps in c-Src activation. *Structure* **2005,** *13*, 861–871.
(22) Davis, M.I.; Hunt, J.P.; Herrgard, S.; Ciceri, P.; Wodicka, L.M.; Pallares, G.; Hocker, M.; Treiber, D.K.; Zarrinkar, P.P. Comprehensive analysis of kinase inhibitor selectivity. *Nat. Biotechnol*. **2011,** 29, 1046–1051.
(23) Namboodiri, H.V.; Bukhtiyarova, M.; Ramcharan, J.; Karpusas, M.; Lee, Y.; Springman, E.B. Analysis of imatinib and sorafenib binding to p38alpha compared with c-Abl and b-Raf provides structural insights for understanding the selectivity of inhibitors targeting the DFG-out form of protein kinases. *Biochemistry* **2010,** *49*, 3611–3618.
(24) Fabbro, D.; Cowan-Jacob, S.W.; Moebitz, H. Ten things you should know about protein kinases: IUPHAR Review 14. *Brit. J. Pharmacol*. **2015,** *172*, 2675–2700.
(25) Pan, Z.; Scheerens, H.; Li, S.J.; Schultz, B.E.; Sprengeler, P.A.; Burrill, L.C.; Mendonca, R.V.; Sweeney, M.D.; Scott, K.C.; Grothaus, P.G.; Jeffery, D.A.; Spoerke, J.M.; Honigberg, L.A.; Young, P.R.; Dalrymple, S.A.; Palmer, J.T. Discovery of selective irreversible inhibitors for Bruton's tyrosine kinase. *ChemMedChem* **2007,** *2*, 58–61.
(26) Bollag, G.; Tsai, J.; Zhang, J.; Zhang, C.; Ibrahim, P.; Nolop, K.; Hirth, P. Vemurafenib: The first drug approved for BRAF-mutant cancer. *Nature Reviews Drug Discovery* **2012,** *11*, 873–886.
(27) Liu, Y. and Gray, N. S. Rational design of inhibitors that bind to inactive kinase conformations. *Nat. Chem. Biol*. **2006,** *2*, 358–364.
(28) Lombardo, L.J.; Lee, F.Y.; Chen, P.; Norris, D.; Barrish, J.C.; Behnia, K.; Castaneda, S.; Cornelius, L.A.; Das, J.; Doweyko, A.M.; Farichild, C.; Hunt, J.T.; Inigo, I.; Johnston, K.; Kamath, A.; Kan, D.; Klei, H.; Marathe, P.; Pang, S.; Peterson, R.; Pitt, S.; Schieven, G. L.; Schmidt, R.J.; Tokarski, J.; Wen, M.L.; Wityak, J.; Borzilleri, R.M. Discovery of N-(2-chloro-6-methyl-phenyl)-2-(6-(4-(2-hydroxyethyl)-piperazin-1-yl)-2-methylpyrimidin-4-ylamino)thiazole-5-carboxamide (BMS-354825), a dual Src/Abl kinase inhibitor with potent antitumor activity in preclinical assays. *J. Med. Chem*. **2004,** *47*, 6658−6661.
(29) Tokarski, J.S.; Newitt, J.A.; Chang, C.Y.; Cheng, J.D.; Wittekind, M.; Kiefer, S.E.; Kish, K.; Lee, F.Y.; Borzillerri, R.; Lombardo, L.J.; Xie, D.; Zhang, Y.; Klei, H.E. The structure of dasatinib (BMS-354825) bound to activated ABL kinase domain elucidates its inhibitory activity against imatinib-resistant ABL mutants. *Cancer Res*. **2006,** *66*, 5790–5797.
(30) Okram, B.; Nagle, A.; Adrián, F.J.; Lee, C.; Ren, P.; Wang, X.; Sim, T.; Xie, Y.; Wang, X.; Xia, G.; Spraggon, G.; Warmuth, M.; Liu, Y.; Gray, N.S. A general strategy for creating ''inactive-conformation'' Abl inhibitors. *Chem. & Biol*. **2006,** *13*, 779–786.

(31) van Linden, O.P.J.; Kooistra, A.J.; Leurs, R.; de Esch, I.J.P.; de Graaf, C. KLIFS: a knowledge-based structural database to navigate kinase-ligand interaction space. *J. Med. Chem*. **2014,** *57*, 249–277.
(32) Wood, E.R.; Truesdale, A.T.; McDonald, O.B.; Yuan, D.; Hassell, A.; Dickerson, S.H.; Ellis, B.; Pennisi, C.; Horne, E.; Lackey, K.; Alligood, K.J.; Rusnak, D.W.; Gilmer, T. M.; Shewchuk, L. A unique structure for epidermal growth factor receptor bound to GW572016 (Lapatinib): Relationships among protein conformation, inhibitor off-rate, and receptor activity in tumor cells. *Cancer Research* **2004,** *64*, 6652–6659.
(33) Hari, S.B.; Merritt, E.A.; Maly, D.J. Conformation-selective ATP-competitive inhibitors control regulatory interactions and noncatalytic functions of mitogen-activated protein kinases. *Chem. & Biol*. **2014,** *21*, 1–8.
(34) Levinson, N.M.; Kuchment, O.; Shen, K.; Young, M.A.; Koldobskiy, M.; Karplus, M.; Cole, P.A.; Kuriyan, J. A Src-like inactive conformation in the Abl tyrosine kinase domain. *PLOS Biology* **2006,** *4*, 753–767.
(35) Fabian, M.A.; Biggs, W.H.; Treiber, D.K.; Atteridge, C.E.; Azimioara, M.D.; Benedetti, M.G.; Carter, T.A.; Ciceri, P.; Edeen, P.T.; Floyd, M.; Ford, J.M.; Galvin, M.; Gerlach, J.L.; Grotzfeld, R.M.; Herrgard, S.; Insko, D.E.; Insko, M.A.; Lai, A.G.; Lelias, J.-M.; Mehta, S.A.; Milanov, Z.V.; Velasco, A.M.; Wodicka, L.M.; Patel, H.K.; Zarrinkar, P.P.; Lockhart, D.J. A small-molecule-kinase interaction map for clinical kinase inhibitors. *Nat. Biotechnol.* **2005,** *23*, 329−336.
(36) Schindler, T.; Bornmann, W.; Pellicena, P.; Miller, W.T.; Clarkson, B.; Kuriyan, J. Structural mechanism for STI-571 inhibition of abelson tyrosine kinase. *Science* **2000,** *289*, 1938–1942.
(37) Nagar, B.; Bornmann, W.G.; Pellicena, P.; Schindler, T.; Veach, D.R.; Miller, W.T.; Clarkson, B.; Kuriyan, J. Crystal structures of the kinase domain of c-Abl in complex with the small molecule inhibitors PD173955 and imatinib (STI-571). *Cancer Res.* **2002,** *62*, 4236–4243.
(38) Hari, S.B.; Perera, B.G.K.; Ranjitkar, P.; Seeliger, M.A.; Maly, D.J. Conformation-selective inhibitors reveal differences in the activation and phosphate-binding loops of the tyrosine kinases Abl and Src. *ACS Chem. Biol*. **2013,** *8*, 2734–2743.
(39) Wodicka, L.M.; Ciceri, P.; Davis, M.I.; Hunt, J.P.; Floyd, M.; Salerno, S.; Hua, X.H.; Ford, J.M.; Armstrong, R.C.; Zarrinkar, P.P.; Treiber, D.K. Activation state-dependent binding of small molecule kinase inhibitors: structural insights from biochemistry. *Chem. Biol*. **2010,** *17*, 1241−1249.
(40) Weisberg, E.; Manley, P.W.; Breitenstein, W.; Bruggen, J.; Cowan-Jacob, S.W.; Ray, A.; Huntly, B.; Fabbro, D.; Fendrich, G.; Hall-Meyers, E.; Kung, A.L.; Mestan, J.; Daley, G.Q.; Callahan, L.; Catley, L.; Cavazza, C.; Azam, M.; Neuberg, D.; Wright, R.D.; Gilliland, D.G.; Griffin J.D. Characterization of AMN107, a selective inhibitor of native and mutant Bcr-Abl. *Cancer Cell* **2005,** *7*, 129–141.
(41) O'Hare, T.; Shakespeare, W.C.; Zhu, X.; Eide, C.A.; Rivera, V.M.; Wang, F.; Adrian, L.T.; Zhou, T.; Huang, W.; Xu, Q.; Metcalf III, C.A.; Tyner, J.W.; Loriaux, M.M.; Corbin, A.S.; Wardwell, S.; Ning, Y.; Keats, J.A.; Wang, Y.; Sundaramoorthi, R.; Thomas, M.; Zhou, D.; Snodgrass, J.; Commodore, L.; Sawyer, T.K.; Dalgarno, D.C.; Deininger, M.W.N.; Druker, B.J.; Tim Clackson, T. AP24534, a pan-BCR-ABL

inhibitor for chronic myeloid leukemia, potently inhibits the T315I mutant and overcomes mutation-based resistance. *Cancer Cell* **2009,** *16*, 401–412.
(42) Chan, W.W.; Wise, S.C.; Kaufman, M.D.; Ahn, Y. M.; Ensinger, C.L.; Haack, T.; Hood, M.M.; Jones, J.; Lord, J.W.; Lu, W.P.; Miller, D.; Patt, W.C.; Smith, B.D.; Petillo, P.A.; Rutkoski, T.J.; Telikepalli, H.; Vogeti, L.; Yao, T.; Chun, L.; Clark, R.; Evangelista, P.; Gavrilescu, L.C.; Lazarides, K.; Zaleskas, V.M.; Stewart, L.J.; Van Etten, R.A.; Flynn, D.L. Conformational control inhibition of the BCRABL1 tyrosine kinase, including the gatekeeper T315I mutant, by the switch-control inhibitor DCC-2036. *Cancer Cell* **2011,** *19*, 556−568.
(43) Pargellis, C.; Tong, L.; Churchill, L.; Cirillo, P.F.; Gilmore, T.; Graham, A.G.; Grob, P.M.; Hickey, E.R.; Moss, N.; Pav, S.; Regan, J. Inhibition of p38 MAP kinase by utilizing a novel allosteric binding site. *Nat. Struct. Biol*. **2002,** *9*, 268–272.
(44) Sullivan, J.E.; Holdgate, G.A.; Campbell, D.; Timms, D.; Gerhardt, S.; Breed, J.; Breeze, A.L.; Bermingham, A.; Pauptit, R.A.; Norman, R.A.; Embrey, K. J.; Read, J.; VanScyoc, W. S.; Ward, W. H. J. Prevention of MKK6-dependent activation by binding to p38α MAP kinase. *Biochemistry* **2005,** *44*, 16475–16490.
(45) Seeliger, M.A.; Ranjitkar, P.; Kasap, C.; Shan, Y.; Shaw, D.E.; Shah, N.P.; Kuriyan, J.; Maly, D.J. Equally potent inhibition of c-Src and Abl by compounds that recognize inactive kinase conformations. *Cancer Research*, **2009,** *69*, 2384–2392.
(46) Agafonov R.V.; Wilson, C.; Otten, R.; Buosi, V.; Kern D. Energetic dissection of Gleevec's selectivity toward human tyrosine kinases. *Nat. Mol. Struc. Biol.* **2014,** *21*, 848–853.
(47) Wilson, C.; Agafonov, R.V.; Hoemberger, M.; Kutter, S.; Zorba, A.; Halpin, J.; Buosi, V.; Otten, R.; Waterman, D.; Theobald, D. L.; Kern, D. Using ancient protein kinases to unravel a modern cancer drug's mechanism. *Science* **2015,** *347*, 882–886.
(48) Dar, A.C.; Lopez, M.S.; Shokat, K.M. Small molecule recognition of c-Src via the Imatinib-binding conformation. *Chem. Biol*. **2008,** *15*, 1015–1022.
(49) Simard, J.R.; Klüter, S.; Grütter, C.; Getlik, M.; Rabiller, M.; Rode, H.B.; Rauh, D. A new screening assay for allosteric inhibitors of cSrc. *Nat. Chem. Biol.* **2009,** *5*, 394–396.
(50) Aleksandrov, A. and Simonson, T. Molecular dynamics simulations show that conformational selection governs the binding preferences of imatinib for several tyrosine kinases. *J. Biol. Chem*. **2010,** *285*, 13807–13815.
(51) Lovera, S.; Sutto, L.; Boubeva, R.; Scapozza, L.; Dölker, N.; Gervasio, F. L. The different flexibility of c-Src and c-Abl kinases regulates the accessibility of a druggable inactive conformation. *J. Am. Chem. Soc*. **2012,** *134*, 2496–2499.
(52) Lin, Y.-L.; Meng, Y.; Jiang, W.; Roux, B. Explaining why Gleevec is a specific and potent inhibitor of Abl kinase. *Proc. Natl. Acad. Sci. U.S.A*. **2013,** *110*, 1664–1669.
(53) Jester, B.W.; Cox, K.J.; Gaj, A.; Shomin, C.D.; Porter, J.D.; Ghosh, I. A coiled-coil enabled split-luciferase three-hybrid system: applied toward profiling inhibitors of protein kinases. *J. Am. Chem. Soc*. **2010,** *132*, 11727−11735.
(54) Jester, B.W.; Gaj, A.; Shomin, C.D.; Cox, K.J.; Ghosh, I. Testing the promiscuity of commercial kinase inhibitors against the AGC kinase group using a split-luciferase screen. *J. Med. Chem*. **2012,** *55*, 1526−1537.

(55) Bosc, N.; Wroblowski, B.; Aci-Sèche, S.; Meyer, C.; Bonnet, P. A proteometric analysis of human kinome: insight into discriminant conformation-dependent residues. *ACS Chem. Biol*. **2015,** ASAP. DOI: 10.1021/acschembio.5b00555
(56) Gray, N.S.; Fabbro, D. Chapter Seven. Discovery of Allosteric Bcr–Abl Inhibitors from Phenotypic Screen to Clinical Candidate. *Methods In Enzymology* **2014,** *548*, 173–188.
(57) Warmuth, M.; Kim, S.; Gu, X.; Xia, G.; Adrián, F. Ba/F3 cells and their use in kinase drug discovery. *Curr. Opin. Oncol*. **2007,** *19*, 55–60.
(58) Copeland, R.A.; Pompliano, D.L.; Meek, T.D. Drug-target residence time and its implications for lead optimization. *Nat. Rev. Drug Discov*. **2006,** *5*, 730–739.
(59) Copeland, R.A. The dynamics of drug-target interactions: drug-target residence time and its impact on efficacy and safety. *Expert Opin. Drug Discov*. **2010,** *5*, 305–310.
(60) Lu, H.; Tonge, P.J. Drug-target residence time: critical information for lead optimization. *Curr. Opin. Chem. Biol*. **2010,** *14*, 467–474.
(61) Guo, D.; Hillger, J.M.; IJzerman, A.P.; Heitman, L.H. Drug-target residence time—a case for G protein-coupled receptors. *Med. Res. Rev*. **2014,** *34*, 856–892.
(62) Vetter, M.L, Zhang, Z., Shuai, L., Wang, J., Cho, H., Zhang, J., Zhang, W., Gray, N.S., Yang, P.L. Fluorescent Visualization of Src by Using Dasatinib-BODIPY. *ChemBioChem* **2014,** *15*, 1317–1324.
(63) Seeliger, M.A.; Young, M.; Henderson, M.N.; Pellicena, P.; King, D.S.; Falick, A.M.; Kuriyan, J. High yield bacterial expression of active c-Abl and c-Src tyrosine kinases. *Protein Sci*. **2005,** *14*, 3135−3139.
(64) Otwinowski, Z. and Minor, W. Processing of X-ray diffraction data collected in oscillation mode. *Methods in Enzymology* **1997,** *276*, 307–326.
(65) McCoy, A.J.; Grosse-Kunstleve, R.W.; Adams, P.D.; Winn, M.D.; Storoni, L.C.; Read, R.J. Phaser crystallographic software. *J. Appl. Cryst*. **2007,** *40*, 658–674.
(66) Emsley, P.; Lohkamp, B.; Scott, W. G.; Cowtan, K. Features and development of Coot. *Acta Crystallogr. Sect. D: Biol. Crystallogr*. **2010,** *66*, 486–501.
(67) Bricogne, G.; Blanc, E.; Brandl, M.; Flensburg, C.; Keller P.; Paciorek, W.; Roversi, P.; Sharff, A.; Smart, O.S.; Vonrhein, C.; Womack. T.O. *Buster version 2.10.0 Ed.*, **2011,** Global Phasing Ltd., Cambridge, UK.
(68) Smart, O.S.; Womack, T.O.; Sharff, A.; Flensburg, C.; Keller, P.; Paciorek, W.; Vonrhein, C.; Bricogne, G. *GRADE version 1.1.1* **2011**.
(69) Chen, V.B.; Arendall, W.B. III, Headd J.J.; Keedy, D.A.; Immormino, R.M.; Kapral, G.J.; Murray, L.W.; Richardson, J.S.; Richardson D.C. (2010). MolProbity: all-atom structure validation for macromolecular crystallography. *Acta Crystallographica* **2010,** *D66*, 12–21.
(70) Obtained from PDB validation report.
(71) Ranjitkar, P.; Brock, A.M.; Maly, D.J. Affinity reagents that target a specific inactive form of protein kinases. *Chem. & Biol*. **2010,** *17*, 195–206.

CHAPTER V

Divergent P-loop Conformations in Homologous Kinases and its Implications for Inhibitor Selectivity

Abstract

Kinase inhibitor development has grown tremendously over the last two decades, yet identifying molecular determinants for controlling inhibitor selectivity is significantly lacking. Herein we have developed methodology for characterizing the P-loop (phosphate-binding loop) conformation of homologous kinases. The P-loop is a dynamic and flexible region of the kinase that often not resolved in traditional NMR or X-ray crystallographic experiments. Using inhibitor selectivity data, molecular dynamics simulations and labeling studies with a 'molecular ruler' series of covalent inhibitors, we have demonstrated that can characterize the in-solution conformation of the kinase P-loop and correlate this positioning to observed trends in inhibitor selectivity.

Introduction

Kinases regulate a number of biological processes and are a therapeutic target in diseases such as cancer, diabetes and arthritis.[1] Consequently, a multitude of inhibitors have been produced to control aberrant cellular phosphosignaling pathways. Predicting an optimal inhibitor selectivity profile, however, has proven to be very challenging given the homology amongst all kinases.[2-3] Thus, it is of great importance to identify any specific kinase determinants for controlling inhibitor-binding tendencies.

Several methods have been designed to address this issue by targeting nonconserved kinase regions outside or adjacent to the ATP pocket. These have included non-ATP competitive[4-5], bivalent[6-8] and allosteric[9-10] modes of inhibition (to name a few). Recent work has begun to explore the conformational variability of the kinase phosphate-binding loop (P-loop) as an additional means for achieving kinome selectivity.[11-14] The P-loop or glycine-rich loop forms the 'roof' of the ATP-binding pocket and is located

between the ß1 and ß2 strands of the N-terminal ß-sheet region (**Figure 5.1A**).[15-16] The P-loop has a –[K/R]$_{-4}$LGXG$_0$XXG[E/D]$_{+4}$V– conserved motif, where the hydrophobic positions (G$_0$-3, G$_0$+5) and glycine residues work together to coordinate adenine ring and phosphate binding (**Figure 5.1B**).[11] Past binding analysis has demonstrated that small molecules can also interact with the kinase P-loop, as most inhibitors tend to make 2 to 4 hydrophobic contacts with this loop region.[11] Additionally, these interactions can occur with the P-loop in either an extended or kinked conformation (**Figure 5.1C**). Only a few kinases (ABL, AURA, MET, FGFR1, p38α, MAP4K4, ACK1) are known to adopt the more unique kinked P-loop conformation, suggesting that this loop could serve as a potential kinase inhibitor selectivity filter.[12]

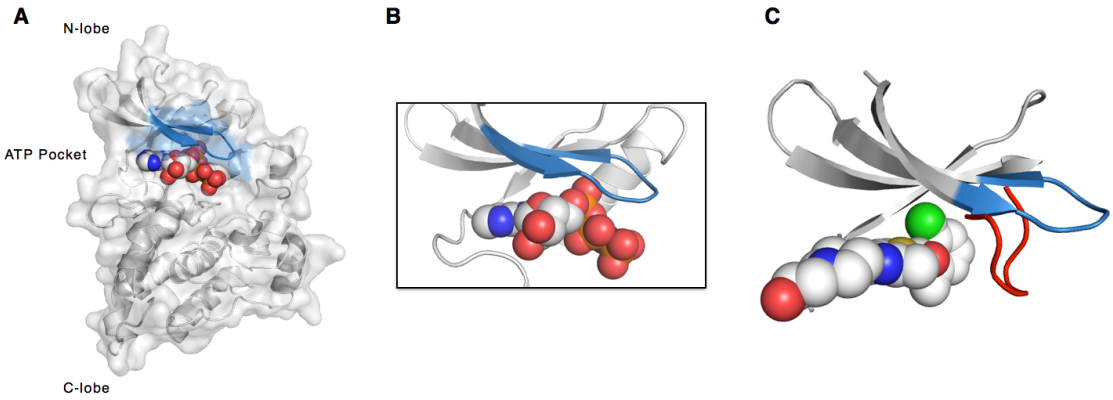

Figure 5.1. Depiction of kinase P-loop. (**A**) Full kinase catalytic domain image with P-loop highlight in blue. (**B**) Zoomed-in view of the ATP pocket and P-loop, coordinating the phosphate groups of an ATP analog. (**C**) Spectrum of P-loop conformations, ranging from fully extended, blue (PDB: 3QLG, c-Src) to kinked in, red (PDB: 2GQG, c-Abl).

Work by our group[13] utilized this information in the design of a highly selective, c-Src inhibitor (**Table 5.1**). Cocrystal structure evaluation of PP2 bound to c-Src and Src-family kinases (PDBs: 3GEQ, c-Src; 2ZV9, Lyn; 1QPE, Lck), illustrated that PP2 could be modified to complement the extended P-loop positioning of c-Src (**Appendix Figure D.1**). A subsequent SAR campaign discovered an inhibitor, KB-SRC-4, that significantly inhibited only c-Src and two other kinases (c-Raf, B-Raf) in a panel of 96 kinases (3%). Molecular models suggested that this selective inhibitor was binding within the 'P-loop pocket' of c-Src, or the region beneath the extended P-loop of the kinase.[13]

Research by the Knapp group has also validated the existence of the P-loop pocket for ERK1/2 as a means for selective inhibition.[14] They confirmed the binding of SCH772984 to this region in both ERK1 and ERK2 and found that this unique binding mode resulted in a highly selective inhibitor (14 total kinases inhibited in a panel of 456 kinases, 3%). Additional cocrystal structures with lower affinity kinase off-targets, haspin and JNK1, revealed the P-loop pocket as being nonconserved, as reflected by the superior specificity of SCH772984 for ERK1/2.

While explicit examples exist for targeting the P-loop pocket of kinases (see above), a comprehensive analysis of this binding pocket has not been performed. Moreover, although kinases with distorted P-loops have been identified, it is not clear what contributes to this structural phenomenon. The kinked P-loop structure does not appear to be a property of primary sequence[13, 17] or limited to a particular kinase group (see **Appendix Figure D.2** for P-loop sequence data).[12] We decided to investigate factors that could influence the relative conformation of the P-loop, including the effect the regulatory spine (R-spine) of the kinase has on this loop. Moreover, we sought to characterize the conformational variability of the P-loop for any kinase, utilizing a variant of our previously described chemical genetic targeting approach (**Chapter II**).[18] Here, we looked at the labeling rates for a series of covalent inhibitors with kinases containing a nucleophilic cysteine group in the P-loop to report on its relative positioning. We determined that our method could robustly identify kinases with kinked P-loop structures and that kinase–inhibitor cocrystal structures are not always the best predictor of selectivity in the design of future kinase inhibitors.

Inhibitor Selectivity Basis for P-loop Conformation Divergence

We initially decided to revisit the selectivity of PP2[19], a non-discriminatory tyrosine kinase inhibitor and KB-SRC-4[13], our aforementioned Src-selective inhibitor (**Table 5.1**). We utilized a continuous kinase activity assay[20] to calculate inhibitory constants (K_i) for both inhibitors with c-Src and a set of three additional homologous kinases (c-Abl, Hck and c-Yes) that each share ≥70% similarity to c-Src within their catalytic domains. As expected, all four kinases were comparably inhibited by PP2 (8.7-, 2.0- and 1.2-fold selectivity for Src over Abl, Hck and Yes)[4], while KB-SRC-4 showed a

considerable binding preference for c-Src (2,800-, 68- and 5.7-fold selectivity over Abl, Hck and Yes).[13] It has been hypothesized that the *meta*-substituted biphenyl group of KB-SRC-4 can be accommodated by the P-loop pocket that is present in c-Src but not in these other closely related kinases. An overlay of kinase-dasatinib complexes for c-Src (PDB: 3QLG) and c-Abl (PDB: 2GQG) supports this fact, seeing as the extended conformation of the P-loop in c-Src is more accessible for ligand binding as compared to closed form of c-Abl (**Figure 5.1C**).

Table 5.1. Biochemical comparison of PP2 and KB-SRC-4.

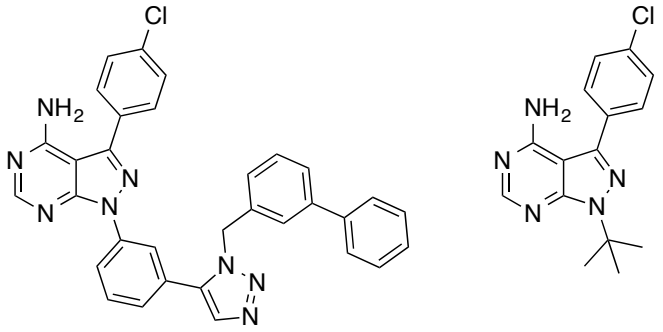

	K_i values	
Kinase	**KB-SRC-4** (fold change)	**PP2** (fold change)
wt c-Src	44 ± 11 nM	45 ± 1 nM
wt c-Abl	>125,000 nM (>2,800)	390 ± 17 nM (8.7)
wt Hck	3,000 ± 540 nM (68)	88 ± 5 nM (2.0)
wt c-Yes	250 ± 39 nM (5.7)	55 ± 7 nM (1.2)

This analysis, however, does not hold true for KB-SRC-4 binding to Hck. An overlay of kinase-pyrazolopyrimidine complexes for c-Src (PDB: 3GEQ) and Hck (PDB: 1QCF) show at most a 0.8 Å average difference between the conformations of the two P-loops, suggesting that Hck has a comparable P-loop pocket for inhibitor binding (**Figure 5.2**). Yet, experimentally KB-SRC-4 has a strong preference for c-Src over Hck (68-fold selectivity) and Hck has previously not been shown to adopt a kinked P-loop structure.[12]

Further obscuring the role of the P-loop in inhibitor selectivity is the fact that KB-SRC-4 does show modest selectivity (5.7-fold) for c-Src over c-Yes, despite both kinases sharing 90% identity (95% similarity) and identical P-loop amino acid compositions. No c-Yes crystal structures or computational models have been reported to support a possible kinked P-loop. The inhibition studies of KB-SRC-4 with both Hck and c-Yes led us to formulate methodology that was more predictive of inhibitor selectivity trends.

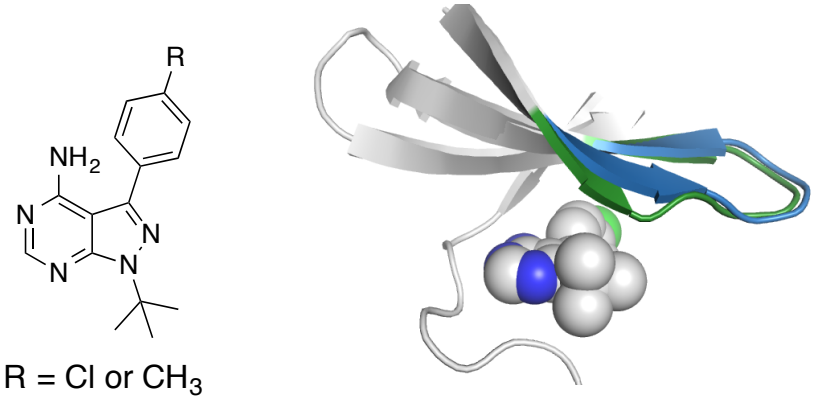

Figure 5.2. P-loop overlay for c-Src (blue) and Hck (green). Both kinases are bound to a similar hinge binding ligand. PP2 (R = Cl) is bound to c-Src (PDB: 3GEQ) while PP1 (R = CH_3) is bound to Hck (PDB: 1QCF).

Correlating P-loop Labeling to Relative Conformation

Past work by our group[18] took a promiscuous kinase inhibitor scaffold and demonstrated that it could be made Src-selective by appending an electrophile onto it for targeting a nonconserved cysteine residue (Cys277) located within the P-loop of the kinase (see **Chapter II**). We also showed that the rate at which a single covalent inhibitor (compound **2.7**) was inactivating the kinase could be used to approximate the relative positioning of the P-loop (see **Chapter II**). We decided to extend this methodology to other kinases with a set of covalent inhibitors to (1) demonstrate that we could characterize the P-loop conformation of any desired kinase and (2) have this information correlate to trends in reversible inhibitor selectivity.

As a proof-of-principle, we first studied the relative P-loop conformation of E280G c-Src, a mutation known to disrupt Src-family kinase P-loop stability (**Figure 5.3**). The identical mutation has been described for Lyn kinase and is known to disrupt

the conserved $[K/R]_{-4}$ to $[E/D]_{+4}$ salt bridge within the P-loop that normally restricts its relative positioning.[21-22] We hypothesized that we could approximate the destabilized P-loop conformation of this c-Src mutant relative to wt by measuring P-loop labeling rates (of Cys277) with a series of covalent inhibitors varying in length.

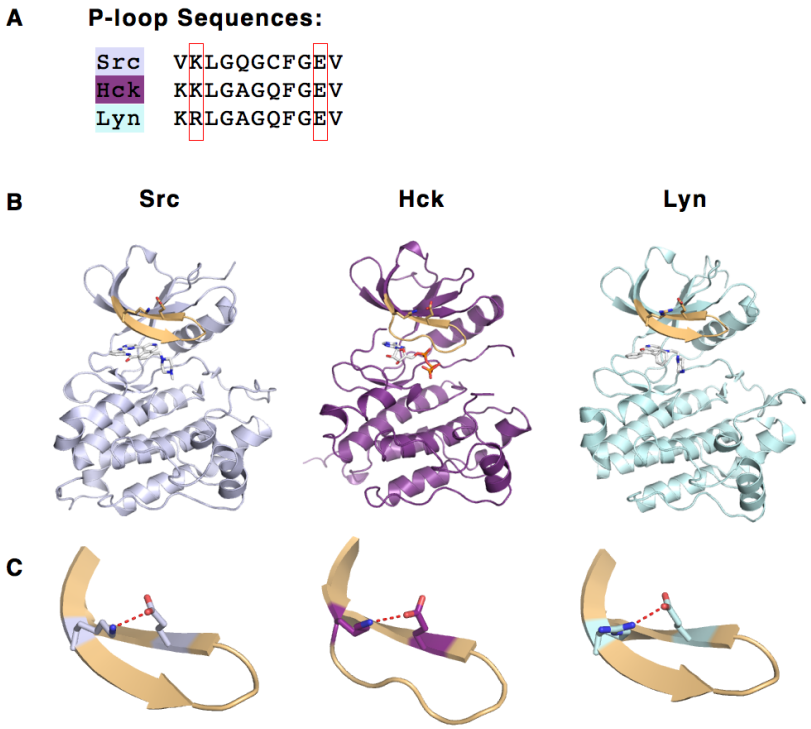

Figure 5.3. P-loop analysis of Src-family kinases Src, Hck and Lyn. (**A**) P-loop sequence alignment shows conserved $[K/R]_{-4}$ to $[E/D]_{+4}$ salt bridge helping to stabilize P-loop positioning. (**B**) Full kinase domains are displayed with extended P-loops highlighted (gold) for each. (**C**) Zoomed-in view of individual P-loop salt bridges.

The synthesis of our covalent 'molecular ruler' series was adapted from the identical amino-pyrazolyl pyrimidine scaffold of compound **2.7** (**Figure 5.4A**). Linker length diversity was introduced at the 3-amino-phenyl position using standard amide coupling techniques with carboxylic acids of different lengths (compounds **2.4** and **5.1**–**5.3**). To ensure consistent cysteine P-loop reactivity, all of the irreversible inhibitors were constructed with an identical vinyl sulfonamide electrophile. A final, shortest covalent inhibitor, compound **5.4**, was also synthesized to better characterize kinases with kinked P-loop structures. Instead of introducing a short amide linker, compound **5.4** had its vinyl sulfonamide installed directly off of the 3-amino-phenyl ring. In total, this set of six

irreversible inhibitors spanned 8.8 Å (5.1 Å – 13.9 Å) and extended ~14 Å outward from the C3-phenyl position of the core scaffold.

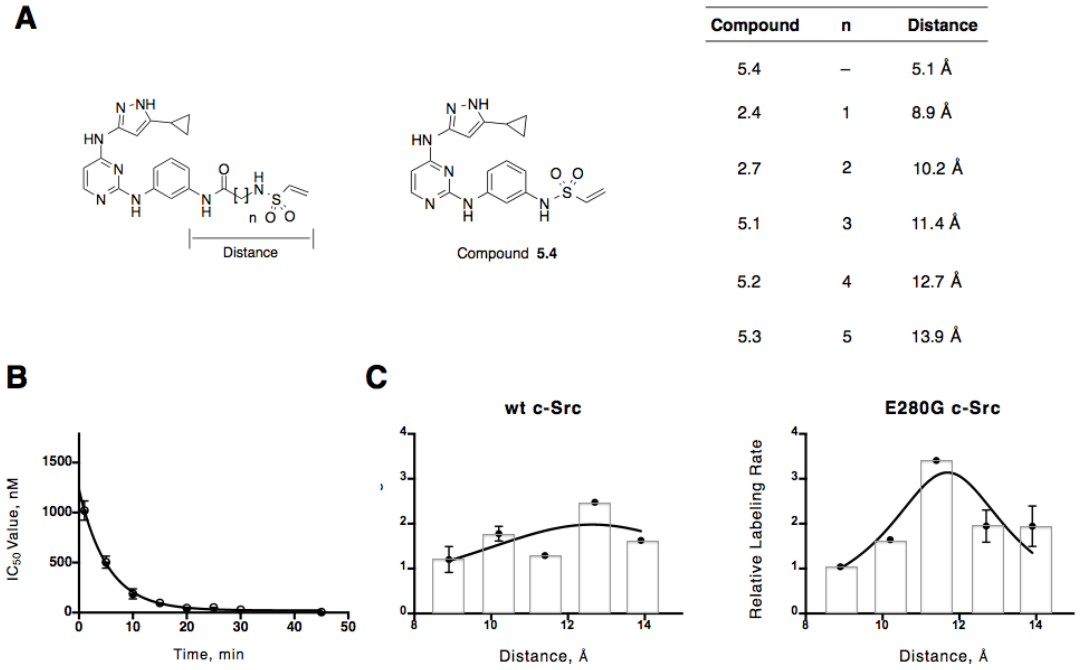

Compound	n	Distance
5.4	–	5.1 Å
2.4	1	8.9 Å
2.7	2	10.2 Å
5.1	3	11.4 Å
5.2	4	12.7 Å
5.3	5	13.9 Å

Figure 5.4. Methodology for determining inhibitor labeling rates. Kinases with kinked P-loops should have a shorter optimal linker length corresponding to its maximal labeling rate. (**A**) Molecular ruler series with for determining P-loop conformation with C3-phenyl to terminal alkene atom distances listed. (**B**) Representative one-phase decay curve fit of time-dependent IC_{50} data for compound **2.7**. (**C**) Comparison of wt c-Src (left) and E280G c-Src (right) inhibitor series labeling rate data.

To evaluate our methodology, covalent modification rates for the entire series of compounds were determined for E280G c-Src and compared to wt c-Src. The labeling rates correspond to half-life ($t_{1/2}$) values that were calculated from inhibitor time-dependent IC_{50} value plots (**Figure 5.4B**). A smaller half-life value is indicative of a faster labeling rate and a more kinked-in P-loop structure. Our calculated labeling rates agree well with other literature protocols for the determination of irreversible inhibitor rate of inactivation constants (progress curves[23] and time-dependent IC_{50} values[24]). We attribute this to the fact that our inhibitory assays maintain constant, saturating amounts of substrate (ATP and peptide) and that the reversible-binding portion of the inhibitor series (see **Chapter II**, compound **2.1**) has identical inhibitory constant values (K_i) for all kinases examined in our study.

The molecular ruler series inactivated E280G c-Src at a greater rate on average (Avg $t_{1/2}$ = 3.5 min) in comparison to wt c-Src (Avg $t_{1/2}$ = 10.2 min), as displayed in **Figure 5.4C**. Compound **5.1** (n = 3 linker) was the optimal inhibitor for E280G c-Src labeling ($t_{1/2}$ = 1.8 ± 0.002 min), displaying nearly a 10-fold improvement over wt c-Src and about a 2-fold improvement over the average half-life for the set. Compound **5.2** (n = 4 linker) had the greatest labeling rate ($t_{1/2}$ = 6.4 ± 0.1 min) for wt c-Src, with a more than 2-fold increase in labeling relative to compound **2.4** (n = 1 linker). For both E280G and wt c-Src, the labeling rates for the molecular ruler set (n = 1, 2, 3, 4, & 5 linkers) followed a Gaussian distribution with wide tail regions, so specific inhibitor distances were calculated using a Lorentizian distribution fit. Using this analysis, E280G c-Src had an optimal inhibitor–to–P-loop distance of 11.7 Å, while wt c-Src had a value of 12.6 Å. This distance specifically refers to the separation between the C3 carbon atom of the amino-phenyl ring on the inhibitor and the alpha carbon of the Cys277 residue of the kinase P-loop. Consequently, this result demonstrates that the disruption of the K_{-4} to E_{+4} P-loop salt bridge in c-Src causes a slight kinking or bending, as evidenced by the shorter optimal linker distance for E280G c-Src over wild type.

Interestingly, compound **5.4**, the shortest covalent inhibitor within the set (5.1 Å linker), did not display time-dependent inhibition of wt c-Src (Avg IC_{50} value = 1.5 μM). Compound **5.4**, however, did label the P-loop destabilized E280G c-Src mutant version, albeit very slowly ($t_{1/2}$ > 45 min). This results supports the above data and past research demonstrating the importance of this salt bridge in the maintenance of the extended P-loop conformation of c-Src.[21]

Covalent P-loop Labeling Studies of Src and Abl

We next evaluated the labeling rate of a P-loop Cys-containing c-Abl mutant, Q252C c-Abl, relative to wt c-Src. c-Abl represents one of the more distinct P-loop conformations (kinked) observed within the protein data bank (**Figure 5.1C**).[12]

Half-life values were determined for the entire set of covalent modifiers (**5.4**, **2.4**, **2.7**, **5.1**–**5.3**) with Q252C c-Abl. Compounds **2.4** (n = 1 linker; $t_{1/2}$ = 4.6 ± 0.2 min), **2.7** (n = 2 linker, $t_{1/2}$ = 4.9 ± 0.1 min) and **5.1** (n = 3 linker, $t_{1/2}$ = 4.9 ± 0.1 min) had significantly shorter half-life values with Q252C c-Abl compared to wt c-Src, indicative

of a kinked P-loop. This was verified with compound **5.4**, which displayed rapid, time-dependent inhibition with Q252C c-Abl ($t_{1/2}$ = 3.8 ± 0.6 min) but not with wt c-Src (see above). The two longest inhibitors of the set, compounds **5.2** (n = 4 linker, $t_{1/2}$ = 7.2 ± 0.4 min) and **5.3** (n = 5 linker, $t_{1/2}$ = 5.8 ± 0.2 min), had noticeably longer labeling rates in comparison to the rest of the inhibitor set.

Since a Lorentizian (or any) distribution fit could not be applied to the Q252C c-Abl data (no maximal experimental labeling rate was determined), the shortest inhibitor length (5.1 Å) was used as the inhibitor–to–P-loop distance for the maximal labeling rate. This value, along with the previously determined wt c-Src value (12.6 Å) was then compared to its crystal structure distance. While the exact 10.3 Å distance for c-Src is known (PDB: 3F6X), a crystal structure overlay between c-Src and c-Abl with a common ligand bound (see **Appendix Figure D.3**) was used to determine a 5.6 Å inhibitor–to–P-loop distance for c-Abl. The optimal calculated inhibitor length for c-Src kinase (12.6 Å) is ~2 Å greater than the value obtained from the crystal structure (**Table 5.2**). This indicates that the P-loop conformation of c-Src can potentially extend outward even more than what is observed crystallographically. Conversely, the two c-Abl distance values are within 0.5 Å of one another, suggesting that the P-loop positioning from its crystal structure appears to be a suitable predictor of its native, in-solution conformation.

Table 5.2. Comparison of static crystal structure distances to the in-solution, determined optimal inhibitor linker distance.

Kinase	Crystal Structure Distance	Optimal Linker Distance	KB-SRC-4, K_i
c-Src	10.3 Å	12.6 Å	44 nM
c-Abl	5.6 Å	5.1 Å	>125,000 nM
Hck	10.1 Å	11.8 Å	3,000 nM

MD Validation of Src and Abl P-loop Conformations

As mentioned, c-Src cocrystal structures predominantly maintain an extended P-loop while a third of all c-Abl structures adopt a kinked P-loop.[12] Our covalent labeling

studies suggested that these static crystal structures represent the most commonly observed P-loop state in solution for both c-Src and c-Abl. To further validate this, we performed molecular dynamics (MD) simulations and determined the frequency at which each kinase P-loop adopted its preferred conformational state.

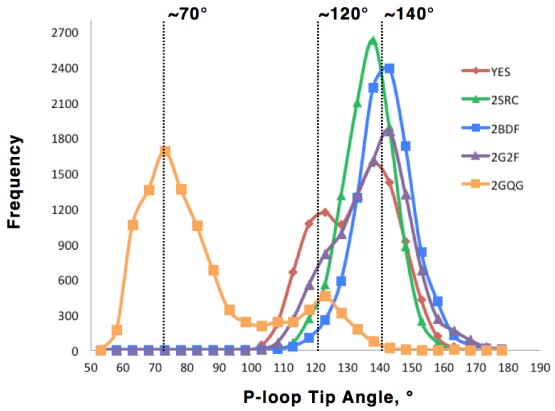

Figure 5.5. MD trajectory data for c-Src (green, 2SRC; blue, 2BDF), c-Abl (purple, 2G2F; orange, 2GQG) and c-Yes (red, homology model).

Two sets of MD simulations (10 x 20 ns; 200 ns total) were conducted for both c-Src (PDBs: 2SRC and 2BDF) and c-Abl (PDBs: 2G2F and 2GQG) to determine if the P-loop was primarily sampling a more open or closed conformation. A histogram of the various angle populations sampled by the P-loop tip (V281–E280–F278 for c-Src; V256–E255–Y253 for c-Abl) and their frequency across the MD trajectory is found in **Figure 5.5**. P-loop angles of 125° or greater are considered to be open states. The starting P-loop angles for the two c-Src simulations were 132.9° and 133.9° (from crystal structures 2SRC and 2BDF respectively), with an observed maximum frequency peak at ~140° during both simulations. Neither P-loop significantly sampled the closed state, suggesting that the P-loop in the static crystal structures of c-Src are good approximations of its native conformation.

For c-Abl, two distinct starting crystal structure P-loop conformations were utilized: 116° for 2G2F and 71.8° for 2GQG, both of which are closed states. The histogram for the P-loop of 2G2F shows a broad distribution of angles with a peak at 140° and a 'bump' near 120°. The 2GQG simulation has a pronounced maximum frequency at 70° and another smaller peak at 120°. This analysis demonstrates that c-Abl can sample both open and closed conformations, although a significant population is in

the closed state. A comparison between c-Src and c-Abl shows that the two c-Src simulations only adopt a closed P-loop conformation (P-loop tip angle <125°) less than 14% of the time (13.4% for 2SRC; 5.4% for 2BDF), whereas 20.5% (2G2F) and 95.7% (2GQG) of c-Abl conformations are sampling this closed state.

Covalent P-loop Labeling Studies of Other PTKs: Hck

We confirmed that our methodology could be applied to any kinase by investigating the labeling rate of a P-loop Cys-containing Hck mutant, Q272C, with our covalent inhibitor set. In crystal structures, Hck adopts an extended P-loop conformation that is quite comparable to that of c-Src (**Figure 5.2**). Despite being from the same kinase family and sharing 80% similarity to one another in the kinase catalytic domain, several inhibitors have been shown to selectively target c-Src over Hck (or vice versa).[13, 25] Our KB-SRC-4 inhibitor data suggests that Hck can adopt a closed or partially closed P-loop with enough frequency to influence inhibitor binding.

We determined half-life values for our entire set of covalent modifiers (**5.4**, **2.4**, **2.7**, **5.1**–**5.3**) with Q272C Hck to test this concept. As with our c-Abl data, all of the compounds tested saw reduced half-life values with Q272C Hck in comparison to wt c-Src. This data supports the hypothesis that the P-loop of Hck can assume a more kinked structure relative to what is depicted through static crystal structures. Testing of Q272C Hck with compound **5.4** did not result in time-dependent inhibition (Avg IC_{50} value = 1.1 μM). This means that the Hck P-loop is not nearly as collapsed as it is for c-Abl (did show time-dependence with **5.4**).

The Q272C Hck labeling results show an optimal C3–to–P-loop distance of 11.8 Å using the aforementioned Lorentizian distribution fit, a closer P-loop positioning relative to the ATP pocket in comparison to c-Src (**Table 5.2**). This helps rationalize the observed 68-fold c-Src over Hck selectivity difference for KB-SRC-4, given that it can bind to a P-loop pocket of Src that is not available as often in Hck. Our measured optimal C3–to–P-loop distance was nearly 2 Å greater than our calculated crystal structure distance for Hck (10.1 Å; determined using overlay with Src PDB 3GEQ and Hck PDB 1QCF; see **Appendix Figure D.4**). This suggests that the in-solution kinase P-loop conformation of

Hck, like that of c-Src, has the potential to extend outward from what is observed in known crystal structures.

P-loop Conformations for Uncharacterized Kinases: Yes

Our covalent labeling studies demonstrated that we could identify the positioning of kinase P-loops relevant for inhibitor binding. We took this one step further by examining the P-loop conformation of a Src-family kinase that has no available structural data, c-Yes. A recent interest in c-Yes inhibitor development has resulted from its role in regulating oncogenic signaling pathways important for colorectal cancer progression.[26] In addition, compounds that do not inhibit c-Yes but do target c-Src have application in the manipulation of embryonic stem cells.[27] Our methodology provided for an unprecedented tool in studying the P-loop positioning of c-Yes.

Compound	n	Rel. Labeling Rate
2.4	1	4.3 ± 0.6
2.7	2	1.9 ± 0.3
5.1	3	3.0 ± 0.1
5.2	4	1.1 ± 0.08
5.3	5	2.4 ± 0.4

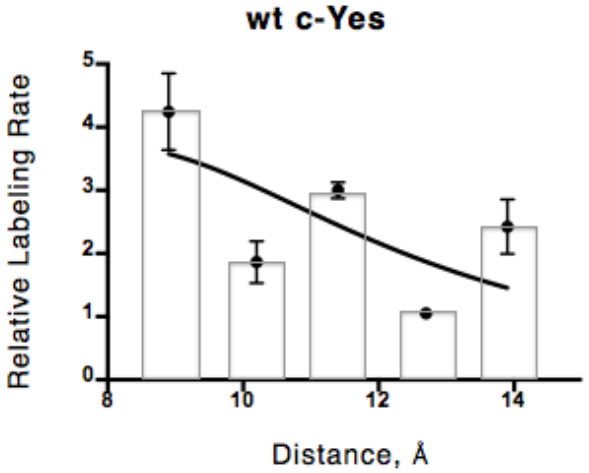

Figure 5.6. Molecular ruler inhibitor series labeling rate data for wt c-Yes.

We tested our entire set of covalent inhibitors against wt c-Yes (native Cys285 in P-loop). Initial observations showed that the molecular ruler series inactivated c-Yes at much greater rate overall (Avg $t_{1/2}$ = 3.1 min) in comparison to wt c-Src (Avg $t_{1/2}$ = 10.2 min) as shown in **Figure 5.6**. The most optimal inhibitor for c-Yes was compound **2.4** ($t_{1/2}$ = 1.5 ± 0.2 min), displaying nearly a 10-fold improvement in labeling over c-Src and a 2-fold improvement over the average half-life for the set. The skewed c-Yes distribution could not be properly fit to a Lorentizian distribution, so the inhibitor length of compound **2.4** (8.9 Å) was used as an overestimate for the inhibitor–to–P-loop

distance required for the maximal labeling rate. This value is ~1.5 Å less than the observed c-Src crystal structure distance and nearly 4 Å less than our measured value of c-Src. Additionally, Compound **5.4** (shortest linker) did not show time-dependent inhibition with c-Yes (Avg IC_{50} value = 1.4 μM). Taken together, we can conclude that the P-loop of c-Abl adopts a significantly more kinked conformation over c-Yes and Hck, although both of these appear to experience at least a partial kinking event in solution.

Based on the above data, one would expect the P-loop pocket binder, KB-SRC-4, to have dramatically weaker affinity against c-Yes relative to c-Src. This is not the case though, as KB-SRC-4 demonstrates only a 5.7-fold improvement in binding to c-Src. This led us to postulate that the P-loop of c-Yes can favorably adopt both an extended and partially kinked P-loop structure. To verify this, we performed MD simulations of c-Yes to determine the frequency of its P-loop in both (kinked and extended) conformations.

Table 5.3. P-loop tip angle data for c-Src, c-Abl and c-Yes from MD simulations.

	PK	Ref Angle	<150°	< 145°	< 140°	<135°	< 130°	< 125°	< 120°	< 115°	< 110°
c-YES	c-Yes	-	96.6%	89.3%	77.3%	61.3%	47.2%	**35.6%**	24.7%	13.2%	4.7%
2SRC	c-Src	132.9°	98.3%	92.9%	78.4%	53.9%	29.4%	13.4%	5.1%	1.5%	0.2%
2BDF	c-Src	133.9°	89.5%	76.7%	54.9%	30.0%	14.0%	5.4%	2.1%	0.6%	0.1%
2G2F	c-Abl	116°	91.2%	80.7%	63.7%	45.9%	31.6%	**20.5%**	11.9%	5.0%	1.4%
2GQG	c-Abl	71.8°	100.0%	100.0%	99.9%	99.4%	98.5%	**95.7%**	91.5%	87.5%	84.8%

A homology model of c-Yes was generated using c-Src as a template given their extremely high sequence homology. With this model, MD simulations (10 x 20 ns; 200 ns total) were conducted to analyze the frequency of each c-Yes P-loop tip angle (V281-E280-F278) across the MD trajectory. c-Yes follows a similar trend as c-Abl (**Figure 5.5**). There are two distinct peaks at ~140° and ~120° in nearly a 1:1 ratio demonstrating that c-Yes also samples both the open and closed P-loop states. The fact that the P-loop of c-Yes does not completely adopt the extended P-loop of c-Src is very intriguing since both kinases share 100% sequence identity in the P-loop region. A breakdown of P-loop angles (**Table 5.3**) shows that 35.6% of c-Yes conformations are sampling the closed state (tip angle less than 125°), an ~4-fold increase over the average closed P-loop sampling of c-Src.

The experimental and MD simulation data suggest that the P-loop of c-Yes may not always be optimally positioned for KB-SRC-4 binding. Molecular docking using Glide from the Schrödinger Suite of Programs[28-29] was subsequently performed to rationalize the different binding affinities of KB-SRC-4 for c-Src and c-Yes. The top predicted binding pose for KB-SRC-4 with c-Src (2BDF, **Figure 5.7A**) shows canonical pyrazolopyrimidine scaffold binding (2 hydrogen bond contacts) to the hinge of the kinase. This was an expected result based on a past c-Src cocrystal structure with PP2 (PDB 3GEQ). Most important, the *meta*-biphenyl moiety of KB-SRC-4 was found docked into the P-loop pocket of c-Src. This predicted interaction contributes to the experimental potency (K_i = 44 nM, c-Src) and specificity (inhibits ~3% of kinome) exhibited by KB-SRC-4.

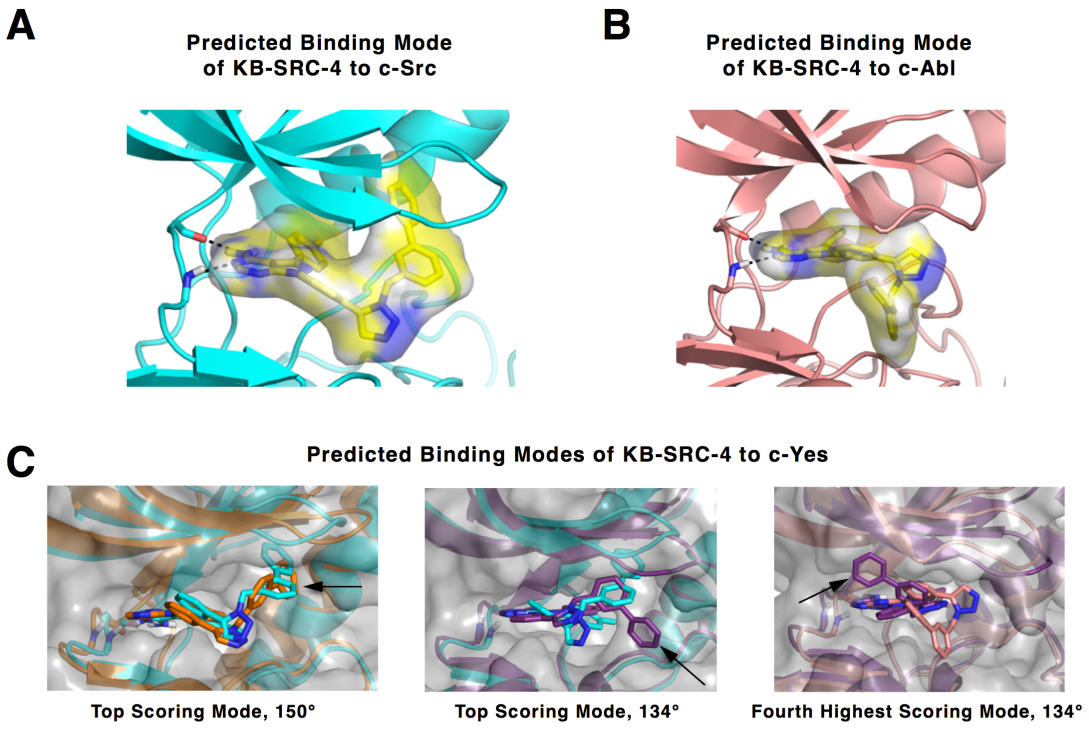

Figure 5.7. Molecular docking data for KB-SRC-4. Data for (**A**) c-Src, (**B**) c-Abl and (**C**) c-Yes is displayed. Arrows denote positioning of *meta*-biphenyl moiety of KB-SRC-4 in c-Yes docking models.

Docking studies with c-Yes utilized six starting structures based on snapshots from its previously described MD trajectory. Representative structural images were

identified from six separate categories, each sorted according to their P-loop conformation. P-loop tip angles from the six groups ranged from 115.9° – 150.0° (**Figure 5.7C**).

Poses were only identified for KB-SRC-4 docked into three of the six total structures. These three structures coincidentally corresponded to the ones with the most extended P-loop tip angles (150.0°, 144.8° and 134°). The two most open P-loop conformations (150.0° and 144.8°) had a top-scoring pose very similar to that obtained for c-Src where the *meta*-biphenyl substituent of KB-SRC-4 was bound within the kinase P-loop pocket (**Figure 5.7C**, left panel). The structure with the 134.0° P-loop tip angle, however, resulted in two interesting binding modes. The predominant binding mode (top three scoring poses) saw the *meta*-biphenyl substituent pointed toward the P-loop pocket but flipped ~90° relative to the top scoring pose for c-Src, causing only partial pocket occupancy (**Figure 5.7C**, middle panel**)**. The alternative-binding mode at the 134.0° P-loop tip angle (fourth highest scoring pose) saw the core of KB-SRC-4 docked into the hinge region for c-Yes, but has the entire *meta*-biphenyl substituent pointing out into solvent. We hypothesized that this binding mode was also the principal pose for KB-SRC-4 docking to c-Abl as shown above. A subsequent docking study of KB-SRC-4 with c-Abl showed an identical outward projection of the *meta*-biphenyl group for its top pose (**Figure 5.7C**, right panel). In these two structures, a closed kinase P-loop conformation is incompatible with P-loop pocket formation. For c-Yes, which can also adopt an extended P-loop conformation, a P-loop tip angle cutoff ~135° appears to be necessary to accommodate the *meta*-biphenyl group of KB-SRC-4. This may demonstrate why KB-SRC-4 displays moderate affinity for c-Yes (K_i = 250 ± 39 nM) while not binding at all to c-Abl (K_i > 125 μM).

Identifying Determinants that Control the P-loop Conformation for Src and Yes

It is well established that the primary sequence of the P-loop does not correspond to either an open or closed state.[12-13, 17] Furthermore, it has been speculated that specific, drug-resistant point mutations in the kinase P-loop can alter its relative positioning,[30] yet this has never been conclusively determined. We decided to investigate primary sequence differences between c-Src (extended P-loop) and c-Yes (postulated kinked P-loop) distal

to the P-loop region that could serve as a molecular determinant for controlling its conformation.

A sequence alignment of the catalytic domains of c-Src and c-Yes revealed only a 29 amino acid residue difference between the two kinases (see **Appendix Figure D.5**). This high sequence identity (90%) significantly narrowed down the number of areas potentially affecting the P-loop conformation of the kinase. Upon closer inspection, we observed that most of these differences were distributed throughout the C-lobe of kinase domain and not neighboring the P-loop. We also noticed that five of the amino acid differences (Src → Yes; V313I, Q324P, V377I, V383I and V402I) were spatially adjacent (within 5 Å) to the regulatory spine (R-spine) of the kinase (**Figure 5.8A**). The R-spine of the kinase (Met314, Leu325, His384 and Phe405) is part of larger skeletal assembly (which includes the catalytic spine and surrounding shell residues) that facilitates ATP and protein substrate binding in order for catalysis to occur.[31-35] We hypothesized that any amino acid substitution around this sensitive spine region could result in a broader conformational effect on the kinase. Specifically, we predicted that the substitution of bulkier residues (valine → isoleucine) into c-Src would contribute to a 'bulging' within the R-spine and ultimately a closed P-loop conformation.

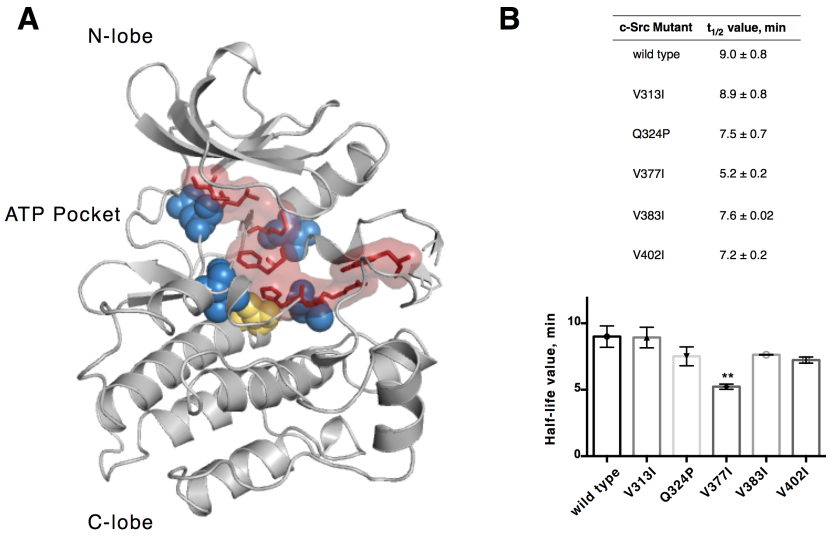

Figure 5.8. Comparison of c-Src mutant labeling rates. (**A**) Location of Src→Yes amino acid differences (spheres) adjacent to the R-spine (red, sticks) of the kinase. (**B**) Labeling rate data of compound **2.7** shows that V377I (gold) c-Src is labeled at a significantly faster rate than wt c-Src ($p < 0.01$).

Each one of the five Src → Yes mutations near the R-spine was prepared via standard mutagenesis protocols and displayed identical stability to wt c-Src, as assessed with melting temperature data (**Appendix Figure D.6**). We then used our covalent labeling methodology to determine the labeling rate of each kinase mutant with compound **2.7** (n = 2 linker) and compared that half-life value to the one for wt c-Src (**Figure 5.8B**). A mutation disrupting the R-spine of the kinase was predicted to kink the P-loop and would be detected through a greater rate of covalent modification. Data for the V313I c-Src mutant ($t_{1/2}$ = 8.9 ± 0.8 min) produced a labeling rate identical to wt c-Src ($t_{1/2}$ = 9.0 ± 0.8 min), while the Q324P ($t_{1/2}$ = 7.5 ± 0.7 min), V383I ($t_{1/2}$ = 7.6 ± 0.02 min) and V402I ($t_{1/2}$ = 7.2 ± 0.2 min) mutants each saw a marginal increase in the rate of P-loop labeling. We only observed a statistically significant ($p < 0.01$) difference between the labeling rates of wt c-Src and the V377I c-Src mutant ($t_{1/2}$ = 5.2 ± 0.2 min), which is located at the base of the R-spine. The data suggest that mutation of this residue can influence a broader kinase structural network and propagate its effect to the P-loop region more than 20 Å away.

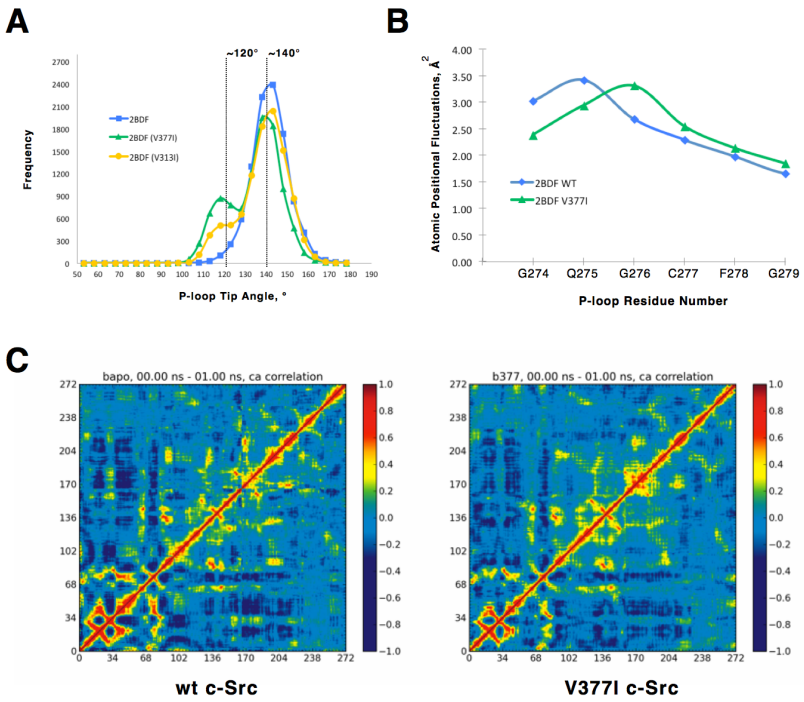

Figure 5.9. MD simulation data comparison for wt, V313I, and V377I c-Src. (**A**) MD trajectory for all three kinases. (**B**) P-loop flexibility comparison of wild type and V377I c-Src. (**C**) Correlated dynamics analysis demonstrating influence of Val377→Ile mutation on R-spine stability.

A MD simulation (10 x 20 ns; 200 ns total) was performed to further analyze the P-loop tendencies for the V377I c-Src mutant. As a negative control, we also ran a simulation (10 x 20 ns; 200 ns total) for V313I c-Src, the mutant that experimentally did not influence the in-solution positioning of the P-loop. The MD trajectory for V377I c-Src shows two distinct peaks at ~140° and ~120° that demonstrates a pattern of open and closed P-loop behavior very similar to that of c-Yes, not c-Src (**Figure 5.9A**). Conversely, V313I c-Src only partially sampled the ~120° P-loop tip angle bin (closed state), primarily residing in an extended P-loop conformation. 17.3% of the V313I c-Src population sampled a P-loop conformation of 125° or less, whereas 28.9% of V377I c-Src sampled this closed state, consistent with the P-loop labeling results.

Additionally, the flexibility of the P-loop for V377I c-Src was analyzed by calculating atomic positional fluctuations, which are the mean square distances from the average position across the trajectory (similar to a B-factor). We observed that the flexibility of the P-loop tip is quite similar (within error of the measurements) for V377I c-Src when compared to wt c-Src and c-Yes (**Figure 5.9B**). Hence, while the P-loop is a highly flexible and dynamic structure for all three kinases, only V377I c-Src and Yes can occupy both an open and closed state for extended periods of time.

Over the course of the MD sampling for wt c-Src, correlated dynamics analysis clearly showed frequent, organized motion between the P-loop (residues 276–279) and the N-lobe residues 293–310 of ß3 and αC and 328–336 of ß4 and ß5 (**Figure 5.9C**). An identical analysis for V377I found these same trends as well as top correlations for residues 316–323, 409 and 508. While the shared correlations between wt and V377I c-Src mainly correspond to a region located above the R-spine of the kinase, the V377I c-Src correlations for the loop residues (316–323) connecting to the ß4 strand directly surround the kinase R-spine and appear to play a role in both inhibitor binding and kinase stability. First, Val323 in this region can directly influence inhibitors binding to the ATP pocket. In fact, this residue is within van der Waals contact of KB-SRC-4, according to our earlier molecular docking studies. Moreover, this area is directly adjacent to Leu325 of the R-spine and thus influences the overall stability and activity of the kinase (**Figure 5.8A**).

Table 5.4. V377I c-Src evaluation with PP2 and KB-SRC-4.

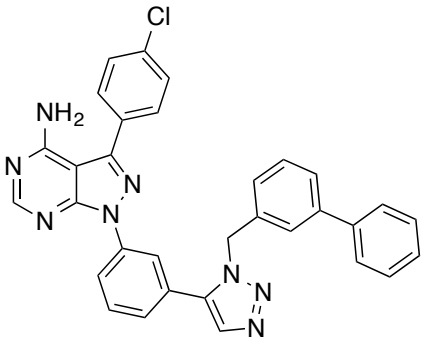

KB-SRC-4

wt c-Src, K_i = 44 ± 11 nM

V377I c-Src, K_i = 200 ± 15 nM (4.5)

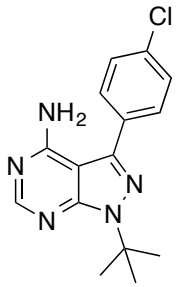

PP2

wt c-Src, K_i = 45 ± 1 nM

V377I c-Src, K_i = 77 ± 11 nM (1.7)

We decided to evaluate KB-SRC-4 inhibition of V377I c-Src in order to verify the correlated dynamics analysis data from our MD studies. We reasoned that if the Val377 → Ile mutation showed a computational contribution to the closure of the P-loop tip angle (28.9% population in closed state), then we should be able to characterize this effect in terms of inhibitor selectivity. Inhibition data for KB-SRC-4 with V377I c-Src (K_i = 200 ± 15 nM) showed a 4.5-fold decrease in potency relative to wt c-Src (**Table 5.4**). The Yes-like propensity of V377I c-Src to adopt a partially kinked P-loop is responsible for the disruption of the P-loop pocket and subsequent inhibitor binding. A control compound that does not bind to the P-loop pocket, PP2, was also evaluated against V377I c-Src. PP2 maintained its high potency for this construct (K_i = 77 ± 11 nM), only showing a less than 2-fold difference in binding relative to wt c-Src. This result demonstrates the allosteric effect distal regions of the protein kinase can have on the ATP pocket and corresponding P-loop conformation.

Conclusions

Kinase drug discovery efforts have created a multitude of inhibitors with diverse selectivity profiles. Understanding what kinase features contribute to their specificity, however, has been difficult at best. To address this need, we designed a 'molecular ruler' series of covalent inhibitors to study the conformation of the kinase P-loop, an element implicated in inhibitor selectivity.[12]

Covalent labeling studies with our inhibitor set demonstrated that homologous kinases can adopt different P-loop conformations. Specifically, we showed that the protein tyrosine kinase c-Yes, which has no reported crystal structure, adopts a kinked P-loop despite sharing 90% identity to c-Src, a kinase with an extended P-loop.

Molecular dynamics simulations also supported this experimental data and suggested that binding to the P-loop pocket of c-Src can improve inhibitor selectivity. Additional work in this area coupled with known kinase structural data should help to identify kinases that have an available P-loop pocket for inhibitor binding. Labeling studies with c-Src mutants also indicated that hydrophobic bulk near the regulatory spine of a kinase might destabilize the P-loop of a kinase, although this has only been explored in c-Src.

Our 'molecular ruler' series of covalent inhibitors presents an unprecedented tool for studying the P-loop conformation of kinases, complementing existing selectivity data for help in the design of future selective kinase inhibitors.

Materials and Methods

General Synthetic Methods

Unless otherwise noted, all reagents were obtained via commercial sources and used without further purification. ^{1}H, ^{13}C, and ^{19}F NMR spectra were measured with a Varian MR400 or Inova 500 spectrometer. Mass spectrometry (HRMS) was carried out by the University of Michigan Mass Spectrometry Facility (J. Windak, director).

Synthetic Protocols

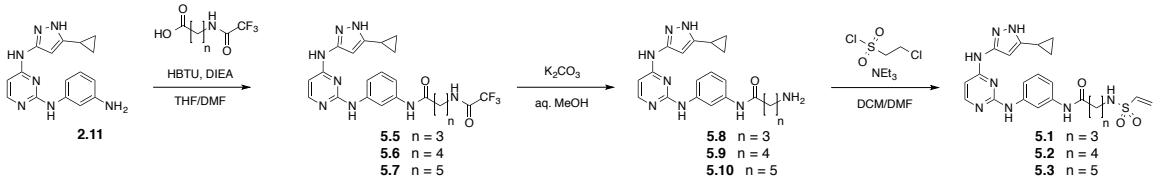

Scheme 5.1. Synthesis of compounds **5.1**–**5.3**, **5.5**–**5.10**.

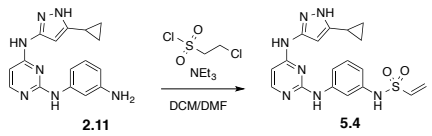

2.11 5.4

Scheme 5.2. Synthesis of compound **5.4**.

Synthesis of 5.1: Crude compound **5.8** (25 mg, 0.061 mmol) was dissolved in anhydrous DMF (1.5 mL) and cooled to 0 ^{o}C prior to addition of 2-chloro-1-ethane sulfonyl chloride (9.6 µL, 0.092 mmol) and TEA (18 µL, 0.13 mmol). The reaction was warmed to rt and stirred for 2 h and then purified via reverse-phase chromatography (linear gradient of 10 → 60% CH_3CN in H_2O) to yield compound **5.1** as an off-white solid (2.1 mg, 7% yield over 2-steps). **Spectral data.** δ 11.95 (s, 1H), 9.81 (s, 1H), 9.46 (s, 1H), 9.01 (s, 1H), 7.99 – 7.91 (m, 1H), 7.83 – 7.76 (m, 1H), 7.47 (d, *J* = 7.6 Hz, 1H), 7.33 – 7.28 (m, 1H), 7.27 – 7.20 (m, 1H), 7.19 – 7.10 (m, 1H), 6.70 (dd, *J* = 10.0, 16.5 Hz, 1H), 6.49 – 6.25 (m, 1H), 6.02 (dd, *J* = 0.4, 16.5 Hz, 1H), 5.96 (dd, *J* = 0.4, 10.0 Hz, 1H), 2.87 (tt, *J* = 6.8, 7.3 Hz, 2H), 2.35 (t, *J* = 7.3 Hz, 2H), 1.88 – 1.80 (m, 1H), 1.75 (tt, *J* = 7.3, 8.1 Hz, 2H), 0.94 – 0.83 (m, 2H), 0.71 – 0.63 (m, 2H). ^{13}C NMR (125 MHz, DMSO-d_6) δ 170.51, 159.66, 155.81, 145.35, 141.19, 139.31, 136.86, 128.33, 125.48, 114.55, 112.33, 110.49, 98.33, 92.94, 41.98, 33.39, 25.38, 7.72, 6.92. HRMS-ESI (*m/z*): $[M + H]^+$ calcd for $C_{22}H_{26}N_8O_3S$, 483.1921; found 483.1917.

Synthesis of 5.2: Crude compound **5.9** (28 mg, 0.069 mmol) was dissolved in anhydrous DCM (1.5 mL) and anhydrous DMF (0.5 mL) and cooled to 0 ^{o}C prior to addition of 2-chloro-1-ethane sulfonyl chloride (8.7 µL, 0.083 mmol) and TEA (19 µL, 0.14 mmol). The reaction was warmed to rt and stirred for 1.5 h. Then the DCM was removed in vacuo and the resultant mixture was purified via reverse-phase chromatography (linear gradient of 5 → 95% CH_3CN in H_2O) to yield compound **5.2** as an off-white solid (3.6 mg, 11% yield over 2-steps). **Spectral data.** ^{1}H NMR (500 MHz, DMSO-d_6): δ 9.79 (s, 1H), 9.14 (s, 1H), 7.99 – 7.95 (m, 1H), 7.86 – 7.82 (m, 1H), 7.47 (d, *J* = 8.2 Hz, 1H), 7.25 – 7.20 (m, 1H), 7.18 – 7.12 (m, 1H), 6.68 (dd, *J* = 10.0, 16.3 Hz, 1H), 6.41 – 6.25 (m, 1H), 6.01 (dd, *J* = 0.7, 16.3 Hz, 1H), 5.95 (dd, *J* = 0.7, 10.0 Hz, 1H), 2.84 (t, *J* = 7.2 Hz, 2H), 2.30 (t, *J* = 7.2 Hz, 2H), 1.88 – 1.80 (m, 1H), 1.65 – 1.55 (m, 2H), 1.53 – 1.43 (m,

2H), 0.92 – 0.84 (m, 2H), 0.70 – 0.64 (m, 2H). ^{13}C NMR (125 MHz, DMSO-d_6) δ 170.49, 160.24, 156.18, 146.16, 141.15, 139.34, 136.93, 129.33, 125.32, 114.32, 112.70, 109.58, 96.82, 93.04, 42.16, 35.86, 29.01, 22.40, 7.72, 6.85. HRMS-ESI (*m/z*): $[M + H]^+$ calcd for $C_{23}H_{28}N_8O_3S$, 497.2078; found 497.2074.

Synthesis of 5.3: Crude compound **5.10** (16 mg, 0.038 mmol) was dissolved in anhydrous THF (1.5 mL) and anhydrous DMF (0.5 mL) and cooled to 0 ^{o}C prior to addition of 2-chloro-1-ethane sulfonyl chloride (4.8 μL, 0.046 mmol) and TEA (11.7 μL, 0.084 mmol). The reaction was warmed to rt and stirred for 1.5 h. Then the DCM was removed in vacuo and the resultant mixture was purified via reverse-phase chromatography (linear gradient of 5 → 95% CH_3CN in H_2O) to yield compound **5.3** as an off-white solid (2 mg, 11% yield over 2-steps). **Spectral data.** ^{1}H NMR (400 MHz, DMSO-d_6): δ 11.95 (s, 1H), 9.80 (s, 1H), 9.48 (s, 1H), 9.00 (s, 1H), 8.01 – 7.93 (m, 1H), 7.89 – 7.79 (m, 1H), 7.46 (d, *J* = 7.9 Hz, 1H), 7.30 – 7.18 (m, 1H), 7.18 – 7.10 (m, 1H), 6.68 (dd, *J* = 10.2, 16.4 Hz, 1H), 6.52 (s, 1H), 6.48 – 6.18 (m, 1H), 6.00 (dd, *J* = 1.9, 16.4 Hz, 1H), 5.94 (dd, *J* = 1.9, 10.2 Hz, 1H), 2.85 – 2.78 (m, 2H), 2.33 – 2.26 (m, 2H), 1.88 – 1.80 (m, 1H), 1.61 – 1.53 (m, 2H), 1.51 – 1.43 (m, 2H), 1.35 – 1.27 (m, 2H), 0.93 – 0.83 (m, 2H), 0.71 – 0.63 (m, 2H). ^{13}C NMR (125 MHz, DMSO-d_6) δ 171.03, 159.60, 155.80, 145.35, 141.15, 139.39, 136.93, 128.31, 125.26, 114.45, 112.31, 110.47, 98.29, 93.00, 42.25, 36.28, 29.18, 25.86, 24.78, 7.70, 6.88. HRMS-ESI (*m/z*): $[M + H]^+$ calcd for $C_{24}H_{30}N_8O_3S$, 511.2235; found 511.2234.

Synthesis of 5.4: Compound **2.11** (7.5 mg, 0.024 mmol) was dissolved in anhydrous THF (1.5 mL) and cooled to 0 ^{o}C prior to addition of 2-chloro-1-ethane sulfonyl chloride (3.1 μL, 0.029 mmol) and TEA (7.5 μL, 0.054 mmol). The reaction was warmed to rt and stirred for 1.5 h. Then the THF was removed in vacuo and the resultant mixture was purified via reverse-phase chromatography (linear gradient of 5 → 95% CH_3CN in H_2O) to yield compound **5.4** as an off-white solid (8.9 mg, 85% yield). **Spectral data.** ^{1}H NMR (400 MHz, DMSO-d_6): δ 11.98 (s, 1H), 9.87 (s, 1H), 9.43 (s, 1H), 9.08 (s, 1H), 8.03 – 7.93 (m, 1H), 7.59 – 7.49 (m, 1H), 7.19 – 7.11 (m, 1H), 6.76 (dd, *J* = 10.0, 16.4 Hz, 1H), 6.71 (d, *J* = 8.1, 1H), 6.52 (s, 1H), 6.48 – 6.26 (m, 1H), 6.16 (dd, *J* = 0.7, 16.4 Hz, 1H),

6.04 (dd, J = 0.7, 10.0 Hz, 1H), 1.90 – 1.82 (m, 1H), 0.96 – 0.84 (m, 2H), 0.74 – 0.65 (m, 2H). ^{13}C NMR (125 MHz, DMSO-d_6) δ 159.53, 155.82, 148.15, 145.49, 141.69, 138.08, 136.35, 128.73, 127.44, 114.69, 112.41, 110.58, 98.40, 92.97, 7.71, 6.88. HRMS-ESI (*m/z*): $[M + H]^+$ calcd for $C_{18}H_{19}N_7O_2S$, 398.1394; found 398.1389.

Synthesis of 5.5: Compound **2.11** (78 mg, 0.25 mmol), HBTU (106 mg, 0.28 mmol), N-TFA-butanoic acid (53 mg, 0.28 mmol) and DIEA (49 μL, 0.28 mmol) were added to an oven-dried flask. Anhydrous THF (5 mL) and anhydrous DMF (1.5 mL) were added. The reaction mixture was stirred under N_2 at room temperature for 18 h. THF was removed in vacuo and the crude contents were poured into water (30 mL). The aqueous layer was ethyl acetate extracted (3X) and then brine washed (3X). The organic layers were collected and dried over sodium sulfate. The solvent was then removed under reduced pressure and crude product was purified via silica gel chromatography using a Biotage Isolera One (1 → 8% MeOH in EtOAc with 0.1% TEA) to yield compound **5.5** as a light, tan solid (59 mg, 47% yield). **Spectral data.** ^{1}H NMR (400 MHz, DMSO-d_6): δ 11.99 (s, 1H), 9.85 (s, 1H), 9.63 (s, 1H), 9.51 – 9.42 (m, 1H), 9.15 (s, 1H), 8.02 – 7.90 (m, 1H), 7.90 – 7.76 (m, 1H), 7.45 (d, J = 8.0 Hz, 1H), 7.29 – 7.21 (m, 1H), 7.21 – 7.13 (m, 1H), 6.53 (s, 1H), 6.46 – 6.22 (m, 1H), 3.25 (tt, J = 6.6 Hz, 7.4 Hz, 2H), 2.35 (t, J = 7.4 Hz, 2H), 1.88 – 1.76 (m, 3H), 0.93 – 0.84 (m, 2H), 0.70 – 0.63 (m, 2H). ^{19}F NMR (376 MHz, DMSO-d_6) δ -69.27, -71.16, -74.39. HRMS-ESI (*m/z*): $[M + H]^+$ calcd for $C_{22}H_{23}F_3N_8O_2$, 489.1969; found 489.1968.

Synthesis of 5.6: Compound **2.11** (78 mg, 0.25 mmol), HBTU (106 mg, 0.28 mmol), N-TFA-pentanoic acid (57 mg, 0.27 mmol) and DIEA (49 μL, 0.28 mmol) were added to an oven-dried flask. Anhydrous THF (5 mL) and anhydrous DMF (1.5 mL) were added. The reaction mixture was stirred under N_2 at room temperature for 18 h. THF was removed in vacuo and the crude contents were poured into water (30 mL). The aqueous layer was ethyl acetate extracted (3X) and then brine washed (3X). The organic layers were collected and dried over sodium sulfate. The solvent was then removed under reduced pressure and crude product was purified via silica gel chromatography using a Biotage Isolera One (1 → 8% MeOH in EtOAc with 0.1% TEA) to yield compound **5.6** as a tan solid (86 mg, 67% yield). **Spectral data.** ^{1}H NMR (400 MHz, DMSO-d_6): δ 11.93 (s,

1H), 9.81 (s, 1H), 9.58 (s, 1H), 9.47 – 9.39 (m, 1H), 9.10 (s, 1H), 8.02 – 7.91 (m, 1H), 7.91 – 7.77 (m, 1H), 7.46 (d, *J* = 8.0 Hz, 1H), 7.30 – 7.20 (m, 1H), 7.20 – 7.12 (m, 1H), 6.52 (s, 1H), 6.48 – 6.19 (m, 1H), 3.21 (tt, *J* = 6.5 Hz, 7.3 Hz, 2H), 2.33 (t, *J* = 6.5 Hz, 2H), 1.88 – 1.80 (m, 1H), 1.64 – 1.47 (m, 2H), 0.94 – 0.84 (m, 2H), 0.71 – 0.63 (m, 2H). ^{19}F NMR (376 MHz, DMSO-*d*$_6$) δ -69.24, -71.13, -74.38. HRMS-ESI (*m/z*): $[M + H]^+$ calcd for $C_{23}H_{25}F_3N_8O_2$, 503.2125; found 503.2124.

Synthesis of 5.7: Compound **2.11** (78 mg, 0.25 mmol), HBTU (106 mg, 0.28 mmol), N-TFA-pentanoic acid (54 mg, 0.24 mmol) and DIEA (44 µL, 0.25 mmol) were added to an oven-dried flask. Anhydrous THF (5 mL) and anhydrous DMF (1.5 mL) were added. The reaction mixture was stirred under N_2 at room temperature for 20 h. THF was removed in vacuo and the crude contents were poured into water (40 mL). The aqueous layer was ethyl acetate extracted (3X) and then brine washed (3X). The organic layers were collected and dried over sodium sulfate. The solvent was then removed under reduced pressure and crude product was purified via silica gel chromatography using a Biotage Isolera One (1 → 8% MeOH in EtOAc with 0.1% TEA) to yield compound **5.7** as a tan solid (85 mg, 72% yield). **Spectral data.** ^{1}H NMR (400 MHz, DMSO-*d*$_6$): δ 11.95 (s, 1H), 9.77 (s, 1H), 9.50 – 9.37 (m, 2H), 9.00 (s, 1H), 8.01 – 7.91 (m, 1H), 7.85 – 7.75 (m, 1H), 7.47 (d, *J* = 8.0 Hz, 1H), 7.29 – 7.20 (m, 1H), 7.20 – 7.10 (m, 1H), 6.52 (s, 1H), 6.48 – 6.22 (m, 1H), 3.19 (tt, *J* = 6.6 Hz, 7.5 Hz, 2H), 2.30 (t, *J* = 7.5 Hz, 2H), 1.88 – 1.80 (m, 1H), 1.60 (tt, *J* = 7.5 Hz, 8.0 Hz, 2H), 1.52 (tt, *J* = 8.0 Hz, 7.1 Hz, 2H), 1.30 (tt, *J* = 8.5 Hz, 8.6 Hz, 2H), 0.94 – 0.85 (m, 2H), 0.71 – 0.64 (m, 2H). ^{19}F NMR (376 MHz, DMSO-*d*$_6$) δ -69.24, -71.13, -74.38. HRMS-ESI (*m/z*): $[M + H]^+$ calcd for $C_{24}H_{27}F_3N_8O_2$, 517.2282; found 517.2281.

Synthesis of 5.8: Compound **5.5** (42 mg, 0.087 mmol) and potassium carbonate (60 mg, 0.43 mmol) were added to a round-bottom flask containing 90% MeOH (5 mL) and stirred at rt for 16 h. MeOH was removed in vacuo and the remaining aqueous layer was ethyl acetate extracted (3X) and brine washed (3X). The organic layers were collected and dried over sodium sulfate. The solvent was removed under reduced pressure to reveal **5.8** as a white solid (25 mg yield) that was carried forward without further characterization.

Synthesis of 5.9: Compound **5.6** (53 mg, 0.11 mmol) and potassium carbonate (73 mg, 0.53 mmol) were added to a round-bottom flask containing 90% MeOH (5 mL) and stirred at rt for 16 h. MeOH was removed in vacuo and the remaining aqueous layer was ethyl acetate extracted (3X) and brine washed (3X). The organic layers were collected and dried over sodium sulfate. The solvent was removed under reduced pressure to reveal **5.9** as a white solid (41 mg) that was carried forward without further characterization.

Synthesis of 5.10: Compound **5.7** (48 mg, 0.11 mmol) and potassium carbonate (53 mg, 0.39 mmol) were added to a round-bottom flask containing 90% MeOH (5 mL) and stirred at rt for 20 h. MeOH was removed in vacuo and the remaining aqueous layer was ethyl acetate extracted (3X) and brine washed (3X). The organic layers were collected and dried over sodium sulfate. The solvent was removed under reduced pressure to reveal **5.10** as a white solid (25 mg) that was carried forward without further characterization.

Spectral Data for Compounds

Spectral data (^{1}H, ^{13}C and ^{19}F NMR) for compounds **5.1**-**5.10** is shown in **Appendix D**.

General Biochemical Methods

Black, opaque-bottom 96 well plates were used for fluorescence assays and were purchased from Nunc. wt c-Src, wt c-Abl and wt Hck plasmids containing a TEV protease cleavable N-terminal 6x-His tag were a generous gift from M. Seeliger (SUNY, Stony Brook) and J. Kuriyan (UC Berkeley) and were expressed in *E. coli* and purified by C. Fox using previously published procedures (see ***Kinase Expression and Purification*** below). The preparation of Q252C c-Abl and c-Yes were described earlier, **Chapter II** and **Chapter III** respectively. The V313I, V377I, V383I and V402I c-Src mutants were prepared by C. Fox. All others were prepared by F. Kwarcinski using standard PCR techniques (see ***Mutant Kinase Production*** below). Chicken c-Src and human c-Abl 1a numbering is used unless otherwise noted. Data was obtained using a Molecular Devices SpectraMax M5 plate reader or Biotek Synergy 4 plate reader. Curve fitting was performed using GraphPad Prism 4 software.

Determination of Kinase T_m Value

Kinase melting curves were performed using modified literature protocols.[36] Briefly, 180 µL of 1 µM kinase was prepared in a DSF compatible buffer (50 mM HEPES pH 8, 200 mM NaCl). Then 3.6 µL of a 250X SYPRO Orange dye (Sigma Aldrich) was added to the kinase solution (2% DMSO final) and 40 µL of this mix was added to 4 separate PCR tubes. Each tube was sealed off with clear plate tape and centrifuged (2000 rpm x 30 s) prior to data collection (25 ^{o}C → 95 ^{o}C at 1 ^{o}C per min). Data was worked up in Microsoft Excel according to the guidelines outlined in the DSF data analysis manual, version 3.0.[37] Representative melting curves can be found in **Appendix D.6**.

Determination of Inhibitor IC_{50} and K_i Values

A continuous fluorescence assay[20] was used to determine IC_{50} and K_i values. Reaction volumes of 60 µL were used in 96-well plates. 51 µL of enzyme in buffer was added to each well. 1.5 µL of the appropriate inhibitor dilution (typically 62.5, 20.8, 6.9, 2.3, 0.77, 0.26, 0.086, 0.029, 0.0095, 0 µM in DMSO) was then added. 1.5 µL of a substrate peptide ("compound 3" as described in Wang et al)[20] solution (1.8 mM in DMSO) was added for any Src-family kinase, while an Abl substrate peptide (2.4 mM in DMSO) was utilized for Q252C and Q252C + Y253F c-Abl assays. The reaction was initiated with 6 µL of ATP (0.25 mM in H_2O), and reaction progress was immediately monitored at 405 nm (ex. 340 nm) for 10 min. Reactions had final concentrations of 30 nM enzyme, 45 µM peptide substrate, 25 µM ATP, 100 µM Na_3VO_4, 100 mM Tris buffer (pH 8), 10 mM $MgCl_2$, 0.01% Triton X-100. The initial rate data collected was used for determination of IC_{50} values. For IC_{50} determination, the kinetic values were obtained directly from nonlinear regression of substrate-velocity curves in the presence of various concentrations of the inhibitor. The equation Y = Bottom + (Top – Bottom)/(1 + 10^X – LogEC50), X = log(concentration) and Y = binding; was used in the nonlinear regression. Inhibitor K_i values (where applicable) were determined using the appropriate ATP Km values for each enzyme. Some K_m values were calculated previously[4, 8, 18, 38] while the K_m values for Q252C + Y253F c-Abl, Q272C Hck, V313I, Q324P, V377I, V383I & V402I c-Src were determined in this work. Some K_i values for compound KB-

SRC-4 (c-Src & c-Abl) and PP2 (c-Src, c-Abl, Hck, c-Yes) were determined previously.[4, 13] A representative inhibition curve is shown in **Appendix D**.

Determination of Inhibitor-Enzyme Half-Life Values and Optimal Linker Distances

The aforementioned continuous fluorescence assay[20] was used to determine time-dependent IC_{50} values. 51 μL of the appropriate enzyme in buffer was incubated with 1.5 μL of inhibitor dilution (typically 62.5, 20.8, 6.9, 2.3, 0.77, 0.26, 0.086, 0.029, 0.0095, 0 μM in DMSO) at room temperature with varying enzyme pre-incubation times (1, 5, 10, 15, 20, 25, 30, 45 min). Then 1.5 μL of a substrate peptide solution (1.8 mM in DMSO) was added followed by addition of 6 μL of ATP (1 mM in H_2O), and reaction progress was immediately monitored at 405 nm (ex. 340 nm) for 10 min. Reactions had final concentrations of 30–100 nM enzyme, 45 μM peptide substrate, 100 μM ATP, 100 μM TCEP, 100 μM Na_3VO_4, 100 mM Tris buffer (pH 8), 10 mM $MgCl_2$ and 0.01% Triton X-100. IC_{50} values were determined as previously described.

For inhibitor–enzyme half-life determination, IC_{50} values were plotted against time and fit to one-phase decay curves: Y = (Y0 – Plateau)*exp(-K*X) + Plateau, where Y0 is the Y value when time is zero, Plateau is the Y value at infinite times and K is the rate constant (expressed in inverse time units). The half-life for each system was computed as $t_{1/2} = \ln(2)/K$. Each inhibitor–enzyme $t_{1/2}$ value was determined using at least two independent time course experiments; the time-dependent IC_{50} value decay curves are shown in **Appendix D**.

For optimal inhibitor linker length determination, normalized labeling rates (inverse half-life values) were plotted against the exact lengths of the molecular ruler series and fit to a Lorentizian distribution. This fit takes into account potential outliers and corrected for the wide tail regions of the data as well. Inhibitor C3-phenyl to terminal vinyl sulfonamide atom lengths were determined using PDB files generated using ChemBio3D Ultra software via the MM2 energy minimization function.

Determination of ATP K_M

The previously described fluorescence assay[20] was used to determine K_m values. Reaction volumes of 60 µL were used in 96-well plates. 51 µL of enzyme in buffer was added to each well. 1.5 µL of DMSO was then added followed by 1.5 µL of a substrate peptide ("compound 3" as described in Wang et al)[20] solution (1.8 mM in DMSO). The reaction was initiated with 6 µL of the appropriate ATP dilution (typically 2000, 1000, 500, 250, 125, 62.5, 31.3, 15.6, 7.8, 3.9, 1.9, 0.98 µM in H_2O) and reaction progress was immediately monitored at 405 nm (ex. 340 nm) for 10 min. Reactions had final concentrations of 30 nM enzyme, 45 µM peptide substrate, 100 µM Na_3VO_4, 100 mM Tris buffer (pH 8), 10 mM $MgCl_2$, 0.01% Triton X-100. The initial rate data collected was used for determination of K_m values. For K_m determination, the kinetic values were obtained directly from nonlinear regression of substrate-velocity curves in the presence of varying concentrations of ATP. The equation Y = (Vmax * X)/(Km + X), X = substrate concentration (µM) and Y = enzyme velocity (RFU/s); was used in the nonlinear regression. Each ATP K_m value was determined using at least three independent experiments; a representative K_m curve is shown in **Appendix D**.

Mutant Kinase Production

The V313I, V377I, V383I and V402I c-Src mutants were prepared by C. Fox. All others were prepared by F. Kwarcinski. The unmodified wt plasmid (chicken c-Src kinase domain, human c-Abl kinase, human Hck kinase) in pET28a (or pSKBR3, Hck) modified with a TEV protease cleavable N-terminal 6x-His tag, was provided to the lab by M. Seeliger (SUNY, Stony Brook) and J. Kuriyan (UC Berkeley). The desired mutation for Y253F c-Abl, Q272C Hck, V313I, Q324P, V377I, V383I, V402I c-Src was added to its respective plasmid (Q252C c-Abl, wt Hck & wt c-Src) using a standard PCR protocol with DpnI digest and transformation. The mutated plasmid was then transformed by electroporation into Bl21DE3 electrocompetent cells containing YopH in pCDFDuet-1 for cell growth, kinase expression and purification (below).

Kinase Expression and Purification

E. Coli cell growth, kinase expression and purification were performed using modified literature protocols for expression of wild-type c-Src kinase domain.[39] Briefly,

the plasmid containing the kinase (pET28a) was transformed into *E. Coli* BL21DE3 cells already containing YopH phosphatase (pCDFDuet-1 plasmid) and plated on LB agar with kanamycin (50 μg/mL, kan) and streptomycin (50 μg/mL, SM) and grown overnight at 37 ^{o}C. The pET28a plasmid containing the c-Yes DNA was transformed into *E. Coli* BL21DE3 cells already containing YopH phosphatase (pCDFDuet-1 plasmid) and GroEL and plated on LB agar with kanamycin (50 μg/mL, kan), streptomycin (50 μg/mL, SM) and chloramphenicol (34 μg/mL, cam) and grown overnight at 37 ^{o}C. E. Coli cells for c-Yes expression without exogenously expressed GroEL did not yield discernable amounts of active kinase. A single colony was picked for a starter culture (LB containing kan/SM or LB containing kan/SM/cam) and subsequently grown overnight at 37 ^{o}C. The next day, scaled up cultures (TB containing kan/SM or TB containing kan/SM/cam) were grown to an OD_{600nm} of 1.2 at 37 ^{o}C and cooled to 18 ^{o}C with shaking prior to induction for 16 h at 18 ^{o}C with 0.2 mM IPTG. Cells were harvested by 20 min centrifugation at 4,000 rpm at 4 ^{o}C and resuspended in 50 mM Tris (pH 8.0), 500 mM NaCl, 5% glycerol, 25 mM imidazole (buffer A) supplemented with 0.1 mM PMSF for immobilized Ni metal affinity chromatography. Cells were lysed via sonication and insoluble protein and cell debris was sedimented through a 50-min centrifugation at 14,000 rpm at 4 ^{o}C. The clear supernatant was loaded onto the Ni-NTA agarose affinity column (batch, QIAGEN) column. The resin was washed with 50 column volumes of buffer A and five column volumes (3X) of buffer QB (20 mM Tris, pH 8.0, 5% glycerol, 1 M NaCl). Protein was eluted with five column volumes (4X) of buffer B (buffer A plus 0.5 M imidazole). The buffer B fractions were pooled together and cleaved with 0.1 mg of TEV per 2.5 mg of crude kinase.

Cleaved protein was loaded onto an anion exchange column (Q Sepharose, Fast Flow, GE Healthcare Life sciences) equilibrated with buffer QA (buffer QB without 1 M NaCl). Proteins were eluted with a linear gradient of 0–35% buffer QB and peak fractions were combined (based on kinase activity assay). A majority of kinases were pure (via SDS-PAGE) after this point, but several had to be concentrated down in order to be loaded onto a size-exclusion column (HiLoad Superdex S75, GE Healthcare Life sciences) equilibrated with buffer D (50 mM Tris, pH 8.0, 5% glycerol, 200 mM NaCl, 1 mM DTT). Pure fractions from the size-exclusion column via SDS-PAGE were

combined and used for biochemical assays.

c-Yes Homology Model

As no crystal structures are available to date, the homology modeling tool Prime[40], from the Schrödinger Suite of Programs, was used to generate a model of the active form of the kinase domain of c-Yes. The human Src structure 2BDF[41] (open loop form) was utilized as the template applying default parameters. Additionally, the open loop region of the human structure 2BDF was refined using the chicken Src structure 3DQW[31] (the chicken and human forms of Src are nearly identical) as it is not fully resolved.

Molecular Dynamics Simulations

Unrestrained, all-atom MD simulations were initiated from the crystallographic coordinates of the apo monomer of wild-type c-Src (PDBs: 2SRC[42] and 2BDF[41]), the apo monomer of wild-type c-Abl (PDBs: 2GQG[43] and 2G2F[44]), and the apo monomer of the mutants V377I and V313I c-SRC created from the PDB structure 2BDF, resulting in five sets of c-Src simulations and two sets of c-Abl simulations. An additional set was performed from the homology model of c-Yes (described above). In total, across c-Src, c-Abl, and c-Yes, eights sets of MD simulations were performed. Hydrogen atoms were added via the tLEaP module in AMBER11 suite of programs[45] using the FF99SB force field.[46] The Antechamber module with the GAFF[47] force field and AM1-BCC charges[48] was used to determine force field parameters for SUB1 and PP2. The N-terminal and C-terminal ends of the proteins were capped with ACE and NME, respectively, using MOE 2011.[49]

Each set of explicit-solvent MD simulations was performed for 20 ns using ten random-number seeds for a total of 200 ns of simulation time. The simulations were carried out using the FF99SB force field[46] and the sander module in the AMBER11 suite of programs.[45] The hydrogen atoms were first minimized, and then the system was solvated using truncated octahedral boundary conditions with TIP3P water molecules[50], a buffer distance of 12 Å, and closeness parameter of 0.5. The -1e charge of c-Src (2BDF) was neutralized by the addition of 4 sodium counter ions placed 10 Å from the protein surface in the most electropositive regions, 1 sodium counter ions for c-Src (2SRC), 8

sodium counter ions for c-Abl (2G2F), 10 sodium counter ions for c-Abl (2GQG), and 5 sodium counter ions for c-Yes. The simulation was run in the NPT ensemble, and SHAKE was used to constrain all bonds to hydrogen atoms. A 2 fs time step was used, along with a 10-Å cutoff for nonbonded interactions and particle mesh Ewald (PME) for long-range electrostatics. For the solvated system, the hydrogen atoms were first minimized, followed by side chains, and lastly all atoms. The system was equilibrated in a series of four stages: a gradual heating of water from 10 to 310 K over 50 ps, followed by water equilibration with protein restrained for 250 ps at 310K, then a full system heating from 10 to 310 K over 50 ps, and finally, full system equilibration with the protein unrestrained at 310K for 500 ps. The production phase was run for 20 ns at 310 K.

Analyses of the P-loop conformations from the simulations were performed using the Ptraj module from the AMBER11 suite of programs.[45] Each MD trajectory was aligned to the fully minimized kinase structure, the last common structure between the simulations. The movement of the P-loop was quantified by measuring the angle between P-loop residues (V281-E280-F278 for c-SRC/c-Yes; V256-E255-Y253 for c-Abl) using Cα atoms. The correlated dynamics were calculated using the Ptraj module, augmented with in-house scripts for visualization and parsing subsets of data. Additionally, atomic fluctuations were calculated for the Cα atoms of P-loop residues 275-280 across the entire trajectory using Praj.

Molecular Docking

Glide from the Schrödinger Suite of Programs[28-29] was used to dock KB-SRC-4 into c-Src (PDB ID 2BDF[41] with activation loop refined, as described above), c-Abl (PDB ID 2G2F[44]), and six c-Yes kinase structures. As a crystal structure of c-Yes is not available, c-Yes snapshots were taken from the 200 ns molecular dynamics trajectory every 25 ns resulting in 20 structures and visually clustered based on their P-loop conformation. Six representative structures were chosen to take forward for docking. All kinase structures were set-up using the same protocol within the Protein Preparation Wizard. Heteroatoms were removed and only hydrogen atoms were minimized in the final preparation step. Receptor grid generation was completed using default parameters

and the active site was defined using the position of PP2, a low nanomolar ATP-competitive inhibitor in complex with Lck, another member of the SFK (PDB: 1QPE[51]). Two constraints were placed on the backbone carbonyl oxygen of Glu339 and backbone amide nitrogen of Met341. KB-SRC-4 is an analog of PP2 thus it should maintain both hydrogen bonds with the hinge region of the ATP-binding site similar to ATP. Default parameters were used for molecular docking with the exception of applying both constraints in some docking runs (docking was done with and without constraints) and including ten ligands for post-docking minimization. The docking score/glide gscore along with visual inspection was employed to determine if a binding pose was reasonable. Reasonable binding poses were similar when constraints and no constraints were used.

References

(1) Zhang, J.; Yang, P. L.; Gray, N. S. Targeting cancer with small molecule kinase inhibitors. *Nat. Rev. Cancer.* **2009,** *9*, 28–39.

(2) Knight, Z. A.; Shokat, K. M. Features of selective kinase inhibitors. *Chem. Biol.* **2005,** *12*, 621–637.

(3) Vulpetti, A.; Bosotti, R. Sequence and structural analysis of kinase ATP pocket residues. *Farmaco.* **2004,** *59*, 759–765.

(4) Breen, M. E.; Steffey, M. E.; Lachacz, E. J.; Kwarcinski, F. E.; Fox, C. C.; Soellner, M. B. Substrate activity screening with kinases: discovery of small-molecule substrate-competitive c-Src inhibitors. *Angew. Chem. Int. Ed. Engl.* **2014,** *53*, 7010–7013.

(5) Breen, M. E.; Soellner, M. B. Small molecule substrate phosphorylation site inhibitors of protein kinases: approaches and challenges. *ACS Chem. Biol.* **2015,** *10*, 175–189.

(6) Gower, C. M.; Chang, M. E.; Maly, D. J. Bivalent inhibitors of protein kinases. *Crit. Rev. Biochem. Mol. Biol.* **2014,** *49*, 102–115.

(7) Brandvold, K. R.; Santos, S. M.; Breen, M. E.; Lachacz, E. J.; Steffey, M. E.; Soellner, M. B. Exquisitely specific bisubstrate inhibitors of c-Src kinase. *ACS Chem. Biol.* **2015,** *10*, 1387–1391.

(8) Kwarcinski, F. E.; Steffey, M. E.; Fox, C. C.; Soellner, M. B. Discovery of bivalent kinase inhibitors via enzyme-templated fragment elaboration. *ACS Med. Chem. Lett.* **2015,** *6*, 898–901.

(9) Lamba, V.; Ghosh, I. New directions in targeting protein kinases: focusing upon true allosteric and bivalent inhibitors. *Current Pharmaceutical Design.* **2012,** *18*, 2936–2945.

(10) Gray, N. S.; Fabbro, D. Discovery of allosteric BCR-ABL inhibitors from phenotypic screen to clinical candidate. *Methods Enzymol.* **2014,** *548*, 173–188.

(11) Patel, R. Y.; Doerksen, R. J. Protein Kinase–inhibitor database: Structural variability of and inhibitor interactions with the protein kinase P-loop. *J. Proteome Res.* **2010,** *9*, 4433–4442.

(12) Guimaraes, C. R.; Rai, B. K.; Munchhof, M. J.; Liu, S.; Wang, J.; Bhattacharya, S. K.; Buckbinder, L. Understanding the impact of the P-loop conformation on kinase selectivity. *J. Chem. Inf. Model.* **2011,** *51*, 1199–1204.

(13) Brandvold, K. R.; Steffey, M. E.; Fox, C. C.; Soellner, M. B. Development of a highly selective c-Src kinase inhibitor. *ACS Chem. Biol.* **2012,** *7*, 1393–1398.

(14) Chaikuad, A.; Tacconi, E. M. C.; Zimmer, J.; Liang, Y.; Gray, N. S.; Tarsounas, M.; Knapp, S. A unique inhibitor binding site in ERK1/2 is associated with slow binding kinetics. *Nat. Chem. Biol.* **2014,** *10*, 853–862.

(15) Hanks, S. K.; Hunter, T. The eukaryotic protein kinase superfamily: kinase (catalytic) domain structure and classification. *The FASEB Journal.* **1995,** *9*, 576–596.

(16) Hubbard, S. R.; Till, J. H. Protein tyrosine kinase structure and function. *Annu. Rev. Biochem.* **2000,** *69*, 373–398.

(17) Seeliger, M. A.; Nagar, B.; Frank, F.; Cao, X.; Henderson, M. N.; Kuriyan, J. c-Src binds to the cancer drug imatinib with an inactive Abl/c-Kit conformation and a distributed thermodynamic penalty. *Structure.* **2007,** *15*, 299–311.

(18) Kwarcinski, F. E.; Fox, C. C.; Steffey, M. E.; Soellner, M. B. Irreversible inhibitors of c-Src kinase that target a nonconserved cysteine. *ACS Chem. Biol.* **2012,** *7*, 1910–1917.
(19) Hanke, J. H.; Gardner, J. P.; Dow, R. L.; Changelian, P. S.; Brissette, W. H.; Weringer, E. J.; Pollok, B. A.; Connelly, P. A. Discovery of a novel, potent, and Src family-selective tyrosine kinase inhibitor. *J. Biol. Chem.* **1996,** *271*, 695–701.
(20) Wang, Q.; Cahill, S. M.; Blumenstein, M.; Lawrence, D. S. Self-reporting fluorescent substrates of protein tyrosine kinases. *J. Am. Chem. Soc.* **2006,** *128*, 1808–1809.
(21) Barouch-Bentov, R.; Che, J.; Lee, C. C.; Yang, Y.; Herman, A.; Jia, Y.; Velentza, A.; Watson, J.; Sternberg, L.; Kim, S.; Ziaee, N.; Miller, A.; Jackson, C.; Fujimoto, M.; Young, M.; Batalov, S.; Liu, Y.; Warmuth, M.; Wiltshire, T.; Cooke, M. P.; Sauer, K. A conserved salt bridge in the G loop of multiple protein kinases is important for catalysis and for in vivo Lyn function. *Mol. Cell.* **2009,** *33*, 43–52.
(22) Georghiou, G.; Kleiner, R. E.; Pulkoski-Gross, M.; Liu, D. R.; Seeliger, M. A. Highly specific, bisubstrate-competitive Src inhibitors from DNA-templated macrocycles. *Nat. Chem. Biol.* **2012,** *8*, 366–374.
(23) Kitz, R.; Wilson, I. B. Esters of methansulfonic acid as irreversible inhibitors of acetylcholinesterase. *J. Biol. Chem.* **1962,** *237*, 3245–3249.
(24) Krippendorff, B. F.; Neuhaus, R.; Lienau, P.; Reichel, A.; Huisinga, W. Mechanism-based inhibition: deriving K(I) and k(inact) directly from time-dependent IC(50) values. *J. Biomol. Screen.* **2009,** *14*, 913–923.
(25) Davis, M. I.; Hunt, J. P.; Herrgard, S.; Ciceri, P.; Wodicka, L. M.; Pallares, G.; Hocker, M.; Treiber, D. K.; Zarrinkar, P. P. Comprehensive analysis of kinase inhibitor selectivity. *Nat. Biotechnol.* **2011,** *29*, 1046–1051.
(26) Sancier, F.; Dumont, A.; Sirvent, A.; Paquay de Plater, L.; Edmonds, T.; David, G.; Jan, M.; de Montrion, C.; Coge, F.; Leonce, S.; Burbridge, M.; Bruno, A.; Boutin, J. A.; Lockhart, B.; Roche, S.; Cruzalegui, F. Specific oncogenic activity of the Src-family tyrosine kinase c-Yes in colon carcinoma cells. *PLoS One.* **2011,** *6*, e17237.
(27) Zhang, X.; Meyn, M. A., III; Smithgall, T. E. c-Yes tyrosine kinase is a potent suppressor of ES cell differentiation and antagonizes the actions of its closest phylogenetic relative, c-Src. *ACS Chem. Biol.* **2014,** *9*, 139–146.
(28) Friesner, R. A.; Banks, J. L.; Murphy, R. B.; Halgren, T. A.; Klicic, J. J.; Mainz, D. T.; Repasky, M. P.; Knoll, E. H.; Shelley, M.; Perry, J. K.; Shaw, D. E.; Francis, P.; Shenkin, P. S. Glide: a new approach for rapid, accurate docking and scoring. 1. Method and assessment of docking accuracy. *J. Med. Chem.* **2004,** *47*, 1739–1749.
(29) Halgren, T. A.; Murphy, R. B.; Friesner, R. A.; Beard, H. S.; Frye, L. L.; Pollard, W. T.; Banks, J. L. Glide: a new approach for rapid, accurate docking and scoring. 2. Enrichment factors in database screening. *J. Med. Chem.* **2004,** *47*.
(30) Krishnamurty, R.; Maly, D. J. Biochemical mechanisms of resistance to small-molecule protein kinase inhibitors. *ACS Chem. Biol.* **2010,** *5*, 121–138.
(31) Azam, M.; Seeliger, M. A.; Gray, N. S.; Kuriyan, J.; Daley, G. Q. Activation of tyrosine kinases by mutation of the gatekeeper threonine. *Nat. Struct. Mol. Biol.* **2008,** *15*, 1109–1118.

(32) Kornev, A. P.; Haste, N. M.; Taylor, S. S.; Eyck, L. F. Surface comparison of active and inactive protein kinases identifies a conserved activation mechanism. *Proc. Natl. Acad. Sci. U S A.* **2006,** *103*, 17783–17788.
(33) Roskoski, R., Jr. Src protein-tyrosine kinase structure, mechanism, and small molecule inhibitors. *Pharmacol. Res.* **2015,** *94*, 9–25.
(34) Kornev, A. P.; Taylor, S. S.; Ten Eyck, L. F. A helix scaffold for the assembly of active protein kinases. *Proc Natl Acad Sci U S A.* **2008,** *105*, 14377-14382.
(35) Wang, Q.; Zorn, J. A.; Kuriyan, J. A structural atlas of kinases inhibited by clinically approved drugs. *Methods Enzymol.* **2014,** *548*, 23–67.
(36) Niesen, F. H.; Berglund, H.; Vedadi, M. The use of differential scanning fluorimetry to detect ligand interactions that promote protein stability. *Nat. Protoc.* **2007,** *2*, 2212–2221.
(37) Niesen, F. H. Excel script for the analysis of protein unfolding data acquired by differential scanning fluorimetry (DSF). *Manual Version 3.0.* **2010**.
(38) Ko, K. S.; Steffey, M. E.; Brandvold, K. R.; Soellner, M. B. Development of a chimeric c-Src kinase and HDAC inhibitor. *ACS Med. Chem. Lett.* **2013,** *4*, 779–783.
(39) Seeliger, M. A.; Young, M.; Henderson, M. N.; Pellicena, P.; King, D. S.; Falick, A. M.; Kuriyan, J. High yield bacterial expression of active c-Abl and c-Src tyrosine kinases. *Protein Sci.* **2005,** *14*, 3135–3139.
(40) Jacobson, M. P.; Pincus, D. L.; Rapp, C. S.; Day, T. J.; Honig, B.; Shaw, D. E.; Friesner, R. A. A hierarchical approach to all-atom protein loop prediction. *Proteins.* **2004,** *55*, 351–367.
(41) Dalgarno, D.; Stehle, T.; Narula, S.; Schelling, P.; van Schravendijk, M. R.; Adams, S.; Andrade, L.; Keats, J.; Ram, M.; Jin, L.; Grossman, T.; MacNeil, I.; Metcalf, C. r.; Shakespeare, W.; Wang, Y.; Keenan, T.; Sundaramoorthi, R.; Bohacek, R.; Weigele, M.; Sawyer, T. Structural basis of Src tyrosine kinase inhibition with a new class of potent and selective trisubstituted purine-based compounds. *Chem. Biol. Drug Des.* **2006,** *67*, 46–57.
(42) Xu, W.; Harrison, S. C.; Eck, M. J. Three-dimensional structure of the tyrosine kinase c-Src. *Nature.* **1997,** *385*, 595–602.
(43) Tokarski, J. S.; Newitt, J. A.; Chang, C. Y. J.; Cheng, J. D.; Wittekind, M.; Kiefer, S. E.; Kish, K.; Lee, F. Y. F.; Borzillerri, R.; Lombardo, L. J.; Xie, D. L.; Zhang, Y. Q.; Klei, H. E. The structure of dasatinib (BMS-354825) bound to activated ABL kinase domain elucidates its inhibitory activity against imatinib-resistant ABL mutants. *Cancer Research.* **2006,** *66*, 5790–5797.
(44) Levinson, N. M.; Kuchment, O.; Shen, K.; Young, M. A.; Koldobskiy, M.; Karplus, M.; Cole, P. A.; Kuriyan, J. A Src-like inactive conformation in the Abl tyrosine kinase domain. *PLoS Biol.* **2006,** *4*, e144.
(45) Case, D. A.; Darden, T. A.; Cheatham II, I. T. E.; Simmerling, C. L.; Wang, J.; Duke, R. E.; Luo, R.; Walker, R. C.; Zhang, W.; Merz, K. M.; Roberts, B.; Wang, B.; Hayik, S.; Roitberg, A.; Seabra, G.; Kolossváry, I.; Wong, K. F.; Paesani, F.; Vanicek, J.; Liu, J.; Wu, X.; Brozell, S. R.; Steinbrecher, T.; Gohlke, H.; Cai, Q.; Ye, X.; Wang, J.; Hsieh, M.-J.; Cui, G.; Roe, D. R.; Mathews, D. H.; Seetin, M. G.; Sagui, C.; Babin, V.; Luchko, T.; Gusarov, S.; A., K.; P.A., K. AMBER 11, University of California, San Francisco. **2010**.

(46) Hornak, V.; Abel, R.; Okur, A.; Strockbine, B.; Roitberg, A.; Simmerling, C. Comparison of multiple amber force fields and development of improved protein backbone parameters. *Proteins-Structure Function and Bioinformatics.* **2006,** *65*, 712–725.
(47) Wang, J.; Wolf, R. M.; Caldwell, J. W.; Kollman, P. A.; Case, D. A. Development and testing of a general amber force field. *J. Comput. Chem.* **2004,** *25*, 1157–1174.
(48) Jakalian, A.; Bush, B. L.; Jack, D. B.; Bayly, C. I. Fast, efficient generation of high-quality atomic charges. AM1-BCC model. *J. Comp. Chem.* **2000,** *21*, 132–146.
(49) Molecular Operating Environment (MOE), C. C. G. I., 1010 Sherbooke St. West, Suite #910, Montreal, QC, Canada, H3A 2R7. **2011**.
(50) Jorgensen, W. L.; Chandrasekhar, J. D.; Madura, R. W.; Impey, R. W.; Klein, M. L. Comparison of simple potential functions for simulating liquid water. *J. Chem. Phys.* **1983,** *79*, 926–935.
(51) Zhu, X.; Kim, J. L.; Newcomb, J. R.; Rose, P. E.; Stover, D. R.; Toledo, L. M.; Zhao, H.; Morgenstern, K. A. Structural analysis of the lymphocyte-specific kinase Lck in complex with non-selective and Src family selective kinase inhibitors. *Structure.* **1999,** *7*, 651–661.

CHAPTER VI

Conclusions

Abstract

Kinases have become a primary focus in the current development of targeted molecular therapies. Research creating novel methodologies for more specific and selective kinase inhibitors, however, has been lacking as roughly two thirds of the kinome has no viable small inhibitor option available. The work presented in this dissertation has helped create new solutions for selectively targeting deregulated kinases and for understanding inhibitor specificity. Although kinase inhibitor selectivity trends are still difficult to exploit pharmacologically, our work regarding four separate targeting strategies (covalent, bivalent, conformation-selective and P-loop pocket inhibition) has significantly advanced our knowledge in this area and will aid in the design of future chemical probes and clinical therapeutics.

Utilizing Covalent Inhibition for Kinase Selectivity and Characterizing P-loop Conformations

Irreversible inhibition has only recently been viewed as an acceptable kinase inhibitor strategy. Concerns of idiosyncratic toxicity from resultant drug-protein adducts have largely been alleviated with the recent FDA approval of ibrutinib and afatinib. These inhibitors benefit from a non-ATP-competitive mode of action and a drug-protein residence time only limited by kinase turnover.

Most covalent kinase inhibitors are based off of reversible-binding scaffolds that already display moderate to high potency and selectivity for the target. This makes measuring the contribution of an appended electrophile on the selectivity of the inhibitor quite difficult. We decided to characterize selectivity via irreversibility by synthesizing a covalent version of a validated, promiscuous kinase inhibitor. We hypothesized that we could obtain considerable gains in selectivity for our model target system, c-Src tyrosine

kinase, by targeting a nonconserved cysteine residue (found in < 2% of all kinases) located within the P-loop or 'ceiling' of the kinase. The uniqueness of the chemical scaffold (binds ~60% of kinases at 2 μM) created a particularly stringent test for our selectivity study.

A small series of covalent inhibitors was synthesized and an optimal inhibitor for c-Src was identified, compound **2.7**, based on a thorough rate of inactivation constant (k_{inact}) analysis. We discovered that k_{inact} values correlated well with predicted electrophile reactivity trends (reactivity: vinyl sulfonamide > α-chloro-ketone) in targeting the non-catalytic Cys277 residue of c-Src. Selectivity analysis of **2.7** with a small panel of homologous kinases demonstrated that we improved selectivity by having an ~8-fold improvement in potency for c-Src over a reversible analog, compound **2.1** and by having suboptimal binding of **2.7** to tyrosine kinases c-Abl and Hck. Both points resulted in a greater than 80-fold improvement in selectivity for c-Src with compound **2.7**.

The modular nature of our targeting strategy allowed us to explore improvements in selectivity on an alternative dasatinib scaffold (FDA-approved kinase inhibitor), while also evaluating its ability to target clinically relevant kinase mutations. The latter point is of particular interest, given the growing number kinase resistant mutations being discovered. We found that we could make dasatinib, a double-digit micromolar inhibitor of gatekeeper mutated c-Src, into one of the most potent T338M c-Src inhibitors (compound **2.8**) known to date (IC_{50} value, 2 h = 44 nM). Selectivity profiling of both dasatinib and **2.8** revealed a modest increase in selectivity (dasatinib, S_{35} = 12%; **2.8**, S_{35} = 7%). This is likely attributed to the high starting potency of dasatinib (picomolar inhibitor of wt c-Src), strictly making any gain in selectivity resultant from incompatible off-target kinase binding to compound **2.8**.

Our k_{inact} characterization with compound **2.7** resulted in a unique ability to describe the relative P-loop conformation of several protein tyrosine kinase systems (eg. wt, P~wt, T338M). We found that an increased k_{inact} values would represent a closer or more kinked-in kinase P-loop conformation, relative to inhibitor. A proof-of-principle analysis using Q252C c-Abl further supported this finding and also demonstrated that we

could apply a chemical genetic targeting approach to study the P-loop of kinases without native cysteine residues, setting the stage for our P-loop studies in **Chapter V**.

The work from this project shows that considerable gains in selectivity can be achieved with covalent kinase inhibition. Irreversibility increases target potency and subsequently improves selectivity (in most normal examples), but absolute specificity results from a combination of covalent inhibition and reversible scaffold binding interactions. If the reversible starting point cannot even weakly bind to the desired kinase, no electrophile can be added to improve target potency. Much work is still left to be done in this area, especially regarding the evaluation of cellular off-targets for covalent kinase inhibitors. Additional projects could also focus on covalently inhibiting kinases in their inactive conformations, for use in either a biochemical or cellular context.

A Novel Enzyme-Templated Fragment-Based Screen for Discovering Bivalent Kinase Inhibitors

In a field with a countless number of small molecule inhibitors, it becomes increasingly important to develop unbiased methods for inhibitor discovery. This allows for the potential detection of novel inhibitor scaffolds with improved physiochemical properties and ideally compounds with little to none intellectual property protection.

Work in **Chapter III** of this thesis detailed our efforts in the design of a novel, proximity-based, enzyme-templated fragment screen. Our goal was to create a hybrid fragment screen, where small molecule fragment hits could be identified without prior structural knowledge using a high throughput activity assay, as opposed to using more time-consuming biophysical or mass spectrometry detection methods.

To this means, we modified our previously described promiscuous kinase inhibitor scaffold with a reactive thiol handle for use in Michael acceptor fragment tethering. This approach differs from traditional tethering in that 1) our small molecule thiol, compound **3.1**, replaces the routinely employed native or engineered cysteine group on the protein surface and that 2) our fragments contain an acrylamide reactive group for Michael acceptor chemistry to occur. We screened for c-Src kinase inhibition via in situ bivalent inhibitor assembly with the simultaneous dosing of **3.1** and a member of the acrylamide library. A library of 110 fragments resulted in four hits, two of which were

followed further for bivalent hit reconstitution (resynthesized without the labile thioether bond). We found that R-enantiomers of both putative inhibitors, compounds **3.8** and **3.10**, did show improved c-Src potency and selectivity relative to compounds **3.1** and **3.2** (all carbon version of **3.1**). We speculated that the fragment portion of both lead compounds were binding within the P-loop pocket of c-Src, contributing to their ~10-fold increase in average selectivity over the control hinge-only-binding compound, **3.2**.

Even with a small library of acrylamides, our screening method rapidly identified fragments that were useful in synthesizing two Src-selective kinase inhibitors. This screen could also easily be applied to any kinase (or suitable protein) with a known hinge binding chemical moiety and without reactive cysteine residues. Improvements in final compound ligand efficiency values could occur with the screening of a larger library or with selection a slightly more ligand efficient starting point (eg. smaller MW hinge binder). Variations on this methodology could also look to direct fragments to other areas of the kinase (eg. substrate site, accessary domains) to improve inhibitor potency and selectivity.

The Effect of Conformation-Selective Inhibition on Kinase Selectivity

The discovery of the selective, DFG-out inactive inhibitor imatinib contributed to the development of numerous Type II kinase inhibitors in an effort to target a 'less conserved' conformation of the kinase. The resultant research produced both selective and non-selective Type II inhibitors, however, the overall convention in the literature has continued to suggest that DFG-out inactive inhibition improves inhibitor selectivity. An additional inactive kinase conformation, αC-helix out (CHO), has also been described for several selective FDA approved inhibitors. A thorough selectivity analysis of this inactive binding mode has yet to take place.

We consequently produced a complete selectivity comparison for a 'matched set' of conformation-selective dasatinib analogs to identify their effects on kinase inhibitor specificity. The work from **Chapter IV** describes the rational design of a CHO kinase inhibitor, as well as the introduction of the first set of conformation-selective inhibitors to share the same hinge-binding scaffold that has been verified crystallographically.

Kinome profiling for the 'matched set' revealed that Type I (active conformation inhibitor) and Type II inhibitors share very similar selectivity profiles (dasatinib, S_{35} = 21%; **DAS-DFGO-I** & **DAS-DFGO-II**, S_{35} = 24%, 20%). This means that the conversion of a Type I to a Type II inhibitor leads to comparable or reduced selectivity as result of Type II inhibitor binding of non-Thr gatekeeper kinases (eg. FLT1, RET, TIE2). Moreover, CHO inhibition produced the most selective inhibitory profile (**DAS-CHO-I** & **DAS-CHO-II**, S_{35} = 5%, 16%), indicating that fewer kinases (including the Ephrin family) are inclined to adopt this inactive conformation (less conserved across kinome). The selectivity data also suggests that the analysis of inhibitor sets with varied hinge-binding scaffolds will likely report only on the selectivity of the hinge binder.

The results from this study are widely applicable to the design of future conformation-selective inhibitors and can used in a multitude of cellular studies. We performed some initial experiments using Bcr-Abl transformed BaF3 cells (Abl is a target for all five inhibitors) and demonstrated that cellular potency is independent of inhibitor kinetic parameters (k_{on}, k_{off}, $t_{1/2}$), biochemical selectivity and potency (K_d). Ongoing research by our group is looking to investigate how these inactive binding modes can also affect noncatalytic kinase functions (eg. subcellular kinase localization). Furthermore, we are looking to test these inactive dasatinib analogs in dasatinib-resistant cell lines for improved efficacy.

Divergent P-loop Conformations in Homologous Kinases and its Implications for Inhibitor Selectivity

The wealth of kinase structural data can still not accurately predict observed trends in inhibitor selectivity. Some of this may be do to kinase regions that can adopt several relative conformations, such the phosphate-binding loop (P-loop). This dynamic loop coordinates ATP binding and serves a role in inhibitor selectivity and resistance.

Our work in the final chapter of this dissertation sought to correlate trends in inhibitor selectivity to the P-loop conformation of the kinase. We synthesized a 'molecular ruler' series of covalent compounds to help characterize the in-solution positioning of the P-loop for c-Src and c-Yes (native P-loop cysteine residues) and two other kinase systems (c-Abl, Hck) using a chemical genetic approach. We confirmed a

kinked in P-loop structure for c-Abl and then designated a slightly kinked P-loop conformation for Hck and c-Yes. This is particularly useful given that c-Yes has no X-ray crystal structure information available.

Our experimental data was further validated with MD simulations and docking studies using a Src-selective inhibitor in order to help rationalize the diminished binding of KB-SRC-4 to c-Abl, Hck and Yes. Mutational studies utilizing our covalent labeling strategy also showed that bulky residues near the regulatory spine of the kinase can influence the relative P-loop positioning of the kinase.

Further work in this area will look to characterize the P-loop conformation of kinases that are (or are not) frequent inhibitor off-targets. The P-loop positioning of drug-resistant kinase mutants (eg. imatinib-resistant P-loop mutations) can likewise be determined, to see if theories regarding inhibitor–P-loop matching do contribute to inhibitor potency and selectivity. A more detailed study discriminating the contributions of protein flexibility from relative P-loop positioning would also be tremendously helpful in identifying kinases that can potentially accommodate a wide range of kinase inhibitors.

APPENDIX A

Supplemental Information and Analytical Data for Chapter II

Figure A.1. Kinase P-loop sequence alignment.

```
SRC:    [273] LGQG**C**FGEV
YES:    [281] LGQG**C**FGEV
FYN:    [279] LGNG**Q**FGEV
FGR:    [269] LGTG**C**FGDV
LCK:    [251] LGAG**Q**FGEV
HCK:    [268] LGAG**Q**FGEV
BLK:    [247] LGSG**Q**FGEV
LYN:    [253] LGAG**Q**FGEV
FRK:    [240] LGSG**Q**FGEV
ABL:    [248] LGGG**Q**YGEV
FGFR1:  [482] LGEG**C**FGQV
FGFR2:  [487] LGEG**C**FGQV
FGFR3:  [152] LGEG**C**FGQV
FGFR4:  [473] LGEG**C**FGQV
TNK1:   [122] LGSG**C**FGVV
LIMK1:  [345] LGKG**C**FGQA
```

Sequence alignment of kinase P-loops for Src family kinases, c-Abl and kinases with a cysteine in an equivalent position to Cys277 (bolded character) of c-Src.

Figure A.2 Compound 2.1 KINOMEscan profiling results.

1% of control: 10% of control: 35% of control:

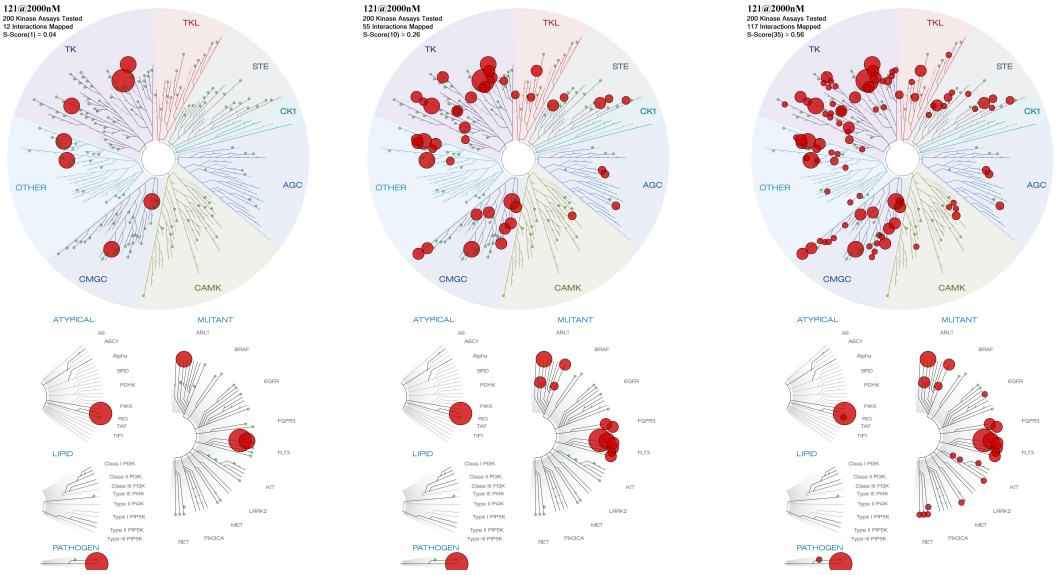

S-scores for Compound **2.1** (2 µM):

S(1) = 4%
S(10) = 26%
S(35) = 56%

Treespot analysis and selectivity (*S*-scores) for compound **2.1** profiled at 2 µM. Complete panel of kinases tested can be found in later in **Appendix A**.

Figure A.3 Gel filtration results with irreversible inhibitors.

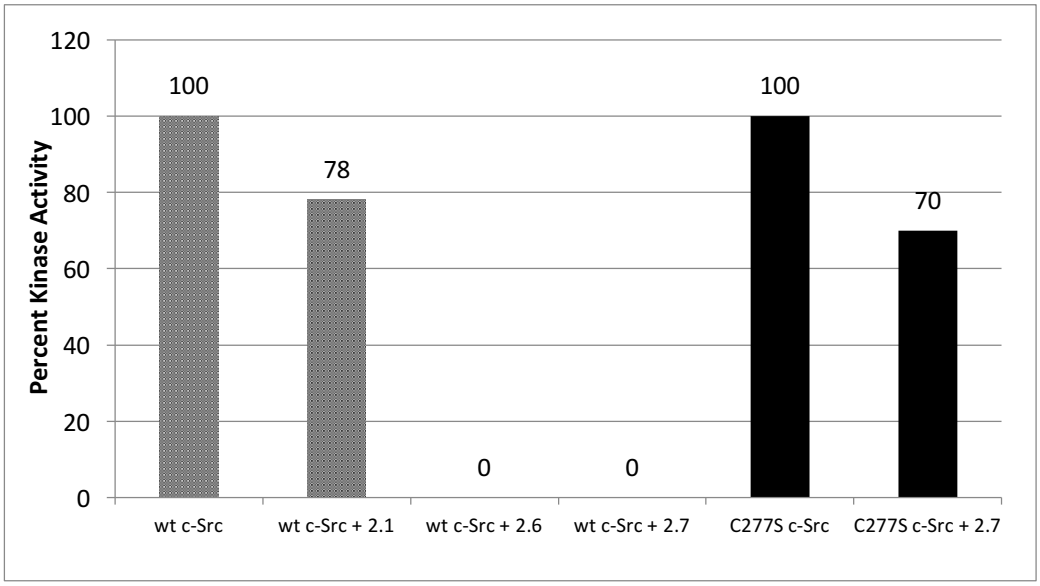

Column graph of percent kinase activity remaining after enzyme was treated with specified inhibitor for 60 min at RT followed by gel filtration through a G25 Sephadex column.

Figure A.4 Mass spectrometry results of enzyme-inhibitor complexes.

Description	Mass Observed
WT c-Src	32,690.1 (no adduct)
WT c-Src + Compound **2.6**	32,690.1 (no adduct) & 33,108.6 (single adduct)
WT c-Src + Compound **2.7**	33,158.6 (single adduct)
C277S c-Src + Compound **2.7**	32,674.5 (no adduct)

Table of observed masses for various 60 min incubations of c-Src enzyme (wt & C277S) and inhibitor (compounds **2.6** & **2.7**) after being passed through separate G25 Sephadex columns. Procedure and spectra can be found in later in **Appendix A**.

Table A.1 Endogenous nucleophile testing.

Compound	IC_{50}, wt c-Src (no DTT/GSH)	IC_{50}, wt c-Src (1 mM DTT)	IC_{50}, wt c-Src (1 mM GSH)
2.7	93 ± 20 nM	95 ± 15 nM	< 30 nM

Table of IC_{50} values for compound **2.7** with wt c-Src after 120 min with no DTT, 1 mM DTT and 1 mM glutathione (GSH). IC_{50} curves can be found in later in **Appendix A**.

Figure A.5 Cellular characterization of compounds **2.1** and **2.7.**

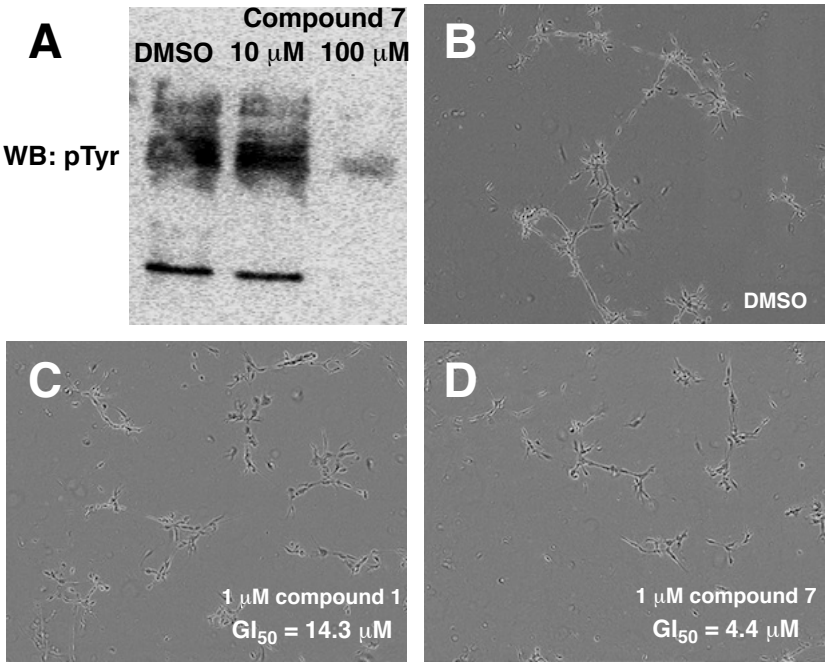

(A) Western blot analysis of compound **2.7** with stably transfected v-Src 3T3 cells. 3D cell Essen IncuCyte camera imaging of **(B)** vehicle **(C)** compound **2.1** at 1 μM and **(D)** compound **2.7** at 1 μM after 24 h of growth.

Spectral Data for Compounds 2.1–2.21

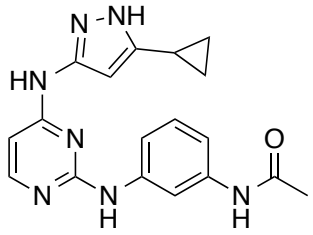

2.1

2.1 ^{1}H:

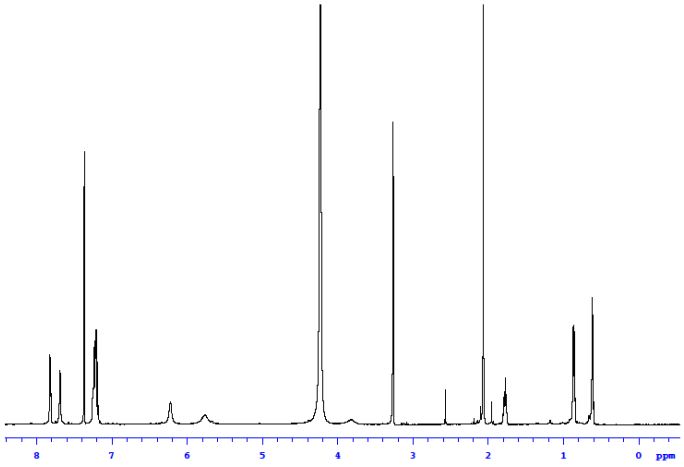

2.1 ^{13}C:

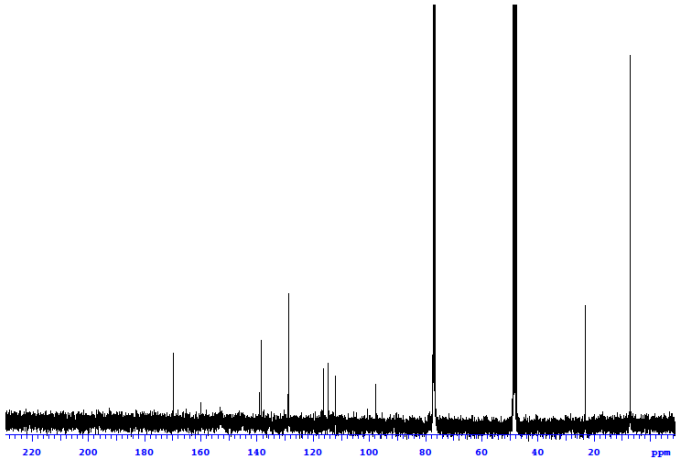

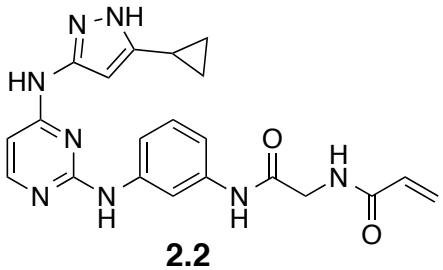

2.2

2.2 ^{1}H:

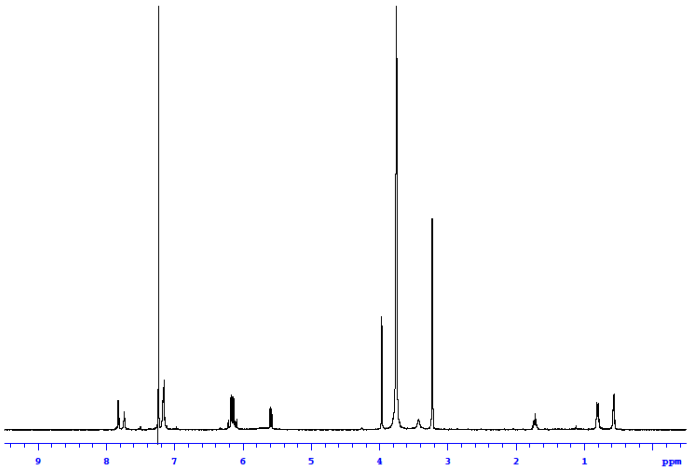

2.2 ^{13}C:

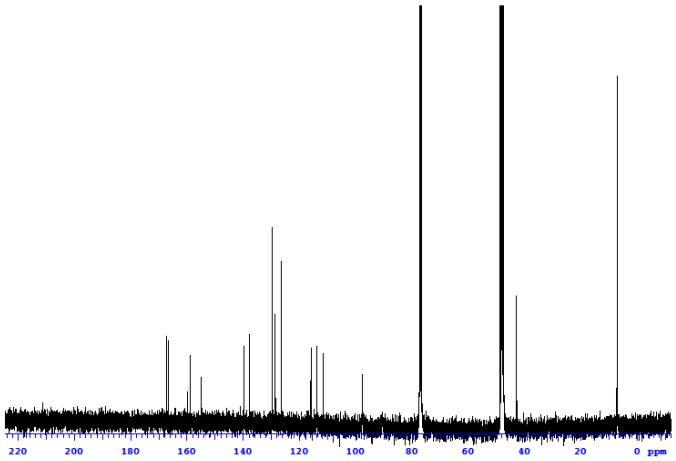

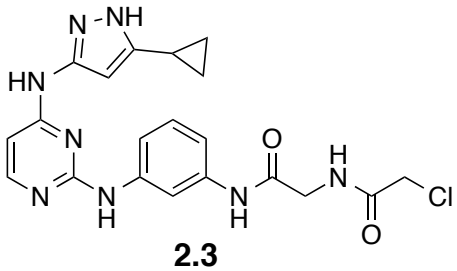

2.3

2.3 ^{1}H:

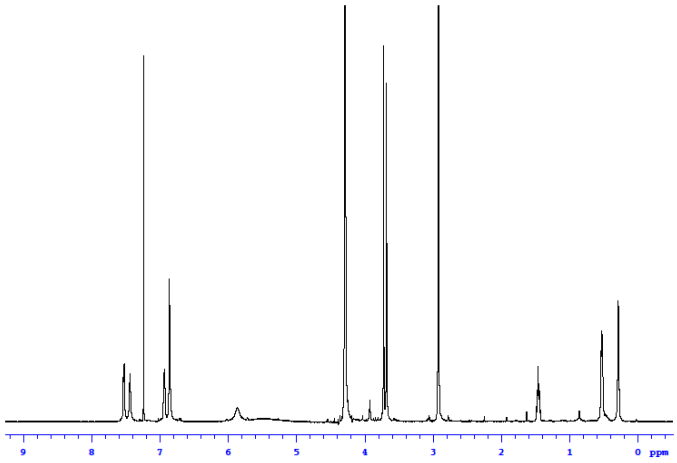

2.3 ^{13}C:

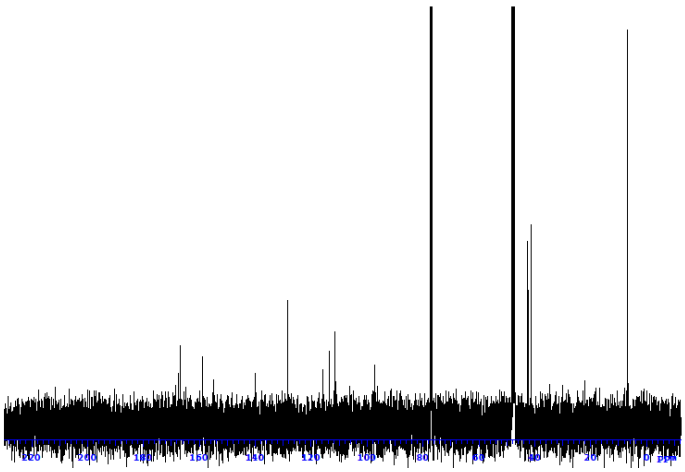

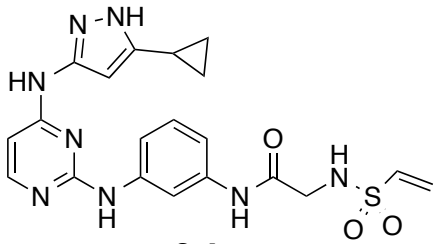

2.4

2.4 ^{1}H:

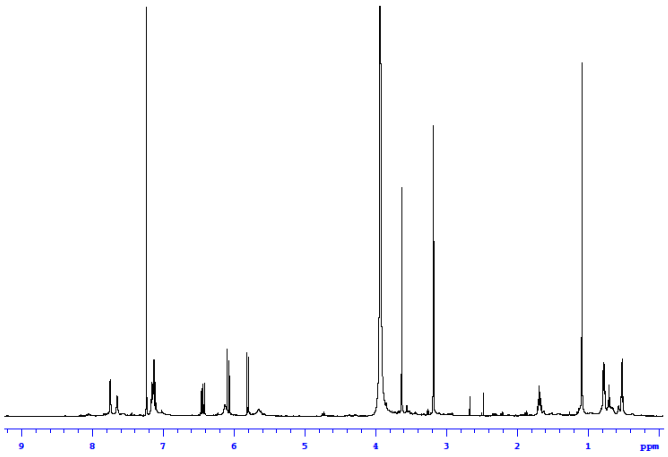

2.4 ^{13}C:

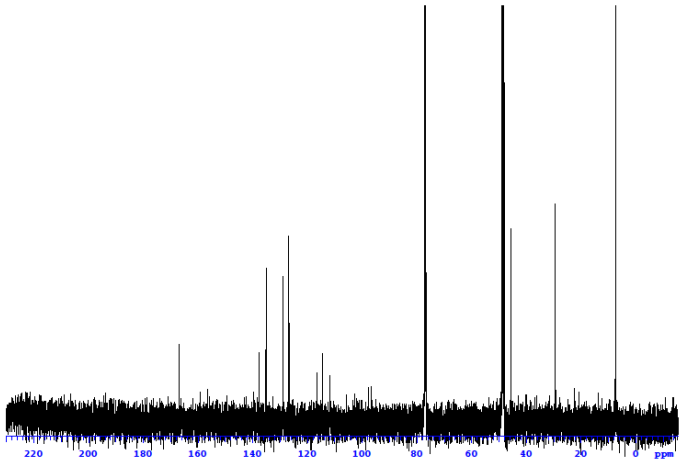

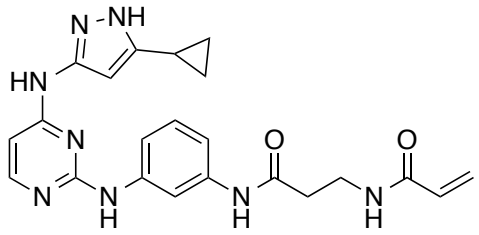

2.5

2.5 ^{1}H:

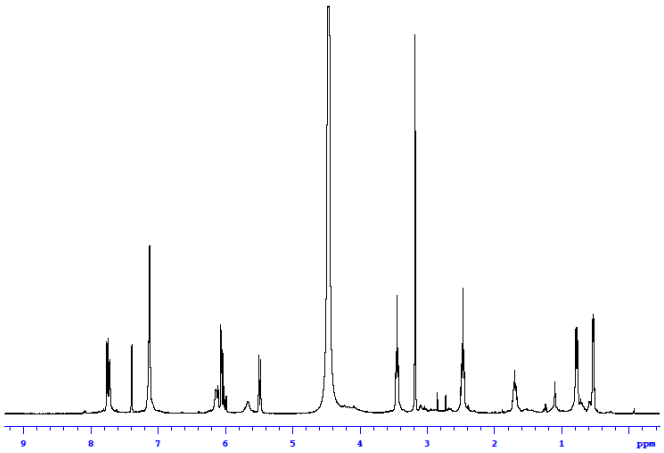

2.5 ^{13}C:

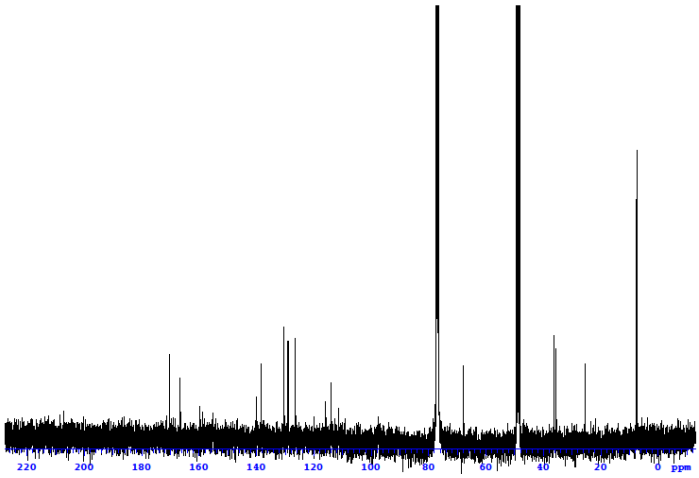

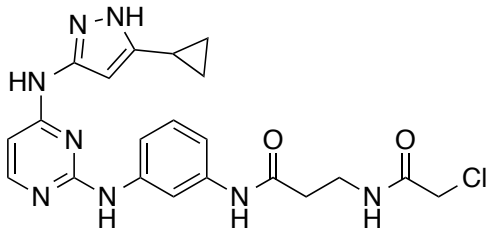

2.6

2.6 ^{1}H:

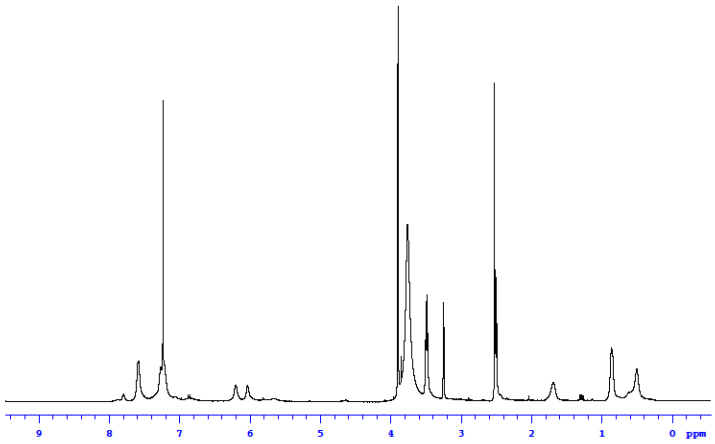

2.6 ^{13}C:

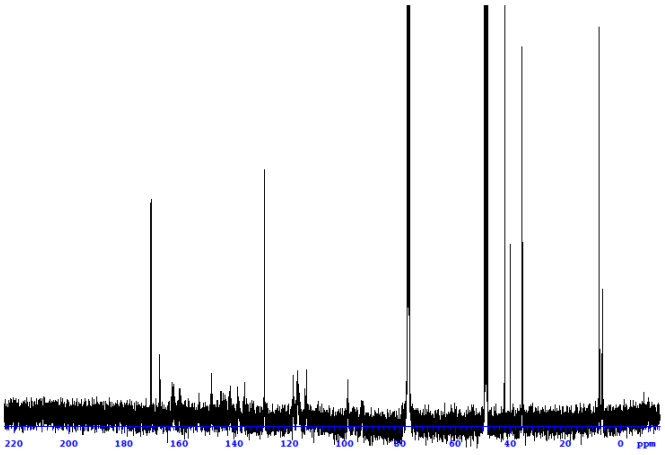

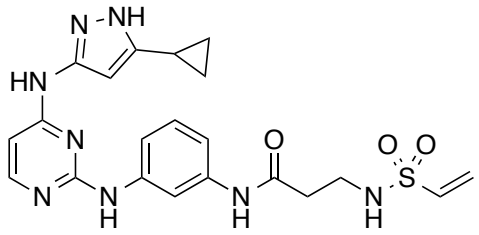

2.7

2.7 ^{1}H:

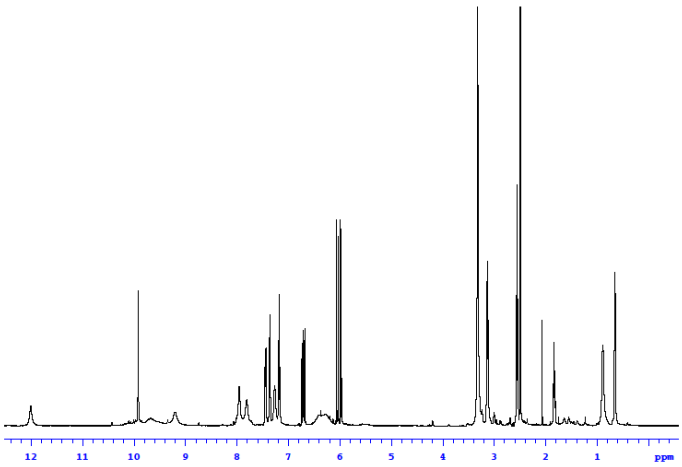

2.7 ^{13}C:

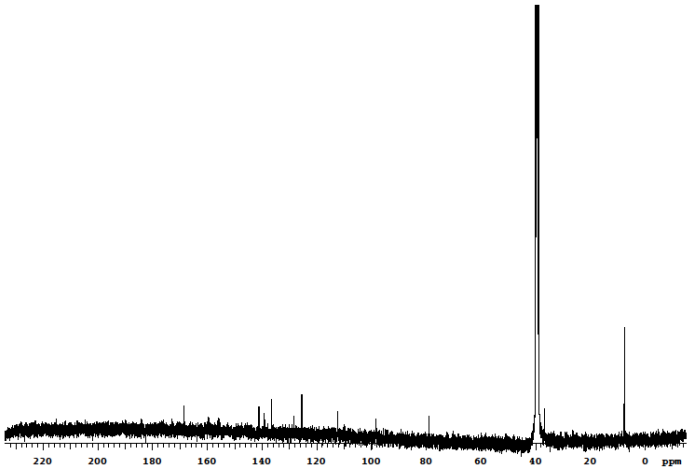

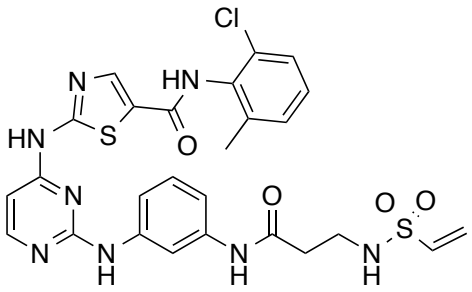

2.8

2.8 ^{1}H:

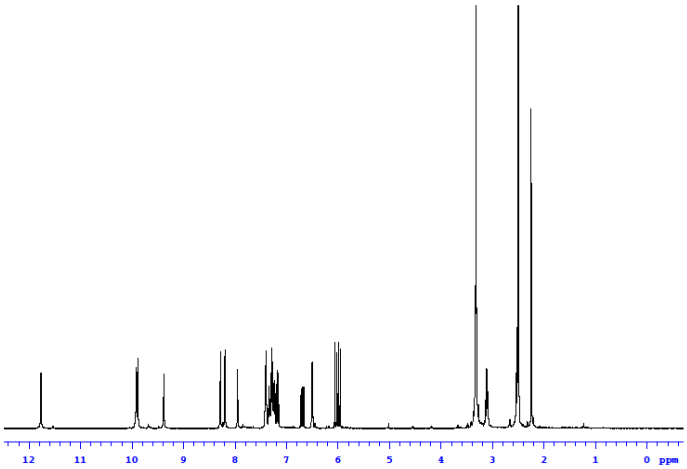

2.8 ^{13}C:

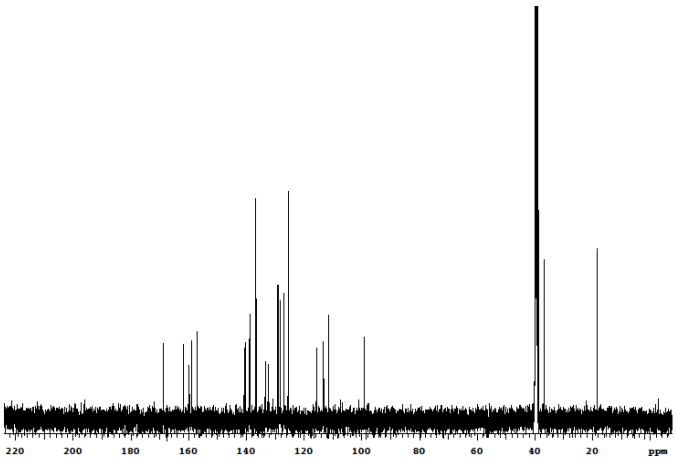

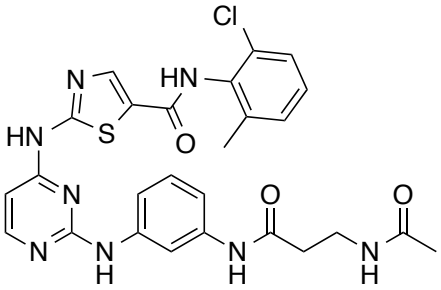

2.9

2.9 ^{1}H:

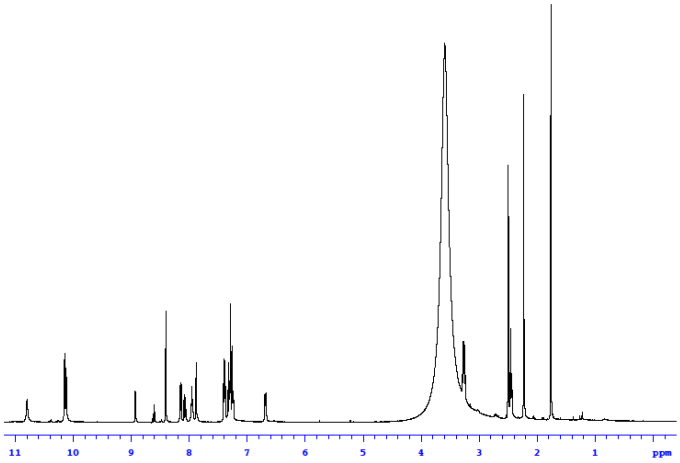

2.9 ^{13}C:

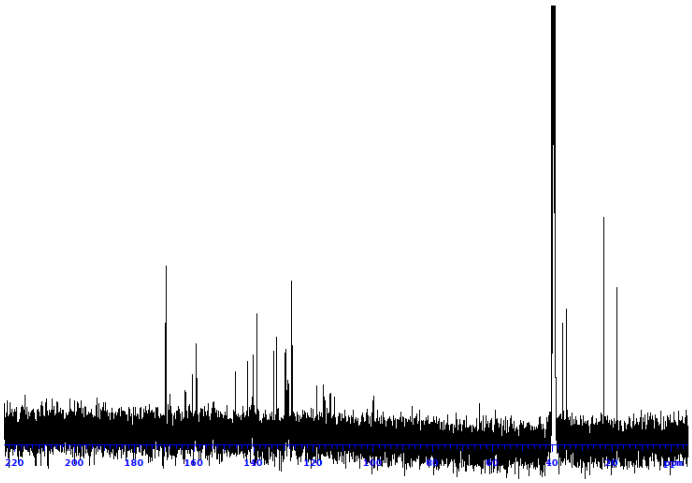

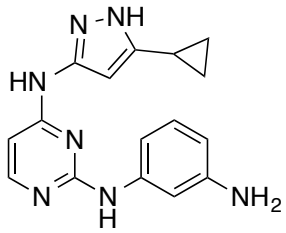

2.11

2.11 ^{1}H:

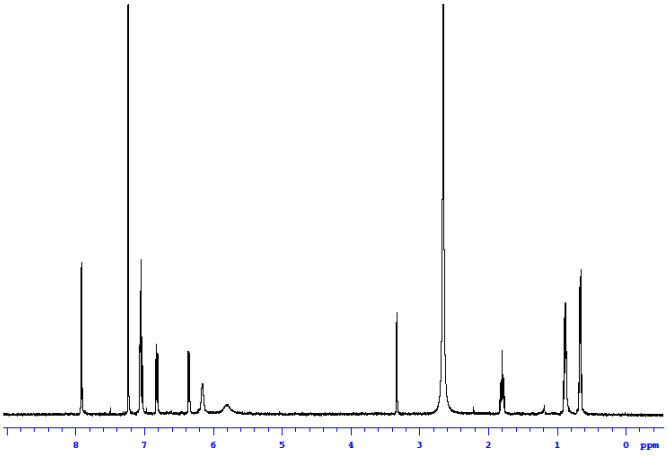

2.11 ^{13}C:

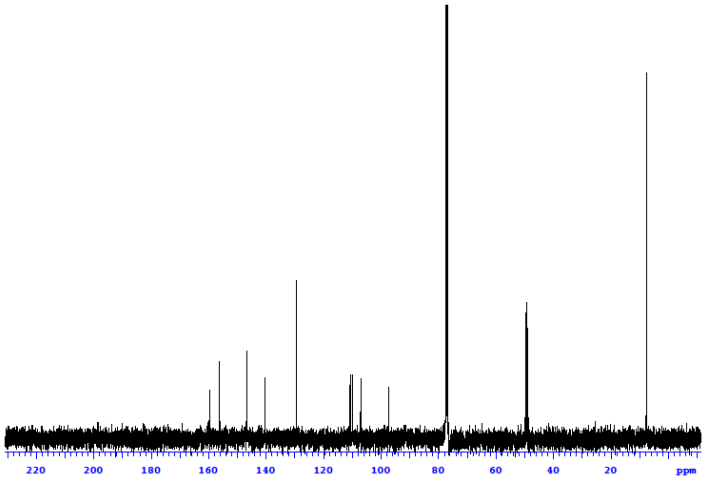

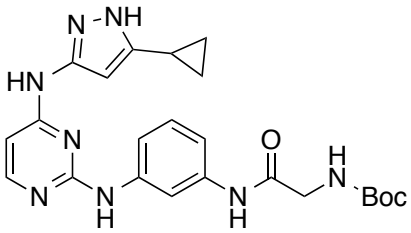

2.12

2.12 ^{1}H:

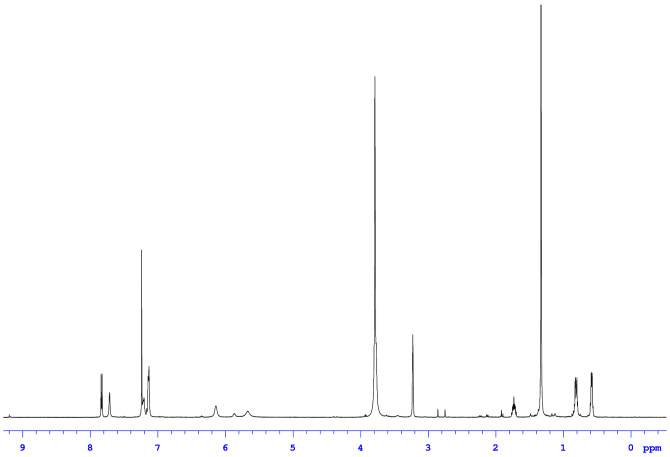

2.12 ^{13}C:

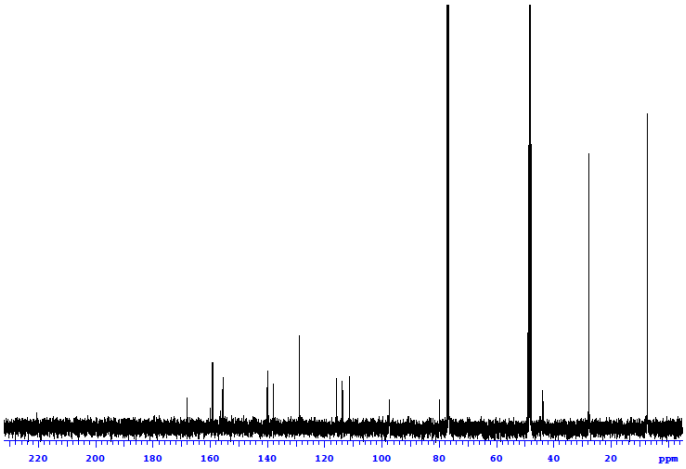

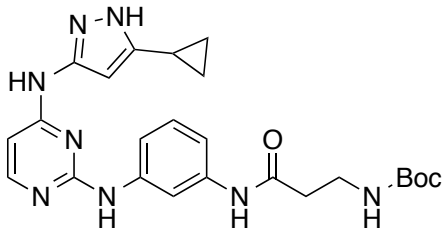

2.13

2.13 ^{1}H:

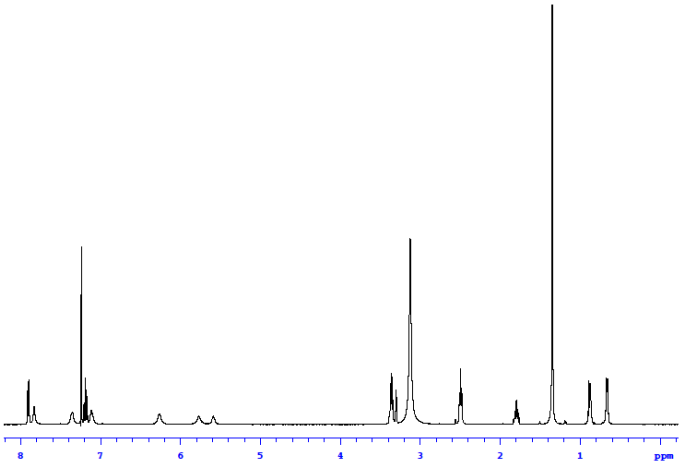

2.13 ^{13}C:

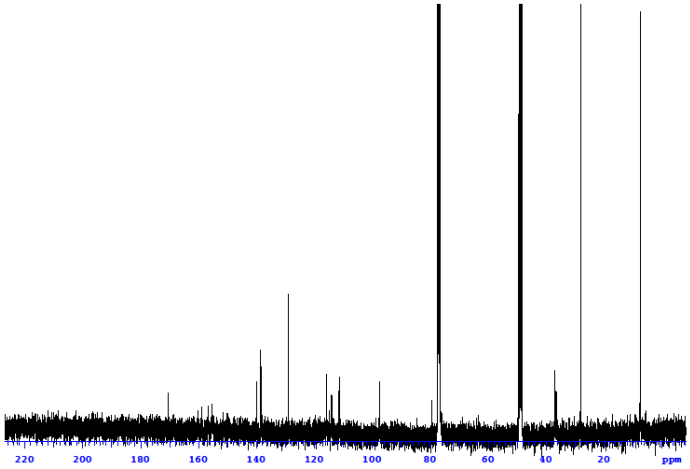

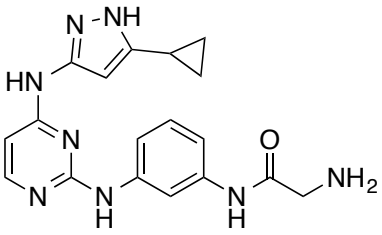

2.14

2.14 ^{1}H:

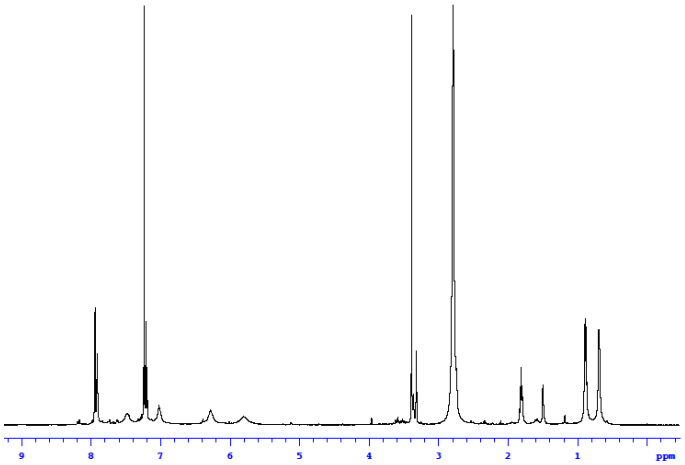

2.14 ^{13}C:

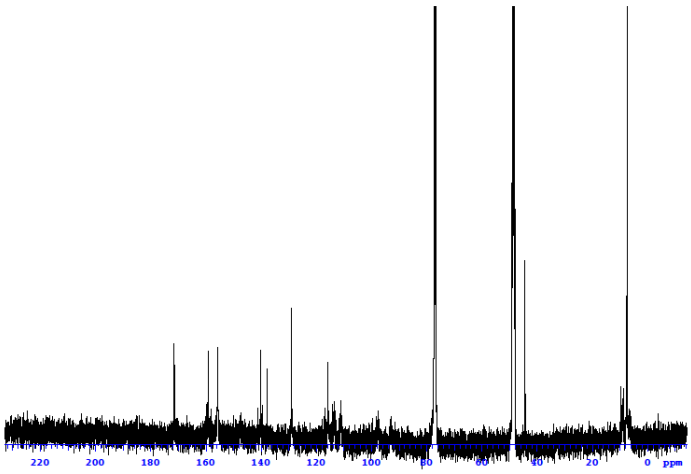

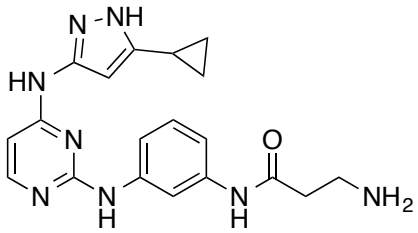

2.15

2.15 ^{1}H:

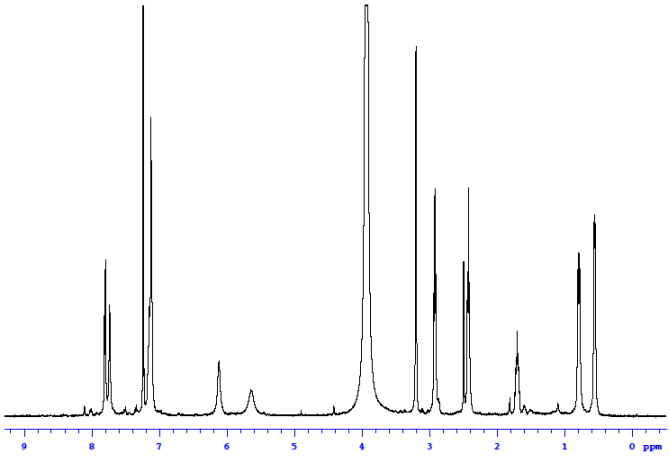

2.15 ^{13}C:

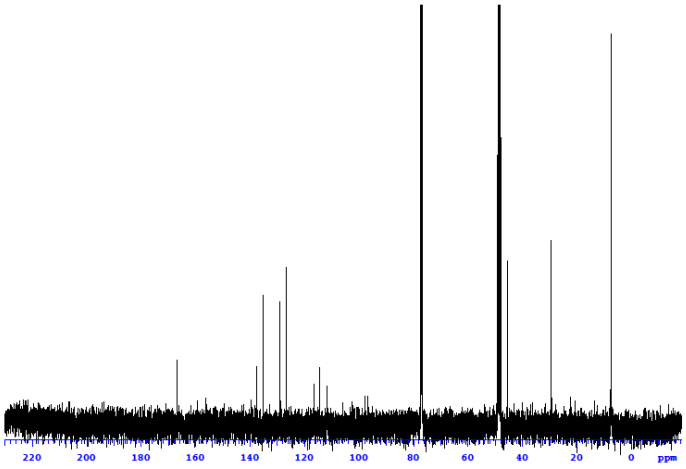

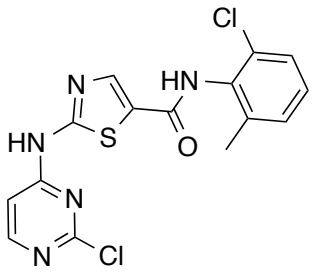

2.17

2.17 ^{1}H:

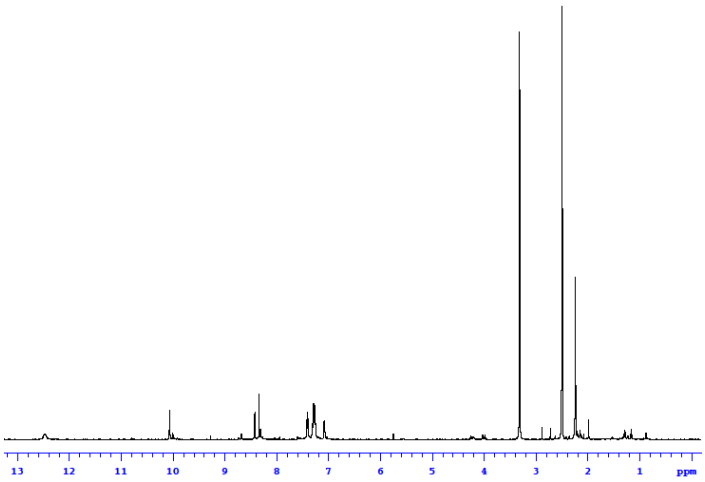

2.17 ^{13}C:

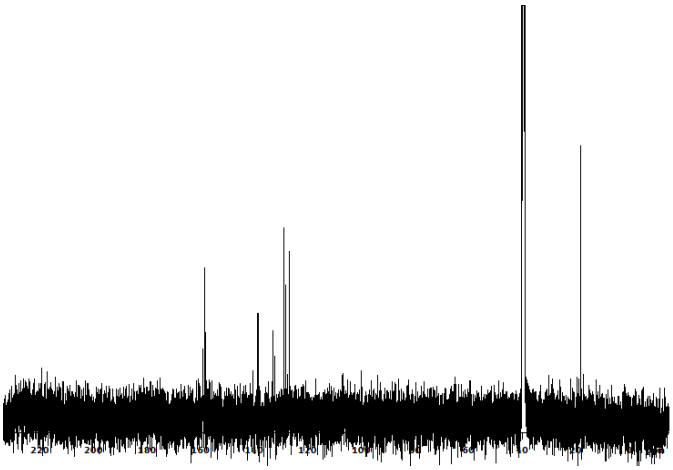

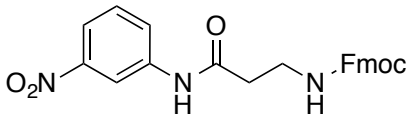

2.18

2.18 ^{1}H:

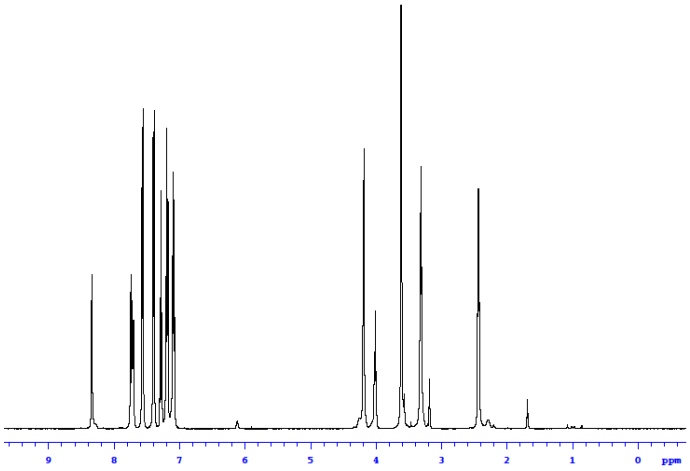

2.18 ^{13}C:

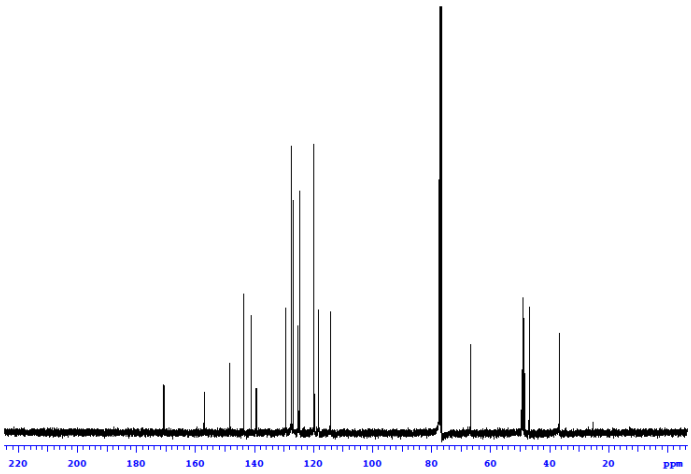

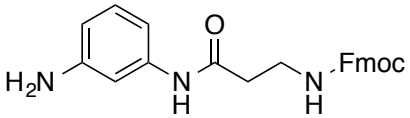

2.19

2.19 ^{1}H:

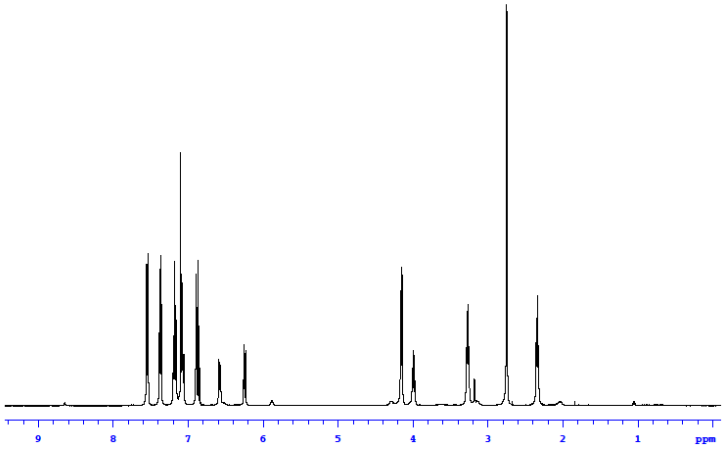

2.19 ^{13}C:

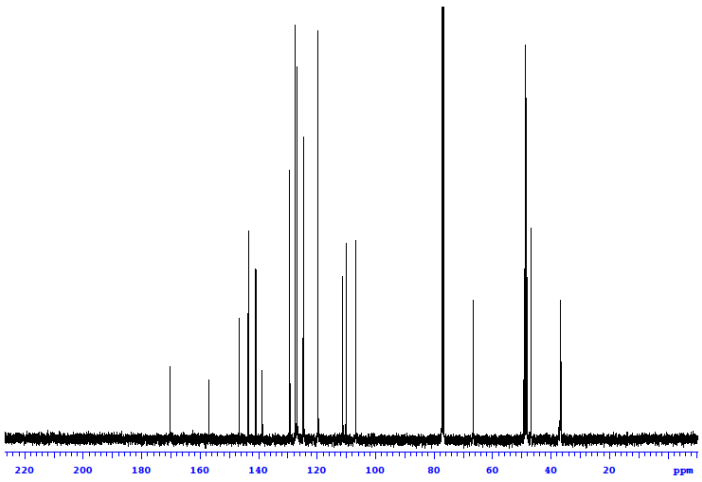

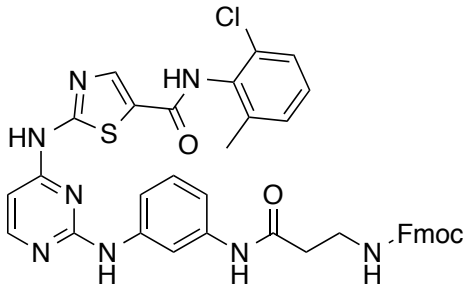

2.20

2.20 ^{1}H:

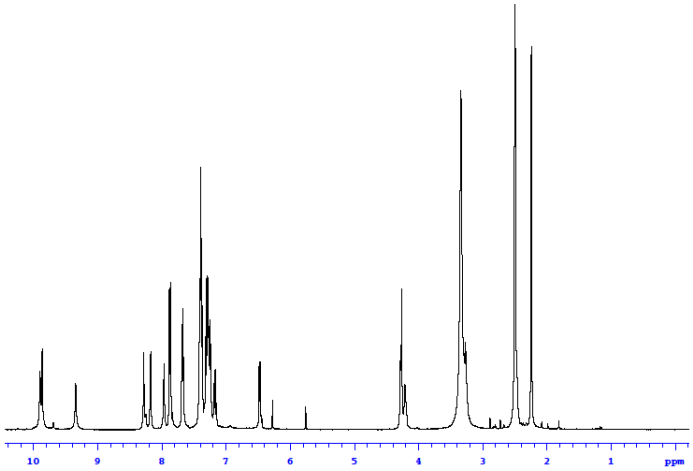

2.20 ^{13}C:

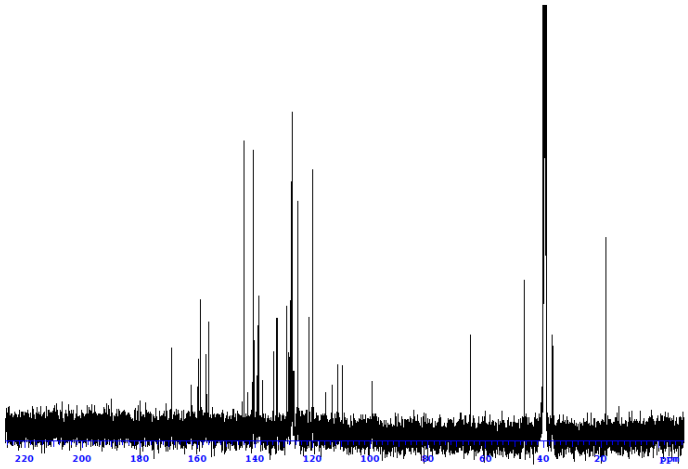

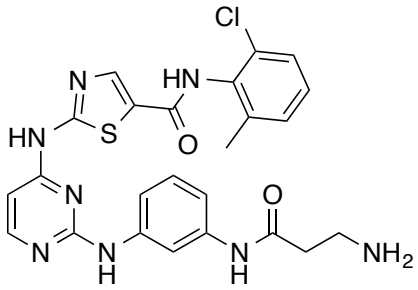

2.21

2.21 ^{1}H:

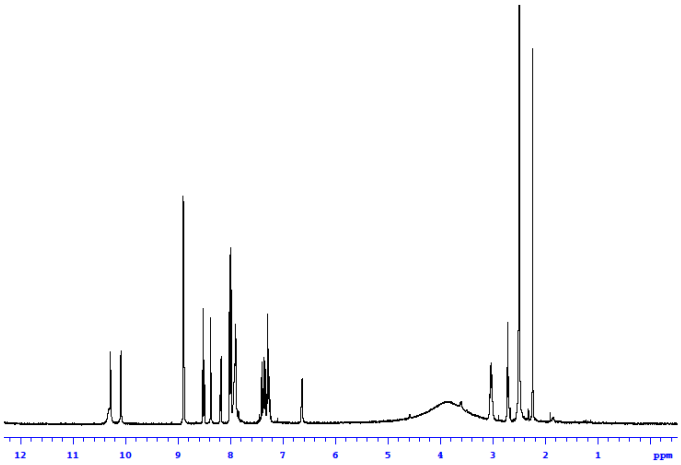

2.21 ^{13}C:

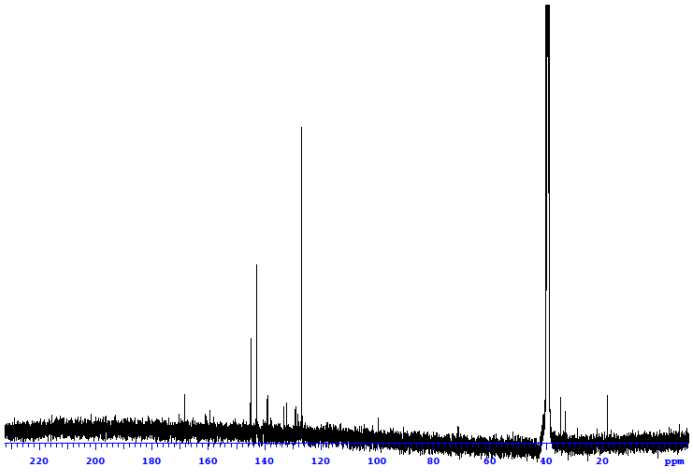

Inhibitor IC_{50} Values

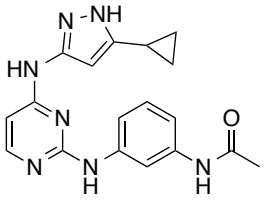

2.1

Compound **2.1** with wt c-Src:

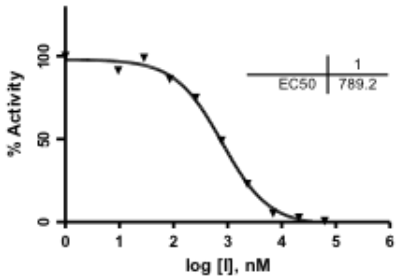

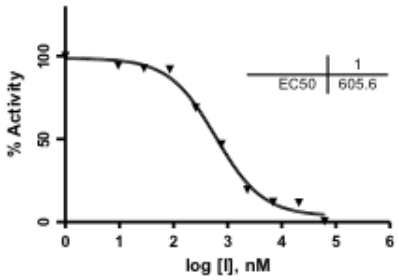

0 min IC_{50} Value = 670 ± 180 nM

120 min IC_{50} Value = 720 ± 170 nM

Compound **2.1** with C277S c-Src:

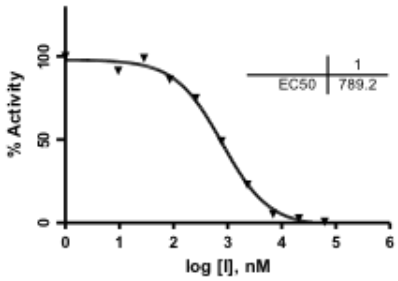

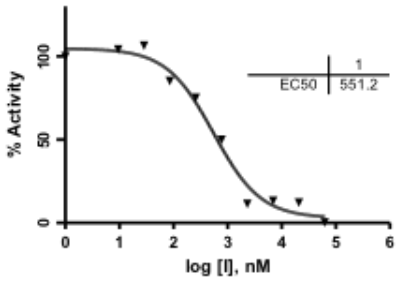

0 min IC_{50} Value = 270 ± 39 nM

120 min IC_{50}Value = 810 ± 360 nM

Compound **2.1** with wt c-Abl:

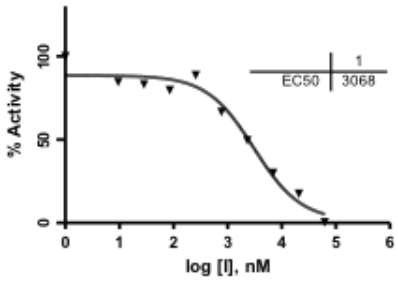

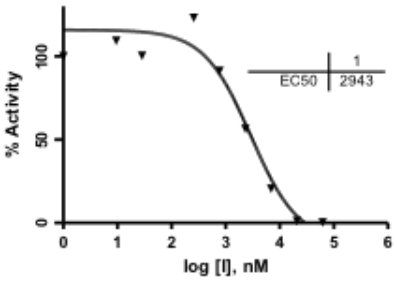

0 min IC_{50} Value = 2,700 ± 470 nM

120 min IC_{50}Value = 2,100 ± 1,200 nM

Compound **2.1** with Q252C c-Abl:

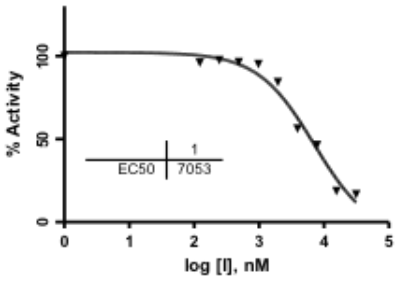

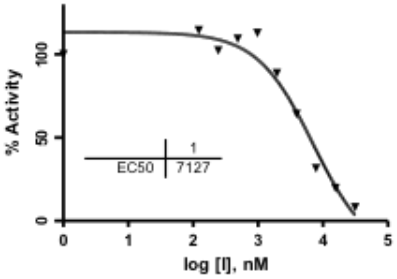

0 min IC_{50} Value = 6.500 ± 760 nM

120 min IC_{50}Value = 7.600 ± 1,500 nM

Compound **2.1** with wt Hck:

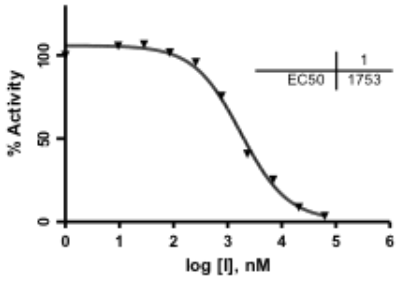

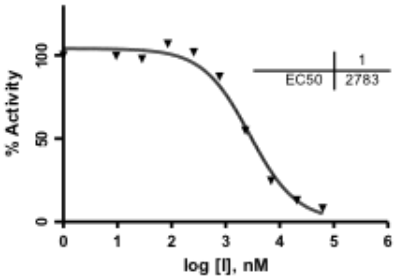

0 min IC_{50} Value = 2,000 ± 230 nM

120 min IC_{50}Value = 2,800 ± 90 nM

Compound **2.1** with T338M c-Src:

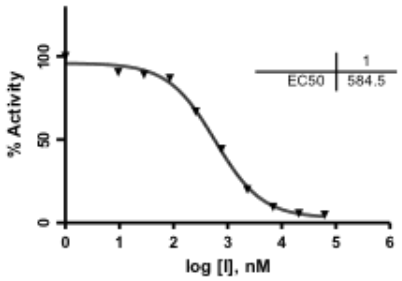

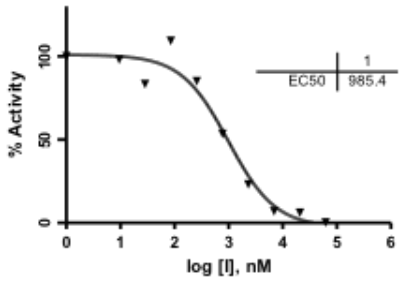

0 min IC_{50} Value = 690 ± 93 nM

120 min IC_{50}Value = 870 ± 160 nM

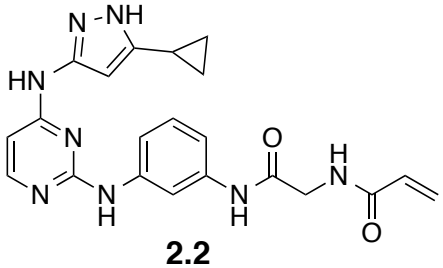

2.2

Compound **2.2** with wt c-Src:

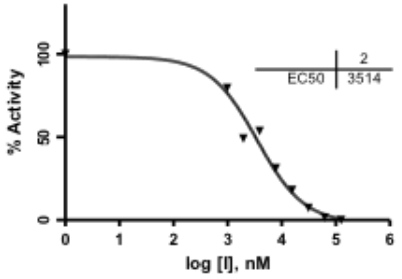

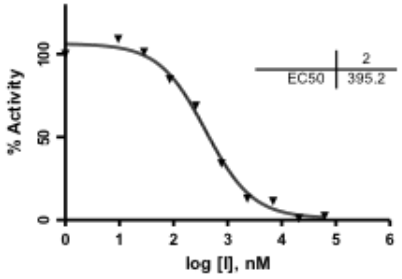

0 min IC_{50} Value = 4,400 ± 1,200 nM

120 min IC_{50}Value = 350 ± 60 nM

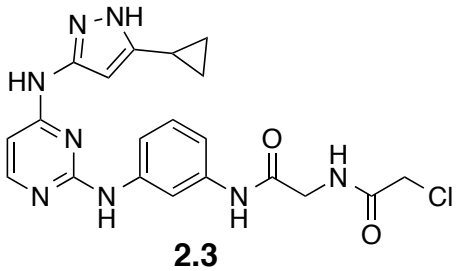

2.3

Compound **2.3** with wt c-Src:

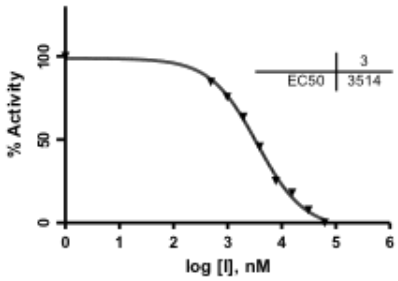

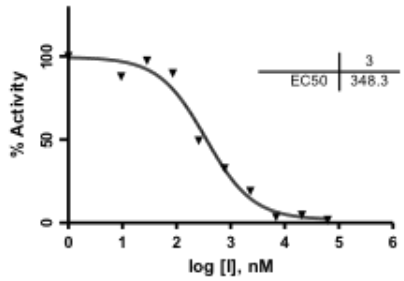

0 min IC_{50} Value = 3,200 ± 390 nM

120 min IC_{50}Value = 340 ± 11 nM

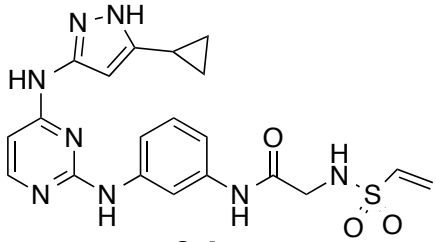

2.4

Compound **2.4** with wt c-Src:

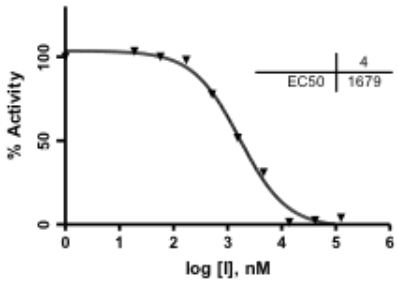

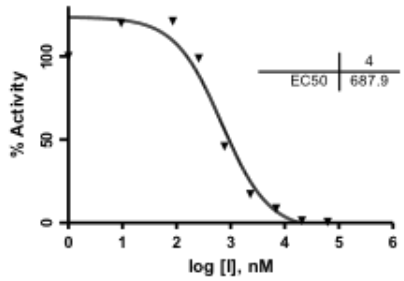

0 min IC_{50} Value = 1,700 ± 21 nM

120 min IC_{50}Value = 570 ± 170 nM

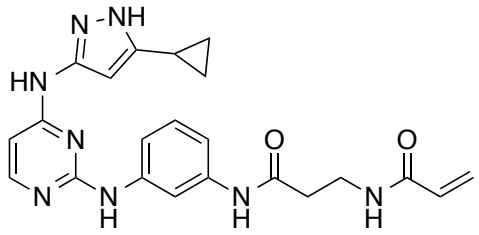

2.5

Compound **2.5** with wt c-Src:

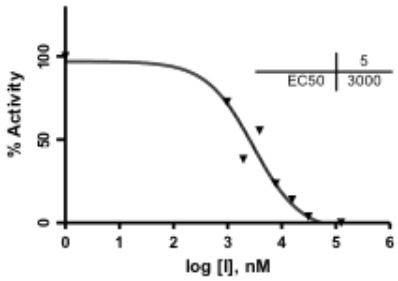

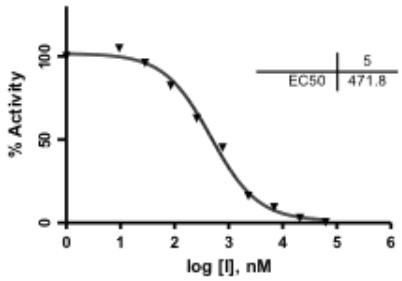

0 min IC_{50} Value = 3,200 ± 740 nM

120 min IC_{50}Value = 610 ± 200 nM

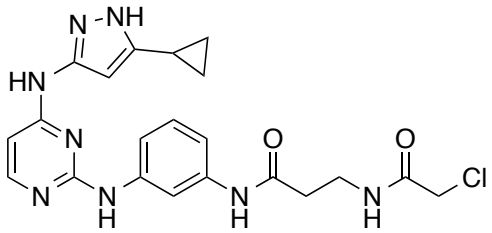

2.6

Compound **2.6** with wt c-Src:

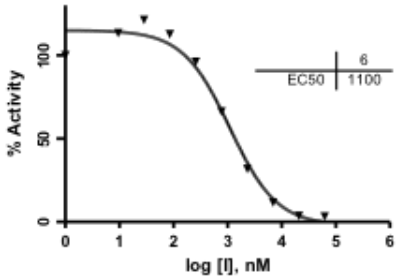

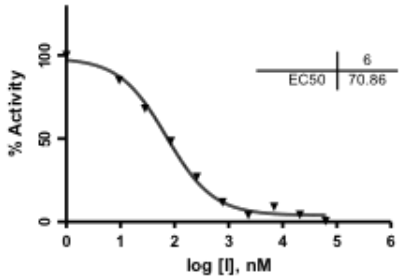

0 min IC_{50} Value = 1,200 ± 170 nM

120 min IC_{50}Value = 91 ± 25 nM

Compound **2.6** with C277S c-Src:

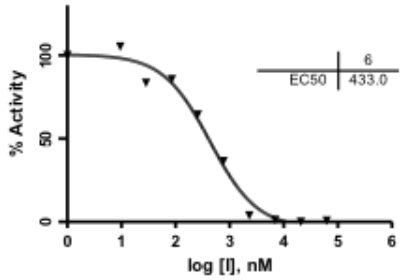

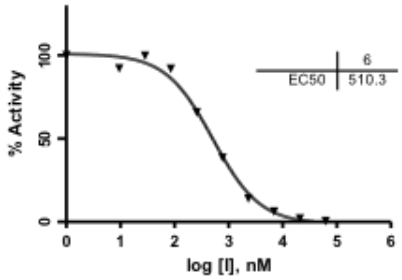

0 min IC_{50} Value = 390 ± 59 nM

120 min IC_{50}Value = 530 ± 30 nM

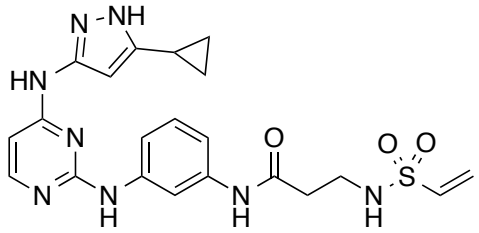

2.7

Compound **2.7** with wt c-Src:

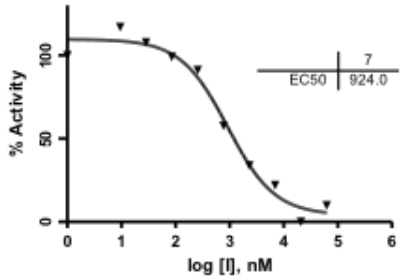

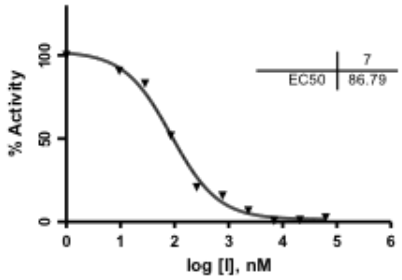

0 min IC_{50} Value = 760 ± 230 nM

120 min IC_{50}Value = 93 ± 20 nM

Compound **2.7** with wt c-Src, 1 mM Glutathione (left) and 1 mM DTT (right):

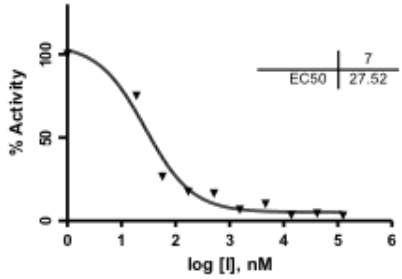

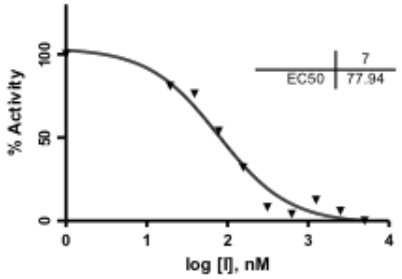

120 min IC_{50}Value < 30 nM

120 min IC_{50}Value = 95 ± 15 nM

Compound **2.7** with C277S c-Src:

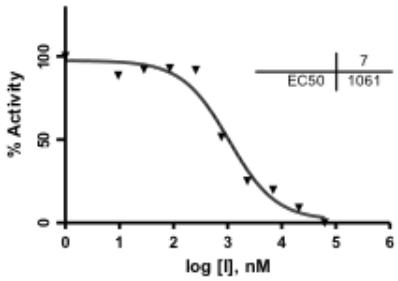

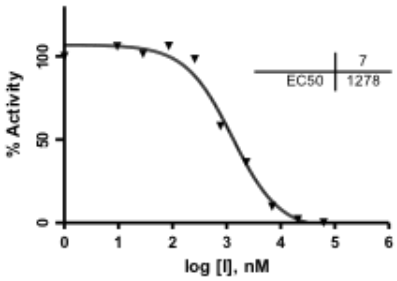

0 min IC_{50} Value = 1,200 ± 210 nM

120 min IC_{50}Value = 1,200 ± 59 nM

Compound **2.7** with wt c-Abl:

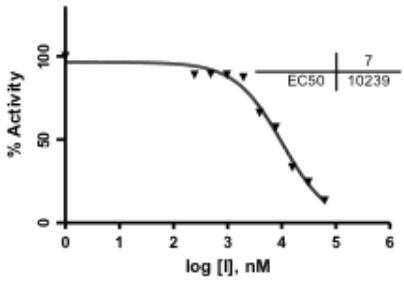

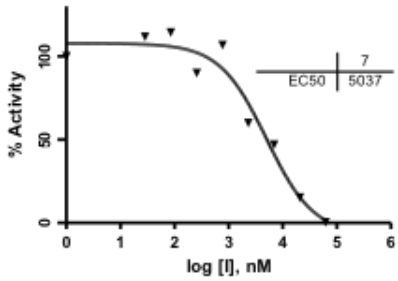

0 min IC_{50} Value = 9.200 ± 2,500 nM

120 min IC_{50}Value = 7,700 ± 1,100 nM

Compound **2.7** with Q252C c-Abl:

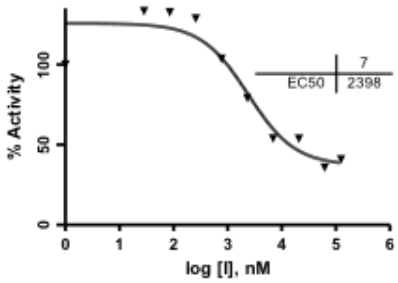

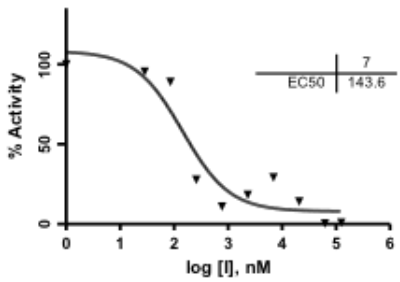

0 min IC_{50} Value = 2,800 ± 1,800 nM

120 min IC_{50}Value = 150 ± 11 nM

Compound **2.7** with wt Hck:

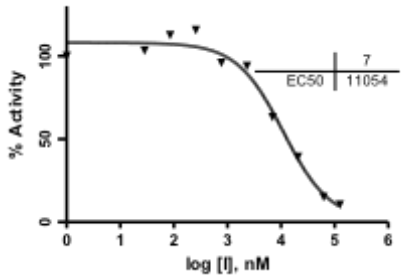

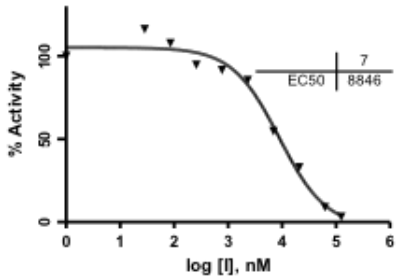

0 min IC_{50} Value = 11,400 ± 2,100 nM

120 min IC_{50}Value = 8,000 ± 900 nM

Compound **2.7** with T338M c-Src:

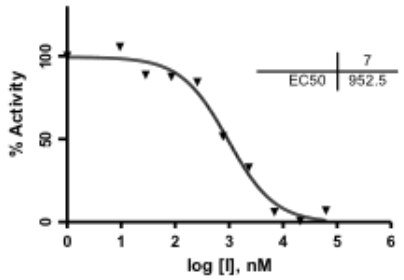

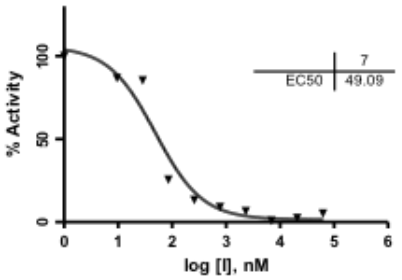

0 min IC_{50} Value = 1,200 ± 350 nM

120 min IC_{50}Value = 48 ± 1 nM

Compound **2.7** with P~c-Src:

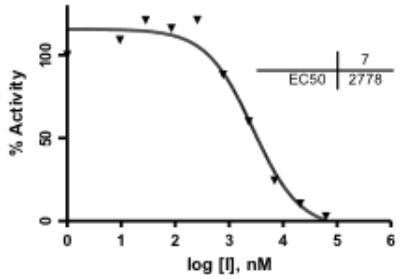

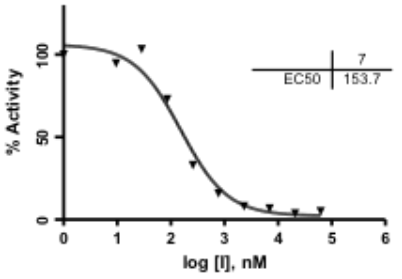

0 min IC_{50} Value = 1,200 ± 240 nM

120 min IC_{50}Value = 130 ± 37 nM

Compound **2.7** with wt c-Yes:

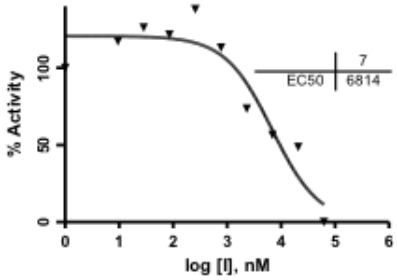

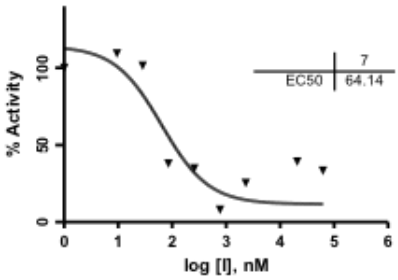

0 min IC_{50} Value = 4,600 ± 3,100 nM

120 min IC_{50}Value = 46 ± 26 nM

Compound **2.7** with P~Q252C c-Abl:

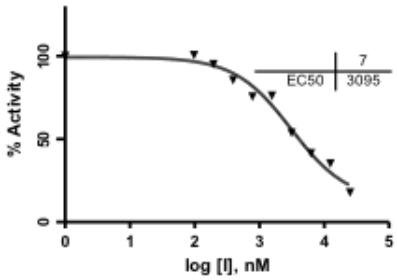

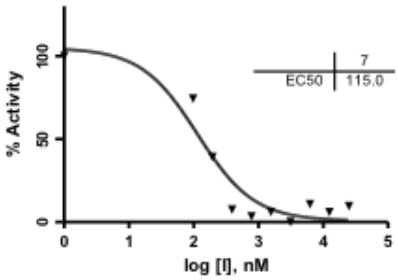

0 min IC_{50} Value = 3,800 ± 980 nM

120 min IC_{50}Value = 110 ± 10 nM

Dasatinib with wt c-Src:

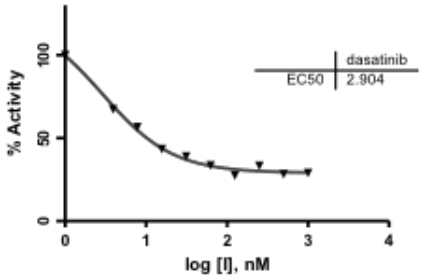

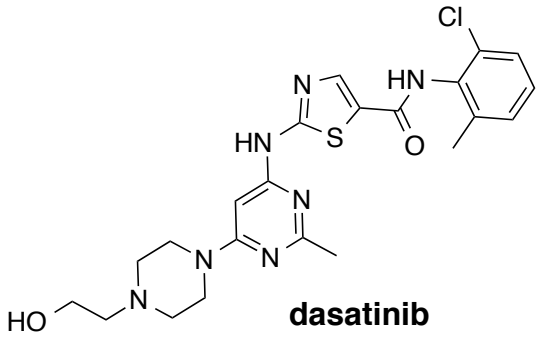

dasatinib

0 min IC_{50} Value < 5 nM

dasatinib with T338M c-Src:

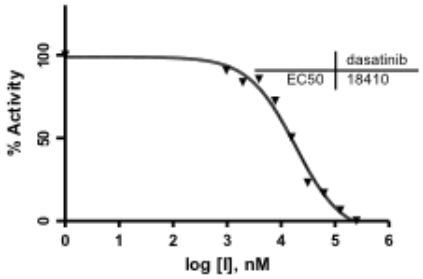

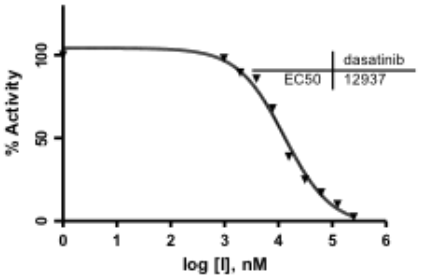

0 min IC_{50} Value = 19.5 ± 2.4 μM

120 min IC_{50}Value = 14.3 ± 2.0 μM

Compound **2.8** with wt c-Src:

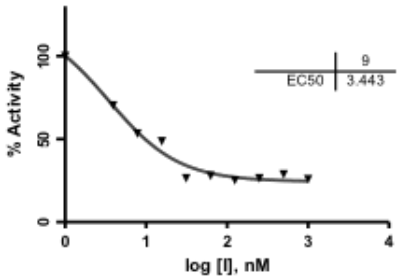

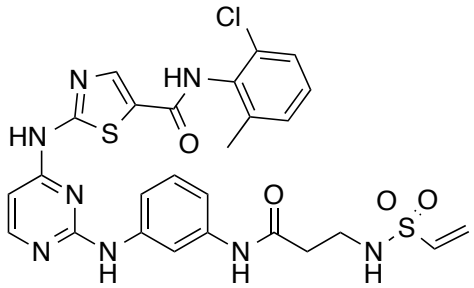

2.8

0 min IC_{50} Value < 5 nM

Compound **2.8** with T338M c-Src:

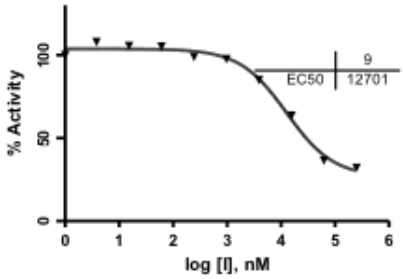

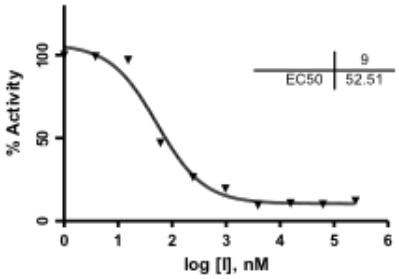

0 min IC_{50} Value = 11.2 ± 2.1 μM

120 min IC_{50}Value = 44 ± 12 nM

Compound **2.9** with wt c-Src:

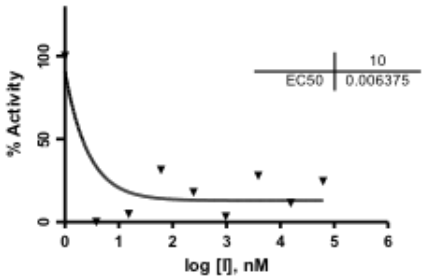

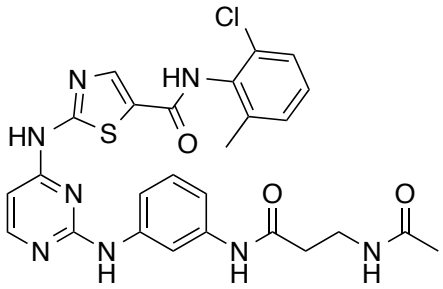

2.9

0 min IC_{50} Value < 5 nM

Compound **2.9** with T338M c-Src:

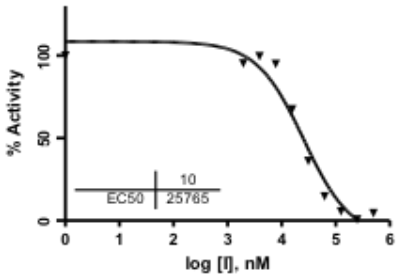

0 min IC_{50} Value = 25.8 ± 4.9 μM

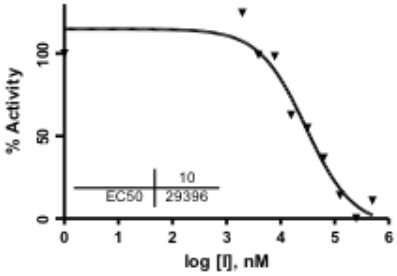

120 min IC_{50}Value = 29.6 ± 7.2 μM

Data for k_{inact} and K_i Determination

IC_{50} value time course of compound **2.6** with wt c-Src:

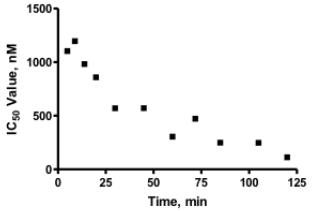

K_i = 600 ± 17 nM
k_{inact} = 1.0 ± 0.1 (x 10^{-3} s^{-1})
(k_{inact} / K_i) = 1,700 ± 61 (M^{-1} s^{-1})

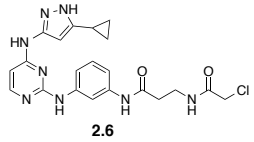

2.6

Time, min	5	9	14	20	30	45	60	72	85	105	120
IC_{50}, nM	1,100	1,193	979	856	567	568	302	469	245	244	109

IC_{50} value time course of compound **2.7** with wt c-Src:

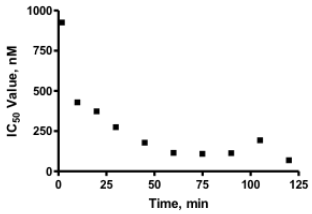

K_i = 360 ± 1 nM
k_{inact} = 1.5 ± 0.3 (x 10^{-3} s^{-1})
(k_{inact} / K_i) = 4,000 ± 870 (M^{-1} s^{-1})

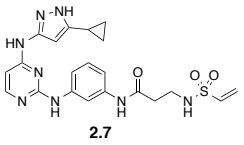

2.7

Time, min	2	10	20	30	45	60	75	90	105	120
IC_{50}, nM	924	427	371	273	176	113	107	111	191	67

IC_{50} value time course of compound **2.7** with P~c-Src:

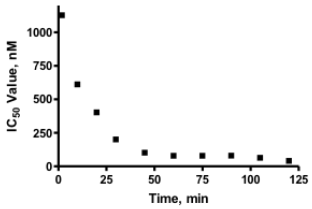

K_i = 510 ± 84 nM
k_{inact} = 4.1 ± 0. 7 (x 10^{-3} s^{-1})
(k_{inact} / K_i) = 8,100 ± 18 (M^{-1} s^{-1})

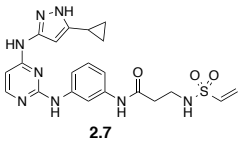

2.7

Time, min	2	10	20	30	45	60	75	90	105	120
IC_{50}, nM	1,125	609	400	198	100	77	77	78	61	38

IC_{50} value time course of compound **2.7** with wt c-Yes:

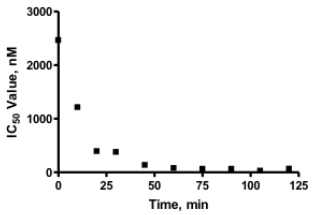

K_i = 190 ± 35 nM
k_{inact} = 2.8 ± 0.5 (x 10^{-3} s^{-1})
(k_{inact} / K_i) = 15,800 ± 5,400 (M^{-1} s^{-1})

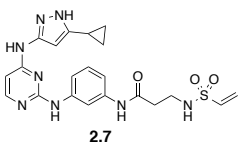

2.7

Time, min	2	10	20	30	45	60	75	90	105	120
IC_{50}, nM	2,464	1,212	391	376	134	75	61	62	26	64

IC_{50} value time course of compound **2.7** with Q252C c-Abl:

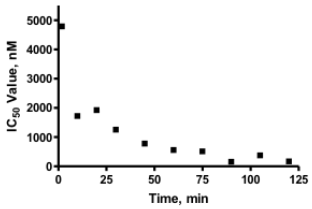

K_i = 1,600 ± 300 nM
k_{inact} = 3.2 ± 0.8 (x 10^{-3} s^{-1})
(k_{inact} / K_i) = 2,000 ± 190 (M^{-1} s^{-1})

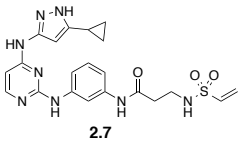

Time, min	2	10	20	30	45	60	75	90	105	120
IC_{50}, nM	4,778	1,714	1913	1243	766	547	504	145	366	156

IC_{50} value time course of compound **2.7** with P~Q252C c-Abl:

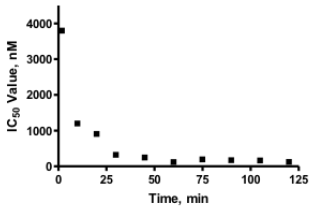

K_i = 910 ± 120 nM
k_{inact} = 6.4 ± 1.1 (x 10^{-3} s^{-1})
(k_{inact} / K_i) = 7,000 ± 280 (M^{-1} s^{-1})

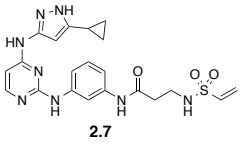

Time, min	2	10	20	30	45	60	75	90	105	120
IC_{50}, nM	3,790	1,192	899	314	238	111	186	163	154	115

IC_{50} value time course of compound **2.7** with T338M c-Src:

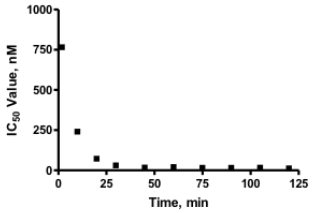

K_i = 53 ± 6 nM
k_{inact} = 5.2 ± 0.1 (x 10^{-3} s^{-1})
(k_{inact} / K_i) = 98,700 ± 10,000 (M^{-1} s^{-1})

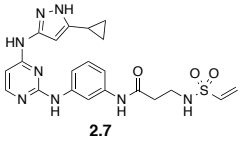

Time, min	2	10	20	30	45	60	75	90	105	120
IC_{50}, nM	764	239	70	29	15	19	14	14	14	11

IC_{50} value time course of compound **2.8** with T338M c-Src:

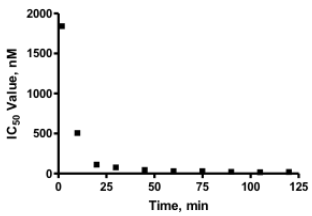

K_i = 98 ± 6 nM
k_{inact} = 38.6 ± 5.2 (x 10^{-4} s^{-1})
(k_{inact} / K_i) = 39,800 ± 7,900 (M^{-1} s^{-1})

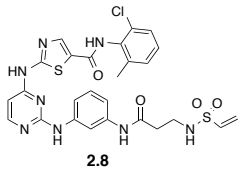

Time, min	2	10	20	30	45	60	75	90	105	120
IC_{50}, nM	1,837	503	108	73	41	26	26	17	13	15

Data for ATP K_m Determination

ATP K_m curve with wt c-Src:

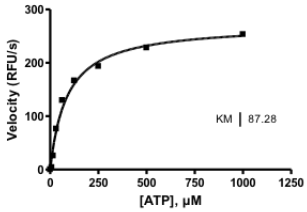

K_m = 98 ± 16 µM
V_{max}= 282 ± 8 (RFU/s)

ATP K_m curve with P~c-Src:

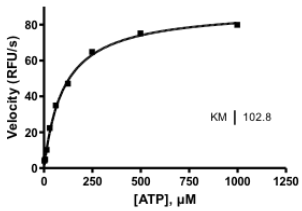

K_m = 95 ± 12 µM
V_{max}= 84 ± 8 (RFU/s)

ATP K_m curve with Q252C c-Abl:

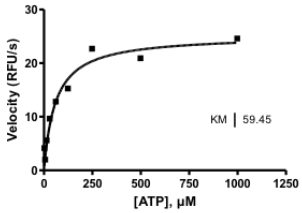

K_m = 63 ± 6 µM
V_{max}= 24 ± 2 (RFU/s)

ATP K_m curve with P~Q252C c-Abl:

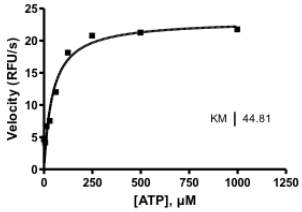

K_m = 36 ± 11 µM
V_{max}= 21 ± 2 (RFU/s)

ATP K_m curve with T338M c-Src:

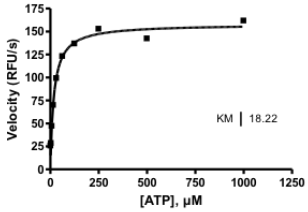

K_m = 20 ± 2 µM
V_{max}= 143 ± 20 (RFU/s)

ESI-MS Characterization

wt c-Src enzyme passed through gel filtration column, then submitted for analysis:

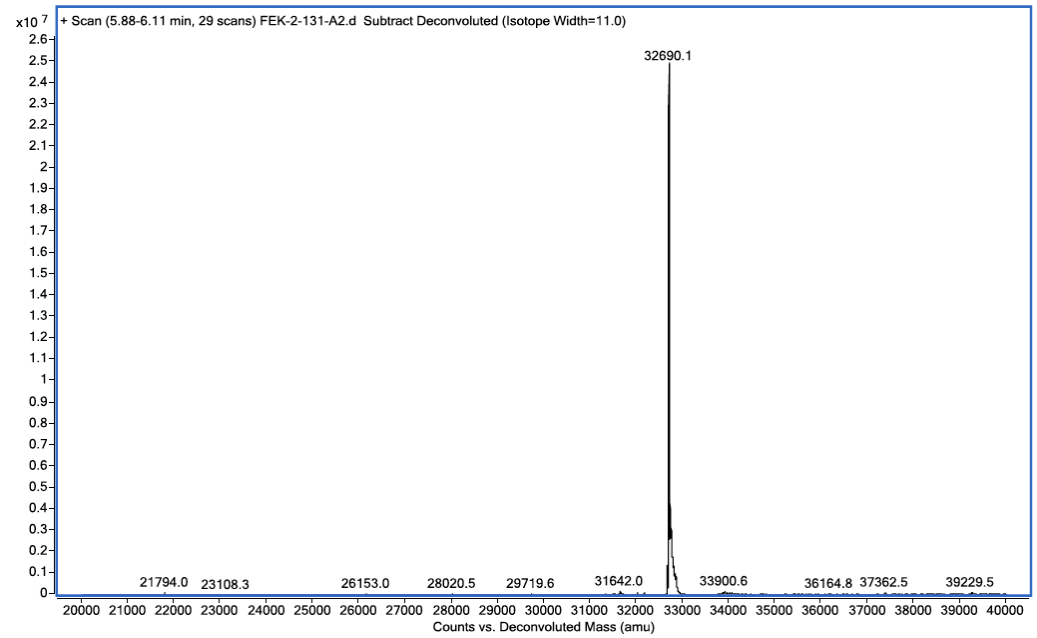

Compound **2.6** incubated with wt c-Src enzyme, passed through gel filtration column, then submitted for analysis:

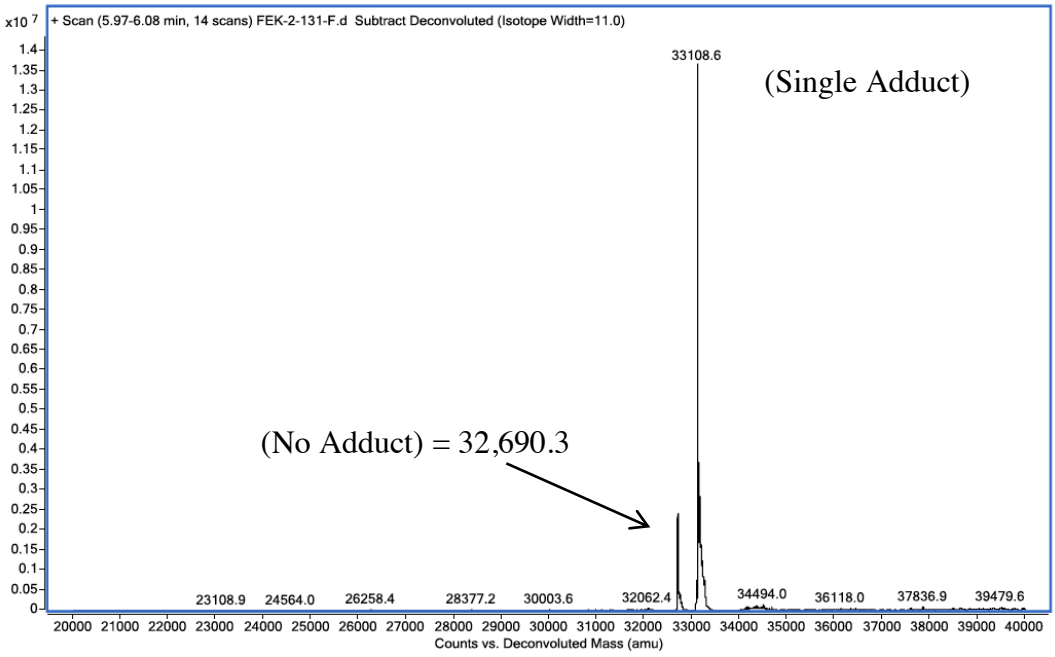

Compound **2.7** incubated with wt c-Src enzyme, passed through gel filtration column, then submitted for analysis:

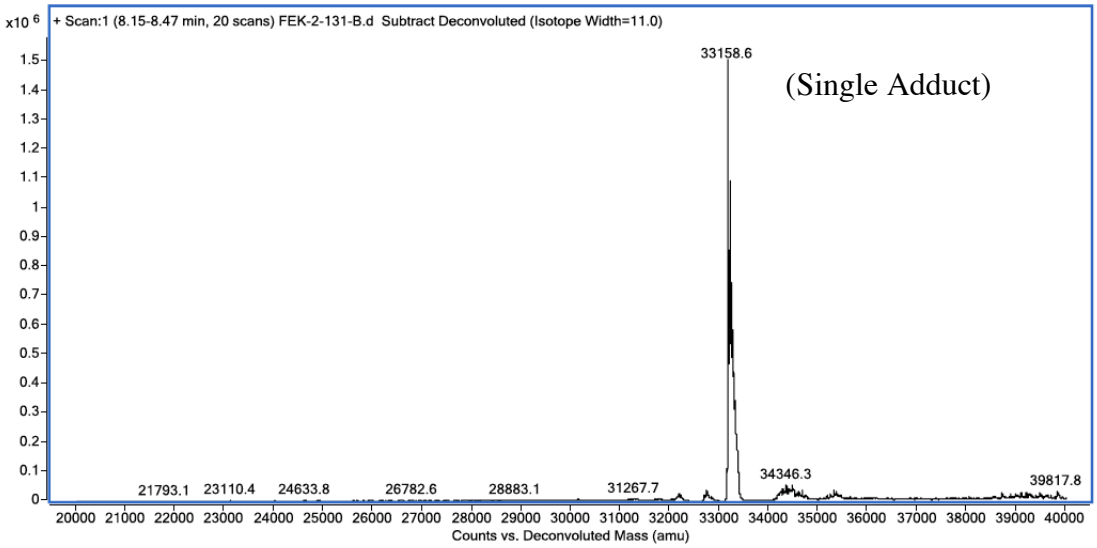

Compound **2.7** incubated with C277S c-Src enzyme, passed through gel filtration column, then submitted for analysis:

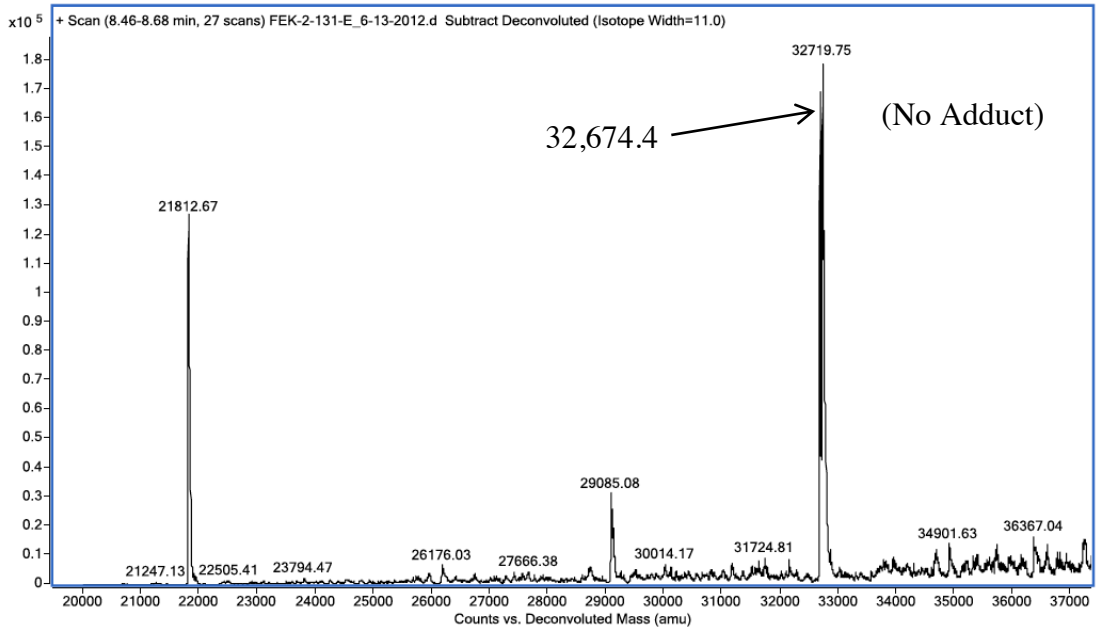

A.12 Cellular Characterization

NIH-3T3, stably tranfected with v-Src cell growth inhibition with compound **2.1** (left) and compound **2.7** (right):

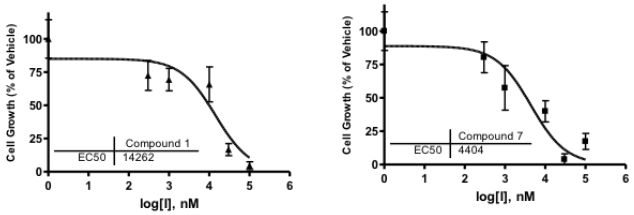

SK-BR-3 (left) and HT-29 (right) cell growth inhibition with dasatinib:

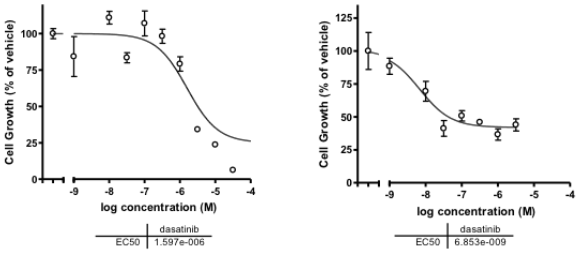

SK-BR-3 (left) and HT-29 (right) cell growth inhibition with compound **2.8**:

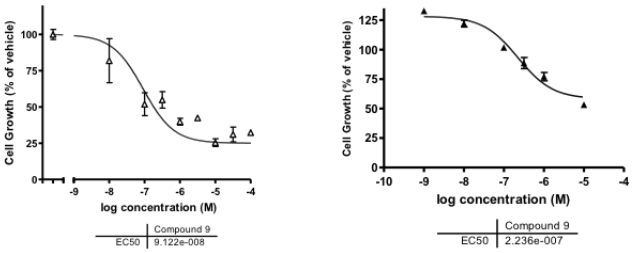

HMEC growth inhibition with dasatinib and compounds **2.8** (compound 9) and **2.9** (compound 10)**.**

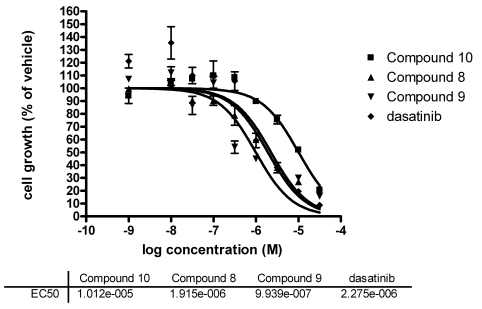

A.13 KINOMEscan Profiling Data

Compound **2.1** was screened at 2 μM.

KINOMEscan Gene Symbol	POC	KINOMEscan Gene Symbol	POC	KINOMEscan Gene Symbol	POC
ABL1(T315I)-nonphosphorylated	2.6	FGR	27	NEK9	26
ABL1(T315I)-phosphorylated	0.45	FLT1	17	NIM1	100
ABL1-nonphosphorylated	8.6	FLT3	4.5	p38-alpha	82
ABL1-phosphorylated	4.4	FLT3(D835H)	3.8	p38-beta	90
ABL2	40	FLT3(D835Y)	0.8	PAK7	34
ACVR1	9.5	FLT3(ITD)	7.2	PCTK1	1.5
AKT1	100	FLT3(K663Q)	4	PCTK2	4
ALK	21	FLT3(N841I)	0	PCTK3	14
ASK1	100	FLT4	44	PDGFRB	20
ASK2	81	FYN	16	PDPK1	82
AURKA	0.45	GCN2(Kin.Dom.2,S808G)	22	PFCDPK1(P.falciparum)	17
AURKB	11	GRK4	7.2	PFPK5(P.falciparum)	80
AURKC	2.4	GRK7	8.8	PFTAIRE2	39
AXL	23	GSK3A	24	PFTK1	32
BIKE	49	GSK3B	74	PIK4CB	44
BLK	16	HCK	49	PIM2	100
BMPR1B	2.2	HIPK1	15	PKNB(M.tuberculosis)	0
BMPR2	12	HIPK2	18	PLK2	81
BRAF	75	HIPK3	16	PRKD2	100
BRAF(V600E)	62	HIPK4	29	PRKD3	68
BTK	22	ICK	2	PRKR	25
CDK2	12	IGF1R	54	RAF1	100
CDK3	23	IKK-alpha	40	RET	17
CDK5	20	IKK-beta	19	RET(M918T)	19
CDK7	3.8	IKK-epsilon	25	RET(V804L)	19
CDK9	55	INSR	9.8	RET(V804M)	13
CDKL3	1.6	INSRR	37	RIOK1	11
CDKL5	0.2	IRAK1	7.1	RIOK3	0
CHEK1	100	ITK	84	RIPK1	48
CLK2	13	JAK1(JH2domain-pseudokinase)	1.2	ROCK1	86
DAPK1	34	JAK2(JH1domain-catalytic)	4.4	ROCK2	77

DCAMKL2	47	JAK3(JH1domain-catalytic)	0	RPS6KA4(Kin.Dom.2-C-terminal)	57
DCAMKL3	49	JNK2	0.95	SBK1	33
DDR1	28	KIT	32	SGK	6
DDR2	46	KIT(D816V)	31	SLK	29
DRAK1	67	KIT(L576P)	22	SRC	3.3
DRAK2	26	KIT(V559D)	22	SRMS	70
DYRK1A	73	LCK	17	SRPK1	2.1
DYRK1B	78	LIMK1	51	SRPK3	4.6
DYRK2	33	LIMK2	60	STK16	5
EGFR	65	LKB1	35	SYK	29
EGFR(L858R)	62	LOK	55	TAK1	21
EGFR(L858R,T790M)	60	**LYN**	50	TAOK1	1.9
EGFR(T790M)	29	LZK	41	TAOK3	18
EPHA3	18	MAK	25	TGFBR1	41
EPHA5	67	MAP3K3	7.6	TGFBR2	53
EPHA6	52	MAP4K2	41	TIE2	43
EPHA7	46	MAPKAPK5	95	TLK1	3.4
EPHB1	70	MARK3	64	TLK2	2.8
EPHB6	5.4	MAST1	40	TNIK	30
ERBB2	76	MEK1	48	TNK1	33
ERBB4	74	MEK2	54	TRKA	1.2
ERK1	90	MEK3	7	TRKB	3.2
ERK2	61	MEK4	18	TRKC	0.75
ERK3	45	MEK6	4.4	TTK	18
ERK4	50	MERTK	34	TYK2(JH1domain-catalytic)	6.2
ERK5	43	MET	26	ULK1	50
ERK8	1.5	MET(M1250T)	50	ULK2	65
ERN1	71	MINK	53	ULK3	7
FAK	55	MLCK	7.4	VEGFR2	26
FER	70	MLK1	77	WEE1	86
FES	94	MST3	20	WEE2	100
FGFR1	0.75	MST4	55	YES	38
FGFR2	6.2	MYLK2	11	YSK1	6.9
FGFR3	1.3	NEK1	41	YSK4	12
FGFR3(G697C)	4.6	NEK6	19	ZAP70	77
FGFR4	59	NEK7	0.45		

A.14 Luceome Profiling Data

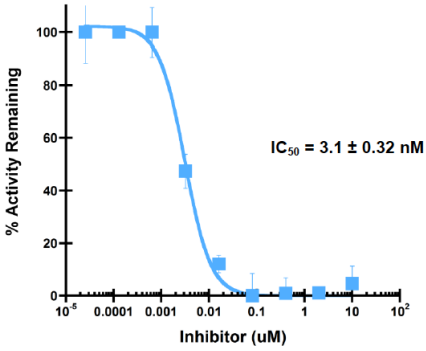

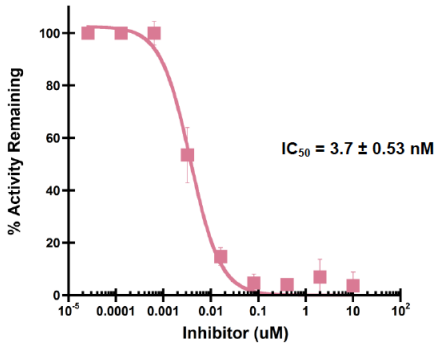

120-min incubation of dasatinib (left) and compound **2.8** (right) with wt c-Src enzyme.

Tabulated Data for dasatinib and compound **2.8** (screened at 15 nM each):

Kinase	dasatinib POC	**2.8** POC	Kinase	dasatinib POC	**2.8** POC
ABL1	18.7	28.5	MST2	98.2	88.9
ABL2	19.7	25.3	MUSK	100	100
AKT1	94.8	97.8	MYLK	100	100
AKT1(FL)	100	100	MYLK2	75.6	84.1
AKT2	100	100	MYT1	100	95.7
AKT2 (S474A)	100	100	p38-¥	100	100
AKT2 (S474D)	91.1	92.2	PAK1	100	100
AKT2(T309A,S474A)	100	100	PAK1(T423A)	100	100
AKT2(T309D,S474D)	95.1	98.3	PAK1(T423E)	100	96.2
AKT3	100	100	PDGFRA	92.6	100
AMPK-¥1	100	100	PDGFRB	100	100
AMPK-¥2	100	93.4	PDK1	97.2	96.5
AURKA	95.9	100	PHKG1	100	92.8
AURKB	100	94.1	PIM1	100	100
AURKC	100	100	PIM2	100	100
AXL	96.9	100	PKAC-¥	100	95.2
BIKE	100	100	PKAC-¥	100	100
BLK	11.9	9	PKC-¥	100	86.4
BTK	92	77.1	PKC-¥	89.8	89.6
CAMK1	100	100	PKC-¥	100	100
CAMK1D	96.6	98.7	PKC-¥	100	100
CAMK1G	98.9	100	PKC-¥	84.3	87.7
CAMK2A	95.7	94.2	PKG1	100	100
CAMK2B	89.4	100	PKN3	96.6	97.4
CAMK2D	100	100	PKX	100	100
CAMKK1	86.2	99.8	PLK4	100	100

CAMKK2	100	100	PRKD2	100	100
CHEK1	100	100	PRKD3	100	100
CK1D	92.3	90.4	PTK2	80	87.4
CLK1	100	96.7	PTK2B	90	93.8
CLK2	100	100	PTK6	96.9	94.6
CSK	100	100	RET	91.8	95
DAPK1	100	100	RIPK2	82.3	100
DAPK2	100	100	RPS6KA1/RSK1	96.4	97.9
DAPK3	86.9	81.3	RPS6KA2/RSK3	100	100
DDR1	7.3	28.6	RPS6KA3/RSK2	100	100
DDR2	10.7	37.1	RPS6KA4/MSK2	99.7	100
DMPK	78.8	100	RPS6KA5/MSK1	80.7	81.8
EPHA1	34.9	73.9	RPS6KA6/RSK4	97.7	93
EPHA2	26.6	69.7	SGK2	100	100
EPHA3	14.1	92.3	SGK3	100	100
EPHA4	16.3	53.9	SIK3	100	97.4
EPHB2	12.1	44.2	SLK	100	100
EPHB3	100	99.8	SNARK	80.7	85
EPHB4	0	11.4	SNF1LK	74.7	89.9
FGFR1(aka FLT2)	100	100	SNF1LK2	99.9	100
FLT1	100	100	SRC	11.2	13.2
FLT3	100	100	STK16	93.5	100
FYN	10.3	17.9	STK33	85.7	93.4
GSK3¥	100	67.1	SYK	87.7	90.5
HCK	53.2	74.5	TBK1	100	69.7
IGF1R	100	100	TEC	100	48.6
IKK-¥	100	100	TESK1	100	100
INSR	100	100	TESK2	52.4	54.2
ITK	100	100	TIE1	100	100
LIMK1	100	100	TIE2	90.9	100
LYN	13.2	29.6	TNK2	100	100
MARK1	92.9	85.1	TNNI3K	100	100
MARK2	100	100	TRKB	96.4	100
MARK3	97.4	98.4	TRKC	100	100
MARK4	97.3	100	TXK	95.3	54.1
MELK	100	100	VEGFR2	100	100
MET	100	100	YANK2	96.7	100
MLK1	100	100	YES1	7	10.7
MLK3	100	100	YSK1	100	100

APPENDIX B

Supplemental Information and Analytical Data for Chapter III

Table B.1. Compound labels and structures for acrylamide library.

The 110-member acrylamide library was obtained from Infarmitik and has an average molecular weight of 235 Da.

Cmpd	Structure	Cmpd	Structure	Cmpd	Structure	Cmpd	Structure	Cmpd	Structure	Cmpd	Structure
EL-1002	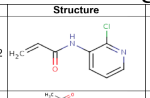	EL-1027	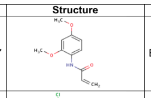	EL-1051	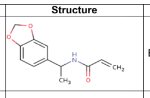	EL-1086	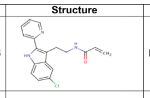	EL-1140	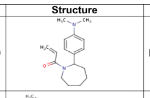	EL-1167	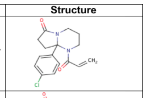
EL-1003	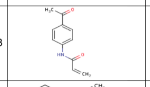	EL-1028	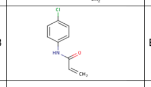	EL-1052	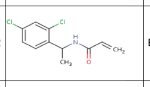	EL-1092	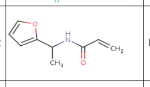	EL-1141	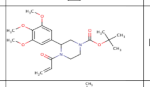	EL-1168	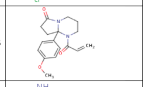
EL-1004	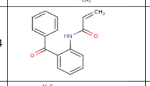	EL-1029	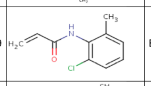	EL-1053	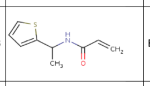	EL-1098	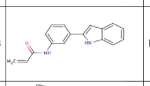	EL-1142	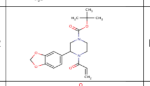	EL-1169	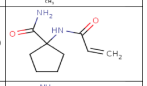
EL-1005	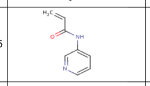	EL-1030	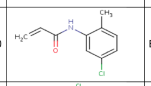	EL-1054	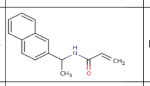	EL-1104	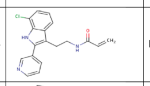	EL-1143	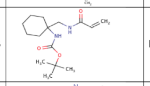	EL-1170	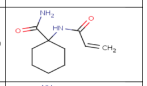
EL-1006	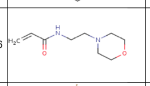	EL-1031	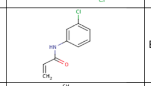	EL-1055	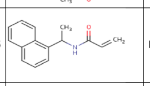	EL-1105	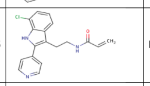	EL-1144	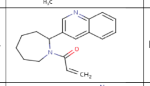	EL-1171	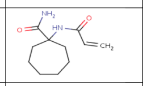
EL-1007	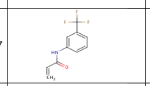	EL-1032	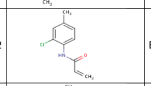	EL-1056	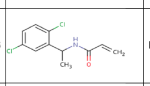	EL-1106	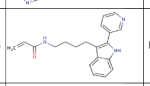	EL-1145	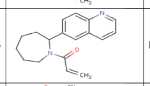	EL-1174	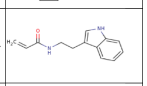
EL-1009	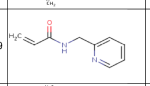	EL-1033	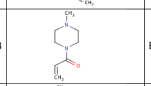	EL-1057	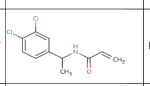	EL-1108	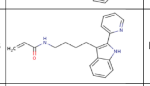	EL-1146		EL-1175	
EL-1010		EL-1034		EL-1058		EL-1109		EL-1147		EL-1176	
EL-1011		EL-1035		EL-1059		EL-1113		EL-1148		EL-1177	
EL-1012		EL-1036		EL-1061		EL-1114		EL-1151		EL-1178	
EL-1015		EL-1037		EL-1062		EL-1115		EL-1152			
EL-1016		EL-1038		EL-1063		EL-1119		EL-1153			
EL-1018		EL-1039		EL-1064		EL-1123		EL-1155			
EL-1019		EL-1040		EL-1065		EL-1124		EL-1156			
EL-1020		EL-1041		EL-1068		EL-1125		EL-1157			
EL-1021		EL-1044		EL-1069		EL-1126		EL-1160			
EL-1022		EL-1046		EL-1071		EL-1132		EL-1161			
EL-1023		EL-1047		EL-1074		EL-1134		EL-1162			
EL-1024		EL-1048		EL-1083		EL-1135		EL-1163			
EL-1025		EL-1050		EL-1084		EL-1137		EL-1164			

Table B.2. Primary screen data.

Single point percent inhibition values after 30 min of incubation for each acrylamide at 20 μM (column 2) and at 20 μM with 1.5 μM compound **3.1** (column 3) added are listed as well as the percent inhibition difference (% ID) values. Fragment/thiol combinations that did not produce any inhibition were not pursued (bottom of table–below black line). The four hits from the screen were considered as having a % ID value >2 standard deviations away from the mean % ID of 14.7%.

Percent Inhibition

Cmpd	Acrylamide	Acr + Thiol	% ID
EL-1061	-42.08	7.73	49.81
EL-1145	-31.15	17.20	48.35
EL-1148	-17.87	27.37	45.24
EL-1092	16.45	59.44	42.99
EL-1037	-16.55	22.70	39.25
EL-1065	-13.73	24.05	37.78
EL-1027	-20.22	16.58	36.80
EL-1047	-10.94	25.82	36.76
EL-1167	-12.02	24.34	36.36
EL-1019	-29.95	5.92	35.87
EL-1048	-12.62	21.04	33.66
EL-1134	-3.81	27.34	31.15
EL-1024	-17.49	13.12	30.60
EL-1054	-13.36	17.07	30.43
EL-1057	-20.99	9.00	29.99
EL-1083	-6.02	23.75	29.77
EL-1119	13.63	42.97	29.34
EL-1064	-4.64	20.61	25.25
EL-1170	1.81	25.21	23.40
EL-1086	18.69	41.82	23.13
EL-1041	-4.55	18.37	22.92
EL-1124	14.98	37.35	22.37
EL-1030	-6.25	15.05	21.30
EL-1021	-13.50	6.14	19.64
EL-1053	-0.26	18.93	19.18
EL-1098	5.44	24.50	19.06
EL-1036	-10.49	5.65	16.14
EL-1052	-1.41	14.20	15.61
EL-1144	-13.79	1.18	14.97
EL-1126	10.41	25.29	14.89
EL-1156	7.09	20.51	13.42
EL-1059	10.12	23.01	12.90
EL-1069	0.65	13.25	12.60
EL-1174	-4.52	7.88	12.40
EL-1046	-9.47	1.73	11.21
EL-1062	-7.24	3.85	11.09
EL-1137	4.78	15.81	11.03
EL-1020	-7.82	2.45	10.27
EL-1152	16.76	26.99	10.23
EL-1141	8.86	17.66	8.80
EL-1105	7.01	14.66	7.65
EL-1055	-3.05	3.49	6.54
EL-1039	-3.67	1.83	5.50
EL-1010	12.22	17.61	5.39

EL-1171	8.80	13.95	5.15
EL-1104	22.08	26.51	4.43
EL-1056	3.58	7.68	4.09
EL-1025	6.57	10.59	4.03
EL-1147	-1.41	2.44	3.85
EL-1161	7.13	10.81	3.68
EL-1004	19.00	22.62	3.62
EL-1068	14.83	18.31	3.48
EL-1175	11.85	13.56	1.71
EL-1143	5.28	5.21	-0.07
EL-1169	3.53	3.44	-0.09
EL-1114	3.46	2.98	-0.48
EL-1164	6.14	2.48	-3.66
EL-1084	12.55	8.83	-3.72
EL-1006	15.17	11.03	-4.14
EL-1142	17.97	13.09	-4.88
EL-1113	15.98	10.13	-5.85
EL-1177	8.37	1.46	-6.90
EL-1063	8.18	1.05	-7.12
EL-1157	30.09	22.71	-7.38
EL-1109	21.31	13.66	-7.65
EL-1005	11.16	3.05	-8.11
EL-1163	25.86	10.74	-15.12
EL-1009	39.19	23.61	-15.58
EL-1176	23.49	3.38	-20.10
EL-1178	31.04	9.34	-21.70
EL-1153	29.11	6.51	-22.60
EL-1003	33.27	8.90	-24.37
EL-1022	-25.56	-24.73	0.83
EL-1012	-78.53	-24.48	54.05
EL-1115	19.28	-24.20	-43.48
EL-1018	-28.89	-16.66	12.23
EL-1029	-42.31	-15.97	26.34
EL-1007	32.85	-14.69	-47.54
EL-1015	-49.50	-14.01	35.49
EL-1032	-10.31	-13.95	-3.64
EL-1074	-6.79	-12.92	-6.12
EL-1140	20.60	-11.86	-32.46
EL-1040	-34.15	-11.59	22.56
EL-1155	21.16	-11.49	-32.65
EL-1132	-2.15	-11.29	-9.14
EL-1002	14.69	-11.05	-25.74
EL-1160	28.33	-9.95	-38.27
EL-1016	-34.67	-9.14	25.52
EL-1108	-23.39	-9.01	14.38
EL-1106	19.64	-8.38	-28.02
EL-1050	-22.75	-7.84	14.91
EL-1058	-13.01	-7.36	5.65
EL-1028	-0.80	-7.04	-6.24
EL-1011	-34.36	-5.72	28.64
EL-1123	21.62	-4.37	-25.99
EL-1023	-60.06	-4.35	55.71
EL-1162	27.59	-3.71	-31.30
EL-1034	3.53	-3.65	-7.18
EL-1033	-12.24	-3.23	9.01
EL-1135	-1.55	-3.15	-1.59

EL-1035	-0.17	-3.03	-2.86
EL-1044	5.34	-2.90	-8.24
EL-1125	5.94	-2.61	-8.55
EL-1031	-20.70	-2.31	18.40
EL-1168	11.59	-1.79	-13.38
EL-1151	-2.74	-1.74	1.00
EL-1146	3.74	-1.38	-5.12
EL-1038	-9.56	-1.18	8.38
EL-1071	8.87	-0.85	-9.72
EL-1051	-29.29	-0.51	28.77

Table B.3. Secondary confirmation screen.

Top seven hits follow-up screen. Triplicate percent inhibition values after 30 min of incubation for each acrylamide at 20 μM (column 2) and at 20 μM with 1.5 μM compound **3.1** (column 3) added are listed as well as the percent difference values. All of the compounds reproduced similar % ID values to the primary screen.

	% Inhibition						% ID
EL-1027	-47.11	8.80	-19.21	8.87	22.99	-11.72	25.89
EL-1037	-36.03	-4.19	-19.94	-0.67	8.68	11.57	18.60
EL-1061	-32.25	-8.17	-25.68	17.08	3.46	8.39	31.68
EL-1065	-14.30	-4.73	-26.42	7.06	25.25	-4.61	24.38
EL-1092	-20.06	18.24	-16.64	-10.24	24.51	10.73	26.68
EL-1145	-22.86	-23.44	-28.94	6.08	12.48	-9.04	28.25
EL-1148	-63.51	-17.83	-10.70	9.69	25.86	-1.05	25.77
DMSO	5.24	0.64	-5.88	15.63	1.79	-17.41	0.00
Staurosporine	67.62	82.02	81.57	65.89	85.58	100.00	6.75
	Acrylamide Only			Acrylamide + Thiol			

Figure B.1. Non-ATP-competitive nature of **EL-1148**.

Biochemical determination of non-ATP-competitive nature of acrylamide fragment, **EL-1148**, with 3M c-Src (mutant described below). Each inhibitor IC_{50} value was determined using at least three independent experiments; a representative inhibition curve is shown.

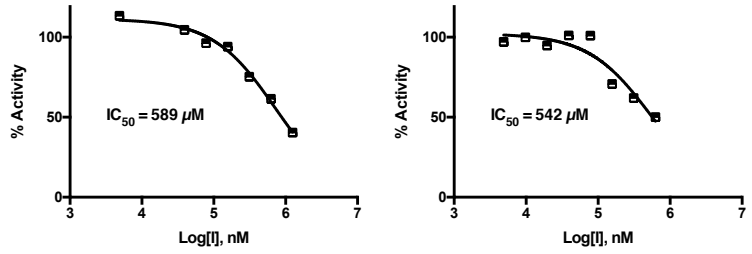

3M c-Src Avg IC_{50} = 465 ± 107 μM (left) at 100 μM ATP
3M c-Src Avg IC_{50} = 490 ± 82 μM (right) at 1000 μM ATP

Figure B.2. Predicted inhibitor binding mode.

A surface depiction of the c-Src P-loop pocket (top, left) is shown alongside an electrostatic interaction map (top, right). An adapted crystal structure of c-Src kinase with the ATP pocket-binding portion of each bivalent inhibitor is also shown (bottom). The amide functionality of compound **3.1** directs the in situ tethering event toward the P-loop pocket of the kinase.

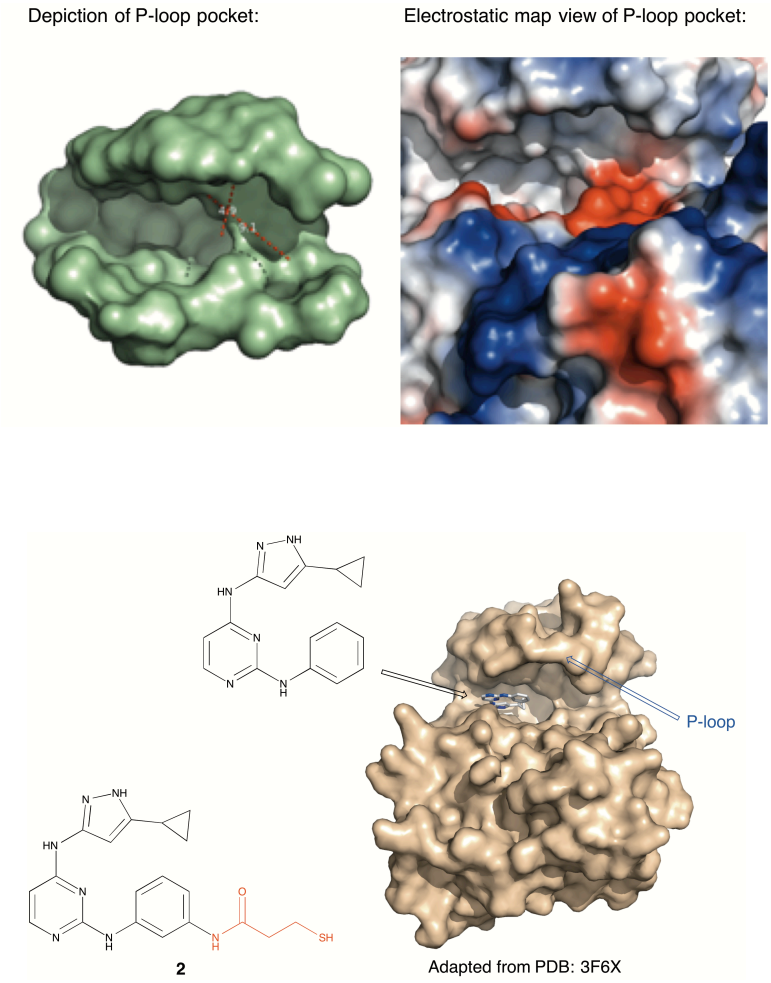

Spectral Data for Compounds 3.1–3.26

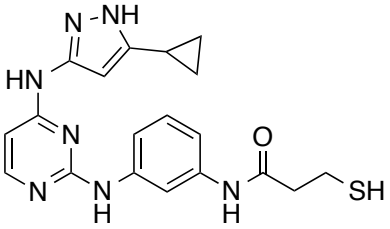

3.1

3.1 ^{1}H:

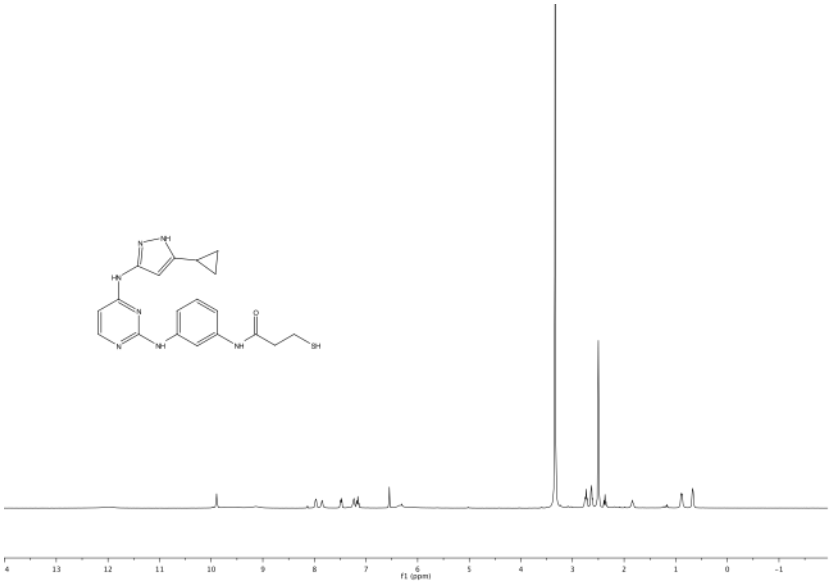

3.1 ^{13}C:

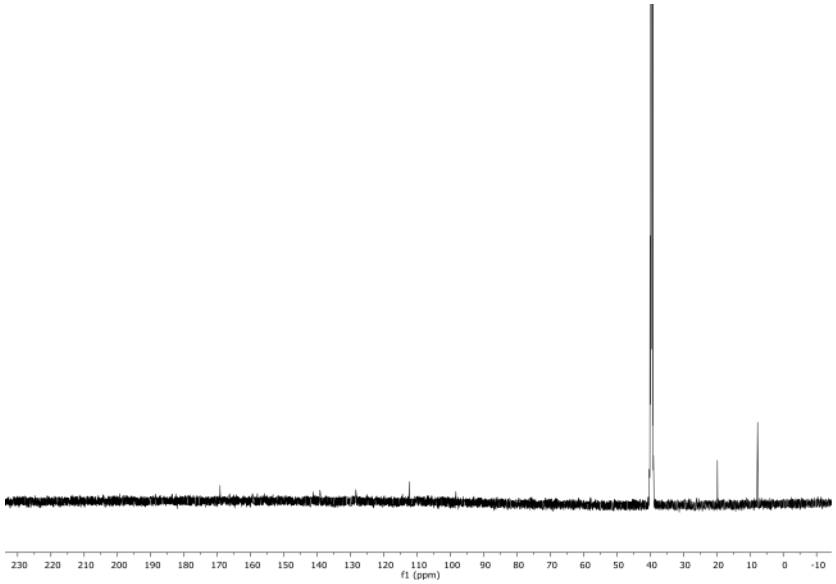

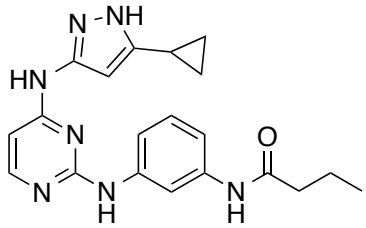

3.2

3.2 ^{1}H:

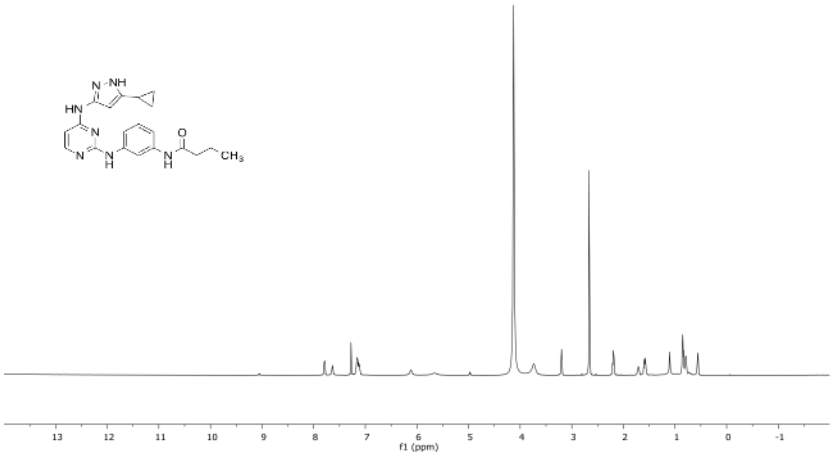

3.2 ^{13}C:

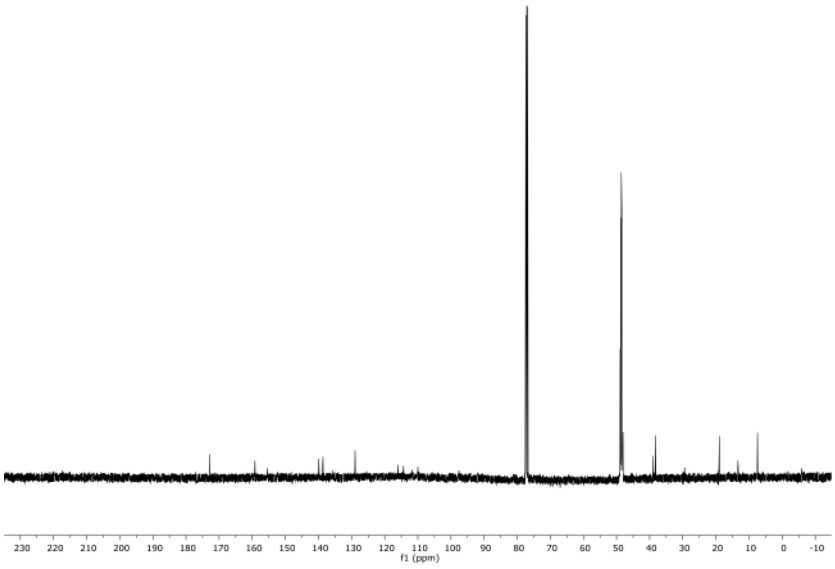

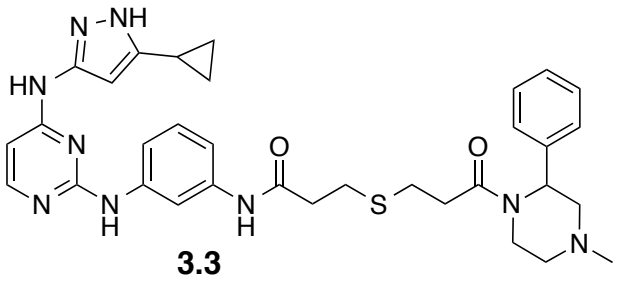

3.3

3.3 ^{1}H:

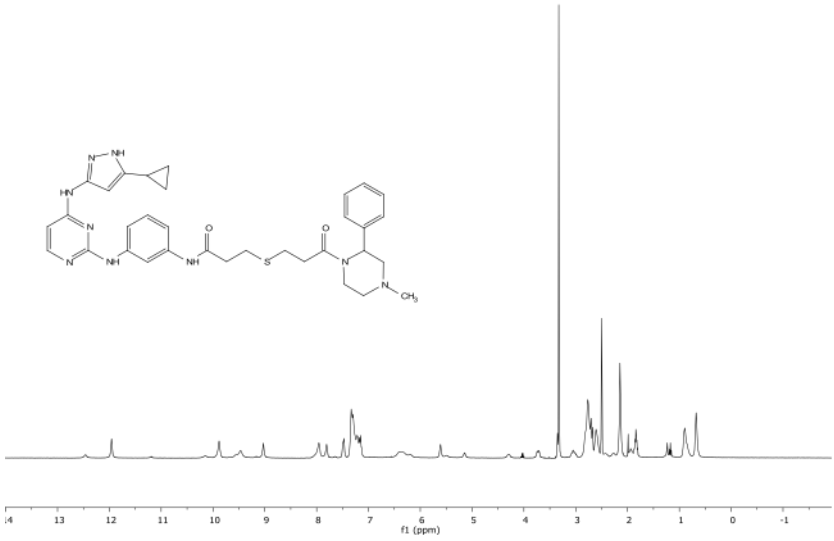

3.3 ^{13}C:

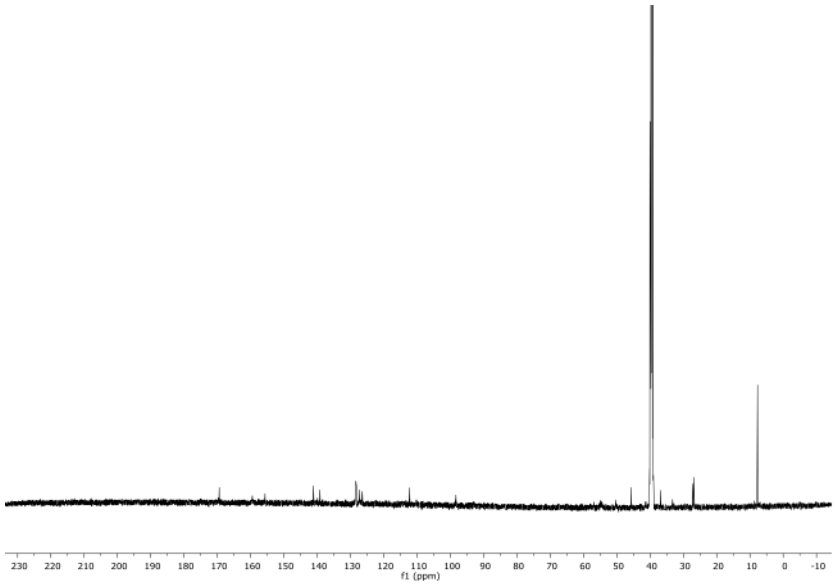

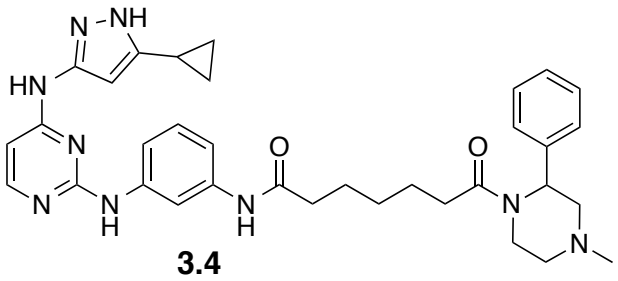

3.4

3.4 ^{1}H:

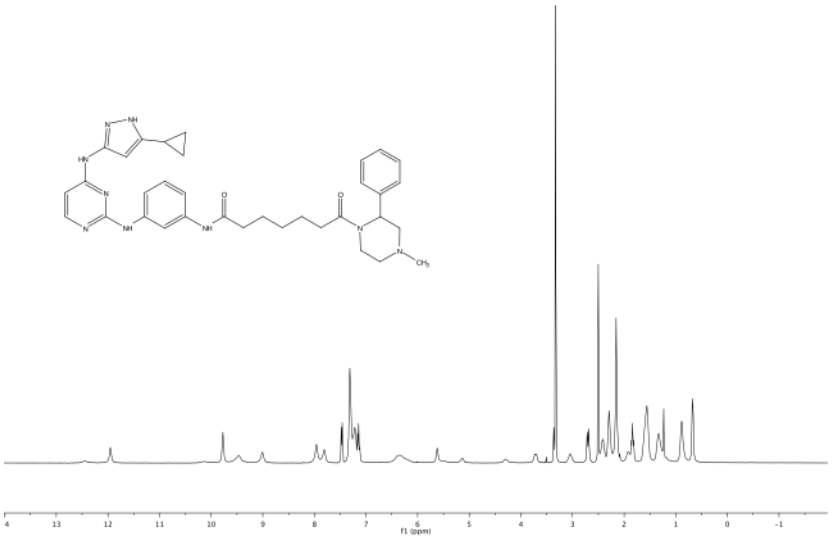

3.4 ^{13}C:

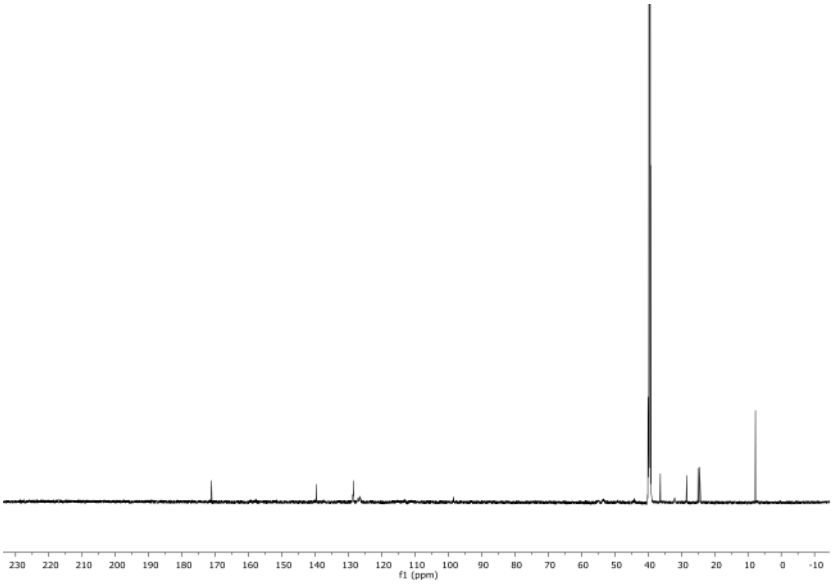

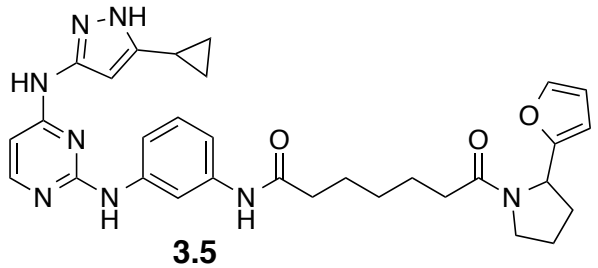

3.5

3.5 ^{1}H:

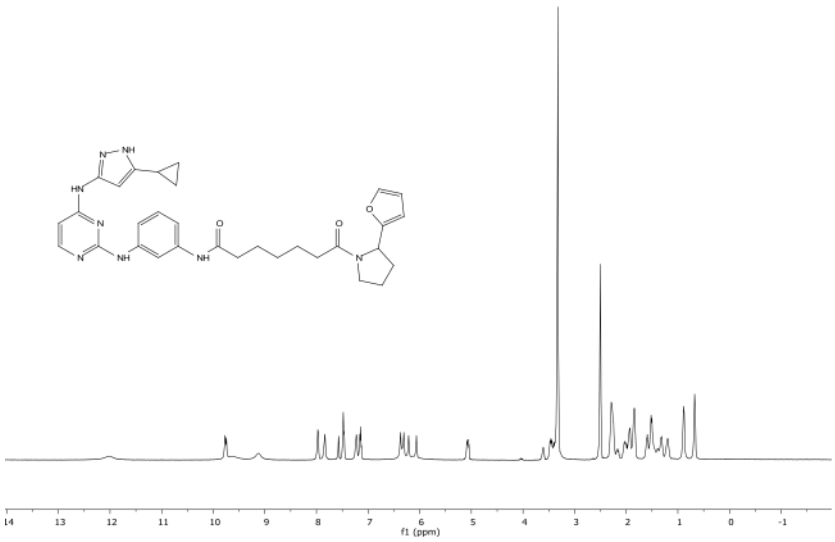

3.5 ^{13}C:

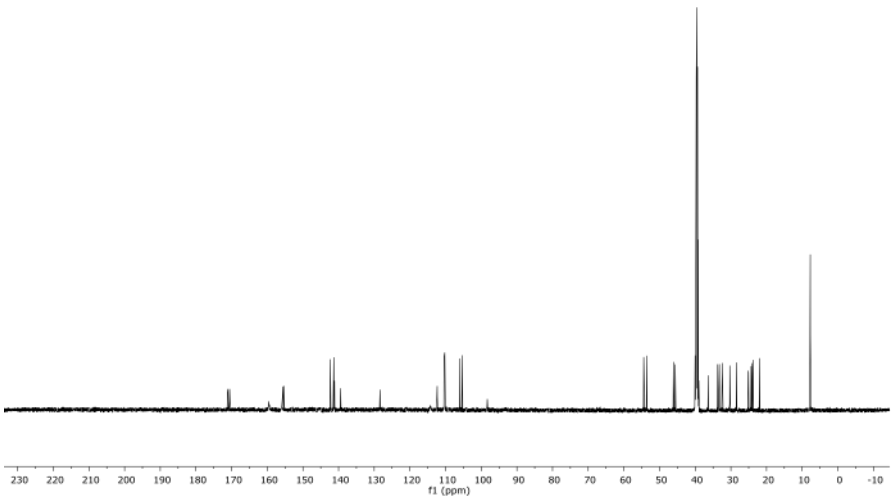

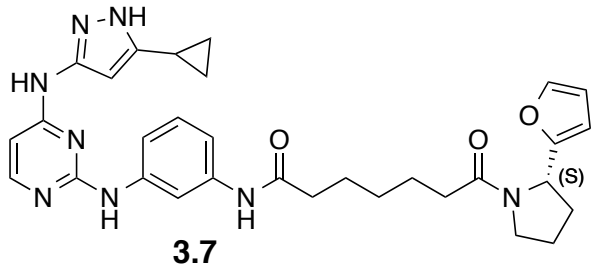

3.7

3.7 ^{1}H:

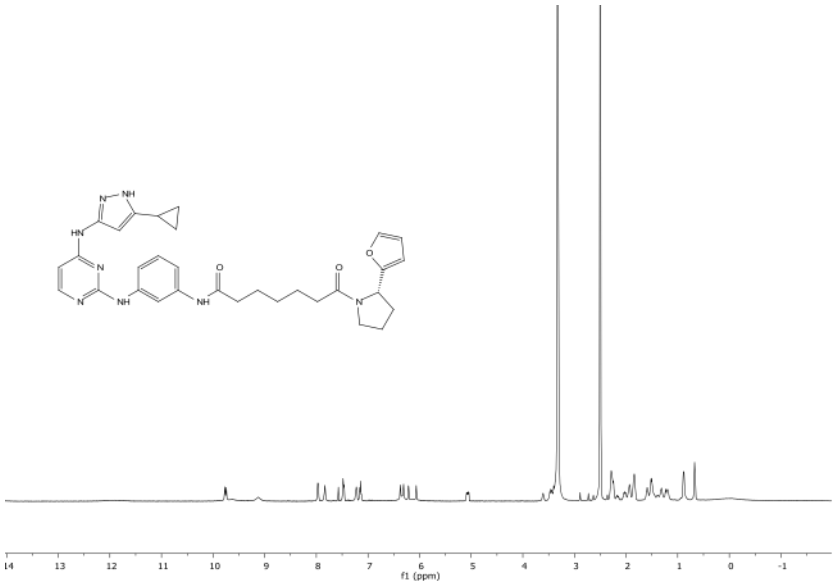

3.7 ^{13}C:

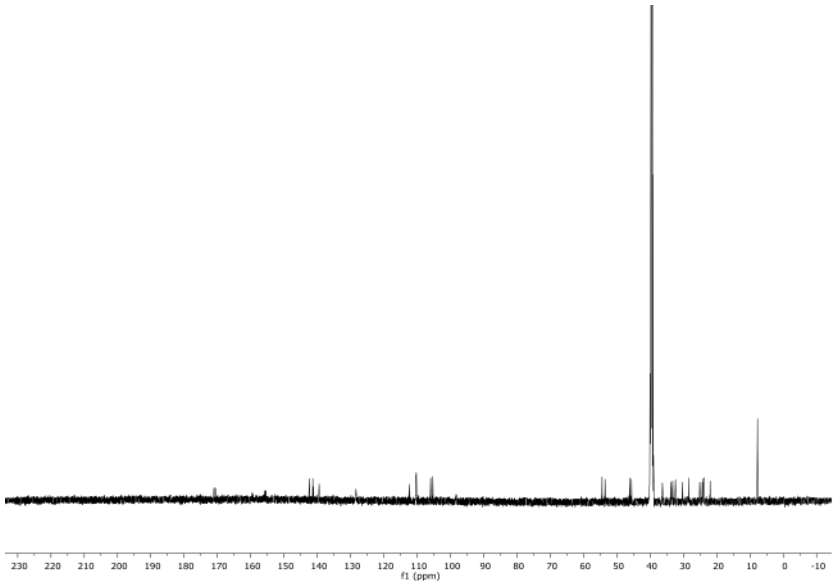

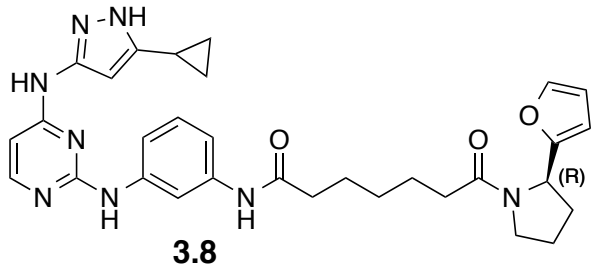

3.8

3.8 ^{1}H:

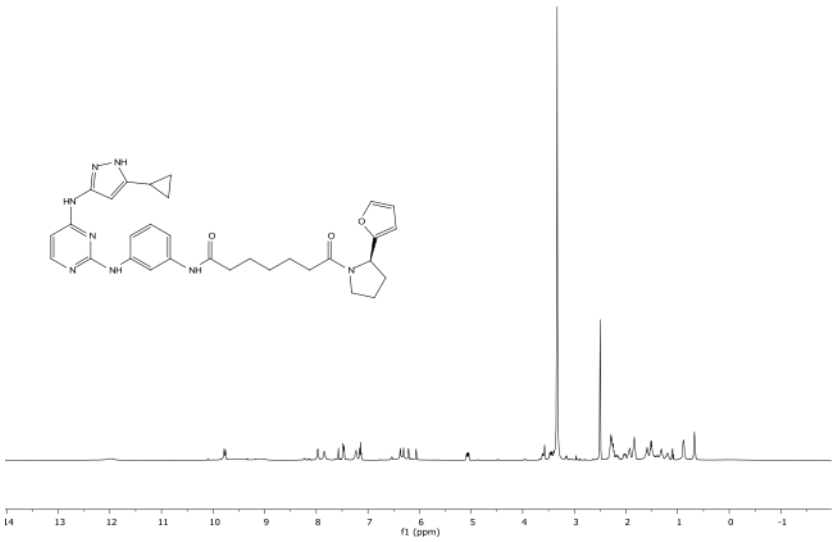

3.8 ^{13}C:

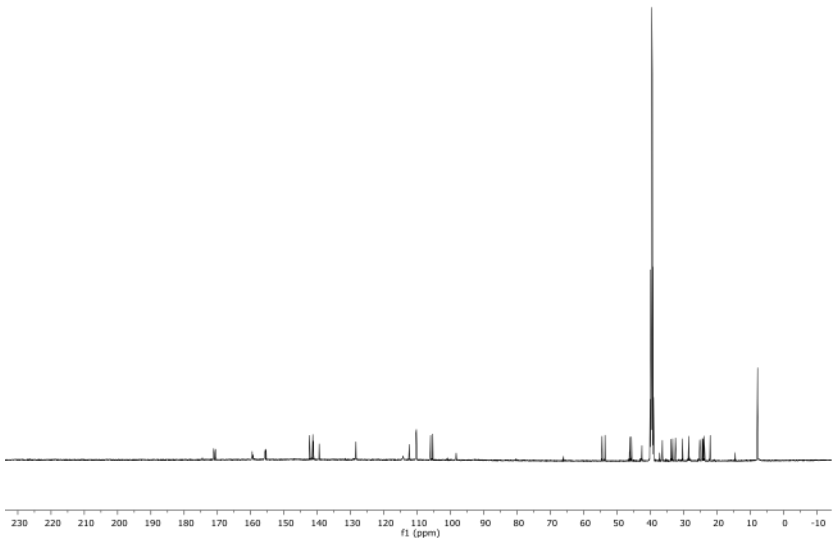

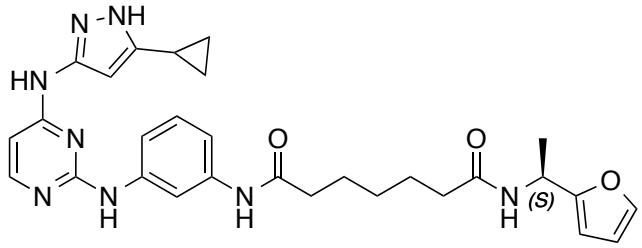

3.9

3.9 ^{1}H:

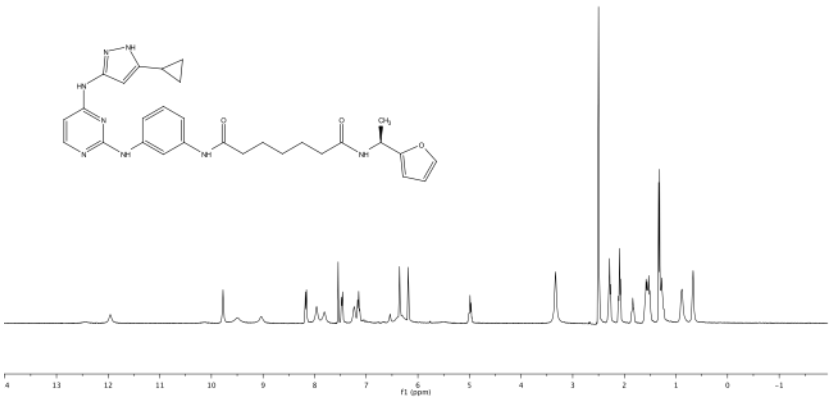

3.9 ^{13}C:

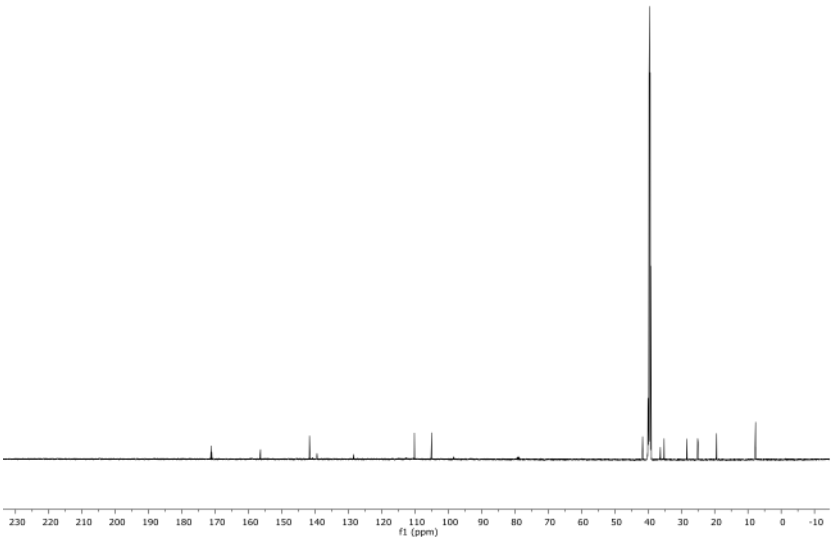

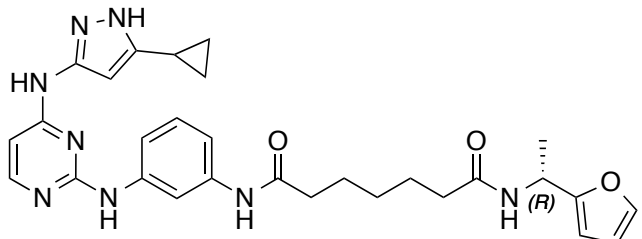

3.10

3.10 ^{1}H:

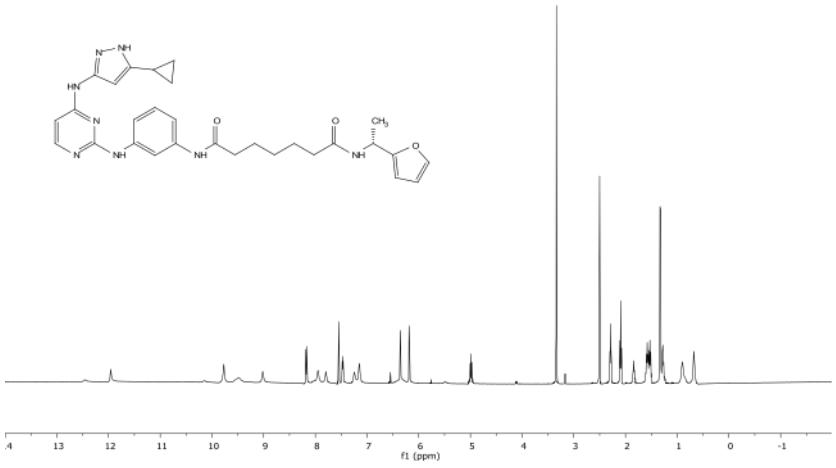

3.10 ^{13}C:

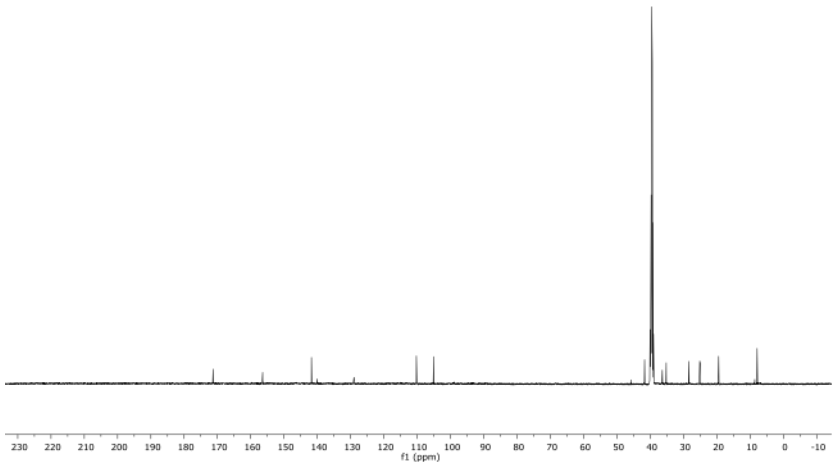

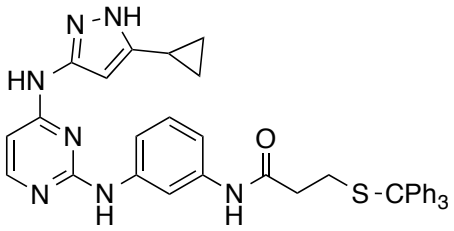

3.11

3.11 ^{1}H:

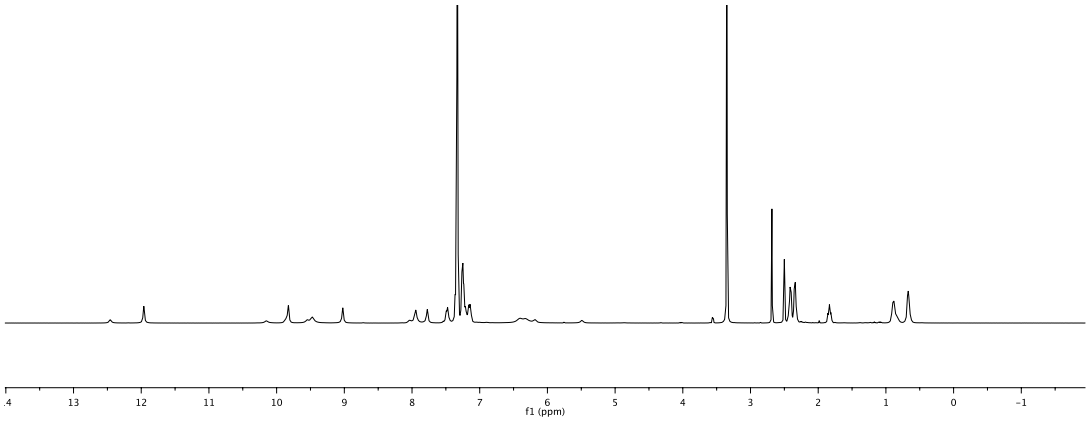

3.11 ^{13}C:

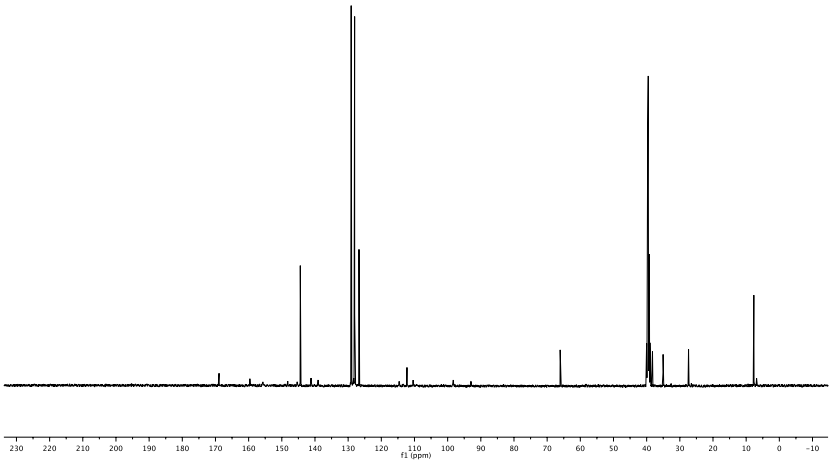

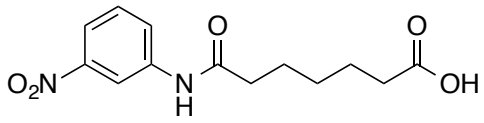

3.12

3.12 ^{1}H:

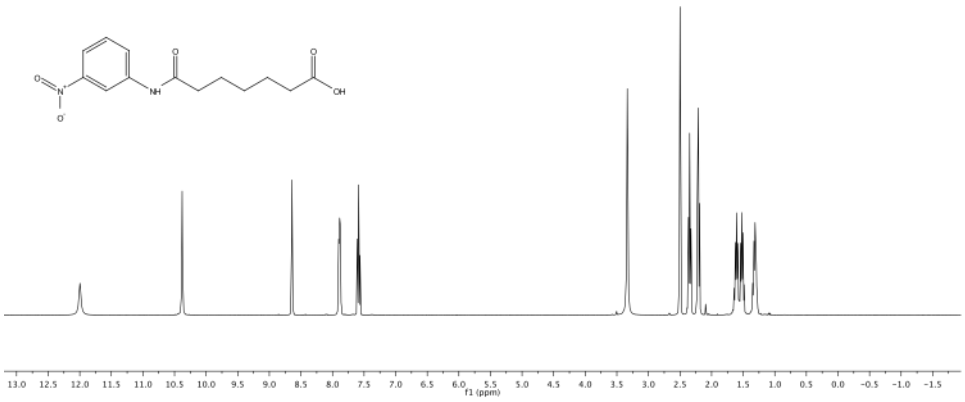

3.12 ^{13}C:

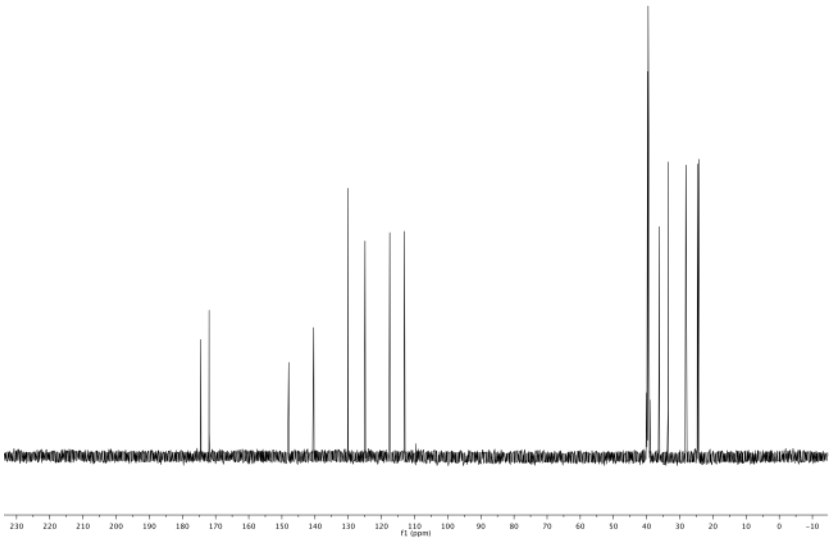

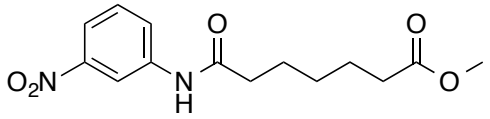

3.13

3.13 ^{1}H:

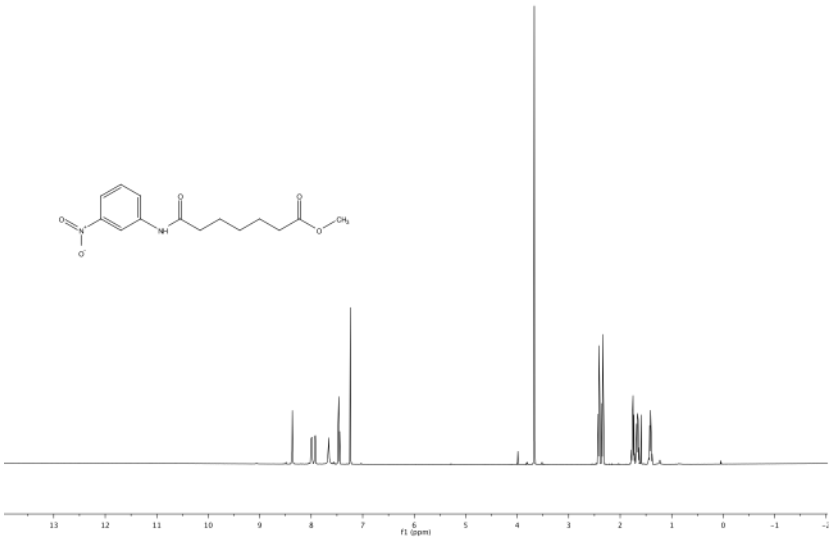

3.13 ^{13}C:

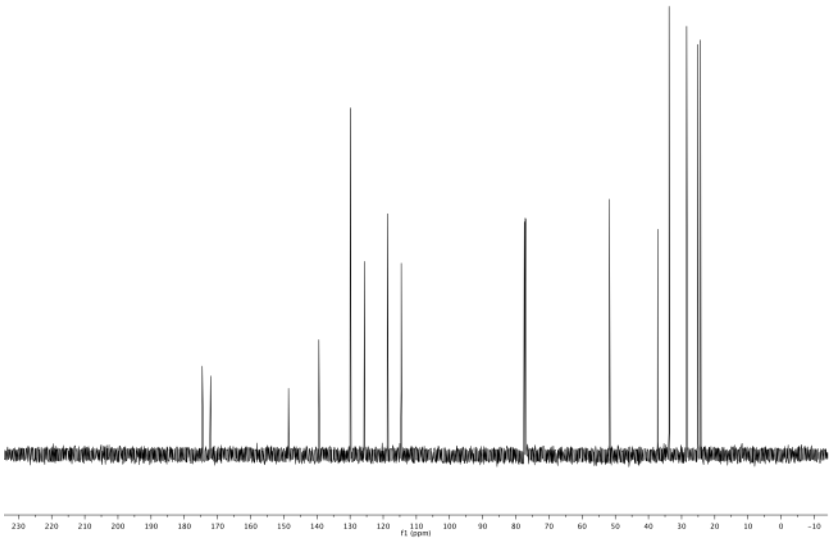

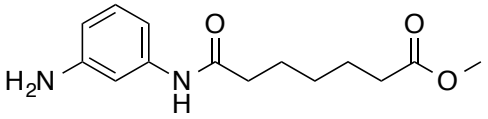

3.14

3.14 ^{1}H:

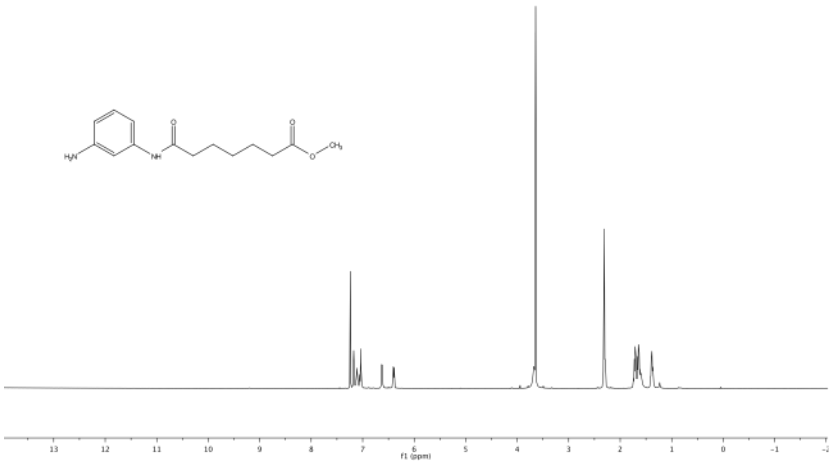

3.14 ^{13}C:

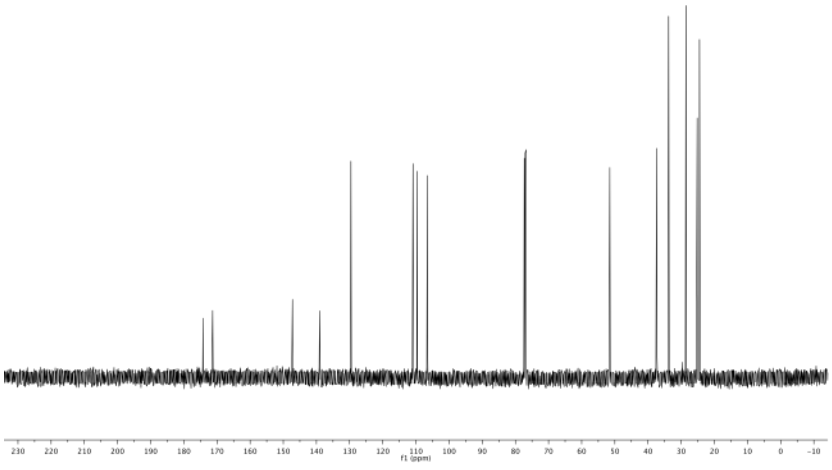

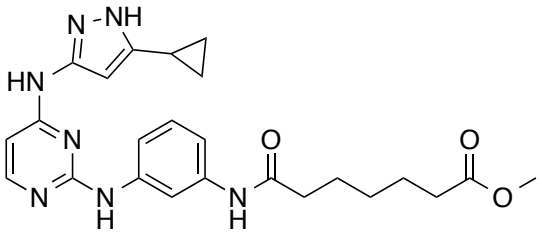

3.15

3.15 ^{1}H:

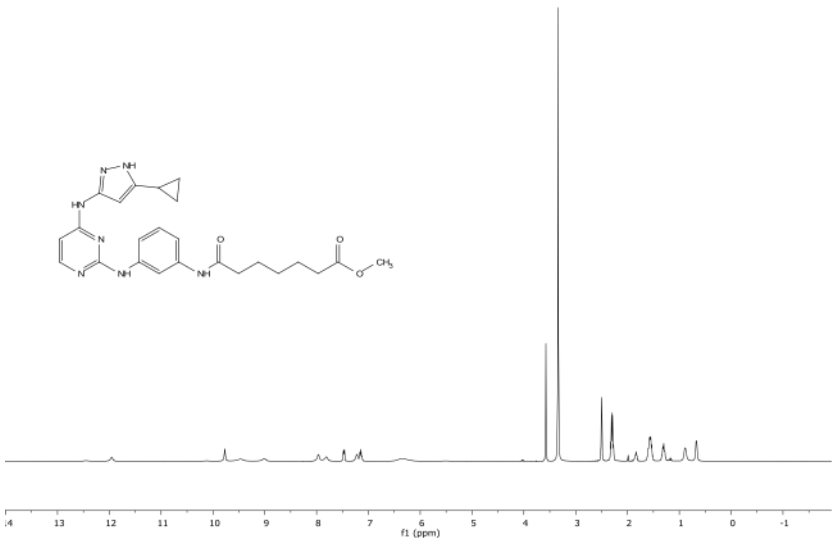

3.15 ^{13}C:

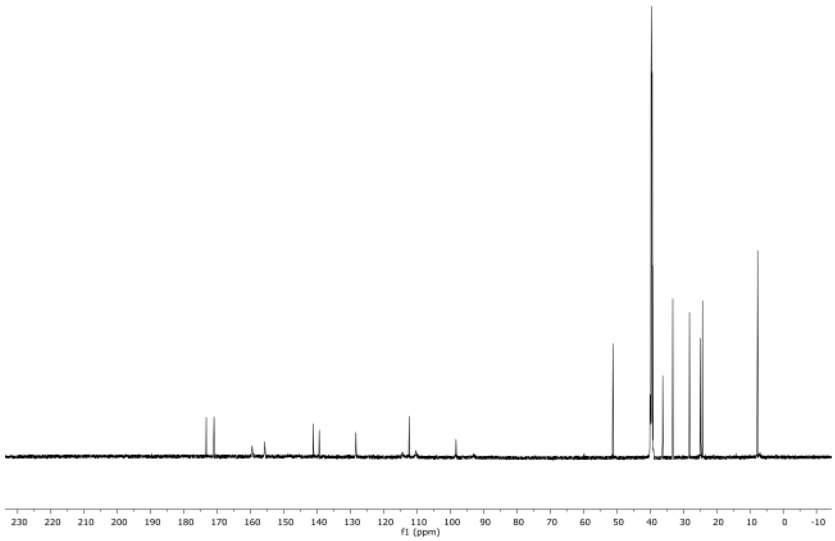

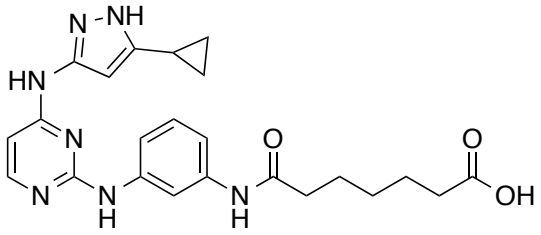

3.16

3.16 ^{1}H:

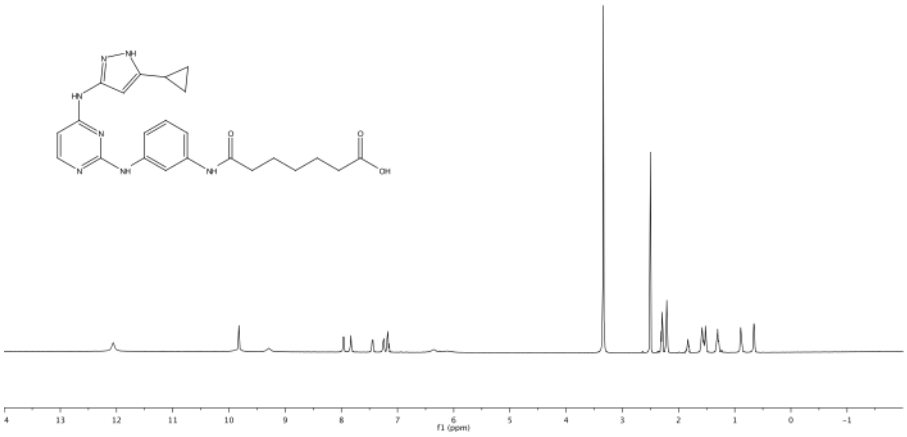

3.16 ^{13}C:

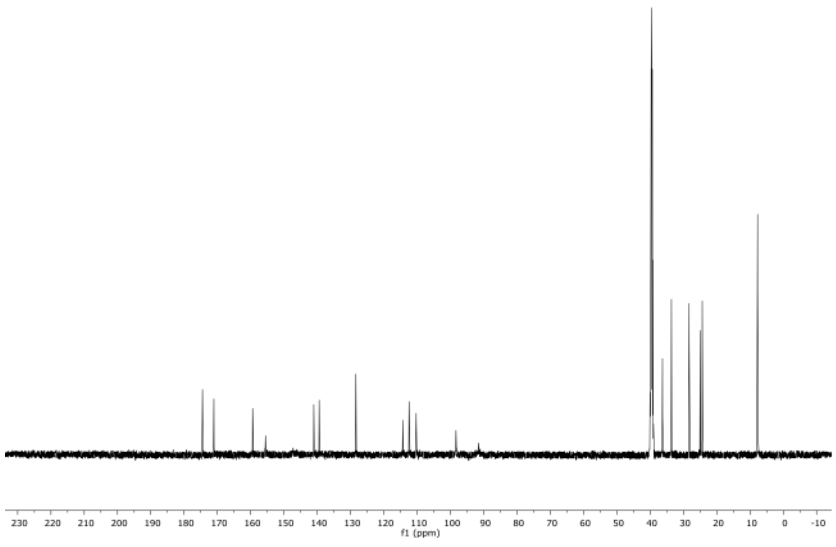

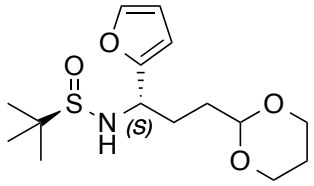

3.18

3.18 ^{1}H:

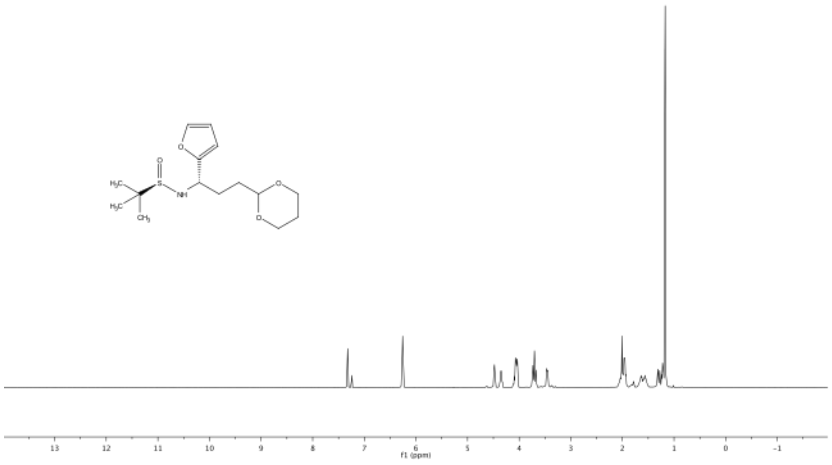

3.18 ^{13}C:

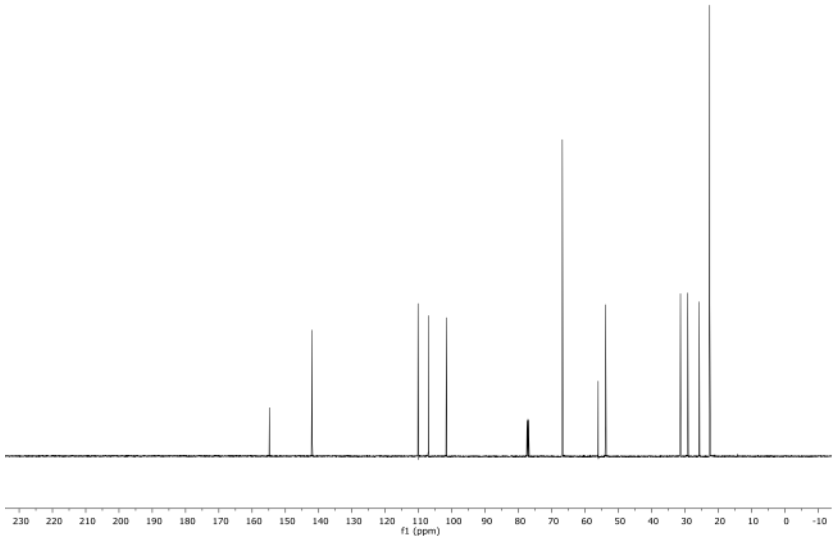

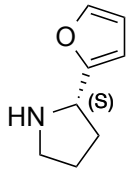

3.19

3.19 ^{1}H:

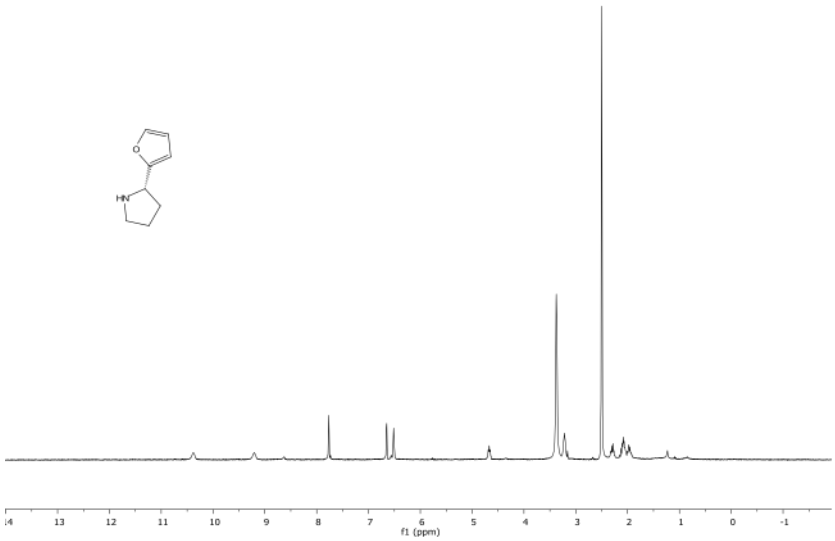

3.19 ^{13}C:

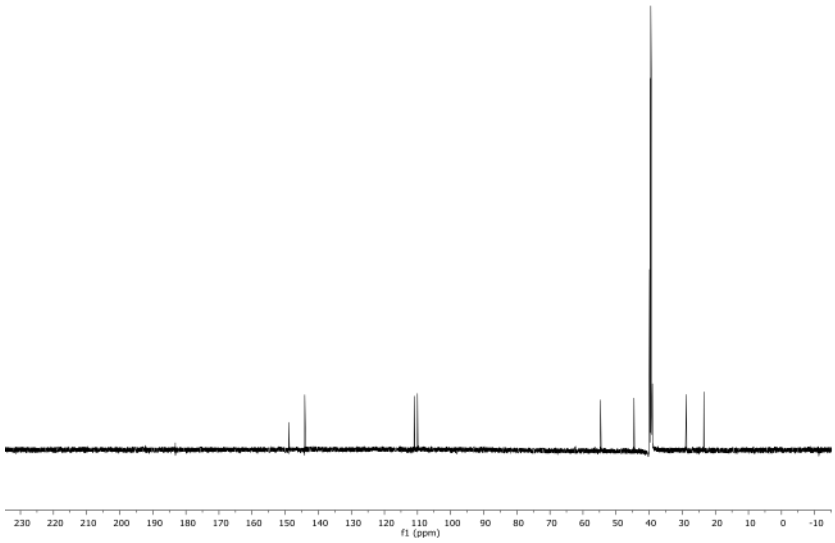

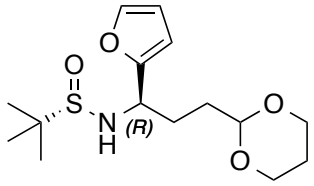

3.21

3.21 ^{1}H:

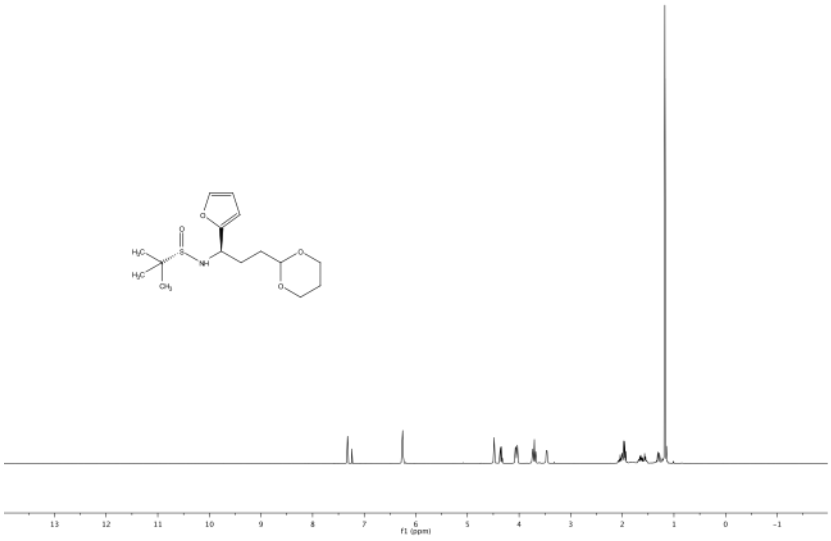

3.21 ^{13}C:

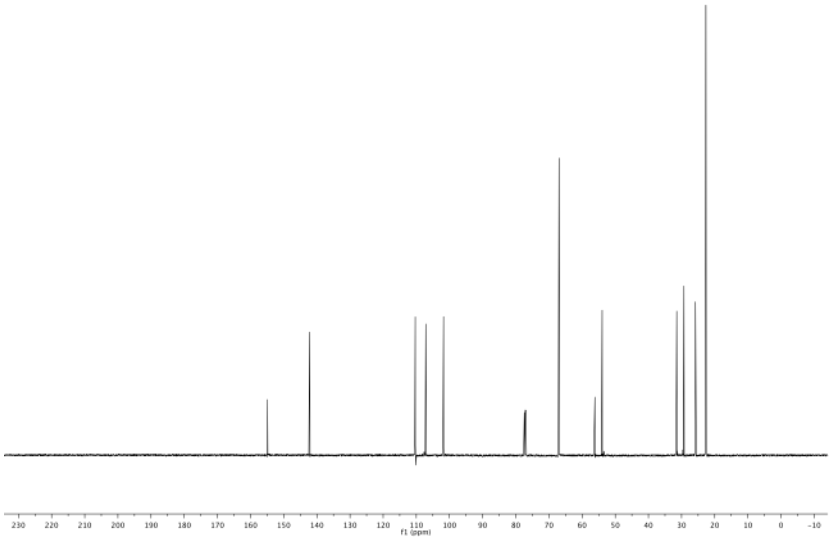

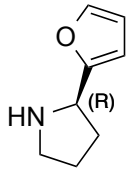

3.22

3.22 ^{1}H:

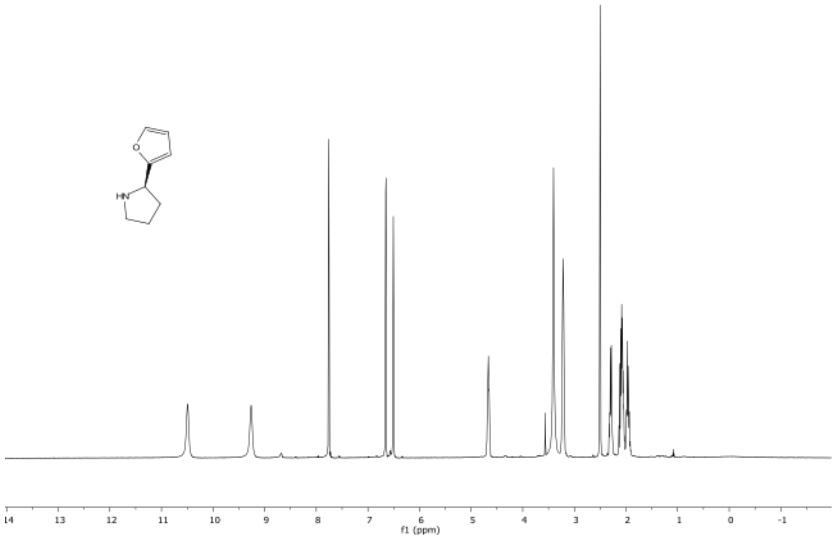

3.22 ^{13}C:

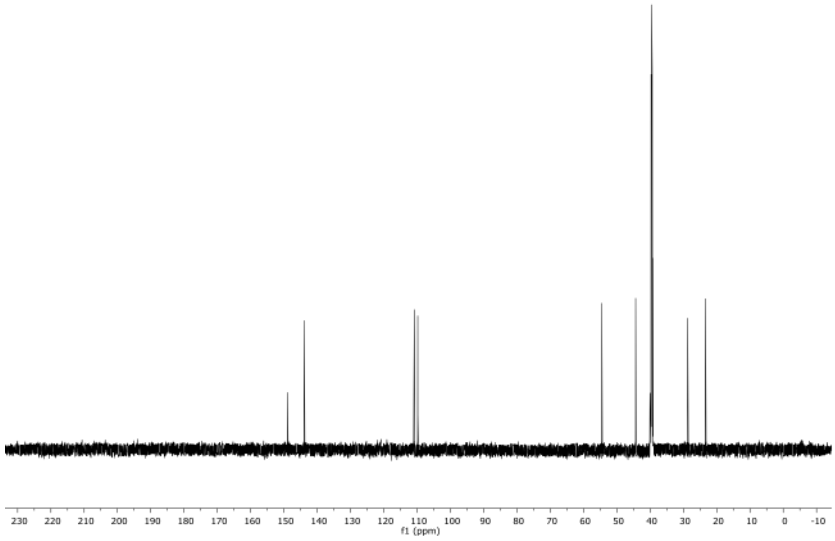

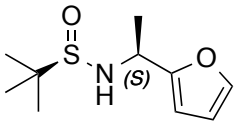

3.23

3.23 ^{1}H:

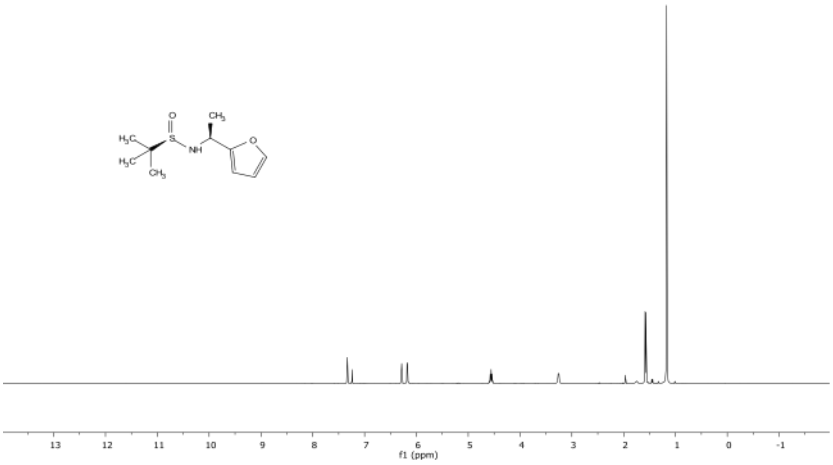

3.23 ^{13}C:

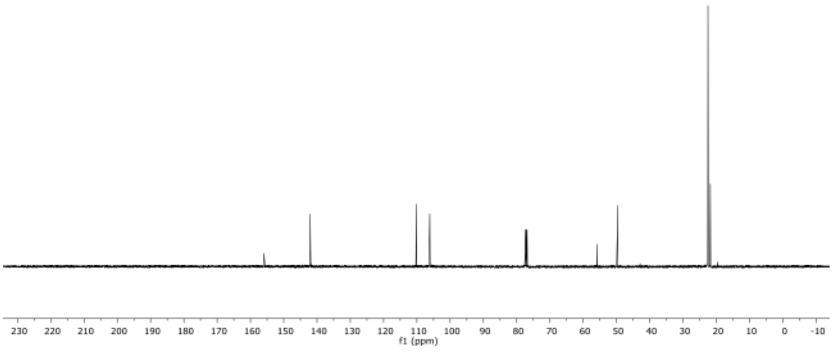

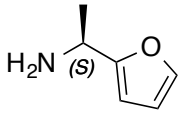

3.24

3.24 ^{1}H:

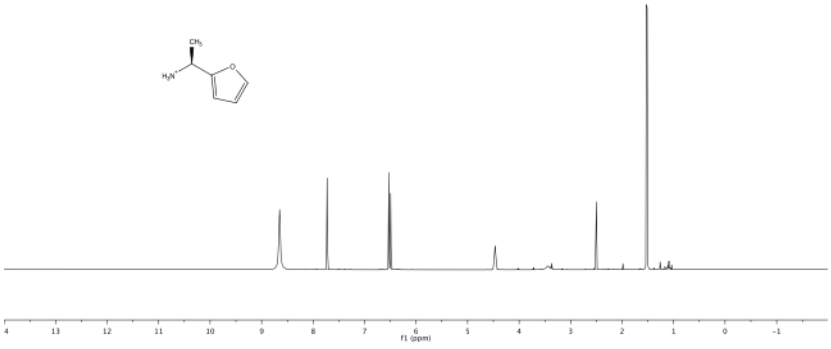

3.24 ^{13}C:

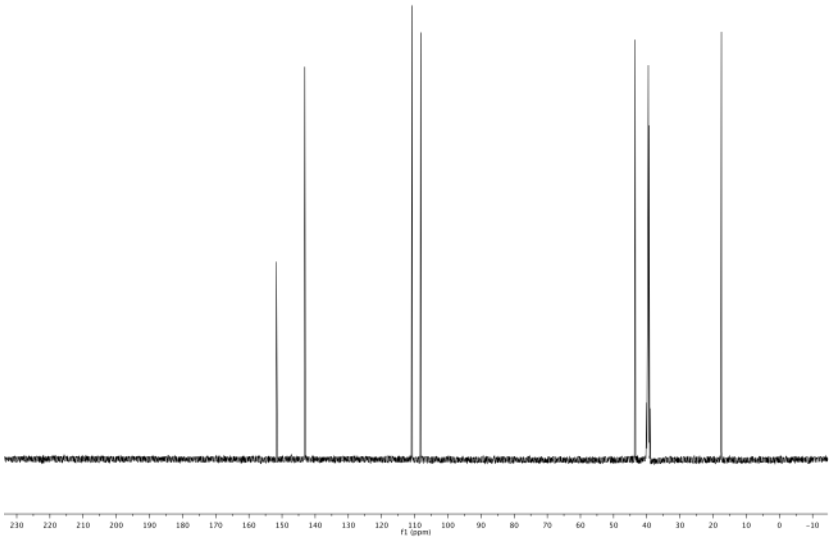

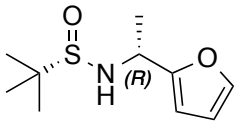

3.25

3.25 ^{1}H:

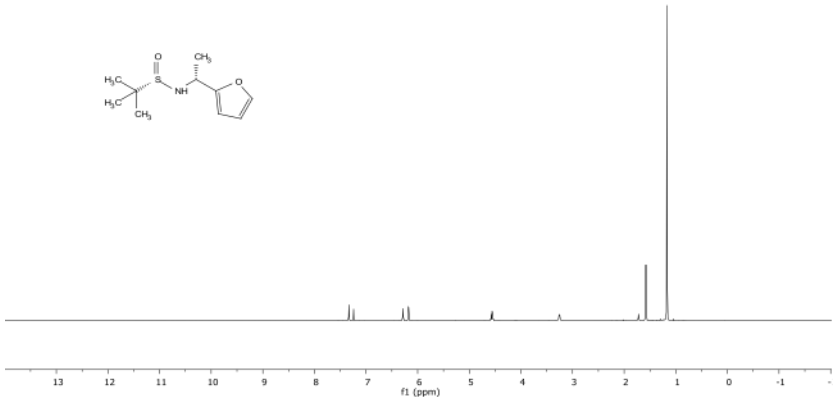

3.25 ^{13}C:

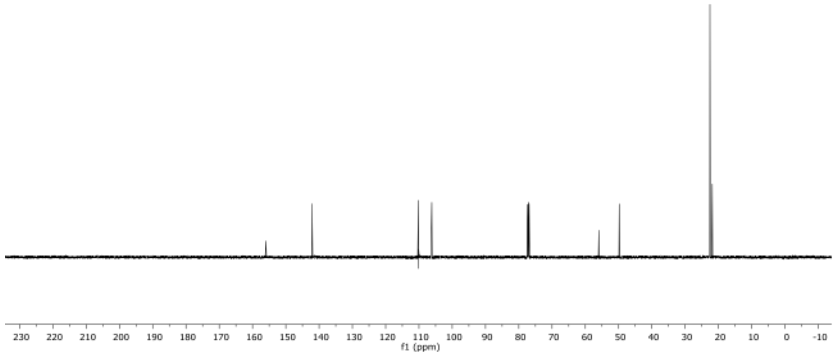

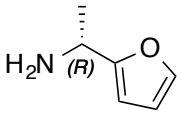

3.26

3.26 ^{1}H:

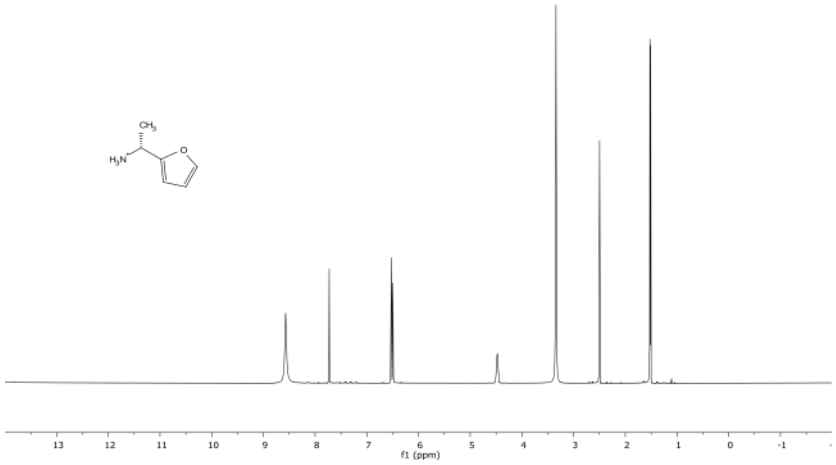

3.26 ^{13}C:

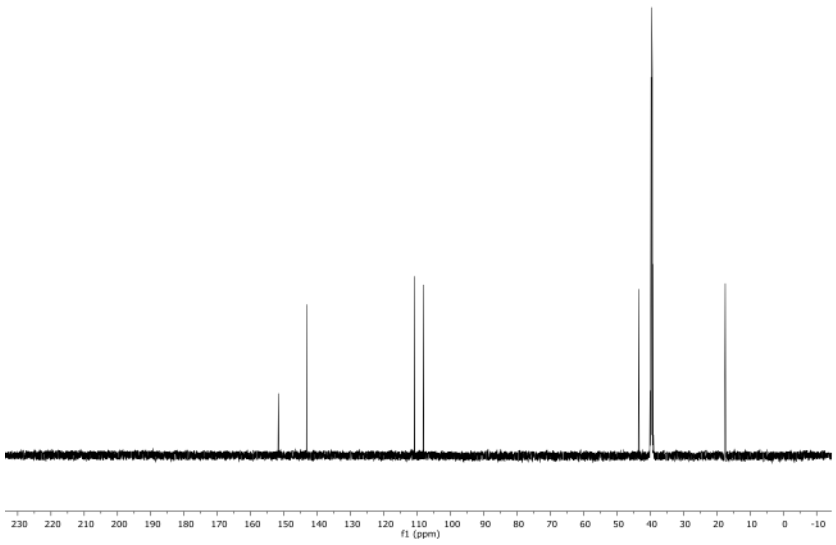

Inhibitor IC_{50} and K_i Values

Analytical data for c-Src IC_{50} & K_i determination. ATP K_m = 98 μM.

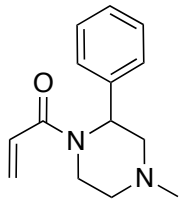

EL-1148

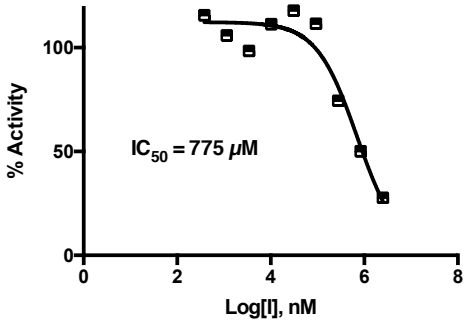

c-Src, 0min Avg IC_{50} = 880 ± 150 μM at 100 μM ATP

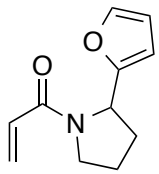

EL-1061

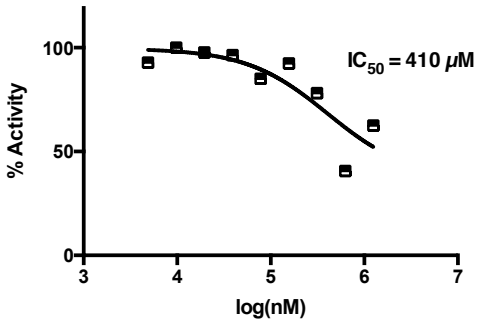

c-Src, 0 min Avg IC_{50} = 500 ± 80 μM at 100 μM ATP

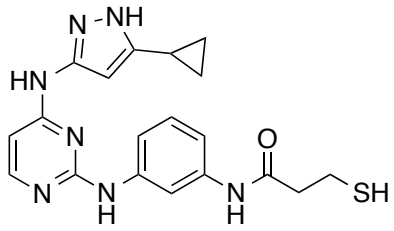

3.1

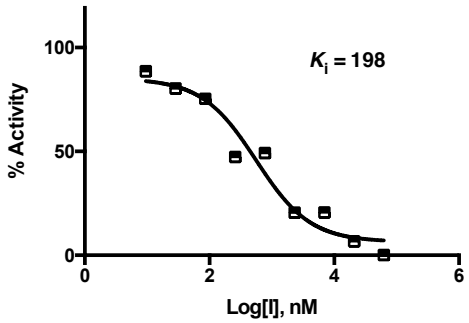

c-Src, 0 min Avg K_i = 190 ± 50 nM

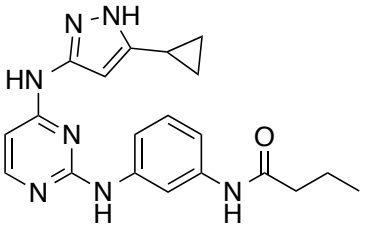

3.2

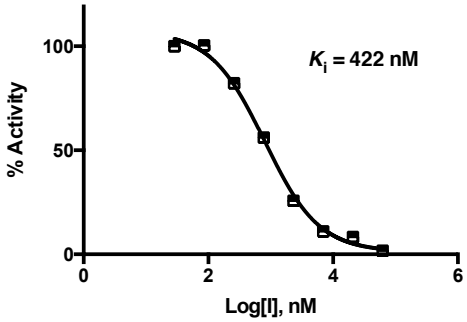

c-Src Avg K_i = 400 ± 20 nM

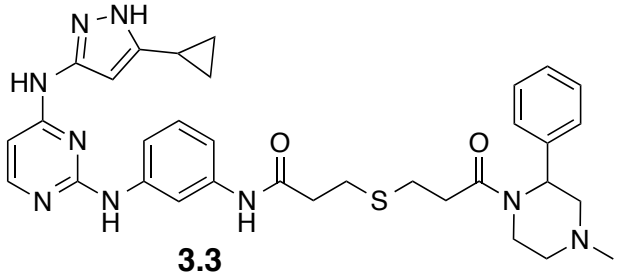

3.3

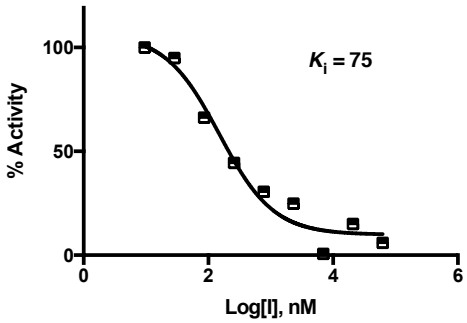

c-Src Avg K_i = 90 ± 20 nM

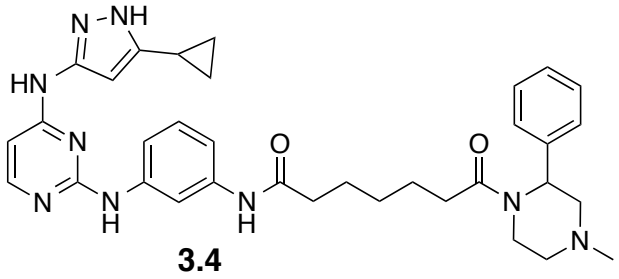

3.4

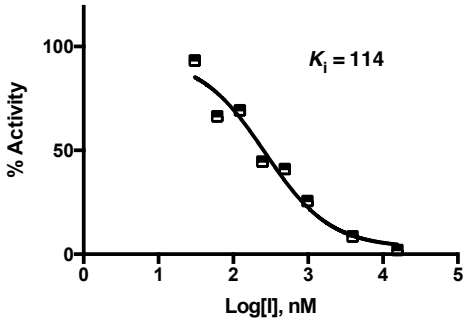

c-Src Avg K_i = 140 ± 30 nM

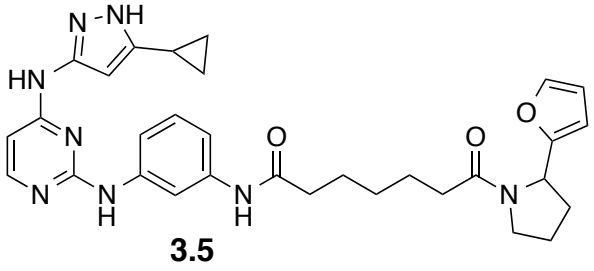

3.5

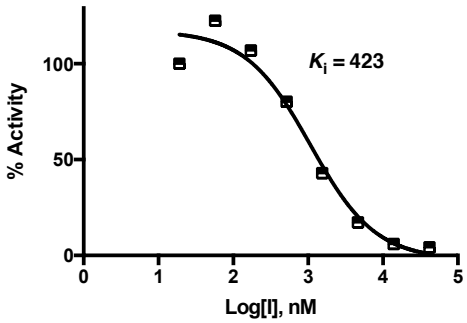

c-Src Avg K_i = 480 ± 50 nM

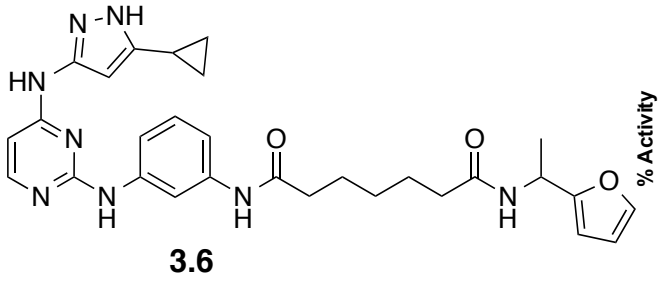

3.6

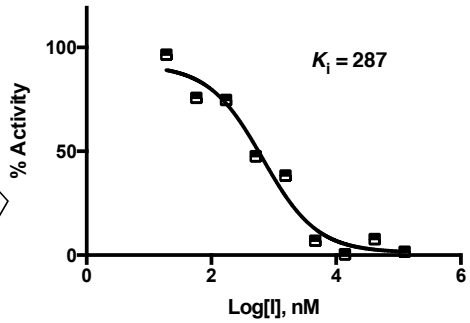

c-Src Avg K_i = 230 ± 60 nM

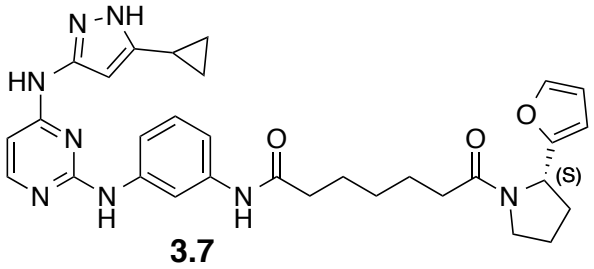

3.7

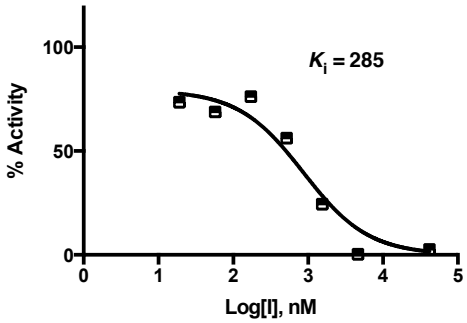

c-Src Avg K_i = 330 ± 50 nM

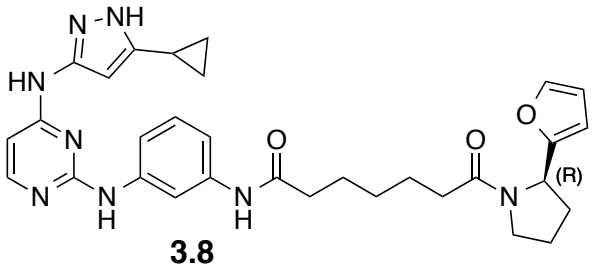

3.8

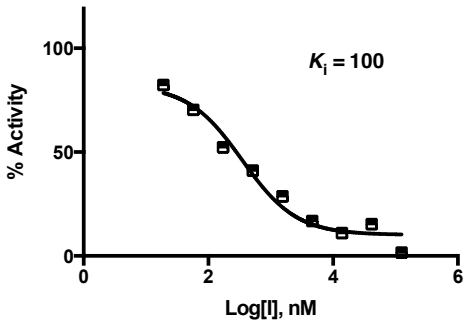

c-Src Avg K_i = 70 ± 20 nM

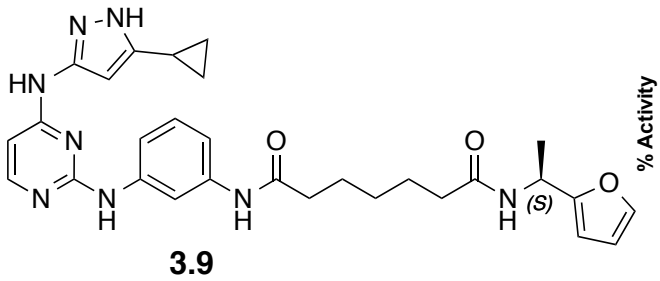

3.9

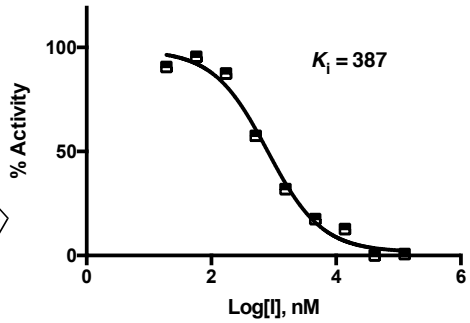

c-Src Avg K_i = 370 ± 20 nM

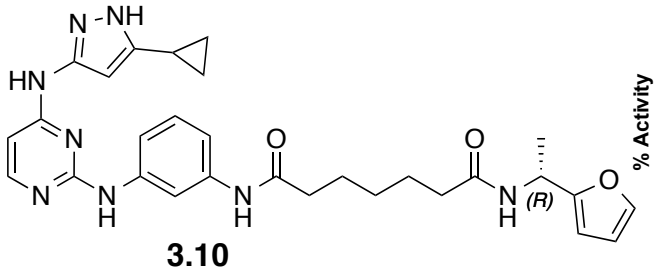

3.10

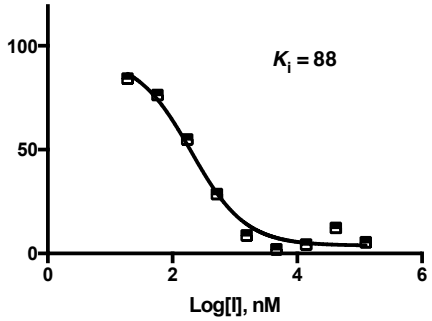

c-Src Avg K_i = 130 ± 60 nM

Analytical data for 3M c-Src IC_{50} & K_i determination. ATP K_m = 28 μM.

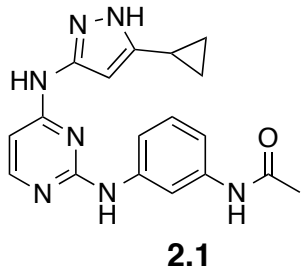

2.1

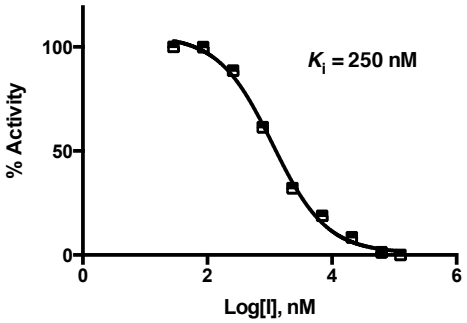

3M c-Src Avg K_i = 240 ± 10 nM

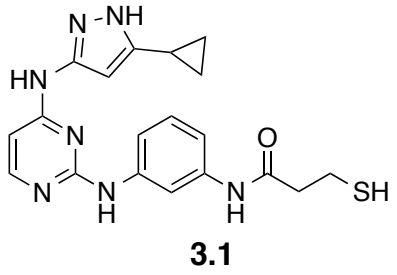

3.1

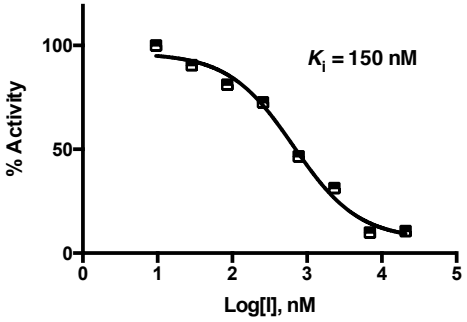

3M c-Src Avg K_i = 200 ± 60 nM

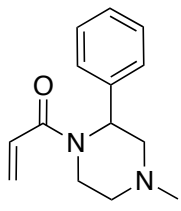

EL-1148

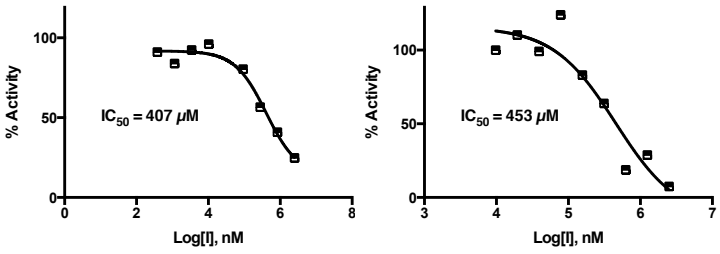

3M c-Src, 0 min Avg IC_{50} = 470 ± 110 μM (left) at 100 μM ATP
3M c-Src, 60 min Avg IC_{50} = 490 ± 50 μM (right) at 100 μM ATP

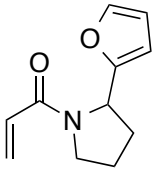

EL-1061

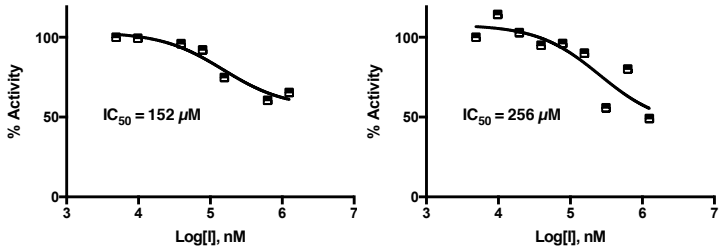

3M c-Src, 0 min Avg IC_{50} = 160 ± 20 μM (left) at 100 μM ATP
3M c-Src, 60 min Avg IC_{50} = 270 ± 30 μM (right) at 100 μM ATP

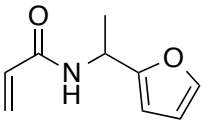

EL-1092

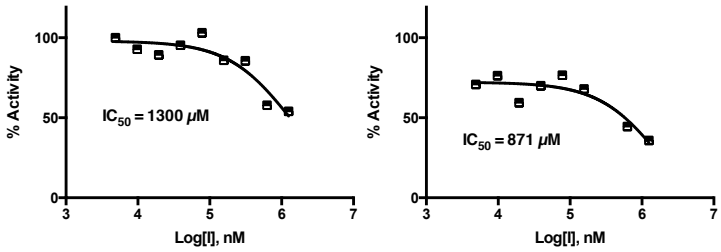

3M c-Src, 0 min Avg IC_{50} = 1260 ± 100 μM (left) at 100 μM ATP
3M c-Src, 60 min Avg IC_{50} = 940 ± 210 μM (right) at 100 μM ATP

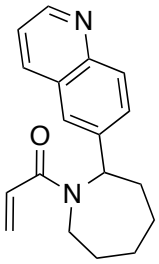

EL-1145

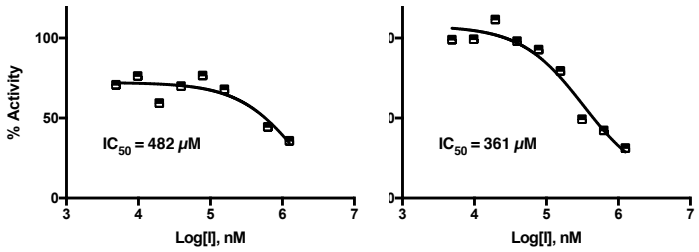

3M c-Src, 0 min Avg IC_{50} = 520 ± 80 μM (left) at 100 μM ATP
3M c-Src, 60 min Avg IC_{50} = 420 ± 50 μM (right) at 100 μM ATP

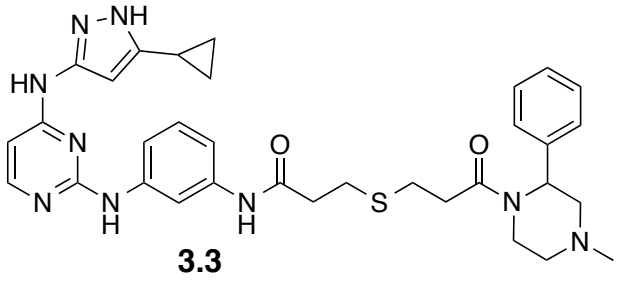

3.3

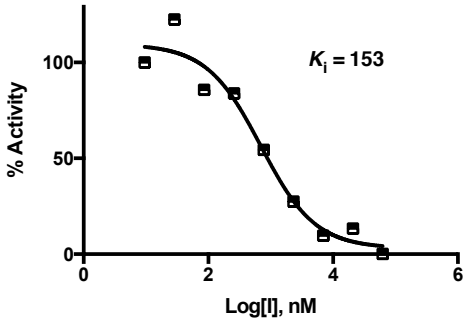

3M c-Src Avg K_i = 120 ± 20 nM

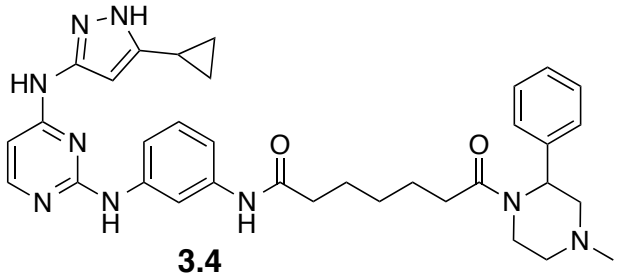

3.4

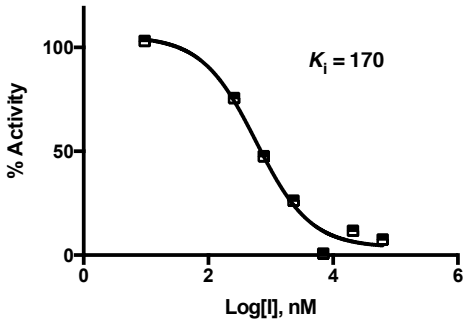

3M c-Src Avg K_i = 180 ± 10 nM

Analytical data for c-Abl K_i determination. ATP K_m = 22 μM.

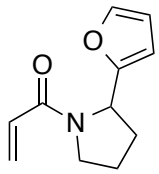

EL-1061

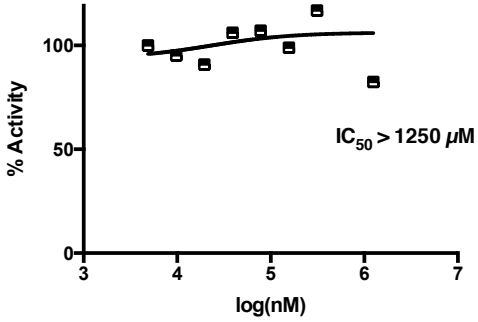

c-Abl Avg IC_{50} > 1250 μM at 100 μM ATP

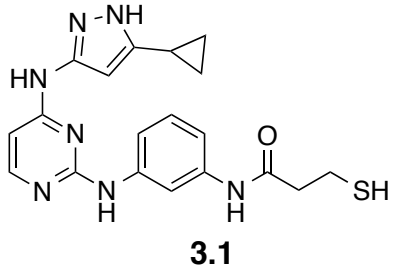

3.1

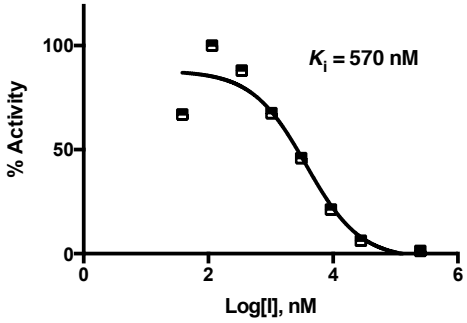

c-Abl Avg K_i = 610 ± 60 nM

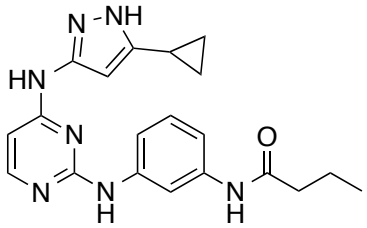

3.2

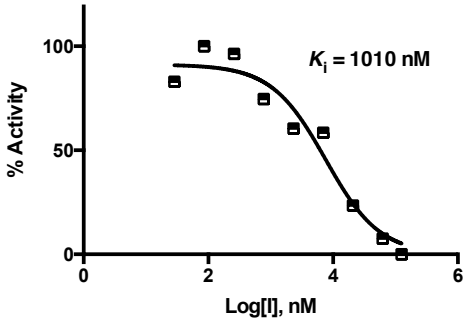

c-Abl Avg K_i = 980 ± 160 nM

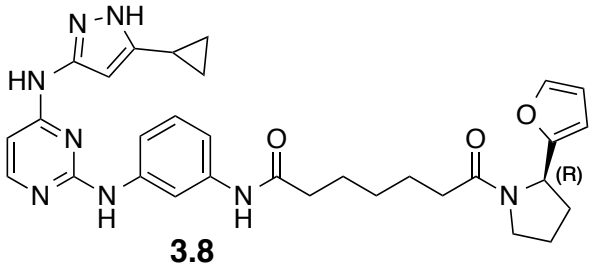

3.8

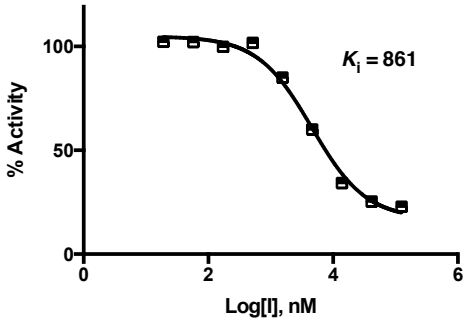

c-Abl Avg K_i = 730 ± 160 nM

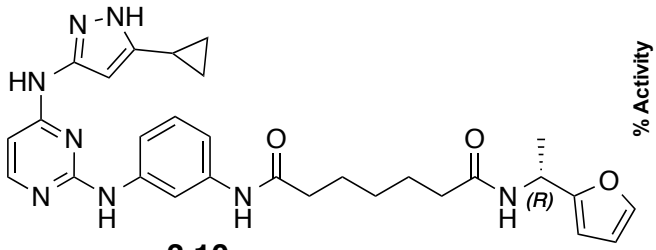

3.10

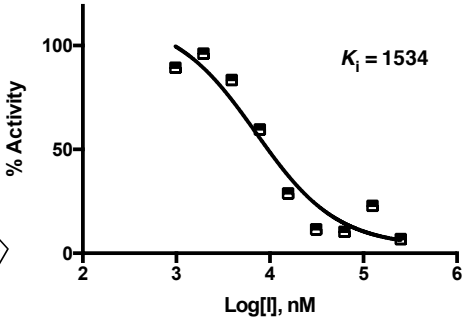

c-Abl Avg K_i = 1150 ± 350 nM

Analytical data for Hck K_i determination. ATP K_m = 20 μM.

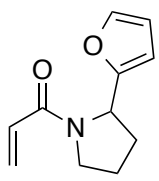

EL-1061

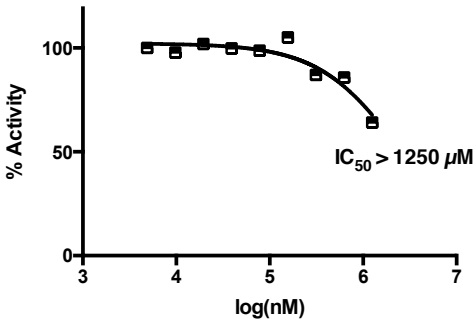

Hck Avg IC_{50} > 1250 μM at 100 μM ATP

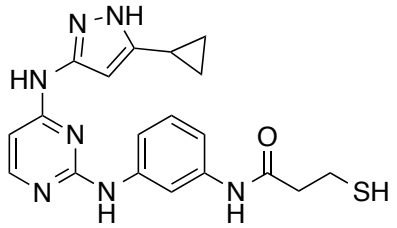

3.1

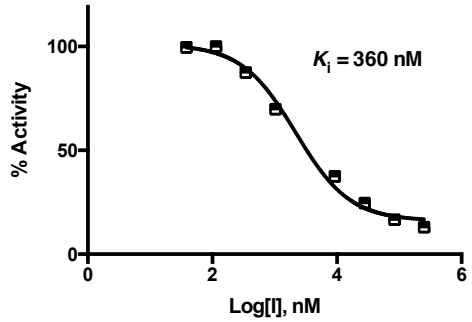

Hck Avg K_i = 410 ± 70 nM

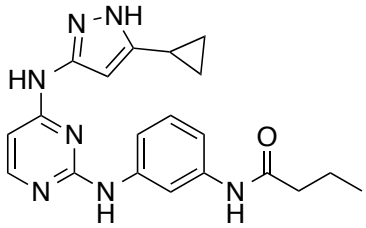

3.2

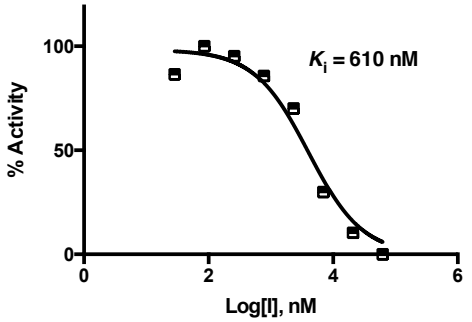

Hck Avg K_i = 650 ± 110 nM

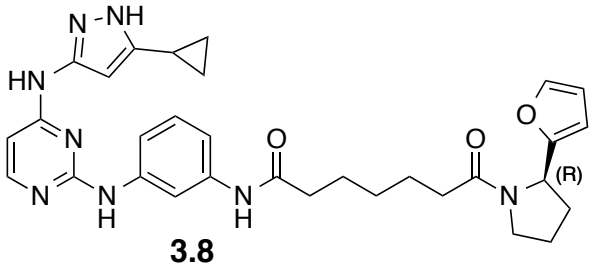

3.8

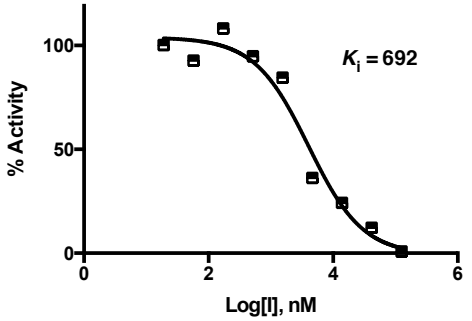

Hck Avg K_i = 710 ± 30 nM

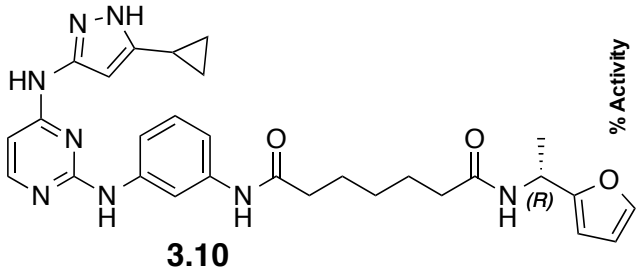

3.10

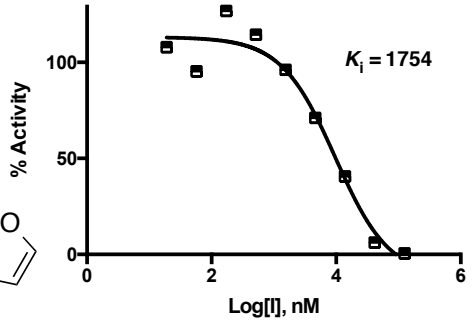

Hck Avg K_i = 1820 ± 80 nM

Analytical data for c-Yes K_i determination. ATP K_m = 105 μM.

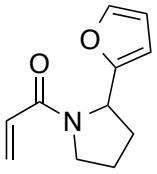

EL-1061

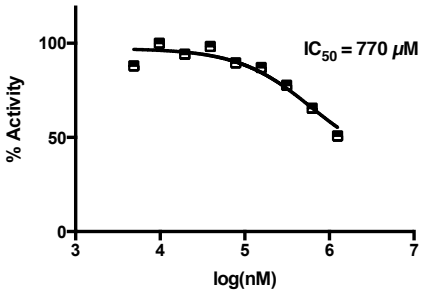

c-Yes, 0 min Avg IC_{50} = 710 ± 140 μM at 100 μM ATP

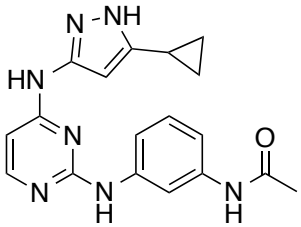

2.1

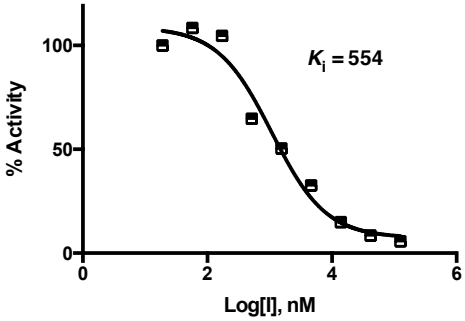

c-Yes Avg K_i = 590 ± 50 nM

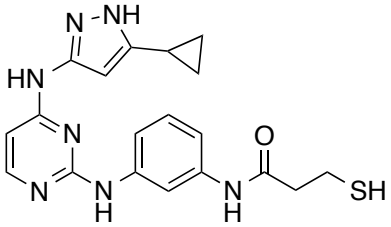

3.1

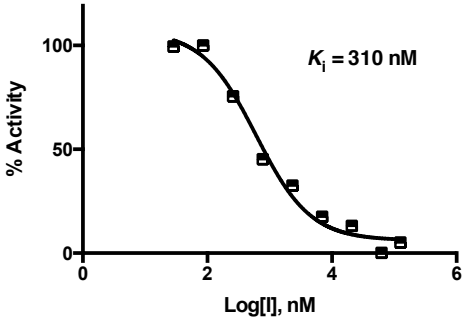

c-Yes, 0 min Avg K_i = 340 ± 20 nM

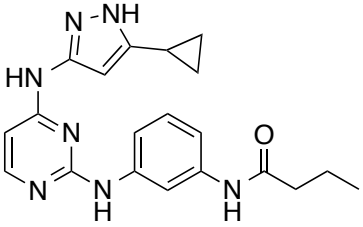

3.2

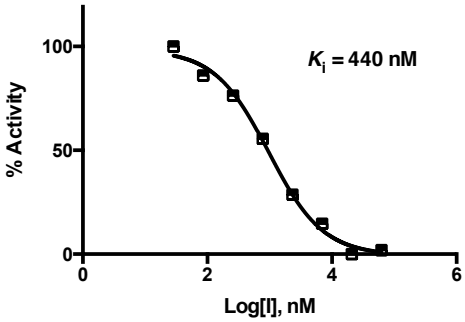

c-Yes Avg K_i = 470 ± 20 nM

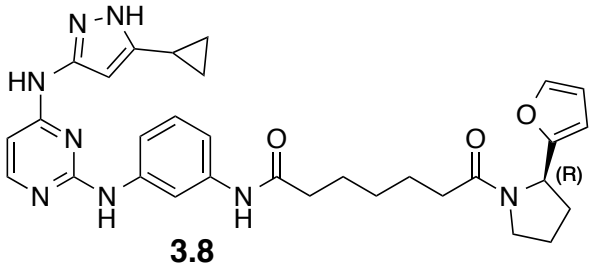

3.8

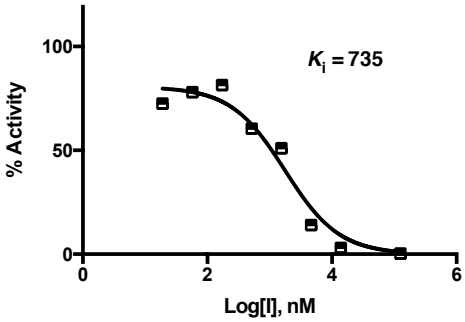

c-Yes Avg K_i = 610 ± 130 nM

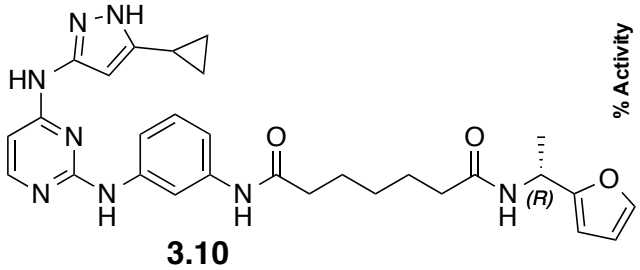

3.10

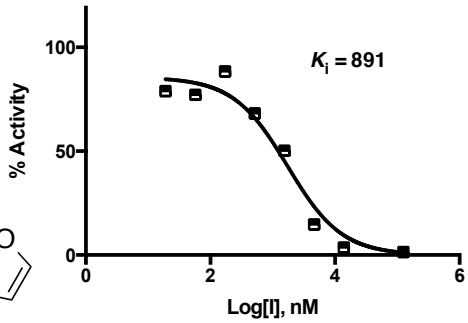

c-Yes Avg K_i = 800 ± 160 nM

Analytical data for E280G c-Src K_i determination. ATP K_m = 102 μM.

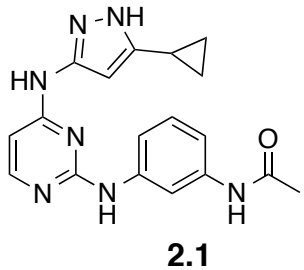

2.1

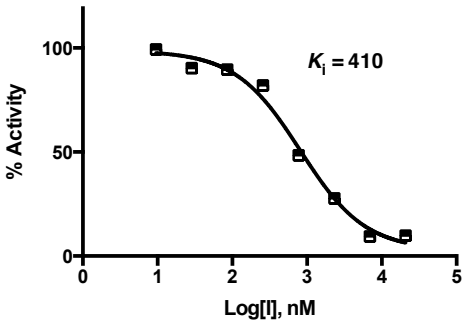

E280G c-Src Avg K_i = 410 ± 30 nM

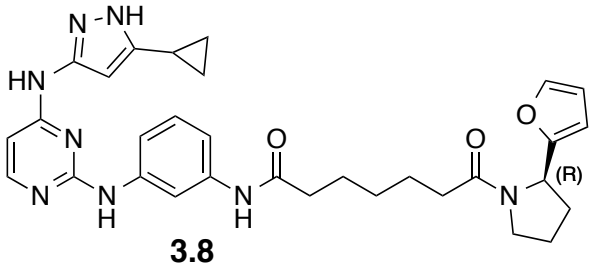

3.8

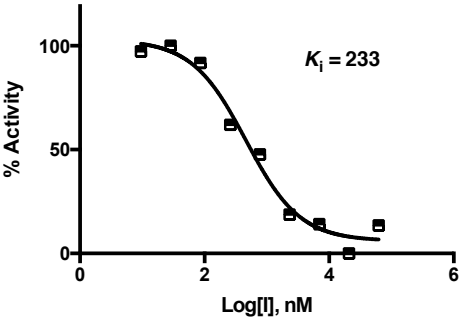

E280G c-Src Avg K_i = 260 ± 30 nM

Data for ATP K_m Determination

ATP K_m curve with 3M c-Src (C277S, C483S, C496S):

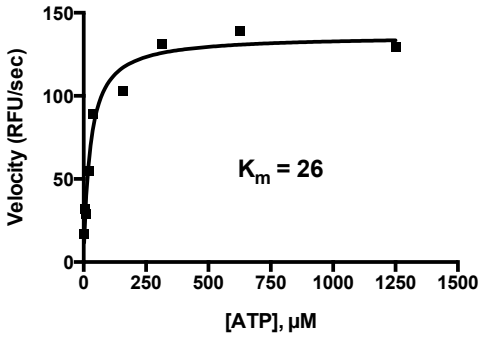

Km = 28 ± 10 µM
Vmax = 135 ± 2 (RFU/s)

ATP K_m curve with E280G c-Src:

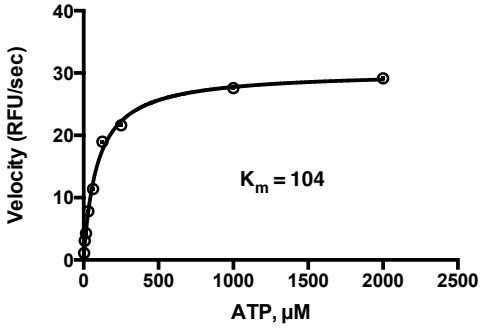

K_m = 102 ± 5 µM
V_{max} = 28 ± 3 (RFU/s)

APPENDIX C

Supplemental Information and Analytical Data for Chapter IV

Figure C.1. Dasatinib and DAS-DFG-out analog biochemical IC_{50} curves.

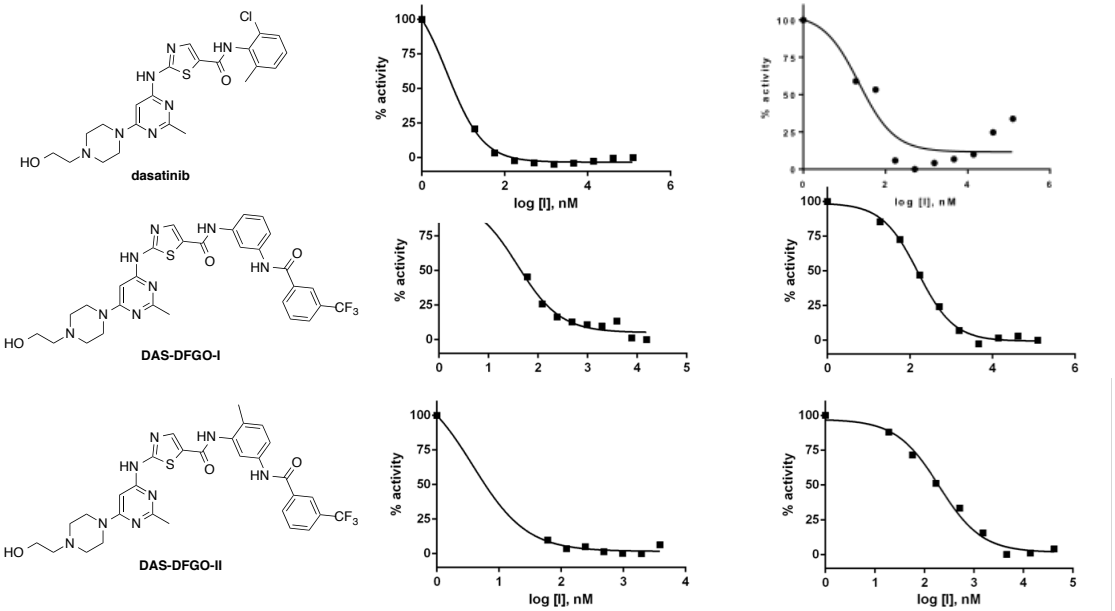

Dasatinib conformation-selective analogs against wt c-Src (left) and wt c-Abl (right). Dasatinib, **DAS-DFGO-I** and **DAS-DFGO-II** have Avg K_i values < 1 nM at 5 mM ATP for both kinases (representative curve shown).

Figure C.2. Overlay of **DAS-DFGO-I** and imatinib.

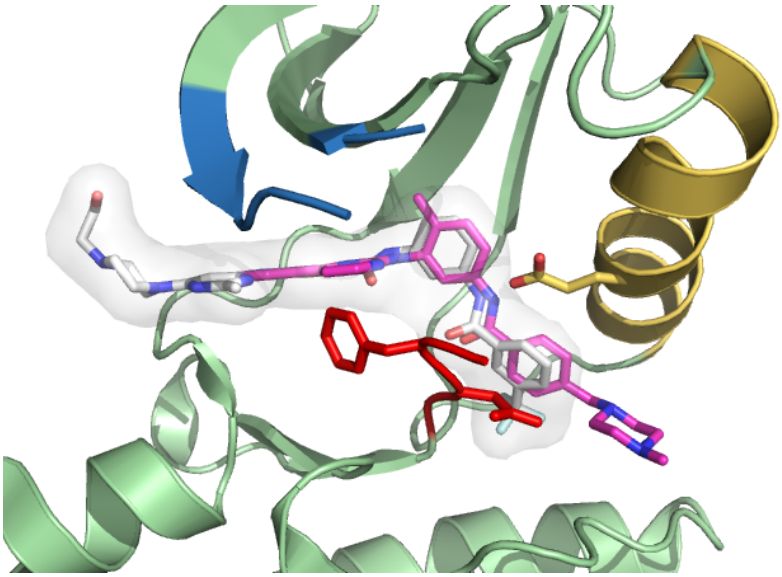

Overlay of **DAS-DFGO-I** (white, PDB: 4YBJ) and imatinib (magenta, PDB: 2OIQ) bound to c-Src. The benzamide group of imatinib makes the identical c-Src interactions as the corresponding trifluoromethyl benzamide group of **DAS-DFGO-I**.

Figure C.3. DAS-CHO analog biochemical IC_{50} curves.

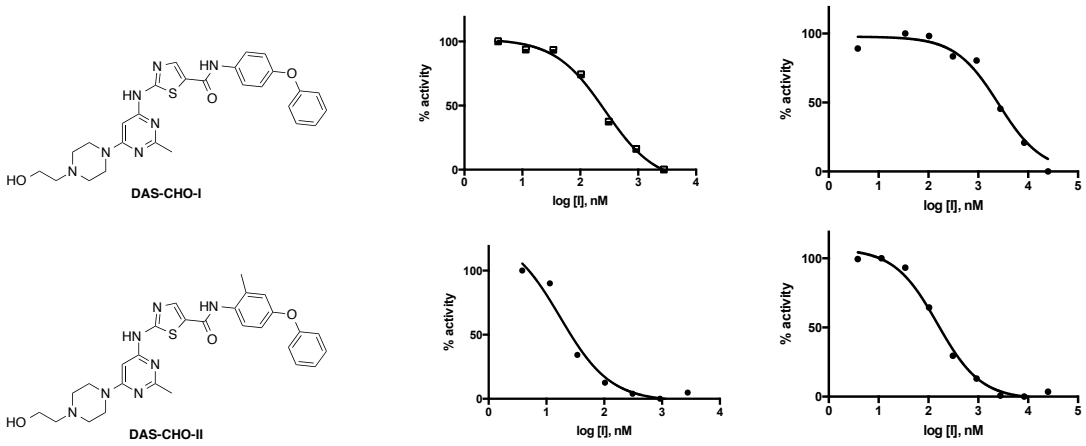

Dasatinib CHO conformation-selective analogs against wt c-Src (left) and wt c-Abl (right). **DAS-CHO-I** has an Avg K_i value < 25 nM at 5 mM ATP for both kinases and **DAS-CHO-II** has an Avg K_i value < 1 nM at 5 mM ATP for both kinases (representative curve shown).

Table C.1. PDB codes used for CHO inhibitor analysis.

PDB	Kinase
4DGG	SRC
3GEN	BTK
1XKK	EGFR
2RGP	EGFR
3BEL	EGFR
3POZ	EGFR
2JIV	T790M EGFR
3PP0	HER2
3RCD	HER2
2R4B	ERBB4
3BBT	ERBB4
2RFN	MET
3EFJ	MET
3EFK	MET

Table C.2. Dasatinib analog BODIPY probes and data.

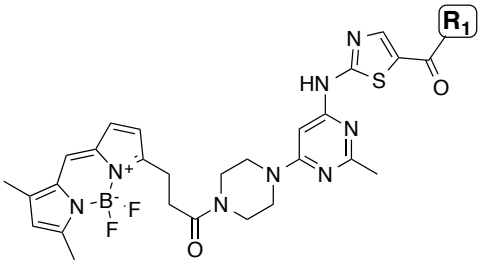

Binding Mode:	active	DFG-out	CHO

R₁ =

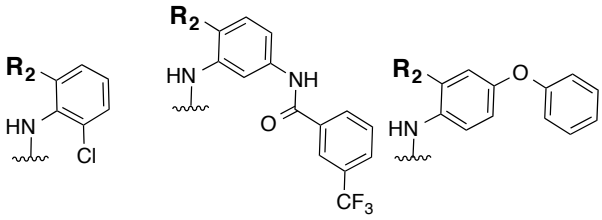

			c-Src				c-Abl			
BODIPY-	**R_1**	**R_2**	**K_d, nM**	**$t_{1/2}$, min**	**k_{on}, sec^{-1}**	**k_{off}, sec^{-1}**	**K_d, nM**	**$t_{1/2}$, min**	**k_{on}, sec^{-1}**	**k_{off}, sec^{-1}**
DAS	active	Me	0.50	15	1.6×10^{-3}	7.9×10^{-4}	0.15	20	3.8×10^{-3}	5.7×10^{-4}
DAS-DFGO-I	DFGO	H	0.67	53	3.3×10^{-4}	2.2×10^{-4}	4.7	79	3.1×10^{-5}	1.5×10^{-4}
DAS-DFGO-II	DFGO	Me	2.8	65	6.4×10^{-5}	1.8×10^{-4}	0.75	75	2.1×10^{-4}	1.5×10^{-4}
DAS-CHO-II	CHO	Me	4.6	13	1.9×10^{-4}	8.6×10^{-4}	0.58	29	3.9×10^{-4}	6.8×10^{-4}

Chemical structures of dasatinib analog BODIPY probes and resultant thermodynamic (K_d) and kinetic (k_{on}, k_{off}) data for wt c-Src and wt-Abl.

Figure C.4. DAS-BODIPY and **DAS-DFGO-II-BODIPY** phospho-Src data.

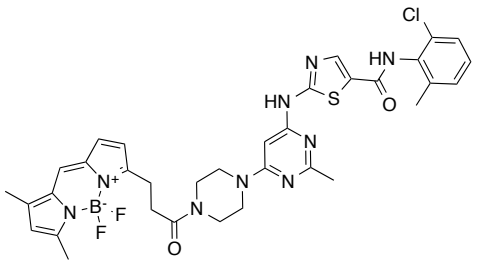

DAS-BODIPY

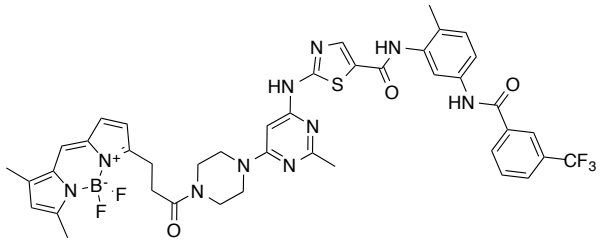

DAS-DFGO-II-BODIPY

c-Src K_d = 0.50 nM	c-Src~pY416 K_d = 0.70 nM
c-Src $t_{1/2}$ = 15 min	c-Src~pY416 $t_{1/2}$ = 23 min
c-Src k_{on} = 1.6×10^{-3} sec^{-1}	c-Src~pY416 k_{on} = 7.4×10^{-4} sec^{-1}
c-Src k_{off} = 7.9×10^{-4} sec^{-1}	c-Src~pY416 k_{off} = 5.2×10^{-4} sec^{-1}

c-Src K_d = 2.8 nM	c-Src~pY416 K_d = 3.0 nM
c-Src $t_{1/2}$ = 65 min	c-Src~pY416 $t_{1/2}$ = 78 min
c-Src k_{on} = 6.4×10^{-5} sec^{-1}	c-Src~pY416 k_{on} = 4.9×10^{-5} sec^{-1}
c-Src k_{off} = 1.8×10^{-4} sec^{-1}	c-Src~pY416 k_{off} = 1.5×10^{-4} sec^{-1}

Thermodynamic (K_d) and kinetic (k_{on}, k_{off}) data for wt c-Src and c-Src~pY416 for **DAS-** and **DAS-DFGO-II-BODIPY**.

Table C.3. Non-Thr gatekeeper kinases inhibited by DFG-out analog.

		K_d values	
target	**GK**	**dasatinib**	**DAS-DFGO-I**
FLT1	Val	5,000 nM	9.3 nM
RET	Val	730 nM	2.2 nM
TIE2	Ile	> 10,000 nM	160 nM

Table C.4. Kinases not inhibited by CHO analog.

	K_d values	
target	**dasatinib**	**DAS-CHO-I**
EPHB2	0.39 nM	17,000 nM
PDGFRA	0.47 nM	3,700 nM
TXK	2.1 nM	910 nM

Spectral Data for Dasatinib Analogs and Compounds 4.1–4.16

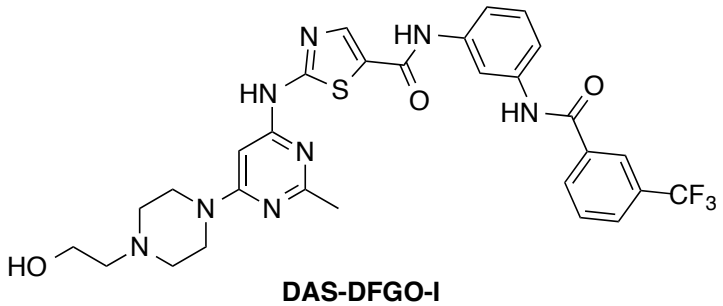

DAS-DFGO-I

DAS-DFGO-I ^{1}H:

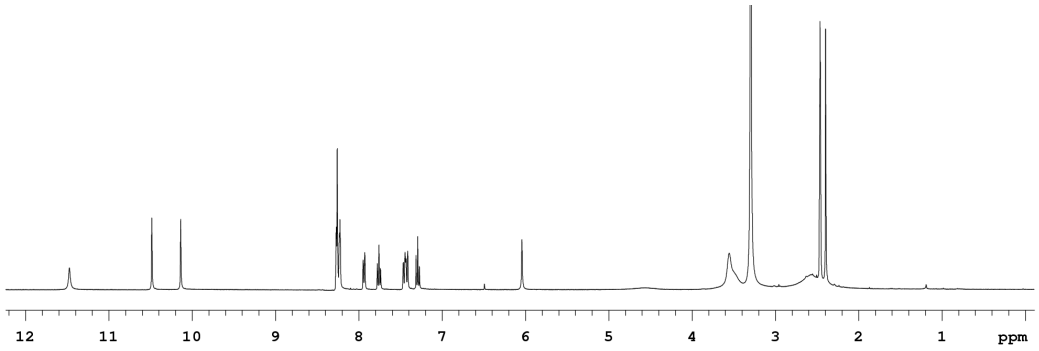

DAS-DFGO-I ^{19}F:

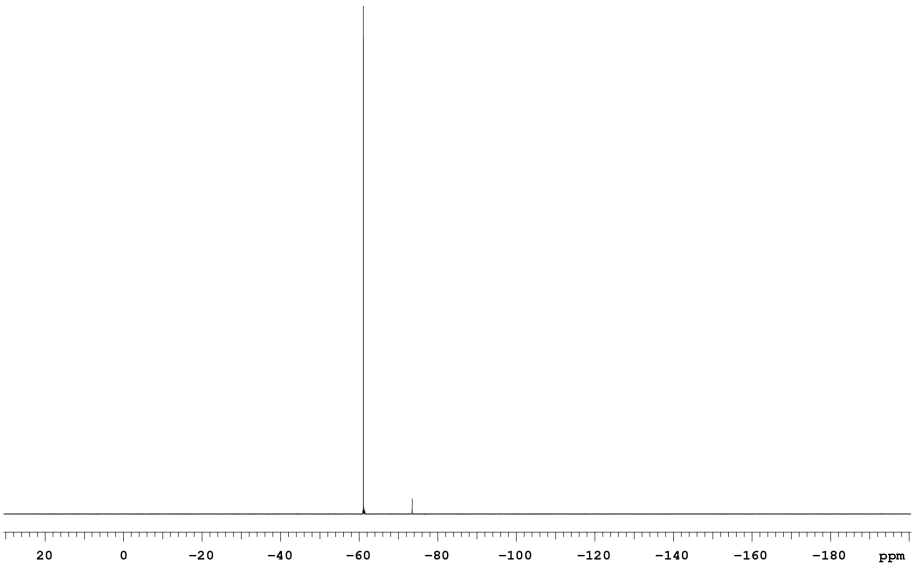

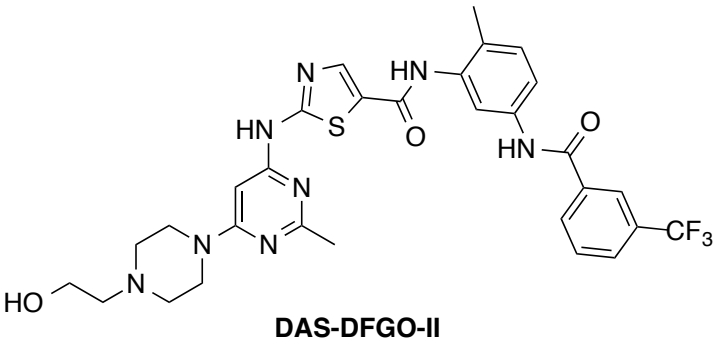

DAS-DFGO-II

DAS-DFGO-II ^{1}H:

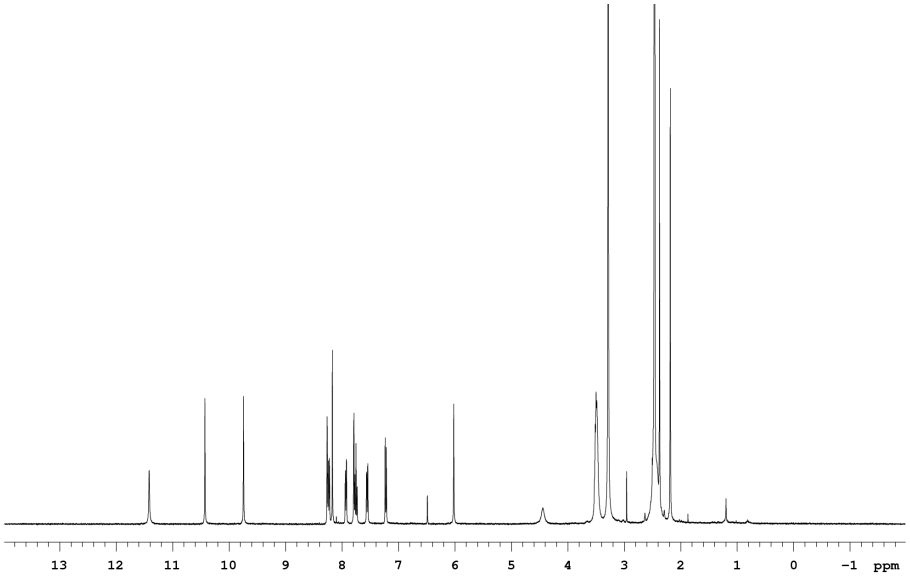

DAS-DFGO-II ^{19}F:

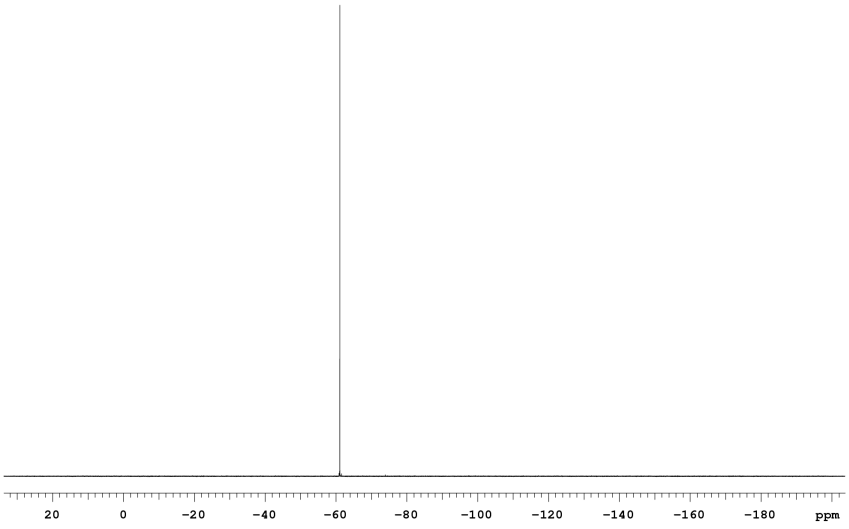

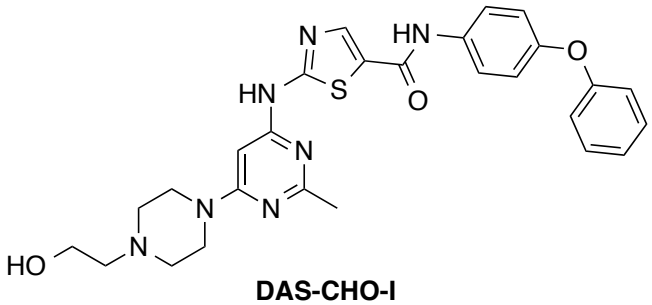

DAS-CHO-I

DAS-CHO-I ^{1}H:

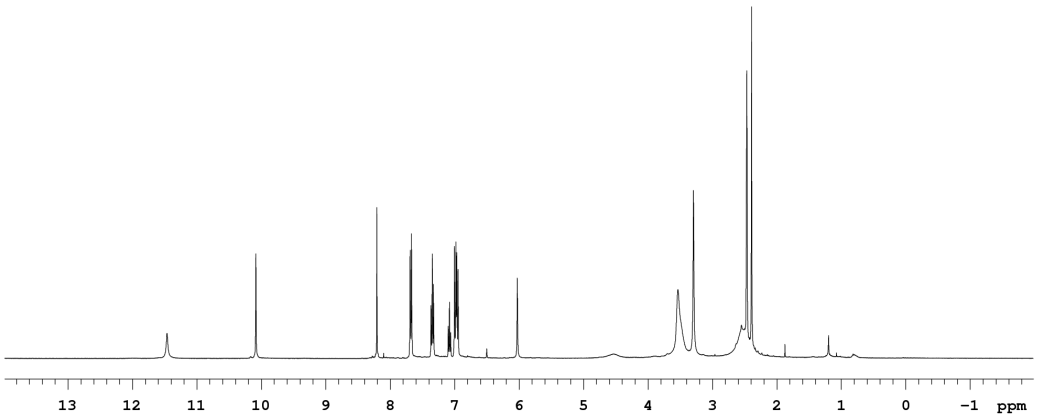

DAS-CHO-I ^{13}C:

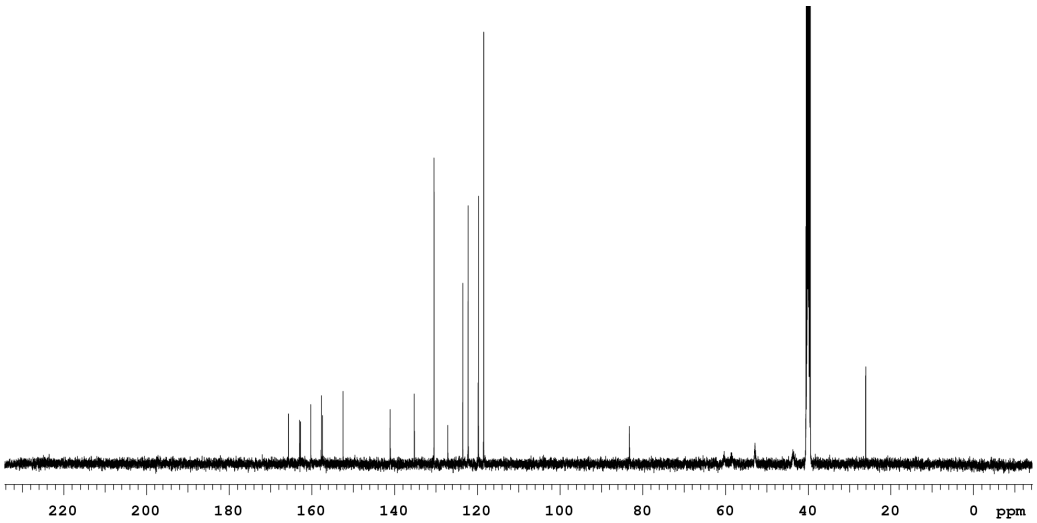

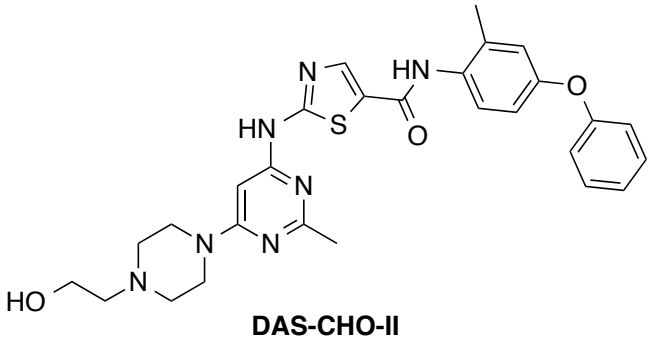

DAS-CHO-II

DAS-CHO-II ^{1}H:

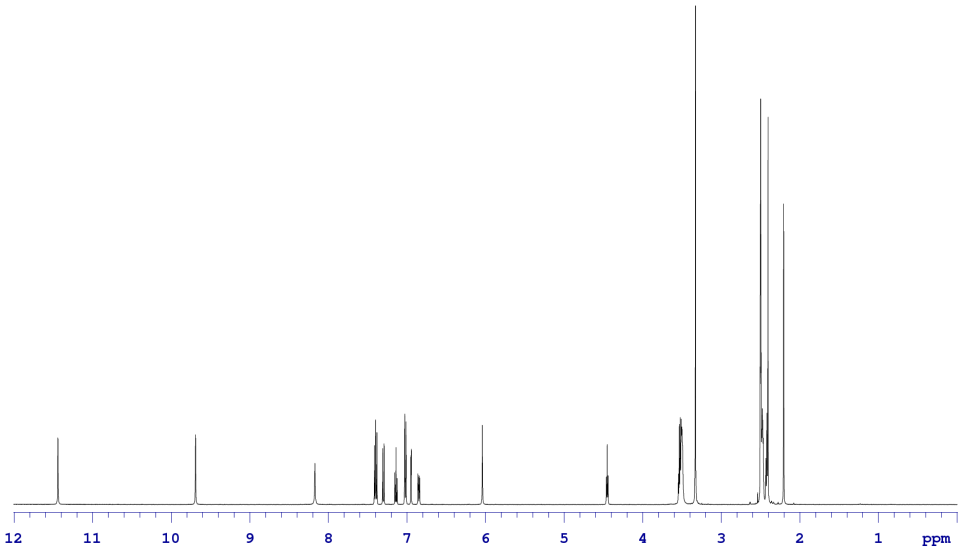

DAS-CHO-II ^{13}C:

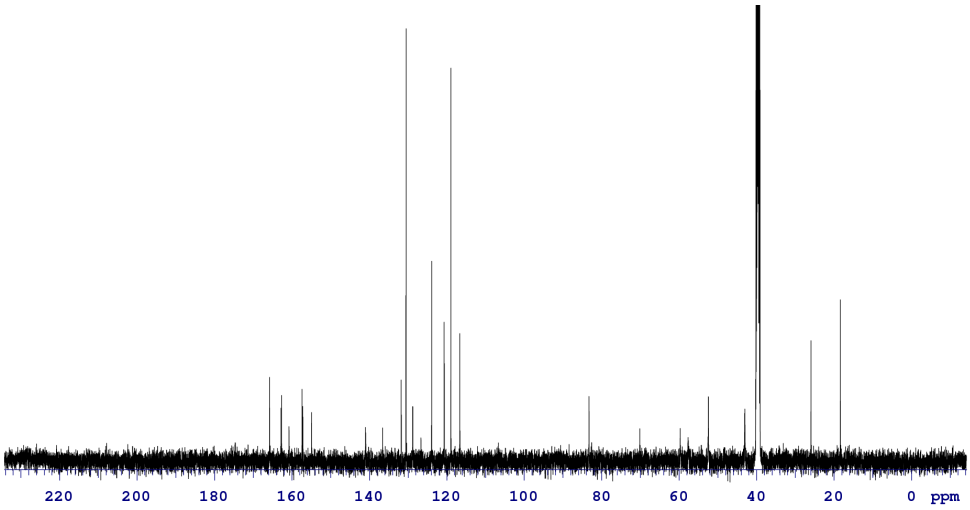

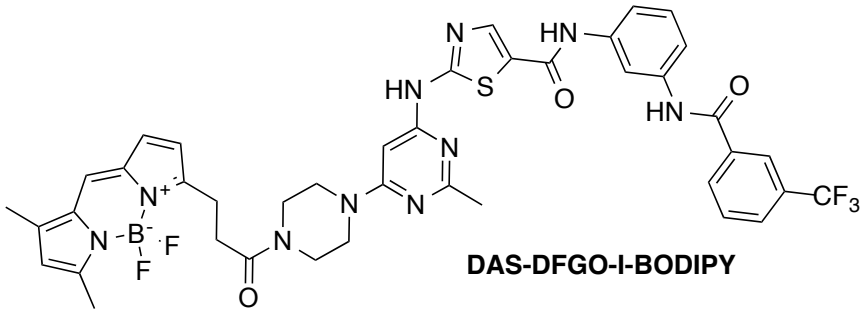

DAS-DFGO-I-BODIPY

DAS-DFGO-I-BODIPY ^{1}H:

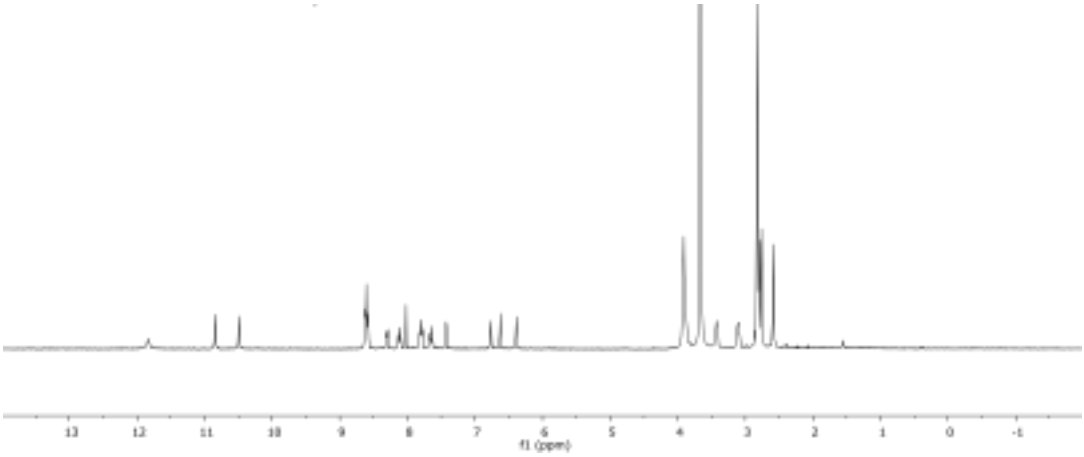

DAS-DFGO-I-BODIPY ^{19}F:

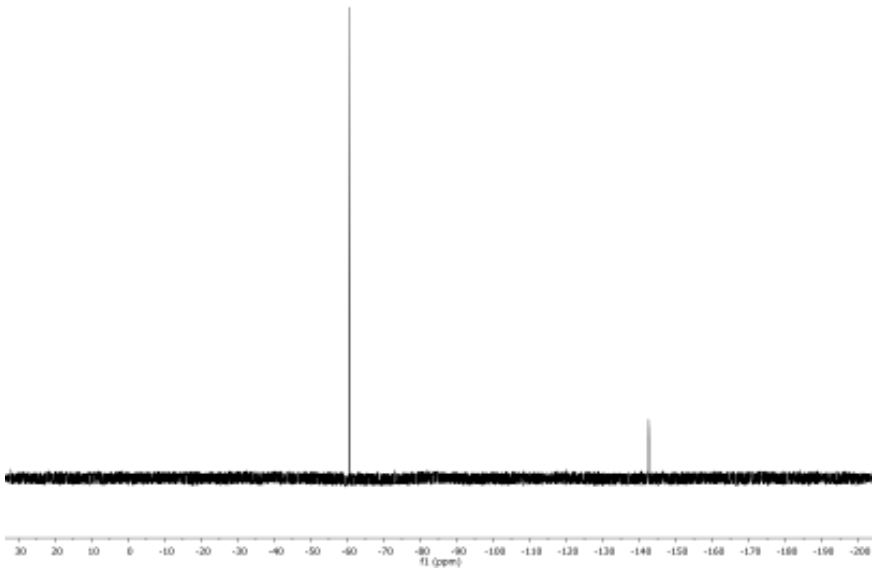

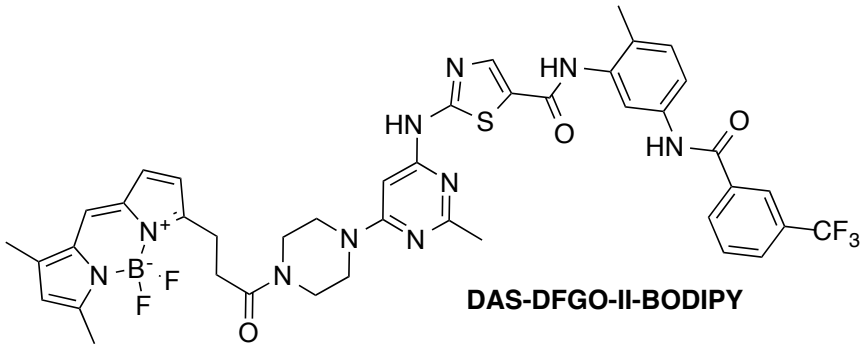

DAS-DFGO-II-BODIPY

DAS-DFGO-II-BODIPY ^{1}H:

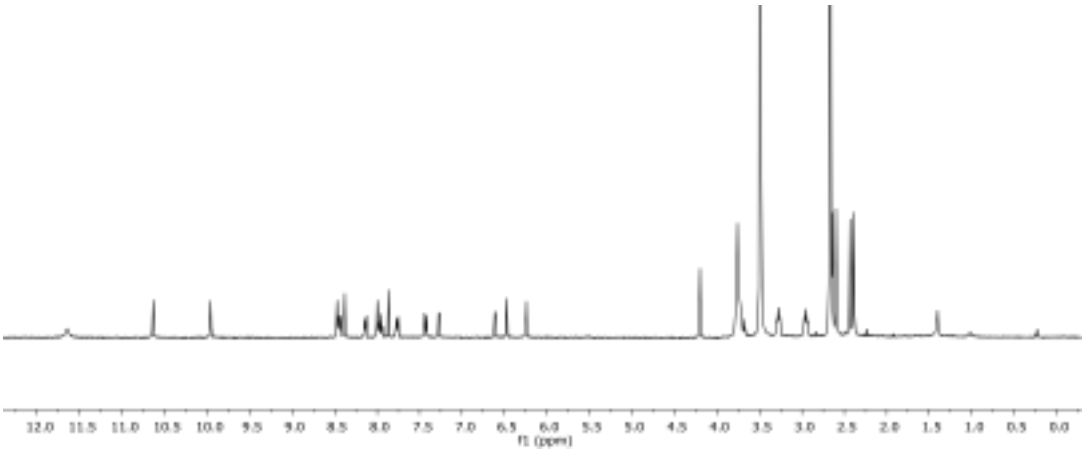

DAS-DFGO-II-BODIPY ^{19}F:

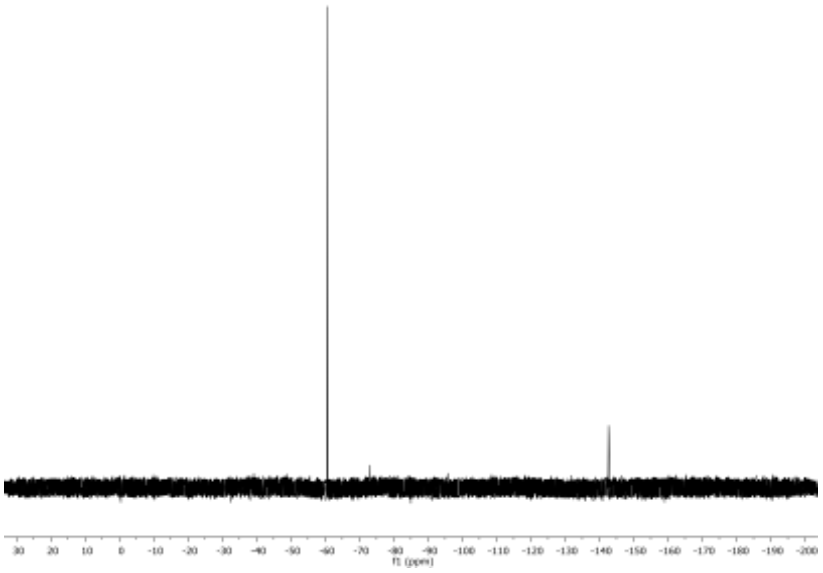

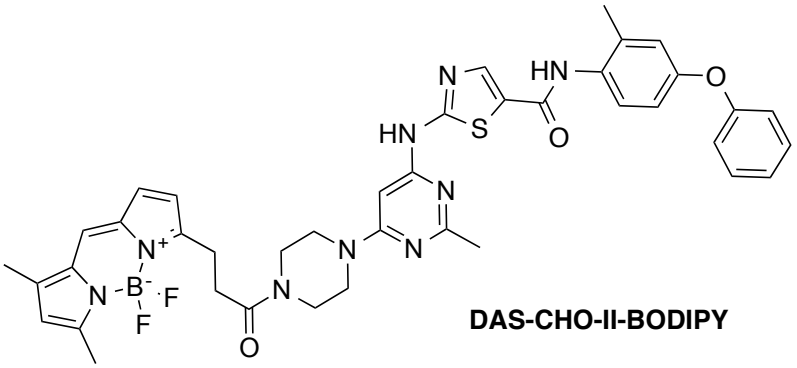

DAS-CHO-II-BODIPY

DAS-CHO-II-BODIPY ^{1}H:

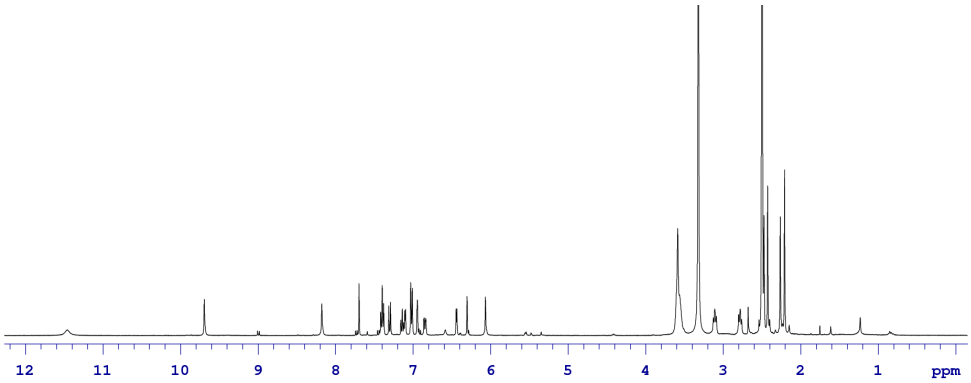

DAS-CHO-II-BODIPY ^{19}F:

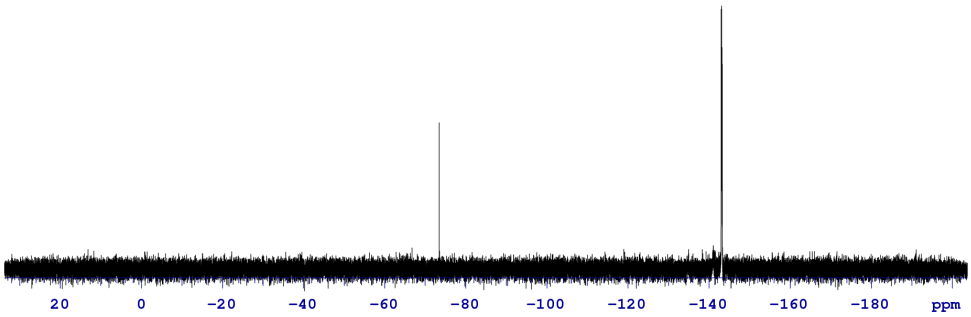

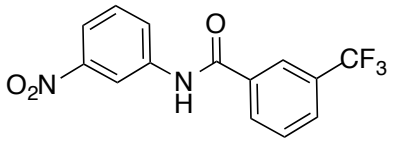

4.1

4.1 ^{1}H:

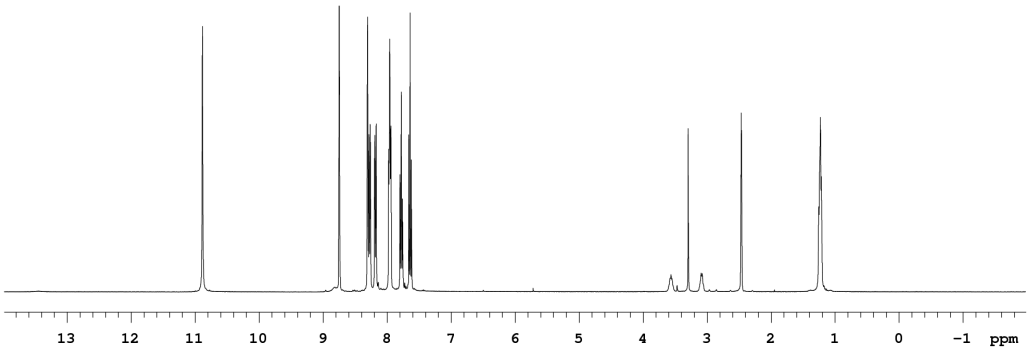

4.1 ^{19}F:

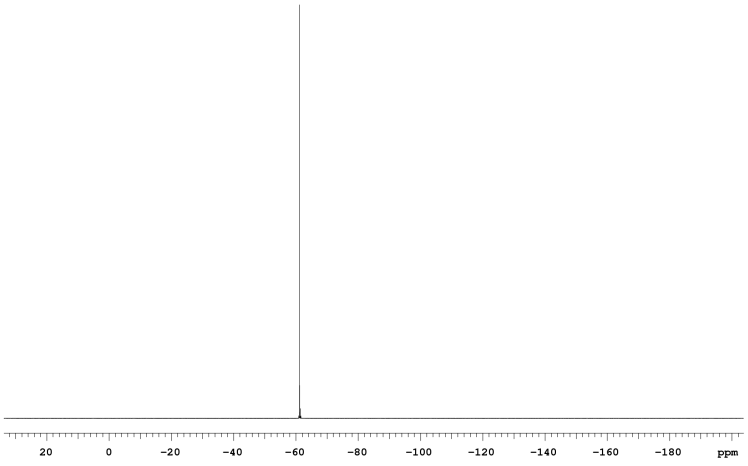

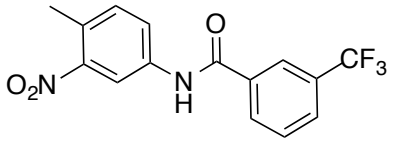

4.2

4.2 ^{1}H:

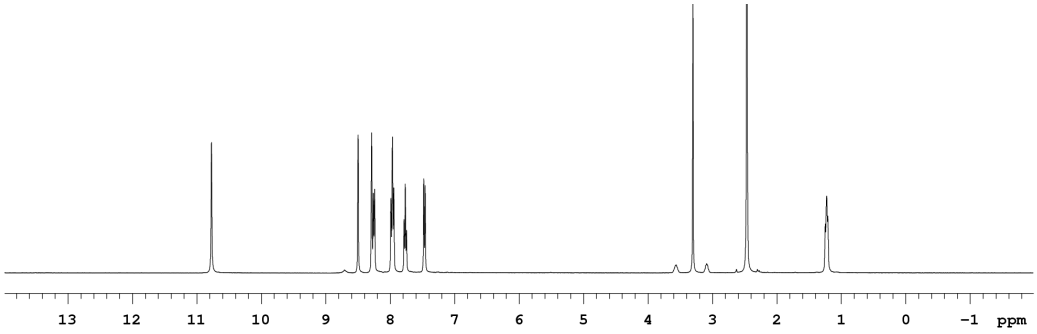

4.2 ^{19}F:

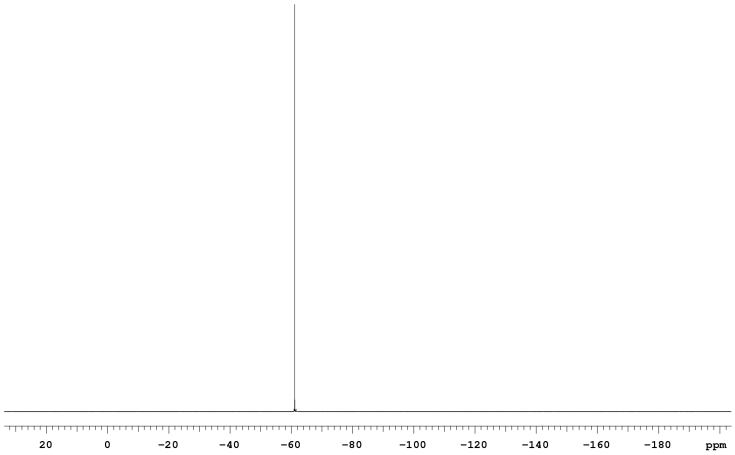

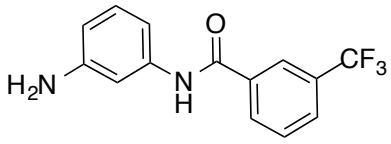

4.3

4.3 ^{1}H:

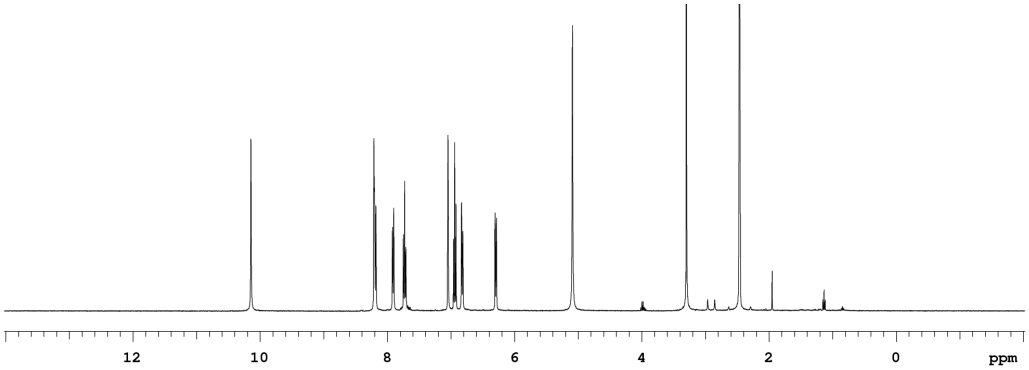

4.3 ^{19}F:

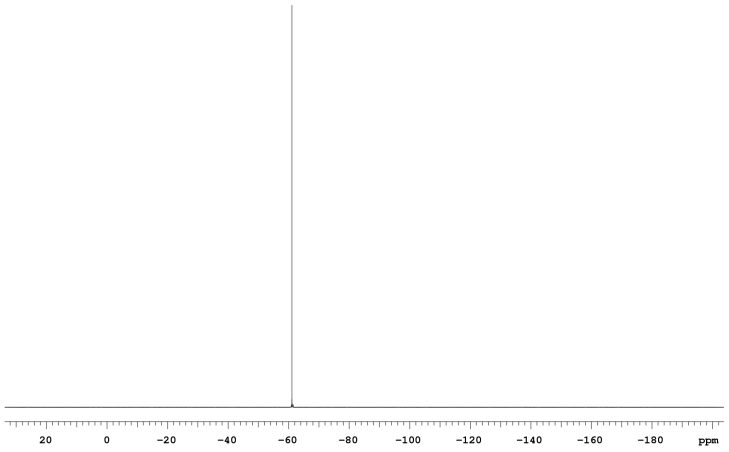

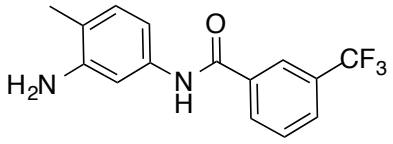

4.4

4.4 ^{1}H:

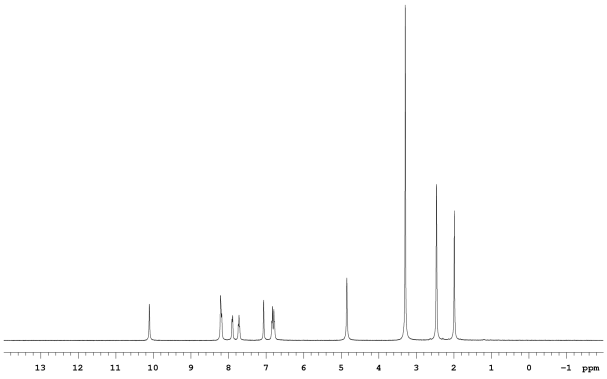

4.4 ^{19}F:

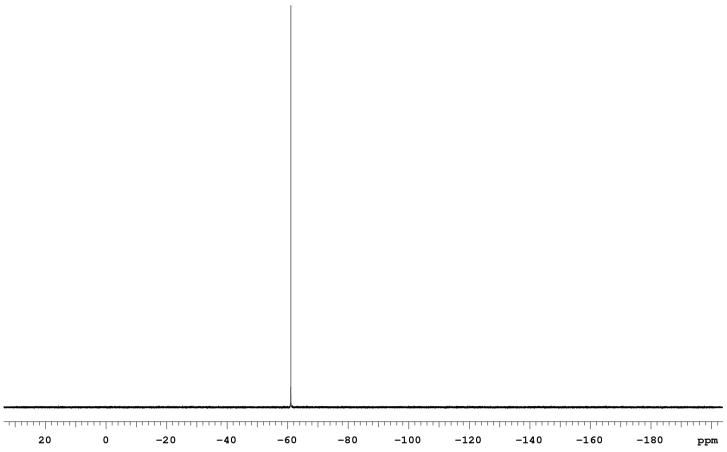

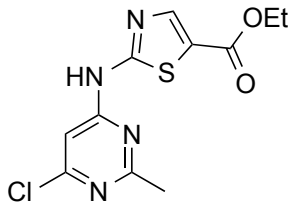

4.6

4.6 ^{1}H:

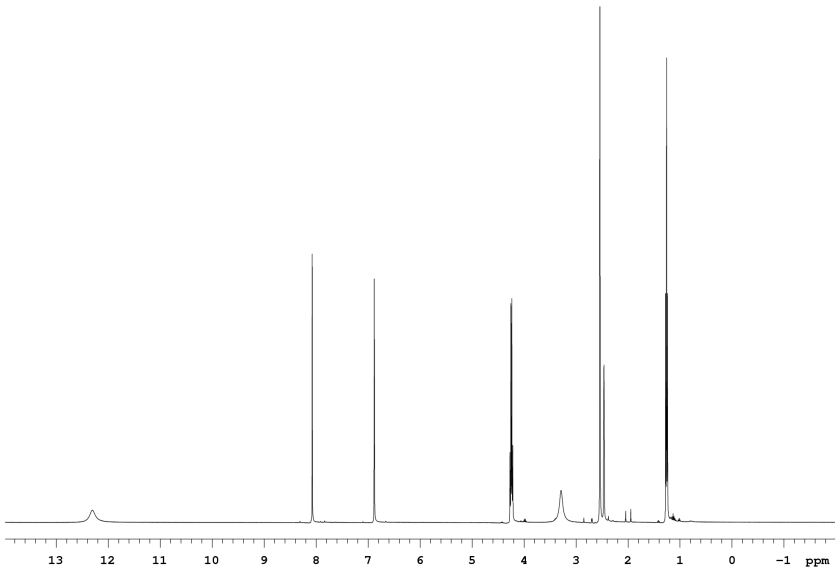

4.6 ^{13}C:

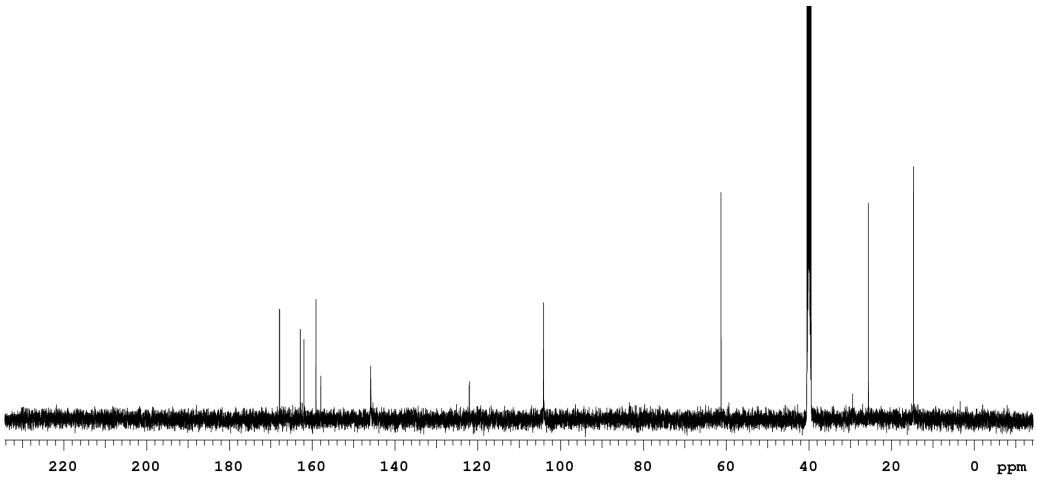

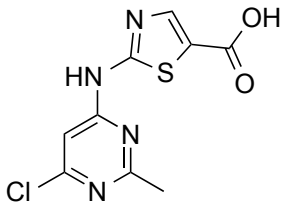

4.7

4.7 ^{1}H:

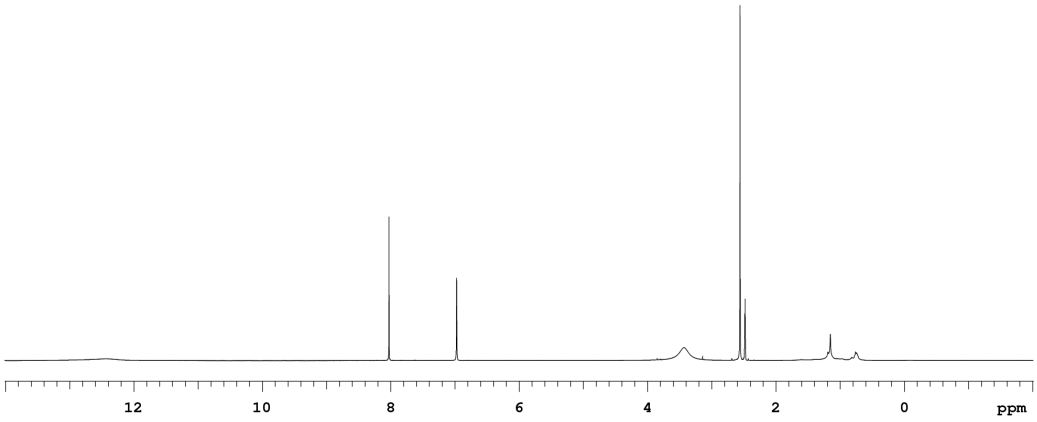

4.7 ^{13}C:

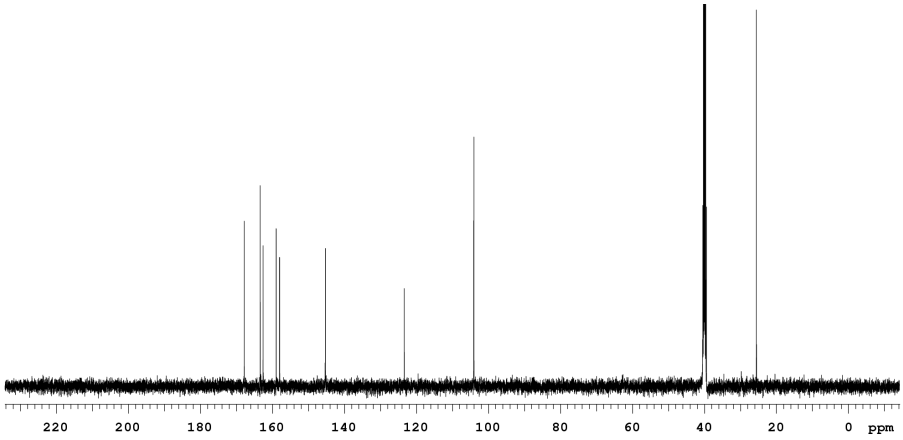

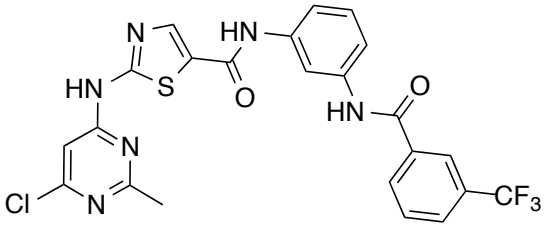

4.8

4.8 ^{1}H:

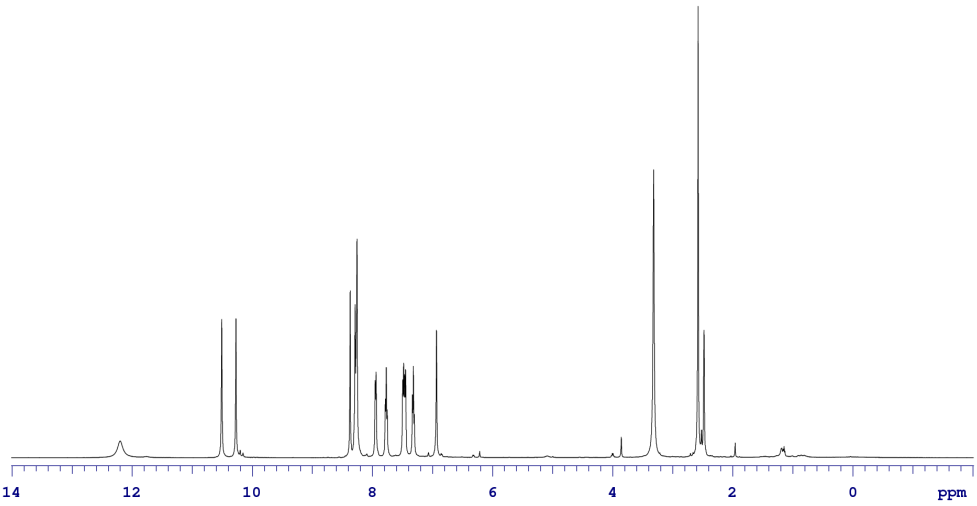

4.8 ^{19}F:

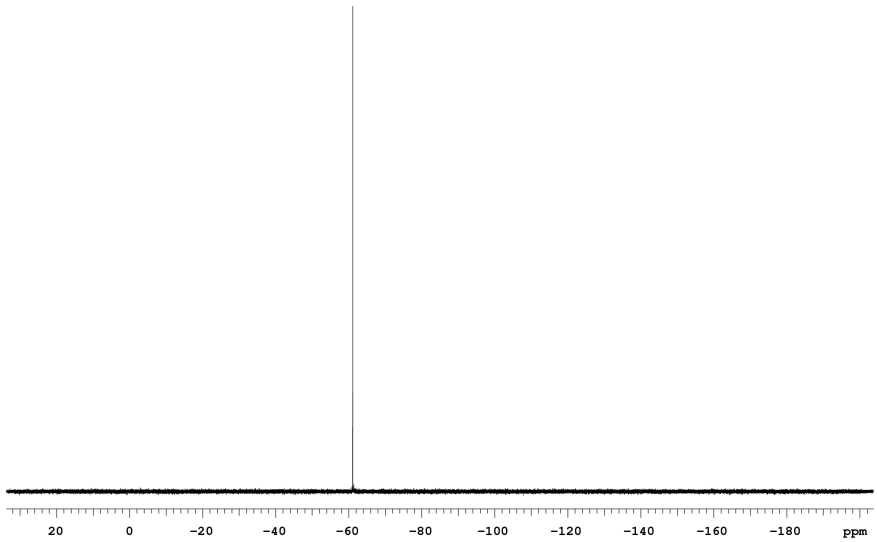

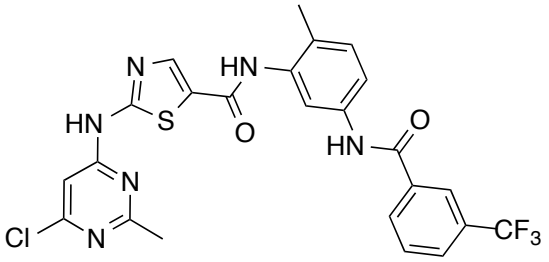

4.9

4.9 ^{1}H:

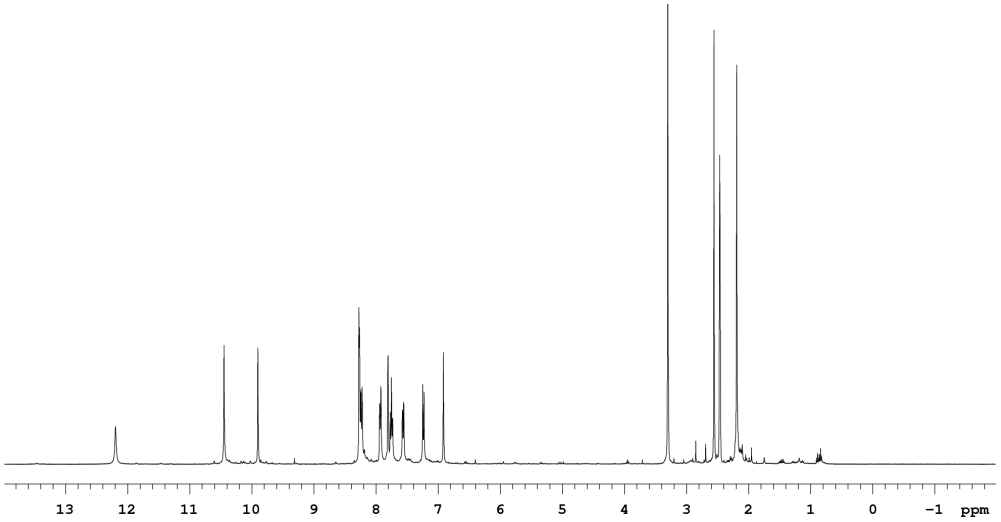

4.9 ^{19}F:

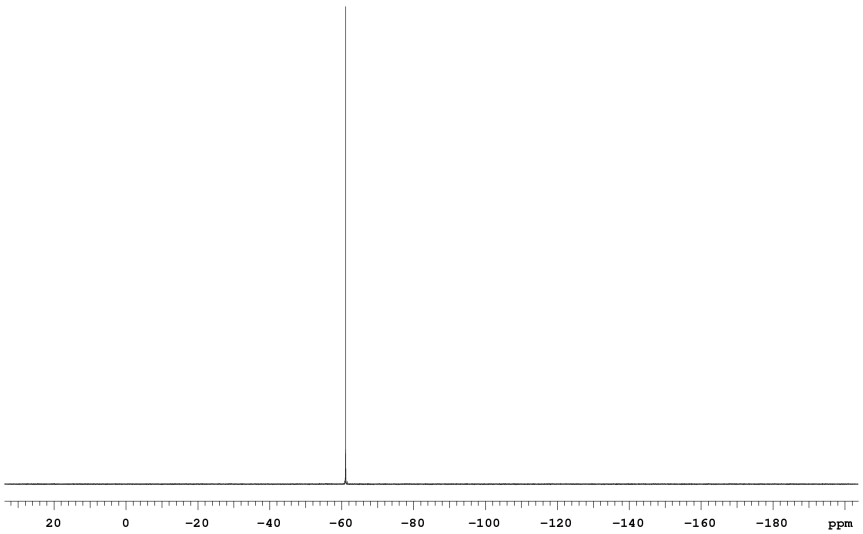

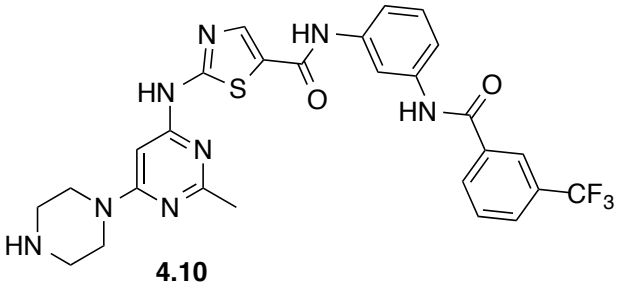

4.10

4.10 ^{1}H:

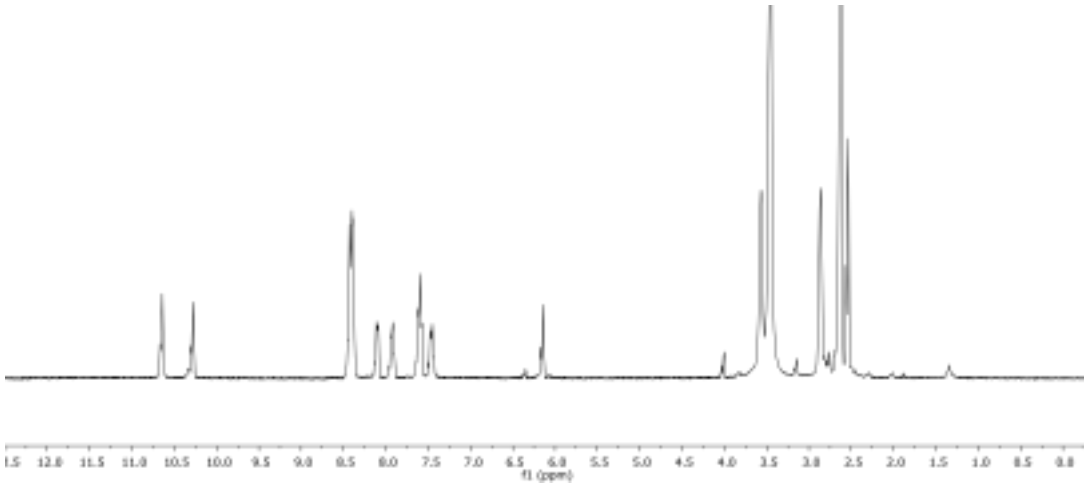

4.10 ^{19}F:

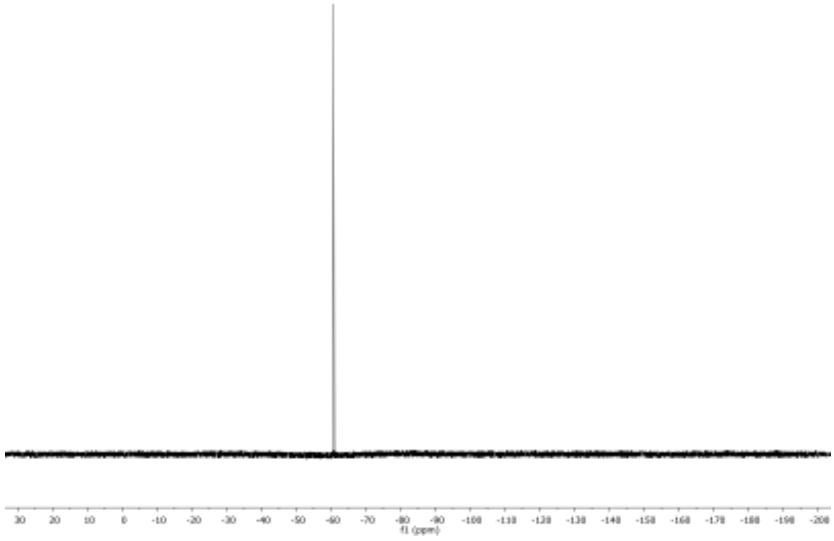

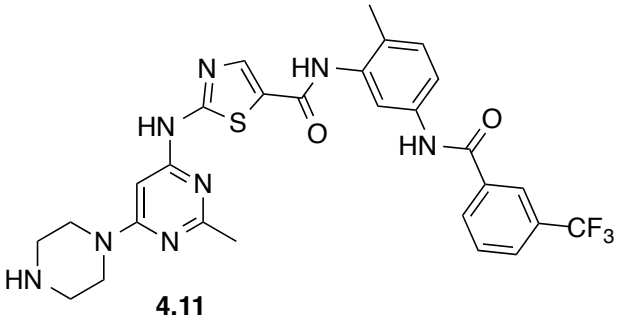

4.11

4.11 ^{1}H:

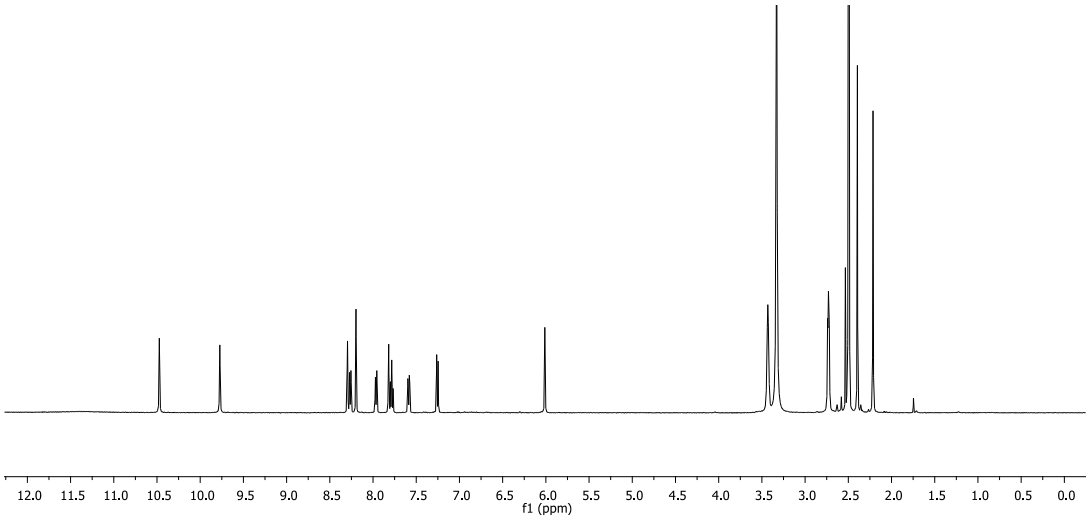

4.11 ^{19}F:

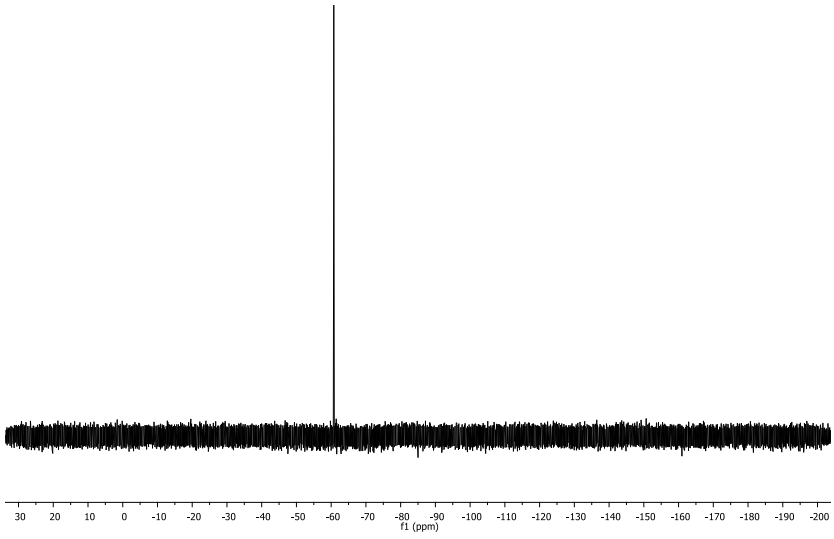

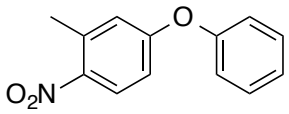

4.12

4.12 ^{1}H:

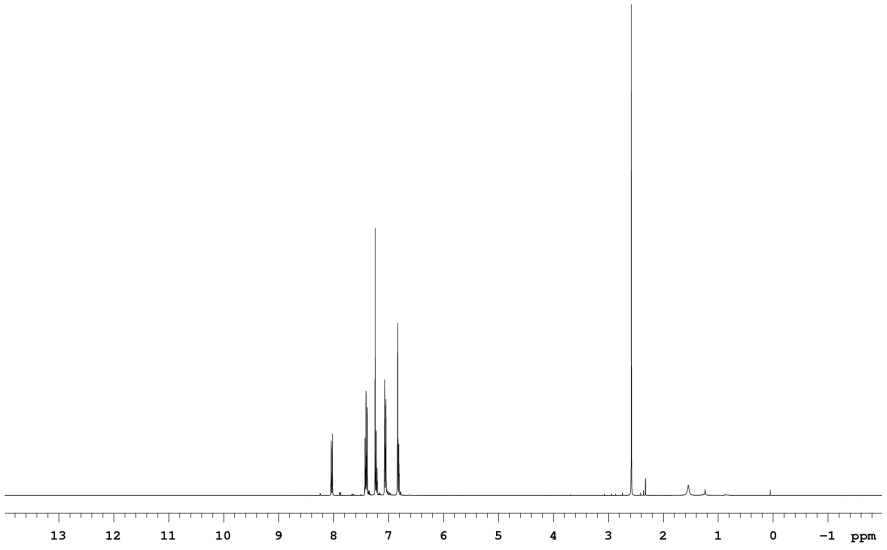

4.12 ^{13}C:

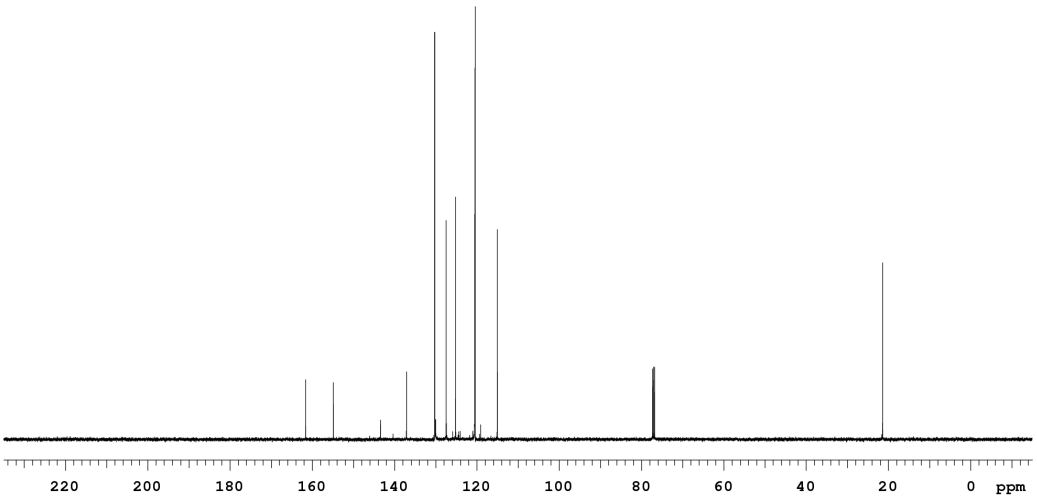

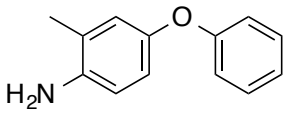

4.13

4.13 ^{1}H:

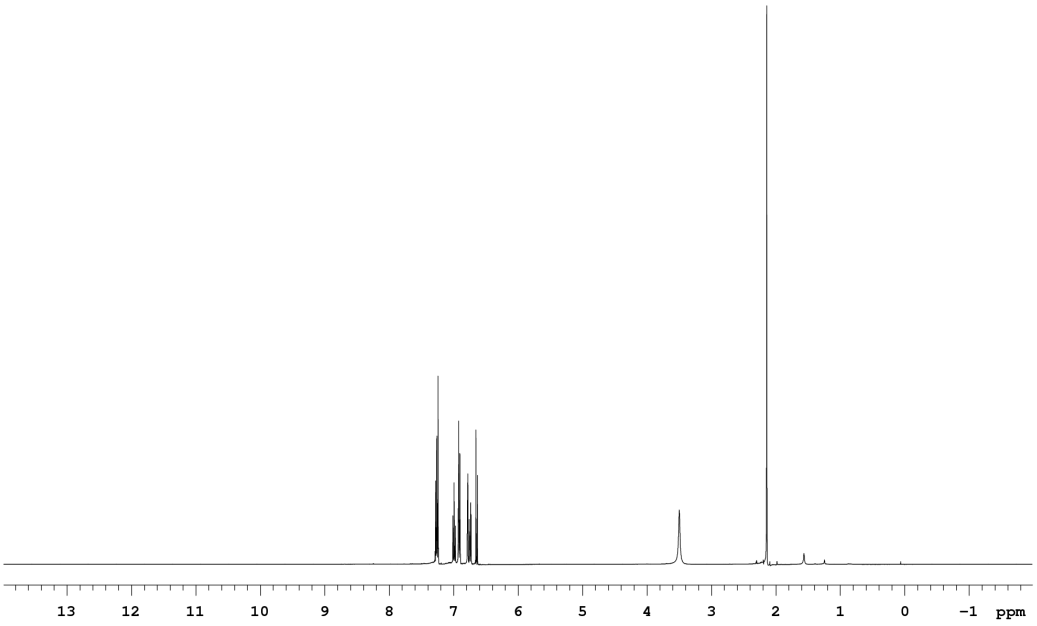

4.13 ^{13}C:

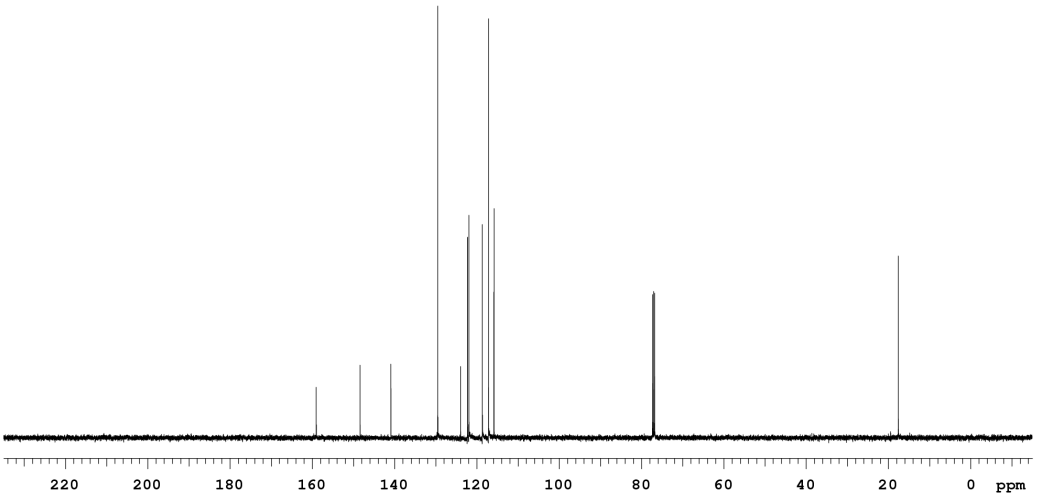

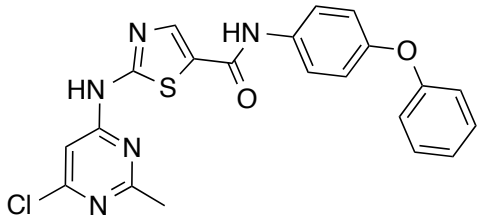

4.14

4.14 ^{1}H:

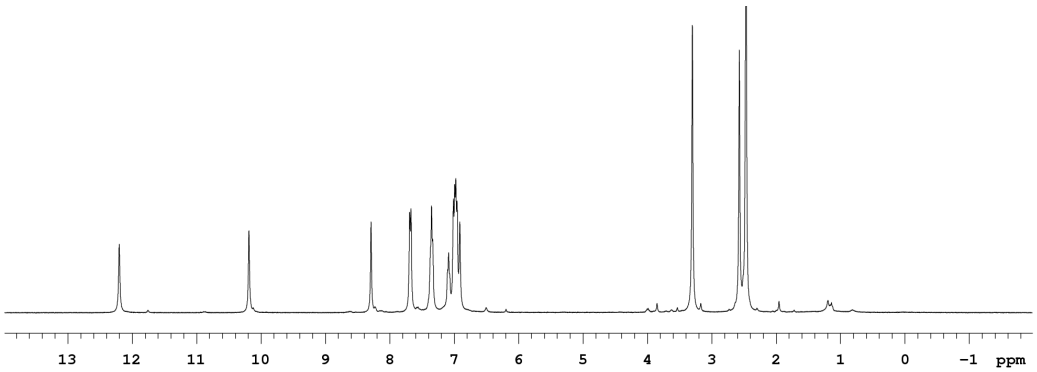

4.14 ^{13}C:

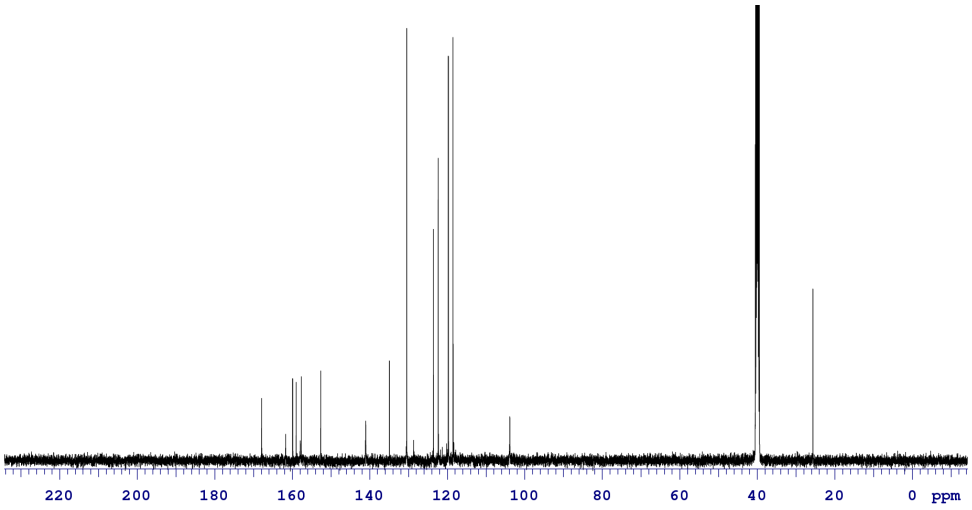

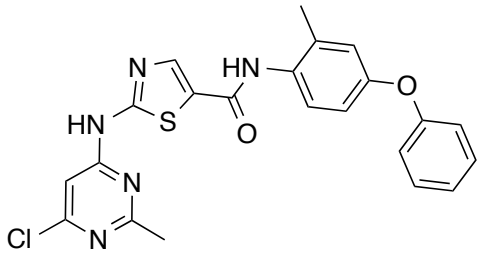

4.15

4.15 ^{1}H:

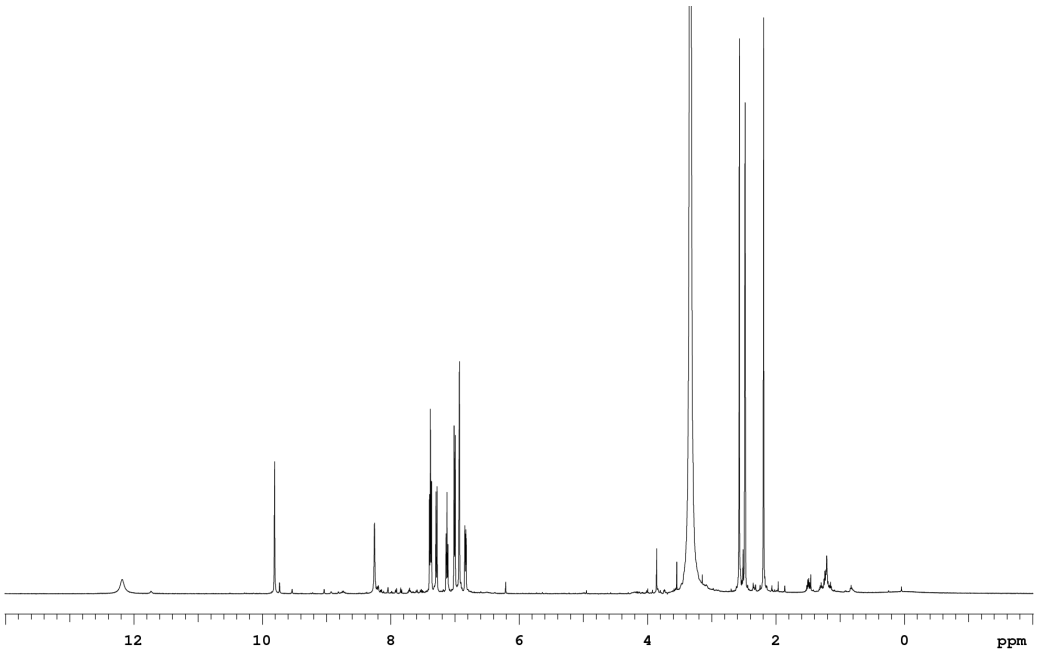

4.15 ^{13}C:

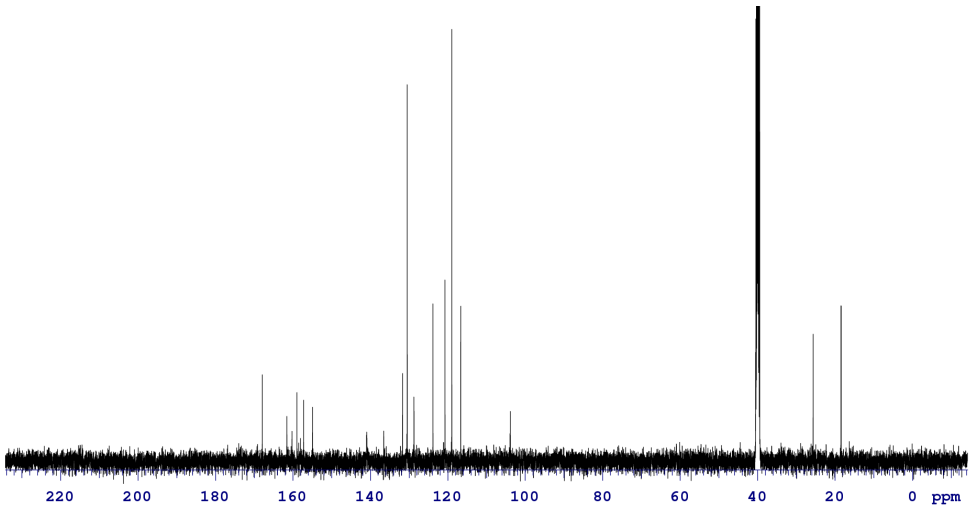

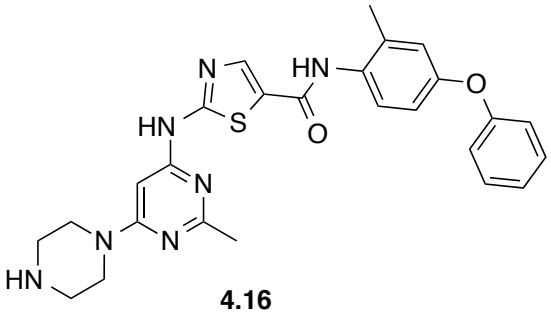

4.16

4.16 ^{1}H:

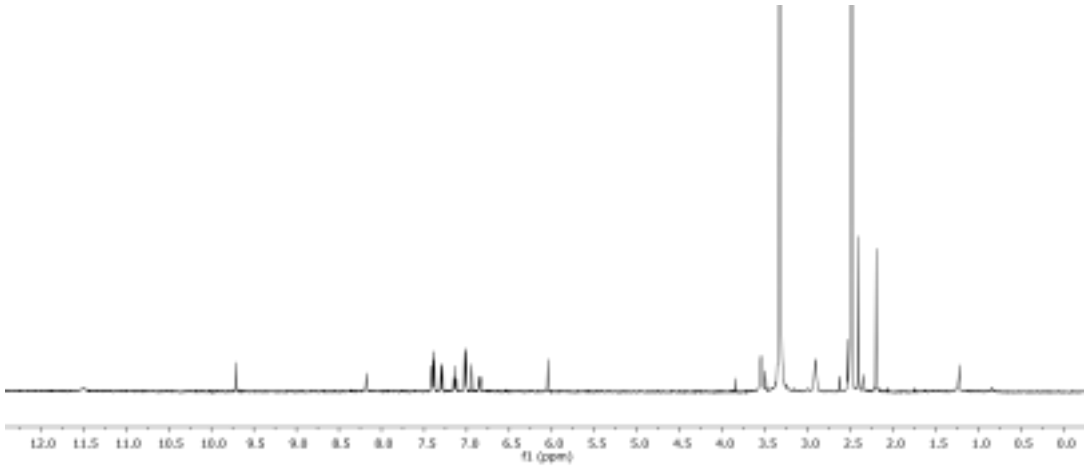

4.16 ^{13}C:

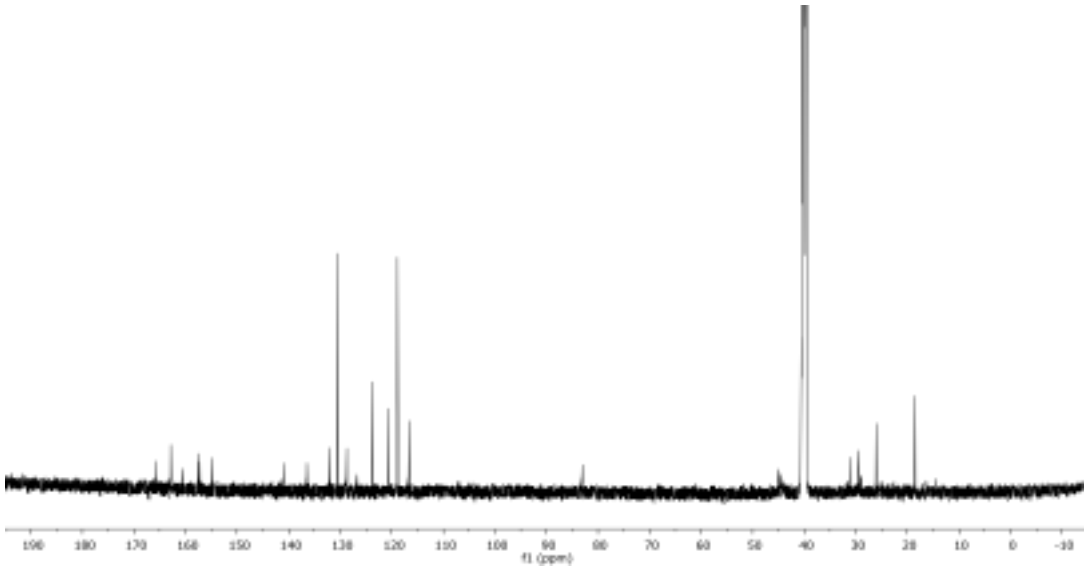

Data Collection and Phasing Statistics

	Src–**DAS-DFGO-I** complex	Src–**DAS-CHO-I** complex	Abl–**DAS-CHO-I** complex
PDB ID	4YBJ	4YBK	4YC8
space group	p2(1)	p2(1)2(1)2(1)	p2(1)2(1)2
unit cell	a = 42.12 b = 120.06 c = 63.32 α= 90.00° β= 90.26° γ = 90.00°	a = 41.33 b = 62.21 c = 102.80 α= 90.00° β= 90.00° γ = 90.00°	a = 112.77 b = 127.10 c = 57.17 α= 90.00° β = 90.00° γ = 90.00°
wavelength (Å)	0.9787	0.9787	0.9793
molecules per asymmeric unit	2	1	2
resolution (Å)[i]	43.56–2.61 (2.61–2.66)	39.62–2.50 (2.50–2.56)	47.32–2.90 (2.90–2.95)
R_{sym} (%)[ii]	7.4 (41.4)	7.4 (41.4)	10.0 (49.3)
total reflections	145715	9990	134144
<I/σI>[iii]	20 (5.21)	20 (3)	20 (3)
completeness (%)[iv]	99.9 (99.9)	99.8 (100)	99.9 (99.8)
redundacy	7.6 (7.3)	12.9 (13.4)	7.1 (7.1)
Refinement Statistics			
Rwork (%)[v]	21.83	20.62	19.60
Rfree (%)[vi]	25.00	25.17	24.00
protein atoms	3937	2099	4073
ligand atoms	212	119	208
water molecules	64	51	11
unique reflections	19137	9952	17477
correlation coefficient	0.91	0.92	0.91
Rm.s.d[vii]			
bond length (Å)	0.0081	0.0082	0.010
bond angle (deg)	0.91	0.97	1.04
ramachandran plot			
preferred (%)	97.98	98.09	95.71
allowed (%)	1.82	1.91	4.29
outliers (%)	0.20	0.00	0.00
MolProbity Score[21]	0.85	0.95	1.46
Clash Score[21]	1.28	1.9	3.76
average Bfactor (Å^2)	43.0	28.0	35.0
RSRZ[12] {A/B/all}	-0.13/0.06/-0.03	-0.06	-0.37/-0.08/-0.22
Ligand Statistics			
Real-space R-value, RSR (A/B)	0.24/0.22	0.21	0.17/0.19
Real-space Correlation Coefficient, % (A/B)	88.0/90.6	89.8	94.8/94.0

[i]Statistics for highest resolution bin of reflections in parentheses.

[ii]Rsym =ΣhΣj l Ihj-<Ih> l /ΣhΣjIhj, where Ihj is the intensity of observation j of reflection h and <Ih> is the mean intensity for multiply recorded reflections.

[iii]Intensity signal-to-noise ratio.

[iv]Completeness of the unique diffraction data.

[v]R-factor = Σh I IFoI – IFcI I / ΣhIFoI, where Fo and Fc are the observed and calculated structure factor amplitudes for reflection h.

[vi]Rfree is calculated against a 10% random sampling of the reflections that were removed before structure refinement.

[vii]Root mean square deviation of bond lengths and bond angles.

Electron Density Maps

DAS-DFGO-I bound to c-Src:

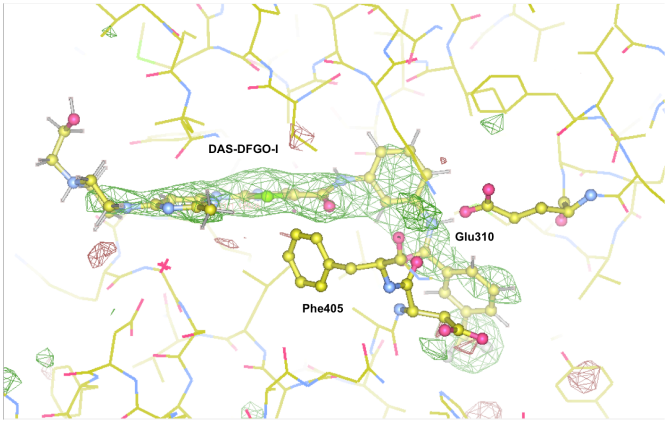

Difference electron density (Fo-Fc, green) inhibitor omit map for the Src–**DAS-DFGO-I** cocrystal structure contoured at 3σ.

DAS-CHO-I bound to c-Src:

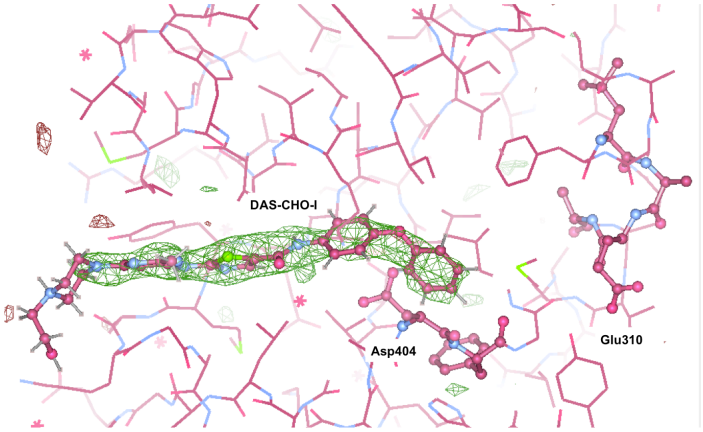

Difference electron density (Fo-Fc, green) inhibitor omit map for the Src–**DAS-CHO-I** cocrystal structure contoured at 3σ.

DAS-CHO-I bound to c-Abl:

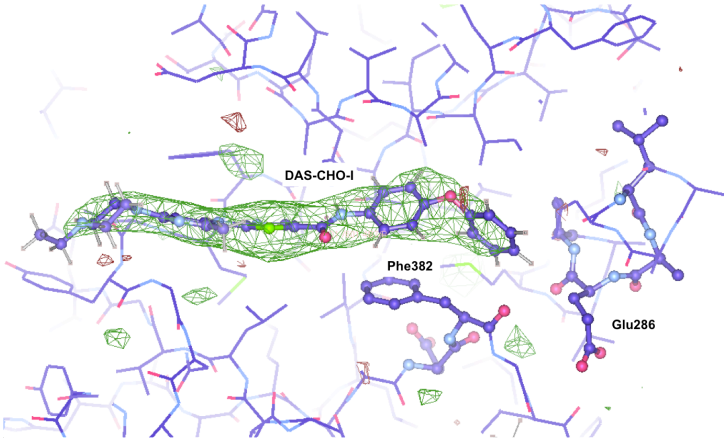

Difference electron density (Fo-Fc, green) inhibitor omit map for the Abl–**DAS-CHO-I** cocrystal structure contoured at 3σ.

Biochemical Characterization

Analytical data summary for wt c-Src, wt c-Abl, P~wt c-Abl & T315I c-Abl determination with each inhibitor.

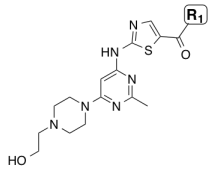

Binding Mode: active | inactive: DFG-out | inactive: C-Helix-out

R_1 =

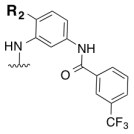

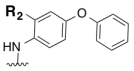

inhibitor	R_1	R_2	c-Src K_d, nM	c-Abl K_d, nM	P~c-Abl K_d, nM	T315I c-Abl K_d, nM
dasatinib	active	Me	0.07	0.03	0.05	890
DAS-DFGO-I	DFG-out	H	0.53	2.2	1.8	>40000
DAS-DFGO-II	DFG-out	Me	2.7	3.0	2.0	66
DAS-CHO-I	CHO	H	15	14	46	>1000
DAS-CHO-II	CHO	Me	1.7	0.32	0.71	>1000

Representative Binding Curves for dasatinib analogs from KINOMEscan:

wt c-Src Values:

dasatinib, K_d = 0.074 nM

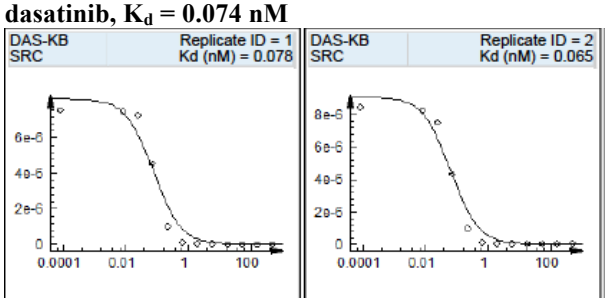

DAS-DFGO-I, K_d = 0.53 nM

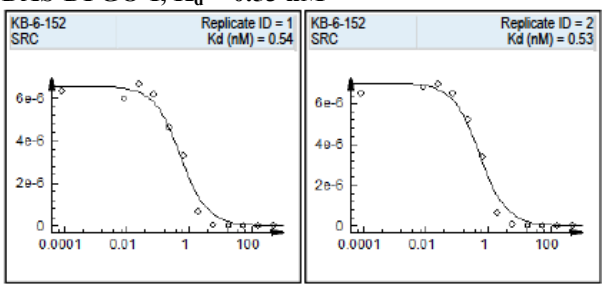

DAS-DFGO-II, K_d = 2.7 nM

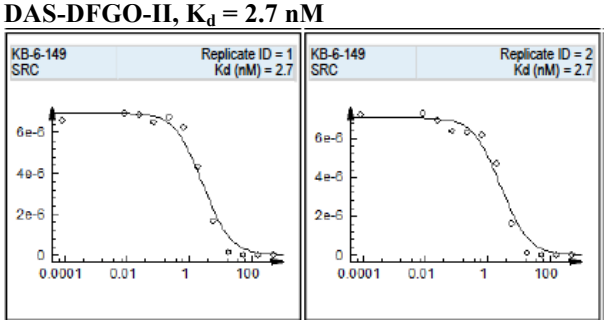

DAS-CHO-I, K_d = 15 nM

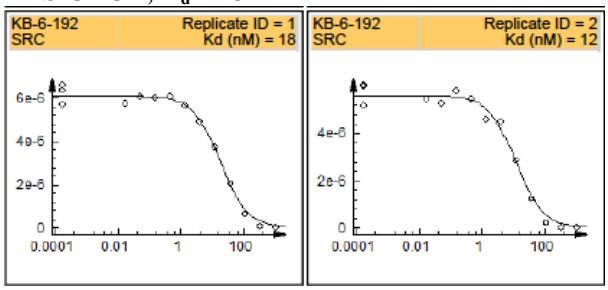

DAS-CHO-II, K_d = 1.7 nM

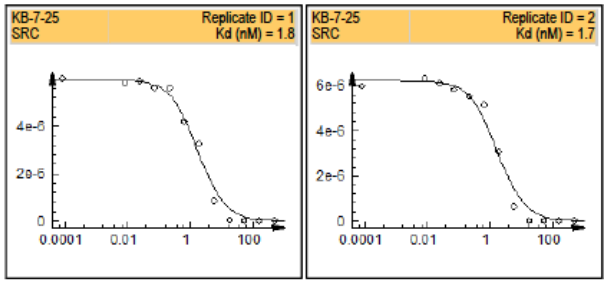

wt c-Abl Values (non-phosphorylated):

dasatinib (Davis et al., 2011)**, K_d = 0.03 nM**

DAS-DFGO-I, K_d = 2.2 nM

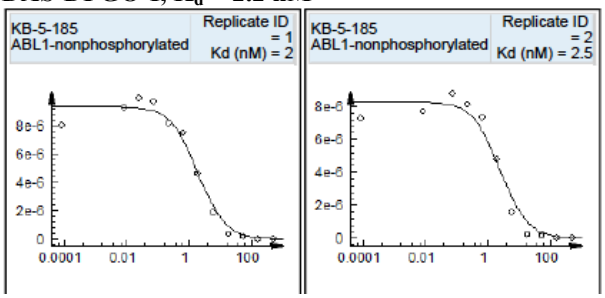

DAS-DFGO-II, K_d = 2.9 nM

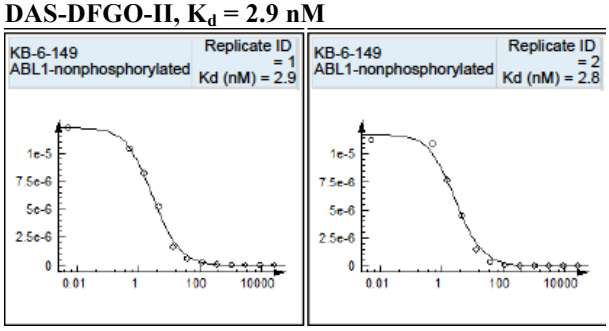

DAS-CHO-I, K_d = 14 nM

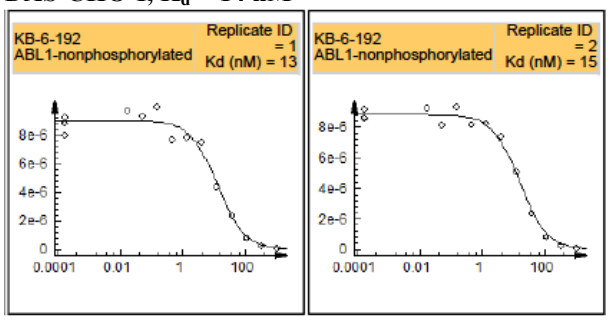

DAS-CHO-II, K_d = 0.32 nM

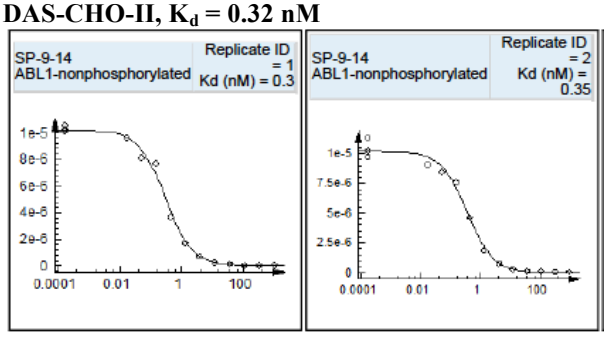

wt c-Abl Values (phosphorylated):

dasatinib (Davis et al., 2011)**, K_d = 0.05 nM**

DAS-DFGO-I, K_d = 1.8 nM

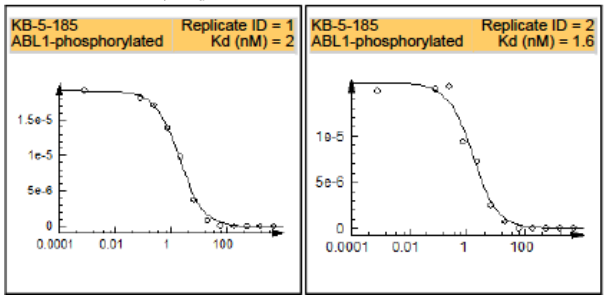

DAS-DFGO-II, K_d = 2 nM

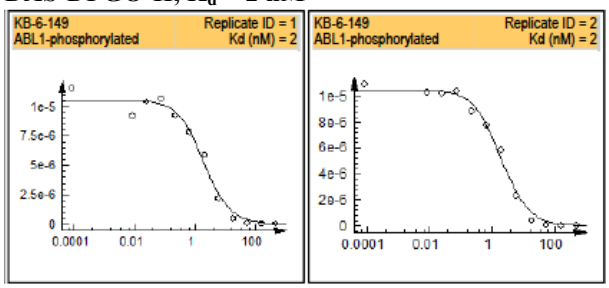

DAS-CHO-I, K_d = 46 nM

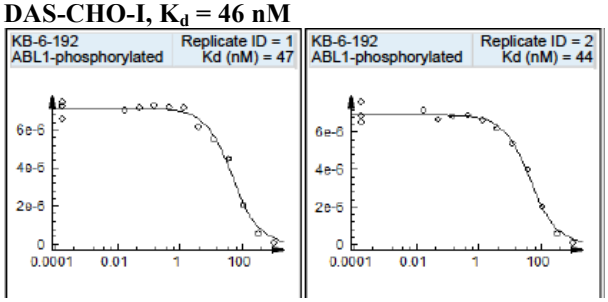

DAS-CHO-II, K_d = 0.71 nM

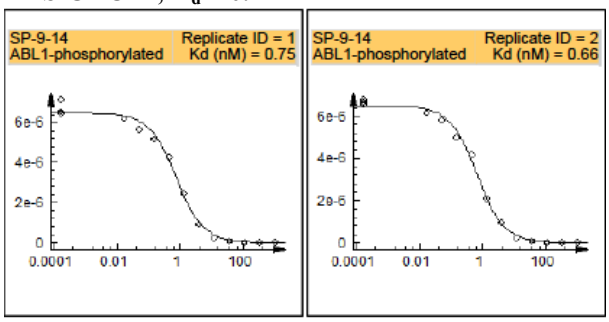

T315I c-Abl Values (non-phosphorylated):

Dasatinib (Davis et al., 2011)**, K_d = 890 nM**

DAS-DFGO-I, K_d > 40000 nM

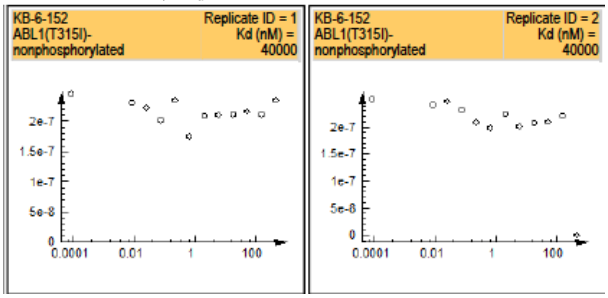

DAS-DFGO-II, K_d = 66 nM

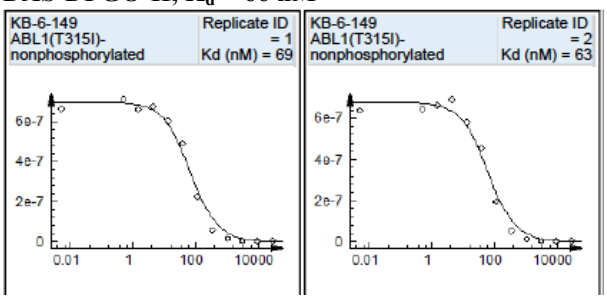

DAS-CHO-I, K_d > 1000 nM

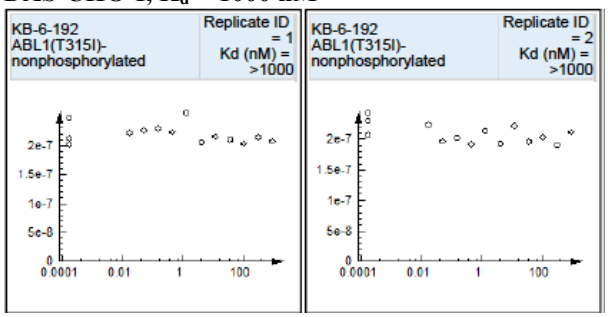

DAS-CHO-II, K_d > 1000 nM

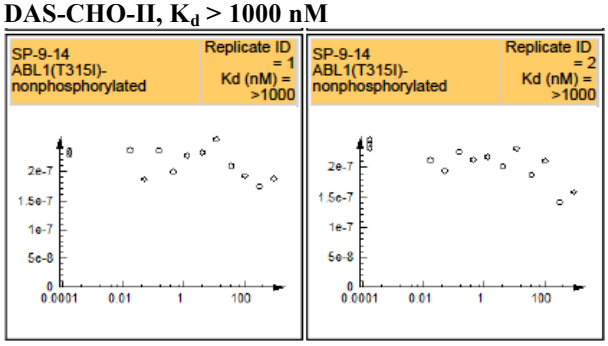

FLT1 Values:

Dasatinib (Davis et al., 2011)**, K_d = 5,000 nM**

DAS-DFGO-I, K_d = 9.3 nM

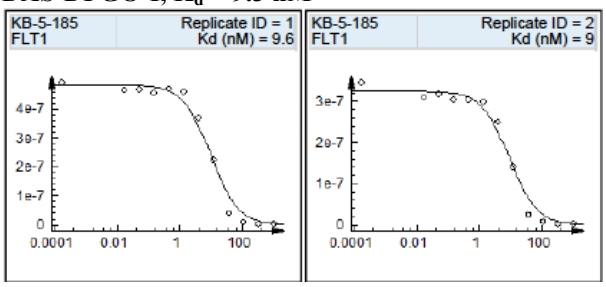

RET Values:

Dasatinib (Davis et al., 2011)**, K_d = 730 nM**

DAS-DFGO-I, K_d = 2.2 nM

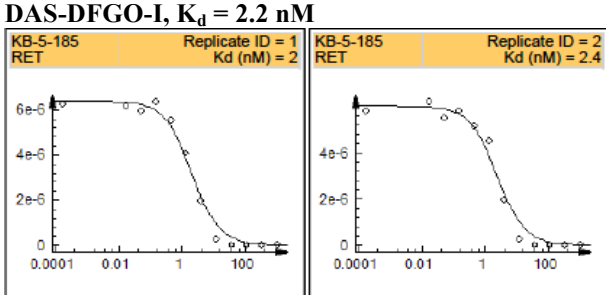

TIE2 Values:

Dasatinib (Davis et al., 2011)**, K_d > 10,000 nM**

DAS-DFGO-I, K_d = 160 nM

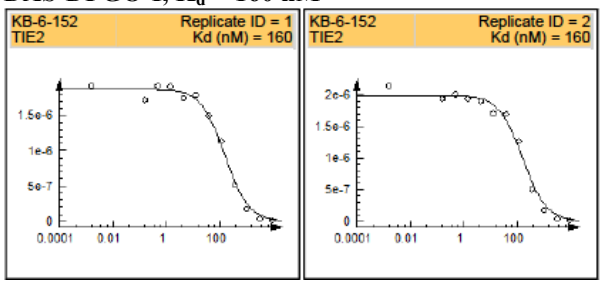

EPHB2 Values:

Dasatinib (Davis et al., 2011)**, K_d = 0.39 nM**

DAS-CHO-I, K_d = 17,000 nM

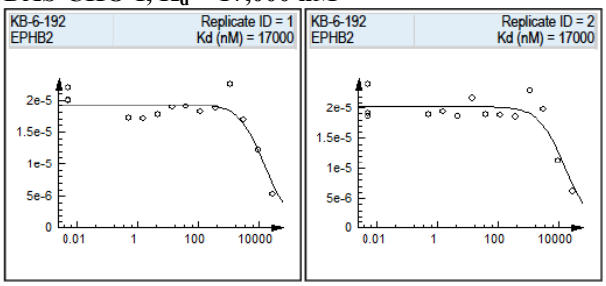

PDGFRA Values:

Dasatinib (Davis et al., 2011)**, K_d = 0.47 nM**

DAS-CHO-I, K_d = 3,700 nM

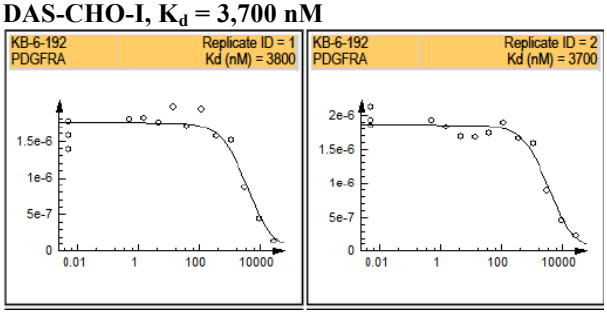

TXK Values:

Dasatinib (Davis et al., 2011)**, K_d = 2.1 nM**

DAS-CHO-I, K_d = 910 nM

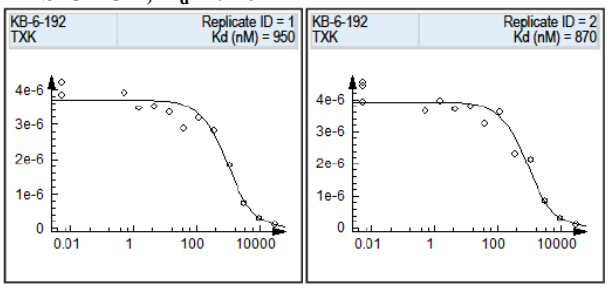

Data Summary for K_d values for additional inhibitors from KINOMEscan:

Gene Target	nilotinib, K_d	ponatinib, K_d	rebastinib, K_d	imatinib, K_d
Abl1-np	11	0.68	7.2	1.5
Abl1-P	15	0.66	11	24
T315I Abl1	740	1.0	9.2	20,000

All values are in nM

Representative binding curves for clinical inhibitors from KINOMEscan:

wt c-Abl Values (non-phosphorylated):

nilotinib, K_d = 11 nM

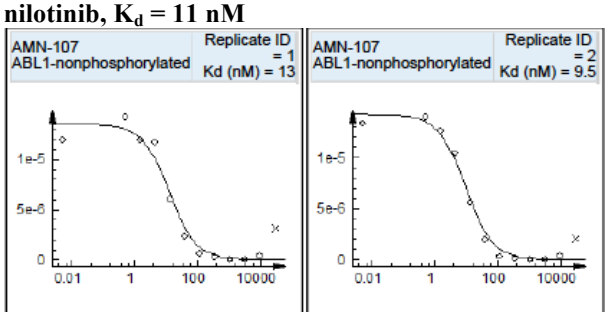

ponatinib, K_d = 0.68 nM

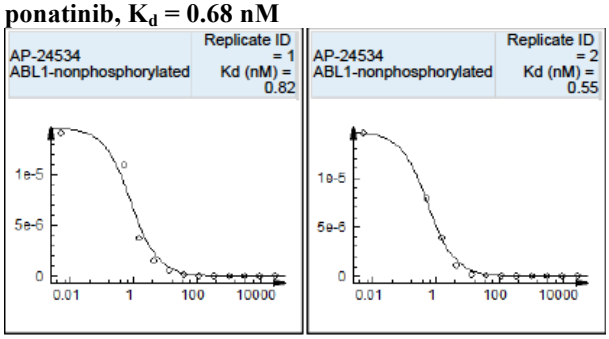

rebastinib, K_d = 7.2 nM

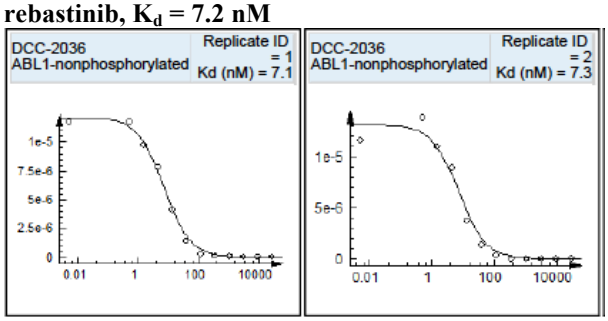

imatinib, K_d = 1.5 nM

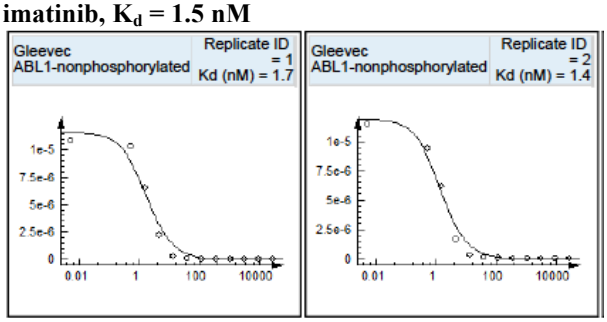

wt c-Abl Values (Phosphorylated):

nilotinib, K_d = 15 nM

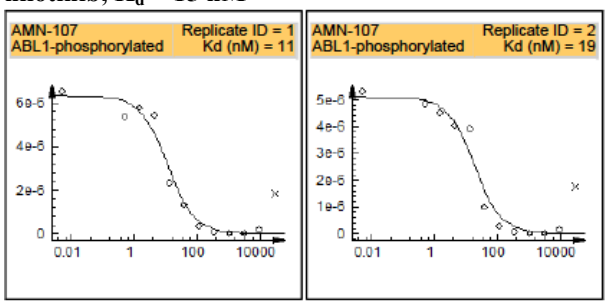

ponatinib, K_d = 0.66 nM

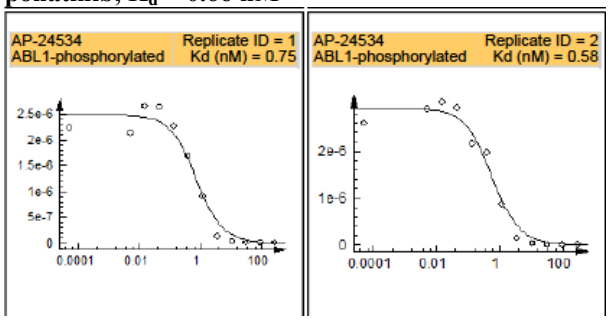

rebastinib, K_d = 11 nM

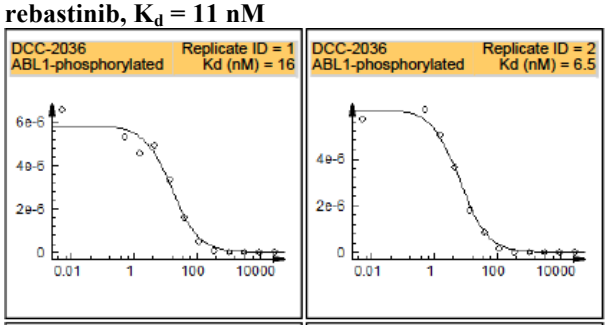

imatinib, K_d = 24 nM

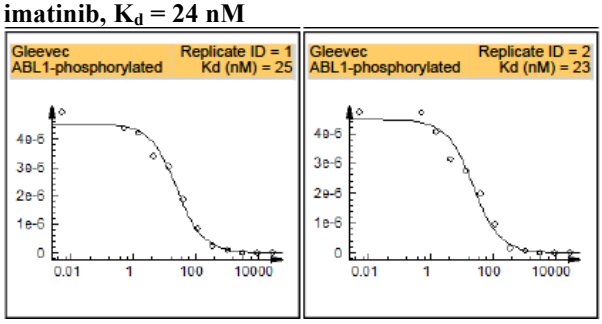

T315I c-Abl Values (non-phosphorylated):

nilotinib, K_d = 740 nM

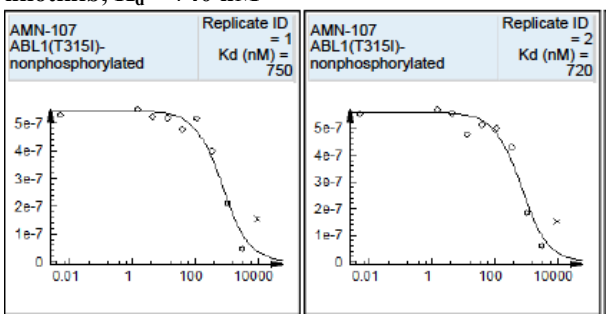

ponatinib, K_d = 1.0 nM

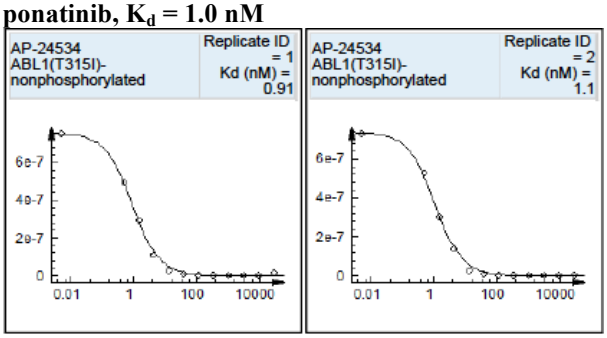

rebastinib, K_d = 9.2 nM

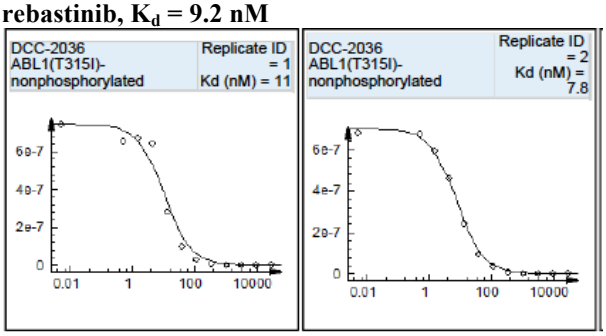

imatinib, K_d = 20,000 nM

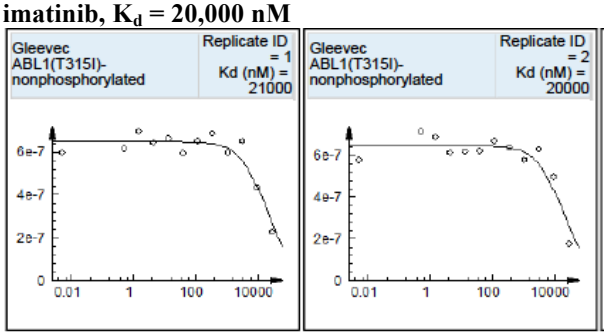

BODIPY Probe Data

wt c-Src Data

	K_d Src, nM	Half-life, min	k_{off}, sec^{-1}	k_{on}, sec^{-1}
DAS-BODIPY	0.50	15	7.88E-04	1.58E-03
DAS-DFGO-I-BODIPY	0.67	53	2.18E-04	3.26E-04
DAS-DFGO-II-BODIPY	2.8	65	1.79E-04	6.38E-05
DAS-CHO-II-BODIPY	4.6	13	8.61E-04	1.87E-04

wt c-Abl KD Data

	K_d Abl, nM	Half-life, min	k_{off}, sec^{-1}	k_{on}, sec^{-1}
DAS-BODIPY	0.15	20	5.66E-04	3.78E-03
DAS-DFGO-I-BODIPY	4.7	79	1.46E-04	3.11E-05
DAS-DFGO-II-BODIPY	0.75	75	1.54E-04	2.06E-04
DAS-CHO-II-BODIPY	0.58	29	3.93E-04	6.78E-04

P~c-Src KD Data

	K_d P~Src, nM	Half-life, min	k_{off}, sec^{-1}	k_{on}, sec^{-1}
DAS-BODIPY	0.70	23	5.15E-04	7.35E-04
DAS-DFGO-I-BODIPY	N.T.	N.T.	N.T.	N.T.
DAS-DFGO-II-BODIPY	3.0	78	1.48E-04	4.94E-05
DAS-CHO-II-BODIPY	N.T.	N.T.	N.T.	N.T.

wt c-Src 3D Data

	K_d 3D Src, nM	Half-life, min	k_{off}, sec^{-1}	k_{on}, sec^{-1}
DAS-BODIPY	0.16	33	3.48E-04	2.17E-03
DAS-DFGO-I-BODIPY	N.T.	N.T.	N.T.	N.T.
DAS-DFGO-II-BODIPY	N.T.	N.T.	N.T.	N.T.
DAS-CHO-II-BODIPY	0.84	45	2.55E-04	3.03E-04

T338I c-Src KD Data

	K_d T338I Src, nM	Half-life, min	k_{off}, sec^{-1}	k_{on}, sec^{-1}
DAS-BODIPY	> 4500	N/A	N/A	N/A
DAS-DFGO-I-BODIPY	N.T.	N.T.	N.T.	N.T.
DAS-DFGO-II-BODIPY	340	43	2.70E-04	7.94E-07
DAS-CHO-II-BODIPY	N.T.	N.T.	N.T.	N.T.

*N.T. = not tested; N/A = not available

Raw data for K_d determination with wt c-Src, wt c-Abl, P~Src KD, c-Src 3D and T338I Src KD:

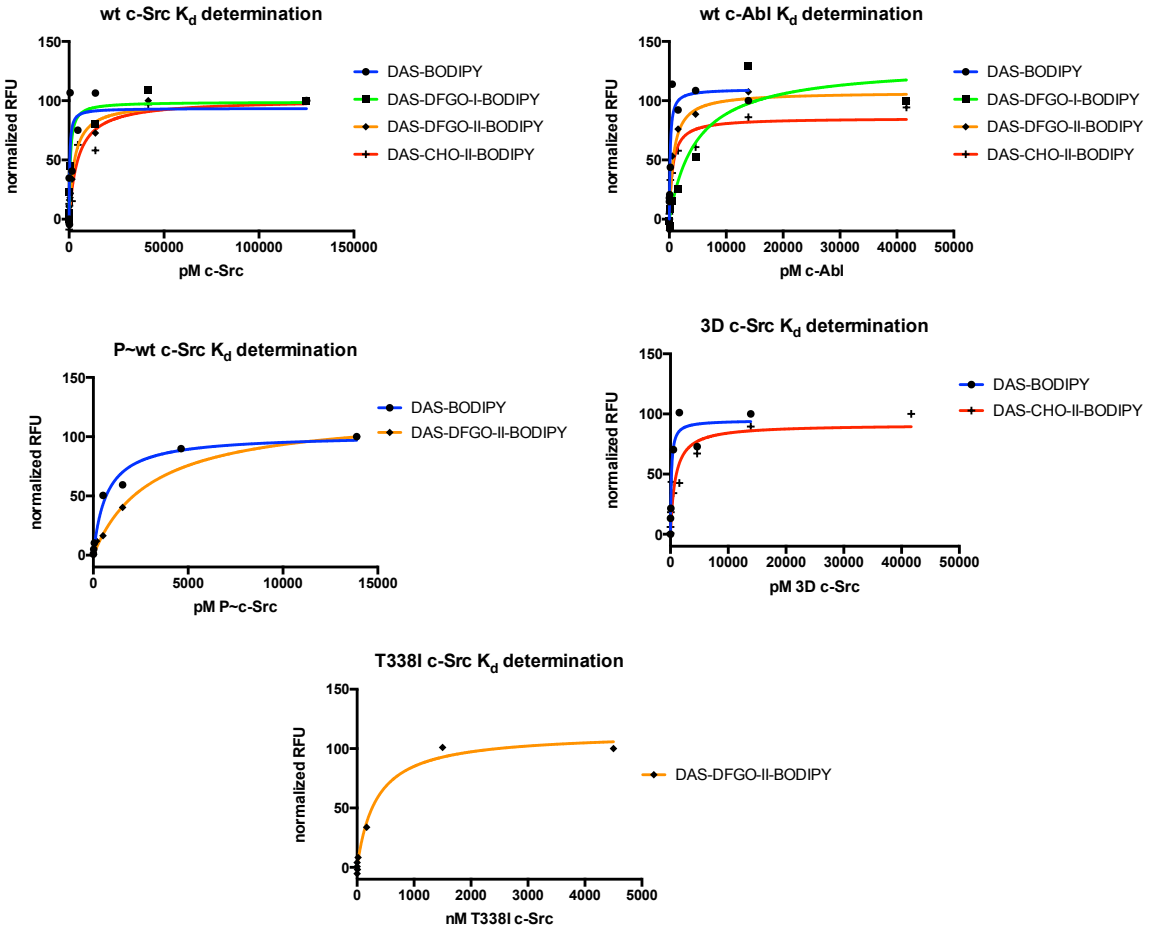

Raw data for k_{off} determination with wt c-Src, wt c-Abl, P~c-Src KD, c-Src 3D and T338I c-Src KD:

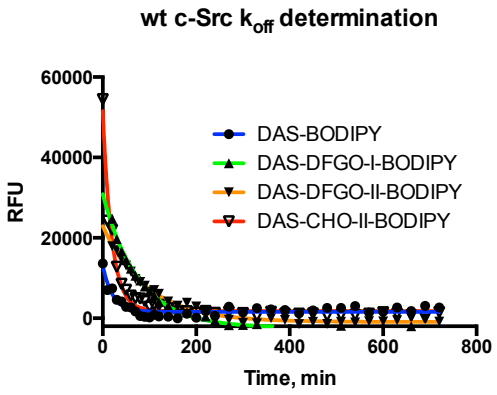

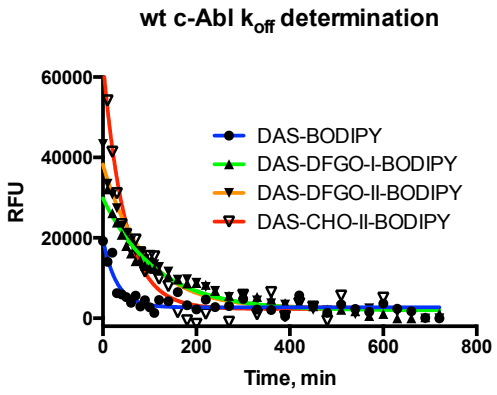

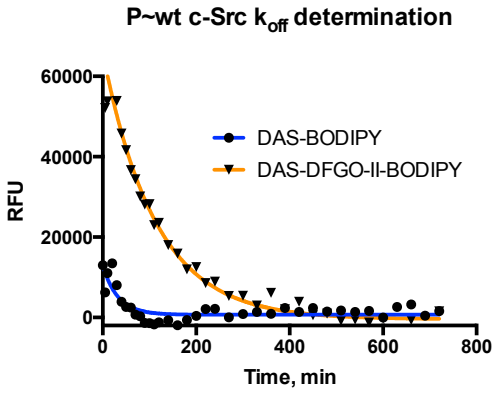

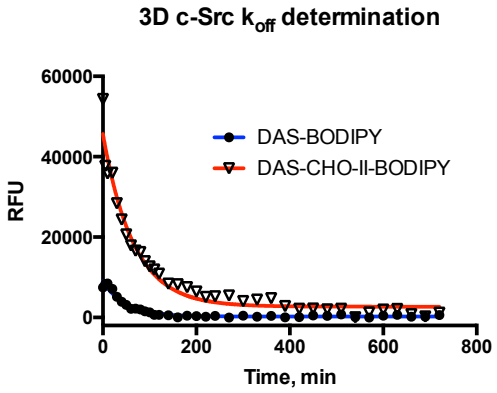

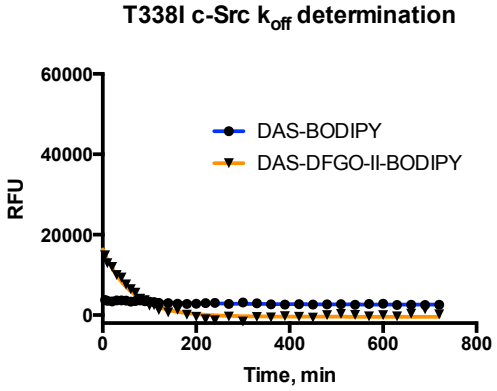

Kinome-wide Screening Data

Inhibitor selectivity profiles were obtained through Luceome Biotechnologies (Tuscon, AZ). Each inhibitor was screened at 0.5 µM against a panel of 124 wt kinases.

Kinome profiling data summary.

	S(50) Score	# of S(50) Targets	S(35) Score	# of S(35) Targets
dasatinib	0.31	38	0.21	26
DAS-DFGO-I	0.29	35	0.24	29
DAS-DFGO-II	0.25	30	0.2	24
DAS-CHO-I	0.08	10	0.05	6
DAS-CHO-II	0.17	21	0.16	19

S(50) scores depicted below:

dasatinib

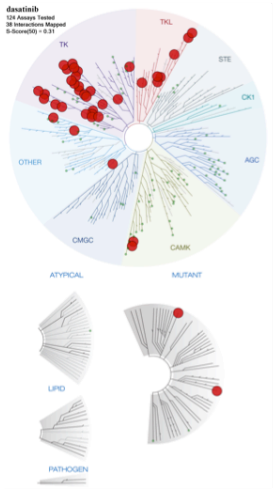

DAS-DFGO-I

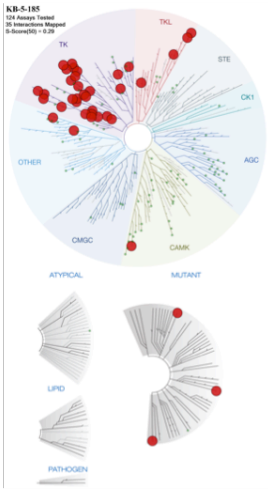

DAS-CHO-I

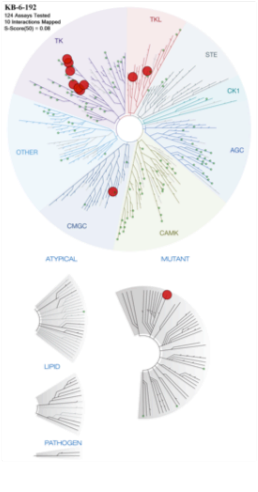

DAS-DFGO-II

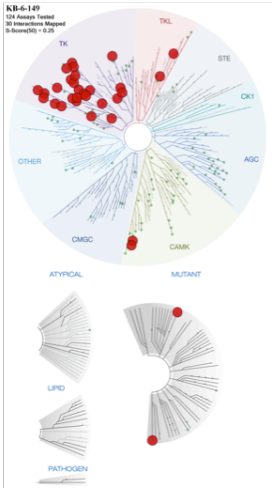

DAS-CHO-II

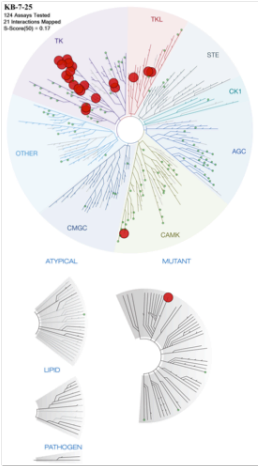

Tabulated Luceome selectivity profiling data:

		Percent of Control			
Kinase Target	**dasatinib**	**DAS-DFGO-I**	**DAS-DFGO-II**	**DAS-CHO-I**	**DAS-CHO-II**
ABL1-phosphorylated	1.9	4.2	10.9	45.7	8.1
ABL2	50.7	6.1	12.2	49.7	9
AKT1	95.1	97.5	100	96.2	100
AKT2	100	100	100	100	100
AKT3	73.3	92.2	100	100	100
AMPK-alpha1	93	100	100	100	100
AMPK-alpha2	67.8	70.6	100	100	100
AURKA	100	100	93.9	100	91.4
AURKB	100	100	100	84	100
AURKC	80.7	86.2	94.1	94.1	96
AXL	27.4	30.5	100	100	100
BIKE	100	97	100	100	100
BLK	0	0	6.2	30.6	6.6
BTK	35.5	73.9	26.4	50	15.5
CAMK1	100	100	100	100	100
CAMK1D	99.3	88.2	100	100	100
CAMK1G	100	100	97.2	100	93
CAMK2A	85.8	95.6	100	100	100
CAMK2B	68.4	92.6	100	100	100
CAMK2D	79.8	100	100	91.7	100
CAMKK1	75	78	100	100	100
CAMKK2	78.9	100	100	100	100
CHEK1	90.9	100	100	95	100
CLK1	100	100	100	93.1	100
CLK2	100	100	100	100	100
CSK	31.3	78.9	11.5	37.8	6.1
CSNK1D	100	100	100	100	100
DAPK1	100	100	97.4	98.7	100
DAPK2	100	100	100	100	100
DAPK3	100	100	100	100	100
DDR1	84.8	85.6	1.1	90.8	18.6
DDR2	51.8	49.2	9.1	76.8	28.9
DMPK	100	100	100	95.7	100
EPHA1	1.1	3.3	7.9	84.2	14
EPHA2	1.3	1.1	68.9	100	96.1
EPHA3	5.8	2.3	11.7	95.6	63.7
EPHA4	0	0	2.7	99.1	77.4
EPHB2	0	0	4.4	99.4	100
EPHB3	35.2	81.1	47.6	99.1	100
EPHB4	1.8	2.1	4	85.5	92.9

Kinase Target	dasatinib	DAS-DFGO-I	DAS-DFGO-II	DAS-CHO-I	DAS-CHO-II
FGFR1	57.2	62.2	56.7	89.7	100
FGFR2	100	67.9	30.1	100	100
FLT1	100	4.8	6.7	95.2	95.7
FLT3	36.8	41.5	91.5	89.7	95.1
FYN	3.8	0.7	53.7	65.4	21
GSK3A	100	67.7	100	84.3	100
HCK	16.6	4.2	10	56.7	12.7
IGF1R	75.7	64	94.5	100	100
IKK-epsilon	100	100	100	99.2	100
INSR	100	100	64.2	100	97.6
ITK	42.3	50	100	97.1	100
LIMK1	50	82.1	63.9	15.9	8.1
LYN	5.9	5.9	54.1	91.4	34.4
MARK1	100	100	100	100	100
MARK2	100	100	100	100	100
MARK3	100	100	100	92.3	100
MARK4	100	100	100	91.9	100
MELK	92	100	95.9	100	100
MET	100	100	97	100	100
MLK1	38.4	40.9	100	100	100
MLK3	18.3	22.6	96.6	96.4	100
MST2	83.3	61.5	97.6	99	100
MUSK	86.4	20.6	60.6	100	100
MYLK	75.4	94.8	100	95.6	100
MYLK2	100	97	100	100	98.8
p38-delta	100	100	100	96.4	100
PAK1	100	100	100	98.8	90.6
PDGFRA	21.3	31.9	79.1	98.9	74.9
PDGFRB	38.4	37.5	57.8	69.5	38.8
PDK1	100	100	100	98.3	100
PHKG1	95.7	99.5	98.2	100	63.9
PIM1	96.1	100	97.5	98.8	99
PIM2	97.4	89.6	100	92.1	100
PKAC-alpha	95.1	96.3	97.7	98.8	98.2
PKMYT1	46.9	59.9	100	94.2	100
PKN3	92	83.8	67	99	88.4
PLK4	12.4	0	100	100	100
PRKACB	78.1	96.7	100	100	100
PRKCD	100	100	92.3	100	100
PRKCE	100	100	100	100	100
PRKCG	100	100	100	100	100
PRKCH	100	100	100	100	100

Kinase Target	dasatinib	DAS-DFGO-I	DAS-DFGO-II	DAS-CHO-I	DAS-CHO-II
PRKCQ	92.4	100	100	100	96.6
PRKD2	100	100	97.9	100	100
PRKD3	100	100	100	100	100
PRKG1	100	100	97.4	100	94.8
PRKX	72.8	89.3	100	95.9	100
PTK2	100	100	100	100	100
PTK2B	100	95.2	100	100	100
PTK6	33.8	0.1	27	25.2	6.2
QSK	57	95.1	95	93.8	91.1
RET	92.2	1	11.9	95.3	100
RIPK2	0.1	37.2	51.8	24	2.7
RPS6KA4(Kin.Dom.1-N-terminal)	100	87.2	100	97.4	96.5
RPS6KA5(Kin.Dom.1-N-terminal)	88.3	96.7	100	93.3	100
RSK1(Kin.Dom.1-N-terminal)	92.5	100	100	84.4	100
RSK2(Kin.Dom.1-N-terminal)	100	100	99.1	94.8	100
RSK3(Kin.Dom.1-N-terminal)	100	94.6	100	100	100
RSK4(Kin.Dom.1-N-terminal)	100	100	100	100	100
SGK2	74.3	91.3	96.4	98.8	100
SGK3	100	100	100	99.4	100
SLK	100	96.2	95.3	95.6	98.8
SNARK	81.3	89.8	100	97.9	100
SNF1LK	12.9	28.8	10	54.7	23.9
SNF1LK2	41.3	74	47.9	98.4	84
SRC	8.8	10.6	16	34.2	9.2
STK16	79.4	75	100	100	100
STK33	100	100	100	97.7	100
SYK	73.3	89.9	100	100	100
TBK1	39.5	35.7	100	100	97
TEC	41.6	86	28.8	88.8	22.2
TESK1	49.1	94.1	78.3	89.1	67.8
TESK2	45.1	93.7	50.4	80.1	23.4
TIE1	100	27.4	64.9	92.7	100
TIE2	100	33.3	15.2	81.6	100
TNK2	24.8	91.9	39.6	93.2	61.3
TNNI3K	25.9	12.7	20.1	100	77.6
TRKB	100	70.6	54.8	100	100
TRKC	100	77.8	48.3	100	100
TXK	16.2	32.5	18	93.9	41.5
VEGFR2	100	15.2	49.3	97.6	100
YANK2	100	100	88.2	90.3	100
YES	8	0	12.7	26.2	6.3
YSK1	100	100	98.6	100	100

Cellular Characterization

Analytical data for GI_{50} determination in WT Abl Ba/F3 cells. Each GI_{50} value was determined using at least three independent experiments. The curves with error bars are shown below. For curves that did not reach full inhibition, the bottom was set to -10.

dasatinib
GI_{50} = 6.1 nM

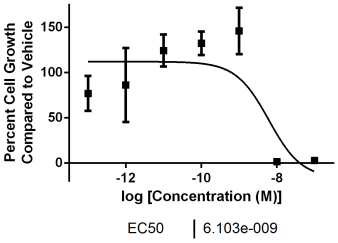

DAS-DFGO-I
GI_{50} = 54 nM

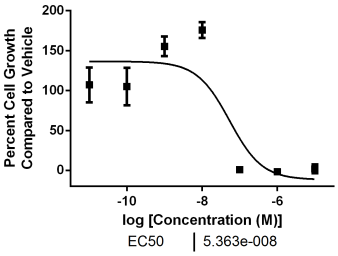

DAS-DFGO-II
GI_{50} = 59 nM

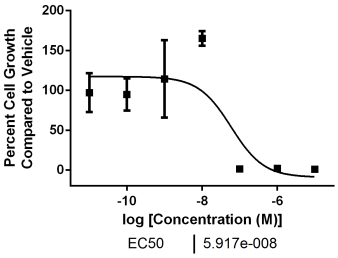

DAS-CHO-I
GI_{50} = 1.1 μM

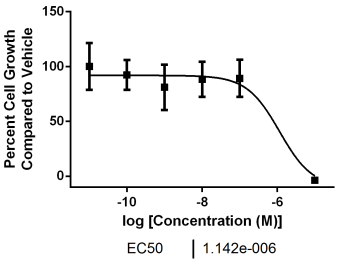

DAS-CHO-II
GI_{50} = 540 nM

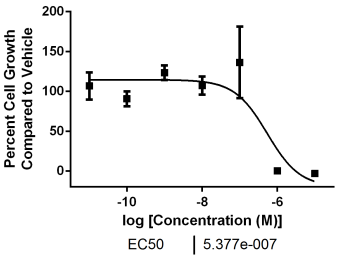

Analytical data for GI_{50} determination in T315I Abl Ba/F3 cells. Each GI_{50} value was determined using at least three independent experiments. The curves with error bars are shown below. For curves that did not reach full inhibition, the bottom was set to -10.

dasatinib
GI_{50} = 4.4 μM

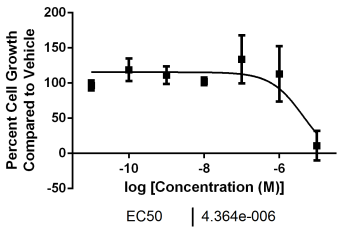

DAS-DFGO-I
GI_{50} = 4.5 μM

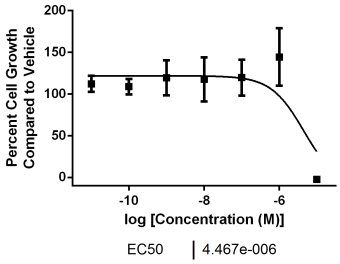

DAS-DFGO-II
GI_{50} = 480 nM

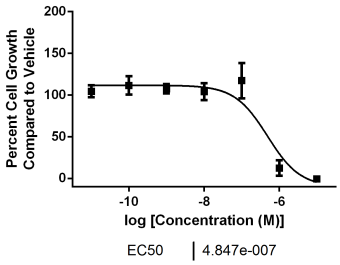

DAS-CHO-I
GI_{50} = 4.2 μM

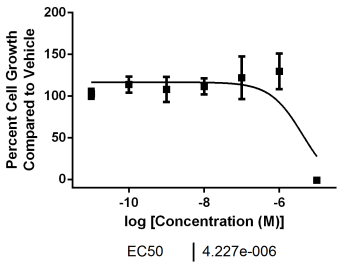

DAS-CHO-II
GI_{50} = 3.1 μM

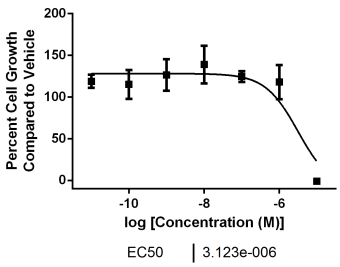

Analytical data for GI_{50} determination in Parental Ba/F3 cells. Each GI_{50} value was determined using at least three independent experiments. The curves with error bars are shown below. For curves that did not reach full inhibition, the bottom was set to -10.

dasatinib
GI_{50} = Does Not Inhibit

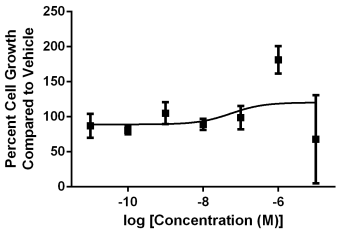

DAS-DFGO-I
GI_{50} = 5.2 μM

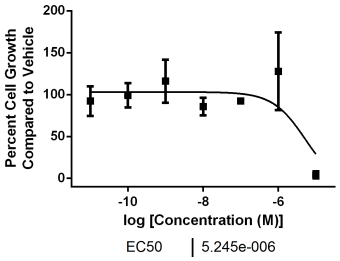

DAS-DFGO-II
GI_{50} = 350 nM

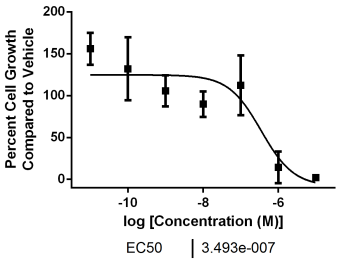

DAS-CHO-I
GI_{50} = 2.5 μM

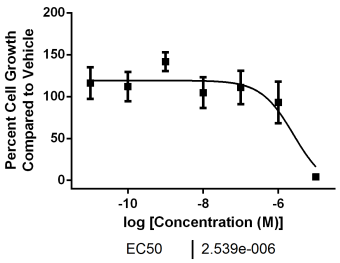

DAS-CHO-II
GI_{50} = 3.2 μM

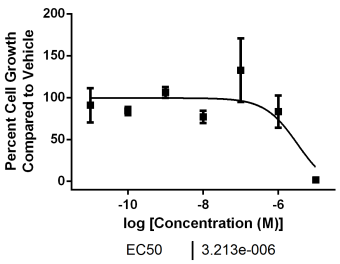

APPENDIX D

Supplemental Information and Analytical Data for Chapter V

Figure D.1. PP2 binding to c-Src kinase.

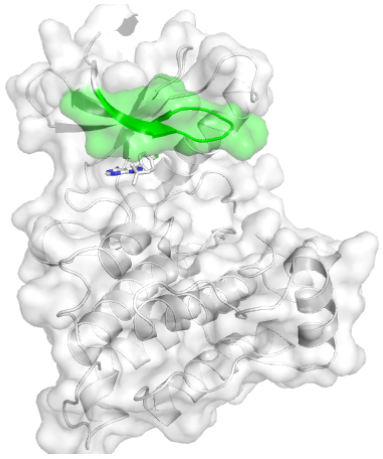

PP2 (sticks) bound to c-Src (surface/cartoon) is displayed (PDB: 3GEQ). The P-loop is shown in green.

Figure D.2. Kinase P-loop sequence alignment.

```
SRC:    [272] KLGQG<b>C</b>FGEV
YES:    [280] KLGQG<b>C</b>FGEV
FYN:    [278] RLGNG<b>Q</b>FGEV
FGR:    [268] RLGTG<b>C</b>FGDV
LCK:    [250] RLGAG<b>Q</b>FGEV
HCK:    [267] KLGAG<b>Q</b>FGEV
BLK:    [246] KLGSG<b>Q</b>FGEV
LYN:    [252] RLGAG<b>Q</b>FGEV
FRK:    [239] RLGSG<b>Q</b>FGEV
ABL:    [247] KLGGG<b>Q</b>YGEV
```

Sequence alignment of kinase P-loops for Src family kinases and c-Abl. Cys277 (and SFK equivalent) position in c-Src is bolded.

Figure D.3. Inhibitor–to–P-loop distance for c-Abl.

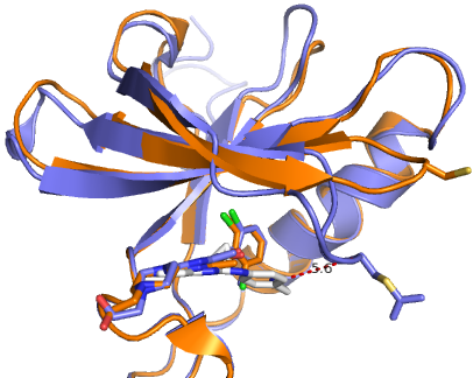

An N-lobe overlay of two c-Src structures (PDBs: 3F6X, white ligand; 3QLG, dasatinib, orange) with the N-lobe of a c-Abl structure bound to dasatinib (PDB: 2GQG). The C3-phenyl to alpha carbon distance of 5.6 Å was determined.

Figure D.4. Inhibitor–to–P-loop distance for Hck.

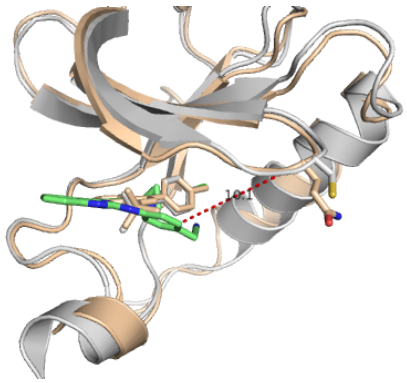

An N-lobe overlay of two c-Src structures (PDBs: 3F6X, white ligand; 3GEQ, PP2, gray) with the N-lobe of a Hck structure bound to PP1 (PDB: 1QCF). The C3-phenyl to alpha carbon distance of 10.1 Å was determined.

Figure D.5. Sequence alignment of c-Src and c-Yes catalytic domains.

```
                260              277         289              306    313 317
c-Yes (green)   WEIPRESLRLEVKLGQGCFGEVWMGTWNGTTKVAIKTLKPGTMMPEAFLQEAQIMKKLRHDKLVPLYAVVSEEP
c-Src (red)     WEIPRESLRLEVKLGQGCFGEVWMGTWNGTTRVAIKTLKPGTMSPEAFLQEAQVMKKLRHEKLVQLYAVVSEEP

    338                 360              377          393            404              420
IYIVTEFMSKGSLLDFLKEGDGKYLKLPQLVDMAAQIADGMAYIERMNYIHRDLRAANILVGENLVCKIADFGLARLIEDNEYTARQGA
IYIVTEYMSKGSLLDFLKGEMGKYLRLPQLVDMAAQIASGMAYVERMNYVHRDLRAANILVGENLVCKVADFGLARLIEDNEYTARQGA

                    443                                                 489        500
KFPIKWTAPEAALYGRFTIKSDVWSFGILQTELVTKGRVPYPGMVNREVLEQVERGYRMPCPQGCPESLHELMNLCWKKDPDERPTFEY
KFPIKWTAPEAALYGRFTIKSDVWSFGILLTELTTKGRVPYPGMVNREVLDQVERGYRMPCPPECPESLHDLMCQCWRKDPEERPTFEY

        520
IQSFLEDYFTATEPQYQPGENL
LQAFLEDYFTSTEPQYQPGENL
```

The 29 different amino acids between c-Yes (top, green) and c-Src (bottom, red) are highlighted.

Figure D.6. DSF data for wt c-Src and c-Src mutants.

c-Src Mutant	T_m, °C
wild type	52.02 ± 0.15
E280G	51.10 ± 0.21
V313I	52.05 ± 0.22
Q324P	51.12 ± 0.10
V377I	52.81 ± 0.06
V383I	51.36 ± 0.07
V402I	52.19 ± 0.08

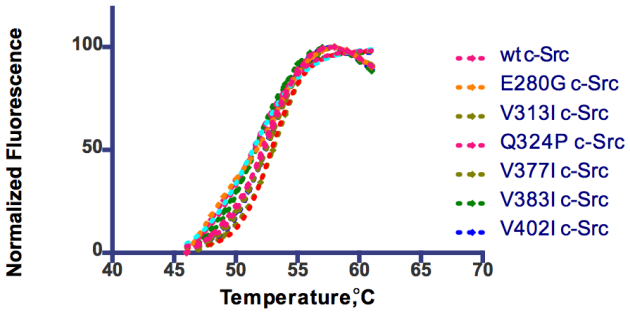

Spectral Data for Compounds 5.1–5.10

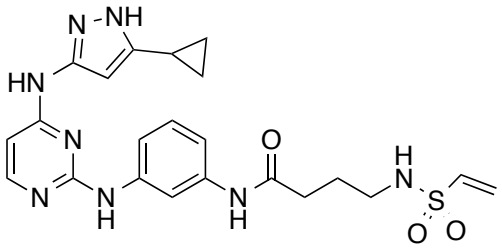

5.1

5.1 ^{1}H:

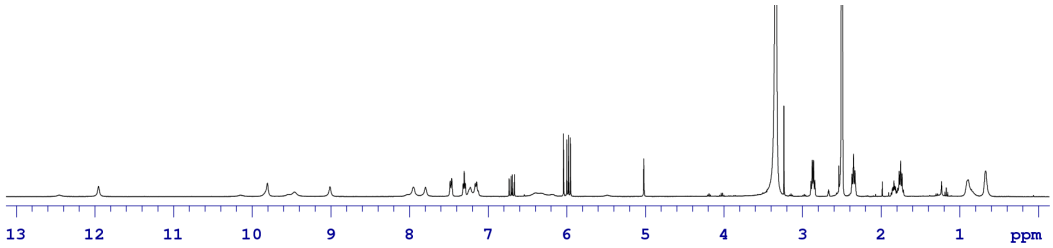

5.1 ^{13}C:

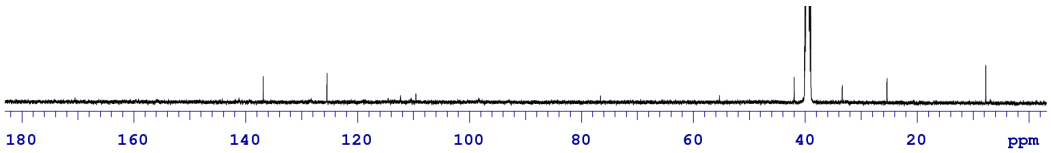

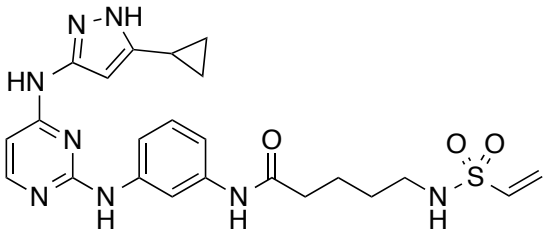

5.2

5.2 ^{1}H:

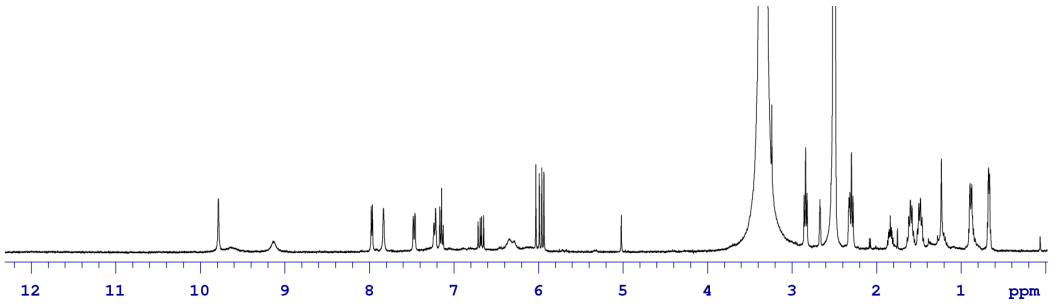

5.2 ^{13}C:

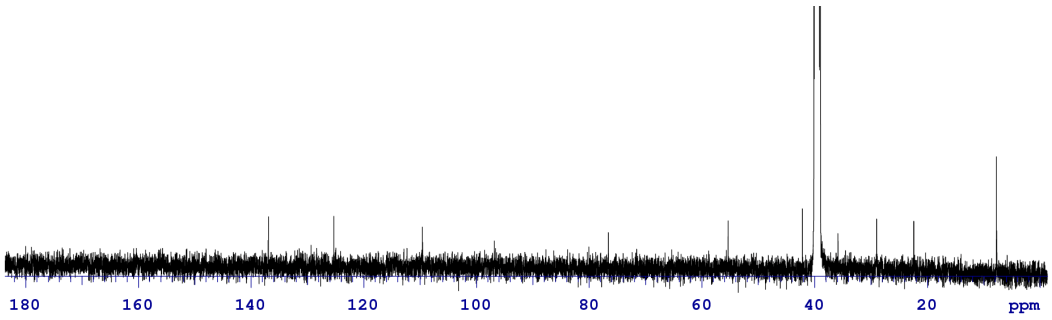

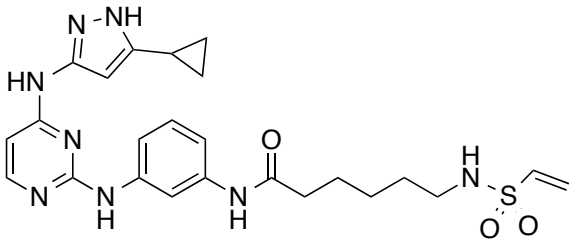

5.3

5.3 ^{1}H:

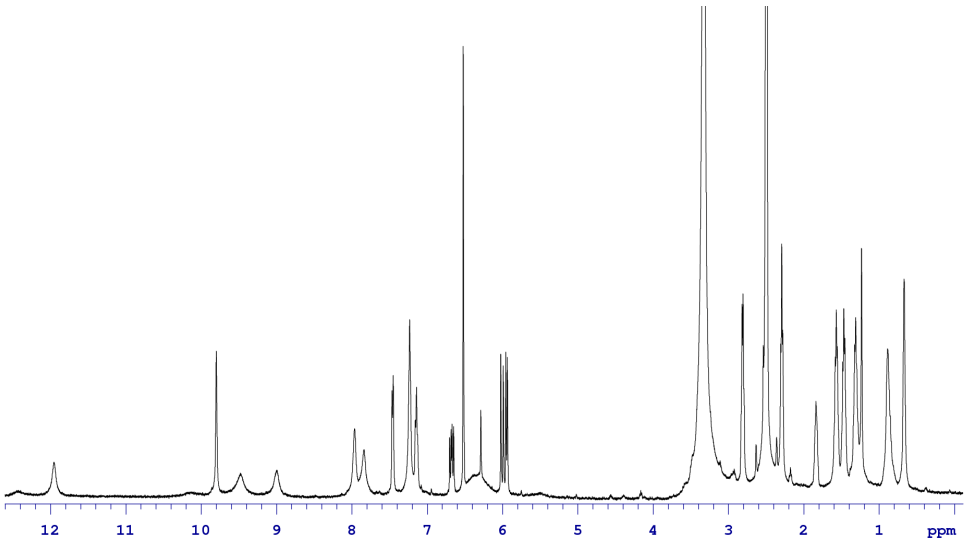

5.3 ^{13}C:

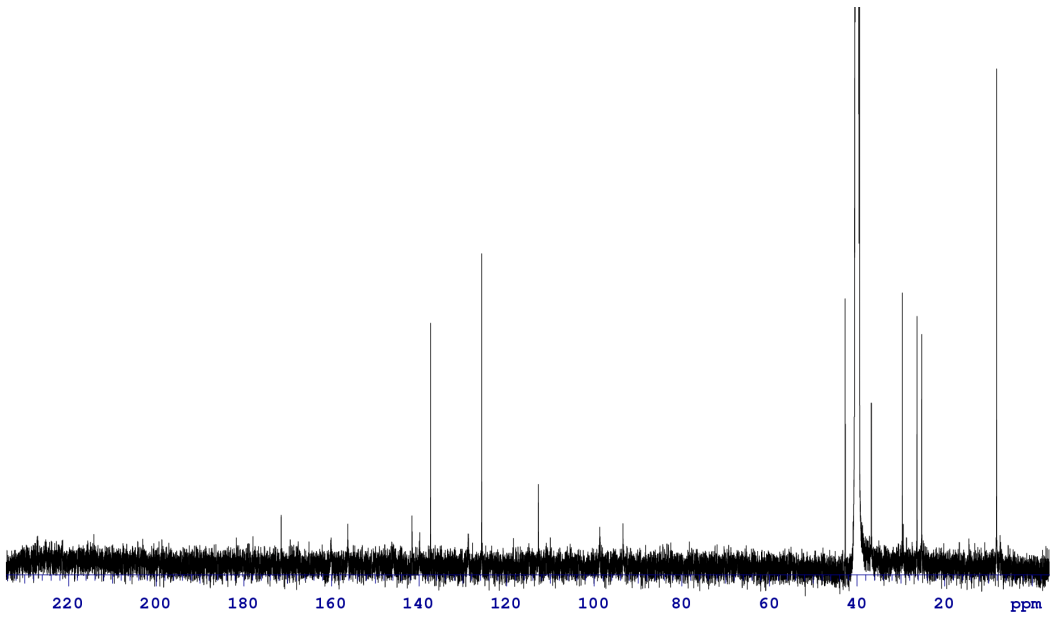

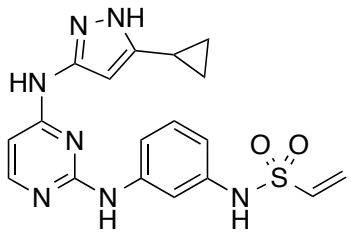

5.4

5.4 ^{1}H:

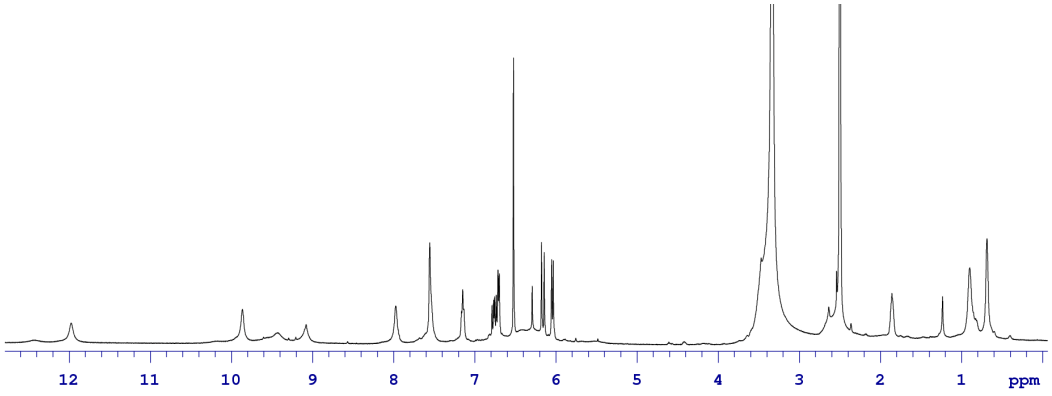

5.4 ^{13}C:

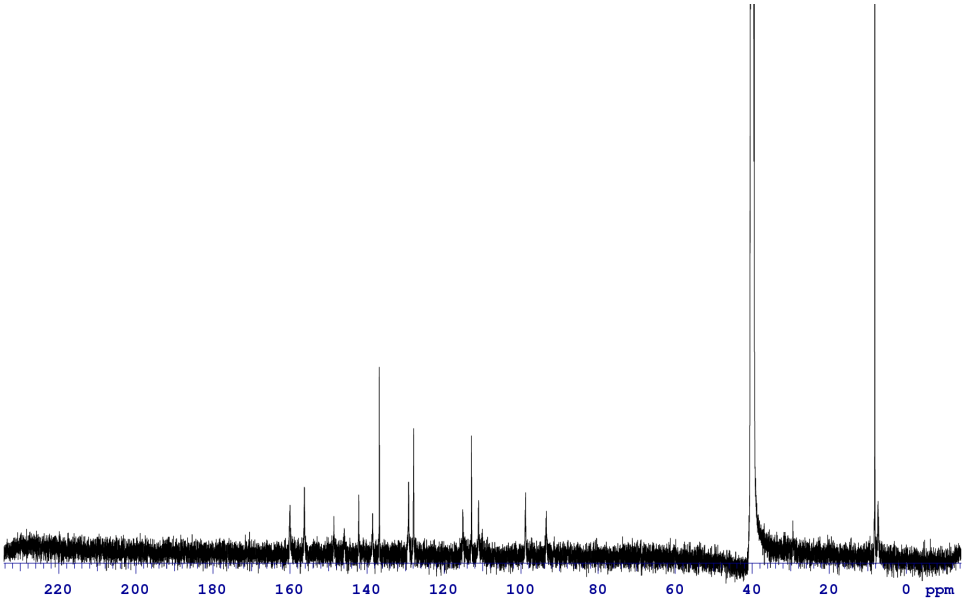

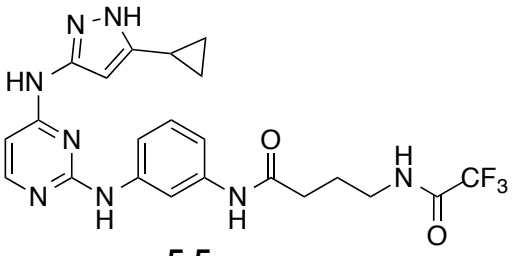

5.5

5.5 ^{1}H:

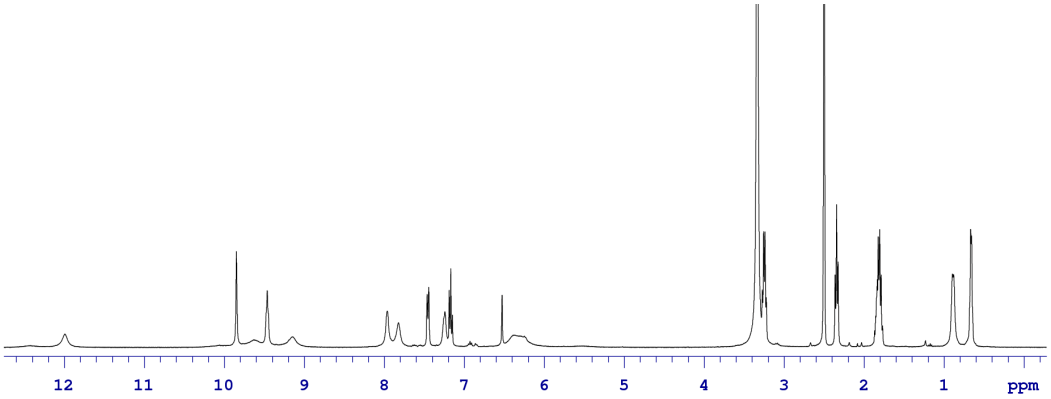

5.5 ^{19}F:

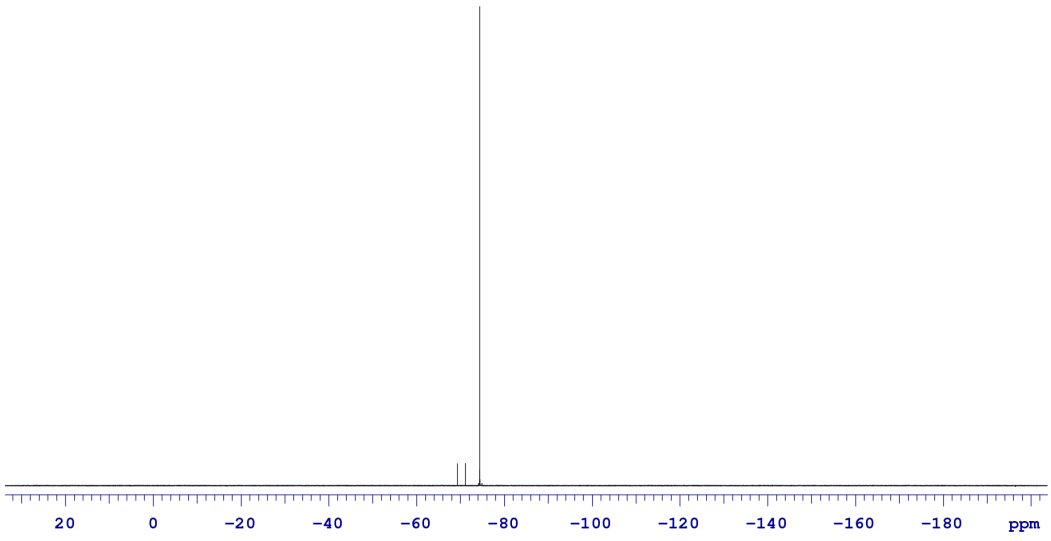

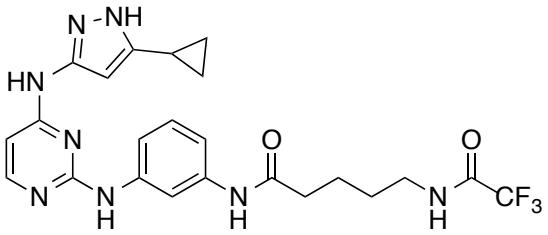

5.6

5.6 ^{1}H:

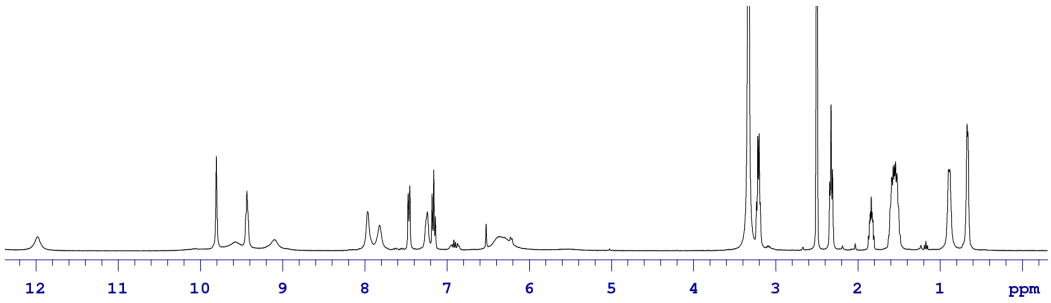

5.6 ^{19}F:

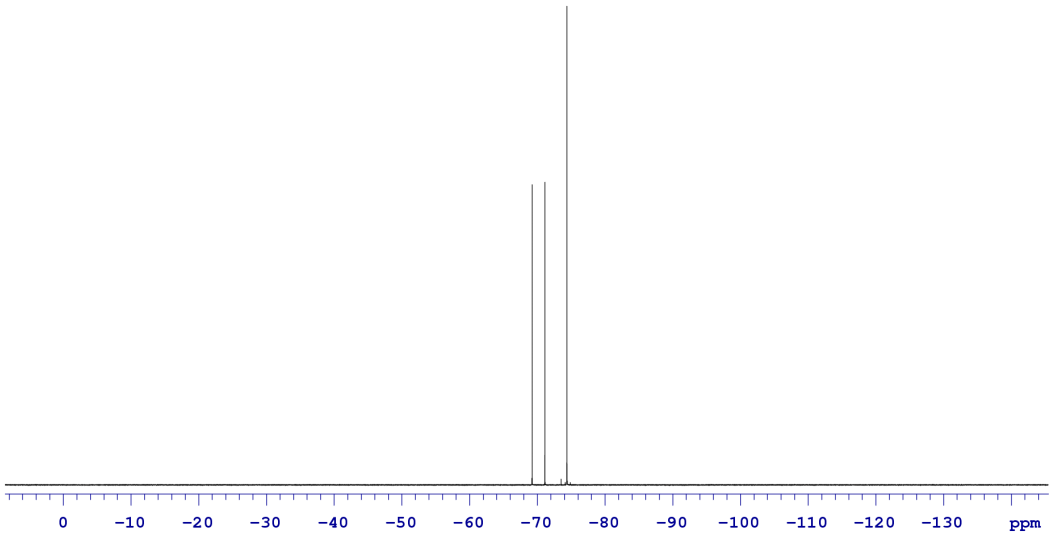

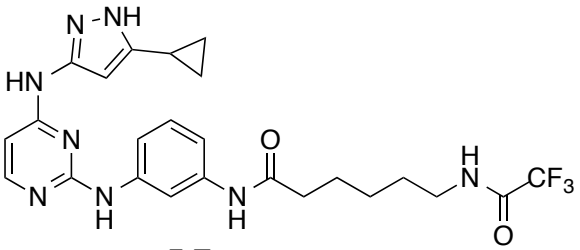

5.7

5.7 ^{1}H:

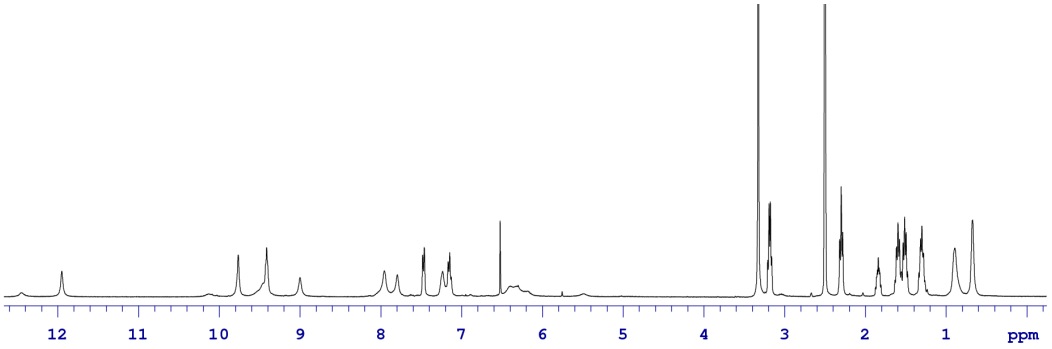

5.7 ^{19}F:

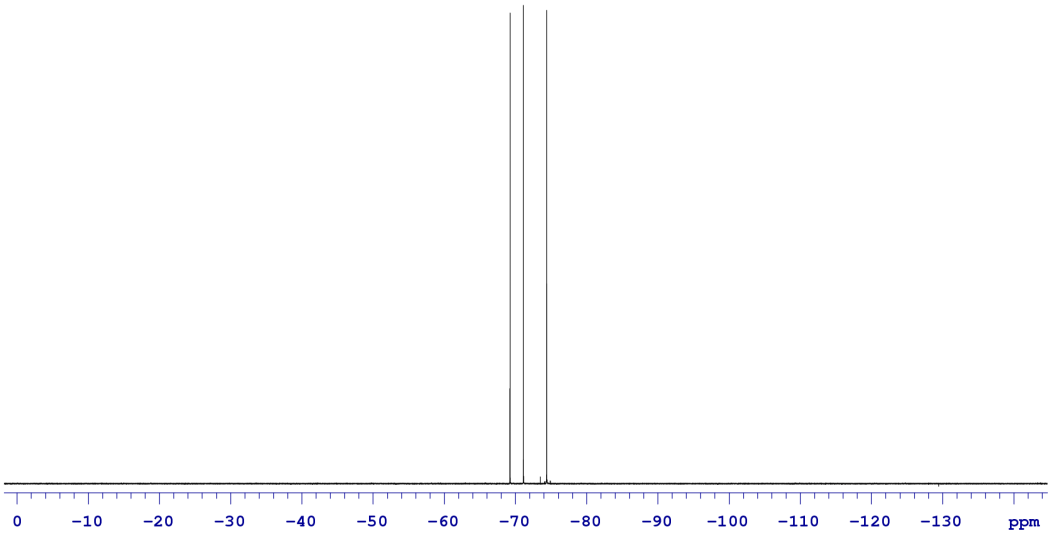

Inhibitor K_i Values

Representative Binding Curves:

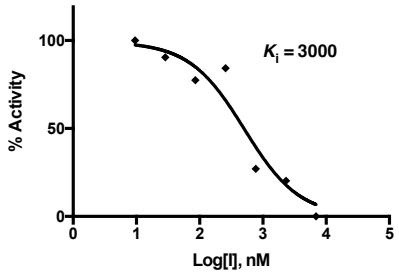

KB-SRC-4, wt Hck K_i = 3000 ± 540 nM

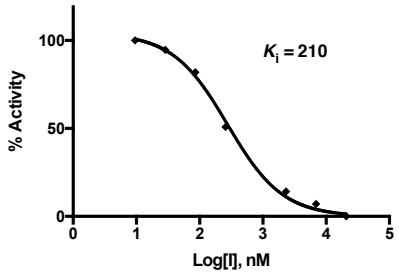

KB-SRC-4, wt c-Yes K_i = 250 ± 39 nM

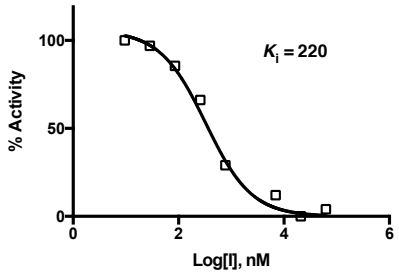

KB-SRC-4, V377I c-Src K_i = 200 ± 15 nM

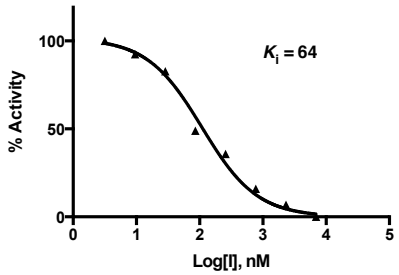

PP2, V377I c-Src K_i = 77 ± 11 nM

Data for Labeling Rate Determination

Data summary for $t_{i1/2}$ data:

Compound	c-Src	c-Yes	Q272C Hck	Q252C c-Abl
5.4	Did not label	Did not label	Did not label	3.8 ± 0.6
2.4	13.6 ± 3.3	1.5 ± 0.2	6.4 ± 0.3	4.6 ± 0.2
2.7	9.0 ± 0.8	3.4 ± 0.6	6.8 ± 0.4	4.9 ± 0.1
5.1	12.3 ± 0.4	2.1 ± 0.1	3.8 ± 0.4	4.9 ± 0.1
5.2	6.4 ± 0.1	6.0 ± 0.3	5.1 ± 0.6	7.2 ± 0.4
5.3	9.8 ± 0.1	2.6 ± 0.5	5.6 ± 0.4	5.8 ± 0.2

c-Src Kinase Mutant	$t_{1/2}$, min
wt c-Src	9.0 ± 0.8
E280G	3.7 ± 0.2
V313I	8.9 ± 0.8
Q324P	7.5 ± 0.7
V377I	5.2 ± 0.2
V383I	7.6 ± 0.02
V402I	7.2 ± 0.2

A. IC_{50} Value Time Courses with wt c-Src Enzyme:

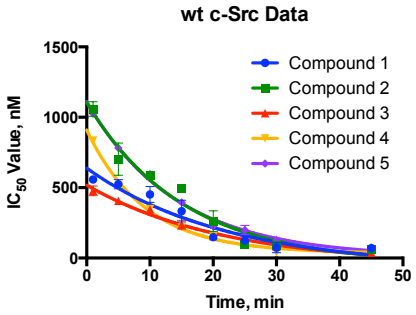

	Compound **2.4 (1)**		Compound **2.7 (2)**		Compound **5.1 (3)**		Compound **5.2 (4)**		Compound **5.3 (5)**	
Time, min	Run 1	Run 2	Run 1	Run 2	Run 1	Run 2	Run 1	Run 2	Run 1	Run 2
1	560	550	1400	1020	500	450	840	830	1040	1000
5	550	500	780	620	420	370	520	510	800	770
10	410	330	600	580	330	250	350	340	600	590
15	390	280	490	410	220	220	220	210	400	390
20	150	150	310	210	160	150	150	150	230	220
25	130	120	110	81	130	130	100	87	220	180
30	100	49	110	72	100	64	55	47	150	110
45	72	69	71	55	37	38	53	45	74	74

IC_{50} Values, nM

B. IC_{50} Value Time Courses with wt c-Yes Enzyme:

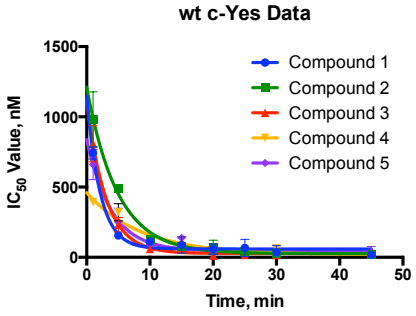

	Compound **2.4 (1)**		Compound **2.7 (2)**		Compound **5.1 (3)**		Compound **5.2 (4)**		Compound **5.3 (5)**	
Time, min	Run 1	Run 2	Run 1	Run 2	Run 1	Run 2	Run 1	Run 2	Run 1	Run 2
1	770	710	1120	850	900	720	410	380	740	590
5	170	140	500	490	270	200	360	280	320	180
10	120	110	140	110	80	39	1300	130	110	77
15	130	48	90	65	130	48	86	73	160	120
20	85	33	110	38	14	11	71	28	41	30
25	110	24	41	35	21	12	55	31	30	6
30	70	3	36	24	25	7	68	61	46	14
45	22	14	28	18	26	19	21	11	66	13

IC_{50} Values, nM

C. IC_{50} Value Time Courses with Q252C c-Abl Enzyme:

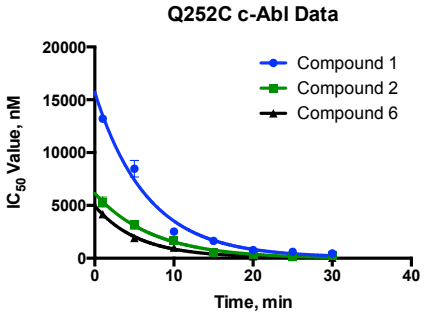

	Compound **5.4 (0)**		Compound **2.4 (1)**		Compound **2.7 (2)**		Compound **5.1 (3)**		Compound **5.2 (4)**		Compound **5.3 (5)**	
Time, min	Run 1	Run 2	Run 1	Run 2	Run 1	Run 2	Run 1	Run 2	Run 1	Run 2	Run 1	Run 2
1	4300	4100	14000	13000	5700	5000	4400	4200	9200	8200	8100	7800
5	2100	1800	9000	7900	3200	2900	3000	2900	7300	5800	5200	5000
10	1200	810	2500	2500	1900	1400	980	870	4000	3600	3200	3000
15	440	360	180	1500	610	540	490	480	2000	1900	1900	1700
20	250	140	890	660	450	290	250	220	1600	1200	1200	1100
25	130	120	650	580	140	110	210	190	1200	1100	1200	890
30	60	60	480	440	250	190	160	160	720	680	790	510
45	60	60	310	260	190	180	100	78	420	360	390	330

IC_{50} Values, nM

D. IC_{50} Value Time Courses with Q272C Hck Enzyme:

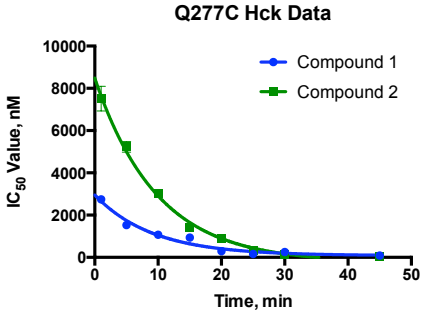

	Compound **2.4 (1)**		Compound **2.7 (2)**		Compound **5.1 (3)**		Compound **5.2 (4)**		Compound **5.3 (5)**	
Time, min	Run 1	Run 2	Run 1	Run 2	Run 1	Run 2	Run 1	Run 2	Run 1	Run 2
1	2900	2600	7900	7100	4300	4300	4800	4100	4600	4400
5	1600	1500	5400	5100	2300	1900	2700	2700	3800	3200
10	1100	1000	3100	3000	870	810	1200	1200	1400	1200
15	960	920	1500	1300	460	380	990	930	400	300
20	310	270	940	870	170	160	360	340	300	200
25	180	140	350	260	140	130	260	210	180	170
30	300	210	120	120	100	95	210	180	130	110
45	96	78	46	35	90	59	150	100	99	88

IC_{50} Values, nM

E. IC_{50} Value Time Courses with E280G c-Src Enzyme:

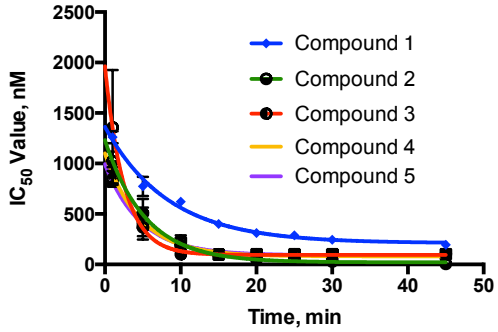

	Compound **2.4 (1)**		Compound **2.7 (2)**		Compound **5.1 (3)**		Compound **5.2 (4)**		Compound **5.3 (4)**	
Time, min	Run 1	Run 2	Run 1	Run 2	Run 1	Run 2	Run 1	Run 2	Run 1	Run 2
1	1300	1219	1100	950	1800	960	940	830	850	790
5	840	707	550	460	450	280	610	410	320	490
10	630	618	220	150	100	100	102	92	270	170
15	430	370	99	95	100	100	100	100	100	95
20	320	302	58	34	100	100	100	100	100	100
25	291	286	58	46	100	100	100	100	100	100
30	265	227	39	19	100	100	100	100	100	100
45	196	195	9	2	100	100	100	100	100	100

IC_{50} Values, nM

F. IC_{50} Value Time Courses with wt, V313I, Q324P, V377I, V383I, V402I c-Src Enzyme for Compound 2.7:

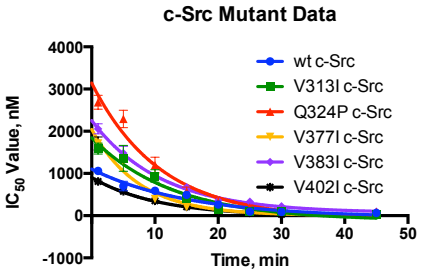

	wt c-Src		V313I		Q324P		V377I		V383I		V402I	
Time, min	Run 1	Run 2	Run 1	Run 2	Run 1	Run 2	Run 1	Run 2	Run 1	Run 2	Run 1	Run 2
1	1100	1020	1700	1500	2800	2600	1800	1600	2100	2000	810	810
5	780	620	1600	1100	2400	2200	1300	1200	1600	1400	590	560
10	600	580	1050	840	1300	1100	420	370	960	870	360	330
15	500	490	430	380	650	490	210	190	690	660	220	210
20	310	210	190	120	390	250	150	120	360	360	100	94
25	110	81	120	100	200	190	120	82	330	330	87	48
30	110	72	99	78	130	120	110	92	230	220	39	25
45	71	55	47	27	91	91	22	12	120	74	28	26

IC_{50} Values, nM

Data for ATP K_m Determination

ATP K_m curve with Q272C Hck:

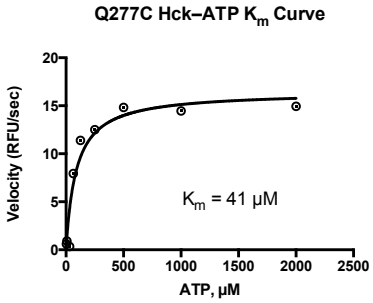

K_m = 47 ± 7 µM
V_{max}= 15 ± 2 (RFU/s)

ATP K_m curve with V313I c-Src:

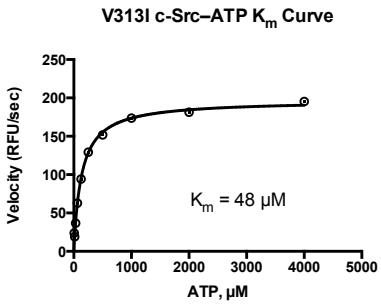

K_m = 49 ± 4 µM
V_{max}= 179 ± 18 (RFU/s)

ATP K_m curve with Q324P c-Src:

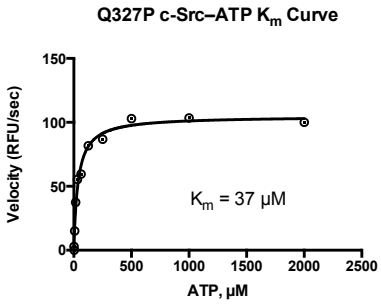

K_m = 45 ± 7 µM
V_{max}= 119 ± 6 (RFU/s)

ATP K_m curve with V377I c-Src:

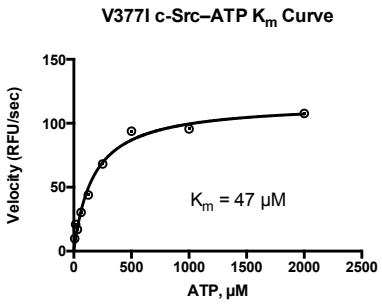

K_m = 45 ± 2 µM
V_{max}= 97 ± 9 (RFU/s)

ATP K_m curve with V383I c-Src:

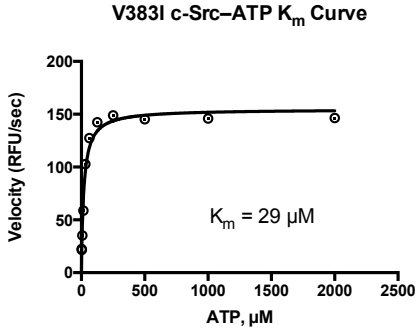

K_m = 27 ± 3 µM
V_{max}= 147 ± 6 (RFU/s)

ATP K_m curve with V402I c-Src:

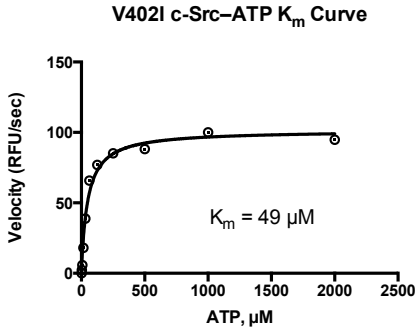

K_m = 45 ± 4 µM
V_{max}= 140 ± 4 (RFU/s)